

Investigations of DNA and anthracene as agents for drug release

Charlotte Meri Amber Farrow

A thesis submitted to the

University of Birmingham

for the degree of

Doctor Of Philosophy

School of Chemistry

College of Engineering and Physical Sciences

University of Birmingham

October 2021

UNIVERSITY OF
BIRMINGHAM

University of Birmingham Research Archive

e-theses repository

This unpublished thesis/dissertation is copyright of the author and/or third parties. The intellectual property rights of the author or third parties in respect of this work are as defined by The Copyright Designs and Patents Act 1988 or as modified by any successor legislation.

Any use made of information contained in this thesis/dissertation must be in accordance with that legislation and must be properly acknowledged. Further distribution or reproduction in any format is prohibited without the permission of the copyright holder.

Abstract

Targeted drug release has been a strong focus in the pharmaceutical industry in recent decades in an attempt to minimise the often severe side effects observed in therapeutics. Many methods of targeted drug release look at incorporating the drug moiety into nanoparticles, but other techniques can involve an organic drug donor with an attached targeting vector. Aptamers, single stranded oligonucleotides which can fold into complex structures capable of binding to non-DNA analytes with high selectivity and specificity, have often been highlighted as possible vectors for drug delivery. This thesis aims to contribute to the field of therapeutic delivery by investigations into both organic drug donor molecules and aptamer-derived directing capabilities.

The first approach of this project primarily involved the synthesis, characterisation, and study of a range of anthracene-derived nitroxyl (HNO) donors for potential therapeutics. A number of 9- and 9,10-substituted anthracene diols were designed as dienes for a Diels-Alder cycloaddition to create an HNO donating molecule capable of photo-initiated release. Further investigations into the stability of cycloadducts formed, and the conjugation of such moieties to a range of targeting vectors were attempted. Following this HNO donating theme, an anthracene-derived Piloty's acid analogue was also prepared and its behaviour under photo-irradiation investigated.

In a different approach, aptamers for controlled drug capture and release were designed and investigated for reversible drug binding. By designing short segments of complementary DNA that would disrupt the secondary structure of the aptamer species, reversible binding could be demonstrated.

Finally, the challenge of the Covid-19 pandemic led to the use of anthracene-modified oligonucleotides in the diagnosis of variant species of the virus. Anthracene tags were designed and synthesised, incorporated into short oligonucleotide probe strands and the

fluorescence changes of the anthracene upon interaction with single base mutations of the Covid-19 spike protein genome were investigated.

Acknowledgements

First, I need to thank my supervisors Professor James Tucker, Dr Richard Grainger, and Dr Paco Fernandez-Trillo for their continual support throughout this project, you have supported me through the lows and celebrated with me through the highs. Jim, thank you for welcoming me into your group and lab and for giving me the freedom to explore every side avenue of this thesis that I could think of. Richard, thank you for continually believing in me more than I believe in myself, and for turning me into an organic chemist (I'll admit it just this once). Paco, thank you for supporting me in every single aspect of this stage of my career and for being a friendly face to see at the pub at the end of a tough week.

I also need to thank the members of all my groups, without whom I would definitely not have finished. I could write pages about the good times, but thank you to Jake, Francia, Georgina, Marium, Klaudia, Ed, Aysha, Media, Liyao, Jack, Yifeng, Lydia, Aldrich and Ruba from the Tucker group, to Izzy, Kesar, Greg, Nick, Connor, Alya, Joseph, Ian and Sandra from the Grainger group, and to Oliver, Andy, Adam, Pavan, Nick, Andrey, Tom, Alex, Amit and Teyfik from the FFT group.

Many others in the department also supported me throughout these years who I need to thank. Russell, Richard, Alex, Harry, George, Alice, Jamie, Elena, Patricia, Asier, Angus, Sam, Lizzie (D and S!), Steven, Sajni, Nicola and Laura, thank you all for being a large part of the best times these past four years. Menisha, thank you for being my RSLC partner in crime, we had a good run!

I need to dedicate a special thank you to the staff at the analytical facilities for their advice and support, I would not have been able to do this without you. Cécile, Chris, Louise, Chi, Peter, Bridget and Allen, thank you! Also, a huge thanks to Todd from Biosciences for his help with a range of mass spectrometry instruments. To the other staff in the department: Phil and Rob – thank you for supporting me through the teaching side of my PhD, and for

making me laugh even in the most stressful times, Katherine, Trevor and Richard – thank you for somehow keeping this department going throughout everything, even a pandemic!

Finally, the biggest thanks need to go to my family and friends who have been my strength throughout the past four years. To Leanne and Matt, you're the best friends I could hope for, even when we're dotted all over the country. To everyone at the yard, thank you for keeping me sane, helping with Alfie when I couldn't leave the lab and for generally reminding me there is more to life than science. Dad, Fei Chin, John and Kim, thank you for being there for me whenever I've needed – the Midlands Farrows have been a great support system throughout and I love you all. Mum, you know exactly how much I have needed you and you have got me through this more than anyone else will ever know, I did this for you. Nan and grandad, I'm sorry you couldn't see me finish this PhD but I'm nearly there!

To dad, I miss you. You never doubted I'd make it and I wish you could have made it to see me graduate.

Contents:

CHAPTER 1: INTRODUCTION TO DRUG DELIVERY 1

1.1 Introduction 1

1.2 Congestive heart failure (CHF) and its treatment 1

1.2.1 Congestive heart failure 1

1.3 Polymers and oligomers for drug transport and delivery 8

1.3.1 Prodrug design and conjugation 8

1.3.2 Aptamers as delivery agents 12

1.4 Thesis aims 22

1.5 References 23

CHAPTER 2: SYNTHETIC STRATEGIES FOR HNO DELIVERY 28

2.1 Introduction 28

2.2 Aim 38

2.3 Design of an anthracene-derived diene 39

2.4 Synthesis of 9-,10-difunctionalised anthracene 2.43 42

2.5 Synthesis of 9,10-difunctionalised anthracene 2.50 45

2.6 DMT protection of diols 2.43 and 2.50 47

2.6.1 DMT protection of anthracene-9,10-dipropan-1-ol 47

2.6.2 DMT protection of anthracene-9,10-dimethan-1-ol 51

2.7 Anthracene-derived monomer syntheses and polymerisation attempts 53

2.8 Syntheses of hydroxyureas 2.64 and 2.70 58

2.9 Diels-Alder cyclo-additions on symmetrical anthracene derivatives 62

2.10 Alkoxy-substituted anthracene Diels-Alder cycloadditions 67

2.11 Conclusions and Future Work 73

2.11 References 74

CHAPTER 3: DEVELOPMENT OF DNA-BASED HNO DELIVERY SYSTEMS 77

3.1 INTRODUCTION 77

3.1.1 DNA delivery and therapeutics 77

3.1.2 Photo-activation of DNA modifications 79

3.2 AIM 82

..... 83

3.3 DESIGN AND SYNTHESIS OF ANTHRACENE TAG PHOSPHORAMIDITE 84

3.3.1 Design of an ideal anthracene tag 84

3.3.2 Synthesis of an alkoxy-substituted anthracene derivative 85

3.3.3 Selective hydroxyl protection 86

..... 87

3.3.4 Phosphoramidite synthesis 87

3.4 DNA SYNTHESIS 89

3.4.1 Introduction 89

3.4.2 Linear and hairpin DNA design 90

3.4.3 Synthesis and purification of modified DNA 92

3.4.5 Diels-Alder reaction on DNA 93

3.4.5 Characterisation of DNA cycloadducts 97

3.4.6.4 PAGE 103

3.4.6.5 Circular Dichroism (CD) 104

3.5 RELEASE OF HNO 107

3.6 CONCLUSIONS AND FUTURE WORK 110

3.7 REFERENCES 112

CHAPTER 4 INVESTIGATIONS INTO PILOTY'S ACID ANALOGUE *N*-(ANTHRACEN-9-YLMETHOXY)-2-NITROBENZENESULFONAMIDE AS AN HNO DONOR 114

4.1 INTRODUCTION 114

4.2 AIMS 118

4.3 Synthesis of anthracene analogue 4.22 120

4.4 Release of HNO by photo-irradiation 127

4.5 Photophysical investigations into Piloty's acid analogue 4.22 145

4.5.1 Absorption and fluorescence in fluorophores 145

4.5.2 Excimer and exciplex formation of anthracene-derived complexes 145

*4.5.3 UVvis and fluorescence experiments on Piloty's acid analogue **4.22** 148*

4.6 Conclusions and future work 153

4.6 References 154

CHAPTER 5 APTAMER CHEMISTRY 156

5.1 Introduction 156

5.1.1 Aptamers as drugs 156

5.1.2 Aptamers as conjugated drug delivery systems 157

5.1.3 Thrombin binding aptamer 159

5.2 Aims 161

5.3 Design and Synthesis of modified thrombin binding aptamer 162

5.3.1 Thermal characterisation of TBA-derived strands 164

5.3.2 CD determination of DNA secondary structure 171

5.3.3 PAGE analysis of thrombin binding aptamers 179

5.4 Studies into the reversible binding ability of thrombin binding aptamers 186

5.5 Conclusions and future work 192

5.6 References 193

CHAPTER 6 COVID-19: DIAGNOSIS OF VARIANTS 195

6.1 Introduction 195

6.1.1. Origin and spread 195

6.1.2 Genomics of SARS-CoV 2 196

6.1.3 Clinical pathogenesis of SARS-CoV-2 197

6.1.4 Genetic variants of SARS-CoV-2 198

6.1.5 Diagnosis of SARS-CoV-2 and variant detection *199*

6.2 AIMS 201

6.3 DESIGN AND SYNTHESIS OF ANTHRACENE-MODIFIED DNA STRANDS 203

6.4 INVESTIGATIONS INTO DUPLEXES OF PROBE AND TARGET STRANDS 207

6.4.1 Fluorescence of N501 probe strand *207*

6.4.2 Fluorescence of E484 probe strand *212*

6.4.3 Fluorescence anisotropy for base variant sensing *217*

6.4.4 Melting temperatures of E484 system duplexes *219*

6.5 CONCLUSIONS AND FUTURE WORK 221

6.6 REFERENCES 222

CHAPTER 7 TECHNIQUES, EXPERIMENTAL AND METHODS I

7.1 TECHNIQUES I

7.2 GENERAL EXPERIMENTAL XI

7.2.1 Materials ..... *XI*

7.2.2 General procedures ..... *XI*

7.1.2 DNA synthesis and characterisation general procedure ..... *XIII*

7.2.3 Experimental ..... *XVII*

Compound 2.56: *2-(bis(4-methoxyphenyl)(phenyl)methoxy)ethan-1-ol* ..... *XXV*

Compound 2.57*:9-((2-(bis(4-methoxyphenyl)(phenyl)methoxy)ethoxy)methyl)-10-(chloromethyl)anthracene* ..... *XXVI*

Compound 2.71: *1-(4-nitrophenyl)-3-((tetrahydro-2H-pyran-2-yl)oxy)urea* ..... *XXX*

Compound 2.65: *1-hydroxy-3-(4-nitrophenyl)urea* ..... *XXXI*

Compound 2.74: *methyl 4'-nitro-[1,1'-biphenyl]-4-carboxylate* ..... *XXXII*

Compound 2.75: *4'-nitro-[1,1'-biphenyl]-4-carboxylic acid* ..... *XXXIII*

Compound 2.76: *1-(4'-nitro-[1,1'-biphenyl]-4-yl)-3-((tetrahydro-2H-pyran-2-yl)oxy) urea* ..... *XXXIV*

Compound 2.78: *1-((9S,10Ss)-9,10-dimethyl-9,10-dihydro-9,10-(epoxyimino) anthracen-11-yl) ethan-1-one* ..... *XXXVII*

***Compound 2.89**: (9R,10R,11R,15R)-9-methoxy-9,10-dihydro-9,10-[3,4] epipyrroloanthracene-12,14-dione ..... XXXIX*

***Compound 2.88:** 1-((9s,10s)-9-methoxy-9,10-dihydro-9,10-(epoxyimino)anthracen-11-yl)ethan-1-one ....XL*

***Compound 3.9**: ethyl 5-(anthracen-9-yloxy) pentanoate.....XLII*

***Compound 3.10:** 5-(anthracen-9-yloxy)pentanoic acid.....XLIV*

***Compound 3.11**: 5-(anthracen-9-yloxy)-N-((2S,3S)-1,3-dihydroxybutan-2-yl)pentanamide.....XLV*

***Compound 3.12**: 5-(anthracen-9-yloxy)-N-((2S,3S)-1-(bis(4-methoxyphenyl) (phenyl)methoxy)-3-hydroxybutan-2-yl)pentanamide.....XLVII*

***Compound 3.13:** (2S,3S)-3-(5-(anthracen-9-yloxy) pentanamido)-4-(bis(4-methoxyphenyl)(phenyl)methoxy)butan-2-yl (2-cyanoethyl) diisopropyl phosphoramidite .....XLIX*

DNA cycloaddition general experimental.....LI

***Compound 4.28:** tert-butyl (allyloxy)carbamate.....LIII*

***Compound 4.30:** 2-(anthracen-9-ylmethoxy)isoindoline-1,3-dione .....LIV*

***Compound 4.27**: O-(anthracen-9-ylmethyl)hydroxylamine .....LV*

***Compound 4.22:** N-(anthracen-9-ylmethoxy)-2-nitrobenzenesulfonamide.....LVI*

***Compound 4.17**: 2-nitrobenzenesulfinic acid.....LVIII*

***Compound 6.4**: ethyl 2-(anthracen-9-yloxy)acetate .....LIX*

***Compound 6.6**: 2-(anthracen-9-yloxy) acetic acid .....LX*

***Compound 6.8**: 2-(anthracen-9-yloxy)-N-((2R,3R)-1,3-dihydroxybutan-2-yl) acetamide.....LXI*

***Compound 6.10**: 2-(anthracen-9-yloxy)-N-((2R,3R)-1-(bis(4-methoxyphenyl)(phenyl) methoxy)-3-hydroxybutan-2-yl) acetamide .....LXIII*

***Compound 6.12:** (2R,3R)-3-(2-(anthracen-9-yloxy)acetamido)-4-(bis(4-methoxyphenyl)(phenyl)methoxy)butan-2-yl (2-cyanoethyl) diisopropyl phosphoramidite .....LXV*

***Compound 6.5:** ethyl 6-(anthracen-9-yloxy) hexanoate .....LXVII*

***Compound 6.7:** 6-(anthracen-9-yloxy) hexanoic acid .....LXVIII*

***Compound 6.9:** 6-(anthracen-9-yloxy)-N-((2R,3R)-1,3-dihydroxybutan-2-yl) hexanamide.....LXIX*

***Compound 6.11**: 6-(anthracen-9-yloxy)-N-((2R,3R)-1-(bis(4-methoxyphenyl)(phenyl) methoxy)-3-hydroxybutan-2-yl)hexanamide .....LXXI*

Compound 6.13: *(2R,3R)-3-(6-(anthracen-9-yloxy)hexanamido)-4-(bis(4-methoxy phenyl)(phenyl)methoxy)butan-2-yl (2-cyanoethyl) diisopropyl phosphoramidite* ..... *LXXIII*

7.2 EXPERIMENTAL REFERENCES LXXV

CHAPTER 8 APPENDICES I

2.1 ^{1}H NMR STACK OF POLYMERISATION ATTEMPT (2.61) I

2.2 ^{1}H NMR OF 4-NITROANILINE II

3.1 HPLC TRACES AND MS OF CHAPTER 3 DNA III

*Lin-A - 5'-TGGACTC(**X**)CTCAATG-3'* ..... *III*

*Lin-U - 5'-TGGACTC**C**CTCAATG-3'* ..... *V*

*HP-A - 5'-CACGTT(**X**)TTCGTG-3'* ..... *VII*

*HP-U - 5'-CACGTT**T**TTCGTG-3'* ..... *IX*

HP-C - 5'-GTGCAAAAAGCAC-3' ..... *XI*

3.2 HPLC TRACE OF HP-CYCLOADDITION XIII

3.3 MS OF HP-CYCLOADDITION XIV

Fraction 3: ..... *XIV*

Crude: ..... *XV*

3.4 EXTENDED RANGE MS OF HP-CYCLOADDITION (RAW DATA) XVI

3.5 FT-ICR MS OF HP-CYCLOADDITION XVII

3.6 UVVIS OF HP-U XIX

4.1 ^{1}H NMR STACK OF PILOTY'S ACID ANALOGUE 4.22 PHOTO-IRRADIATION USING 125 W MERCURY LAMP AND 365 NM BANDPASS FILTER XX

4.2 IRRADIANCE OF 125 W MERCURY LAMP (0 MM AND 50 MM DISTANCE OF SENSOR FROM THE LAMP) XXI

5.1 HPLC TRACES AND MS OF APTAMER DNA STRANDS XXII

TBA: ..... *XXII*

TBA_L: ..... *XXIV*

TBA_C: ..... *XXVI*

TBA_{LC}: ..... *XXVIII*

$Short_C$: ..... *XXX*

$Long_C$: ..... *XXXII*

6.1 HPLC TRACES AND MS OF COVID-19 TARGET STRANDS XXXIV

E484K WT ..... *XXXIV*

E484K Mut ..... *XXXVI*

N501Y WT ..... *XXXVIII*

N501Y Mut ..... *XL*

Full TS WT ..... *XLII*

Full TS Mut1 ..... *XLIV*

Full TS Mut2 ..... *XLVI*

Full TS Mut3 ..... *XLVIII*

6.2 HPLC TRACES AND MS OF MODIFIED COVID-19 PROBE STRANDS L

E484K Probe ..... *L*

N501Y Probe ..... *LII*

6.3 IDT HAIRPIN SECONDARY STRUCTURE POSSIBILITIES[1] LIV

6.4 GRAPHICAL REPRESENTATION OF MELTING TEMPERATURES OF E484K PROBE DUPLEXES WITH LONGER TARGET STRANDS LVIII

7.1 ^{1}H AND ^{13}C NMR OF 2.89 LIX

7.2 ^{1}H AND ^{13}C NMR OF 2.88 LX

7.3 ^{1}H AND ^{13}C NMR OF 4.22 LXII

List of abbreviations

Ac- Acyl

ATP – Adenosine triphosphate

cGMP – cyclic guanosine monophosphate

CD – Cyclodextrins

CHF – Congestive heart failure

CHO – Chinese hamster ovary (cell line)

CPP – Cell penetrating peptide

Da - Daltons

DIPEA – *N, N*-Diisopropylethylamine

DMAP – 4-(*N, N*-Dimethylamino)pyridine

DMF – *N, N*-Dimethylformamide

DMSO – Dimethyl sulfoxide

DMT– 4,4'-Dimethoxytrityl

DNA – Deoxyribonucleic acid

Dox – Doxorubicin

DTX - Docetaxol

EDTA – Ethylenediaminetetraacetic acid

ENVs – Exosome mimetic nanovesicles

Et – Ethyl

FBS – Fetal bovine serum

FDA – Food and Drug administration

FRET – Fluorescence resonance energy transfer

GFP – Green fluorescent protein

HBTU – *N, N, N', N'*-Tetramethyl-O-(1*H*-benzotriazol-1-yl)uranium hexafluorophosphate

HPLC – High pressure liquid chromatography

Hz – Hertz

IR – Infrared

LHS – Left Hand Side

Me - Methyl

MS – Mass spectrometry

MUC1 – Mucin1

MW – Molecular weight

NMR – Nuclear magnetic resonance

NSHP – Naturally supercharged human proteins

PAGE – Polyacrylamide gel electrophoresis

PEG – Polyethylene glycol

PEI - Polyethylenimine

Ph – Phenyl

Ppm – Parts per million

PrP – Prion protein

RHS – Right Hand Side

RNA – Ribonucleic acid

RT – Room temperature

siRNA – Short interfering RNA

S. I. – Supplementary information

SNALPs – Stable nucleic acid lipid particles

TBA – Thrombin binding aptamer

TBA_C – TBA complementary

TBA_L – TBA + linker

TBA_{LC} – TBA_L complementary

TEAA – Triethylammonium acetate

THF – Tetrahydrofuran

THP – Tetrahydro-2*H*-pyran-2-yl

TLC – Thin layer chromatography

Ts - Tosyl

UV – Ultra-violet

VEGF – Vascular endothelial growth factor

Chapter 1: Introduction to drug delivery

1.1 Introduction

This thesis covers a range of subject areas unified by a common theme of using DNA to improve targeted delivery of therapeutics to the human body. This chapter provides a short and general introduction to the concept of drug delivery by summarising the current research literature on:

- Congestive heart failure as an exemplar of a particular disease and how it may be treated through the delivery of small-molecules therapeutics (e.g., HNO).
- The use of various oligomeric and polymeric structures to deliver drugs with a particular focus on DNA aptamers.

1.2 Congestive heart failure (CHF) and its treatment

Drug treatments in the medical industry are hampered by a lack of *in vivo* stability and specificity in the most efficacious therapeutics, leading to negative side effects and sub-optimal loading doses.[1-3] Therefore, academia and the pharmaceutical industries are continually looking for improved methods for targeting therapies towards certain cell or tissue types as well as stabilising more powerful drugs. Research on CHF provides a good example of such endeavours, as outlined below.

1.2.1 Congestive heart failure

Congestive heart failure (CHF) presents numerous problems in intensive care, both through diagnosis of the condition and its treatment.[4] Presentation of the disease in intensive care usually occurs as shortness of breath, hypoxemia and infiltrates (white spots) on a chest radiograph. Physicians must determine if the presentation is due to cardiac- or noncardiac-induced pulmonary edema.[4] CHF can occur from systolic or diastolic dysfunction where

systolic dysfunction causes low forward flow and cardiac output and the diastolic dysfunction causes normal to high cardiac output and blood pressure.[4]

Diagnosis of CHF occurs primarily through non-invasive imaging; echocardiography can be used to evaluate left and right ventricular systolic function whilst Doppler patterns can differentiate between normal and impaired relaxation physiology.[5] Less common techniques for diagnosis include pulmonary artery catheterisation[6] and cardiac catheterisation[7] but these are invasive and as such carry more risk. Once diagnosed, treatment options can be considered.

1.2.1.1 Current treatments for CHF

Most randomised studies into the treatment of CHF have focused on systolic dysfunction, primarily looking at relieving symptoms and stabilising hemodynamics rather than reversing the failure of the cardiac tissue.[4]

Diuretics such as Spironolactone[4] reduce the acute symptoms of congestion and can be used to adjust biventricular chamber dilation by reducing preload.[8] Certain loop diuretics reversibly inhibit ion transporters and are more effective with CHF-induced acute pulmonary edema, reducing pulmonary capillary wedge pressure and increasing venous capacity.[5, 9, 10]

Outpatients with CHF can use ß-adrenergic blocking agents, though care should be taken with this method as ß-blockers cause an initial deterioration in hemodynamics and symptoms, showing improvement again over the next 6 – 12 months.[4, 11]

One of the largest classes of treatments for CHF are vasodilators, used to reverse maladaptive neurohumoral and hemodynamic responses.[12] Nitrates are one such class of endothelial-independent vasodilators, providing exogenous nitric oxide. The therapeutic utility of the nitric oxide (NO) radical signalling pathway has been recognised within vasodilators for over a century, but the efficacy of such donors has reduced the potential for this treatment in clinic.[13] Other vasodilators include angiotensin-converting enzyme (ACE) inhibitors such as

trandolapril and ramipril which have shown long-term mortality and morbidity benefits in trials in the last 25 years (Figure 1).[4, 14] Some patients were found to have side effects when using ACE inhibitors and were preferentially treated with angiotensin II receptor blockers.[11, 15]

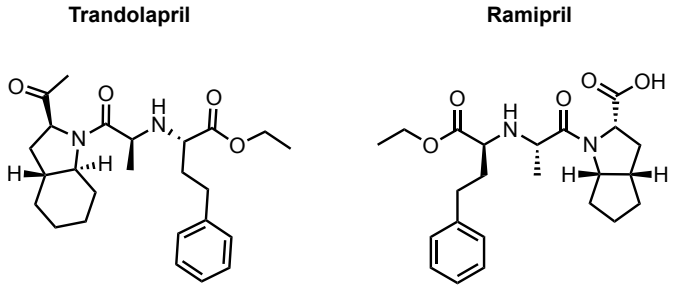


Figure 1 Structures of trandolapril and ramipril

Each treatment option shows benefits and limitations, with vasodilators providing much of the more current research into CHF therapeutics, as described below.

1.2.1.2 Investigations into NO• and HNO activity

As successful vasodilators have relied on nitric oxide in the majority, the nitric oxide radical (•NO) has been proven to have an integral role in various physiological processes including vascular homeostasis and angiogenesis.[11] The oxidised nitrogen oxides including peroxynitrite ($ONOO^-$), nitrite (NO_2^-) and nitrogen dioxide (NO_2) have also received attention, but the protonated one electron reduced nitroxyl (HNO) has been more overlooked in comparison (Figure 2).[16]

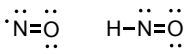


Figure 2 Lewis acid structures of NO radical and HNO

The differences between •NO and HNO have been discussed in great detail in the review by Kemp-Harper and co-workers,[17] and the abilities of nitroxyl to target thiols[18, 19] and increase plasma levels of calcitonin gene-related peptide (CGRP)[20] were highlighted as desirable traits in new therapeutics for CHF. HNO in particular displays a larger number of interactions with biomolecules by interacting with thiols directly and activating vascular voltage-dependent K^+ channels.[11] In addition, the cardiotropic activity of HNO appears to be related to its ability to activate cardiac sarcoplasmic ryanodine receptors, a trait not shared by the function of NO•.[11, 21]

A few years ago (2008), a comprehensive mechanism giving an overview of the actions of nitroxyl was put together by Irvine *et al.* (Figure 3).[11]

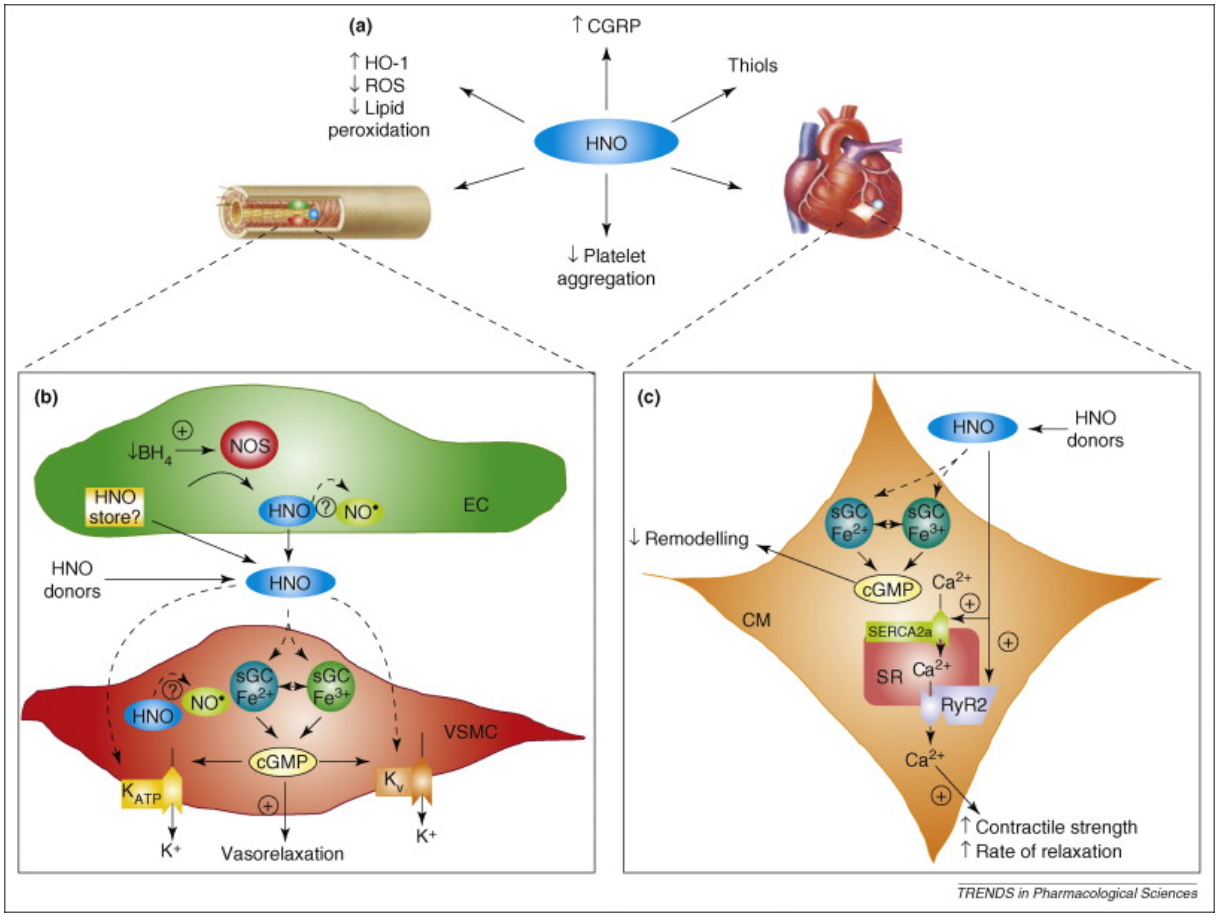
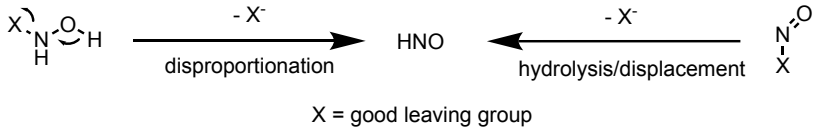


Figure 3 Overview of the activity of HNO in the cardiovascular system as described by Irvine et al. 2008.[11] Abbreviations: CM, cardiomyocyte; EC, endothelial cell; HO-1, haem-oxygenase; ROS, reactive-oxygen species; VSMC, vascular smooth muscle cell, sGC, soluble guanylate cyclase; cGMP, cyclic GMP; CGRP, calcitonin gene-related peptide.

The treatment of CHF can also be compromised by superoxide scavenging[22] and a preference for targeting ferrous haem proteins over ferric.[23] These challenges could be overcome via the use of HNO, should a suitable method of nitroxyl delivery be found (see below).

Given the potential for HNO in the treatment of CHF, an ongoing challenge has been to provide an effective means for delivering the species therapeutically using a donor molecule. A number of potential therapeutics donating either nitric oxide or nitroxyl have been continually developed over the past few decades, though the focus here will look at donor developments since the mid-2000s. HNO donation has tended to rely on either the disproportionation of hydroxylamine derivatives or decomposition of nitroso compounds (Scheme 1). The review by Miao and King[24] discussed both methods of donation in great detail.



Scheme 1 HNO release strategies as detailed by Miao and King, 2016

HNO donors will be discussed in more depth in Chapter 2 (section 2.1), though several designs have focused on dual HNO and NO donors. One such example was a primary amine-derived diazeniumdiolate (IPA/NO) which donated both nitroxyl and nitric oxide at neutral pH.[25] This drug was then adapted to reduce the amount of nitric oxide delivered, and has resulted in a range of HNO donors based on the diazeniumdiolate which have a wide-range of half-lives and show promise in cancer cell targeting as well (Figure 4).[11]

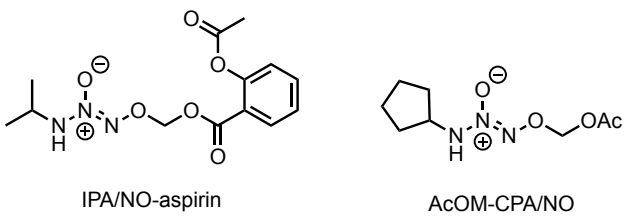
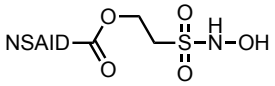


Figure 4 IPA/NO derivatives with HNO donating capabilities

Nitric oxide donors have also been designed from Piloty's acid, another well-known HNO donor. By creating ethanesulfohydroxamic acid esters of indomethancin and ibuprofen, Knaus synthesised a series of potential clinical prodrugs (Figure 5) which displayed a range of biological activities and increased NO release.[26]



NSAID = indomethacin, ibuprofen

Figure 5 Piloty's acid derived prodrug series designed by Knaus, 2011

Having shown that HNO and NO donors compounds can be attached to known drug moieties for reduced cytotoxicity, the idea of combining donor molecules with targeting vectors could still be explored further.

1.3 Polymers and oligomers for drug transport and delivery

1.3.1 Prodrug design and conjugation

Prodrugs have been of great interest in the development of therapeutics for a range of diseases, as they require biological or chemical transformation before a pharmacological response, meaning they can be transported through the body in an inactive state. As of 2018, 5 – 7% of approved drugs are prodrugs, reflecting the rise in popularity for the therapeutics that can minimise side effects.[27] Attaching a prodrug to an oligomeric or polymeric targeting vector can result in increased drug loading as well as further reduced side effects.

1.3.1.1 Prodrugs and polymers

The conjugation of a drug with a polymeric species led to the coining of the phrase 'polymeric prodrug' which was defined as a polymeric form of drug that remained inactive during delivery to the site of action and is activated by specific conditions at the target site.[28] The Ringsdorf model was developed in 1975 (Figure 6), creating a rationale that consisted of five components; a polymeric backbone, the drug, the spacer, the targeting agent and a solubilising agent.[28]

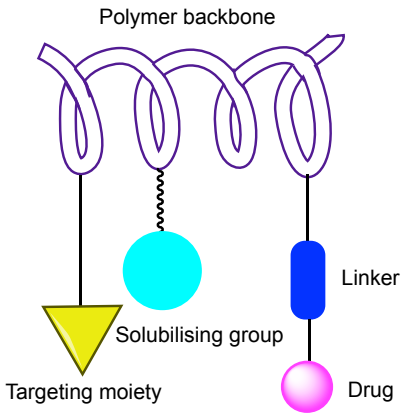


Figure 6 Ringsdorf model of polymeric pro-drug adapted from Gao, 2018

The polymeric backbone could be either inert or biodegradable but should not be an active component of the drug. The spacer was designed to control the site and rate of release of the active drug from the conjugate, typically by either hydrolytic or enzymatic cleavage.[28] The targeting moiety was designed to guide the conjugate to the correct area, with the solubilising moiety enabling its operation under physiological conditions.[28]

Certain general strategies improve the design of polymeric prodrugs; these include the availability of suitable functional groups for covalent coupling of the polymer with the drug, biocompatibility of the polymer, water solubility and low polydispersity.[28]

Common polymers used in such conjugations fit into three classifications: synthetic, natural and pseudosynthetic. Frequently used polymers include synthetic polyethylene glycol (PEG) and vinyl polymers, natural polymers such as chitosan and proteins and synthetic poly α-amino acids.[28, 29] There are limitations to each type, and to the use of polymeric prodrugs in general. The steric hindrances of large polymers can cause issues when conjugating drugs to the backbone, but the presence of a linker species can be used to counteract this. More problematic is the possibility of the prodrug being internalised by endocytosis if the drug is not released upon recognition of the target site.[28]

1.3.1.2 Prodrugs and peptides

One of the biggest challenges in delivering therapeutics is cell penetration to allow the drug access to the targeted organelle. In conjunction to this, many therapeutics are often DNA or protein based, and as such also suffer from low cell permeability.[30] Cell penetrating peptides (CPPs) are small (<30 amino acids) peptides capable of permeating through the cell membrane. In particular, several abnormal CPPs, known as naturally supercharged human proteins (NSHPs) are capable of transporting fused proteins through a lipid bilayer with high efficiency.[30] Miyata and co-workers[31] adapted a peptide-based approach conjugated to anthracene in an attempt to improve cell internalisation of their HNO donor. The group

discuss their highly hydrophilic design as a potential advantage for incorporating the cycloadduct into biological systems, but found the compound to be less stable under ambient conditions.[32]

1.3.1.3 Pro-drugs and DNA aptamers

Use of DNA as a targeting vector for pro-drugs has primarily focused on aptamers, short single-stranded DNA or RNA moieties that bind proteins and peptides with high target selectivity. Aptamers have advantages over antibodies in that they are equally selective but are non-immunogenic and more easily synthesised on mass.[33] RNA-based aptamers suffer from quick degradation by nucleases in biological media, with DNA systems more stable.[34] One method to counteract this was found to be modification of the nucleic acid backbone to increase resistance.[34]

Aptamers have been used as active targeting agents for platinum containing drugs, though this has typically required the use of liposomes[35] or intercalation into double-stranded sections of aptamer secondary structures.[33, 36] Other anti-cancer drugs such as doxorubicin (DOX) can also be incorporated into A10 PSMA aptamers for targeted delivery, indicating that research into aptamer-based delivery has shown success over the past two decades (Figure 7).[37] Aptamers as a targeted delivery agent will be discussed in more detail below.

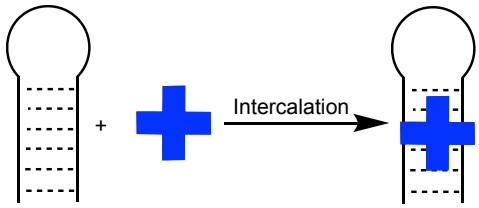


Figure 7 General schematic for intercalation of doxorubicin into an A10 PSMA aptamer based on Bagalkot et al. 2006

Aptamer conjugation to pro-drugs is less well-known, indicating a potential gap in the development of therapeutics, and this theme will be explored throughout this body of work.

Improved methods in synthetic DNA production have enabled the generation of large amounts of oligodeoxynucleotides using systematic evolution of ligands by exponential enrichment (SELEX).[38] A SELEX experiment typically generates a random sequence library of approximately 1×10^{13} to 1×10^{15} strands of approximately 20-100 residues in length, and each nucleotide is flanked by the sequences required for enzymatic manipulation.[39] Suitable members of the library are then successively partitioned for binding and amplified, leaving individual nucleotides that can bind to the identified target.

Aptamers frequently compete with small molecules and antibodies for therapeutic applications, as they have properties more suitable for systemic administration, in particular against targets in the bloodstream or on cell surfaces such as epidermal growth factors (EGFR).[39] As of 2020, one aptamer has been marketed for therapeutics and more are in clinical trials, though results from trials have been mixed.[40, 41] Where clinical trials were terminated, the reasoning was typically low activity of the aptamer or the trial was stopped without reason.[40] Pegaptanib, a pegylated 27 nucleotide RNA that specifically binds to the main form of vascular endothelial growth factor (VEGF), is currently approved in the US, Europe, Canada, Brazil and Australia.[40] More aptamers have been commercialised in the case of diagnostic applications, including OTA-Sense for the detection of Ochratoxin A, AflaSense for the detection of aflatoxins and AptoCyto, a range of aptamer products that detect a number of growth factor receptors.[40]

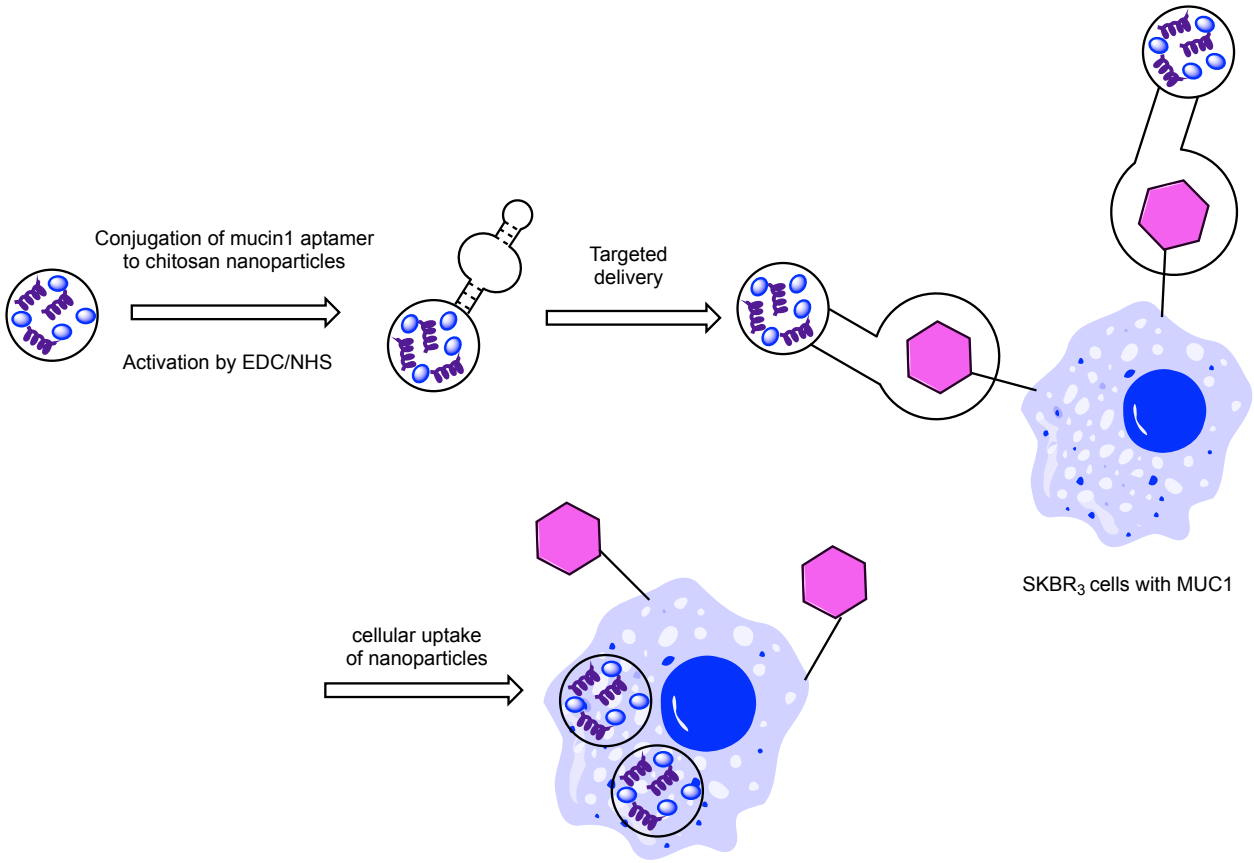
Aptamers can be the therapeutic themselves as anti-coagulants. The prevention and treatment of thrombotic disorders relies heavily on heparin, due to the low cost of production and its safety of use.[42] The limitations of heparin include platelet aggregation and the necessity of protamine as an antidote, which in turn can have serious side effects.

Thrombin, a coagulation protein with many effects in the coagulation cascade, transforms fibrinogen to the insoluble fibrin and catalyses other coagulation-related reactions.[42] When finding anti-coagulant agents, thrombin has always been a strong candidate for targeting, due to its recognition of multiple macro molecular substrates and ability to function as both a procoagulant and an anti-coagulant.[42, 43] Multiple aptamers have been developed to interact with thrombin, with a conserved sequence of GGTTGG in almost every clone. Other anti-coagulant aptamers include the anti-factor IX aptamer, which was capable of prolonging the coagulation of plasma from human species *in vitro*. [42]

1.3.2 Aptamers as delivery agents

For aptamers to work well as delivery agents for therapeutics, the mechanism of their conjugation or intercalation must be discussed. Many aptamers on the market work in conjugation with siRNAs (small interfering RNA),[44] which suppress gene expression by targeting the mRNA expression, and targeted delivery of these have been coupled to aptamers since 1998.[45] Since this time, many aptamer platforms have been developed to support targeted siRNA delivery, using nanoparticles,[46-48] nanorings,[49, 50] nanovectors[51] and stable nucleic lipid particles (SNALPs).[52] Aptamer-functionalised siRNA designs typically fall into two categories, incorporation into the nanoparticle or conjugation onto the nanoparticle surface.[44] Nayebi's group[53] have shown an elegant approach to co-deliver chemotherapeutic agents and siRNA within nanoparticles, improving the delivery using the Mucin1 aptamer. The Mucin1 aptamer targets MUC1, a member of the membrane-bound mucin sub-family which is overexpressed in many cancers, in particular invasive lung cancers.[54] A number of aptamers were found by SELEX to have activity against MUC1. [53] The siRNA was entrapped along with docetaxel into chitosan nanoparticles, then the Mucin1 aptamer was conjugated by the same EDC/NHS method (Scheme 2). These nanocomposites were measured on incubation with $SKBr_3$ cells which are mucin positive, and CHO cells that are mucin negative to determine the additional targeting efficacy of the aptamer conjugate.[53] By running these

experiments at pH 7.4 and 5.5, both docetaxel and siRNA release could be emulated in both normal and tumour-type cells. Native gels of the nanoparticles showed release of both drug types over 70 hours and appeared independent of the environment's pH.



Scheme 2 Diagrammatic scheme of co-delivery of siRNA and docetaxel in chitosan nanoparticles conjugated to Mucin1 aptamer as described by Zolbanin et al., 2018

Shokri's investigations into the efficacy of siRNA-loaded nanoparticles in cancer therapeutics kickstarted this area of interest.[55] The group loaded siRNA on chitosan lactate (ChLa) nanoparticles by ionic gelation of the nanoparticles with a mixture of siRNA and sodium tripolyphosphate (TPP). The overall stability of the siRNA inside the nanoparticles was determined by incubation with serum and heparin (a polyanion used to emulate negatively-charged cellular environments).[55] *In vitro* release was seen gradually up until 60 hours and equilibrium was seen after 72 hours in both pH types tested. This style of nanoparticle also

showed 50% release of encapsulated siRNA in the first 36 hours, in a similar manner to that of which Nayebi[53] found with the chitosan nanoparticles. Research by Katas[56] into siRNA and chitosan nanoparticles also showed good entrapment by the use of cross-linkers, stabilising the siRNA inside the nanoparticles for up to 15 days.

Nanoparticles are increasingly used within the world of therapeutics as effective carriers of drugs, in particular in the case of cancer treatments that rely on co-administration of multiple drug types.[57] Such nanocarriers are often polymer- or lipid-based, metallic, inorganic or biologically-derived – where each type has differing advantages and disadvantages. One common feature to each nanoparticle subset is the need to functionalise them with a vector for targeted delivery.[57] As such, aptamers have been shown to be conjugated to nanoparticles to facilitate this. In the case of cancer therapeutics, most drugs used for treatment are non-specific and therefore attack healthy cells too. For this purpose, choosing a targeting vector that is specific to cancer cells can improve the delivery of drug loaded nanoparticles, minimising toxicity without increasing the overall size of the therapeutic device dramatically.

Many aptamer-based drug delivery systems have used the AS1411 aptamer due to the stability of the G-quadruplex structure in serum.[58] The AS1411 aptamer (sequence: 5'-GGT GGT GGT GGT TGT GGT GGT GGT GG-3')[59] binds the multifunctional cellular protein nucleolin. As such, it is a good selector for higher nucleolin-expressing cancer cells. Several types of cancer cells with high proliferation rates such as breast cancer cells, lymphocytic leukaemia and prostate carcinoma, all express higher levels of nucleolin.[58] The G-quadruplex structure made AS1411 aptamer a good candidate for carrying a quadruplex ligand like 5,10,15,20-tetrakis(1-methylpyridinium-4-yl) porphyrin (TMPyP4).[58] The quadruplex ligand can bind and stabilise G-quadruplexes in the human telomere, inhibiting function and causing cellular senescence, but TMPyP4 is poorly selective and toxic to some cell lines.[58, 60] By

incorporating TMPyP4 into the AS1411 G-quadruplex, targeted delivery and a reduction of non-specific toxicity could be achieved.[58]

The Zheng group[61] covalently conjugated cholesterol-PEG chains to AS1411 (nucleolin-targeting) aptamers then bound these to living mouse dendritic cell membrane. These cells were subsequently extruded via microconstrictions to yield exosome-mimetic ENVs. Paclitaxel was loaded into the ENVs by sonication with a loading efficiency of 5% and was found to demonstrate burst release within the first hour, then sustained release with over 70% paclitaxel unloaded within 24 hours. *In vitro* tests on MDA-MB-231 cells showed good membrane crossing of the ENVs and 90% of cells were blocked in the G2-M phase. When studied *in vivo*, the aptamer bound ENVs accumulated in tumours and reduced the tumour volume from 169.6 mm^3 to 35.34 mm^3 (Figure 8).[61] Similarly, Zhang and co-workers also investigated aptamer bound extracellular nanovesicles and their effect on osteosarcoma cellular phenotypes.[62]

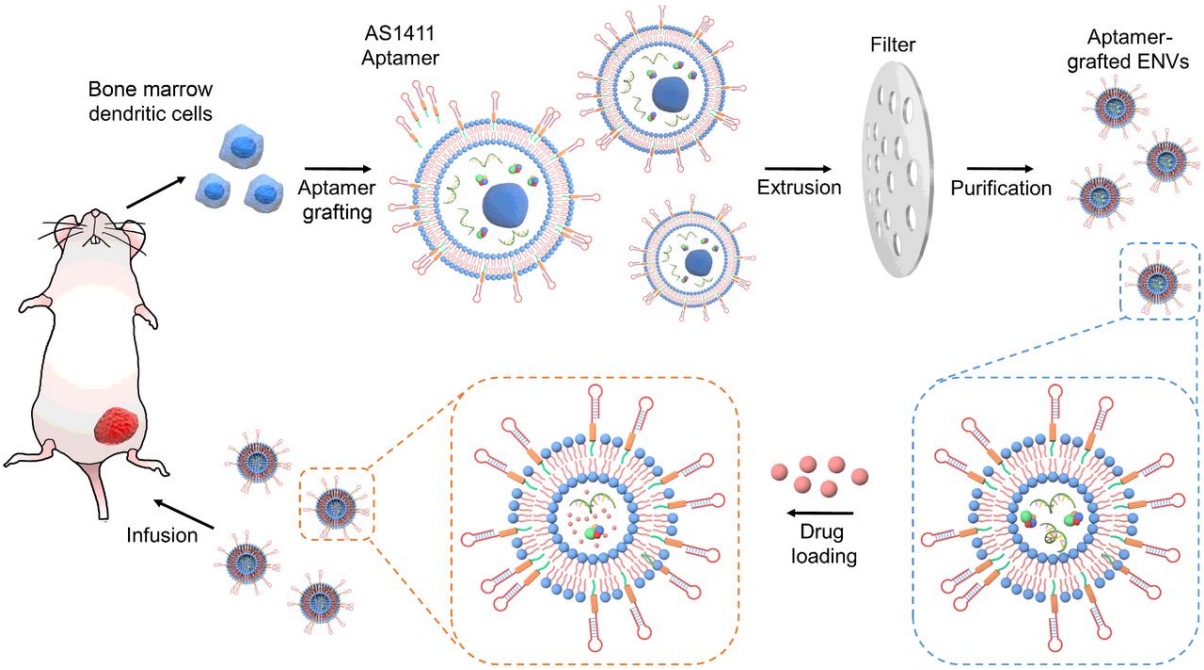


Figure 8 Schematic taken from work carried out by Zheng and co-workers[49]

As cancer cells have increased expression of MUC1 receptor, Sayari *et al.*[63] chose to conjugate a MUC1 aptamer (described earlier) to chitosan nanoparticles pre-loaded with SN38 – an active metabolite of irinotecan for cancer cell specific therapeutics.[64] This conjugation was carried out by adding 5'-NH_2 modified aptamers to EDC/NHS reacted nanoparticles.[63] When testing the cytotoxicity of the loaded nanoparticles, it was noted that the inclusion of the aptamer did not affect the efficacy of the drug. Atyabi and their group[63] tested these conjugated systems on two cell lines, HT-29 and CHO. The nanoparticle-aptamer moieties were determined to be more efficiently incorporated into the cells in the HT-29 cell line, though there was little difference in the CHO cell line.[63] The study concluded by demonstrating the improved delivery and increased solubility of the drug when contained within the nanoparticles. The same method of conjugating nanoparticles to aptamers has been used since 2004, and was demonstrated in the binding of the 3'-NH_2 modified A10 PSMA aptamer to the nanoparticle in the original work by Langer and co-workers.[65] The enhanced uptake was determined to be approximately 77-fold higher than the control nanoparticle group.

As ferromagnetic and superparamagnetic nanoparticles have been applied for medical purposes previously, Kichkailo[66] worked to improve the delivery of these by the conjugation of aptamers to such nanostructures. By functionalising the ferroarabinogalactan nanoparticles with AS-14 and AS-42 aptamers, the biocompatibility and colloidal stability of the compounds *in vivo* was improved.[66] The aptamers were chosen for their binding specificity, with AS-14 binding post-translationally modified fibronectin of the extracellular matrix of cancer cells and AS-42 binding heat shock cognate 71 kDa protein.[66]

1.3.2.1 Aptamer-drug release mechanisms

Aptamers have been investigated with ever growing interest in the sphere of controlled drug release, due to their high specificity for targets. Where drugs can be intercalated into the aptamer strand or covalently conjugated to the DNA via a nanoparticle or another loading

moiety, the targeting nature of these oligomers is most enticing. However, the subsequent release of these therapeutics is as important as sending them to the correct area of the body or cell, and therefore, mechanisms of release must be discussed.

As the secondary structure of aptamers plays a vital role in their targeting nature, changes to the conformational structure upon binding could provide interesting opportunities for therapeutics to be released on that change. For many intercalating drugs, such as DOX, the double-stranded nature of one conformational structure of the DNA allows for binding opportunities, which upon target binding could unfold and release the therapeutic. Such a possibility was made more evident by Long and co-workers when they demonstrated that conformational changes of an ATP-binding aptamer could be observable by monitoring the duration time of translocation across nanopore biosensors.[31]

A similar design template shows an effector-responsive aptamer that was designed to induce a conformational change when an effector strand is introduced (**Error! Reference source not found.**).[32] The three components of this construct consist of the sensing loop, the complementary aptamer and antidote stems. The sensing loop in this instance was designed to recognise a specific nucleic acid effector, here the mRNA of green fluorescent protein (GFP).[67] The prototype used thrombin binding aptamer (TBA) as the complementary aptamer and a short (eight nucleotide) section of complementary DNA to the TBA was designated as the antidote. When the mRNA of GFP was absent, the antidote strand disrupted the G-quadruplex of the TBA, causing a lack of recognition by the aptamer. However, on addition of the GFP, the sensing loop undergoes a conformational change to bind the effector strand and allow the reconfiguration of the TBA to the active form.[68]

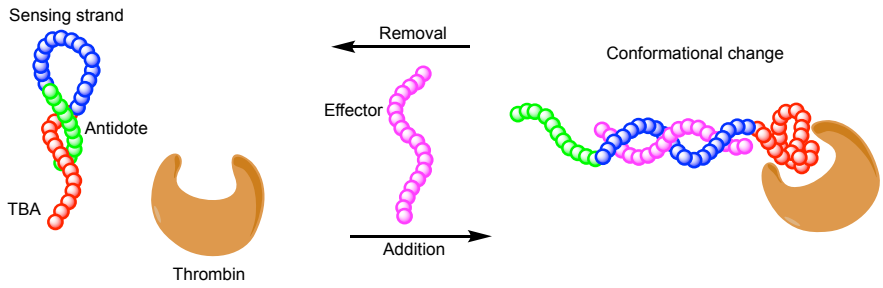


Figure 9 Schematic of the proposed effector-responsive hairpin oligonucleotide designed by Li, 2013

Likewise, the conformational changes in aptamers can be used in surface-based diagnostics (Figure 10). By designing an aptamer for a specific moiety with an additional tail which would be made prominent upon the conformational change seen on target recognition, a solid-surface decorated with 'capture' DNA could be used to bind the aptamer plus target.[68] A mouse prion protein (PrP) aptamer was used with an additional 5' section of DNA that was complementary to an inside region of the aptamer. Following the conformational change upon recognition of PrP, the inside section was revealed and able to be bound by the immobilised complementary region.

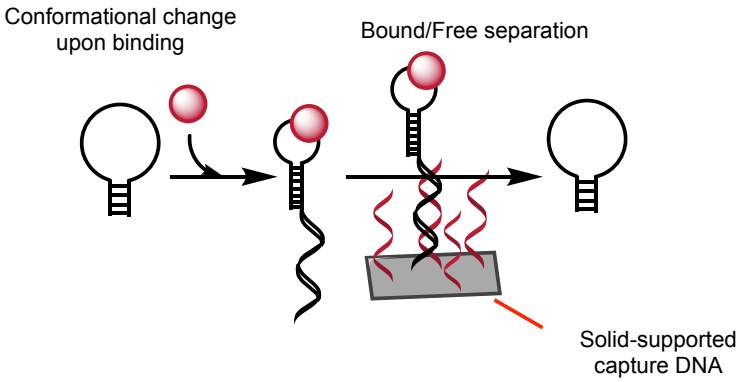


Figure 10 Conformational changes seen on diagnostic use of aptamers designed by Ogasawara et al.[67]

Within the cellular environment, pH changes in tumour cells can cause conformational changes to release DOX from aptamer moieties. The drug release profile of DOX from DNA nano rings was observed at pH 7.4 and pH 5.5, showing that the drug is released more effectively in acidic environments.[68] At physiological pH, the in vitro cumulative release of the nano-ring-DOX conjugate was observed to be 61% after 48 h, indicating mainly passive release of the therapeutic. However, at pH 5.5, DOX release was calculated to be 95% within the same time frame with the release being attributed to the enhanced breakage of the phosphodiester and *N*-glycosidic bonds of the sugar and purine bases that occurs in acidic environments.[68]

In a similar vein, pH-responsive drug release from aptamers has been investigated via the development of allosterically controlled aptamers that could be switched from binding to releasing on addition of an inhibitor.[69] Here, the ATP binding aptamer was used with an inhibitor designed to create a double strand DNA sequence in the centre of the aptamer strand, causing a conformational change (Figure 11). The nicking endonuclease enzyme Nt.BsmAI specifically recognises this stretch of double stranded DNA and cleaves the inhibitor, making the process reversible.[69] The group then extended this work further to encompass allosteric control of the cocaine binding aptamer by labelling the 3' and 5' ends of the DNA strand with a Förster resonance energy transfer (FRET) pair for monitoring binding.

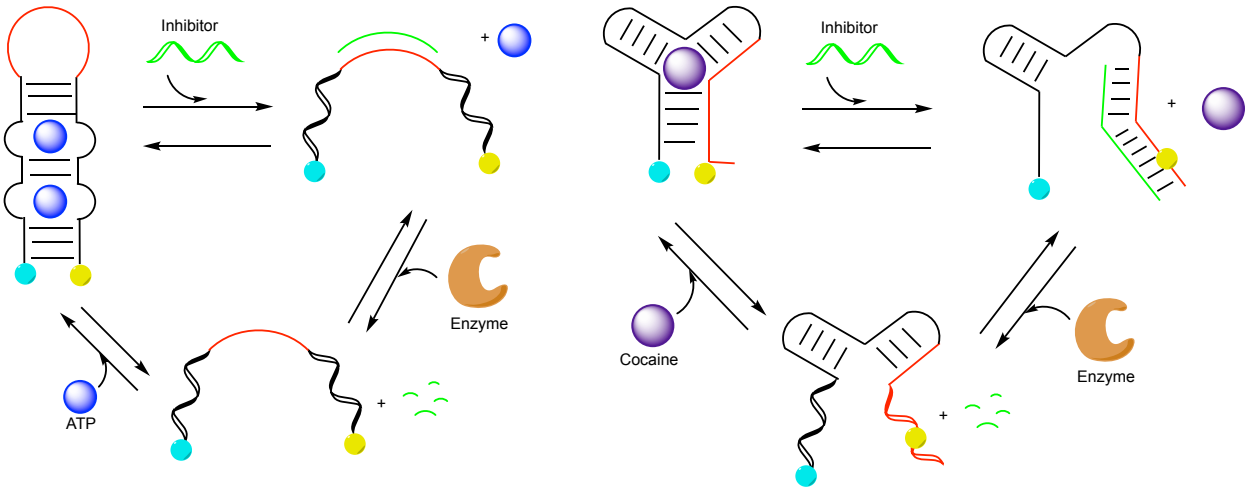


Figure 11 Fuel-responsive aptamer bind and release strategies designed by Ricci and co-workers[69]

More efficient methods utilise fuel-responsive drug release by relying on nucleases to break down the aptamer conjugate, making the delivery faster, if less elegant. One excellent example of the simplicity of this system relies on a construct of aptamer domains within a larger DNA scaffold.[70] The linear regions of the DNA were designed to be double stranded, meaning that intercalating drugs could be loaded efficiently. Interspersed between these double stranded-DNA regions were hairpin loop style aptamers targeting PTK7, a component of the planar cell polarity pathway.[71, 72] The construct was determined to be highly stable, showing little release of the intercalated drug and high specificity to PTK7 expressing cell lines. Once internalised to the cell, the presence of DNase-1, a DNA nuclease, interacts with the substrate, degrading the DNA to release DOX rapidly.[73]

Perhaps a more complex system relies on aptamer-nanoparticle composites. In such designs, the aptamer can act as a gateway for drug release from porous nanomaterials, controlling the discharge until in the presence of a specific fuel.[24, 72, 74] Özalp and Schäfer created fluorescein-loaded mesoporous silica nanoparticles which they conjugated to ATP aptamers. In the absence of ATP, the release of fluorescein was blocked by the DNA but upon the conformational change triggered by ATP binding, the nanoparticles were un-capped and the cargo released (Figure 12).[72]

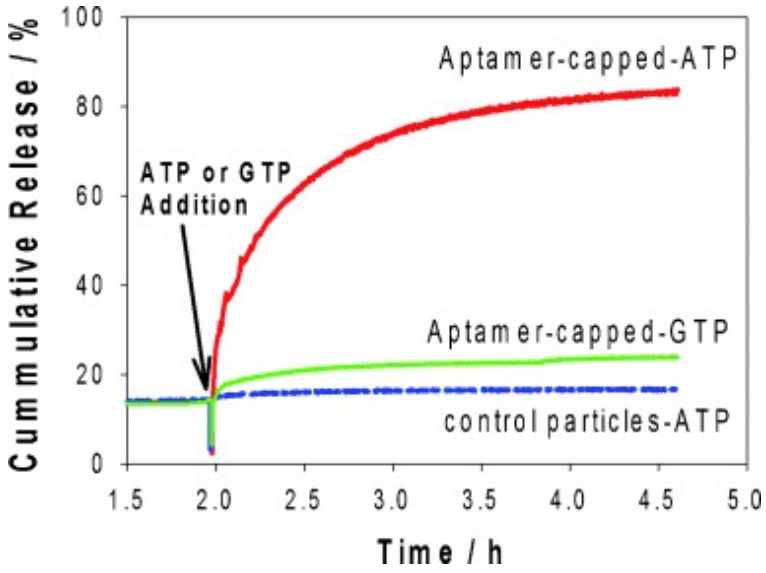


Figure 12 Release of fluorescein on uncapping of aptamer gates. Taken from Özalp and Schäfer, 2011.[72]

1.4 Thesis aims

This thesis looks to contribute to the field of targeted drug delivery via a number of routes, including photo-activation of drug moieties and aptamer-based targeting. A significant amount of effort has been directed towards the incorporation of nitroxyl donors into anthracene-derived diols for vector conjugation and subsequent targeted delivery. This approach is investigated in multiple ways, designing a range of anthracene diols and HNO donor molecules (Chapters 2 – 4) and investigating photo-activated HNO donation. The anthracene diols will be designed for conjugation to oligonucleotides or for polymerisation, and the HNO donating functionalities will be derived from nitroso groups or sulfonamide derivatives.

Targeted drug delivery will also be investigated via the formation of modified aptamers capable of binding and releasing a drug moiety (in this case thrombin). The constructs created in Chapter 5 will investigate reversible binding of thrombin for targeted delivery and release.

In a slightly different vein, the thesis work was adapted to face the challenges presented by the Covid-19 pandemic through the design of several anthracene-modified DNA strands for detecting single base changes in different variants of the SARS-CoV-2 genome (Chapter 6). The detection of variants is achieved by monitoring changes in anthracene emission intensity upon duplex formation with different target sequences.

1.5 Chapter 1 References

1. Fernandez-Fernandez, A.; Manchanda, R.; McGoron, A. J., Theranostic applications of nanomaterials in cancer: drug delivery, image-guided therapy, and multifunctional platforms. *Appl. Biochem. Biotechnol.,* **2011,** *165* (7-8), 1628-51.
2. Ahmed, F.; Khan, M. A.; Haider, N.; Ahmad, M. Z.; Ahmad, J., Recent Advances in Theranostic Applications of Nanomaterials in Cancer. *Curr. Pharm. Des.,* **2021**, 10.2174/1381612827666210916140627.
3. Kim, S.; Shi, Y.; Kim, J. Y.; Park, K.; Cheng, J. X., Overcoming the barriers in micellar drug delivery: loading efficiency, *in vivo* stability, and micelle-cell interaction. *Expert Opin. Drug Deliv.,* **2010,** *7* (1), 49-62.
4. Poppas, A.; Rounds, S., Congestive heart failure. *Am J Respir Crit Care Med* **2002,** *165* (1), 4-8.
5. Pitt, B.; Zannad, F.; Remme, W. J.; Cody, R.; Castaigne, A.; Perez, A.; Palensky, J.; Wittes, J., The effect of spironolactone on morbidity and mortality in patients with severe heart failure. Randomized Aldactone Evaluation Study Investigators. *N. Engl. J. Med.,* **1999,** *341* (10), 709-17.
6. Hunt, S. A.; American College of, C.; American Heart Association Task Force on Practice, G., ACC/AHA 2005 guideline update for the diagnosis and management of chronic heart failure in the adult: a report of the American College of Cardiology/American Heart Association Task Force on Practice Guidelines (Writing Committee to Update the 2001 Guidelines for the Evaluation and Management of Heart Failure). *J. Am. Coll. Cardiol.,* **2005,** *46* (6), e1-82.
7. Allan, J. J.; Smith, R. S.; DeJong, S. C.; McKay, C. R.; Kerber, R. E., Intracardiac echocardiographic imaging of the left ventricle from the right ventricle: quantitative experimental evaluation. *J. Am. Soc. Echocardiogr.,* **1998,** *11* (10), 921-8.
8. Kramer, B. K.; Schweda, F.; Riegger, G. A., Diuretic treatment and diuretic resistance in heart failure. *Am. J. Med.,* **1999,** *106* (1), 90-6.
9. Bristow, M. R., beta-adrenergic receptor blockade in chronic heart failure. *Circulation* **2000,** *101* (5), 558-69.
10. Lechat, P.; Packer, M.; Chalon, S.; Cucherat, M.; Arab, T.; Boissel, J. P., Clinical effects of beta-adrenergic blockade in chronic heart failure: a meta-analysis of double-blind, placebo-controlled, randomized trials. *Circulation* **1998,** *98* (12), 1184-91.
11. Irvine, J. C.; Ritchie, R. H.; Favaloro, J. L.; Andrews, K. L.; Widdop, R. E.; Kemp-Harper, B. K., Nitroxyl (HNO): the Cinderella of the nitric oxide story. *Trends Pharmacol. Sci.,* **2008,** *29* (12), 601-8.
12. Kober, L.; Torp-Pedersen, C.; Carlsen, J. E.; Bagger, H.; Eliasen, P.; Lyngborg, K.; Videbaek, J.; Cole, D. S.; Auclert, L.; Pauly, N. C., A clinical trial of the angiotensin-converting-enzyme inhibitor trandolapril in patients with left ventricular dysfunction after myocardial infarction. Trandolapril Cardiac Evaluation (TRACE) Study Group. *N. Engl. J. Med.,* **1995,** *333* (25), 1670-6.
13. Effect of ramipril on mortality and morbidity of survivors of acute myocardial infarction with clinical evidence of heart failure. The Acute Infarction Ramipril Efficacy (AIRE) Study Investigators. *Lancet* **1993,** *342* (8875), 821-8.
14. Pitt, B.; Segal, R.; Martinez, F. A.; Meurers, G.; Cowley, A. J.; Thomas, I.; Deedwania, P. C.; Ney, D. E.; Snavely, D. B.; Chang, P. I., Randomised trial of losartan versus captopril in patients over 65 with heart failure (Evaluation of Losartan in the Elderly Study, ELITE). *Lancet* **1997,** *349* (9054), 747-52.
15. Moncada, S.; Higgs, E. A., The discovery of nitric oxide and its role in vascular biology. *Br. J. Pharmacol.,* **2006,** *147 Suppl 1*, S193-201.
16. Fukuto, J. M.; Jackson, M. I.; Kaludercic, N.; Paolocci, N., Examining nitroxyl in biological systems. *Methods Enzymol.,* **2008,** *440*, 411-31.

17. Donzelli, S.; Espey, M. G.; Thomas, D. D.; Mancardi, D.; Tocchetti, C. G.; Ridnour, L. A.; Paolocci, N.; King, S. B.; Miranda, K. M.; Lazzarino, G.; Fukuto, J. M.; Wink, D. A., Discriminating formation of HNO from other reactive nitrogen oxide species. *Free Radic. Biol. Med.,* **2006,** *40* (6), 1056-66.
18. Paolocci, N.; Katori, T.; Champion, H. C.; St John, M. E.; Miranda, K. M.; Fukuto, J. M.; Wink, D. A.; Kass, D. A., Positive inotropic and lusitropic effects of HNO/NO- in failing hearts: independence from beta-adrenergic signaling. *Proc. Natl. Acad. Sci. U. S. A.,* **2003,** *100* (9), 5537-42.
19. Paolocci N, S. W., Miranda KM, Martignani C, Isoda T, Hare JM, Espey MG, Fukuto JM, Feelisch M, Wink DA, Kass DA, Nitroxyl anion exerts redox-sensitive positive cardiac inotropy *in vivo* by calcitonin gene-related peptide signaling. *Proc. Natl. Acad. Sci. U. S. A.,* **2001,** *98*, 10463-8.
20. Bolhassani, A.; Jafarzade, B. S.; Mardani, G., In vitro and in vivo delivery of therapeutic proteins using cell penetrating peptides. *Peptides* **2017,** *87*, 50-63.
21. Tocchetti, C. G.; Wang, W.; Froehlich, J. P.; Huke, S.; Aon, M. A.; Wilson, G. M.; Di Benedetto, G.; O'Rourke, B.; Gao, W. D.; Wink, D. A.; Toscano, J. P.; Zaccolo, M.; Bers, D. M.; Valdivia, H. H.; Cheng, H.; Kass, D. A.; Paolocci, N., Nitroxyl improves cellular heart function by directly enhancing cardiac sarcoplasmic reticulum Ca^{2+} cycling. *Circ. Res.,* **2007,** *100* (1), 96-104.
22. Miranda, K. M.; Yamada, K.; Espey, M. G.; Thomas, D. D.; DeGraff, W.; Mitchell, J. B.; Krishna, M. C.; Colton, C. A.; Wink, D. A., Further evidence for distinct reactive intermediates from nitroxyl and peroxynitrite: effects of buffer composition on the chemistry of Angeli's salt and synthetic peroxynitrite. *Arch. Biochem. Biophys.,* **2002,** *401* (2), 134-44.
23. Miranda, K. M.; Nims, R. W.; Thomas, D. D.; Espey, M. G.; Citrin, D.; Bartberger, M. D.; Paolocci, N.; Fukuto, J. M.; Feelisch, M.; Wink, D. A., Comparison of the reactivity of nitric oxide and nitroxyl with heme proteins. A chemical discussion of the differential biological effects of these redox related products of NOS. *J. Inorg. Biochem.,* **2003,** *93* (1-2), 52-60.
24. Miao, Z.; King, S. B., Recent advances in the chemical biology of nitroxyl (HNO) detection and generation. *Nitric Oxide* **2016,** *57*, 1-14.
25. DuMond, J. F.; King, S. B., The chemistry of nitroxyl-releasing compounds. *Antioxid. Redox Signal* **2011,** *14* (9), 1637-48.
26. Huang, Z.; Velazquez, C. A.; Abdellatif, K. R.; Chowdhury, M. A.; Reisz, J. A.; DuMond, J. F.; King, S. B.; Knaus, E. E., Ethanesulfohydroxamic acid ester prodrugs of nonsteroidal anti-inflammatory drugs (NSAIDs): synthesis, nitric oxide and nitroxyl release, cyclooxygenase inhibition, anti-inflammatory, and ulcerogenicity index studies. *J. Med. Chem.,* **2011,** *54* (5), 1356-64.
27. Mishra, A. P.; Chandra, S.; Tiwari, R.; Srivastava, A.; Tiwari, G., Therapeutic Potential of Prodrugs Towards Targeted Drug Delivery. *Open Med. Chem. J.,* **2018,** *12*, 111-23.
28. Gao, Y., Introduction and synthesis of polymeric prodrugs. *MOJ. Bioequiv. Availab.* **2018,** *5*, 125-8.
29. Azori, M., Polymeric prodrugs. *Crit. Rev. Ther. Drug Carrier Syst.,* **1987,** *4* (1), 39-65.
30. Matsuo, K.; Nakagawa, H.; Adachi, Y.; Kameda, E.; Aizawa, K.; Tsumoto, H.; Suzuki, T.; Miyata, N., Photoinduced Upregulation of Calcitonin Gene-Related Peptide in A549 Cells through HNO Release from a Hydrophilic Photocontrollable HNO Donor. *Chem. Pharm. Bull.,* **2012,** *60* (8), 1055-62.
31. Ying, Y. L.; Wang, H. Y.; Sutherland, T. C.; Long, Y. T., Monitoring of an ATP-binding aptamer and its conformational changes using an alpha-hemolysin nanopore. *Small* **2011,** *7* (1), 87-94.
32. Li, N., Reversible regulation of aptamer activity with effector-responsive hairpin oligonucleotides. *J. Lab. Autom.,* **2013,** *18* (1), 77-84.

33. Apps, M. G.; Choi, E. H.; Wheate, N. J., The state-of-play and future of platinum drugs. *Endocr. Relat. Cancer,* **2015,** *22* (4), R219-33.
34. Lakhin, A. V.; Tarantul, V. Z.; Gening, L. V., Aptamers: problems, solutions and prospects. *Acta Naturae,* **2013,** *5* (4), 34-43.
35. Cao, Z.; Tong, R.; Mishra, A.; Xu, W.; Wong, G. C.; Cheng, J.; Lu, Y., Reversible cell-specific drug delivery with aptamer-functionalized liposomes. *Angew. Chem. Int. Ed. Engl.,* **2009,** *48* (35), 6494-8.
36. Shangguan, D.; Tang, Z.; Mallikaratchy, P.; Xiao, Z.; Tan, W., Optimization and modifications of aptamers selected from live cancer cell lines. *ChemBioChem* **2007,** *8* (6), 603-6.
37. Bagalkot, V.; Farokhzad, O. C.; Langer, R.; Jon, S., An aptamer-doxorubicin physical conjugate as a novel targeted drug-delivery platform. *Angew. Chem. Int. Ed. Engl.,* **2006,** *45* (48), 8149-52.
38. Tuerk, C.; Gold, L., Systematic evolution of ligands by exponential enrichment: RNA ligands to bacteriophage T4 DNA polymerase. *Science* **1990,** *249* (4968), 505-10.
39. Keefe, A. D.; Pai, S.; Ellington, A., Aptamers as therapeutics. *Nat. Rev. Drug Discov.,* **2010,** *9* (7), 537-50.
40. Kaur, H.; Bruno, J. G.; Kumar, A.; Sharma, T. K., Aptamers in the Therapeutics and Diagnostics Pipelines. *Theranostics* **2018,** *8* (15), 4016-32.
41. Kumar Kulabhusan, P.; Hussain, B.; Yuce, M., Current Perspectives on Aptamers as Diagnostic Tools and Therapeutic Agents. *Pharmaceutics* **2020,** *12* (7).
42. Gopinath, S. C., Anti-coagulant aptamers. *Thromb. Res.,* **2008,** *122* (6), 838-47.
43. Bock, L. C.; Griffin, L. C.; Latham, J. A.; Vermaas, E. H.; Toole, J. J., Selection of single-stranded DNA molecules that bind and inhibit human thrombin. *Nature* **1992,** *355* (6360), 564-6.
44. Dinis Ano Bom, A. P.; da Costa Neves, P. C.; Bonacossa de Almeida, C. E.; Silva, D.; Missailidis, S., Aptamers as Delivery Agents of siRNA and Chimeric Formulations for the Treatment of Cancer. *Pharmaceutics* **2019,** *11* (12).
45. Guo, P.; Zhang, C.; Chen, C.; Garver, K.; Trottier, M., Inter-RNA interaction of phage phi29 pRNA to form a hexameric complex for viral DNA transportation. *Mol. Cell,* **1998,** *2* (1), 149-55.
46. Afonin, K. A.; Viard, M.; Koyfman, A. Y.; Martins, A. N.; Kasprzak, W. K.; Panigaj, M.; Desai, R.; Santhanam, A.; Grabow, W. W.; Jaeger, L.; Heldman, E.; Reiser, J.; Chiu, W.; Freed, E. O.; Shapiro, B. A., Multifunctional RNA nanoparticles. *Nano Lett.,* **2014,** *14* (10), 5662-71.
47. Zhao, N., Bagaria, H. G., Wong, M. S., Zu, Y., A nanocomplex that is both tumor cell-selective and cancer gene-specific for anaplastic large cell lymphoma. *J. Nanobiotechnology,* **2011,** *9*.
48. Powell, D.; Chandra, S.; Dodson, K.; Shaheen, F.; Wiltz, K.; Ireland, S.; Syed, M.; Dash, S.; Wiese, T.; Mandal, T.; Kundu, A., Aptamer-functionalized hybrid nanoparticle for the treatment of breast cancer. *Eur. J. Pharm. Biopharm.,* **2017,** *114*, 108-18.
49. Li, N.; Ebright, J. N.; Stovall, G. M.; Chen, X.; Nguyen, H. H.; Singh, A.; Syrett, A.; Ellington, A. D., Technical and biological issues relevant to cell typing with aptamers. *J. Proteome Res.,* **2009,** *8* (5), 2438-48.
50. Panigaj, M., Reiser, J., Aptamer guided delivery of nucleic acid-based nanoparticles. *DNA and RNA Nanotech.,* **2015,** *2*, 42-52.
51. Yan, W.; Tao, M.; Jiang, B.; Yao, M.; Jun, Y.; Dai, W.; Tang, Z.; Gao, Y.; Zhang, L.; Chen, X.; Wang, Q. L., Overcoming Drug Resistance in Colon Cancer by Aptamer-Mediated Targeted Co-Delivery of Drug and siRNA Using Grapefruit-Derived Nanovectors. *Cell Physiol. Biochem.,* **2018,** *50* (1), 79-91.
52. Wilner, S. E.; Wengerter, B.; Maier, K.; de Lourdes Borba Magalhaes, M.; Del Amo, D. S.; Pai, S.; Opazo, F.; Rizzoli, S. O.; Yan, A.; Levy, M., An RNA alternative to

human transferrin: a new tool for targeting human cells. *Mol. Ther. Nucleic Acids,* **2012,** *1*, e21.
53. Majidi Zolbanin, N.; Jafari, R.; Majidi, J.; Atyabi, F.; Yousefi, M.; Jadidi-Niaragh, F.; Aghebati-Maleki, L.; Shanehbandi, D.; Soltani Zangbar, M. S.; Nayebi, A. M., Targeted Co-Delivery of Docetaxel and cMET siRNA for Treatment of Mucin1 Overexpressing Breast Cancer Cells. *Adv. Pharm. Bull.,* **2018,** *8* (3), 383-93.
54. Nabavinia, M. S.; Gholoobi, A.; Charbgoo, F.; Nabavinia, M.; Ramezani, M.; Abnous, K., Anti-MUC1 aptamer: A potential opportunity for cancer treatment. *Med. Res. Rev.,* **2017,** *37* (6), 1518-39.
55. Jadidi-Niaragh, F.; Atyabi, F.; Rastegari, A.; Mollarazi, E.; Kiani, M.; Razavi, A.; Yousefi, M.; Kheshtchin, N.; Hassannia, H.; Hadjati, J.; Shokri, F., Downregulation of CD73 in 4T1 breast cancer cells through siRNA-loaded chitosan-lactate nanoparticles. *Tumour Biol.,* **2016,** *37* (6), 8403-12.
56. Raja, M. A.; Katas, H.; Jing Wen, T., Stability, Intracellular Delivery, and Release of siRNA from Chitosan Nanoparticles Using Different Cross-Linkers. *PLoS One,* **2015,** *10* (6), e0128963.
57. Fontana, F.; Liu, D.; Hirvonen, J.; Santos, H. A., Delivery of therapeutics with nanoparticles: what's new in cancer immunotherapy? *Wiley Interdiscip. Rev. Nanomed. Nanobiotechnol.,* **2017,** *9* (1).
58. Shieh, Y. A.; Yang, S. J.; Wei, M. F.; Shieh, M. J., Aptamer-based tumor-targeted drug delivery for photodynamic therapy. *ACS Nano,* **2010,** *4* (3), 1433-42.
59. Perrone, R.; Butovskaya, E.; Lago, S.; Garzino-Demo, A.; Pannecouque, C.; Palu, G.; Richter, S. N., The G-quadruplex-forming aptamer AS1411 potently inhibits HIV-1 attachment to the host cell. *Int. J. Antimicrob. Agents,* **2016,** *47* (4), 311-6.
60. De Cian, A.; Lacroix, L.; Douarre, C.; Temime-Smaali, N.; Trentesaux, C.; Riou, J. F.; Mergny, J. L., Targeting telomeres and telomerase. *Biochimie,* **2008,** *90* (1), 131-55.
61. Wan, Y.; Wang, L.; Zhu, C.; Zheng, Q.; Wang, G.; Tong, J.; Fang, Y.; Xia, Y.; Cheng, G.; He, X.; Zheng, S. Y., Aptamer-Conjugated Extracellular Nanovesicles for Targeted Drug Delivery. *Cancer Res.,* **2018,** *78* (3), 798-808.
62. Li, S.; Pei, Y.; Wang, W.; Liu, F.; Zheng, K.; Zhang, X., Extracellular nanovesicles-transmitted circular RNA has_circ_0000190 suppresses osteosarcoma progression. *J. Cell Mol. Med.,* **2020,** *24* (3), 2202-14.
63. Sayari, E.; Dinarvand, M.; Amini, M.; Azhdarzadeh, M.; Mollarazi, E.; Ghasemi, Z.; Atyabi, F., MUC1 aptamer conjugated to chitosan nanoparticles, an efficient targeted carrier designed for anticancer SN38 delivery. *Int. J. Pharm.,* **2014,** *473* (1-2), 304-15.
64. Ebrahimnejad, P.; Dinarvand, R.; Sajadi, A.; Jaafari, M. R.; Nomani, A. R.; Azizi, E.; Rad-Malekshahi, M.; Atyabi, F., Preparation and in vitro evaluation of actively targetable nanoparticles for SN-38 delivery against HT-29 cell lines. *Nanomedicine* **2010,** *6* (3), 478-85.
65. Farokhzad, O. C.; Jon, S.; Khademhosseini, A.; Tran, T. N.; Lavan, D. A.; Langer, R., Nanoparticle-aptamer bioconjugates: a new approach for targeting prostate cancer cells. *Cancer Res.,* **2004,** *64* (21), 7668-72.
66. Kolovskaya, O. S.; Zamay, T. N.; Zamay, G. S.; Babkin, V. A.; Medvedeva, E. N.; Neverova, N. A.; Kirichenko, A. K.; Zamay, S. S.; Lapin, I. N.; Morozov, E. V.; Sokolov, A. E.; Narodov, A. A.; Fedorov, D. G.; Tomilin, F. N.; Zabluda, V. N.; Alekhina, Y.; Lukyanenko, K. A.; Glazyrin, Y. E.; Svetlichnyi, V. A.; Berezovski, M. V.; Kichkailo, A. S., Aptamer-Conjugated Superparamagnetic Ferroarabinogalactan Nanoparticles for Targeted Magnetodynamic Therapy of Cancer. *Cancers (Basel),* **2020,** *12* (1).
67. Ogasawara, D.; Hachiya, N. S.; Kaneko, K.; Sode, K.; Ikebukuro, K., Detection system based on the conformational change in an aptamer and its application to simple bound/free separation. *Biosens. Bioelectron.,* **2009,** *24* (5), 1372-6.
68. Srivithya, V.; Roun, H.; Sekhar Babu, M.; Jae Hyung, P.; Sung Ha, P., Aptamer-conjugated DNA nano-ring as the carrier of drug molecules. *Nanotechnology,* **2018,** *29* (9), 095602.

69. Del Grosso, E.; Ragazzon, G.; Prins, L. J.; Ricci, F., Fuel-Responsive Allosteric DNA-Based Aptamers for the Transient Release of ATP and Cocaine. *Angew. Chem. Int. Ed. Engl.,* **2019,** *58* (17), 5582-6.
70. Golubkov, V. S.; Chekanov, A. V.; Cieplak, P.; Aleshin, A. E.; Chernov, A. V.; Zhu, W.; Radichev, I. A.; Zhang, D.; Dong, P. D.; Strongin, A. Y., The Wnt/planar cell polarity protein-tyrosine kinase-7 (PTK7) is a highly efficient proteolytic target of membrane type-1 matrix metalloproteinase: implications in cancer and embryogenesis. *J. Biol. Chem.,* **2010,** *285* (46), 35740-9.
71. Zhang, Z.; Ali, M. M.; Eckert, M. A.; Kang, D. K.; Chen, Y. Y.; Sender, L. S.; Fruman, D. A.; Zhao, W., A polyvalent aptamer system for targeted drug delivery. *Biomaterials* **2013,** *34* (37), 9728-35.
72. Ozalp, V. C.; Schafer, T., Aptamer-based switchable nanovalves for stimuli-responsive drug delivery. *Chemistry* **2011,** *17* (36), 9893-6.
73. Golubkov, V. S.; Prigozhina, N. L.; Zhang, Y.; Stoletov, K.; Lewis, J. D.; Schwartz, P. E.; Hoffman, R. M.; Strongin, A. Y., Protein-tyrosine pseudokinase 7 (PTK7) directs cancer cell motility and metastasis. *J. Biol. Chem.,* **2014,** *289* (35), 24238-49.
74. Zhu, C. L.; Lu, C. H.; Song, X. Y.; Yang, H. H.; Wang, X. R., Bioresponsive controlled release using mesoporous silica nanoparticles capped with aptamer-based molecular gate. *J. Am. Chem. Soc.,* **2011,** *133* (5), 1278-81.

Chapter 2: Synthetic strategies for HNO delivery

2.1 Introduction

The delivery of nitroxyl (HNO) has been of interest in pharmaceutical sciences since the suggestion that this protonated, one electron reduced form of nitric oxide with such distinct chemical activity might be produced endogenously.[1, 2] However, is still unknown whether the biological activity of nitroxyl is part of a normal endogenous signalling system, and its mode of action has yet to be determined.[3] The chemical behaviour of HNO was described in depth in section *1.2.1.2* and as such it was determined that any HNO delivery agent designed as a therapeutic agent would have to donate the nitroxyl *in situ*.

Current methods of donating HNO rely on donors which decompose spontaneously to release HNO with other small molecules. The most common donor of this type is Angeli's salt **2.1** (Figure 13), which decomposes in aerobic, neutral and slightly alkaline conditions to generate HNO, NO_2^- and •NO.[2, 3] Decomposition was determined to be first order at pH 4 – 8 with a rate constant of $4 - 5 \times 10^{-3}$ s^{-1} at 37 ˚C. The role of oxygen was determined to be important in accelerating the release of HNO,[4] making this donor a more attractive prospect for therapeutic strategies. However, the release of •NO as a radical species could cause a cytotoxic effect, limiting the possibilities of the salt as an effective treatment. Despite this effect, *in vivo* investigations have been carried out using Angeli's salt – showing that vasodilation still occurs upon treatment with the donor.[5] This study also confirmed the tolerance of cells to Angeli's salt with a low risk of carcinogenesis and an LD_{50} > 130 mg kg^{-1}. However, the decomposition rate was low, meaning slow donation of HNO. In pharmacology this slow release could cause problems if the body cleared the drug moiety before full release of the nitroxyl. This would mean a faster, more controlled release would be optimal in such cases.

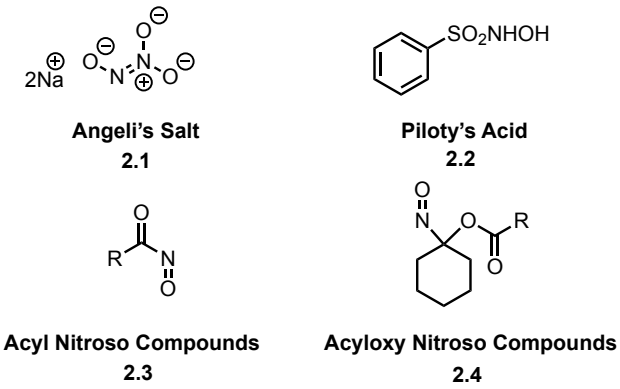
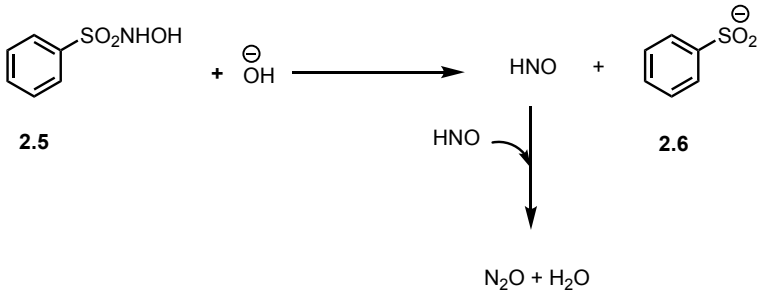


Figure 13 General structures of known HNO donors

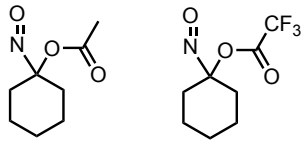
Another common choice for donation of HNO is the use of Piloty's acid **2.2**, a sulfonamide derivative which releases nitroxyl under basic conditions with a rate constant of 1.8×10^{-3} s^{-1} at 37 °C, pH 13 (Scheme 3).[6] However, at neutral pH and under aerobic conditions this decomposition is much slower, and Feelisch[5] and co-workers demonstrated the release of nitric oxide rather than HNO at pH 7.4 and 8.0. The same investigation also showed the vaso-relaxant activity of Piloty's acid was weaker than that of nitric oxide or Angeli's salt.[5] The high pH required means that other HNO donors are more suited to therapeutic activity.



Scheme 3 Self-decomposition of Piloty's acid as reported by Piloty[7] and amended by Angeli.[8] Scheme adapted from Bonner and Ko[6]

Acyloxy nitroso complexes are a more modern HNO donor type with the general structure **2.4** shown in Figure 13, designed for greater control of nitroxyl release.[4] A number of compounds with this general structure have been tested for HNO release, including 1-

nitrosocyclohexylacetate **2.7** and 1-nitrosocyclohexyl trifluoroacetate **2.8** which hydrolyse to release nitroxyl (Figure 14).[4, 7] Of these, the trifluoroacetate analogue **2.8** was determined to release HNO rapidly in buffer at neutral pH, making this an attractive therapeutic prospect in comparison to Angeli's salt. When tested on rat aortic rings, both **2.7** and **2.8** showed similar vasodilation to control tests with Angeli's salt but had a higher EC_{50}.[4]



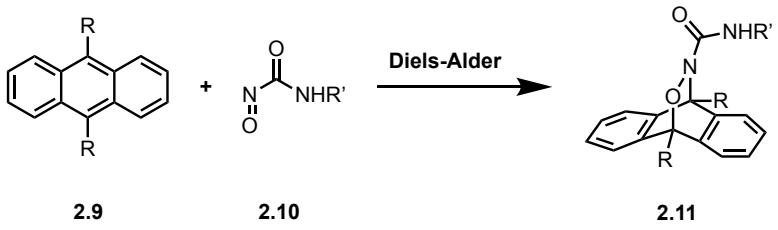
2.7 **2.8**

Figure 14 Acyloxy nitroso complexes tested for HNO release

In contrast to the acyloxy species, acyl nitroso compounds with the general structure **2.3** are more highly reactive and unstable, breaking down easily in aqueous conditions to release HNO.[4] Toscano and co-workers demonstrated the lifetime of the acyl nitroso species to be in the order of 1 ms in organic solvents, using time-resolved infrared spectroscopy.[8] Such compounds are typically formed from the oxidation of *N*-acyl hydroxylamine derivatives by the use of various oxidising reagents such as Swern compounds and tetra-alkyl ammonium periodate.[4, 9] Adaptions of this were designed by Whiting[10] to avoid the need for toxic Swern-based oxidants and also by King and co-workers to trap the acyl nitroso with 1,3-dienes to give Diels-Alder cycloadducts.[10, 11] King developed *N*-hydroxyurea derived acyl nitroso-9,10-dimethylanthracene cycloadducts which could be photo-irradiated to initiate retro Diels-Alder decomposition and regeneration of the acyl nitroso, which could release nitroxyl upon nucleophilic substitution with water. [12]

The Diels-Alder cycloadducts formed from *N*-hydroxyureas and 1,3-dienes became the starting point for many other investigations into HNO release, due to the appealing level of

control derived from the photo-activation and the biologically relevant conditions it can be performed in. Both King's group[13] and Miyata[12, 14] have developed this work further, using anthracene derivatives as the diene and functionalising the hydroxyurea based dienophile to enhance the control of the retro Diels-Alder reaction (Scheme 4).



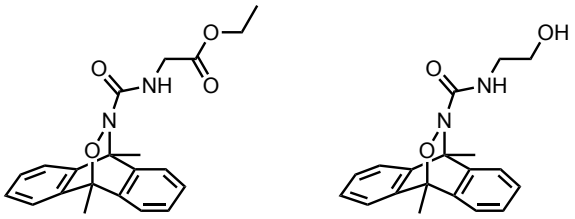
2.9 **2.10** **2.11**

Scheme 4 General scheme for the cycloaddition of anthracenes as 1,3-dienes and acyl nitroso species

Careful adjustments of the acyl nitroso moiety allowed greater stability of the cycloadduct, Adachi *et al*.[15] found that introducing a nitroaryl group improved the thermal stability of the HNO donor and also increased the susceptibility of the adduct to photo-irradiation derived decomposition. This decomposition was determined not to be a formal photochemical process, due to the [4 + 2] electrocyclic reaction being photochemically forbidden according to Woodward-Hoffmann rule.[15, 16] When considering Woodward-Hoffmann rules and the Diels-Alder reaction, a preservation of C_s symmetry along the entire reaction path is considered necessary.[12] When any substitution of the diene or the dienophile occurs, this symmetry is lost and formally the reaction should not proceed. However, ample evidence points to the contrary for this case as substituted dienes and dienophiles frequently undergo Diels-Alder cycloadditions. The mechanism of the decomposition is still undetermined but the retro Diels-Alder was found to be roughly correlated with the absorption maximum and extinction coefficient of the compounds, implying the photo-absorption was critical.[17, 18]

Modifications of the R groups at the 9- and 10-positions of the anthracene derivative **2.9** also improved the water solubility of the cycloadduct. When the Diels-Alder cycloadducts were originally investigated 9,10-dimethyl anthracene was used as the diene of choice, and

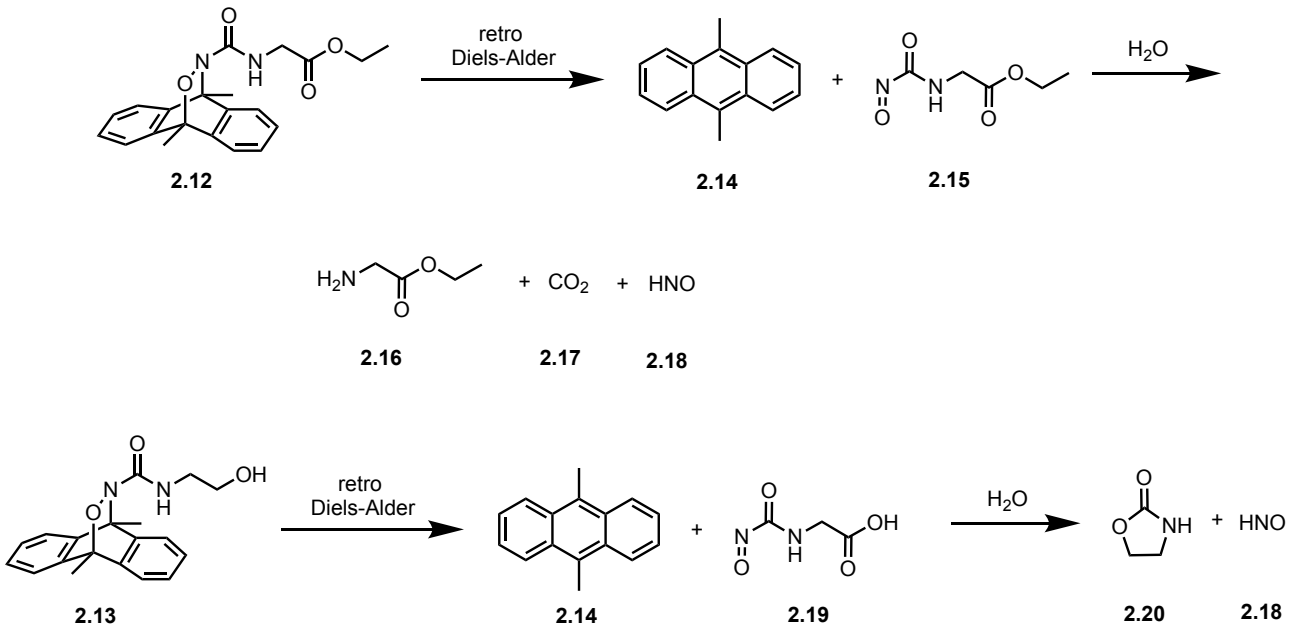
solubility in aqueous media was adjusted only by the R groups of the nitrogen-containing functionality attached to the dienophile.[18] The water solubility of the cycloadduct was improved by the use of the *N*-hydroxyureas of ethanolamine and the HNO release properties were also made evident by thermal decomposition of the cycloadduct formed using the *N*-hydroxyurea of ethyl glycine (Figure 15).



2.12 **2.13**

Figure 15 Second generation cycloadducts designed by King and co-workers, 2004.[17]

The method of releasing HNO was determined to differ slightly upon retro Diels-Alder decomposition. Whilst the ester-based acyl nitroso species was found to release HNO by nucleophilic substitution, decomposing in a first order manner ($k = 1.33 \times 10^{-2}$ min^{-1}), cycloadduct **2.13** decomposed to the acyl nitroso which was trapped by an internal nucleophilic hydroxyl group (Scheme 5).[12]



*Scheme 5 Retro Diels-Alder pathways of compounds **2.12** and **2.13** adapted from Miyata and co-workers[13]*

Miyata chose to investigate making changes to both the diene and dienophile to improve the water solubility and efficacy of HNO release in this style of cycloadduct.[12, 14] In a similar manner to King's work, the first point of variation was at the acyl nitroso dienophile; choosing to add aromaticity to improve stability. By adding aromatic groups to the nitroaryl moiety, a small library of cycloadducts **2.21** – **2.26** was developed to show the varying stability of the Diels-Alder constructs (Figure 16).

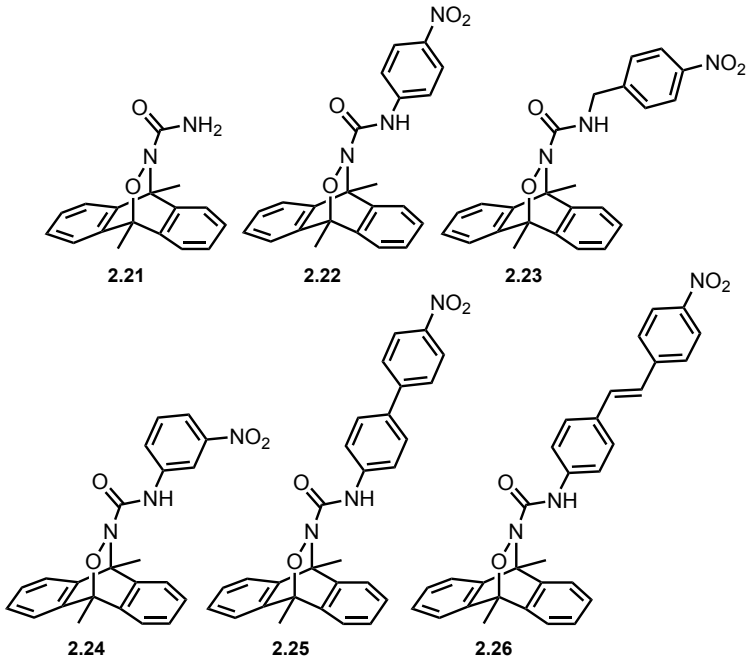
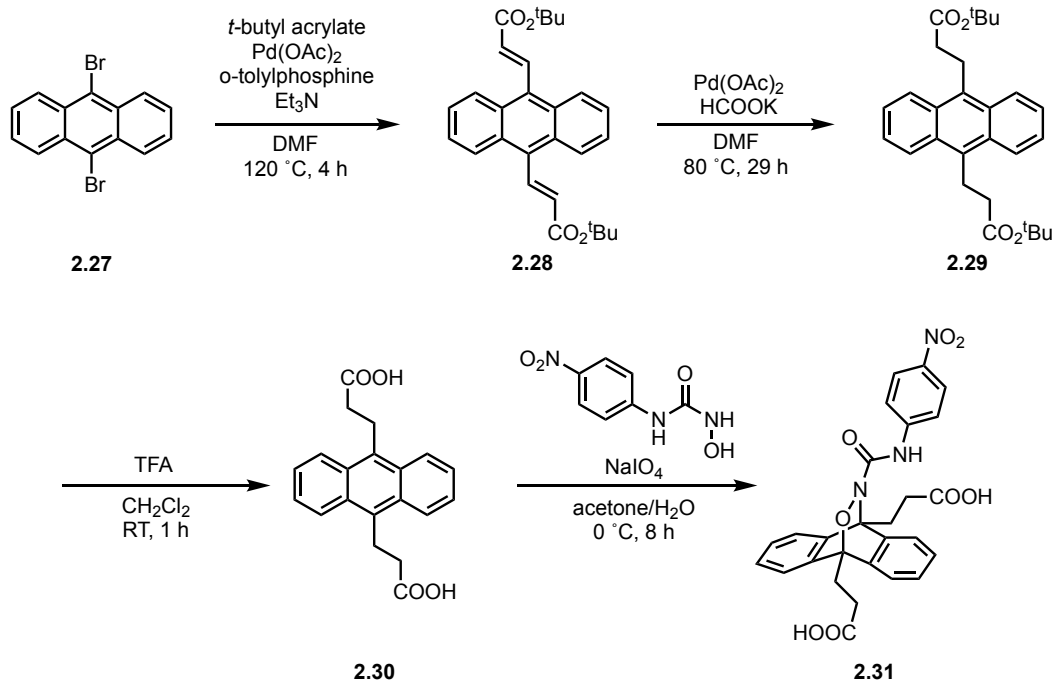


Figure 16 Library of aromatic functionalised acyl nitroso components of the Diels-Alder cycloadducts

Miyata and co-workers discovered that while **2.22** was capable of undergoing a photo-induced retro Diels-Alder reaction to release HNO, the cycloadduct was unstable even in the absence of light at room temperature.[12] The more thermally stable cycloadducts **2.21** and **2.23** were not susceptible to retro Diels-Alder by photo-irradiation and **2.24** showed similar thermal stability to that of **2.22** with significantly less HNO release. The group deduced from these results that the stability was dependent on the steric hindrance of the substituent and as such developed the more sterically unhindered conjugated groups **2.25** and **2.26**.[13] The stability of these components in the dark were an improvement on **2.22** and the HNO release from **2.25** was determined to be of nearly equal capacity to that of Angeli's salt. The group also determined the maximum absorption wavelength of the cycloadducts to be 324 nm for **2.22** and 337 nm for cycloadduct **2.25**, giving an opportunity for UVA light to be used to activate the photo-induced retro Diels-Alder.[19]

In order to both improve the water solubility of the cycloadducts mentioned in their 2008 work and to reduce the cytotoxicity of the anthracene derivative, Miyata's group further

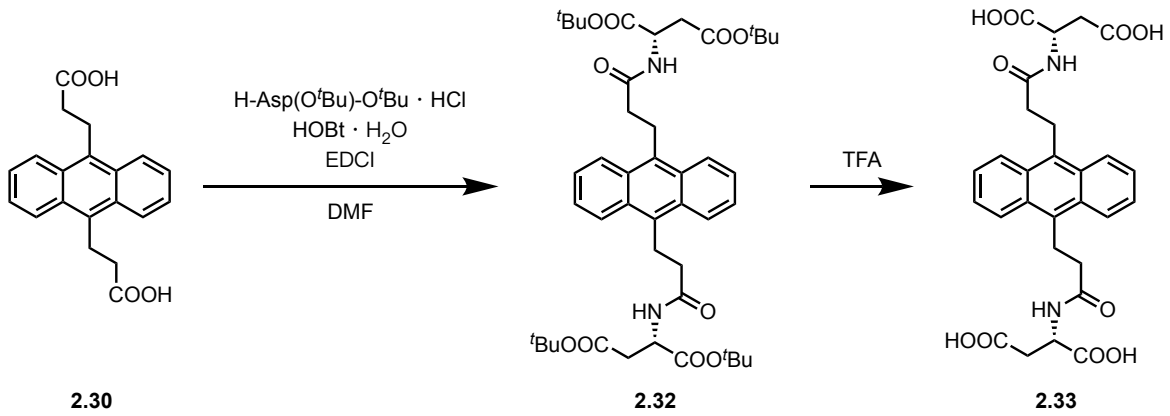
functionalised the 9- and 10-positions of the anthracene diene.[13] The introduction of symmetric 9,10-dialkyl functionalities via palladium-catalysed couplings gave rise to water-soluble anthracene derivatives suitable for Diels-Alder cycloaddition.[13] The use of the Heck reaction here was used by Miyata and co-workers (Scheme 6) to produce the anthracene derivative **2.30**.



*Scheme 6 Miyata's scheme for the synthesis of water-soluble cycloadduct **2.31***

Compared to the cycloadduct **2.22**, derivative **2.31** was found to be soluble at over 100 μM in buffer solutions containing 0.1% DMSO. The addition of carboxylic acid moieties increased the hydrophilicity of the compound and was hypothesised to be more easily excreted, and as such less toxic via metabolic bioactivation.[14] The group determined that the solvent used had an effect on the molecule released upon photo-irradiation too, showing release of nitric oxide in apolar solvents but HNO when performed in aqueous conditions. It was considered that the NO release was due to photo-induced homolytic cleavage but that in the presence of water, nucleophilic attack could lead to the release of HNO.[14]

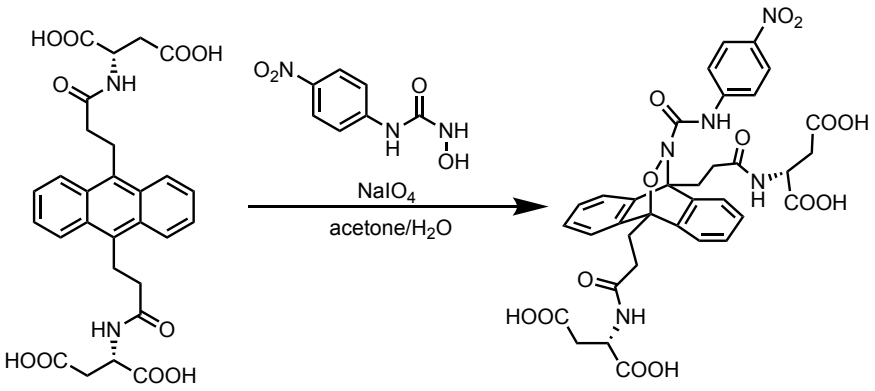
Miyata and co-workers looked to further decorate the anthracene derived diene with four carboxylate groups by a condensation reaction of anthracene derivative **2.30** and protected aspartic acid (Scheme 7) to give the highly hydrophilic **2.33**.[14]



2.30 **2.32** **2.33**

Scheme 7 Further functionalisation of anthracene derivatives with aspartic acid as demonstrated by Miyata and co-workers.[13]

The Diels-Alder cycloadduct of diene **2.33** was found to be soluble in 50 mM Tris buffer (pH 7.5) and the HNO release was found to be accelerated by photo-irradiation (Scheme 8).[14] The group determined that the cycloadduct **2.34** was less stable than that of the previous Diels-Alder product **2.30**, undergoing retro Diels-Alder even in dark conditions. The instability of the cycloadduct **2.34** was considered to be partially due to the linker length between the carboxyl group and the diene moiety.[12] From these results, the group deduced that the intramolecular interaction of the carboxylic acid group with the heterocyclic section of the molecule could lead to the increased stability of **2.31**.



2.33 **2.34**

*Scheme 8 Diels-Alder cycloaddition of the water-soluble anthracene derivative **2.33** as demonstrated by Miyata and co-workers.[13]*

Finally, Miyata looked into the effect of retro Diels-Alder induced HNO release on cellular CGRP levels in cells, in particular the A549 human alveolar basal epithelial carcinoma cells due to their production of CGRP.[13] The group measured the increase of CGRP in cells treated with cycloadduct **2.31** and Angeli's salt and determined it was due to HNO release as the increase was negated when an HNO trap was used for control experiments.

This work by Miyata has highlighted both the potential of these cycloadduct HNO donor systems and the limitations discovered so far. Incorporation of these systems into larger supramolecular systems could give an interesting method of stabilising the cycloadducts and as such has become the focus of the aims of this project.

Supramolecular chemistry will play a role within each research theme of this thesis and is defined as the chemistry of non-covalent interactions forming molecular assemblies.

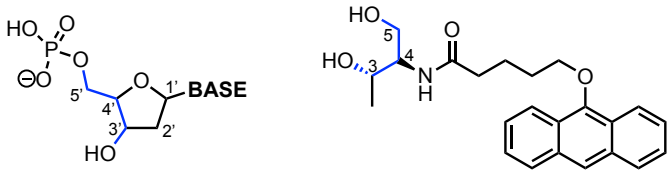
2.2 Aim

Recent work from the Miyata group[14],[12, 13] described an HNO donating compound that is capable of releasing HNO upon photoactivation. It was hypothesised that the limitations of this work could be overcome by incorporating the compound into a larger system which could improve the substrates stability and use under physiological systems. Whilst coupling aspartic acid residues to the anthracene gave the unstable cycloadduct **2.34**, it was thought possible that functionalisation with different moieties could improve the overall stability. Furthermore, incorporating the cycloadduct within polymeric or oligomeric structures would improve the directing ability of the overall construct, leading to better tolerance of physiological environments and improved site-specific targeting. Aptamers have been shown by many in recent decades to aid targeting of drugs, as will be discussed in more detail in Chapter 5, and make a strong case for using DNA as a vector system.[20, 21] By designing anthracene moieties with alcohol functional groups, a wide range of further modification would be achievable, to allow the conjugation of monomers for polymerisation, or solid-phase DNA synthesis for example.

As such, the primary aim of the project was to develop a more stable anthracene-derived cycloadduct that was also capable of further functionalisation for DNA or polymer incorporation. In this respect, it was important for the cycloadduct or its precursor to have an appropriate functional group to allow conjugation to the desired targeting vector.

2.3 Design of an anthracene-derived diene

The Tucker group has previously incorporated anthracene into DNA strands using phosphoramidite chemistry for diagnostic sensing.[20, 22-25] The use of threoninol-coupled anthracene derivatives gives an unsymmetrical diol suitable for solid-phase DNA synthesis (Figure 17).



2.35 **2.36**

Figure 17 Similarities in the three-carbon linker of the two oxygen components in a typical DNA phosphate sugar backbone and a threoninol-anthracene derivative

The challenge when considering the current method developed by the Tucker group[24, 26] of incorporating anthracene into a DNA construct is that the symmetry around the central ring of the anthracene moiety is broken, leading to two possible regioisomers when undergoing the Diels-Alder reaction with an acyl nitroso dienophile (Figure 18). This would cause an issue when characterising the cycloadducts themselves, as it was envisioned that separation of the hemi-aminal **2.37** and acetal **2.38** could be complex and one might prove more accessible for the retro Diels-Alder than the other.

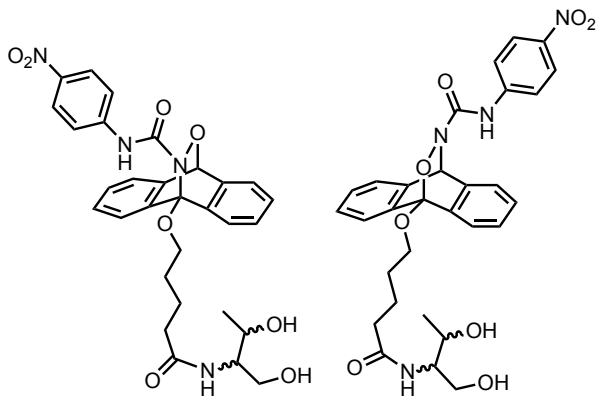


Figure 18 Two regioisomers formed from the Diels-Alder reaction on an anthracene-derived tag showing the hemi-aminal (left) and acetal (right) possibilities

As such, the synthetic approach was split into multiple components: first to design and make symmetrical anthracene derivatives before attempting to de-symmetrise these for solid-phase DNA synthesis or to decorate with monomers for polymerisation (Figure 19a); alternatively to synthesise asymmetric alkoxy-anthracene tagged phosphoramidites for solid-phase DNA synthesis (Figure 19b, discussed in Chapter 3); to synthesise hydroxyurea derivatives suitable for oxidation to the acyl nitroso form (Figure 19c); and finally to make stable Diels-Alder cycloadducts by combining these anthracene and hydroxyurea components (Figure 19d).

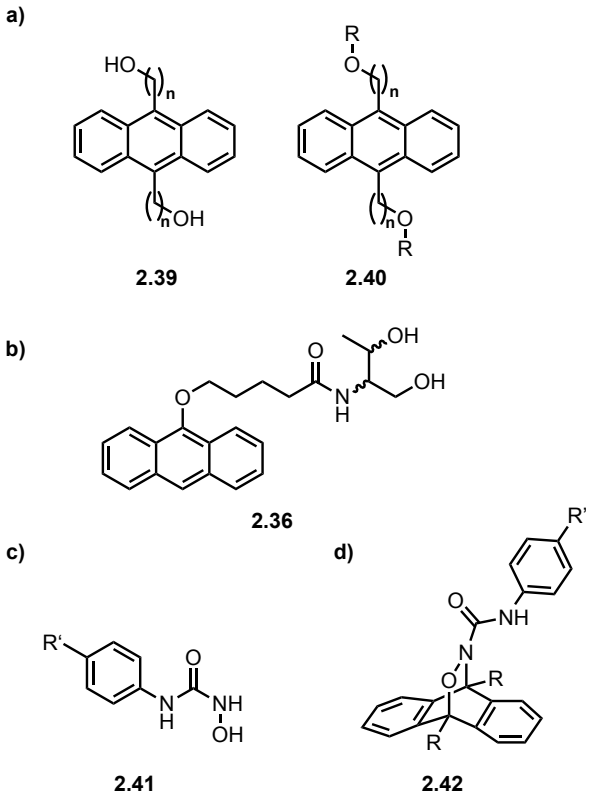
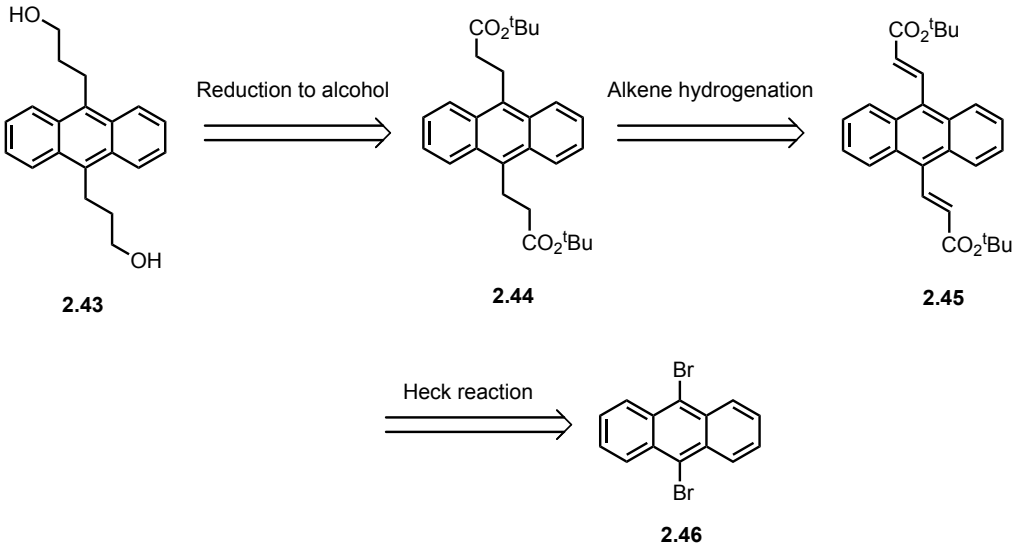


Figure 19 Synthetic aims of the project where a and b show the anthracene-derived dienes where R = phosphoramidites, monomer species or polymer species and n = 1 or 3; c shows the dienophile precursor where R' = NO_2 or 4-nitrophenol and d shows the cycloadduct formed from the dienes in 18a/b.

Following successful synthesis of the diol species of anthracene derivatives **2.36, 2.39, 2.40**, the project aim was to incorporate the diene into either a polymer or an oligonucleotide. For this purpose, a number of monomer conjugations **2.60 – 2.61** were designed to allow for polymerisation (see section 2.7). To incorporate the anthracene **2.36** into an oligonucleotide, the aim was to selectively protect one alcohol of the diol to allow reactions to be carried out on the other. The remaining alcohol functional group could then be phosphitylated to give a phosphoramidite suitable for solid-phase DNA synthesis.

2.4 Synthesis of 9-,10-difunctionalised anthracene 2.43

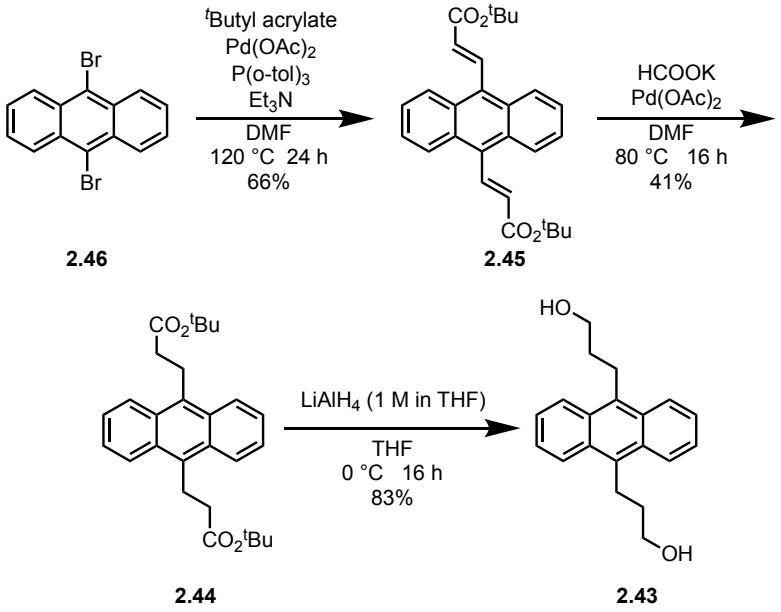
Utilising key methodology from both Miyata[13] and King,[19] dipropanol **2.43** was targeted for synthesis (Scheme 9).



2.43 **2.44** **2.45** **2.46**

Scheme 9 Retrosynthetic analysis of Miyata and King's work to create a di-propanol anthracene derivative

King and co-workers mentioned that they synthesised the dipropanol derivative **2.43** in an attempt to design more water-soluble anthracene systems.[13] However, the work was not continued into the formation of Diels-Alder cycloadducts and the water solubility of the compound not discussed any further in their report. Miyata also used this strategy to design the dipropanoic acid derivative **2.44**, using this as the diene for their work into photo-activatable HNO donors, using palladium-catalysed cross-coupling Heck reactions to create the un-saturated alkyl ester **2.45** from the commercially available 9,10-dibromoanthracene **2.46**.[13] The hydrogenation of **2.46** to give the saturated alkyl derivative **2.44** was also documented by Miyata, using potassium formate as a safer alternative to hydrogen gas.[13] Following the literature procedure from Miyata and co-workers,[13] the saturated alkyl ester **2.44** was synthesised and subsequently reduced to the alcohol **2.46** to create the first diene designed for potential HNO donation (Scheme 10).



Scheme 10 3-step synthesis of diol functionalised anthracene 2.43

Bis-olefination of 9,10-dibromoanthracene with tert-butyl acrylate was followed by a selective di-reduction of the di-α,β-unsaturated ester **2.44** from ester **2.45**. Initially, the reduction proved difficult, with the unsaturated ester **2.44** obtained in reasonable yield but impure, and its separation from the starting material **2.45** proving impossible. Furthermore, the reaction did not go to completion even with longer reaction times and higher catalyst loading (entries 2-3, Table 1). However, rather than move to a harsher hydrogen source, the potassium formate was subsequently recrystallised immediately prior to use which improved the yield by almost 100% to a moderate 41% (entry 4, Table 1). Whilst the reaction appeared to have gone to completion by ^{1}H NMR spectra, with the unsaturated alkene peaks in the vinyl region having disappeared, the yield was negatively affected in the purification step as the substrate tended to be poorly soluble in various column eluents (Ch_2Cl_2: MeOH, EtOAc: hexane, Pet. Ether: Et_2O). It was considered that the flexibility of the alcohol functional groups was too great to disrupt the π-stacking of the anthracene derivative **2.43**.

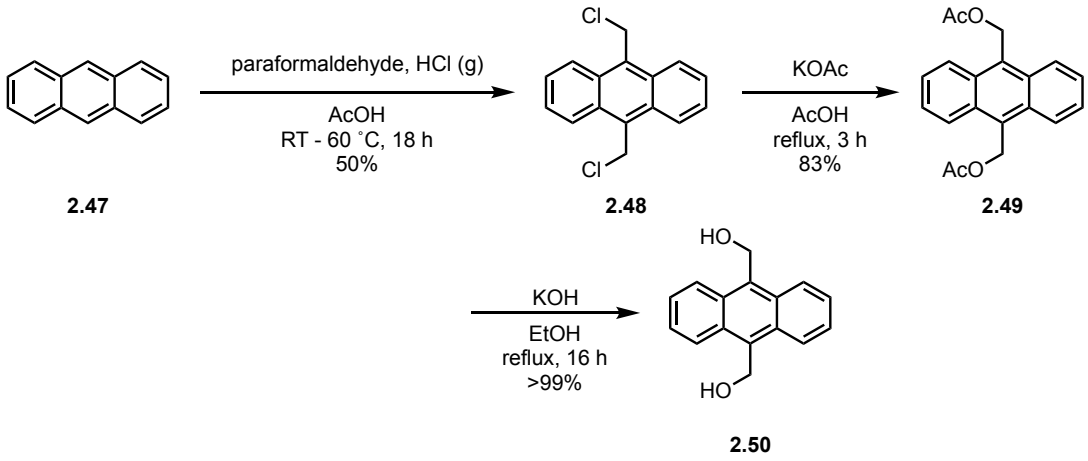
Table 1 Optimisation of reaction conditions for alkene hydrogenation

ENTRY	*CATALYST LOADING (%)*	*HCOOK PURIFICATION*	*REACTION TIME (H)*	*REACTION TEMP (ºC)*	*YIELD (%)*
1	*5*	*N/A*	*46*	*80*	*Impure – unable to separate from t-butanol)*
2	*10*	*N/A*	*30*	*80*	*23 (required 2 columns)*
3	*10*	*N/A*	*60*	*80*	*19*
4	*10*	*Recrystallisation from MeOH/Et_2O*	*17*	*80*	*41*

Ester **2.44** was then reduced to alcohol **2.43** using $LiAlH_4$ in a good 83% yield. The alcohol moiety was required to give two functional groups suitable for solid phase DNA synthesis. The solubility of this species was disappointing however, with the compound only soluble in DMSO or at low concentrations in THF, making the compound more difficult to work with.

2.5 Synthesis of 9,10-difunctionalised anthracene 2.50

In an attempt to improve the initial yield of the protected anthracene-derived diene as well as its overall solubility in common solvents, a different chain length was designed (**Error! Reference source not found.**). It was hoped that this shorter chain would be more soluble as the diol due to less flexibility of the greasy functional groups which could disrupt π-stacking of the aromatic rings. The placement of the methanol functional groups in the 9- and 10-positions of the anthracene was developed by Mattay and co-workers,[27] and this was used as the starting point for the synthetic design (Scheme 11).



*Scheme 11 Synthesis of dimethanol derivative **2.50** developed by Mattay and co-workers, 2008.[27]*

Chloro-methylation of pure anthracene was achieved by subjecting paraformaldehyde to gaseous HCl in acetic acid until it dissolved, then adding the anthracene to the resulting solution and heating for 16 hours. Although purification by recrystallisation from benzene has been reported;[28, 29] due to the potential carcinogenic risks of handling benzene, an alternative recrystallisation from chlorobenzene was performed to mitigate the risk. Mattay demonstrated an excellent 92% yield of the chloro-methylation through this purification strategy,[30] but the fair 50% yield of the bis-haloalkyl derivative **2.48** achieved using chlorobenzene was considered acceptable given its lower risk.

Originally, acetylation to prepare **2.49** was achieved by refluxing with sodium acetate in acetic acid for 6 hours, then stirring at room temperature for a further 5 days. The long reaction times and disappointing 26% yield meant this was quickly adapted to refluxing with potassium acetate for 3 hours to achieve an excellent yield of 83%.[31]

Subsequent basic deprotection of the acetyl group by potassium hydroxide gave the symmetrical diol **2.50** in quantitative yield. This anthracene derivative was more soluble than the 3-carbon chain alternative **2.43**, potentially due to the reduced flexibility of the alcohol chain disrupting the π-stacking of the aromatic groups.

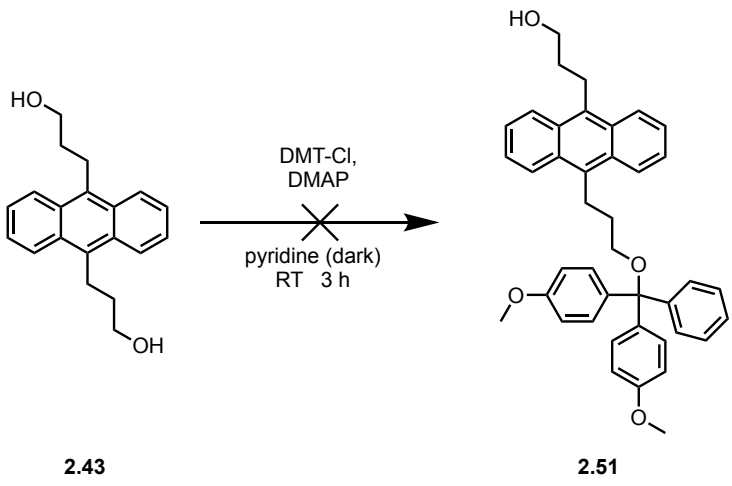
As such, two symmetrical anthracene derivatives **2.43** and **2.50** of differing solubility and alkyl chain length were prepared for future Diels-Alder based cycloadditions.

2.6 DMT protection of diols 2.43 and 2.50

The incorporation of nucleotide analogues into DNA strands using solid-phase DNA synthesis relies on the preparation of a diol and activation of one of the alcohol groups. The dimethoxy trityl (DMT) protecting group has been identified as an optimal intermediate in the synthesis of the required phosphoramidite precursors due to its preference for primary alcohols and its acid lability.[20, 26] The Tucker group has worked on incorporating anthracene derivatives into DNA using solid-phase synthesis over several years.[32, 33] To combine the incorporation of anthracene into oligomer strands via phosphoramidite chemistry with the symmetrical anthracene derivatives synthesised, diols **2.43** and **2.50** were subjected to DMT protection conditions, with the aims of selectively protecting one alcohol group and de-symmetrising the molecule.

2.6.1 DMT protection of anthracene-9,10-dipropan-1-ol

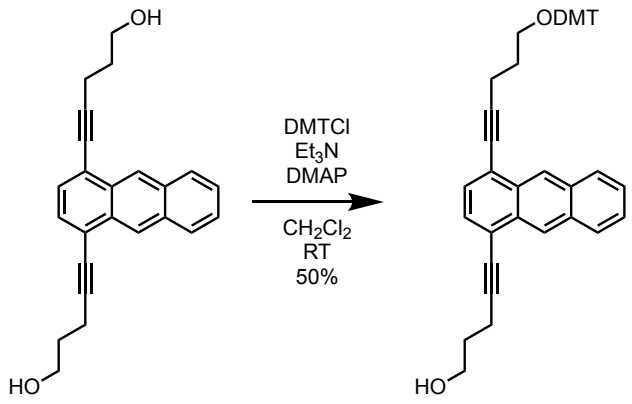
Diol **2.43** was treated with DMAP and 0.6 equivalents of DMT-Cl in the presence of excess base to selectively protect one alcohol functional group (Scheme 12).



Scheme 12 Attempted DMT protection of anthracene-9,10-dipropan-1-ol

When protecting deoxyribose sugars with DMT, the use of pyridine as a basic solvent is enough to ensure nucleophilic substitution of the primary alcohol. When the reaction was attempted using only DMT-Cl it only appeared to work on a small scale, with ^{1}H NMR spectroscopy showing the desired change in the aromatic region but fewer than 20 mg obtained each time, and the compound degrading upon attempts at purification.

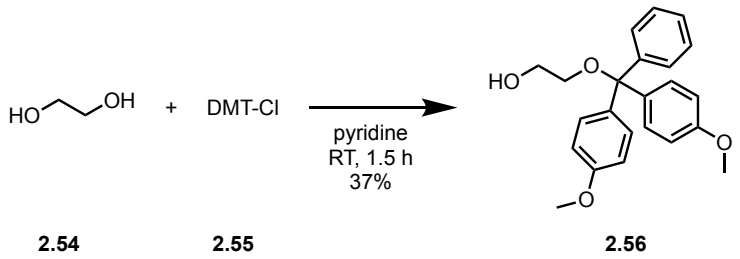
For non-symmetrical diol nucleotide analogues, the use of DMAP in addition to the pyridine is necessary to catalyse the selective tritylation of primary alcohols. This was found to yield the desired product, though upon purification by flash chromatography, the compound degraded to the starting material. As DMT protecting groups are known to be highly acid labile, it was thought that base doping all column solvents with 1% Et_3N would negate any risk of the silica causing the deprotection, but this proved unsuccessful. Work by Häner and co-workers showed successful desymmetrisation of 1,4-anthracene derived diol **2.52** using a combination of DMAP and triethylamine but this approach did not work on this 9,10-functionalised system (Scheme 13).[34]



2.52 **2.53**

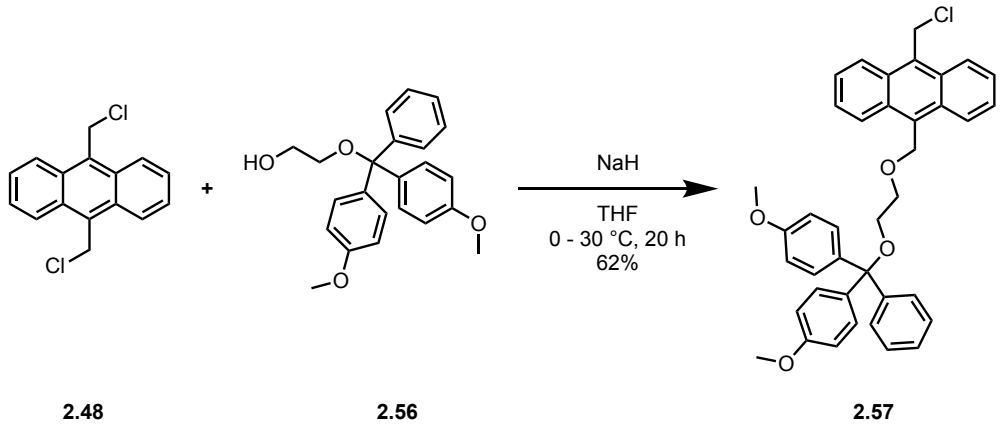
Scheme 13 Asymmetric DMT protection of anthracene-derived diol as demonstrated by Yu and Haner

A new reaction pathway to yield this product was therefore necessary. It was decided to attach the DMT protecting group to an intermediate diol, before coupling this to an anthracene derivative. Using ethylene glycol as the diol, the procedure was carried out using the same reaction conditions (Scheme 14).



Scheme 14 DMT protection of ethylene glycol

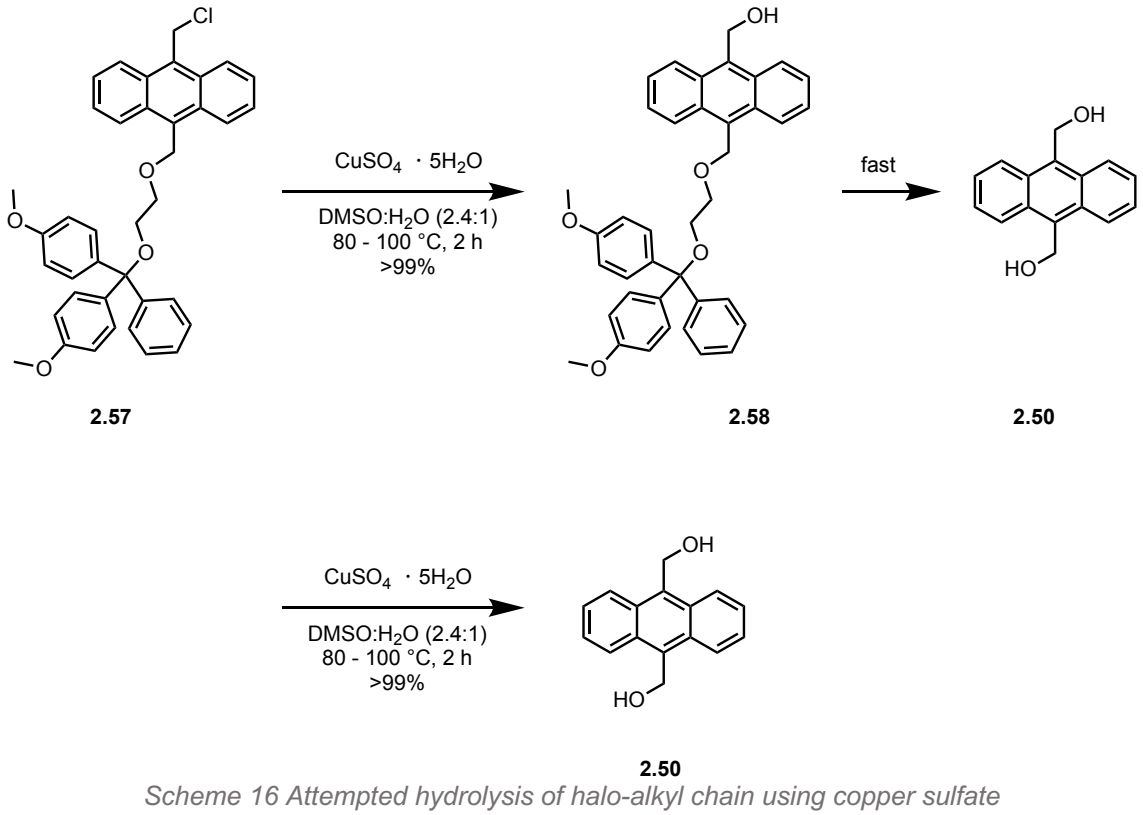
This reaction worked as desired, with the disappointing yields thought to be due to the DMT group only being added in 0.6 equivalents to reduce the risk of bis-protection. Next, addition of this protected alcohol **2.56** with the halo-alkyl derivative **2.48** was attempted. The nucleophilic substitution was aided by the use of excess sodium hydride (NaH) (Scheme 15).



*Scheme 15 Nucleophilic substitution of DMT protected ethylene glycol **2.56** and 9,10-bis(chloromethyl)anthracene **2.48***

Upon monitoring by TLC, it appeared that the reaction had gone to completion, with the UV-active spot corresponding to the anthracene-based starting material disappearing. However, upon aqueous work up and extraction with Et_2O, this spot returned and starting material was isolated. In a second attempt, the NaH (sourced as a 60% dispersion in mineral oil and triturated with hexane prior to use). Upon flash chromatography, the product was obtained in 62% yield.

Unfortunately, further attempts to functionalise the molecule at the remaining halogen however, proved disappointing. First, acid-free hydrolysis of the chlorine to an alcohol group was attempted using copper sulfate as a catalyst.[33] This resulted in hydrolysis of the DMT group however, resulting in formation of diol **2.50** (Scheme 16).



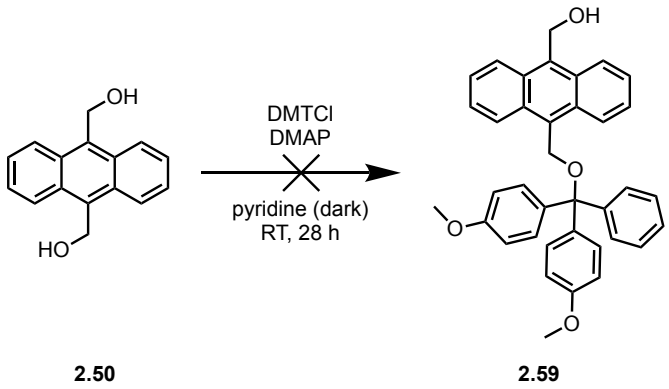
Scheme 16 Attempted hydrolysis of halo-alkyl chain using copper sulfate

The reaction could proceed via a one-step hydrolysis to form the diol **2.50** immediately, although it was considered less likely as TLC showed the presence of DMT in the product

spot when the silica plate was hovered over HCl acid vapour. This compound turns bright orange upon subjection to acid vapour, and as such can be used to check in DMT is present in the compound spot. Therefore, it could be considered to be a two-stage process, forming the desired product in an unstable form which decomposes upon aqueous work up. Whilst the addition of copper sulfate in water was known to give an alcohol from an alkyl halide, the slightly acidic nature of the copper salt in water may have caused deprotection of the DMT group.

2.6.2 DMT protection of anthracene-9,10-dimethan-1-ol

As DMT protection of the anthracene **2.43** proved unsuccessful, the same reactions were tried on the more soluble anthracene derivative (Scheme 17). It was considered that diol **2.50** may have less flexibility around the planar rings, and as such the DMT group might be better placed to stack with the anthracene ring.



*Scheme 17 Attempted DMT protection of anthracene-9,10-dimethan-1-ol **2.50***

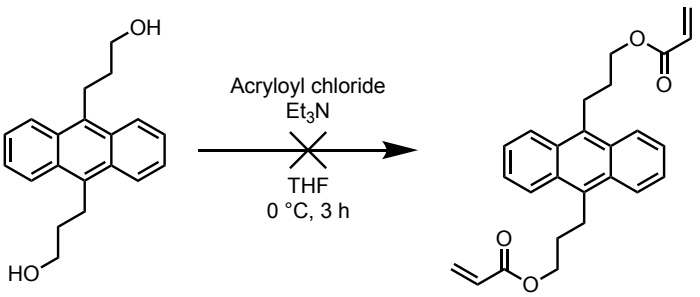
Unfortunately, no reaction was seen to have taken place by TLC as the starting material spot did not appear to shift or disappear throughout the reaction process. When worked up and purified by flash chromatography, one separated spot gave the mass of a sodium adduct of the product, but in yields of <5% and the ^{1}H NMR indicated the DMT peaks were located in a different environment than expected.

As such, and as further attempts to improve this reaction proved unsuccessful, a different approach to produce an asymmetric DMT-protected anthracene derivative was required, building from anthrone rather than a symmetrical anthracene derivative.

2.7 Anthracene-derived monomer syntheses and polymerisation attempts

As developing a symmetrical anthracene linker ready for DNA synthesis proved challenging, a new approach to provide an anthracene-derived monomer compound appropriate for polymerisation was considered. As acrylates are monomers capable of polymerisation by free radical atom transfer and are frequently co-polymerised with water-soluble monomers, it was decided that these would make a good starting point.[10, 35]

From the anthracene-9,10-dipropan-1-ol, a diacrylate could be obtained by the addition of acryloyl chloride. In the first attempt, acryloyl chloride was added with a base in order to reduce the risk of hydrolysis occurring upon work up (Scheme 18).

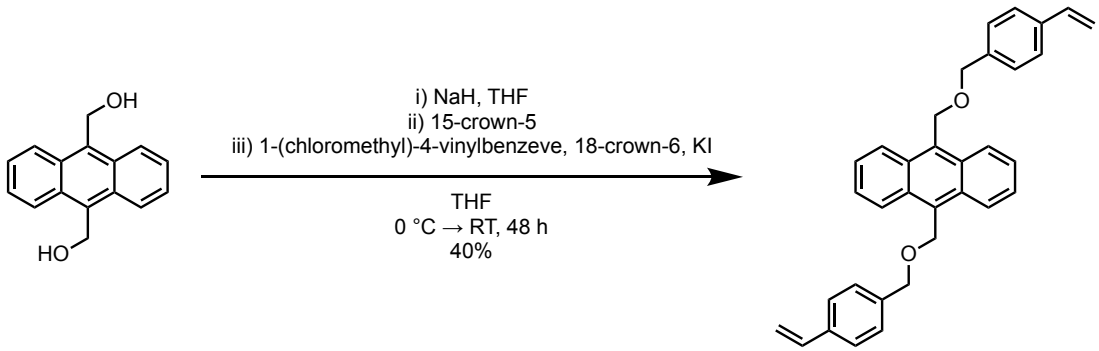


2.43 **2.60**

*Scheme 18 Attempted synthesis of anthracene-9,10-diylbis(propan-3,1-diyl) diacrylate **2.60***

Excess triethylammonium chloride precipitate was removed from the reaction mixture by gravity filtration, and the residue purified by flash chromatography. Subsequent ^{1}H NMR spectroscopy analysis of each of these fractions showed a mixture of mono- and bis-acrylates, indicating some degradation of product over time, as a fraction would initially show one spot by TLC, but later multiple spots.

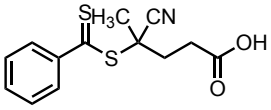
Whilst not as water-soluble as (poly)acrylates, styrene-derived monomers are relatively simple to synthesise and can be later co-polymerised with highly soluble polymeric units such as (poly)ethylene glycol for improved solubility (Scheme 19).



*Scheme 19 Synthesis of an anthracene-derived styrene monomer unit **2.61***

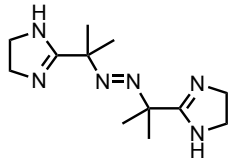
The reaction conditions were taken from work done by Acer and co-workers[12] creating carbazole-based monomers. In comparison to synthesising the diacrylate species, this was a much more robust process and as such this monomer species was used in further investigation into polymerisation.

The polymerisation of styrene monomer **2.61** was first investigated by RAFT polymerisation, using RAFT agent 4-cyano-4-(phenylcarbonothioylthio)pentanoic acid **2.62** and 1,2-bis(2-(4,5-dihydro-1H-imidazol-2-yl)propan-2-yl)diazene dihydrochloride (VA044) **2.63** as an initiator (Figure 20).



4-cyano-4-(phenylcarbonothioylthio pentanoic acid

2.62



2 HCl

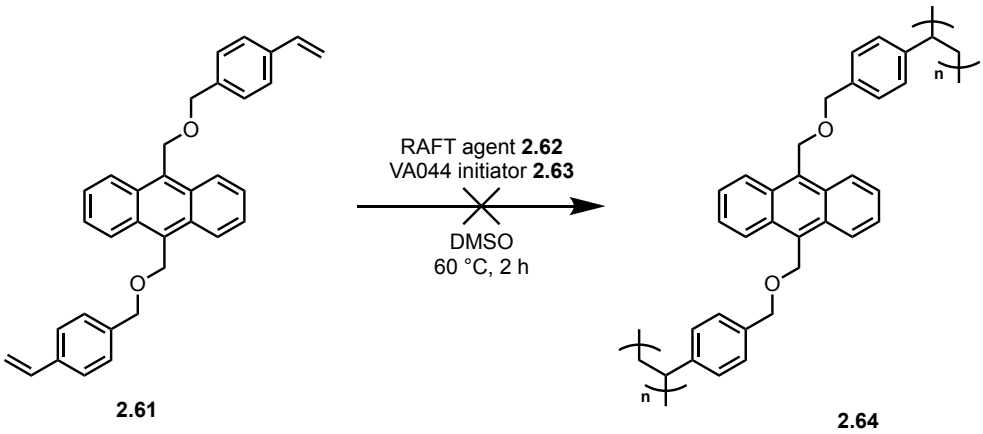
1,2-bis(2-(4,5-dihydro-1H-imidazol-2-yl)propan-2-yl)diazene dihydrochloride

2.63

*Figure 20 Structures of RAFT agent **2.62** and initiator VA044 **2.63***

The solvent chosen for this first polymerisation was DMSO, in an attempt to allow monitoring by ^{1}H NMR spectroscopy throughout the reaction. Unfortunately, the monomer was not soluble in DMSO, but the reaction process was attempted in the assumption that the polymer might become more soluble.

A stock solution of the RAFT agent **2.62** and VA044 **2.63** in DMSO was prepared and degassed with argon for 25 min. Likewise, a suspension of the monomer **2.61** in DMSO was degassed with argon for the same time period. The monomer was added to the RAFT agent and initiator, a time = 0 h aliquot taken, and the resulting suspension was heated at 65 ºC for 2 h (Scheme 20).



2.61 **2.64**

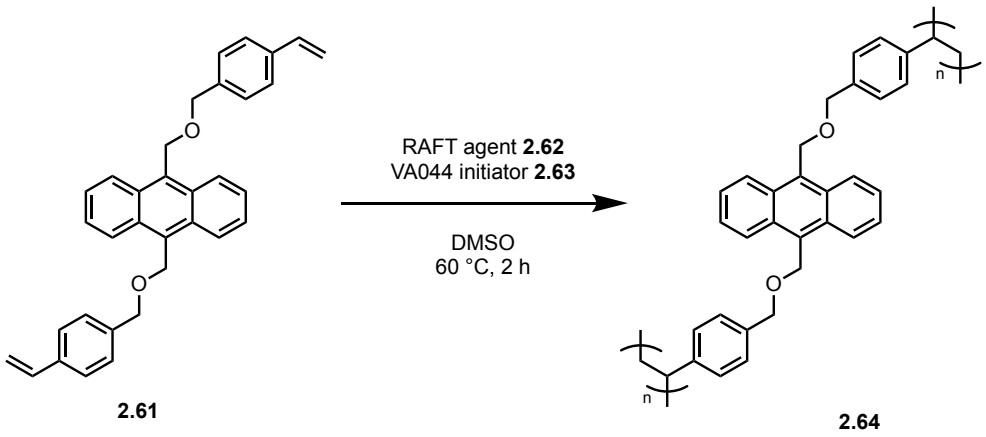
*Scheme 20 Attempted RAFT polymerisation of styrene derived **2.64***

The first polymerisation showed no sign of progression, with analysis of the t = 120 min ^{1}H NMR sample showing only starting material (Appendix 2.1). Due to the lack of any reaction, a different solvent was considered to aid dissolution of the starting material and as such improve the reactivity. As the starting material was known to be soluble in toluene, this solvent was tried but this also meant a new initiator was required to allow all reagents to be homogenous. A number of initiators were tested in this solvent to determine the correct way to proceed (Table 2).

Table 2 Initiators tested for solubility in toluene

INITIATOR	SOLUBILITY IN TOLUENE (3.6 mM)
1,2-bis(2-(4,5-dihydro-1H-imidazol-2-yl)propan-2-yl)diazene dihydrochloride (VA044)	×
4,4'-azobis(4-cyanoveleric acid) (ACVA)	×
Azobisisobutyronitrile (AIBN)	×
Azobisisobutyronitrile (AIBN)	(1.7 mM) -✓

Working at lower concentrations, AIBN was observed to be soluble in toluene and as such the next polymerisation attempt used this initiator for the activation of the RAFT agent. The reaction mixture was degassed for 60 min before being sealed and heated at 70 ºC overnight (Scheme 21). Unfortunately, product analysis ^{1}H NMR was compounded by the lack of solubility of the supposed product in DMSO-d6, which formed an emulsion. Subsequent mass spectrometry analysis of the reaction mixture showed starting material, but the polymer may not have flown under those conditions.



*Scheme 21 Attempted polymerisation of styrene monomer **2.61** in PhMe*

The need for toluene and excessive heat to solubilise the monomer species meant that further polymerisation attempts were abandoned as the limited solubility reduced the practical use of the monomer species **2.61** in drug delivery under physiological conditions. It was decided that further investigation into water soluble polymeric and oligomeric systems would be more appropriate. In summary, symmetrical 9,10-functionalised anthracene monomer **2.60** was proven to be unstable but the styrene derived monomer **2.61** was synthesised and bench stable. However, characterisation of the polymerisation product **2.64** proved unsuccessful.

2.8 Syntheses of hydroxyureas 2.64 and 2.70

So far throughout this chapter, the synthesis of various dienes for the cycloaddition proposed by King[13] and Miyata's[12] groups has been discussed. Of equal importance in creating these cycloadducts is the synthesis of the dienophile for the Diels-Alder reaction. In most cases, the dienophile of choice was determined to be *N*-hydroxy-*N*'-(4-nitrophenyl)urea, based on work done by Adachi *et al*.[36] on the most efficient 4-nitrophenyl substituent.

One of the requirements when designing a retro Diels-Alder focused HNO releasing therapeutic is that the dienophile is capable of forming an acyl nitroso. Miyata's group[10] have already focused on various dienophiles (Figure 21) and have investigated the relative stability of each of these in forming cycloadducts. Based on this previous work, the focus of the current investigation was hydroxyurea **2.65** and **2.69**.

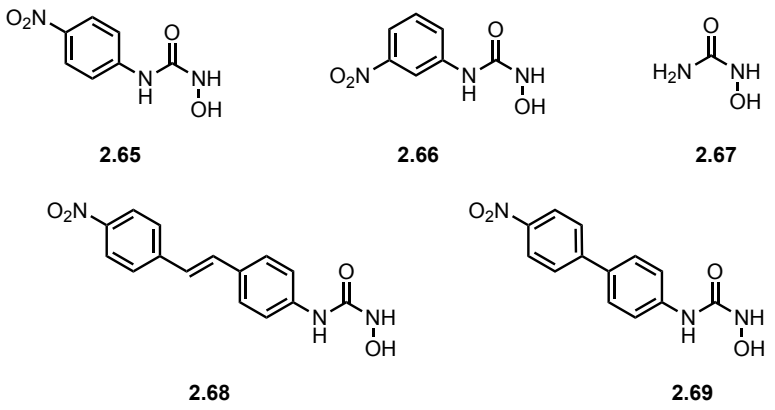
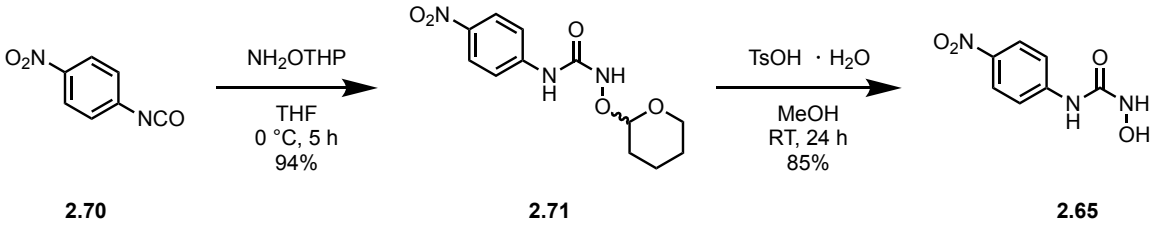


*Figure 21 Varieties of dienophile precursor **2.65 – 2.69** developed by Miyata and co-workers*

First, the synthesis of *N*-hydroxy-*N*'-(4-nitrophenyl) urea **2.65** was completed via a two-step route from 4-nitrophenyl isocyanate (Scheme 22).

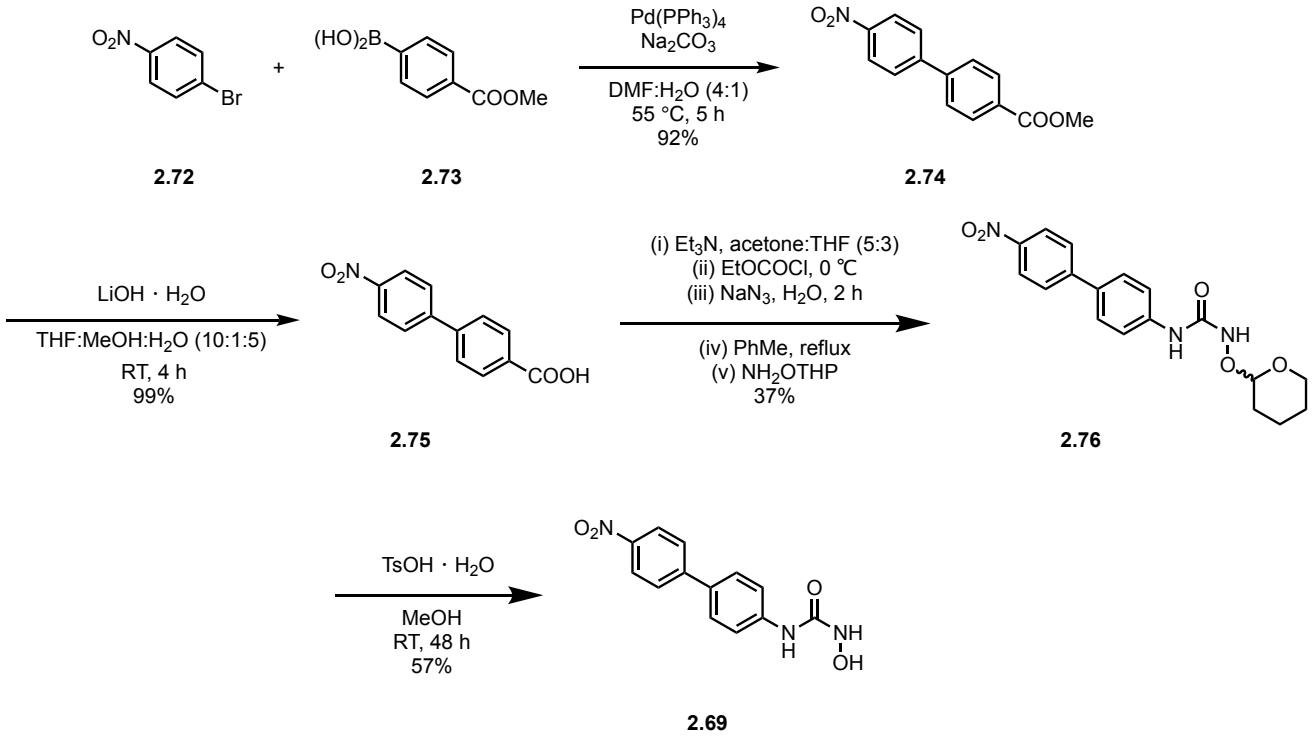


2.70 **2.71** **2.65**

*Scheme 22 Synthesis of N-hydroxy-N'-(4-nitrophenyl) urea **2.65***

A rearrangement from the commercially available isocyanate gave the protected hydroxyurea species in an excellent yield, which could then be deprotected under acidic conditions to give the desired hydroxyurea **2.65** in 85% yield.

To make the hydroxyurea **2.69**, a more drawn-out synthesis was required (Scheme 23). First, the Suzuki coupling of commercially available 1-bromo-4-nitrobenzene **2.72** and 4-methoxycarbonyl phenylboronic acid **2.73** gave the intermediate benzene carboxylate **2.67** in 92% yield. Next, the hydrolysis of the ester to the carboxylic acid **2.68** was achieved in almost quantitative yield using a lithium hydroxide solution.



*Scheme 23 Synthesis of hydroxyurea **2.69***

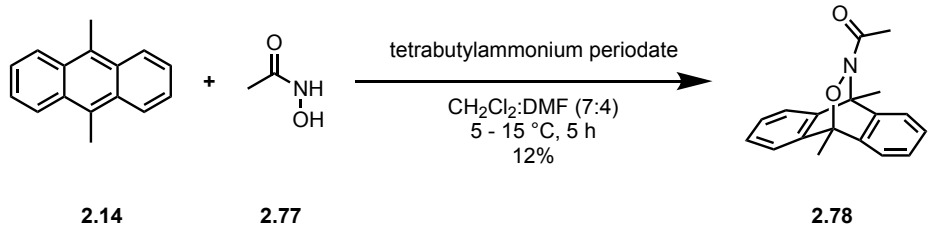
The acid **2.75** was then converted to the protected urea **2.76** by the stepwise formation of an acyl azide via the acyl carbonate, followed *in situ* by a Curtius rearrangement to give the isocyanate which could be trapped by a THP protected amine.[17] This method was used for the formation of the urea **2.69** as previous attempts to form the acyl azide using diphenyl phosphoryl azide (DPPA) proved unsuccessful. This disappointing yield was thought to be due to the wash step which occurred once the acyl azide had been formed. Due to the need for a thermal conversion of the azide to an isocyanate before the amine addition, a solvent suitable for higher temperatures was necessary. Therefore, the reaction mixture was extracted into toluene before being concentrated down. It is possible that some of the azide could have been lost at this stage. Upon reflux, the thermal conversion of the azide to an isocyanate could be followed by IR to allow addition of the amine at the correct point for formation of the urea species. Final deprotection of the tetrahydropyran group was achieved in quantitative yield using *p*-toluene-sulfonic acid to give the desired hydroxyurea **2.69**.

Both compounds **2.65** and **2.69** were synthesised as the hydroxyureas, though they needed to be converted to the acyl nitroso before the Diels-Alder cyclo-addition could take place. This was undertaken by the use of sodium periodate as an oxidising agent prior to the addition of the anthracene-derived diene.

2.9 Diels-Alder cyclo-additions on symmetrical anthracene derivatives

Having prepared a variety of dienes and dienophiles, the potential for forming the Diels-Alder cycloadducts of these constructs was investigated to determine their efficacy for releasing HNO in a controlled manner.

As the nitroso compounds **2.65** and **2.69** used previously when investigating Diels-Alder cycloaddition are known to have limited stability due to their method of HNO release, a more stable dienophile with similar characteristics was required. As such, for these test reactions acetohydroxamic acid **2.77** was used in the presence of tetrabutylammonium periodate to form the acetyl nitroso species **2.78** (Scheme 24). The cycloaddition was then tested on the commercially available symmetrical 9,10-dimethyl anthracene.



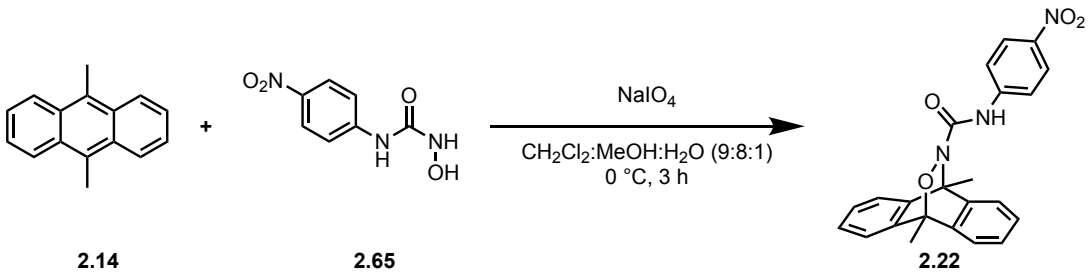
2.14 **2.77** **2.78**

*Scheme 24: Diels-Alder cycloaddition of a simple nitroso with 9,10-dimethyl anthracene **2.14***

The cycloadduct **2.78** was formed in a disappointing 12% yield but appeared stable to natural light and air meaning full characterisation could be attained without decomposition.

Then, following the procedure laid out by both King[12] and Miyata's[13, 14] groups, the cyclo-addition of *N*-hydroxy-*N*'-(4-nitrophenyl)urea **2.65** and 9,10-dimethylanthracene **2.14** was attempted (Scheme 25). All Diels-Alder reactions were undertaken in the absence of light to

prevent any photo-activated retro Diels-Alder occurring during the synthesis and purification processes.



2.14 **2.65** **2.22**

Scheme 25 Diels-Alder reaction as proposed by King and Miyata

This reaction was undertaken following conditions determined by Miyata and co-workers[10] but suffered from a lack of solubility of the anthracene species in CH_2Cl_2: MeOH: H_2O. When monitoring the reaction by TLC, it was evident that the hydroxyurea species **2.65** was used up within the first hour, despite it being in excess, but the anthracene remained. By continuing the reaction for 8 hours, the anthracene derivative was finally deemed to have been consumed and the reaction mixture was allowed to warm slightly from 0 °C to room temperature and poured over H_2O before being extracted into ethyl acetate.

The organic layer was washed with HCl then brine before being concentrated to a yellow oil. Addition of hexane gave a bright yellow precipitate but analysis using ^{1}H NMR spectroscopy at this stage showed broad peaks, indicating a mixture. Flash column chromatography in CH_2Cl_2: MeOH (99:1 - 98:2) separated the components of the reaction mixture and each of these was analysed via ^{1}H NMR spectroscopy.

This showed unreacted 9,10-dimethyl anthracene in the more polar fractions, indicating some degradation during the purification process, and a mixture in the less polar fractions that could not be fully characterised, and which degraded over time despite being kept under an inert atmosphere in the dark (Figure 22). At all points of purification and characterisation this compound was kept in the dark as much as practically possible, with column chromatography being carried out under foil and all NMR spectroscopy carried out using amber NMR tubes.

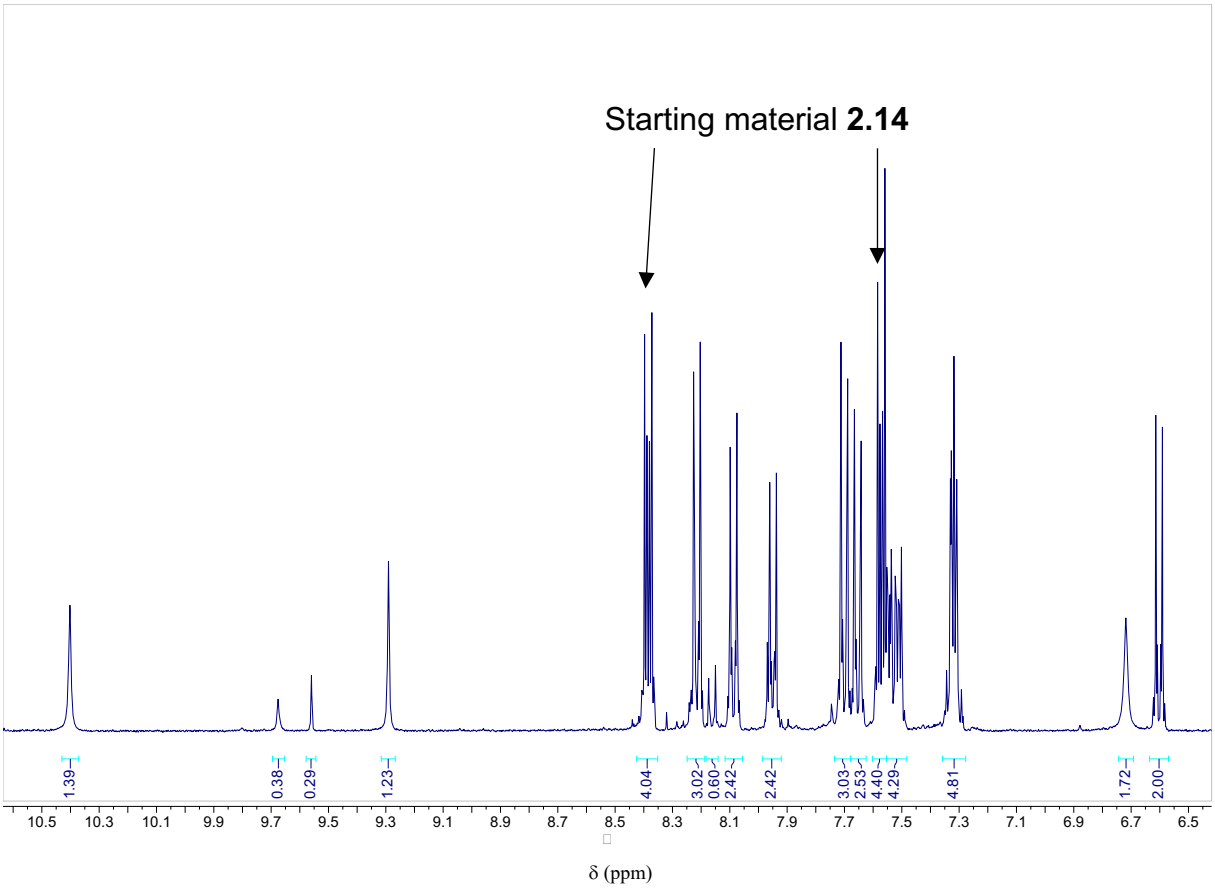


Figure 22 Aromatic region of 9,10-dimethylanthracene based cycloadduct ^{1}H NMR showing degradation of the compound

An expansion of the aromatic region of the less polar compound of the reaction mixture shows a combination of compounds that include 9,10-dimethyl anthracene at 8.38 and 7.55 ppm. The large number of other multiplets suggests that some cyclo-addition had taken

place – but checking against the ^{1}H NMR peaks reported by Miyata's[13] and King's[37] groups indicated a mixture of product and starting materials.

A second attempt at this cyclo-addition with a different work up and purification gave a slightly different ^{1}H spectrum. By extracting the reaction mixture in CH_2Cl_2, the precipitate formed during the reaction could mostly dissolve, allowing for an easier separation. Likewise, the purification eluent system was changed from CH_2Cl_2: MeOH to EtOAc: *n*-hexane: Et_3N (10:200:1 - 10:30:1) to better separate the components of the reaction mixture. This yielded a combination of the desired product with some trace impurities and a small amount of the starting material 9,10-dimethyl anthracene in low yields (<20%). To test the stability of this cyclo-adduct, a second sample of the compound was subjected to ^{1}H NMR 24 hours after the reaction had concluded (Figure 23).

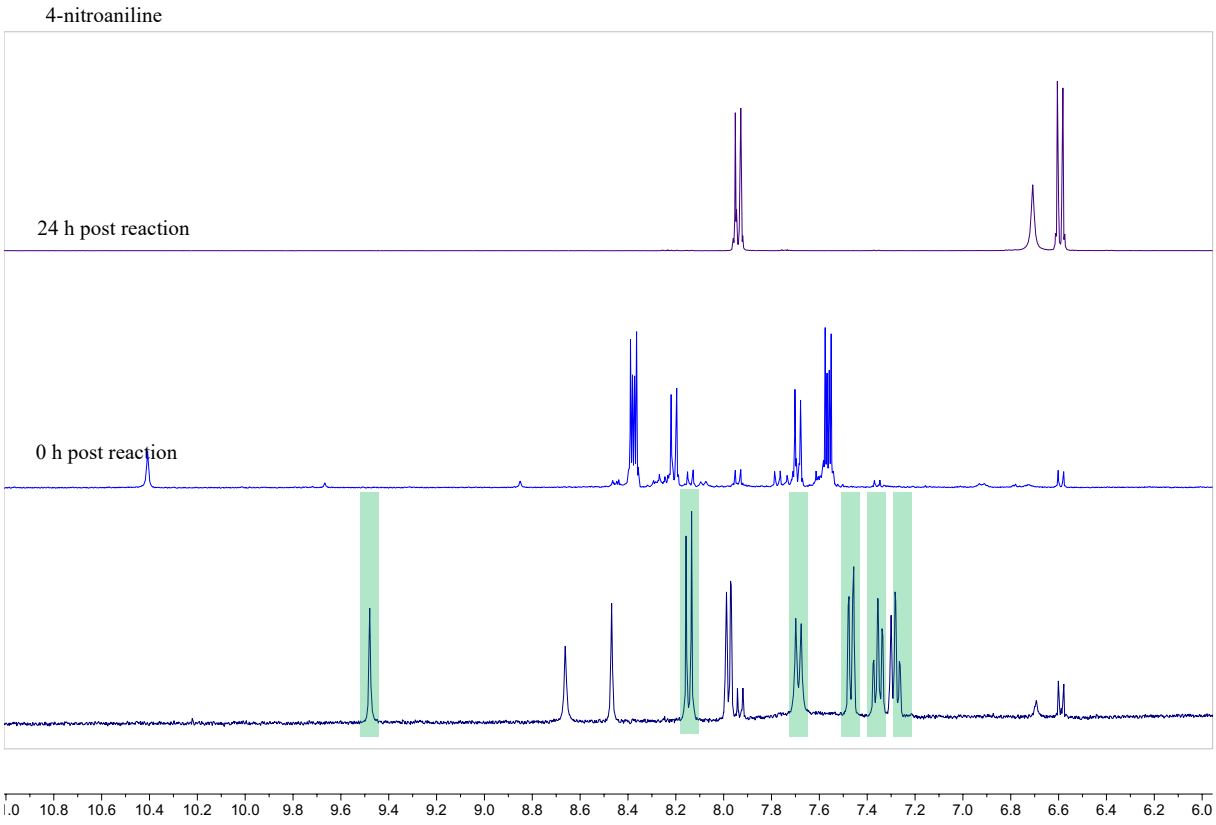
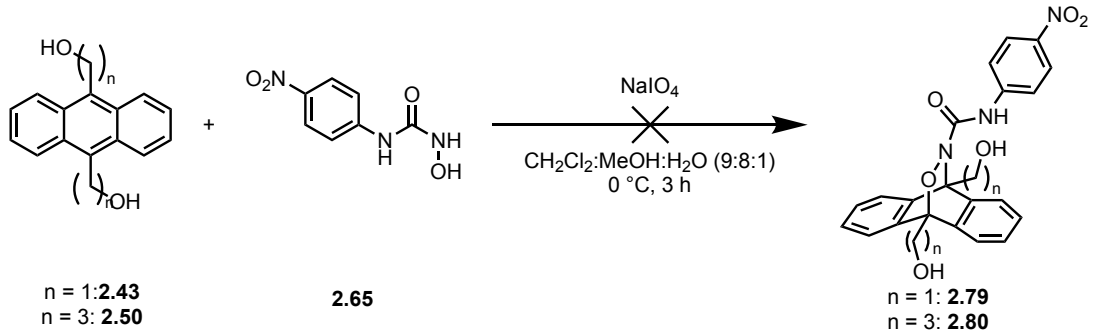


*Figure 23 Stability test of the Diels-Alder cyclo-addition of **2.14** and **2.64** in DMSO-d6.*

From the analysis of the aromatic region of the ^{1}H NMR spectra of the cyclo-adduct, it was clear that the compound had degraded. Whilst the smaller peaks indicated that some impurities remained, the peaks that matched those reported by Miyata[38] (highlighted in green) were replaced by multiplets at approximately 8.45 and 7.51 ppm, matching 9,10-dimethyl anthracene **2.14**, and apparent doublets at 8.20 and 7.69 ppm which were thought to represent 4-nitroaniline – an end product of the HNO release mechanism. The singlet at 10.37 ppm could also be indicative of the NH_2 of the 4-nitroaniline.

To investigate this further, a ^{1}H NMR spectrum of commercially available 4-nitroaniline was analysed in the same solvent conditions, to look for similarities in the peaks. However, when run in DMSO the aromatic peaks corresponding to 4-nitroaniline coincide with the small peaks at 6.70 and 7.85 ppm previously thought to be impurities (Appendix 2.2). This would indicate that the desired product had formed, but that it was unstable, degrading within a short timeframe.

To further test the effects of functionalisation at the 9,10-positions of the anthracene moieties, the cycloaddition of hydroxyurea **2.65** and anthracene diols **2.43** and **2.50** was attempted under the same conditions (Scheme 26). Unfortunately, these proved unsuccessful, indicating that the presence of an alcohol functional group might have a negative effect on the stability of the cycloadduct. Whilst the reaction was shown to proceed partially by TLC, work up gave only the starting materials.



n = 1:**2.43**
n = 3: **2.50**

2.65

n = 1: **2.79**
n = 3: **2.80**

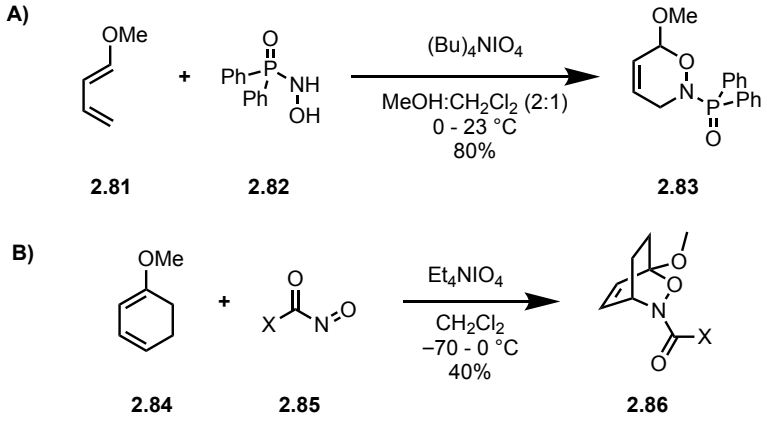
*Scheme 26: Attempted Diels-Alder cycloaddition of anthracene-derived diols **2.43** and **2.50** with nitroso derived from hydroxyurea **2.65***

2.10 Alkoxy-substituted anthracene Diels-Alder cycloadditions

Previous evidence of non-symmetrical anthracene-derived Diels-Alder cycloadducts is minimal.[39, 40] When designing anthracene compounds for incorporation into DNA, anthrone is a typical starting point, being commercially available and easy to derivatise into a variety of ethers. As such, the majority of DNA-incorporated anthracenes have an ether-functionalisation at the 9-position.

Diels-Alder reactions on such anthracene derivatives are unknown in the literature, and the inherent stability of the cycloadduct is of interest when considering a much more complex supramolecular system. As such, Diels-Alder cycloadditions were initially performed on a simple 9-methoxy anthracene **2.87** to investigate the stability thereof as well as the regiochemistry of the dienophile attacking the diene.

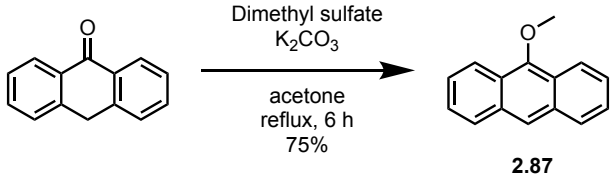
The regiochemistry shown by hetero Diels-Alder reactions has been documented for a number of dienes.[40, 41] When reacting substituted nitroso with alkoxy-substituted dienes such as (*E*)-1-methoxybuta-1,3-diene **2.81** and 1-methoxycyclohexa-1,3-diene **2.84** (Scheme 27), the acetal is formed preferentially.[40, 41]



Scheme 27 Hetero Diels-Alder cycloadditions shown by a) Ware Jr. and King and b) by Gouverneur et al.

From this data, it was assumed that an alkoxy-substituted anthracene diene would have a similar preference for the hemi-acetal. Ware and King noted that the alkoxy-substituted diene gave the opportunity for hydrolysis to occur, reducing the stability of the cycloadduct.[41] Gouverneur *et al*. focused too on the structure of the transition states of the dienophile, predicting the conformational energy differences for nitroso-derived dienophiles.[40]

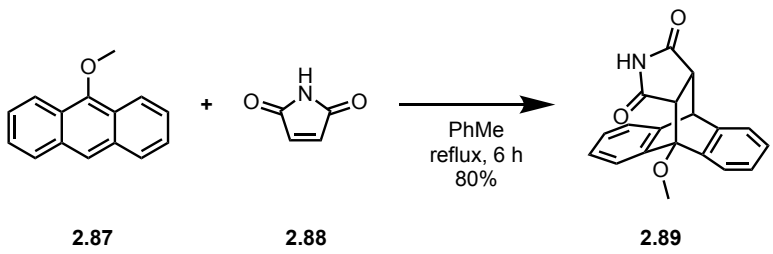
9-Methoxy anthracene **2.87** was not commercially available so this was prepared from anthrone using dimethyl sulfate and potassium carbonate (Scheme 28).[39]



*Scheme 28 Methylation of anthrone for synthesis of 9-methoxy anthracene **2.87***

The crude sample was purified by recrystallisation from CH_2Cl_2 and *hexane* to give the desired compound in 75% yield.

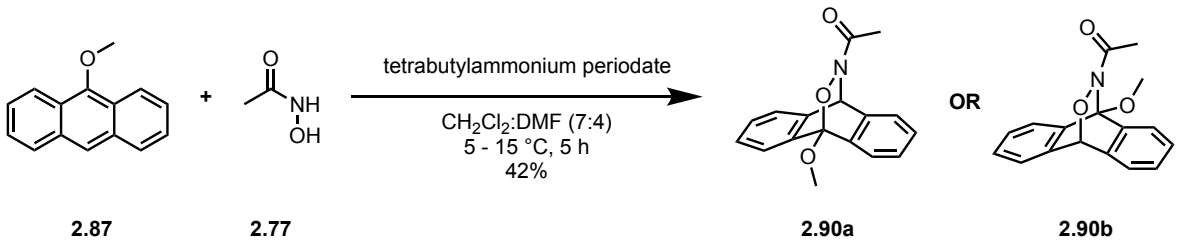
As Diels-Alder reactions with dienes functionalised with oxygen in this way are unusual, a test reaction with the well-known dienophile maleimide was attempted to determine if such cycloadducts were stable. Though cycloadduct **2.89** has been previously recorded,[40] the synthesis relied on the use of a chiral sulfinyl maleimide and samarium diiodide. Preferring to use less hazardous reducing agents, an alternative method using a higher boiling point solvent was attempted (Scheme 29).



*Scheme 29 Diels-Alder reaction of 9-methoxy anthracene **2.87** and maleimide **2.88***

The cycloadduct **2.89** was made without purification, precipitating out of refluxing toluene as the clean product in 80% yield. The sample also proved stable in light on the bench, with no evidence of the photo-induced retro Diels-Alder reaction occurring. With the precedent set for an oxygen-functionalised cycloadduct, further investigations into hetero dienophiles could be performed as detailed below.

The use of hetero-dienophiles on alkoxy-substituted dienes is known[14, 39] but not common using an anthracene derivative. Interestingly, all evidence for the preferred regiochemistry of these points towards the acetal forming over the hemi-aminal. As such, this gave the starting point for the characterisation of any cycloadditions made using the alkoxy-substituted species **2.87**. Subsequently, 9-methoxy anthracene **2.87** was subjected to cycloaddition conditions with acetohydroxamic acid **2.77** and tetrabutylammonium periodate (Scheme 30).



2.87 **2.77** **2.90a** **2.90b**

*Scheme 30 Synthesis of 9-methoxy anthracene-derived cycloadduct **2.90a** or **2.90b***

The cycloadduct was isolated in 42% yield as one regioisomer following column chromatography (1% Et_3N, CH_2Cl_2) but proved to be unstable in solution, light, and air, fully decomposing within 24 h (Figure 24). Clearly there was a detrimental effect on the stability of the cycloadduct when using the alkoxy-substituted diene in comparison to the 9,10-dimethyl anthracenes.

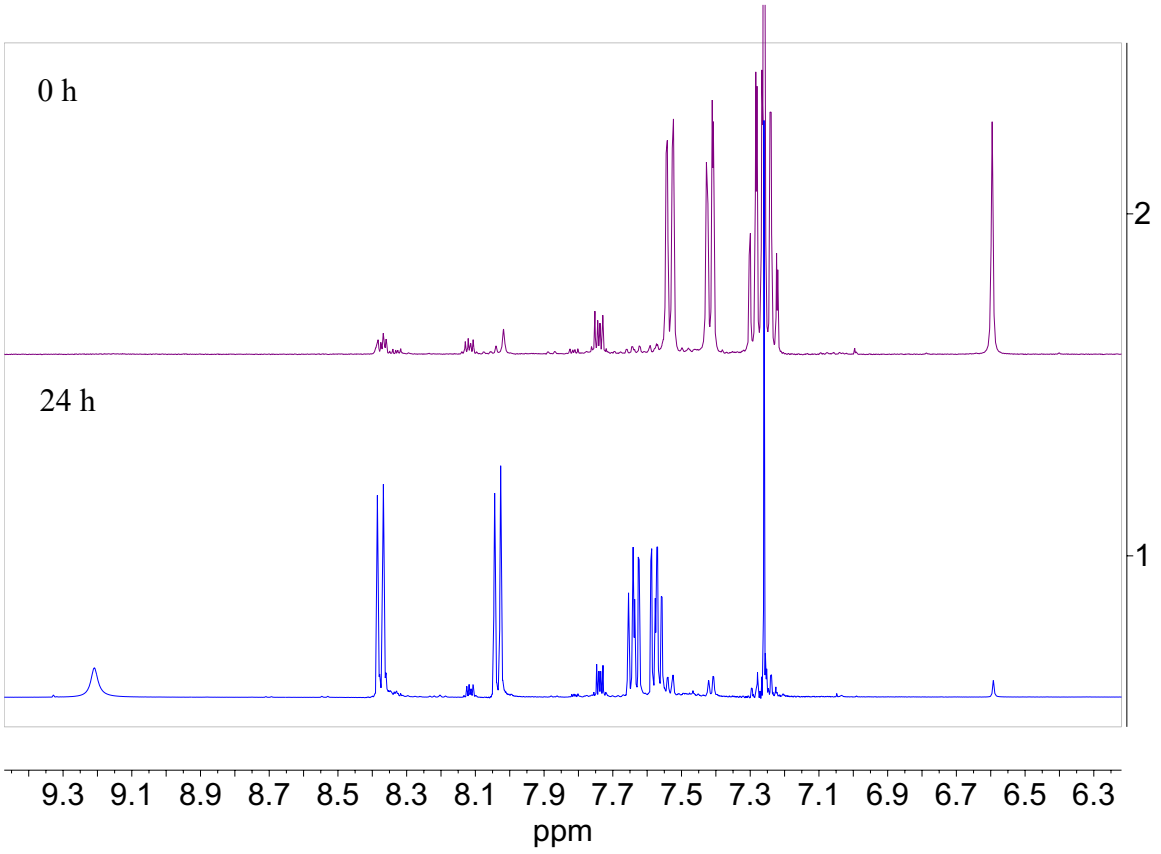


*Figure 24 Aromatic region of ^{1}H NMR spectra of the cycloadduct **2.90** at 0 h (2) and 24 h (1) after purification*

Analysis of the ^{1}H NMR spectrum at 0 and 24 h after isolation clearly showed the decomposition of the cycloadduct as indicated by the disappearance of the bridging singlet proton at 6.6 ppm and the shifting of the aromatic signals downfield.

Having managed to analyse the compound both before and after its decomposition, our attention turned to determining its regiochemistry as well as the structure of the decomposition product. Analysis by ^{1}H and ^{13}C NMR the presence of only one regioisomer, but HSQC, HMBC and COSY NMR spectra were not enough to unambiguously determine the regiochemistry. To fully confirm the presence of either the acetal or hemi-aminal, X-ray crystallography was required (Figure 25).

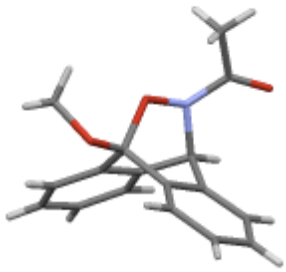


*Figure 25 X-ray crystal structure of the cycloadduct **2.90a** showing to form as the acetal. For more information on the X-ray crystallography data, please see experimental for compound **2.90***

Crystals were formed in fraction tubes straight from flash column chromatography, collected and kept under an inert atmosphere until X-ray crystallography analysis. From the crystal structure in combination with NMR analysis it was clear that the acetal had formed as the sole regioisomer. This regiochemistry matches the pattern shown by Ware and King in their work performing hetero Diels-Alder reactions on alkoxy-substituted dienes where they argued for a steric hindrance to prevent formation of the hemi-aminal.[14]

Calculation of the torsion angles of the bridging atoms and the amide indicated that there was a deviation from planarity of the NH of the amide. Certain aspects of the crystal structure can be determined as planar, including C16 as the carbonyl carbon (Figure 26).

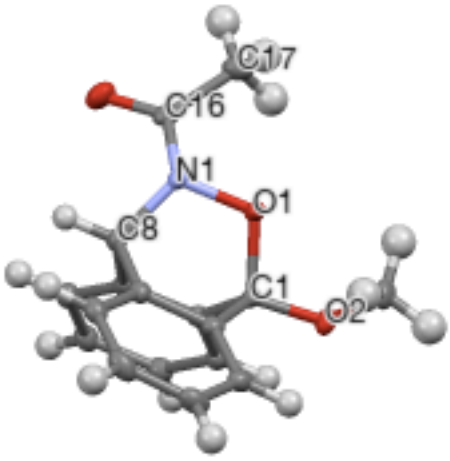
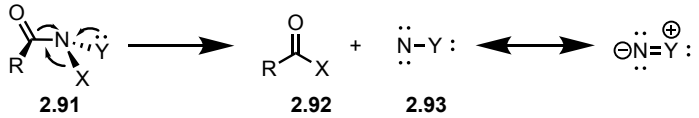


*Figure 26 Crystal structure of cycloadduct **2.90a** with relevant atoms labelled for discussion. Crystal structure data can be obtained in experimental section 7.2.3*

As such, the torsion angles of C17-C16-N1-O1 (–25.96 ˚) and C17-C16-N1-C8 (–163.42 ˚) were calculated, which would both be zero if the nitrogen also showed planar characteristics. This deviation indicated the nitrogen was not displaying sp^2 behaviour, but some tetrahedral characteristics. Similar non-planar nitrogens within a 6-membered hydroxyl amine with an epicyclic amide carbonyl have been shown but are still the minority in such published structures.[42-44]

Typical amides have a strong π-orbital between the nitrogen lone pair and the carbon C16 2pz orbital due to the polarisation of the π-CO orbital.[45] As the amide in question in structure **2.90a** is anomeric, the planarity of the nitrogen can be disturbed with hybridisation towards sp^3 due to the electron density redistribution required by the electronegative oxygen, as necessary according to Bent's rule.[42] From this pyramidalisation, the lone pair on the nitrogen shows great 2s character, resulting in structural, spectroscopic and chemical differences compared to the traditional amide.[42]

Glover and Rosser reviewed such unusual behaviours exhibited by anomeric amides in biological activities, focusing most on *N*-acyloxy-alkoxyamides, which show mutagenic effects on DNA by reacting with the nucleophilic centres.[45] Their work in 1996 looked at the N-C(O) bond length when substituting hydrogens on the amide with heteroatoms showed an increase in length (1.362 Å – 1.380 Å) which matched exactly the bond length measured between N1 and C16 of Figure 26.[46] Glover and Campbell also discovered the heteroatom rearrangement on nitrogen (HERON) reaction of anomeric amides in polar solvents (Scheme 31),[47] which could potentially explain some of the lack of stability observed in the cycloadducts synthesised throughout this chapter.



2.91 **2.92** **2.93**

Scheme 31 Heteroatom rearrangement on nitrogen (HERON) reaction as described by Glover and Rosser

2.11 Conclusions and Future Work

The primary aim of this project was to design stable anthracene-derived cycloadducts capable of incorporation into an oligomeric or polymer macromolecule. The design of the anthracene dienes **2.43**, **2.50**, and **2.61** was to allow for conjugation of the cycloadduct to a targeting vector, whether that was for solid-phase DNA synthesis or polymerisation.

Multiple dienes were created, though there was very limited success in further functionalising any of them due to a disappointing lack of stability of the cycloadduct. As such a different approach was developed, using alkoxy-substituted anthracenes such as **2.87** to develop an easier point of DNA incorporation.

Hydroxyureas **2.65** and **2.69** were also synthesised to form the dienophiles necessary for the desired Diels-Alder reactions *in situ* with a reducing agent. Test cycloadditions were carried out with commercially available 9,10-dimethylanthracene **2.14** and acetohydroxamic acid **2.77** to form the initial cycloadducts and to determine the regiochemistry of the asymmetric hetero-Diels-Alder reaction.

Having shown that synthesis of cycloadduct **2.90** was achievable, the project could conceivably look forwards towards a DNA-incorporated anthracene moiety and the cycloaddition could be tested on the modified oligomer. This will be further investigated in Chapter 3.

2.11 References

1. Fukuto, J. M.; Dutton, A. S.; Houk, K. N., The chemistry and biology of nitroxyl (HNO): a chemically unique species with novel and important biological activity. *ChemBioChem,* **2005,** *6* (4), 612-9.
2. Amatore, C.; Arbault, S.; Ducrocq, C.; Hu, S. H.; Tapsoba, I., Angeli's salt (Na_2N_2O3) is a precursor of HNO and NO: a voltammetric study of the reactive intermediates released by Angeli's salt decomposition. *ChemMedChem,* **2007,** *2* (6), 898-903.
3. Oliveira, C.; Benfeito, S.; Fernandes, C.; Cagide, F.; Silva, T.; Borges, F., NO and HNO donors, nitrones, and nitroxides: Past, present, and future. *Med. Res. Rev.,* **2018,** *38* (4), 1159-87.
4. DuMond, J. F.; King, S. B., The Chemistry of Nitroxyl-Releasing Compounds. *Antioxid. Redox Sign.,* **2011,** *14* (9), 1637-48.
5. Zamora, R.; Grzesiok, A.; Weber, H.; Feelisch, M., Oxidative release of nitric oxide accounts for guanylyl cyclase stimulating, vasodilator and anti-platelet activity of Piloty's acid: a comparison with Angeli's salt. *Biochem. J.,* **1995,** *312 (Pt 2)*, 333-9.
6. Bonner, F. T., Ko, Y, Kinetic, Isotopic, and 15N NMR Study of A Hydroxybenzenesulfonamide Decomposition: An HNO Source Reaction. *Inorg. Chem.* **1992,** *31*, 2514-9.
7. Sha, X.; Isbell, T. S.; Patel, R. P.; Day, C. S.; King, S. B., Hydrolysis of acyloxy nitroso compounds yields nitroxyl (HNO). *J. Am. Chem. Soc.,* **2006,** *128* (30), 9687-92.
8. Christie, C. C., Kirby, G. W., Mcguigan, H., Mackinnon, J. W. M., C-Nitrosoformamides, a new class of transient dienophiles formed by oxidation of N-hydroxyureas. *J. Chem. Soc. Perkin. Trans. I* **1985**, 2469-73.
9. Howard, J. A.; Ilyashenko, G.; Sparkes, H. A.; Whiting, A., Development of new transition metal catalysts for the oxidation of a hydroxamic acid with in situ Diels-Alder trapping of the acyl nitroso derivative. *Dalton Trans.,* **2007**, (21), 2108-11.
10. Xu, Y. P.; Alavanja, M. M.; Johnson, V. L.; Yasaki, G.; King, S. B., Production of nitroxyl (HNO) at biologically relevant temperatures from the retro-Diels-Alder reaction of *N*-hydroxyurea-derived acyl nitroso-9,10-dimethylanthracene cycloadducts. *Tetrahedron Lett.,* **2000,** *41* (22), 4265-9.
11. King, S. B., *N*-hydroxyurea and acyl nitroso compounds as nitroxyl (HNO) and nitric oxide (NO) donors. *Curr. Top Med. Chem.,* **2005,** *5* (7), 665-73.
12. Adachi, Y.; Nakagawa, H.; Matsuo, K.; Suzuki, T.; Miyata, N., Photoactivatable HNO-releasing compounds using the retro-Diels-Alder reaction. *Chem. Commun.,* **2008**, (41), 5149-51.
13. Matsuo, K.; Nakagawa, H.; Adachi, Y.; Kameda, E.; Tsumoto, H.; Suzuki, T.; Miyata, N., Alternative photoinduced release of HNO or NO from an acyl nitroso compound, depending on environmental polarity. *Chem. Commun.,* **2010,** *46* (21), 3788-90.
14. Matsuo, K.; Nakagawa, H.; Adachi, Y.; Kameda, E.; Aizawa, K.; Tsumoto, H.; Suzuki, T.; Miyata, N., Photoinduced Upregulation of Calcitonin Gene-Related Peptide in A549 Cells through HNO Release from a Hydrophilic Photocontrollable HNO Donor. *Chem. Pharm. Bull.,* **2012,** *60* (8), 1055-62.
15. Nakagawa, H., Controlled release of HNO from chemical donors for biological applications. *J. Inorg. Biochem.,* **2013,** *118*, 187-90.
16. Tuvi-Arad, I.; Avnir, D., Symmetry-enthalpy correlations in Diels-Alder reactions. *Chemistry* **2012,** *18* (32), 10014-20.
17. Zeng, B. B.; Huang, J. M.; Wright, M. W.; King, S. B., Nitroxyl (HNO) release from new functionalized *N*-hydroxyurea-derived acyl nitroso-9,10-dimethylanthracene cycloadducts. *Bioorg. Med. Chem. Lett.,* **2004,** *14* (22), 5565-8.

18. Zeng, B. B.; Huang, J.; Wright, M. W.; King, S. B., Nitroxyl (HNO) release from new functionalized *N*-hydroxyurea-derived acyl nitroso-9,10-dimethylanthracene cycloadducts. *Bioorg. Med. Chem. Lett.,* **2004,** *14* (22), 5565-8.
19. King, S. B., Zeng, B. B. , Palladium-Catalyzed Synthesis of Water-Soluble Symmetric 9,10-Disubstituted Anthracenes. *Synthesis,* **2002**, (16), 2335-7.
20. Moran, N.; Bassani, D. M.; Desvergne, J. P.; Keiper, S.; Lowden, P. A. S.; Vyle, J. S.; Tucker, J. H. R., Detection of a single DNA base-pair mismatch using an anthracene-tagged fluorescent probe. *Chem. Commun.,* **2006**, (48), 5003-5.
21. Duprey, J. L. H. A.; Bassani, D. M.; Hyde, E. I.; Ludwig, C.; Rodger, A.; Vyle, J. S.; Wilkie, J.; Zhao, Z. Y.; Tucker, J. H. R., Anthracene-modified oligonucleotides as fluorescent DNA mismatch sensors: discrimination between various base-pair mismatches. *Supramol. Chem.,* **2011,** *23* (3-4), 273-7.
22. Manchester, J.; Bassani, D. M.; Duprey, J. L. H. A.; Giordano, L.; Vyle, J. S.; Zhao, Z. Y.; Tucker, J. H. R., Photocontrolled Binding and Binding-Controlled Photochromism within Anthracene-Modified DNA. *J. Am. Chem. Soc.,* **2012,** *134* (26), 10791-4.
23. Duprey, J. L.; Bullen, G. A.; Zhao, Z. Y.; Bassani, D. M.; Peacock, A. F.; Wilkie, J.; Tucker, J. H., Single Site Discrimination of Cytosine, 5-Methylcytosine, and 5-Hydroxymethylcytosine in Target DNA Using Anthracene-Tagged Fluorescent Probes. *Acs. Chem. Biol.,* **2016,** *11* (3), 717-21.
24. Duprey, J. L. H. A.; Bassani, D. M.; Hyde, E. I.; Jonusauskas, G.; Ludwig, C.; Rodger, A.; Spencer, N.; Vyle, J. S.; Wilkie, J.; Zhao, Z. Y.; Tucker, J. H. R., Rationalisation of a mechanism for sensing single point variants in target DNA using anthracene-tagged base discriminating probes. *Org. Biomol. Chem.,* **2018,** *16* (35), 6576-85.
25. Duprey, J. L. H. A.; Zhao, Z. Y.; Bassani, D. M.; Manchester, J.; Vyle, J. S.; Tucker, J. H. R., Detection of DNA base variation and cytosine methylation at a single nucleotide site using a highly sensitive fluorescent probe. *Chem. Commun.,* **2011,** *47* (23), 6629-31.
26. Duprey, J.-L. H. A. Studies On Anthracene Tagged Oligonucleotides. PhD, University of Birmingham, 2010.
27. Cloninger, M. J.; Whitlock, H. W., A Synthetic Receptor Which Uses Multiple Edge-Face Interactions To Bind Aromatic Guests. *J. Org. Chem.,* **1998,** *63* (18), 6153-9.
28. Schafer, C.; Strube, F.; Bringmann, S.; Mattay, J., Photocyclizable resorcin[4]arene dimers. *Photochem. Photobiol. Sci.,* **2008,** *7* (12), 1457-62.
29. Qiu, L.; Zhu, C. C.; Chen, H. C.; Hu, M.; He, W. J.; Guo, Z. J., A turn-on fluorescent Fe^{3+} sensor derived from an anthracene-bearing bisdiene macrocycle and its intracellular imaging application. *Chem. Communi.,* **2014,** *50* (35), 4631-4.
30. Caruthers, M. H., Chemical Synthesis of DNA. *J. Chem. Educ.,* **1989,** *66* (7), 577-80.
31. Caruthers, M. H., The Chemical Synthesis of DNA/RNA: Our Gift to Science. *J. Biol. Chem.,* **2013,** *288* (2), 1420-7.
32. Yu, H.; Haner, R., Solution-phase synthesis of 1D tubular polymers via preorganization-polymerization. *Chem. Commun. (Camb)* **2016,** *52* (100), 14396-9.
33. Menchikov, L. G., Vorogushin, A. V., Korneva, O. S., Nefedov, O. M., An effective method for alcohol preparation by hydrolysis of organohalides in the presence of copper and its salts in aqueous DMSO. *Mendeleev Commun.,* **1995,** *5*, 223-4.
34. V. Coessens, T. P., K. Matyjaszewski, Functional polymers by atom transfer radical polymerization. *Prog. Polym. Sci.,* **2001,** *26*, 337-77.
35. Gulfidan, D., Koyuncu, E. S., S., Acar, M. H., Neutral state colorless electrochromic polymer networks: Spacer effect on electrochromic performance. *Polymer* **2014,** *55* (23), 5998-6005.
36. Boulahjar, R.; Ouach, A.; Matteo, C.; Bourg, S.; Ravache, M.; le Guevel, R.; Marionneau, S.; Oullier, T.; Lozach, O.; Meijer, L.; Guguen-Guillouzo, C.; Lazar, S.; Akssira, M.; Troin, Y.; Guillaumet, G.; Routier, S., Novel tetrahydropyrido[1,2-a]isoindolone derivatives (valmerins): potent cyclin-dependent kinase/glycogen synthase kinase 3 inhibitors

with antiproliferative activities and antitumor effects in human tumor xenografts. *J. Med. Chem.,* **2012,** *55* (22), 9589-606.
37. Stock, G. L. A. a. L. M., The Preparation of 9-Fluoroanthracenes. *J. Org. Chem.,* **1971,** *36* (8), 1140-2.
38. Franck, B., Zeidler, V. R., U., Model Reactions for Biological Ring Opening of Anthraquinones. *Angewandte Chemie* **1967,** *6* (11), 952-3.
39. Ware, R. W., Jr.; King, S. B., *P*-Nitrosophosphate compounds: new N-O heterodienophiles and nitroxyl delivery agents. *J. Org. Chem.,* **2000,** *65* (25), 8725-9.
40. Gouverneur, V., Mineur, S. J. M. C., Belotti, D., Dive, G., Ghosez, L., New acylnitroso compounds for the asymmetric oxyamination of dienes. *Tetrahedron* **1998,** *54*, 10537-54.
41. Ware Jr., R. W., King, S. B., *N*-Phosphinoylnitroso compounds: new asymmetric N-O heterodienophiles and nitroxyl delivery agents. *J. Am. Chem. Soc.* **1999,** *121*, 6769-70.
42. Memeo, M. G.; Lapolla, F.; Bovio, B.; Quadrelli, P., Three-dimensional heterocycles: new uracil-based structures obtained by nucleophilic substitution at the sp2 carbon of bromoisoxazoline. *Molecules* **2014,** *19* (6), 8661-78.
43. Lu, P. H.; Yang, C. S.; Devendar, B.; Liao, C. C., Syntheses of optically pure conduramines via the strategy of hetero Diels-Alder reaction of masked *o*-benzoquinones with homochiral nitroso dienophiles. *Org. Lett.,* **2010,** *12* (11), 2642-5.
44. Chaiyaveij, D.; Batsanov, A. S.; Fox, M. A.; Marder, T. B.; Whiting, A., An Experimental and Computational Approach to Understanding the Reactions of Acyl Nitroso Compounds in [4 + 2] Cycloadditions. *J. Org. Chem.,* **2015,** *80* (19), 9518-34.
45. Glover, S. A.; Rosser, A. A., Heteroatom Substitution at Amide Nitrogen-Resonance Reduction and HERON Reactions of Anomeric Amides. *Molecules* **2018,** *23* (11).
46. Rauk, A., Glover, S. A. , A computational investigation of the stereoisomerism in bisheteroatom-substituted amides. *J. Org. Chem.* **1996,** *61*, 2337-45.
47. Campbell, J. J., Glover, S. A., Bimolecular reactions of mutagenic *N*-acetoxy-*N*-alkoxybenzamides and *N*-methylaniline. *J. Chem. Soc. Perkin. Trans. II* **1992,** *10*, 1661-3.

Chapter 3: Development of DNA-based HNO delivery systems

3.1 Introduction

Photo-activated release of caged drug systems could lead to a new future in pharmaceutical delivery. HNO delivery systems are often hindered by an inherent instability, reducing the control required for therapeutics. As observed by Miyata[1] the stability of the Diels-Alder cycloadduct from anthracene derivatives and an acyl nitroso moiety was very dependent on the 9- and 10-positions on the anthracene (Scheme 6, Scheme 8, **Chapter 2**). They found that a carboxylic acid group improved stability, but further amide coupling to a peptide reduced this under ambient conditions.[2] Likewise, the work discussed in Chapter 2 demonstrated the potential for an alkoxy-substituted anthracene to act as a diene in non-symmetrical cycloadducts, though with limited success in improving stability.

3.1.1 DNA delivery and therapeutics

The stabilising effect of DNA in therapeutic investigations has, like with the use of peptides, become more prevalent as the use of nanoscale technologies grows. For example, metal nanoclusters have been stabilised in DNA recently[3, 4] and DNA-based hydrogels are also becoming more common in the therapeutic industry, due to the enhanced stability of DNA in comparison to antibodies and protein enzymes.[5] In these systems. The DNA can be manipulated to allow control of the hydrogel, by a combination of duplex bridges, pH-responsive cross bridges and G-quadruplexes.[5]

There are other examples of DNA being used in host guest assemblies, to stabilise nanoparticle formation either for the formation of the DNA strand itself, or for co-delivery of an intercalating drug such as doxorubicin (DOX).[6] Cyclodextrin (CD) containing poly(ethyleneimine) (PEI) nanoparticles are often used in therapeutics due to their high

biocompatibility, making them useful for trapping drug molecules within the cavities. To form such nanoparticles, DNA is condensed alongside a therapeutic, often DOX, with the CD-PEI and the overall molecule is stabilised by the electrostatic interactions.[7]

In addition to its stabilising role, DNA can be used to target certain recognition markers within the body, making it ideal as a targeting vector. In particular, aptamers – short single-stranded DNA that are selected for binding to specific targets – are ideal for the delivery of therapeutic agents with their 3-D nature making them highly selective.[7] As such, drug moieties can be loaded onto DNA strands as long as they do not interfere with the secondary structure of the aptamer.

Potential drawbacks to the use of DNA in delivering therapeutics revolve around the risk of nuclease-triggered degradation. Unmodified DNA strands have very short half-lives *in vivo*, typically under ten minutes, but it has been found that modifications to the DNA at the 2'-position of the sugar backbone can dramatically improve stability both *in vivo* and *in vitro*.[8] Other methods of improving this lifetime can include conjugation of the aptamers to a 40 kDa polyethylene glycol (PEG) chain without too much of an adverse effect on target binding affinity.[8]

Other considerations when attempting to use DNA to deliver therapeutics must include the matter of controlled release of the substrate in question. However, for the investigation described in this thesis, the cycloadduct operates under photo-irradiated control which means that external control of the DNA conformation to trigger release is not required.

3.1.2 Photo-activation of DNA modifications

One avenue of research when considering drug delivery within DNA strands involves looking at photo-activation of modifications within a DNA strand. As far as DNA-based drug systems are concerned, sulfur-substituted purine and pyrimidine nucleoside base analogues have been known since the late 1940s and FDA-approved since the 1950s.[8] These have slightly different properties to unmodified nucleosides, and as such have been used expansively in cancer treatments and immunosuppression (Figure 27).

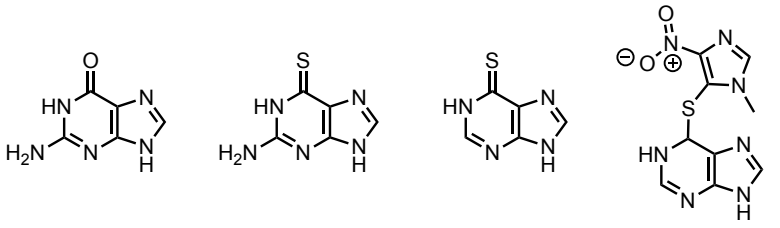


Figure 27 Guanine and sulfur-substituted analogues prevalent in drug syntheses

Interestingly, certain thiopyrimidine derivatives are naturally occurring components of bacterial tRNA strands.[9] In particular, 4-thiouridine **3.5** (and the DNA analogue 4-thio-2'-deoxythymidine **3.6**) have been investigated for their photo-crosslinking capabilities, improving the knowledge around the tertiary structure of tRNAs and also looking at the treatment of certain carcinomas using light-activated therapeutics (Figure 28).[10, 11]

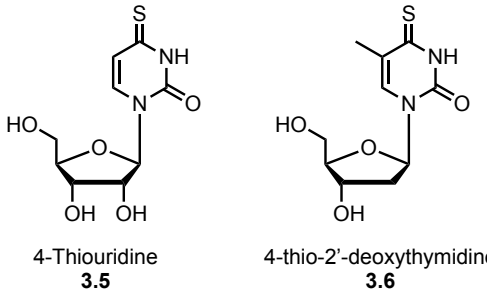


*Figure 28 4-thiouridine **3.5** and DNA analogue **3.6***

The thiopurines used in such therapeutics are known to metabolise into 6-thio-2'-deoxyguanosine, which can then induce DNA inter- and intra-strand crosslinking behaviours under UVA light and as such, DNA damage. The mechanism of action of how this oxidatively generated DNA damage occurs is debated[12, 13] as it was previously assumed to generate singlet oxygen with quantum yields of ~50%. However, Pollum *et al* found significantly lower quantum yields, and as such proposed a new mechanism of action wherein the production of singlet oxygen is in competition (Figure 29).[14]

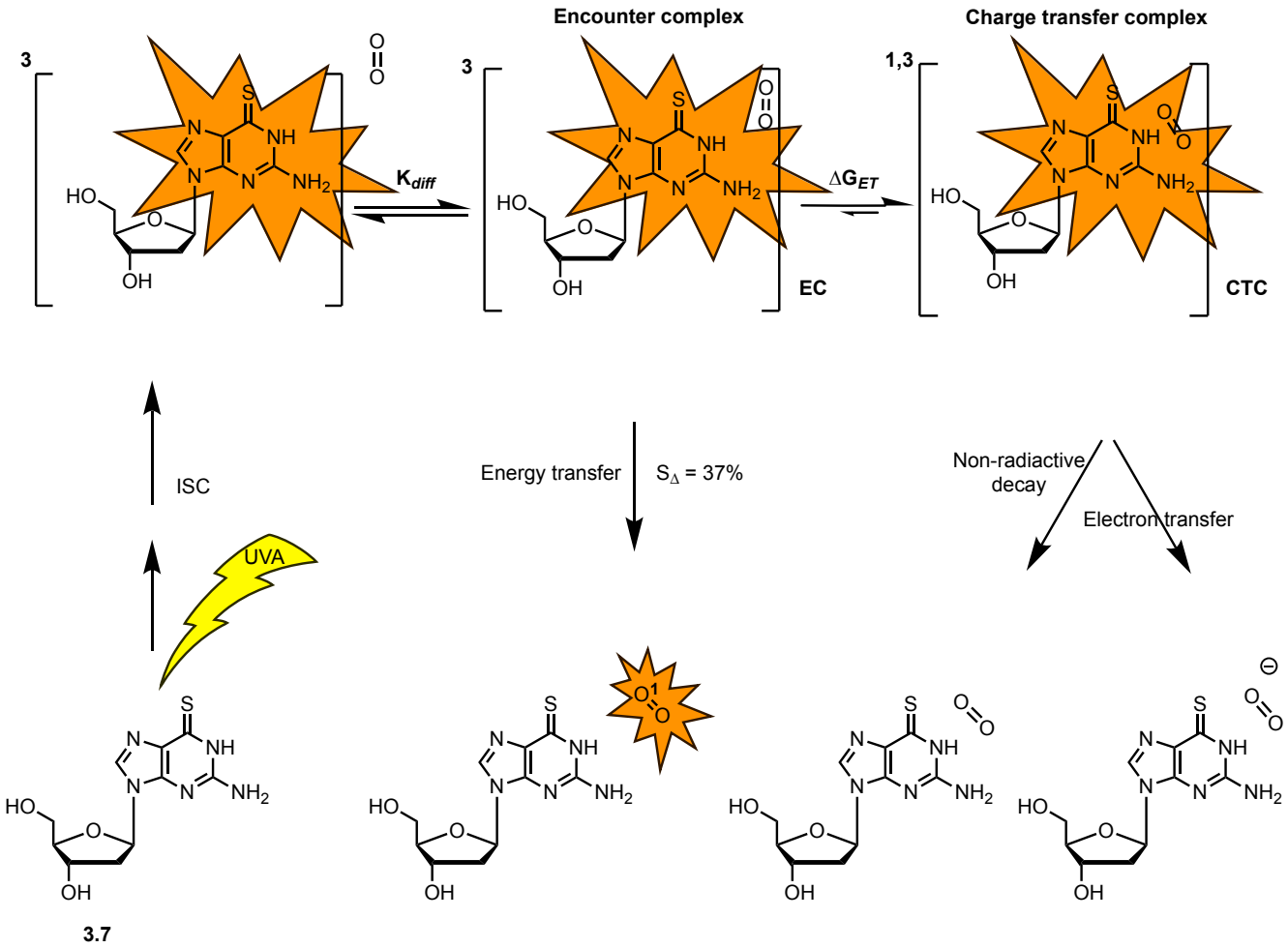


Figure 29 Proposed mechanism of action generating singlet oxygen in competition with other reaction pathways as described by Pollum et al.[14]

From here, therapeutic investigations have evolved further to incorporate the photo-activation of drugs within nano-capsules and vesicles, and even onto developing photo-thermal therapies.[15]

For the work discussed in this chapter, the premise of the photo-activation was to enable the release of the HNO from its inactive state within the confines of a cyclo-adduct. Chapter 2 details the release of HNO by photo-activation, and also highlighted the concerns surrounding the stability of the cyclo-adduct before exposure to light. Work by King[16-18] and Miyata[19, 20] has detailed the retro Diels-Alder reaction required to release the acyl nitroso in aqueous conditions and the cyclo-adduct in this chapter was designed to follow the same mechanism of action.

Even within DNA constructs there is evidence of the photo-controllable nature of anthracene being used to manipulate greater supramolecular interactions. Tucker and co-workers show the controllable disruption of a thrombin binding aptamer (TBA) G-quadruplex by the replacement of certain bases with anthracene moieties which could undergo a [4π + 4π] photo-cyclisation upon photo-irradiation.[21] This light-induced process disrupted the modified aptamer's ability to form a G-quadruplex and bind thrombin, which was considered useful in the design of clotting factor therapeutics.

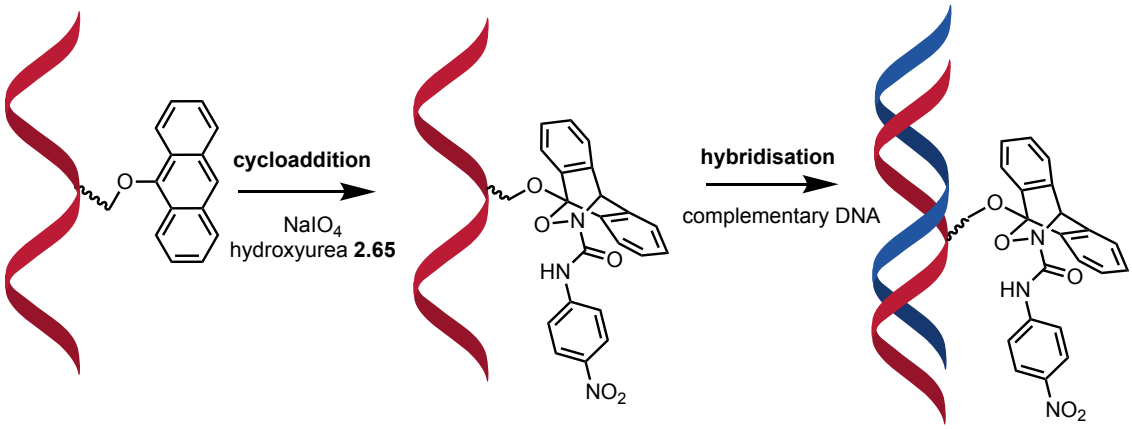
3.2 Aim

As the stability of the cyclo-adduct in Chapter 2 was the main challenge of the synthetic aims of this project, the idea of incorporating the cyclo-adduct within a single strand of DNA was hoped to improve this issue.

As such, the aim of this chapter was to investigate the feasibility of incorporating Diels-Alder derived cycloadducts into single-stranded DNA and to look into their subsequent HNO donating capabilities. Despite previous work showing the destabilising effects of incorporating the cycloadducts into peptides when functionalising at both the 9- and 10-positions of the anthracene starting material,[22] the incorporation of anthracene into DNA was a novel option for stabilising the Diels-Alder photocage.

Therefore, the first objective was to determine whether functionalising the anthracene diene at only the 9- position would allow for improved stability of the cycloadduct, at least within DNA systems. A known anthracene tag synthesis designed by the Tucker group[21, 23] was chosen to build a 9-anthracene derived phosphoramidite which could be incorporated into DNA using solid-phase synthesis. The Diels-Alder reaction would then be performed on the DNA strand to attempt cycloadduct formation.

In the event of successful incorporation of the cycloadduct into a single strand of DNA, the hybridisation of the strand into a duplex and subsequent release of HNO could be investigated (Scheme 32).



Scheme 32 Generalised scheme for incorporation of anthracene into DNA, Diels-Alder cycloaddition, and hybridisation into a duplex

3.3 Design and synthesis of anthracene tag phosphoramidite

3.3.1 Design of an ideal anthracene tag

Previous work by the Tucker group has concentrated on incorporating anthracene moieties with a chiral functionality (Figure 30) into DNA single strands for diagnostic sensing of SNPs.[20, 21, 24-26] Computational modelling of the anthracene within a particular 15-mer DNA strand[26] gave an insight of the positioning of the intercalator within the DNA major and/or minor grooves of duplex DNA. This modelling was performed to investigate differences in anthracene absorption and emission spectra when the tag was in different environments within the oligomer. When duplexed opposite different bases, the anthracene emission spectra were found to differ in intensity, forming the basis of the diagnostic sensing work.[20] Modelling of the strand (n=4 linker to the tag) as a duplex showed how, whilst still a dynamic process, the L anthracene projects more into the major groove of duplex DNA, managing to intercalate well, while the D anthracene is less unable to do so, instead aligning near the minor groove (Figure 30).[21]

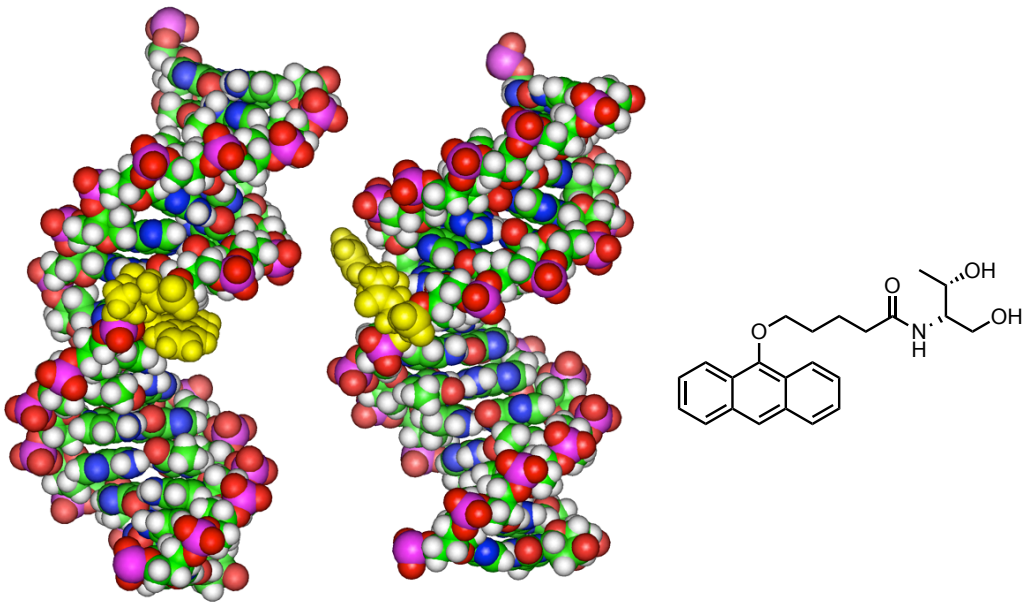


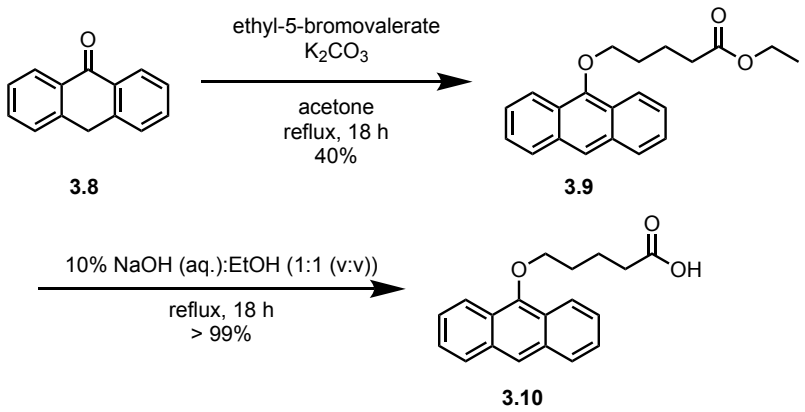
Figure 30 AMBER models of L (left) and D (right) n=4 anthracene tagged 15-mer duplex DNA. Taken from J-L. Duprey, 2010. D isomer of the anthracene derivative shown.

This modelling caused the design of the anthracene tag for the HNO release project to be directed towards forming the D isomer as it was hypothesised that the middle ring of the anthracene would be more available for the cycloaddition. The 15-mer was also kept the same, with the single strand used for the cycloadditions to further improve accessibility of the diene.

Use of the *n* = 4 tag length was also designed to maximise the chances of stability within the complex; this linker length had previously been shown to improve duplex stability as observed by investigating the T_m values of duplexes formed with linker lengths *n* = 1 to *n* = 6.[27] While in this study duplex formation was not the primary objective, evidence of improved stability, presumably by the flexibility of the anthracene moiety to intercalate, was highly desirable for the longer term aim of hybridisation to a complementary vector DNA strand.

3.3.2 Synthesis of an alkoxy-substituted anthracene derivative

As discussed above, an anthracene-derived tag was initially chosen as the ideal diene for Diels-Alder based cyclo-addition studies as its behaviour within single-strand DNA had previously been well studied within the group. It was decided to synthesise the *n* = 4 monomer species, where *n* represents the number of carbons between the carbonyl group and the oxygen species. This is a known synthesis involving a carboxylic acid intermediate derived by saponification of the anthracene alkoxy ester (Scheme 33).[20, 24]

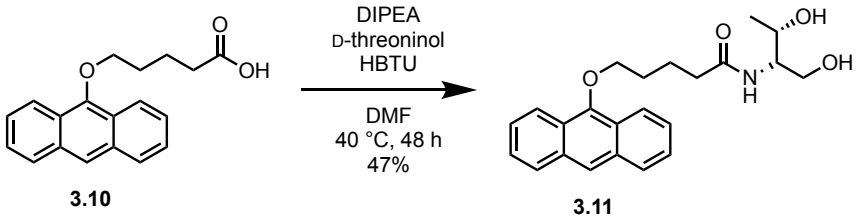


*Scheme 33 Synthesis of anthracene-derived carboxylic acid intermediate **3.10***

From commercially available anthrone, base-induced nucleophilic substitution with ethyl-5-bromovalerate gave the alkoxy-ester **3.9** in 40% yield. This ester was saponified with aqueous sodium hydroxide and precipitated with hydrochloric acid to give the carboxylic acid intermediate **3.10** in quantitative yield.

To create a non-nucleosidic base analogue for solid-phase DNA synthesis, certain moieties must be maintained within the structure. One important feature is the design of the hydroxyl functional groups which occur as the 3'- and 5'-OH groups on a standard nucleoside. By using threoninol (2-amino-1,3-butanediol), the primary and secondary hydroxyl groups mimic that of the nucleoside, giving a reasonable analogue. Another benefit is the presence of the methyl group adjacent to one alcohol, which creates a point of stereogenic distinction and allows for the regioselective protection of one alcohol. These factors make it possible to achieve diastereomically pure phosphoramidites for DNA synthesis.

Use of D-threoninol in the amide coupling reaction (Scheme 34) gives the (*S,S*)-stereoisomer for the resulting compound **3.11**, which can be maintained throughout the next stages of synthesis to result in an *S,S* configured phosphoramidite.



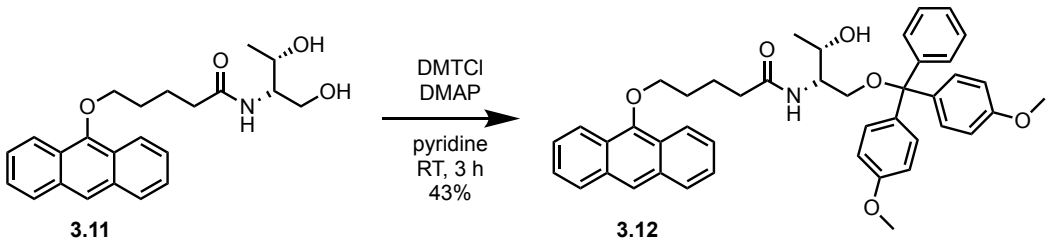
3.10 **3.11**

*Scheme 34 Amide coupling with D-threoninol to give unsymmetrical diol **3.11***

3.3.3 Selective hydroxyl protection

Following the standard Caruthers methodology for solid-phase DNA synthesis,[27] the 5'-alcohol is protected initially with an acid-labile group. Most often, this utilises dimethoxytrityl (DMT) groups for the protection. This protecting group has been used extensively when

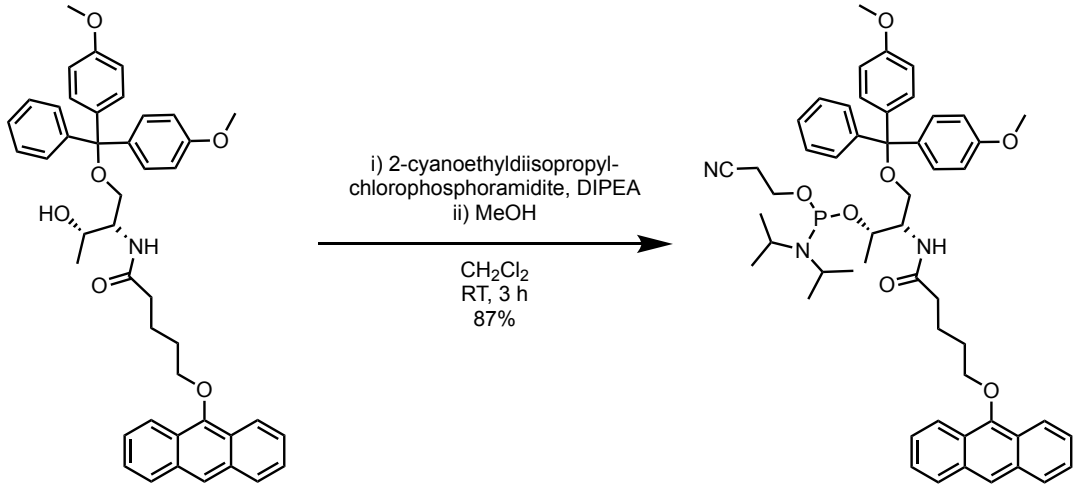
designing phosphoramidites for solid-phase DNA synthesis.[20, 24] The DMT group was added regioselectively to the primary alcohol of the threoninol derived functional group in 43% yield to produce protected species **3.9**. To further catalyse the selective tritylation of the primary alcohol over the secondary, DMAP was added to the reaction mixture (Scheme 35).[20, 28]



*Scheme 35 DMT protection of primary alcohol group on an anthracene derivative to give compound **3.12***

3.3.4 Phosphoramidite synthesis

The final synthetic step to prepare the anthracene derivative ready for solid-phase DNA synthesis requires phosphitylation of the free alcohol group within compound **4** using 2-cyanoethyl *N, N*-diisopropylchlorophosphoramidite and DIPEA, before quenching with methanol for 30 min to give the phosphoramidite **3.13** (Scheme 36). This compound showed as two very close spots by TLC on base-doped silica TLC plates, believed to be the two P(III) diastereomers. On removal of the solvent, the crude compound was re-dissolved in de-gassed EtOAc and washed with saturated sodium hydrogen carbonate then brine (both also degassed). Column chromatography on activated basic alumina in 50:49:1 hexane: EtOAc: Et_3N (degassed) gave the desired compound as a pale-yellow solid in 87% yield.



*Scheme 36 Phosphitylation of secondary alcohol to give anthracene derived phosphoramidite **3.13***

The phosphoramidite monomer was characterised using positive electrospray mass spectrometry, ^{31}P and ^{1}H NMR. ^{13}C NMR was not obtained due to the inherent instability of the phosphoramidite. The ^{31}P NMR spectrum showed two peaks (147.5, 147.0 ppm) that corresponded to the expected region for diastereomeric phosphoramidites (Figure 31).[23]

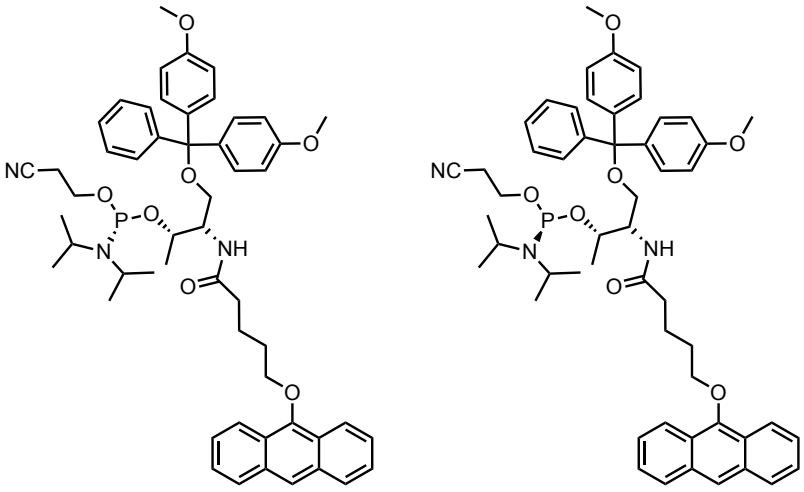


Figure 31 Diastereomeric phosphoramidites

3.4 DNA synthesis

3.4.1 Introduction

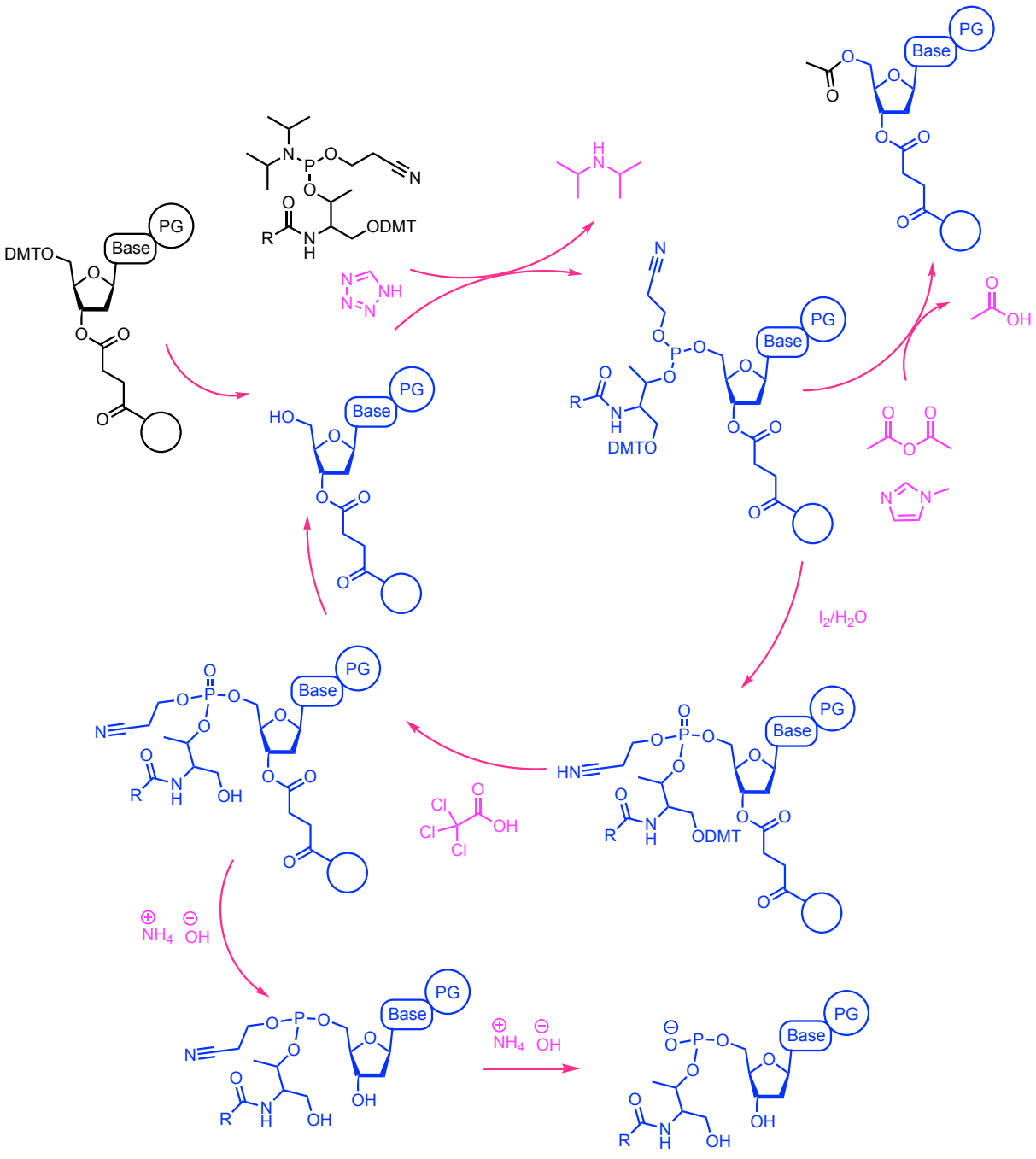
Synthesis of all oligonucleotides discussed throughout was performed using a Beckmann 1000M automated DNA synthesiser, incorporating the 'phosphoramidite' DNA synthesis method.

In this method, the 3' terminus is bought on a controlled pore glass (CPG) solid support, which contains a 5' protected deoxynucleoside (A,C,G or T) attached at the 3' end by a succinimide linker. This acts as the starting point to the DNA synthesis cycle and all subsequent bases and base analogues are coupled onto the support (**Error! Reference source not found.**).

First, detritylation of the solid supported base on the CPG removes the protecting group and leaves a free 5' alcohol for coupling. This is done using an acid-initiated removal with trichloroacetic acid.

To couple the next base, either an unmodified nucleoside or a nucleoside base analogue, tetrazole is used to remove the diisopropylamine from the phosphoramidite. This allows activation of the phosphoramidite which then adds into the deprotected hydroxyl group on the supported nucleoside. Before the next base can be added, any unreacted chains must be capped with acetyl groups and the phosphite ester must be oxidised to the phosphatetriester using iodine and water.

This process can then be repeated as often as required to build the desired sequence strand. To end the DNA sequence, ammonia solutions cleave the succinimide linker and remove the cyanoethyl groups to deprotect the phosphoramidite (Scheme 37).



Scheme 37 Automated DNA synthesis cycle showing addition of an R group base analogue

3.4.2 Linear and hairpin DNA design

The linear sequence chosen for this modified oligonucleotide was used as it was a 15-mer that had been fully characterised with the same anthracene tag modification in previous work

by the Tucker group (Table 3).[17, 29] This would allow a direct comparison for results of the anthracene incorporated oligonucleotide and the Diels-Alder cycloadduct incorporated product. Although the anthracene tag was incorporated into the middle of the linear DNA strand, it was thought the diene would still be sufficiently available for the subsequent Diels-Alder reaction. A hairpin strand was also designed with the anthracene moiety included in the centre of the loop section, which was expected to increase the availability of the anthracene diene for the desired Diels-Alder reaction.

This strand was slightly shorter than the 15-mer linear strand and consisted of a region of 4 bases capable of binding to the other end of the strand with either five thymine bases or four thymines and a modification separating the 5' and 3' binding regions.

Table 3 DNA sequences designed

STRAND NAME	***STRAND SEQUENCE (5'-3')***
Modified sequence (strand LIN-A):	5'-TGGACTC(**X**)CTCAATG-3'
Unmodified sequence (strand LIN-U):	5'-TGGACTC**C**CTCAATG-3'
Complementary sequence (strand LIN-C):	5'-CATTGAGGGAGTCCA-3'
Modified sequence (strand HP-A):	5'-CACGTT(**X)**TTCGTG-3'
Unmodified sequence (strand HP-U):	5'-CACGTT**T**TTCGTG-3'
Complementary sequence (strand HP-C):	5'-GTGCAAAAAGCAC-3'

Each strand option was synthesised both as the modified and the unmodified version, with the corresponding complementary strand for studies on duplex formation.

3.4.3 Synthesis and purification of modified DNA

The synthetic procedure for solid-phase DNA synthesis with a modification requires the dissolution of the base-analogue phosphoramidite in dry MeCN to a concentration of 0.1 M. This concentration of the modified tag is higher than that used for unmodified DNA synthesis, calculated to maximise the coupling yield due to the reactivity of phosphoramidite. The coupling was performed on an ABI 394 DNA synthesiser with an extended coupling time (15 minutes instead of 25 seconds).

Each oligonucleotide was synthesised using ultra-mild conditions, which are less harsh than the standard ones, using slightly different Cap Mix A (pyridine/Pac-anhydride) and a lower concentration of iodine oxidiser (0.02 M instead of 0.1 M). The deprotection conditions are different too, instead of using ammonia to remove the DNA from the resin, the strands are removed from the synthesiser on the resin and left to shake in potassium carbonate (0.05 M in EtOH, 2 mL) for 16 hours. The crude DNA strands must then be concentrated to dryness using a speed-vac and passed through a Nap10 column prior to purification by HPLC.

HPLC was used for the purification of all DNA strands, with varying gradients of acetonitrile and an aqueous TEAA solution (0.1 M) dependent on the strand structure (Table 4).

Table 4 HPLC conditions for purifying DNA strands

DNA	*TIME OF GRADIENT (MIN)*	*MeCN (%) START*	*0.1 M TEAA BUFFER (%) START*	*MeCN (%) END*	*0.1 M TEAA BUFFER (%) END*	*TEMP (ºC)*
LIN-A	*30*	*15*	*85*	*25*	*75*	*24*
LIN-U	*30*	*5*	*95*	*18*	*82*	*60*

LIN-C	*30*	*5*	*95*	*18*	*82*	*60*
HP-A	*30*	*15*	*85*	*25*	*75*	*24*
HP-U	*30*	*5*	*95*	*18*	*82*	*60*
HP-C	*30*	*5*	*95*	*18*	*82*	*60*

Use of semi-preparative reversed-phase HPLC on an oligo clarity column gave clearly separated retention peaks for purification, with truncated DNA strands typically showing much shorter retention times. The purified strands were then characterised by analytical HPLC and mass spectrometry (Appendix 3.1).

The various HPLC temperature choices were due to the potential un-wrapping of the hairpin structure at heat. There was also a risk that the cycloadduct would undergo retro-Diels-Alder at heat, and as such for accurate comparisons the starting material LIN-A and HP-A strands were purified at room temperature.

3.4.5 Diels-Alder reaction on DNA

To carry out the Diels-Alder reaction on the anthracene-incorporated DNA, adjustments had to be made to the reaction conditions. For the small molecule testing of the cycloaddition, a mixture of organic solvents was used to improve the rate of reaction. In DNA however, chlorinated solvents are not suitable, and adjustments were required (Table 5).

Table 5 Conditions attempted for DNA cycloaddition reaction

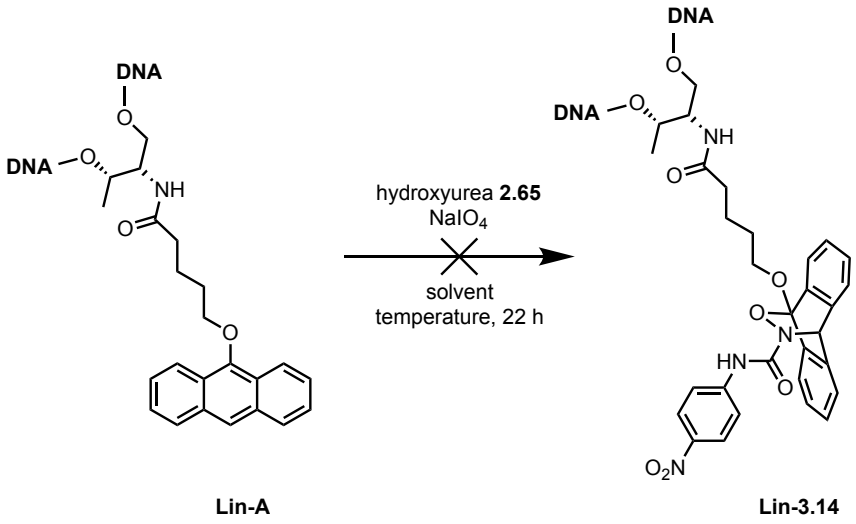
Conditions	*Solvent*	*Temperature (˚C)*	*Reaction time (h)*	*DNA concentration (μM)*	*Hydroxyurea **2.65/2.69** and $NaIO_4$ concentration (μM)*
1	H_2O	0	22	20	100
2	H_2O: DMF (1:4)	4	22	20	100
3	H_2O: MeOH (1:10)	4	22	20	100
4	H_2O: MeOH (1:10)	4	22	90	170
5	H_2O: MeOH (1:10)	4	46	90	170

First, running the reaction in an entirely aqueous solution was tried (condition 1), but the lack of solubility of the hydroxyurea **2.65** made this unsuitable. Next, an aqueous mixture (H_2O: DMF 1:4) was tried (condition 2), to improve the solubility of the DNA strand and the sodium periodate. By degassing the solutions of sodium periodate $NaIO_4$ (100 μM) and hydroxyurea **2.65** (100 μM) and combining them on a vortex in an ice bath (0 ˚C) for 15 minutes, the acyl nitroso species was assumed to have formed *in situ*. A degassed solution of the anthracene-modified DNA (20 μM) was added to the reaction vessel and the mixture vortexed for a further 20 hours in the ice bath. To characterise the reaction products, the solution was first concentrated to dryness using a speed-vac and re-dissolved in H_2O (1 mL). This was passed

through a Nap10 size-exclusion column to de-salt the sample and remove any unreacted urea.

Characterisation of the cycloadduct (section **3.4.6**) indicated that this attempt had not resulted in any reaction occurring, with the UV vis spectra, HPLC retention time and MS results remaining the same as seen in the starting material.

One possible reason for the lack of reaction was thought to have been the aqueous conditions used. As the acyl nitroso species is known to undergo nucleophilic attack from water, it could be that the nitroso does not exist as the dienophile for long enough to undergo the Diels-Alder cycloaddition. Using this assumption, changing the solvent to methanol (condition 3) was thought to negate this possibility. The reaction was also moved to a cold room (4 ˚C) to maintain a more even temperature throughout the experiment (Scheme 38).

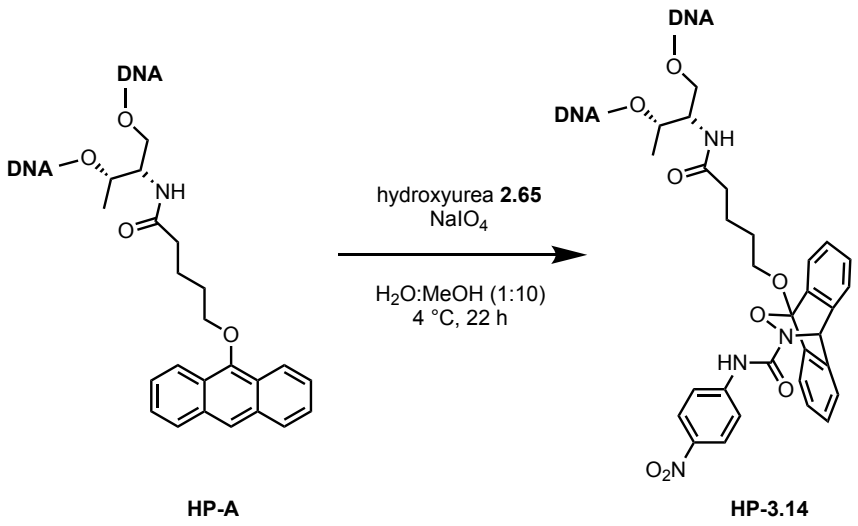


*Scheme 38 Attempted Diels-Alder reaction to form cycloadduct **Lin-3.14***

Using condition 3 (Table 5), the hydroxyurea was vortexed with sodium periodate for a longer period of one hour to ensure the nitroso had formed before the linear DNA was added to the reaction vessel. The same work up was implemented after 22 hours vortexing, and the same characterisation techniques used to study the reaction product. All three forms of

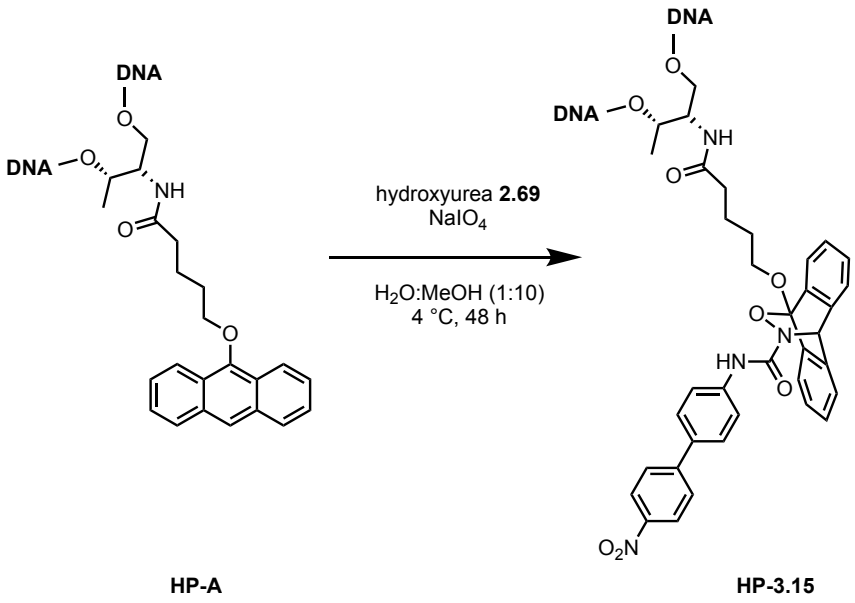
characterisation showed a lack of reaction again, with analogous UV vis results to those seen in Figure 32. From this, focus shifted to the design of the DNA strand: the linear nature of the DNA strand could interfere with the availability of the anthracene diene for the dienophile which may explain the apparent lack of reactivity.

Next, the hairpin loops of anthracene-modified DNA were subjected to the same condition 3 from Table 5 (Scheme 39). Analysis of these products showed a definite change from the starting materials (see next section for further details), indicating a reaction had taken place. However, on attempting to increase the concentration of the reagents, reactivity was reduced and only starting material was observed after 22 h. Increasing the reaction length to 46 h gave some sign of product, as will be discussed in the following section. Following investigations in Chapter 2 where the regiochemistry of the cycloadduct was determined to be most likely an acetal, the following diagrams follow this assumption and only show the acetal regioisomer.



*Scheme 39 Diels-Alder reaction on strand **HP-A** to form cycloadduct **HP-3.14***

A second version of the strand was also prepared using the larger hydroxyurea **2.69** in an attempt to prepare a slightly more stable version of the cycloadduct, based on Miyata's previous findings (Scheme 40).[30]



*Scheme 40 Diels-Alder reaction of DNA strand **HP-A** and the nitroso formed from hydroxyurea **2.69** to form the cycloadduct **HP-3.15***

3.4.5 Characterisation of DNA cycloadducts

3.4.5.1 UV vis

Analysis of the sample was carried out using UVvis, HPLC and mass spectrometry. UVvis of the starting material showed characteristic peaks, from which the reaction could potentially be followed. First, the DNA absorbance band at 260 nm should be present in both the starting material and end DNA cycloadduct. The anthracene absorbance bands however should be disrupted by the Diels-Alder reaction taking place.

Anthracene has been a major component of the chemistry of organic chromophores since the 1830s.[30] The ultraviolet absorption patterns of anthracene were discussed by Jones[30] where he described the two distinguishable parts of the compound's absorption. The multiple

maxima in the 300 – 400 nm wavelength region are thought to be vibrational sub-shells, related to the aromatic C-H bending observed in the infrared spectrum at around 1450 cm^{-1} and expected to be due to the multiple resonance forms possible in the structure.[31] The higher frequency bands are considered to be related to a separate state of electronic excitation.[31] These maxima are hidden in any spectra containing DNA so the bands absorbing at 300-400 nm will be used from here in studying the anthracene fused ring system.

UVvis analysis of the crude (post Nap-10 size-exclusion column) products **Lin-3.14** and **HP-3.14** against the starting materials **Lin-A** and **HP-A** showed initial differences in the reactivity of the strands. For the linear strand, characteristic anthracene absorbance bands were observed in the product sample – a strong indication that either the Diels-Alder had not occurred or that the retro Diels-Alder had taken place under these conditions without need for photo-irradiation (Figure 32).

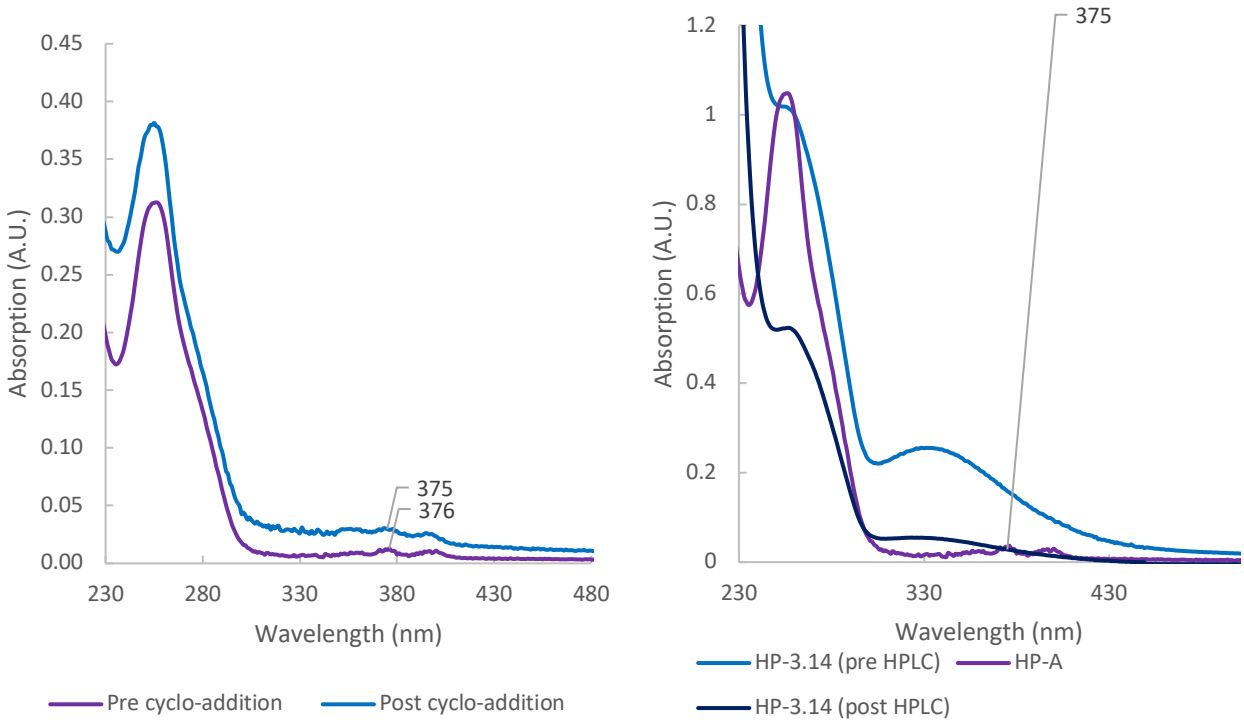


*Figure 32 UVvis absorption spectra before and after cyclo-addition on anthracene modified linear DNA strands **Lin-3.14** (left) and anthracene modified hairpin DNA strands **HP-3.14** (right). Solvent: MeOH, 4 μM*

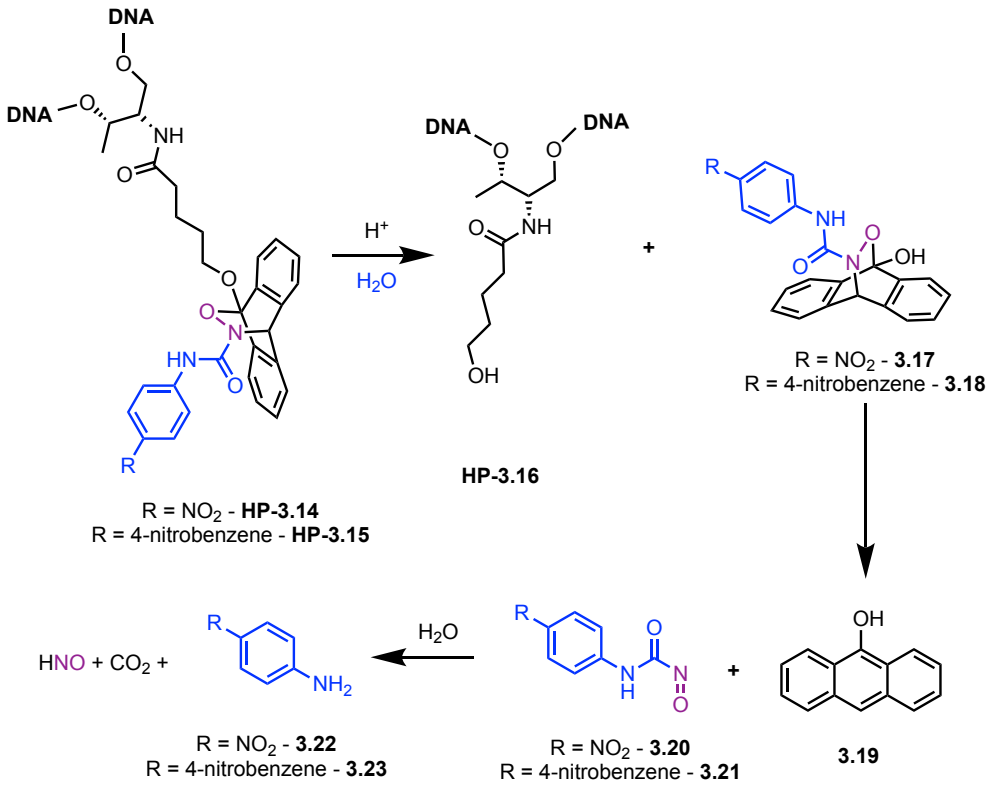
In contrast, analysis of the hairpin DNA **HP-A** system showed that a reaction had taken place, with the characteristic anthracene bands no longer evident and being replaced by a featureless broad band centred at around 340 nm (Figure 32). A higher energy absorption (λ_{max} at 260 nm) was still observed as expected for a DNA system, but this became more like a shoulder, which was perhaps indicative of a new absorbing moiety in this region.

3.4.6.2 HPLC

Analytical HPLC carried out on the hairpin system confirmed that a reaction had taken place with a total of 3 peaks seen by LC-MS (Appendix 3.2), with one relating to the retention time of the starting material. This fraction (t_R = 3.1 min, similar to the starting material), showed weak absorption signals at 260 and 360 nm, indicative of both the DNA and anthracene absorbance patterns. Fraction 2 showed no DNA absorbance (t_R = 3.6 min), so was assumed to be some residual unreacted hydroxyurea **2.65** that had got through the size-exclusion column. The third fraction showed absorption at 260 nm but not at 360 nm. This peak had a slightly shifted retention time compared to the starting material (t_R = 4.2 min), indicating the polarity of the complex had changed slightly and it was considered that the lack of absorption at 360 nm could indicate decomposition of the cycloadduct during the HPLC purification process. This fraction was separated using analytical HPLC and a mass recorded of this sample for further analysis (Appendix 3.3).

3.4.6.3 Mass Spectrometry

Interestingly, the masses of both the crude sample and that of fraction 3 after HPLC (determined using a clarity oligo column on a Waters Xevo G2-XS mass spectrometer) were 3892.640 which were in fact lower that the mass of the starting material **HP-A** (4068.659) and that of the intended cycloadduct (4265.97 for **HP-3.14**, 4342.07 for **HP-3.15**) (Appendix 3.3). Further investigation into the mass observed and possible fragmentation patterns led to the hypothesis that the acetal was undergoing hydrolysis at some point either before or during mass spectrometry (Scheme 41).



*Scheme 41 Possible hydrolysis mechanism of DNA-cycloadduct **HP-3.14** and **HP-3.15** to release HNO spontaneously*

The presence of the alcohol **3.16** would suggest that the desired cycloadduct might still have formed, as the likelihood of an aromatic carbon-oxygen bond (i.e., to anthracene) breaking under the same conditions would be very low. All previous investigations into an anthracene incorporated into DNA strands have not shown such fragility.[19, 20, 26] In an attempt to find further evidence to support this, the MS was run again with a wider search range of molecular weights (Appendix 3.4). This wider search gave extra masses seen within one retention peak on LC-MS, in particular the crude strand showed both the hydrolysed DNA mass (MW: 3892.59, 100%) and a mass which consistent with the sodium adduct of anthracen-9-ol (calculated mass: 217.22, observed mass: 217.00, 35%). As these masses were both observed within one retention peak on LC-MS, it was assumed the hydrolysis might be continuing to occur under MS conditions.

Taking the above into consideration, modifications to the MS conditions were made to try and reduce the chance of hydrolysis occurring. First, a DNAPac RP column was used to replace the Clarity Oligo column, to see if the lack of silica could improve the movement of the cycloadduct through to MS. Using this polymer-based column worked with the anthracene-modified DNA strand, changing the retention time slightly but still showing the correct molecular weight. However, the cycloadduct-modified DNA appeared to stick to the stationary phase of the column, not eluting at all. The small molecule with MW 217.00 eluted again, indicating that either the cycloadduct or the hydrolysed DNA strands were interacting with the stationary phase of the column, negating its use in further investigations.

Next, Fourier-transform ion cyclotron resonance (FT-ICR) was used in an attempt to control the hydrolysis of the cycloadduct. This technique uses the frequency of ion rotation in the magnetic field for the measurement, meaning it currently demonstrates the highest mass resolution (detailed in 7.1.2.9).[31]

A final approach to observing the full mass spectrum was attempted, using an Orbitrap Elite. The Orbitrap is an ion trap mass analyser that is an analogue of the FT-ICR discussed earlier. Use of these analysers is common for work on mass identification of protein species prone to fragmentation and as such it was hoped this would allow observation of the non-fragmented species.

The **HP-3.14** and **HP-3.15** samples were freshly prepared prior to the mass spectrometry and the crude product run on the Orbitrap Elite in MeOH: MeCN (1:1 – 10:1). Unfortunately, the scans did not show the full mass of the cycloadducts **HP-3.14** or **HP-3.15**, giving mainly fragment masses. One scan of the **HP-3.14** crude product showed a more promising result (Figure 33), but deconvolution showed that this mass calculated back to a molecular weight of 4255.90, still lower than the full cycloadduct mass 4265.97 required. From here, it was decided that the accurate mass of the cycloadduct could not be obtained, and as such a

definitive proof of the formation of the desired cycloadduct **HP-3.14** could not be achieved using mass spectrometry.

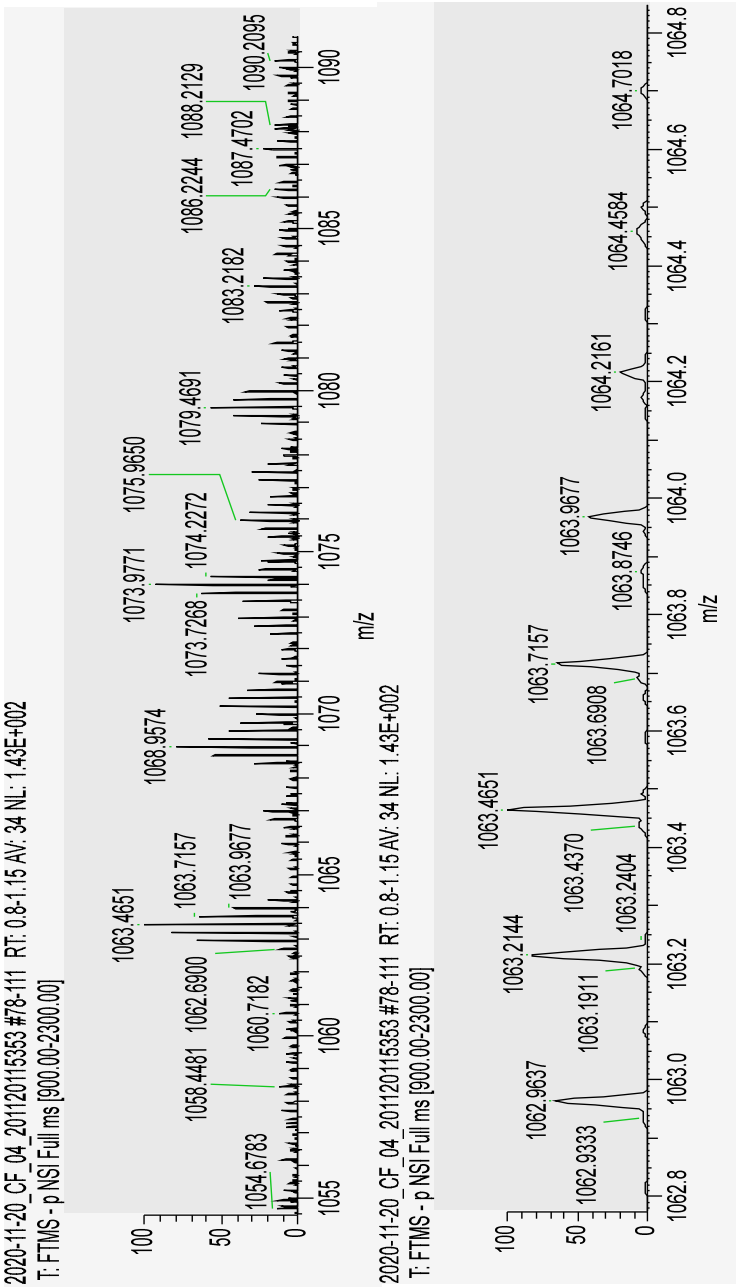
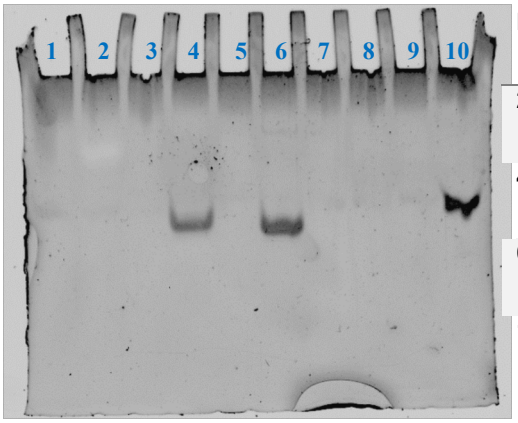


*Figure 33 Raw mass spectrometry data from Orbitrap Elite analysis of **HP-3.14** showing an isotope pattern calculating back to a molecular weight of 4255.9*

3.4.6.4 Polyacrylamide gel electrophoresis

Polyacrylamide gel electrophoresis (PAGE) was also used in an attempt to demonstrate the formation of the cycloadduct-modified DNA **HP-3.14**. As DNA is negatively charged, all the samples were expected to move, and any relative changes in mobility could be attributed to the modification with the cycloadduct possibly expected to run at a slightly different speed to the starting material, and also to the hydrolysed product. 25% Acrylamide gels in tris-borate-EDTA buffer and H_2O were used to run the crude and post-HPLC samples against the anthracene-modified starting material **HP-A**. As Figure 34 shows however, all three bands ran at very similar rates, which perhaps was not unexpected given the similar sizes of the starting materials and expected product. However, if anything, the band in lane 10 (post HPLC sample) ran slightly more slowly than those of the starting material and the crude product. While this might be consistent with the Diels-Alder cycloadduct moving more slowly through the gel due to its increased size, without mass spectrometry, this is impossible to state with any certainty.



LANE	SAMPLE
2	DNA loading gel
4	Hairpin shaped Oligo with Anthracene **HP-A**
6	Hairpin shaped Oligo with Cycloadduct (Crude) **HP-3.14**
10	Hairpin shaped Oligo with Cycloadduct (Post HPLC) **HP-3.14**

*Figure 34 PAGE of hairpin oligo **HP-A** and cycloadduct **HP-3.14***

To further investigate the evidence for the formation of the cycloadduct-modified DNA, a number of control experiments were run to ensure anthracene hydrolysis could not occur in other conditions. First, the anthracene-modified DNA was treated with sodium periodate at

the same concentration in the absence of the acyl nitroso compound. As expected, the resulting UV vis spectrum (Figure 35) indicated no reaction had occurred which shows the retention of the typical anthracene absorption peaks.

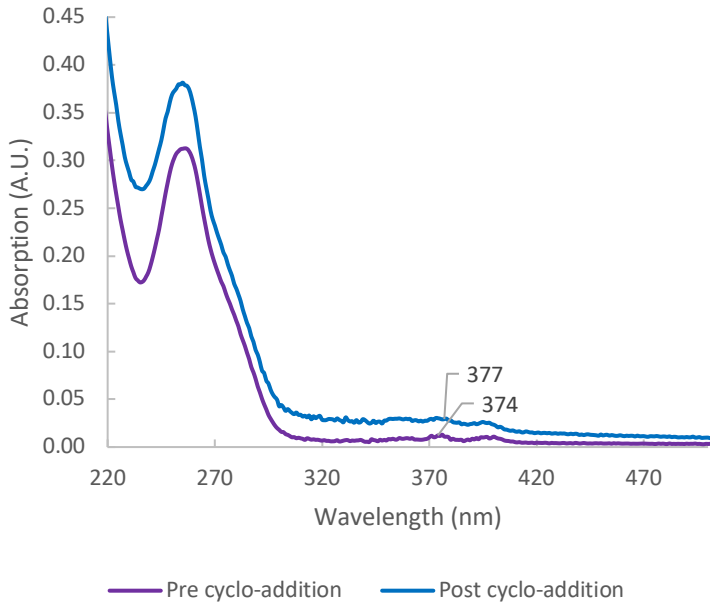


*Figure 35 Control reaction of $NaIO_4$ with anthracene modified DNA **HP-A** in MeOH*

Likewise, unmodified HP-U was subjected to the full reaction conditions, showing a similar lack of reactivity when analysed by UVvis (Appendix 3.6).

3.4.6.5 Circular Dichroism (CD)

CD is the study of differential absorption of left and right circularly polarised light, where it is used to investigate the relative shape of UVvis absorbing chiral structures.[33] It has therefore been used in studying DNA, in particular its secondary structure and the peaks and troughs of different DNA types are well-characterised. This technique will be outlined in detail in Chapter 7 (7.1.2.4).

To start investigating the relative CD spectra of the hairpin strands with and without the anthracene modifications, and after cyclo-addition, a variety of salt and solvent conditions were tested. In salt-free aqueous conditions, the CD spectra of the unmodified and

anthracene-modified strands **HP-U** and **HP-A** were found to have the same basic shape but showed a shift in the main peak from 277 nm to 260 nm (Figure 36) with a slight drop in intensity of approximately 0.8 mdeg.

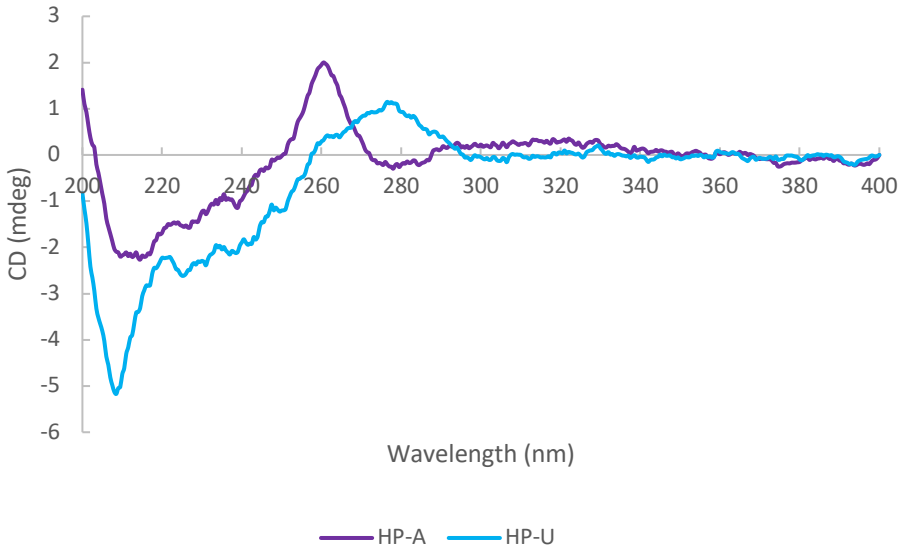


*Figure 36 CD spectra of anthracene-modified strand **HP-A** (10μM) and unmodified strand **HP-U** (10 μM) in H_2O*

Next, these two strands and **HP-3.14** (post HPLC) were studied to determine the CD spectra under the reaction solvent conditions (50 μM $NaIO_4$, MeOH) (Figure 37).

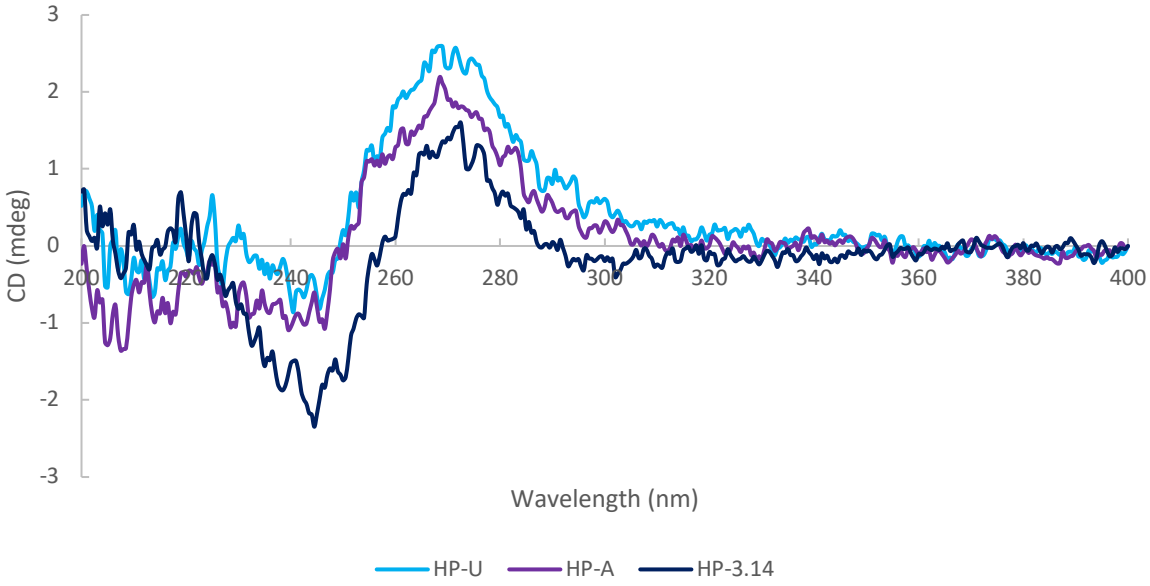


*Figure 37 Differences in CD spectra of anthracene-modified DNA strand **HP-A** (5 μM), unmodified strand **HP-U** (5 μM), and post cyclo-addition strand **HP-3.14**(5 μM)*

Compared to the spectra in water, the anthracene modified **HP-A** and unmodified **HP-U** showed very similar peaks and troughs, with the shifts almost entirely negated. However, the cycloaddition product **HP-3.14** caused a slight change in the spectrum, with a more pronounced trough at 245 nm and the peak at 267 nm showing a slightly lower intensity.

To consider this result against the possible hydrolysed DNA product seen in Scheme 41, it is necessary to discuss the relative chirality of the anthracene-containing DNA, the cyclo-adduct containing DNA and the DNA alcohol product strand HP-OH. As the inclusion of the anthracene into the DNA strand does not appear to have a strong effect on the CD spectra, it could reasonably be assumed that the DNA alcohol hydrolysis product should not show a different ellipticity, as the chiral nature of the DNA strand would not have changed. The cyclo-addition on the other hand, would introduce a new chiral element to the DNA strand through the acetal and as such could possibly cause a shift in the CD spectrum. However, the poor signal to noise ratio (due to the low amount of product material available) precludes a more definitive interpretation of the data at this stage.

3.5 Release of HNO

The characterisation of the cycloadduct containing DNA strand was determined to be inconclusive, and as such further work into this system as an HNO release system was deemed unlikely to be suitable for therapeutic applications. However, to finish the investigation, a brief study into the photo-activated release of HNO was undertaken, with the assumption that visualisation of the anthracene would reappear if the cycloadduct had formed and been stable. Whilst evidence pointed towards the **HP-3.14** product having undergone decomposition throughout the purification process, a retrospective approach to analysis of the compound would allow further investigation into the stability of the cycloadduct.

The isolated strand **HP-3.14** was dissolved in water to provide an aqueous environment for the retro Diels-Alder-derived acyl nitroso to undergo nucleophilic attack. Strand **HP-3.14** (400 µL, 2.732 µM) was dispensed into a quartz cuvette, fitted with a 325 ±4 nm bandpass filter and subjected to photo-irradiation for 30 min intervals, as per the diagram depicted in Figure 38.

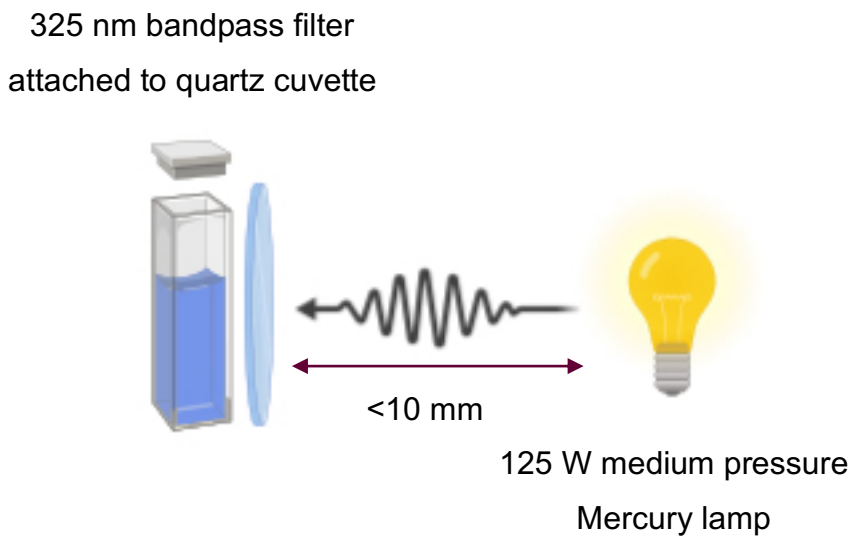


*Figure 38 Diagram of the set up designed to photo-irradiate strand **HP-3.14** at 325 nm to initiate HNO release*

The sample of **HP-3.14** was subjected to photo-irradiation for 30 min intervals and a UV vis spectrum taken at each timepoint (Figure 39).

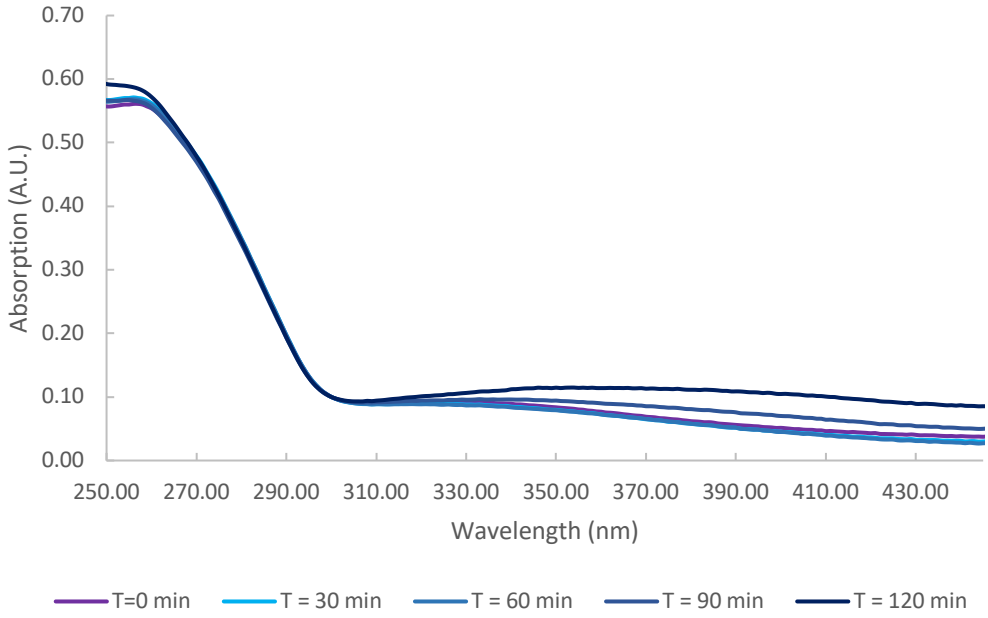


*Figure 39 UV vis spectra of cycloadduct-containing DNA **HP-3.14** in H_2O (2.73 μM) at different timepoints of photo-irradiation, normalised at 300 nm*

Analysis of these UV vis spectra showing a lack of anthracene absorptions bands indicated the starting material **HP-3.14** was the acetal adduct, with MS of the DNA strand showing degradation products that aligned with the cycloaddition having taken place. Observing the UV vis spectra at set timepoints revealed that the photo-irradiation was having little effect on the absorption after 2 hours, indicating that either no reaction was taking place, the retro Diels-Alder was indeed happening but very slowly, or that there was another degradation pathway occurring once the retro Diels-Alder had taken place. After one hour, there was no change at all in the absorption spectrum, but at T = 90 min the absorbance at wavelengths greater than 330 nm started to increase along with a decrease at 260 nm, which points towards some sample degradation occurring. As anticipated, the lack of re-emergence of any

anthracene bands indicated a lack of reversibility of any cycloadduct formation, a contrast to that observed by Miyata and co-workers.[17, 22] Due to the inherent instability of the compound observed by MS, no concrete proof of Diels-Alder cycloaddition can be given using this technique of attempting regeneration of the anthracene adduct **HP-A**.

3.6 Conclusions and future work

In this chapter, investigations into cycloadduct formation on anthracene-DNA were undertaken with the purpose of designing an externally controlled HNO-releasing system for therapeutic applications. The work has demonstrated that a reaction, possibly the desired Diels-Alder cycloaddition was possible on an anthracene group incorporated into a hairpin DNA strand, but not on a modified unstructured strand. While changes in the UVvis spectrum were observed in the forward process to indicate the reaction of the anthracene group, no photo-controlled reversal of the reaction was possible, meaning the efficiency of the HNO release could not be calculated.

From this work, it was decided not to investigate HNO release from DNA-based cycloadducts any further, due to the difficulties in proving both the existence and stability of the supposed Diels-Alder cycloadduct within the DNA, and the lack of evidence for the photo-activated retro Diels-Alder.

Future work on this possible cycloadduct product could include removing the 325 nm bandpass filter to increase the efficiency of HNO release – though this has inherent risks associated with damage to the DNA strand with UV light. A better course of action might be to redesign the linker to the anthracene tag to remove the reliance on an ether, which might improve the overall stability of the cycloadduct by eliminating the potential for hydrolysis (Figure 40).

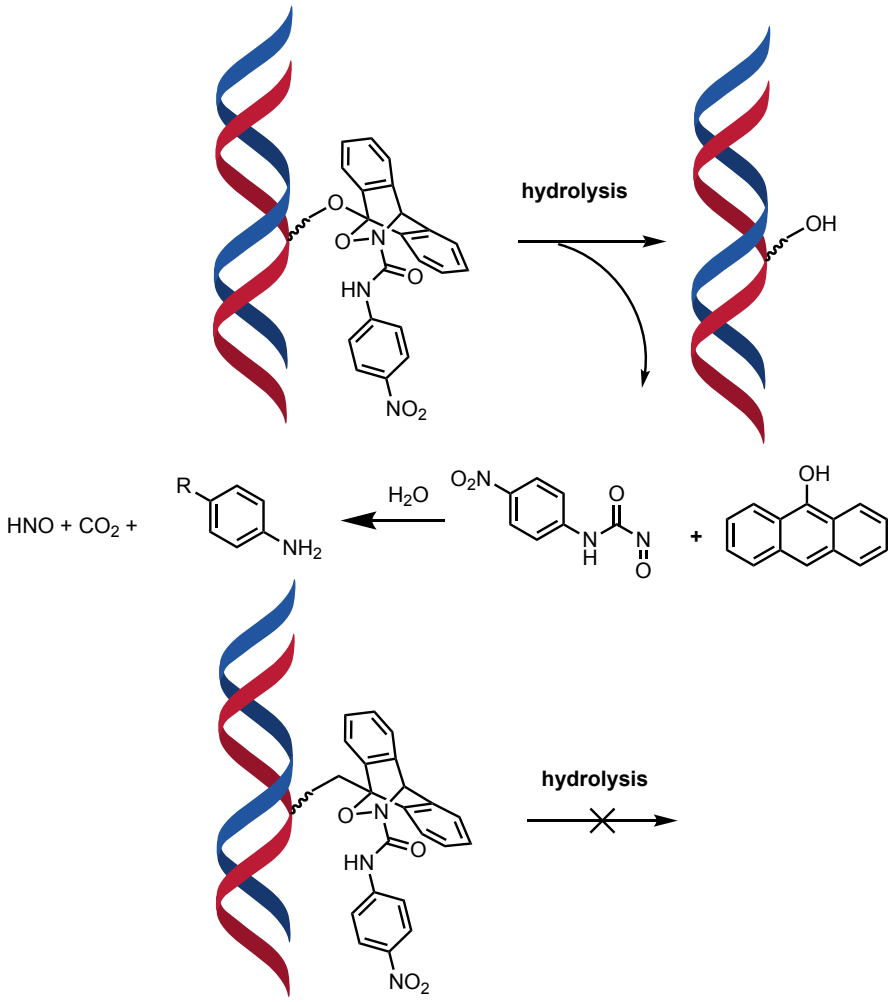


Figure 40 Cartoon representation of the hydrolysis seen on formation of a DNA-bound cycloadduct and possible future work relying on a methylene bridge in place

3.7 References

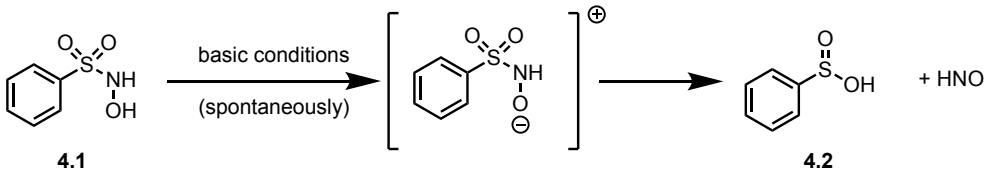
1. Gambucci, M.; Cerretani, C.; Latterini, L.; Vosch, T., The effect of pH and ionic strength on the fluorescence properties of a red emissive DNA-stabilized silver nanocluster. *Methods Appl. Fluoresc.,* **2019,** *8* (1), 014005.
2. Chakraborty, S.; Babanova, S.; Rocha, R. C.; Desireddy, A.; Artyushkova, K.; Boncella, A. E.; Atanassov, P.; Martinez, J. S., A Hybrid DNA-Templated Gold Nanocluster For Enhanced Enzymatic Reduction of Oxygen. *J. Am. Chem. Soc.,* **2015,** *137* (36), 11678-87.
3. Li, J.; Mo, L.; Lu, C. H.; Fu, T.; Yang, H. H.; Tan, W., Functional nucleic acid-based hydrogels for bioanalytical and biomedical applications. *Chem. Soc. Rev.,* **2016,** *45* (5), 1410-31.
4. Liu, X.; Zhang, J.; Fadeev, M.; Li, Z.; Wulf, V.; Tian, H.; Willner, I., Chemical and photochemical DNA "gears" reversibly control stiffness, shape-memory, self-healing and controlled release properties of polyacrylamide hydrogels. *Chem. Sci.,* **2019,** *10* (4), 1008-16.
5. Stoffelen, C.; Huskens, J., Soft Supramolecular Nanoparticles by Noncovalent and Host-Guest Interactions. *Small* **2016,** *12* (1), 96-119.
6. Jeddi, I.; Saiz, L., Three-dimensional modeling of single stranded DNA hairpins for aptamer-based biosensors. *Sci. Rep.,* **2017,** *7* (1), 1178.
7. Healy, J. M.; Lewis, S. D.; Kurz, M.; Boomer, R. M.; Thompson, K. M.; Wilson, C.; McCauley, T. G., Pharmacokinetics and biodistribution of novel aptamer compositions. *Pharm. Res.,* **2004,** *21* (12), 2234-46.
8. Ashwood, B.; Pollum, M.; Crespo-Hernandez, C. E., Photochemical and Photodynamical Properties of Sulfur-Substituted Nucleic Acid Bases. *Photochem. Photobiol.,* **2019,** *95* (1), 33-58.
9. Pollum, M.; Jockusch, S.; Crespo-Hernandez, C. E., Increase in the photoreactivity of uracil derivatives by doubling thionation. *Phys. Chem. Chem. Phys.,* **2015,** *17* (41), 27851-61.
10. Hemmens, V. J.; Moore, D. E., Photochemical sensitization by azathioprine and its metabolites--II. Azathioprine and nitroimidazole metabolites. *Photochem. Photobiol.,* **1986,** *43* (3), 257-62.
11. Brem, R.; Daehn, I.; Karran, P., Efficient DNA interstrand crosslinking by 6-thioguanine and UVA radiation. *DNA Repair (Amst)* **2011,** *10* (8), 869-76.
12. Pollum, M.; Ortiz-Rodriguez, L. A.; Jockusch, S.; Crespo-Hernandez, C. E., The Triplet State of 6-thio-2'-deoxyguanosine: Intrinsic Properties and Reactivity Toward Molecular Oxygen. *Photochem. Photobiol.,* **2016,** *92* (2), 286-92.
13. Manivasagan, P.; Bharathiraja, S.; Santha Moorthy, M.; Oh, Y. O.; Song, K.; Seo, H.; Oh, J., Anti-EGFR Antibody Conjugation of Fucoidan-Coated Gold Nanorods as Novel Photothermal Ablation Agents for Cancer Therapy. *ACS Appl. Mater. Interfaces,* **2017,** *9* (17), 14633-46.
14. DuMond, J. F.; King, S. B., The Chemistry of Nitroxyl-Releasing Compounds. *Antioxid. Redox. Sign.,* **2011,** *14* (9), 1637-48.
15. Xu, Y. P.; Alavanja, M. M.; Johnson, V. L.; Yasaki, G.; King, S. B., Production of nitroxyl (HNO) at biologically relevant temperatures from the retro-Diels-Alder reaction of *N*-hydroxyurea-derived acyl nitroso-9,10-dimethylanthracene cycloadducts. *Tetrahedron Lett.,* **2000,** *41* (22), 4265-9.
16. Zeng, B. B.; Huang, J. M.; Wright, M. W.; King, S. B., Nitroxyl (HNO) release from new functionalized *N*-hydroxyurea-derived acyl nitroso-9,10-dimethylanthracene cycloadducts. *Bioorg. Med. Chem. Lett.,* **2004,** *14* (22), 5565-8.
17. Adachi, Y.; Nakagawa, H.; Matsuo, K.; Suzuki, T.; Miyata, N., Photoactivatable HNO-releasing compounds using the retro-Diels-Alder reaction. *Chem. Commun.,* **2008**, (41), 5149-51.

18. Matsuo, K.; Nakagawa, H.; Adachi, Y.; Kameda, E.; Tsumoto, H.; Suzuki, T.; Miyata, N., Alternative photoinduced release of HNO or NO from an acyl nitroso compound, depending on environmental polarity. *Chem. Commun.,* **2010,** *46* (21), 3788-90.
19. Ali, A.; Bullen, G. A.; Cross, B.; Dafforn, T. R.; Little, H. A.; Manchester, J.; Peacock, A. F. A.; Tucker, J. H. R., Light-controlled thrombin catalysis and clot formation using a photoswitchable G-quadruplex DNA aptamer. *Chem. Commun. (Camb)* **2019,** *55* (39), 5627-30.
20. Duprey, J.-L. H. A. Studies On Anthracene Tagged Oligonucleotides. PhD, University of Birmingham, 2010.
21. Duprey, J. L. H. A.; Bassani, D. M.; Hyde, E. I.; Ludwig, C.; Rodger, A.; Vyle, J. S.; Wilkie, J.; Zhao, Z. Y.; Tucker, J. H. R., Anthracene-modified oligonucleotides as fluorescent DNA mismatch sensors: discrimination between various base-pair mismatches. *Supramol. Chem.,* **2011,** *23* (3-4), 273-7.
22. Matsuo, K.; Nakagawa, H.; Adachi, Y.; Kameda, E.; Aizawa, K.; Tsumoto, H.; Suzuki, T.; Miyata, N., Photoinduced Upregulation of Calcitonin Gene-Related Peptide in A549 Cells through HNO Release from a Hydrophilic Photocontrollable HNO Donor. *Chem. Pharm. Bull.,* **2012,** *60* (8), 1055-62.
23. Moran, N.; Bassani, D. M.; Desvergne, J. P.; Keiper, S.; Lowden, P. A. S.; Vyle, J. S.; Tucker, J. H. R., Detection of a single DNA base-pair mismatch using an anthracene-tagged fluorescent probe. *Chem. Commun.,* **2006**, 10.1039/b611650g (48), 5003-5.
24. Duprey, J. L. H. A.; Zhao, Z. Y.; Bassani, D. M.; Manchester, J.; Vyle, J. S.; Tucker, J. H. R., Detection of DNA base variation and cytosine methylation at a single nucleotide site using a highly sensitive fluorescent probe. *Chem. Commun.,* **2011,** *47* (23), 6629-31.
25. Zhao, Z. Y.; San, M.; Duprey, J. L.; Arrand, J. R.; Vyle, J. S.; Tucker, J. H., Detection of single nucleotide polymorphisms within a sequence of a gene associated with prostate cancer using a fluorophore-tagged DNA probe. *Bioorg. Med. Chem. Lett.,* **2012,** *22* (1), 129-32.
26. Duprey, J. L. H. A.; Bassani, D. M.; Hyde, E. I.; Jonusauskas, G.; Ludwig, C.; Rodger, A.; Spencer, N.; Vyle, J. S.; Wilkie, J.; Zhao, Z. Y.; Tucker, J. H. R., Rationalisation of a mechanism for sensing single point variants in target DNA using anthracene-tagged base discriminating probes. *Org. Biomol. Chem.,* **2018,** *16* (35), 6576-85.
27. Caruthers, M. H., The Chemical Synthesis of DNA/RNA: Our Gift to Science. *J. Biol.Chem.,* **2013,** *288* (2), 1420-7.
28. Wilkinson, C. G. Epigenetic sensing of base modifications using anthracene- and naphthalimide-incorporated dna probes, MSci, University of Birmingham, 2018.
29. Gray, V.; Dzebo, D.; Lundin, A.; Alborzpour, J.; Abrahamsson, M.; Albinsson, B.; Moth-Poulsen, K., Photophysical characterization of the 9,10-disubstituted anthracene chromophore and its applications in triplet-triplet annihilation photon upconversion. *J. Mater. Chem. C.,* **2015,** *3* (42), 11111-21.
30. Jones, R. N., The Ultraviolet Absorption Spectra of Anthracene Derivatives. *Chem. Rev.,* **1947,** *41* (2), 353-71.
31. Nikolaev, E. N.; Kostyukevich, Y. I.; Vladimirov, G. N., Fourier transform ion cyclotron resonance (FT ICR) mass spectrometry: Theory and simulations. *Mass Spectrom Rev.,* **2016,** *35* (2), 219-58.
32. Yu. M. Yevdokimov, V. I. S., S. G. Skuridin, S. V. Semenov, O. N. Kompanets, The CD spectra of double-stranded DNA liquid-crystalline dispersions. In *Circular dichroism: theory and spectroscopy*, Rogers, D. S., Ed. Nova Science Publishers: New York, 2011, pp 1-66.
33. Kelly, S. M.; Jess, T. J.; Price, N. C., How to study proteins by circular dichroism. *Biochim. Biophys. Acta.,* **2005,** *1751* (2), 119-39.

Chapter 4 Investigations into Piloty's acid analogue *N*-(anthracen-9-ylmethoxy)-2-nitrobenzenesulfonamide as an HNO donor

4.1 Introduction

The use of a common sulfonamide derivative **4.1** to release HNO has been of interest since the discovery of Piloty's acid in the late 19th century.[1] Piloty's acid can release nitroxyl spontaneously under basic conditions but is much less efficient under aerobic conditions and at neutral pH (Scheme 42).[2] Indeed, at pH 7.4, nitric oxide is thought to be released rather than HNO.[3]



*Scheme 42 Piloty's acid **4.1** and spontaneous decomposition under basic conditions to form the sulfinic acid **4.2** and HNO*

To create a more stable analogue, Nakagawa and co-workers developed a coumarin derivative of the sulfonamide that could release HNO when photo-irradiated in the visible light range.[2] Based on the reports of Piloty's acid derivatives 2-nitro-*N*-hydroxybenzenesulfonamide **4.3** and 2-bromo-*N*-hydroxybenzensulfonamide **4.4**,[2] the group worked on designing coumarin based compounds **4.5** and **4.6** (Figure 41).

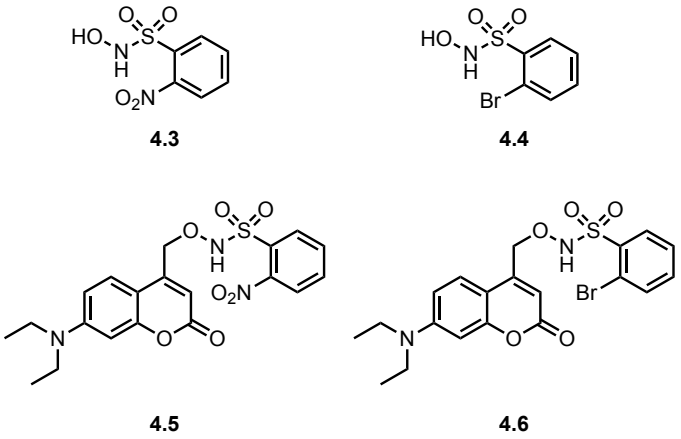
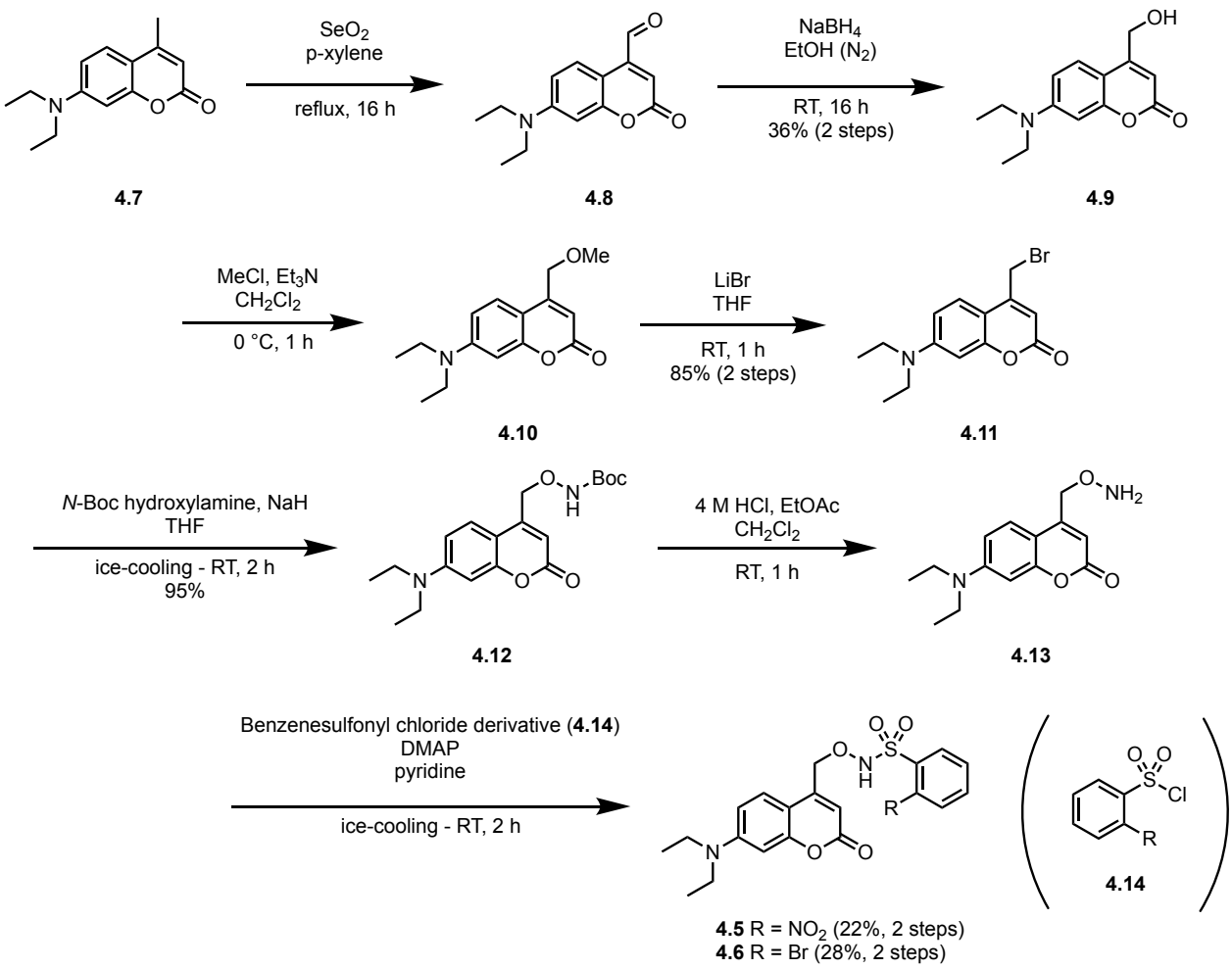


*Figure 41 Sulfonamide derivatives **4.3-4.6***

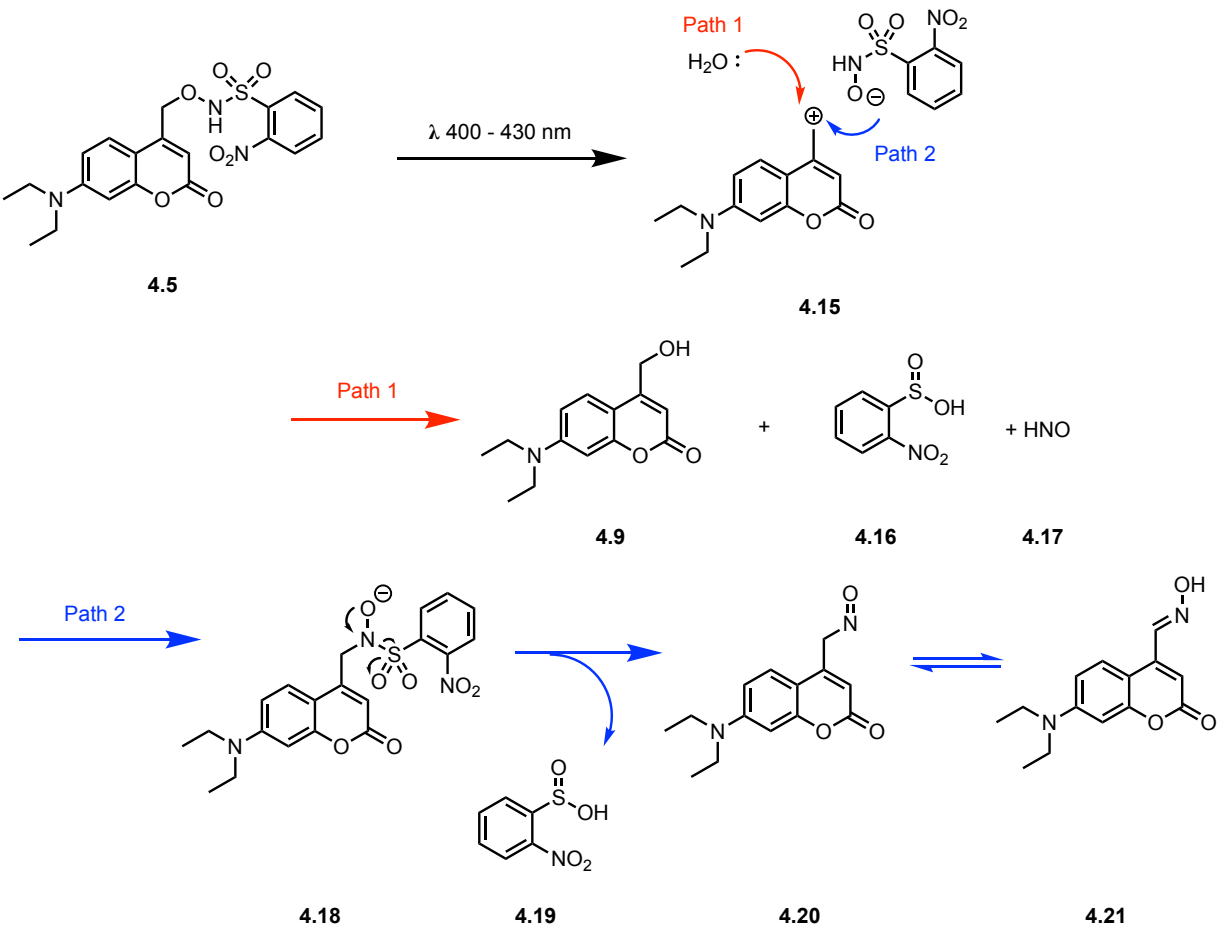
The design of compounds **4.5** and **4.6** show the hydroxyl group to be protected by a (7-diethylaminocoumarin-4-yl) methyl group which is released upon visible light irradiation at near 400 nm.[2] The compounds were synthesised from 7-diethyl-amino-4-methylcoumarin **4.7** over seven steps (Scheme 43). UV vis analysis showed absorption at around 400 nm, expected to be derived from the coumarin moiety.[2]



*Scheme 43 Synthetic scheme for production of derivatives **4.5** and **4.6** designed by Nakagawa and co-workers.*[2]

The photodecomposition of coumarin derivative **4.5** was undertaken using a xenon lamp source fitted with a 400 - 430 nm band pass filter and resulted in a number of new products as detected by HPLC.[2]

Two pathways of photodecomposition were proposed by Nakagawa and co-workers (Scheme 44).[4]



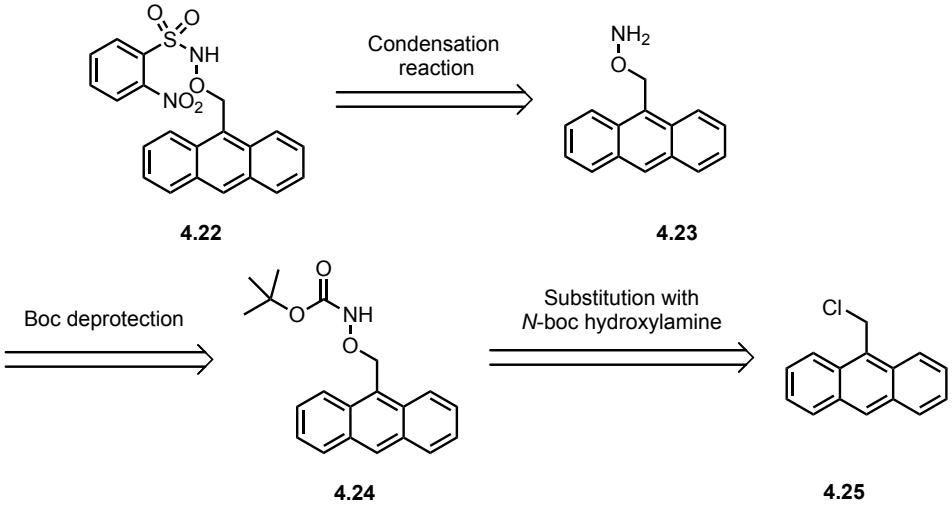
*Scheme 44 Photodecomposition mechanisms of **4.5** as proposed by Nakagawa and co-workers[4]*

Path 1 shown in red described the desired process where heterolytic cleavage of the C-O bond gave a methyl cation that could be attacked by water in aqueous environments and led to release of HNO. Path 2 (in blue) showed another potential pathway where the oxygen from the N-O could attack the methyl cation back again, resulting in the carbaldehyde oxime **4.21**. From this, the efficiency of HNO release by photodecomposition could also be studied. Nakagawa and co-workers estimated the efficiency of HNO release to be at <10%.

4.2 Aims

The possibility of adapting a sulfonamide derivative for both photo-controllable HNO release and DNA incorporation was attractive. By creating an anthracene derived analogue, the photo-controlled nature of nitroxyl donation could be retained with the opportunity for incorporation into DNA. The advanced knowledge of the photo-properties of anthracene-modified DNA within the Tucker group might also lead to adjustments capable of increasing HNO release efficiency.

The aim of this project, therefore, was to design an anthracene-sulfonamide derivative that was capable of releasing HNO upon photo-irradiation at certain wavelengths. The first design looked at creating a non-symmetrical anthracene sulfonamide derivative from the commercially available 9-chloromethyl anthracene **4.25** (Scheme 45).



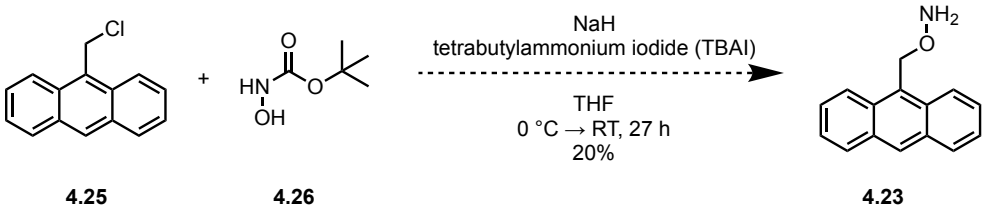
*Scheme 45 Retrosynthetic scheme for proposed synthesis of anthracene-sulfonamide derivative **4.22***

It was considered that a similar approach could also be possible with the symmetrical 9,10-difunctionalised anthracene moieties, making the design robust enough for both alternatives.

Upon successful synthesis of Piloty's acid derivative **4.22**, the secondary aim was to instigate decomposition of the analogue by photo-irradiation and to determine the mechanism by which the photodecomposition occurred.

4.3 Synthesis of anthracene analogue 4.22

Synthesis of the anthracene Piloty's acid derivative **4.22** was based on Nakagawa's work on the coumarin analogue.[2] From a halo-alkyl functional group, a protected hydroxylamine was added via nucleophilic substitution. Whilst Nakagawa demonstrated this through an alkyl bromide functionalised coumarin species, the same reaction was attempted on the commercially available 9-chloromethyl anthracene **4.25** (Scheme 46).



4.25 **4.26** **4.23**

*Scheme 46 Anticipated reaction on addition of N-Boc hydroxylamine **4.26** to 9-chloromethyl anthracene **4.25***

Following the procedure used by Nakagawa and co-workers, the nucleophilic substitution gave unexpected results from ^{1}H NMR spectroscopy analysis, showing the possibility of the nitrogen instead of the oxygen acting as the nucleophile, and loss of the Boc group as well as the intermolecular reaction (Figure 42). The triplet at 1.73 ppm was considered to represent the -NH proton as the peak integrated to 1 and showed triplet splitting, rather than the anticipated NH_2 singlet which would integrate to 2. The procedure proposed by Nakagawa and co-workers did not discuss any sign of the *N*-hydroxylamine in place of the *O*-hydroxylamine.

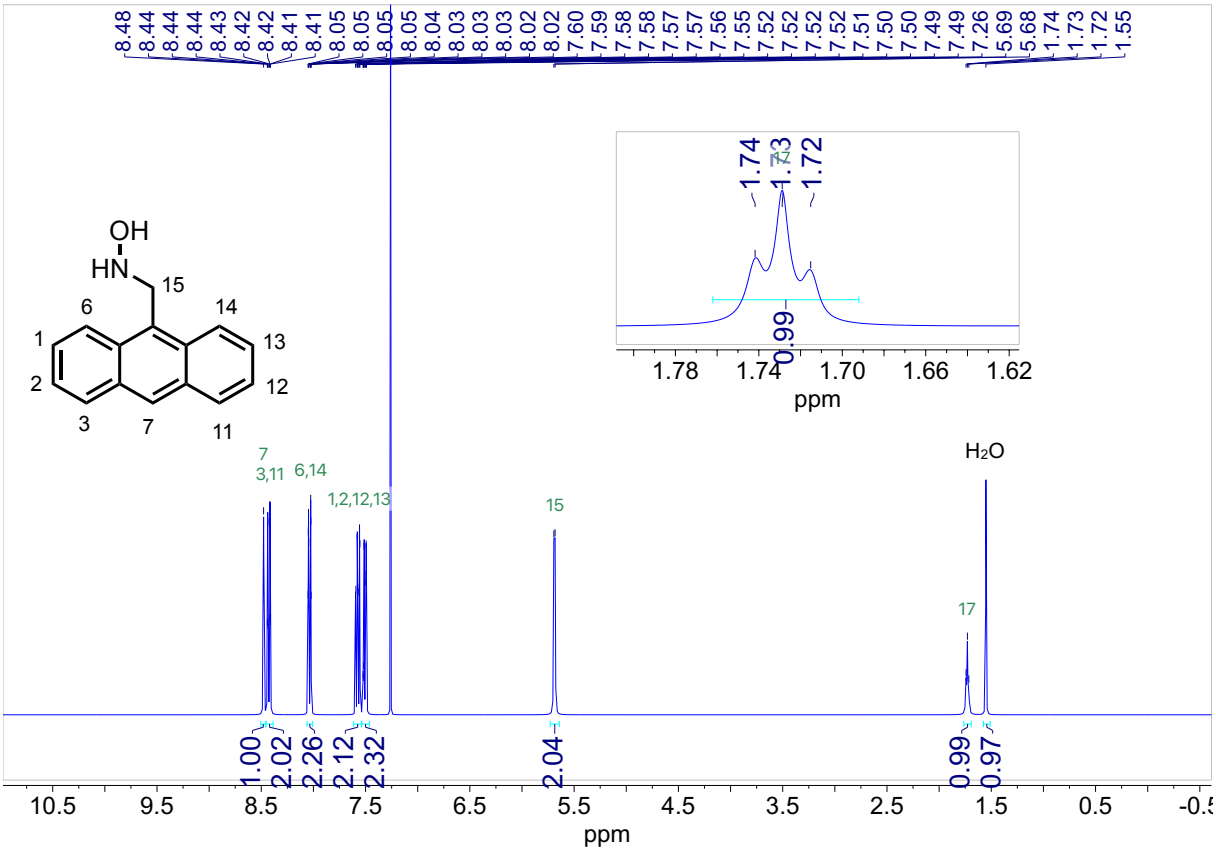
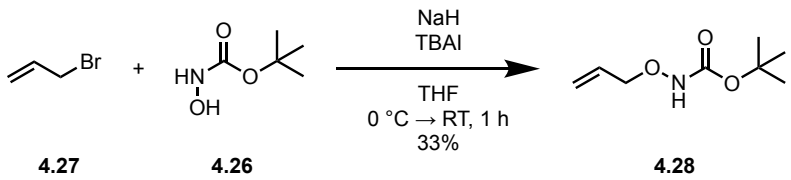


*Figure 42 ^{1}H NMR spectra of anticipated O-hydroxylamine **4.23** in $CDCl_3$ with evidence indicating an N-hydroxylamine formed instead*

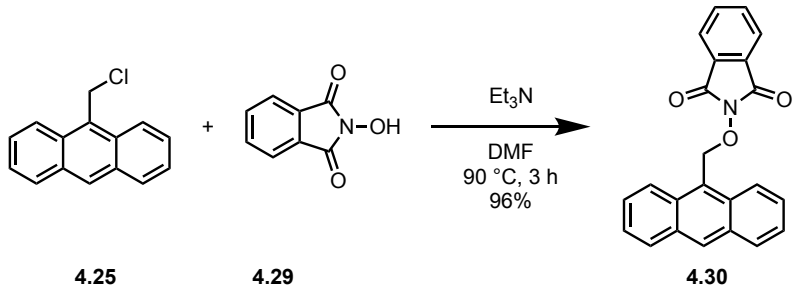
To test this theory, the Boc-protected hydroxylamine was reacted with 3-bromo-prop-1-ene **4.27** using different sodium hydride options, either triturated with hexane or left as the oil emulsion, to determine if this had any effect on the reaction option (Scheme 47). Whilst the ideal test would have used a chloro- group, the bromine substituent was readily available and as such used preferentially.



*Scheme 47 Test reactions of BOC-protected hydroxylamine **4.27** with bromo-propene **4.26***

When sodium hydride was triturated prior to use, the product seemed to be as expected, with evidence of the -NH peak adjacent to the carbonyl and the -CH_3 peaks of the tertiary butyl unit in the ^{1}H NMR spectrum of the crude reaction mixture. Without the trituration step however, the crude reaction mixture was determined to be more mixed, and evidence of the desired reaction having taken place was less clear. As such, it was decided that triturating the sodium hydride from the oil prior to use was necessary for the reaction to take place but was unlikely to have caused the removal of the Boc group seen in the test reaction.

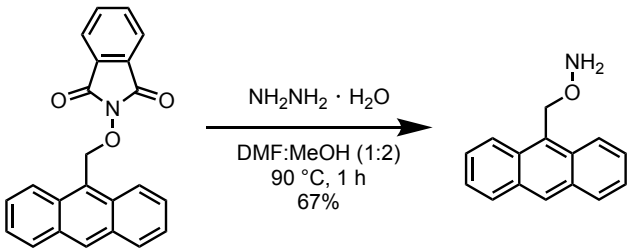
As this step proved to be more complex when attempted on the anthracene analogue **4.25**, a different approach was necessary. Accordingly, the next nucleophilic substitution to be attempted used *N*-hydroxyphthalimide **4.29** as a protected hydroxylamine (Scheme 48).[2]



4.25 **4.29** **4.30**

*Scheme 48 Synthesis of anthracene derivative **4.30***

This nucleophilic substitution was achieved in excellent yield, giving the protected hydroxylamine **4.30**. Subsequent deprotection of the *N*-hydroxyphthalimide was attempted using hydrazine monohydrate (Scheme 49). Analysis of this product by ^{1}H NMR showed the production of a primary amine, indicating that the previous Scheme 46 saw the nitrogen act as the nucleophile as opposed to the oxygen.



4.30 **4.23**

*Scheme 49 Deprotection with hydrazine monohydrate to give **4.23***

In the ^{1}H NMR spectrum of **4.23** (Figure 43), a broad singlet can be seen at 5.57 ppm which corresponds to the NH_2 of the hydroxylamine functional group.

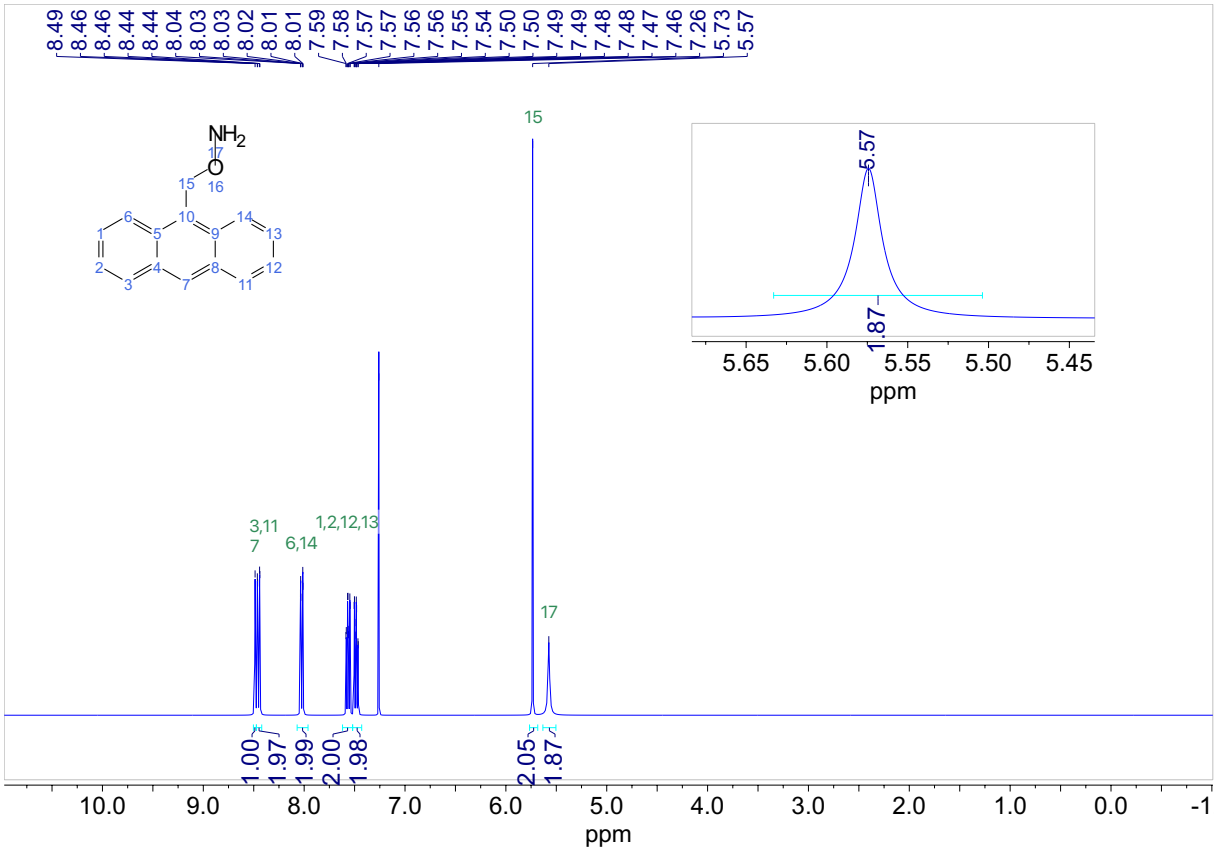
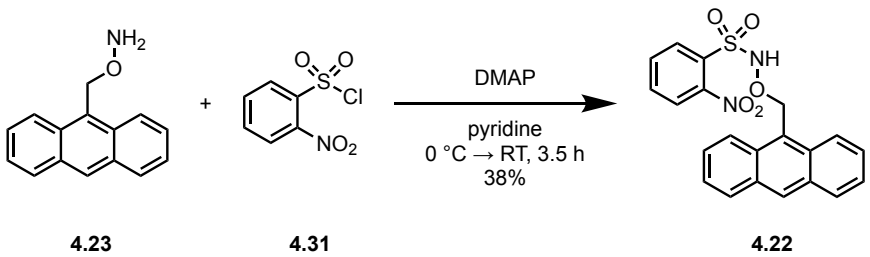


*Figure 43 ^{1}H NMR spectrum of anthracene derivative **4.23** in $CDCl_3$*

With the successful synthesis of hydroxylamine **4.23**, a condensation reaction with 2-nitrobenzene sulfonyl chloride **4.31** was carried out using an adapted procedure from Nakagawa and co-workers to give the product **4.22** (Scheme 50).[2]



4.23 **4.31** **4.22**

*Scheme 50 Condensation reaction for synthesis of Piloty's Acid derivative **4.22***

Crystals of this novel Piloty's acid derivative, grown from CH_2Cl_2 and hexane, were subjected to X-ray crystallography (Figure 44). The resulting structure provided some interesting information into the solid-state packing of the molecule and also suggested that stability was improved compared to other synthesised HNO donors, given that it could be solved before decomposition.

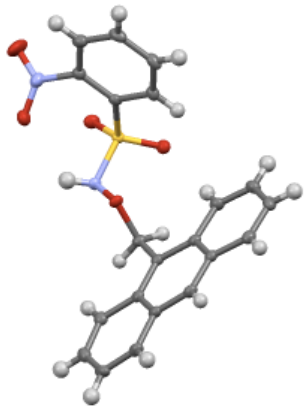


*Figure 44 Crystal structure generated of Piloty's acid derivative **4.22**. The structure is drawn with ellipsoids at 50% probability. For more information, please go to section 7.2.3*

The X-ray structure confirmed the formation of the anticipated *O*-hydroxylamine in **4.22**. The nitrobenzene functionality was orientated away from the anthracene, indicating a lack of π-stacking between the aromatic moieties. Crystal structures of 9-methoxymethyl anthracene have been reported[5] and the orientation of the methoxymethyl substituent matches that shown in Figure 44.

However, the intermolecular packing is quite distinct from that of 9-methoxymethyl anthracene in that the nitro-benzene functionality of **4.22** is π-stacked with the anthracene moiety of a neighbouring molecule (distance of 3.178 Å), whilst the 9-methoxymethyl anthracene unit cell shows no such interaction in its unit cell (Figure 45).[5]

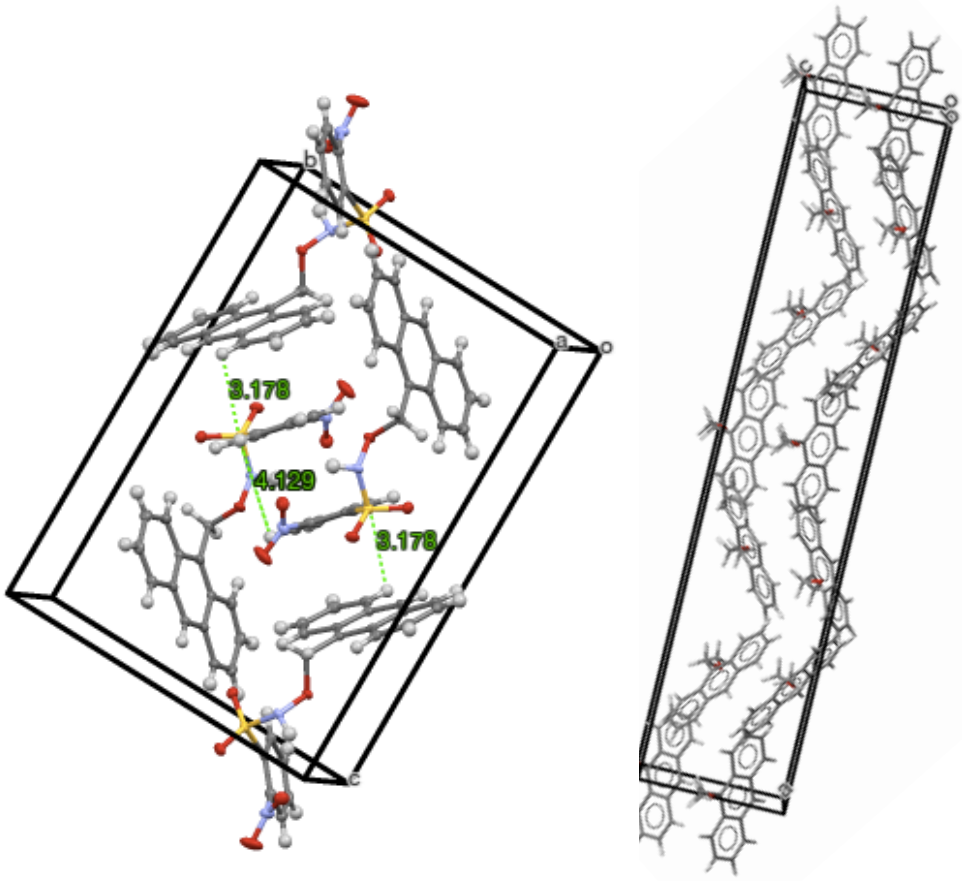


*Figure 45 Packing arrangement of Piloty's acid analogue **4.22** (LHS) and 9-methoxymethyl anthracene (RHS) as determined by Liu et al., 2007*

4.4 Release of HNO by photo-irradiation

Having successfully synthesised the Piloty's acid derivative **4.22**, investigations into the suitability of this HNO donor for photo-activated release were performed. To determine the optimum wavelength for photo-activated release of the HNO, the anthracene was excited in an attempt to try to allow subsequent homolytic cleavage of the NO bond of the hydroxylamine functional group. In Nakagawa's work, the coumarin analogue was excited using a 400-430 nm bandpass filter attached to a Xe lamp due to the UV vis analysis showing the λ_{max} to be at 395 nm.

The UV vis spectrum of **4.22** was obtained in various solvents and analysed to determine the appropriate wavelength to photo-irradiate the anthracene component of the sample for HNO release (Figure 46) which was found to be 365 – 371 nm in a range of solvents.

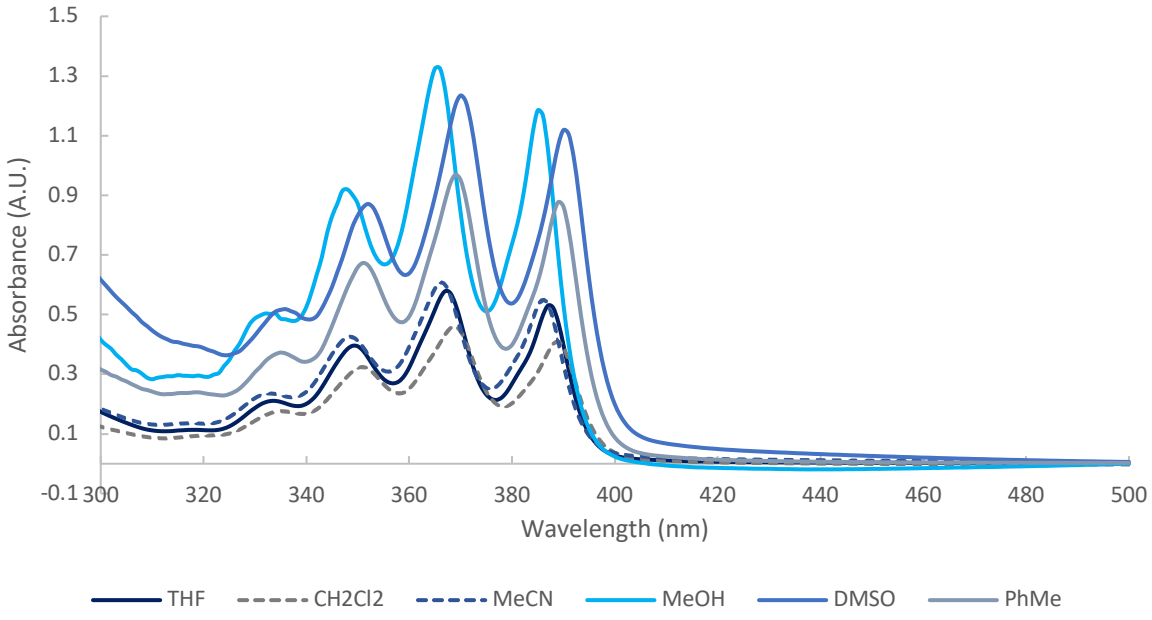


*Figure 46 UV vis analysis of anthracene derivative **4.22** in a range of solvents (100 μM)*

With this information in hand, a photo-irradiation experiment was carried out on an NMR sample, allowing for easy monitoring of the reaction procedure at regular intervals.

Two identical samples (40.8 mM, 600 µl, $CDCl_3$) and a separate control sample of $CDCl_3$ (600 µl) were prepared in borosilicate NMR tubes. Initial ^1H NMR spectra were recorded for each sample and the control. One sample along with the control was placed next to a 125 W mercury lamp as shown in the diagram below (Figure 47).

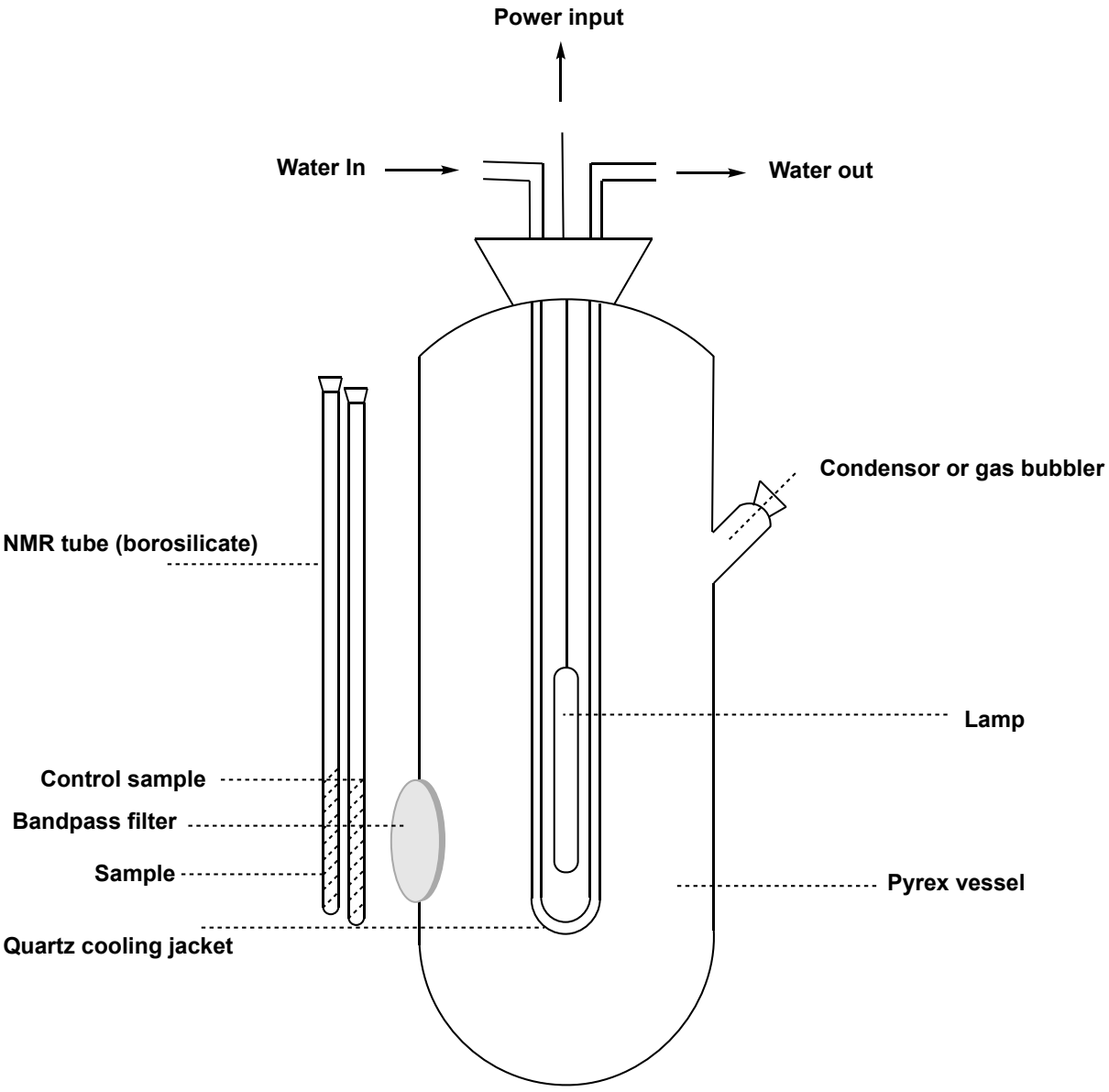
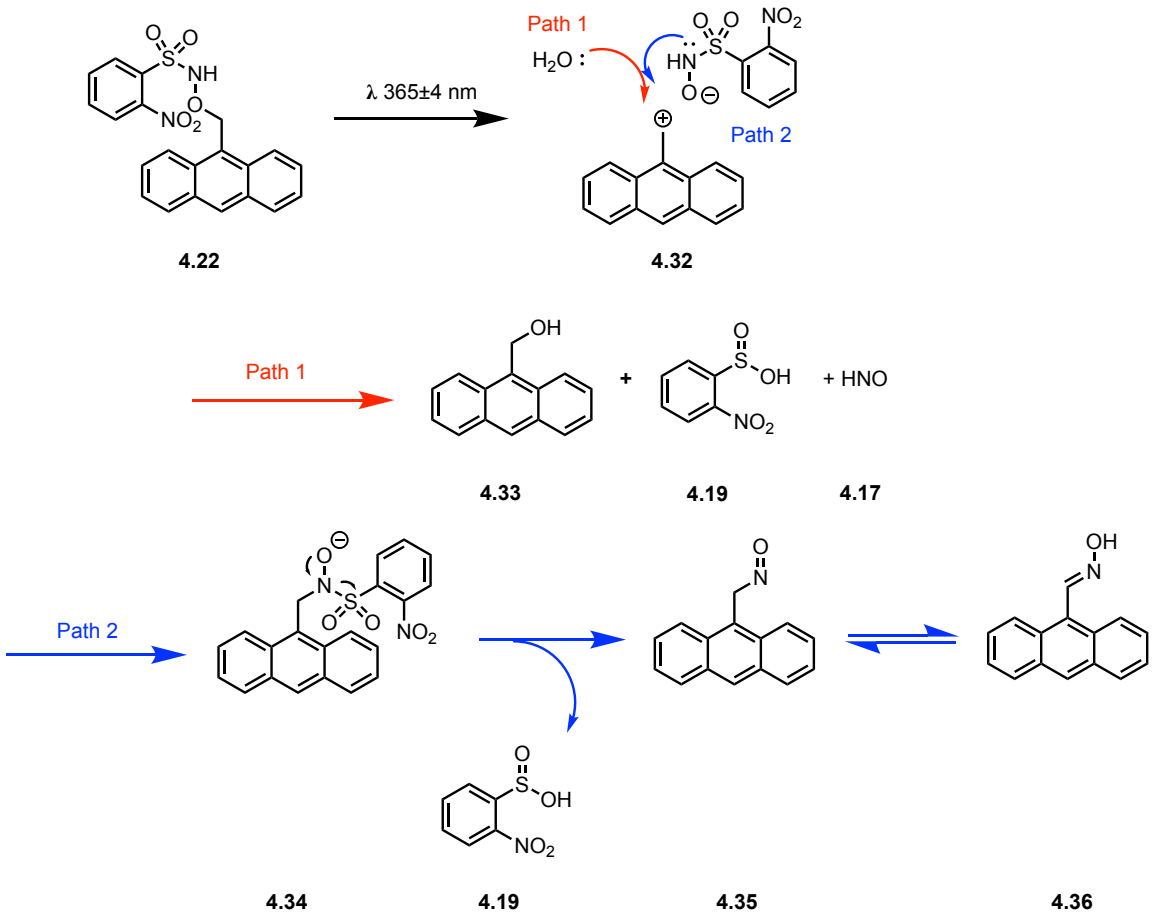


Figure 47 Experimental set up for NMR sample photo-irradiation with 365 nm bandpass filter

The first photo-irradiation (Scheme 51) investigated the effects of photo-irradiation through a 365 nm bandpass filter at set intervals.



*Scheme 51 Anticipated photo-irradiation pathways of Piloty's Acid derivative **4.22** at 365±4 nm*

By subjecting the samples to photo-irradiation for set periods of time (Table 6), any changes could be monitored by ^{1}H NMR analysis to investigate the pathway of decomposition.

*Table 6 Results from the photo-irradiation of Piloty's Acid derivative **4.22** at 365 nm in $CDCl_3$ (40.8 mM)*

	Irradiation (total min)	Sample 1	Sample 2 (no irradiation)	Control $CDCl_3$
T = 0	0	Peaks corresponding to compound **4.22**	Peaks corresponding to compound **4.22**	Chloroform peak
T = 1	20	No change	No change	No change
T = 2	80	No change	No change	No change

Due to the lack of photodecomposition when using a 365 nm bandpass filter (^{1}H NMR - Appendix 4.1), a second experiment was tried using the 125 W mercury lamp without any filter to push the reaction forwards. By removing the bandpass filter, a greater range of wavelengths (UVA wavelength range 315 – 400 nm) would be available to initiate the photodecomposition, but at the risk of more undesired side reactions. A study was first undertaken to determine the wavelengths and power of the mercury lamp at the distance the sample would be held at, determining the power outage of the lamp and as such the power of photo-irradiation seen by the samples (Appendix 4.2). Subsequently, the reaction was repeated under the same conditions but without the filter (Table 7).

*Table 7 Photo-irradiation of Piloty's Acid derivative **4.22** (40.8 mM, $CDCl_3$) without a 365 nm bandpass filter*

	Irradiation (total min)	Sample 1	Sample 2 (no irradiation)	Control $CDCl_3$
T = 0	0	Peaks corresponding	Peaks	$CDCl_3$ peak

		to compound **4.22**	corresponding to compound **4.22**	
T = 1	60	New multiplets: 8.34-8.30, 7.83-7.80 (shown in blue) New singlet 11.54, 5.60 (shown in green)	No change	No change
T =2	120	Increased intensity of new signals	No change	No change
T = 3	180	Increased intensity of new signals	No change	No change

The photo-irradiation showed that a decomposition event was occurring, albeit slowly (Figure 48). Likewise, the change in appearance of the NMR sample from that of the control sample indicated that some reaction was occurring, while at the same time a change from a light orange solution to a brown translucent suspension was observed.

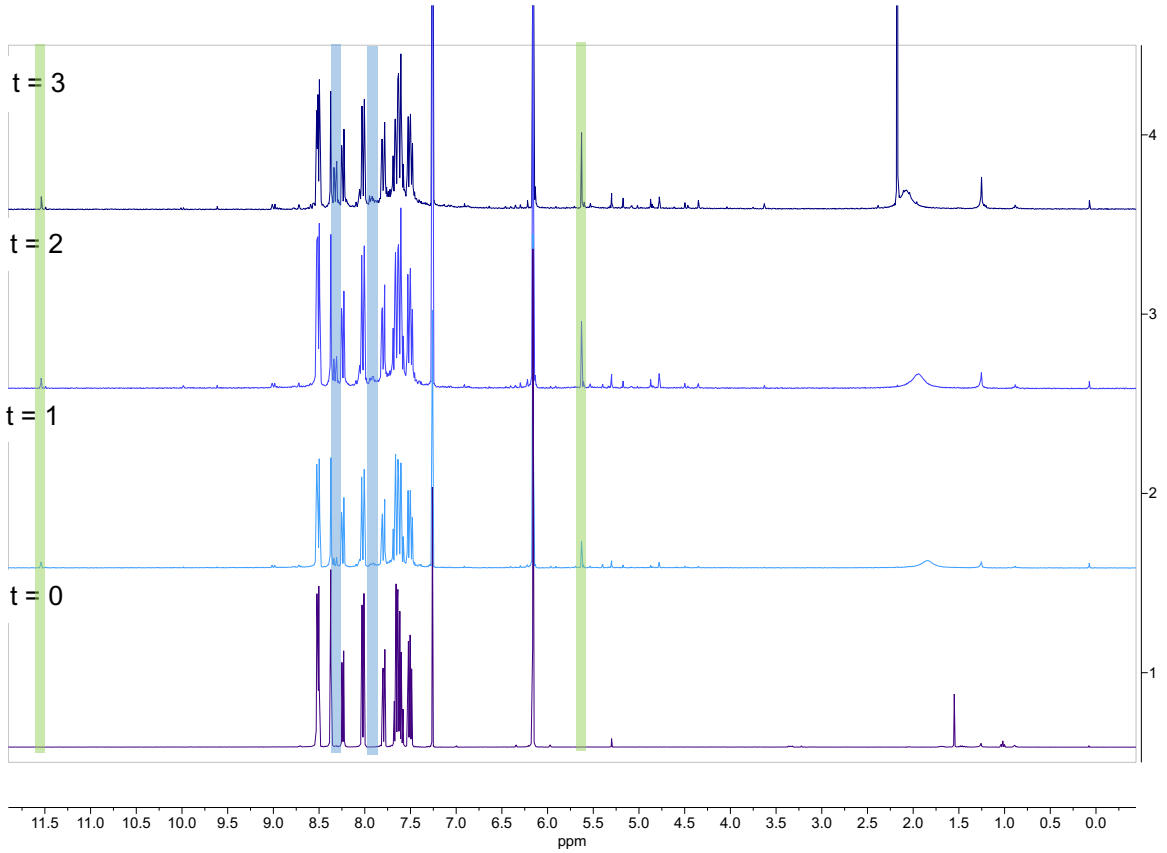
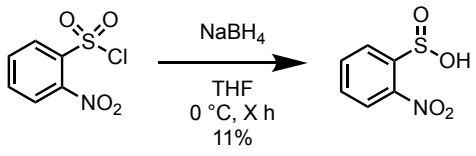


*Figure 48 ^{1}H NMR spectroscopy analysis of photo-irradiation of Piloty's Acid derivative **4.22** without a bandpass filter*

According to Nakagawa's work, there are two HNO generation pathways possible for the photo-irradiation of the Piloty's Acid derivative.[6] As such, the mechanism of photodecomposition was investigated by the separate synthesis of sulfinic acid, a known decomposition product of both mechanistic pathways suggested by Nakagawa and co-workers (Scheme 52).[7] Should the sulfinic acid formation be observed, further investigations into identification of the decomposition pathway could be undertaken.



4.37 **4.19**

*Scheme 52 Synthesis of sulfinic acid **4.19***

Subsequent analysis of the ^{1}H NMR spectrum of sulfinic acid **4.19** against that of the photo-irradiated product allowed for an investigation into the determination of photodecomposition (Figure 49). However, the sulfinic acid peaks in the same solvent were not similar to those in the photo-irradiated sample.

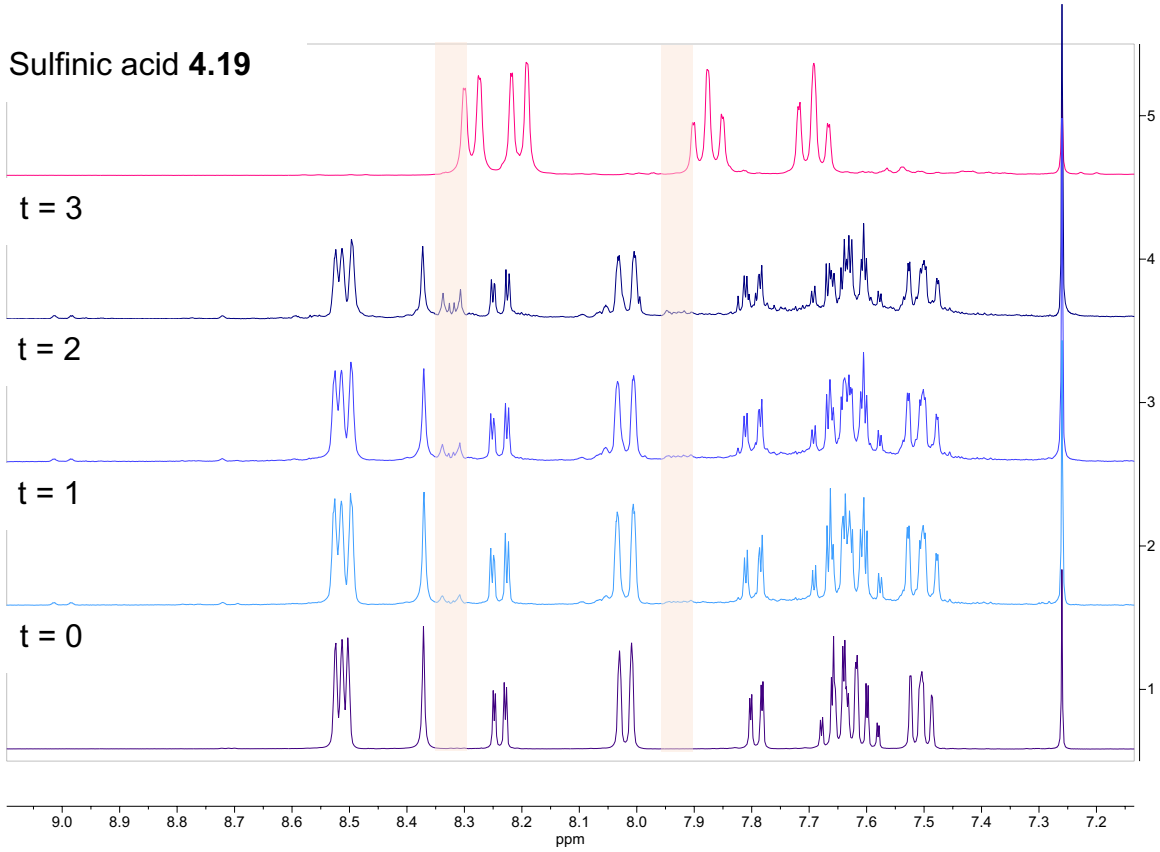


*Figure 49 ^{1}H NMR of the aromatic region of Piloty's acid analogue **4.22** at various timepoints of photo-irradiation against the anticipated photo-decomposition product **4.19***

Highlighted in orange, the new peaks formed did not correspond to those of the sulfinic acid **4.19**. Other expected reaction products were also investigated and the solvent for the photo-irradiation needed to be changed for an accurate comparison of the ^{1}H NMR spectra. The only solvent capable of dissolving both the Piloty's acid derivative and the assorted reaction products anticipated (**Error! Reference source not found.**) was DMSO. Therefore, the

investigation was repeated in deuterated DMSO (Figure 50) at a higher concentration (44.9 mM).

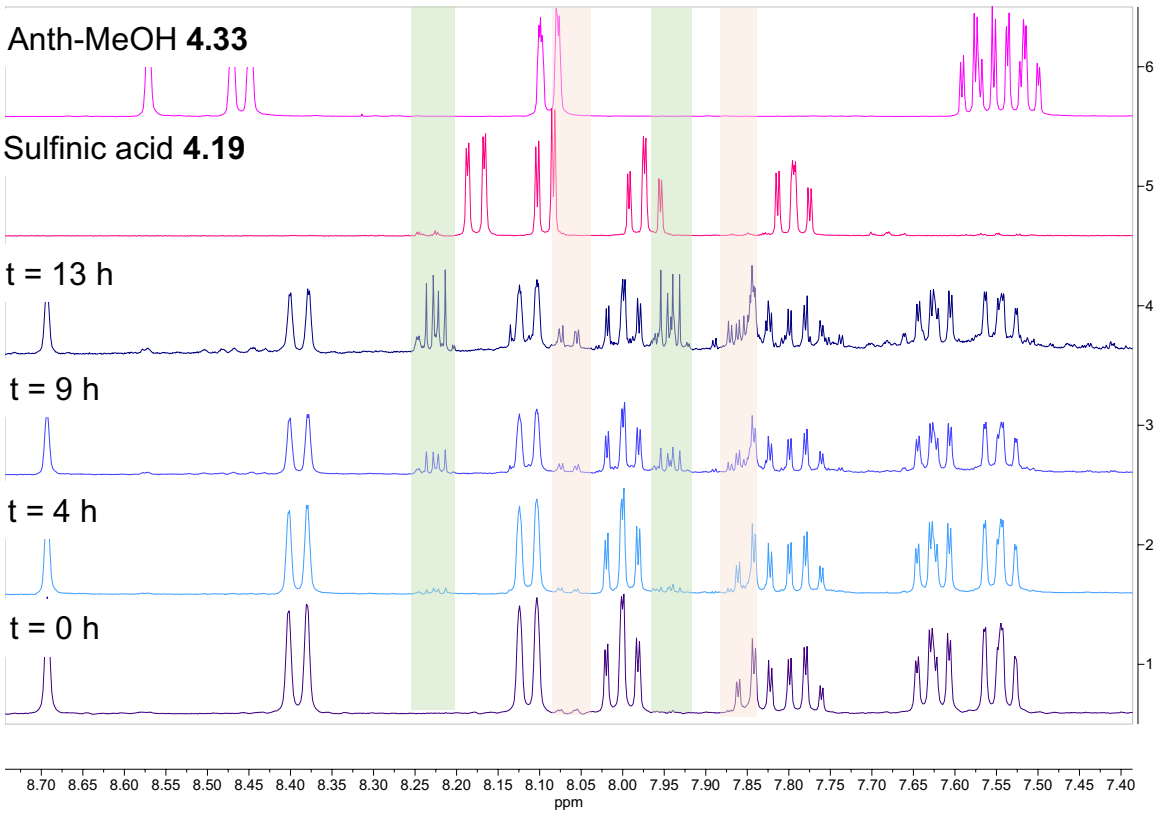


*Figure 50 ^{1}H NMR spectra of the aromatic region of Piloty's acid derivative **4.12** in DMSO and expected products **4.19** and **4.33***

Analysis of the ^{1}H NMR spectra showed that the new peaks formed upon photo-irradiation did not correlate with the anticipated products. The green highlighted sections show formation of anthraquinone whilst the orange highlights show formation of a new uncharacterised product. On such a small scale, the mixture could not be separated easily, and the investigation needed to be carried out on a larger sample to further investigate the products formed. To achieve this, the reactant sample was placed in an immersion well around the lamp and water jacket (Figure 51) and stirring was maintained throughout the reaction by the addition of a stirrer bar and magnetic stirrer plate.

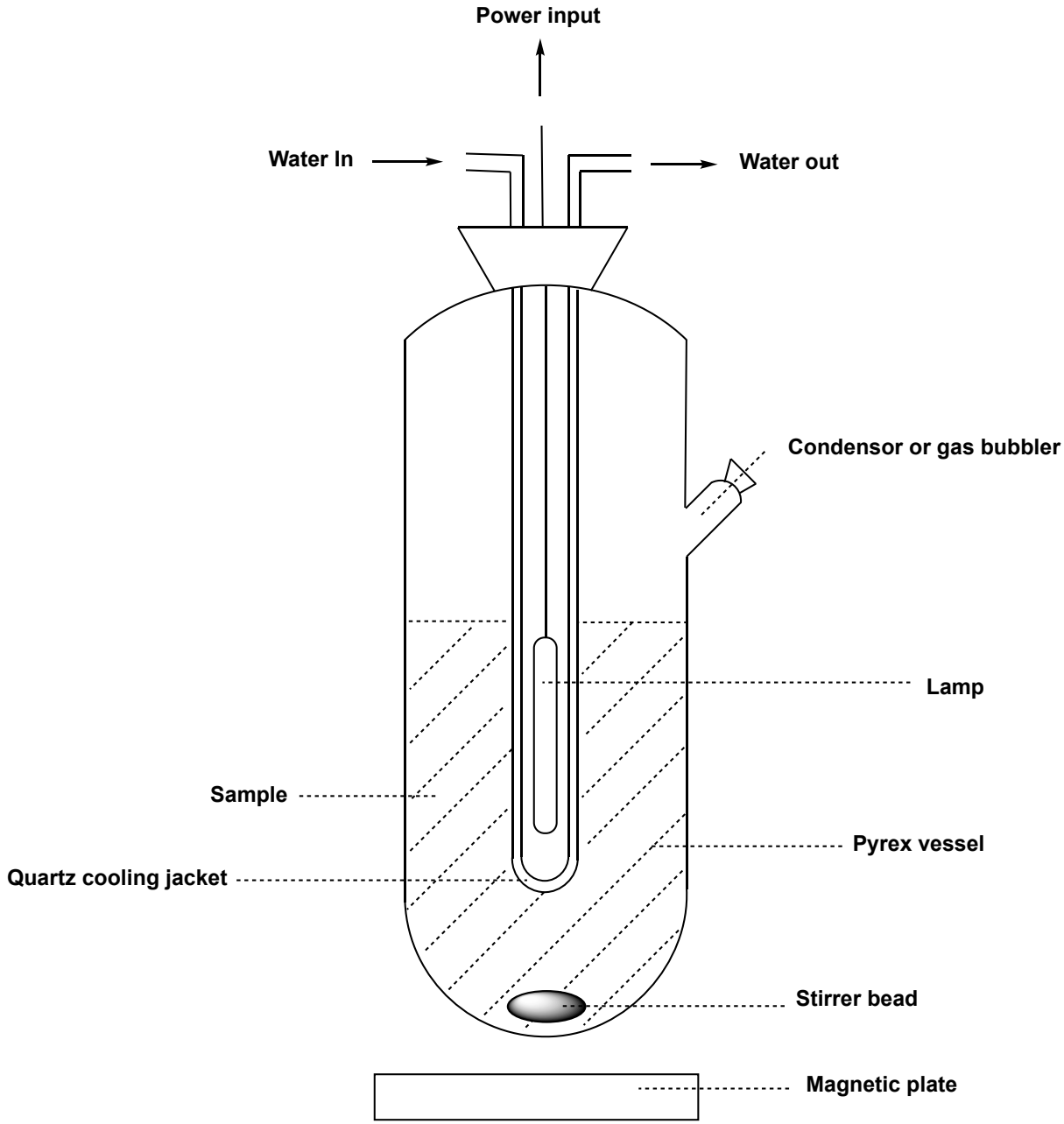


Figure 51 Experimental set up for immersion well photochemistry

This photo-irradiation was carried out in 45-minute intervals on the sample (12 mM) and was monitored by TLC throughout. After a total of 270 min the starting material appeared to have been consumed, leaving a mixture which was analysed by ^{1}H NMR spectroscopy (Figure 52). From these spectra, it was observed that a small amount of 9-anthracenyl methanol **4.33** may have been produced, made evident by the appearance of peaks at 8.57, 8.46 and 8.09

ppm and in the increased signal noise in the baseline over the range of 7.59-7.50 ppm, highlighted in blue.

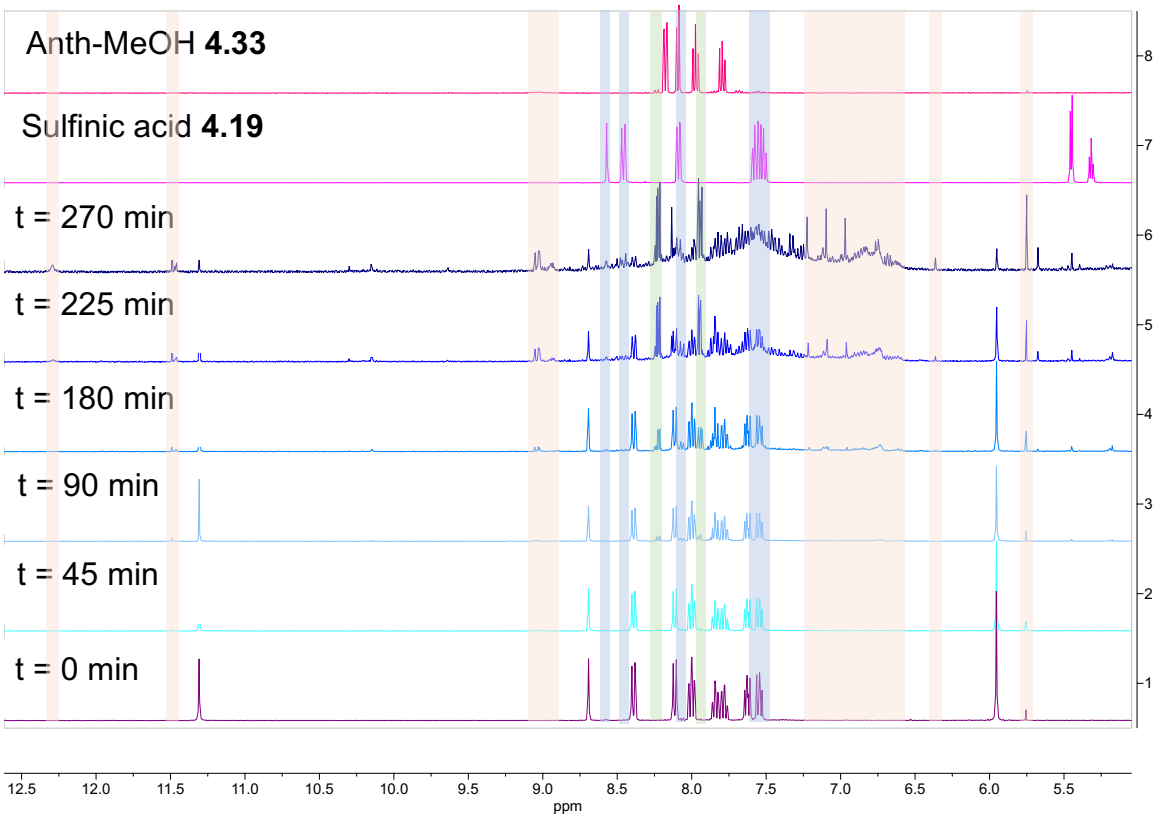


*Figure 52 ^{1}H NMR of immersion well photo-irradiation reaction on **4.22** in DMSO-d6.*

As in Figure 50, anthraquinone peaks were observed to have formed upon photo-irradiation, highlighted in green. Additionally, extra uncharacterised peaks highlighted in orange were observed. Upon vacuum distillation to remove the deuterated DMSO the sample was split into two fractions by volume to investigate different methods of purification. One fraction was subjected to an aqueous work up from a variety of solvents whilst the other fraction was subjected to flash column chromatography (Figure 53).

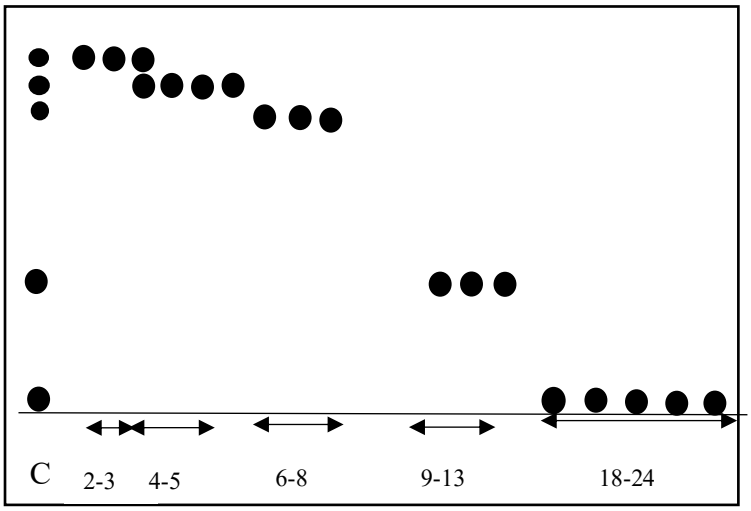


Figure 53 TLC representation of flash chromatography separating fractions of photo-irradiated product by polarity (TLC performed in 99:1 CH_2Cl_2:Et_3N and visualised under 254 nm UV light)

The separated components were then characterised by ^{1}H NMR spectroscopy ($CDCl_3$). From the column chromatography (Figure 54) the separated fractions did not show any anticipated products by ^{1}H NMR spectroscopy. Fractions 6-8 and 4-5 showed anthraquinone peaks as multiplets at 8.35-8.30 and 7.83-7.78 ppm, though in both cases the products were not clean.

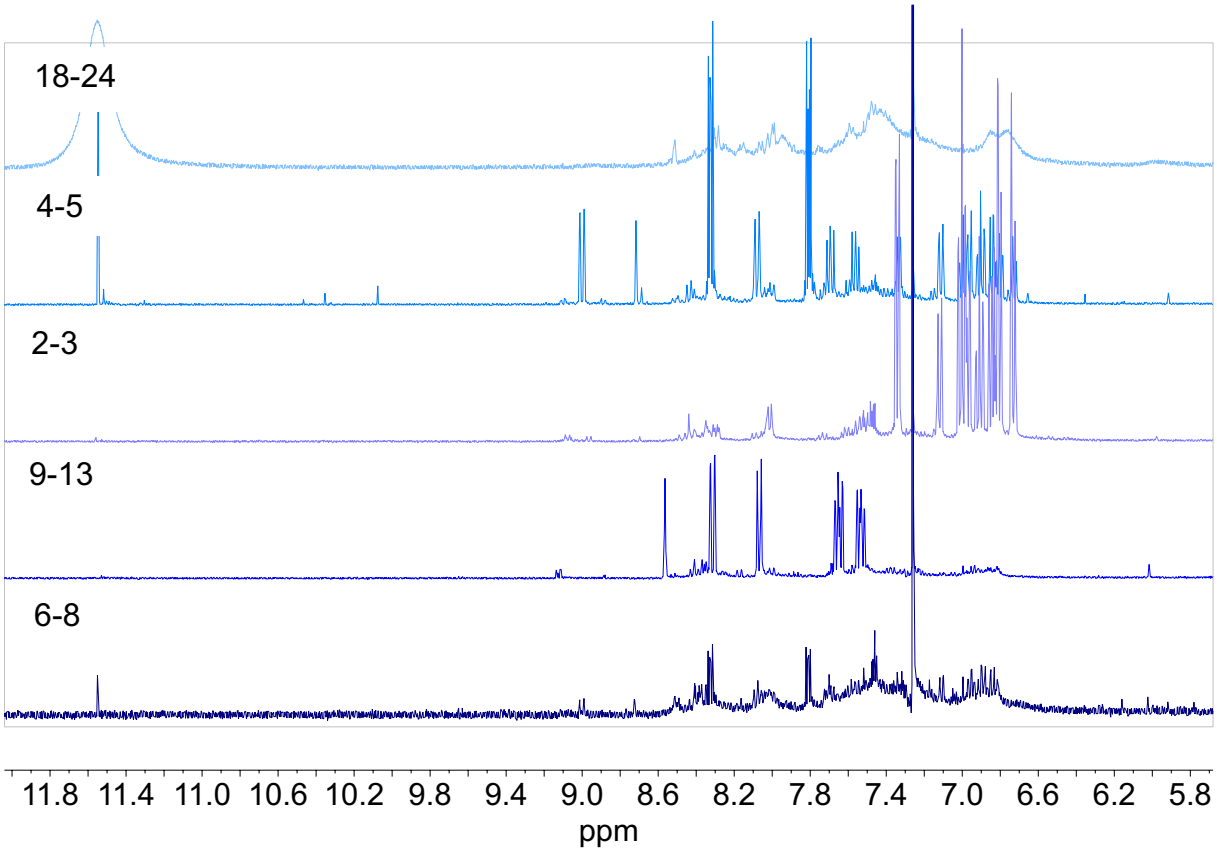


*Figure 54 ^{1}H NMR stacked spectra of the aromatic region of fractions taken from flash chromatography of the photo-irradiated **4.22** ($CDCl_3$)*

The presence of anthraquinone indicated the photo-irradiation had not occurred as expected, and a further investigation was necessary to determine how the Piloty's acid derivative was affected in this manner. One possible explanation for the production of anthraquinone could be via the synthesis of oxygen radicals from the photo-irradiation of the DMSO solvent.[8, 9] In an attempt to remove this possibility, the solvent was freeze-pump-thawed three times to remove as much atmospheric oxygen from the reaction environment as possible. The reaction was then repeated once more for a total of 270 minutes, and the fractions collected by column chromatography were subjected to ^{1}H NMR for analysis (Figure 55). In this instance, the solvent for the NMR was chosen to be DMSO-d6 to allow for a more concentrated sample. Here it was demonstrated that the anthraquinone peaks were not observed in the expected regions (as highlighted in green).

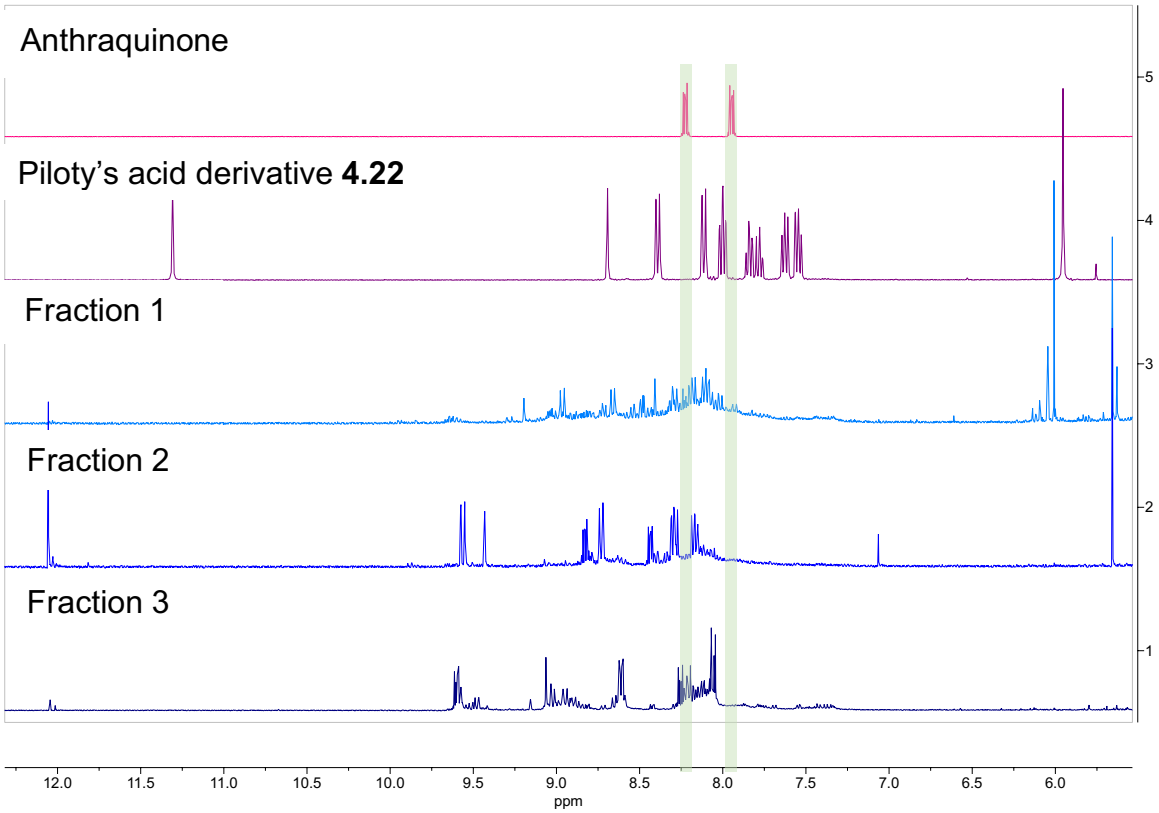


*Figure 55 ^{1}H NMR spectra of the fractions collected from column chromatography of photo-irradiated Piloty's acid derivative **4.22***

However, analysis of the ^{1}H NMR following photo-irradiation of **4.22** under these conditions showed little evidence of the anticipated photodecomposition with the components of the mixture proving difficult to separate by flash column chromatography. As such, the level of HNO anticipated to have been released was minimal.

The 125 W mercury lamp used was thought to be too powerful and too wide-ranging in wavelength for the desired photodecomposition (315 – 400 nm, see Appendix 4.2 for detailed range of wavelengths), resulting in decomposition which could not be assigned to any expected products such as 9-anthracene methanol **4.33** or 9-anthraldehyde oxime **4.36**. Therefore, different methods of photo-irradiating at 360-320 nm were next investigated as outlined below, in order to narrow down the possible decomposition pathways.

A blacklight with a wavelength of approximately 365 nm was used (Figure 56) to limit the wavelengths at which the photo-irradiation could take place.

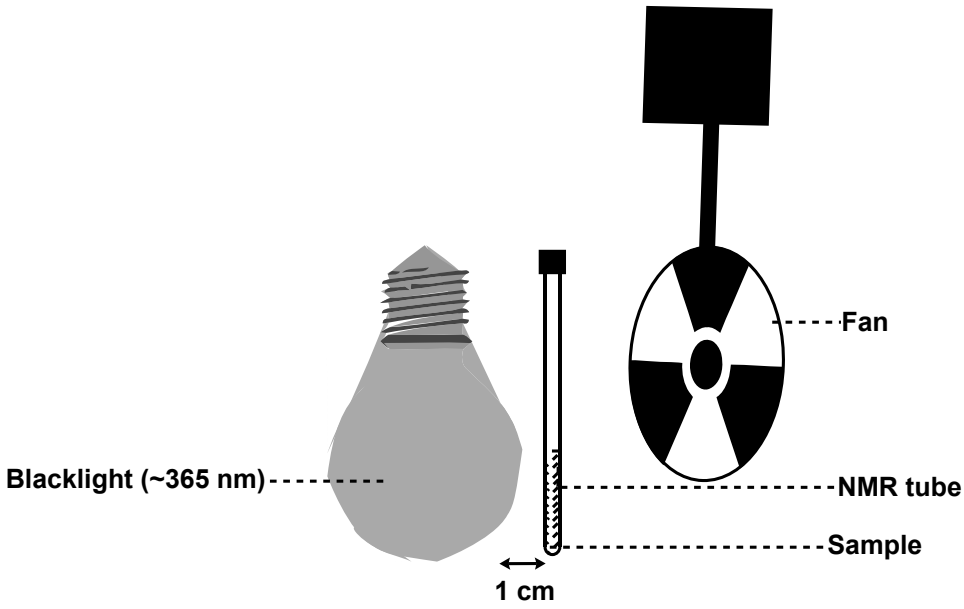
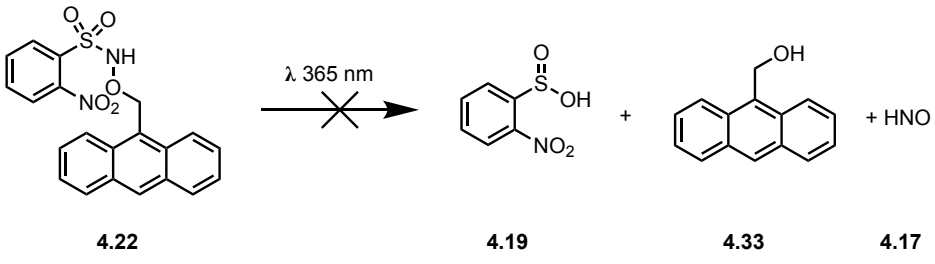


Figure 56 365 nm blacklight set up for photo-irradiation experiments

By keeping the NMR tube of the sample close to the light source, the maximum power of the lamp (15 W) could reach the sample to aid photo-release. The fan was required to keep the NMR tube cool. The reaction was repeated with the new set up (Scheme 53) and the ^{1}H NMR analysed (Figure 57).



*Scheme 53 Proposed photodecomposition of Piloty's acid analogue **4.22** using a blacklight (365 nm)*

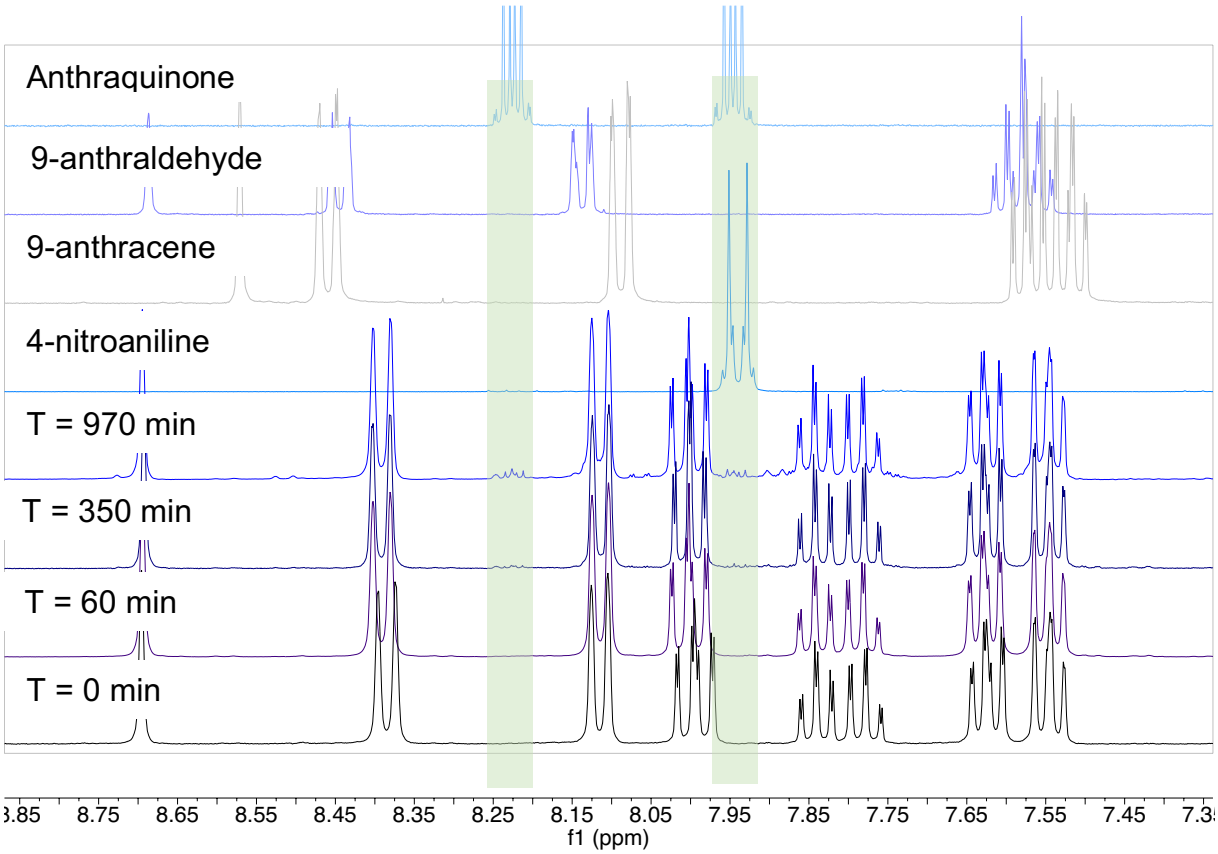


*Figure 57 ^{1}H NMR spectra comparisons of the photo-irradiation of Piloty's acid analogue **4.22** via 365 nm blacklight (DMSO-d6)*

From analysis of the ^{1}H NMR aromatic region, a lack of photodecomposition was evident, where very little reactivity was seen to occur with the 15 W blacklight other than the formation of anthraquinone as highlighted in green.

Considering the loss of power occurring when using an NMR tube in front of a non-directed light source, it seemed reasonable to attempt the photo-irradiation with a more directed approach. It was considered that the use of 365 nm specific LEDs in a circle could potentially increase the overall light directed to the sample. Therefore, a large glass petri dish containing these LEDs was used in an alternative experimental set up (Figure 58).

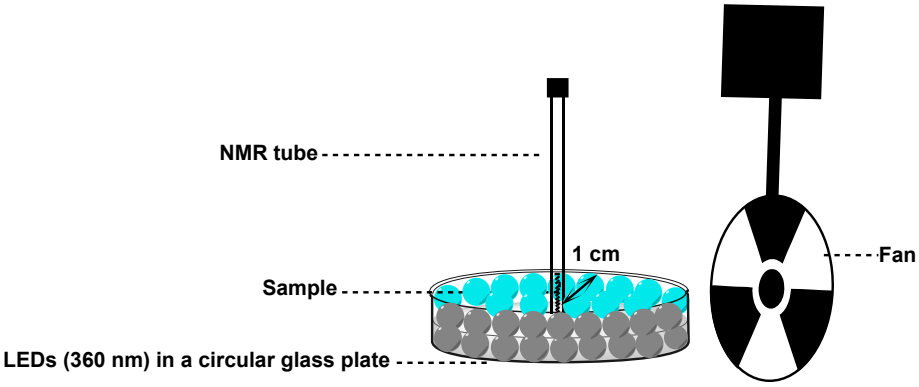


Figure 58 Photo-irradiation set up using 360 nm LEDs in an inward directing circle

Using this modified set-up, the photo-irradiation was carried out as described previously (Scheme 53) and the ^{1}H NMR of the aromatic region once again analysed (Figure 59).

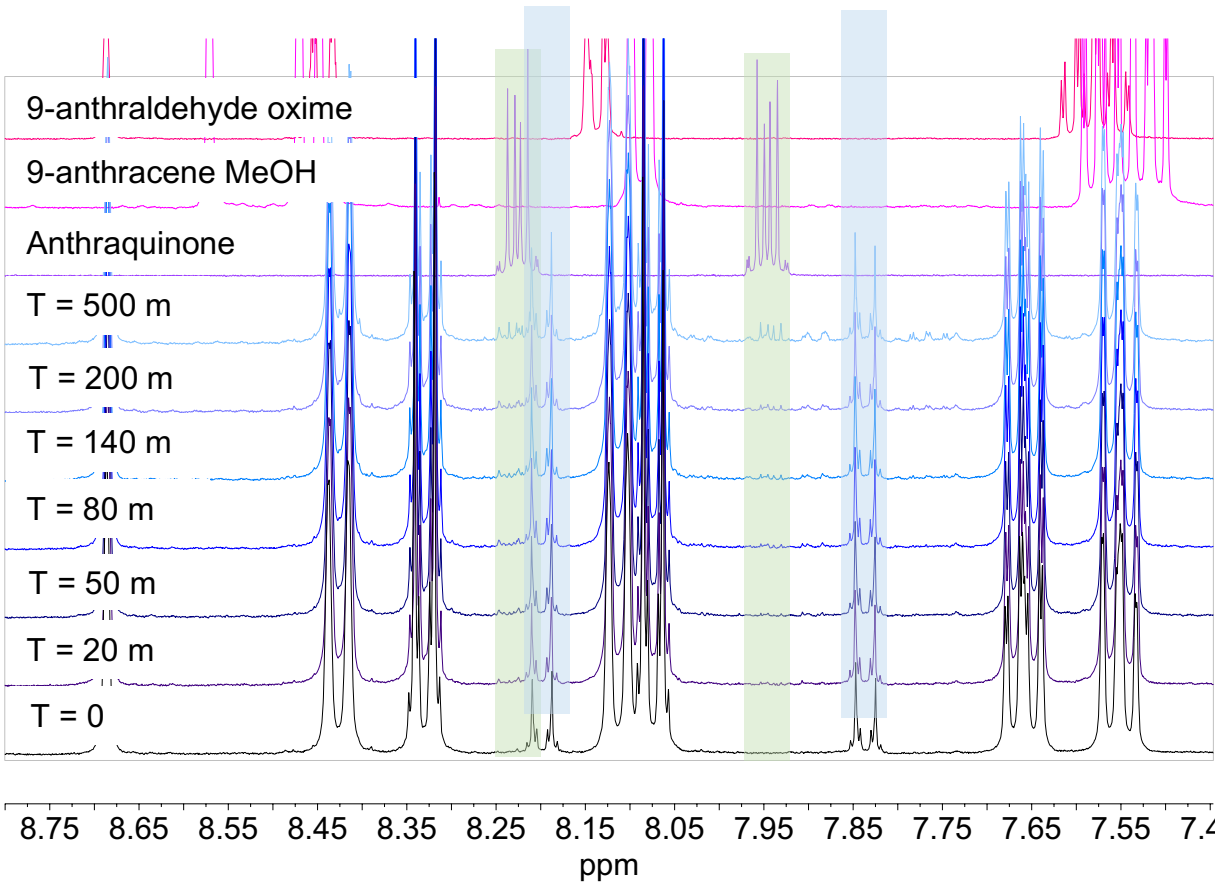


Figure 59 ^{1}H NMR spectra compilation of 360 nm LED light photo-irradiation of Piloty's acid analogue ***4.22***

Figure 59 shows a clear lack of reactivity from the sample. In this reaction, a small amount of a spontaneous decomposition product was observed from the T = 0 min sample onwards (peaks at 7.83 and 8.19 highlighted in blue). It was thought that this side product occurred from the sample being exposed to air for a prolonged period, but this product was kept in the sample to see whether it would be affected by the photo-irradiation. It can be seen however, that no such change occurred, with this decomposition product not appearing to be sensitive to photo-irradiation at 365 nm. A very small amount of anthraquinone appeared to form at T = 500 m (highlighted in green), indicating the generation of small amounts of oxygen radicals over time.

The disappointing lack of susceptibility of Piloty's acid analogue **4.22** to photo-irradiation at the λ_{max} led to the consideration of other photophysical behaviours that could be interfering with the heterolytic cleavage, as described in the next section.

4.5 Photophysical investigations into Piloty's acid analogue 4.22

4.5.1 Absorption and fluorescence in fluorophores

Transitions between the ground and various excited states of a molecule can be described using as a Jablonski diagram (Figure 60).[10]

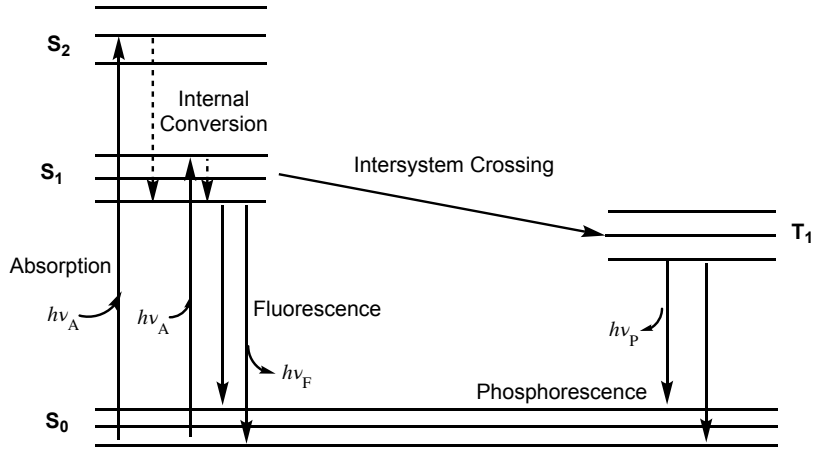


Figure 60 One form of a Jablonski diagram showing absorption and emission energy changes

After absorption of a photon, the fluorophore usually gets excited to higher energy electronic states, either S_1 or S_2. At this point, the molecules in S_2 usually relax quickly ($\leq 10^{-12}$ s) to the lower excited state S_1 via internal conversion, and as such fluorescence emission usually occurs from the thermally equilibrated excited state of S_1.[10] Excited fluorophores can return to the ground state by either fluorescence (from S_1 to S_0) or by undergoing an intersystem crossing to the triplet state T_1 (phosphorescence). This is facilitated by the presence of heavy atoms such as bromine or iodine.[10]

4.5.2 Excimer and exciplex formation of anthracene-derived complexes

Research into the photophysics of complex formation has led to the observation that cyclodimerisations in the excited state can occur via the formation of excimers.[11] Excimers,

dimeric complexes stabilised in the excited state (with one in the excited state and one in the ground state), were first named by Förster[12] in aromatic hydrocarbons and can be identified by structureless fluorescence. The formation of fluorescent intramolecular exciplexes (where one part of the molecule acts as a donor and one acts as an acceptor) in moderately to strongly polar solvents but not in apolar solvents is known for certain arene-amine systems.[13, 14] Excimer formation occurs when two or more molecules of the same type are involved in a photo-absorption event, often but not necessarily beginning when the absorption of one molecule perturbs the electronic state of a neighbour (Figure 61).[9] An exciplex is either the intra-molecular photo-absorption event of the same type or an inter-heteromolecular photo-absorption event. In each figure shown below, the increasing percentage of H_2O showed a change in fluorescence upon aggregation of the 1,8-naphthalimide complex, as the higher frequency emission band decreased in intensity at about 70:30 H_2O: MeCN and higher amounts of water. Similarly, at higher H_2O volume, the lower frequency emission band at approximately 470 nm (LHS graph) and 630 nm (RHS graph) increased.[14]

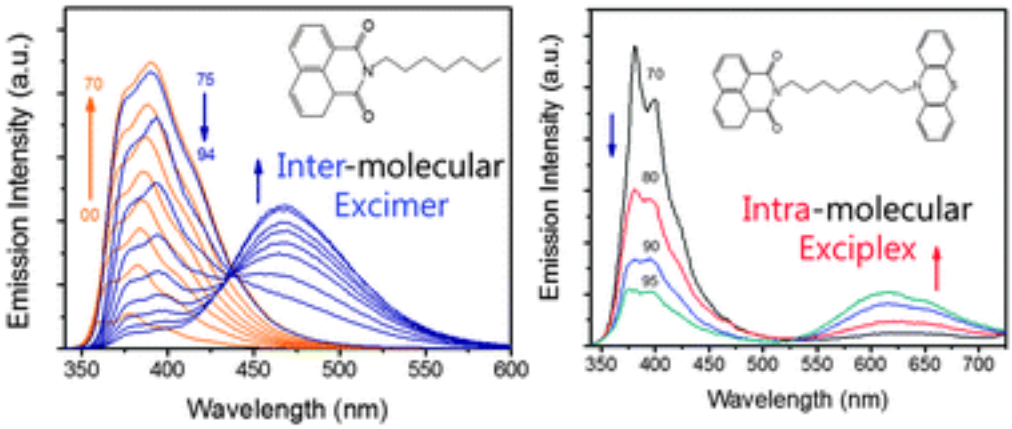


Figure 61 Depiction of excimer and exciplex fluorescence spectra as described by Cho et al., 2014. The emission spectra show changes in the fluorescence behaviour upon increasing water to MeCN ratio.

Excimers and exciplexes do not follow the well-studied mirror image rule typically obeyed by fluorescent compounds. The mirror image rule results in emission spectra mirroring the patterns demonstrated by absorption spectra due to the excitation energy quickly dissipating to leave the fluorophore in the excited energy state (S_1).

Characterisation of exciplexes and excimers represent important steps in understanding the dynamic photophysical and photochemical processes of multi-chromophore systems.[15] Indeed, excimer formation often results in the stabilisation of complexes at geometries that would be unfavourable/repulsive in the ground state and are generally accepted to have sandwich geometry.[11, 16]

Anthracene is known to form a covalent cycloadduct upon photo-irradiation,[17] which is formed from its excimer, whilst pyrene does not photodimerise under any conditions.[18] The behaviour of pyrene led Chandross to develop a method to record excimer emission upon excitation of dianthracene (Figure 62).[19, 20]

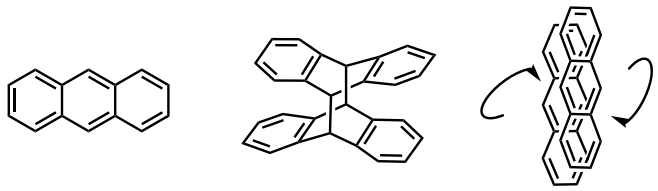


Figure 62 Structures of anthracene, dianthracene and a depiction of an anthracene excimer with one molecule in the ground state and the other in an excited state as depicted by Chandross et al., 1965

Having determined that there are instances where anthracene moieties forms excimers before photodimerising, the lack of photo-release of **4.22** upon photo-irradiation could be explained by exploring the fluorescence.

The intensity of fluorescence emission can be reduced at higher concentrations of the fluorophore due to a variety of mechanisms including a collision of fluorophores, the

formation of non-fluorescent dimers or energy transfer to non-fluorescent dimers.[21] Quenching of anthracene derivatives have been investigated throughout the past 70 years, though the focus has mainly been on phenyl-anthracene and anthracene itself, not on anthracene derivatives with potential exciplex characteristics.[11, 22]

4.5.3 UVvis and fluorescence experiments on Piloty's acid analogue **4.22**

By further investigating the photophysical characteristics of the Piloty's acid analogue **4.22**, some insight into the lack of photo-reactivity could potentially be achieved. First, the fluorescence spectra of the compound in a variety of solvents were recorded (Figure 63) in order to determine if the polarity of the solvent could have an effect on the emission profile.

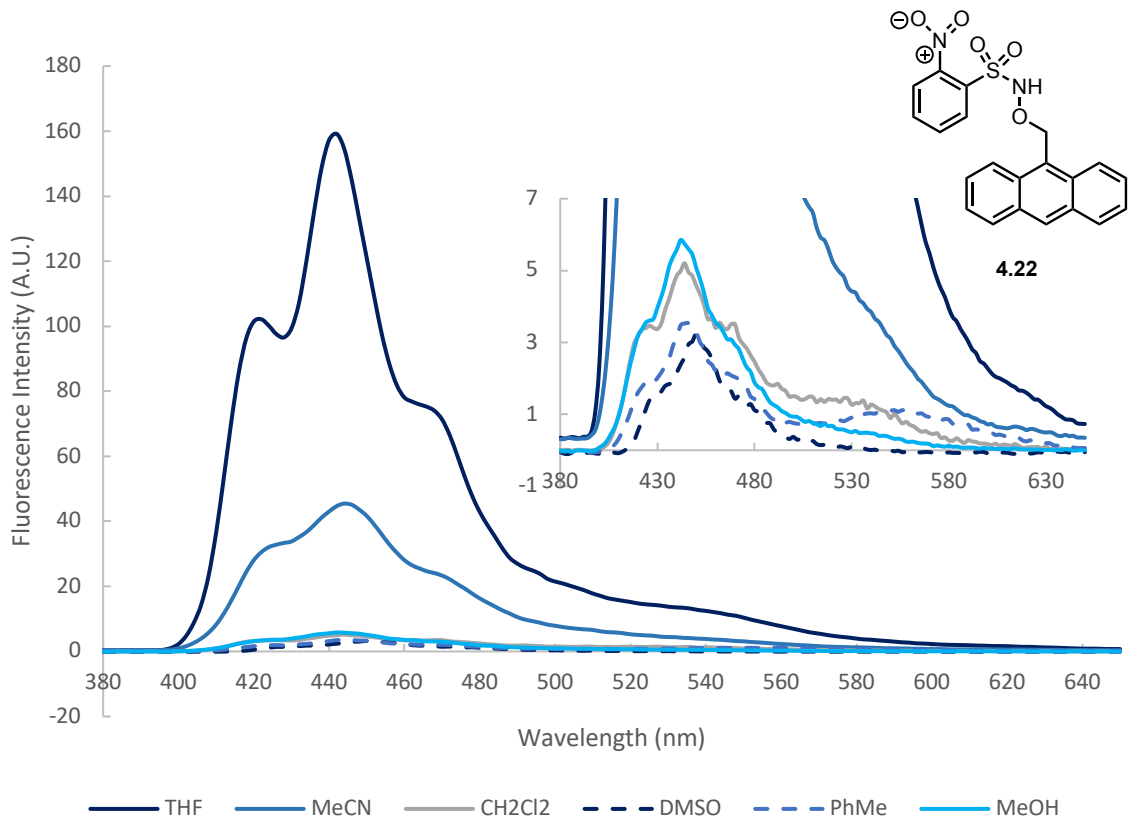


*Figure 63 Fluorescence emission spectra of Piloty's acid analogue **4.22** (Ex 350 nm, 10 mM) in various solvents. Insert shows a magnified view of less emissive solutions.*

The emission spectra of the Piloty's acid analogue **4.22** showed remarkably different behaviour in different solvents. For each solvent, the emission was lower than that expected, indicating that some form of quenching was occurring.[21, 22] Whilst the UV vis spectra could be recorded at 100 μM, a 10-fold increase in concentration was needed to observe the emission spectra.

More interestingly, a different quenching effect could be seen in the individual solvents, with apolar solvents such as PhMe and CH_2Cl_2 showing an additional emission shoulder at 520 – 580 nm.

To investigate this effect further, particularly in the less emissive solvents, each sample was diluted to 5 mM and the emission analysed in comparison (Figure 64).

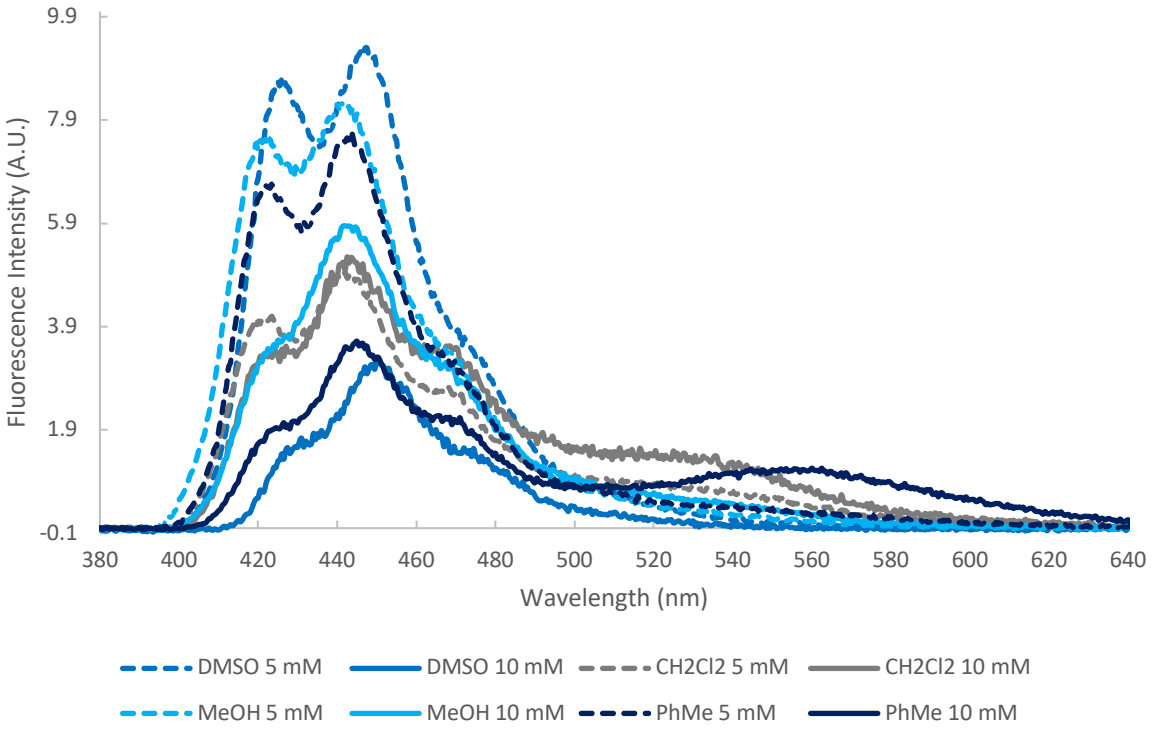
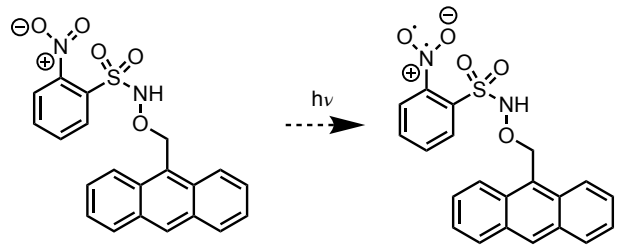


*Figure 64 Fluorescence emission spectra of Piloty's Acid analogue **4.22** in various solvents (Ex 360 nm, 5 and 10 mM)*

From the difference in emission at lower concentrations (Figure 64), diluting the sample tended to lead to more emission, but in the apolar solvents it also removed the additional shoulder band. The lack of emission in the additional shoulder band at >540 nm in lower concentrations indicated an intermolecular effect of the exciplex system, as an intramolecular interaction would be expected to be concentration independent.

In CH_2Cl_2, the emission of **4.22** did not appear to differ too much except in the first vibrational band and the red-shifted shoulder band (Figure 64). Indeed, in each case the emission of the first vibrational band showed the most difference upon dilution, indicating that this aspect of the anthracene is the most affected.

It was considered that solvent polarity might play a key role in the formation and photophysical properties of the intermolecular excimer, potentially by the localised quenching of emission. If the nitro group of **4.22** could be photoactivated to a radical species, as found in Nakatsuji's work on dual-chromophore nitroxides, then self-quenching might be a viable option for the complex (Scheme 54).[16] However, this conversion could be more likely to occur when photo-irradiating due to the formation of a radical species than when fluorescing.



*Scheme 54 Photoactivation of the nitro group in Piloty's acid analogue **4.22** to a radical nitro species as a possible mechanism of self-quenching*

The ^{1}H NMR spectra of the Piloty's acid analogue **4.22** from section 4.4 showed that no dimerisation of the anthracene functionality took place upon photoirradiation. Interestingly, the first vibronic band sees the most change when the fluorescence was measured under different conditions, becoming more evident as the concentration decreases (Figure 64). When taking the fluorescence using right-angle observation, some of the emission bands of anthracene are selectively reduced in different concentrations. In particular, the short wavelength first vibronic emission bands reduce at higher concentrations (Figure 65).[2]

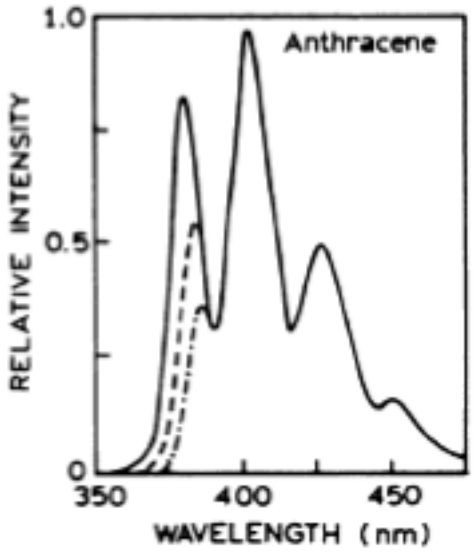


Figure 65 Diagram of anthracene emission at different concentrations showing the reduction in emission of the first vibronic band. Diagram taken from Lakowicz, 1999[13]

Looking at the concentration dependent changes in the short wavelength emission demonstrated by Lakowicz,[23] the increased intensity of the 5 mM first vibronic bands compared the 10 mM samples in Figure 64 followed the same pattern.

In summary, the photophysical characteristics of the Piloty's acid analogue **4.22** showed an interesting intermolecular behaviour that reduced its efficacy for HNO release, making it an unsuitable option for nitroxyl delivery.

4.6 Conclusions and future work

The aim of this project adjusted over time from the design and synthesis of a photo controllable HNO donor to a photophysical investigation into the anthracene derivative **4.22**. The synthesis of an anthracene-derived Piloty's acid analogue was successful and achieved in reasonable yield, but the photo-irradiation to induce heterolytic cleavage of the C-O bond was found to be ineffective. Future work in this area should involve looking into the use of HPLC to separate compounds post photo-irradiation and LCMS for characterisation of unknown products. So far, the primary effort of the investigation has focused on exciting the anthracene to induce heterolytic cleavage of the compound, but investigations into pH control of the Piloty's acid analogue **4.22** could also be carried out.

Looking further into the photophysical characteristics of the analogue **4.22** showed a solvent dependent shift in the fluorescence emission but also a high level of self-quenching. Future work could look into the photophysics of this Piloty's acid derivative in comparison to compounds with similar functionality, such as Nakagawa's coumarin analogue **4.5**[2] and other fluorescent derivatives.

4.6 References

1. Piloty, O., Ueber eine Oxydation des Hydroxylamins durch Benzolsulfochlorid. *Koenigs Ber. dtsch. Chem. Ges.* **1896,** *11*, 1590.
2. Kawaguchi, M.; Tani, T.; Hombu, R.; Ieda, N.; Nakagawa, H., Development and cellular application of visiblelight- controllable HNO releasers based on caged Piloty's acid. *Chem. Commun.,* **2018,** *54* (73), 10371-4.
3. Aizawa, K.; Nakagawa, H.; Matsuo, K.; Kawai, K.; Ieda, N.; Suzuki, T.; Miyata, N., Piloty's acid derivative with improved nitroxyl-releasing characteristics. *Bioorg. Med. Chem. Lett.,* **2013,** *23* (8), 2340-3.
4. Teng, Y.; Suwanarusk, R.; Ngai, M. H.; Srinivasan, R.; Ong, A. S.; Ho, B.; Renia, L.; Chai, C. L., An amidation/cyclization approach to the synthesis of *N*-hydroxyquinolinones and their biological evaluation as potential anti-plasmodial, anti-bacterial, and iron(II)-chelating agents. *Bioorg. Med. Chem. Lett.,* **2015,** *25* (3), 607-10.
5. Liu, J., Wei, G.-H., Ping, G.-J., Ma, J.-F., 9-(Methoxy-meth-yl)anthracene. *Acta Crystallographica Section E: Structure Reports Online* **2007,** *63*, 04442.
6. Hashemi, M., M., Beni, Y. A., Regeneration of carbonyl compounds by oxidative cleavage of carbon-nitrogen double bonds with molecular oxygen in the presence of copper(I) chloride/ kieselghur as catalyst. *Synthetic Commun.,* **2001,** *31*, 295-9.
7. Opeida, I. A., Kas'yanchuk, M. G., Oxidation of Anthrone with Oxygen in DMSO. *Russ. J. Org. Chem.,* **2002,** *38* (6), 905-6.
8. Wang, H., Zhang, B. W., Cao, Y., Intramolecular charge transfer and exciplex formation in anthracene bichromophoric compounds. *J. Photochem. Photobiol. A: Chemistry* **1995,** *92*, 29-34.
9. Krueger, R. A.; Blanquart, G., Exciplex Stabilization in Asymmetric Acene Dimers. *J. Phys. Chem. A* **2019,** *123* (9), 1796-806.
10. Lakowicz, J. R., Principles of fluorescence spectroscopy. ProQuest Ebook Central: 1999. https://ebookcentral.proquest.com (accessed 26 August 2021).
11. Mattes, S. L., Farid, S., Photochemical cycloadditions via exciplexes, excited complexes, and radical ions. *Acc. Chem. Res.* **1982,** *15*, 80-6.
12. Forster, T., Kasper, K., Ein Konzentrationsumschlag der Fluoreszenz. *Zeitschrift für Physikalische Chemie* **1954,** *1*, 275-7.
13. Schmidbaur, H.; Raubenheimer, H. G., Excimer and Exciplex Formation in Gold(I) Complexes Preconditioned by Aurophilic Interactions. *Angew. Chem. Int. Ed. Engl.,* **2020,** *59* (35), 14748-71.
14. Cho, D. W., Excimer and exciplex emissions of 1,8-naphthalimides caused by aggregation in extremely polar or nonpolar solvents. *New J. Chem.,* **2014,** *38*, 2233-6.
15. Likhtenstein, G. I.; Ishii, K.; Nakatsuji, S., Dual chromophore-nitroxides: novel molecular probes, photochemical and photophysical models and magnetic materials. *Photochem. Photobiol.,* **2007,** *83* (4), 871-81.
16. Tang, C., Zhu, X., Song, Y., Liu, W., Yang, Q., Lv, Z., Yang, Y., Revealing the origin of excimer emission in anthracene crystals: The role of T excitation wavelength and pressure. *J. Photochem. Photobiol. A: Chemistry* **2019,** *376*, 263-8.
17. Bouas-Laurent, H., Castellan, A., Desvergne, J.-P., Lapouyade, R., Photodimerization of anthracenes in fluid solutions: (part 2) mechanistic aspects of the photocycloaddition and of the photochemical and thermal cleavage. *Chem. Soc. Rev.,* **2001,** *30*, 248-63.
18. Das, A.; Danao, A.; Banerjee, S.; Raj, A. M.; Sharma, G.; Prabhakar, R.; Srinivasan, V.; Ramamurthy, V.; Sen, P., Dynamics of Anthracene Excimer Formation within a Water-Soluble Nanocavity at Room Temperature. *J. Am. Chem. Soc.,* **2021,** *143* (4), 2025-36.

19. Chandross, E. A., Photolytic dissociation of dianthracene. *J. Chem. Phys.,* **1965,** *43*, 4175-6.
20. Chandross, E. A., Ferguson, J., Absorption and fluorescence of sandwich dimers. Theory of the excimer state. *J. Chem. Phys.,* **1966,** *45*, 397-8.
21. Bae, W.; Yoon, T. Y.; Jeong, C., Direct evaluation of self-quenching behavior of fluorophores at high concentrations using an evanescent field. *PLoS One* **2021,** *16* (2), e0247326.
22. Saltiel, J., Marchand, G. R., Dabestani, R., Pecha, J. M., The quenching of anthracene triplets by ground-state anthracene. *Chem. Phys. Lett.,* **1983,** *100*, 219-22.
23. Chen, K.; Liu, B.; Yu, B.; Zhong, W.; Lu, Y.; Zhang, J.; Liao, J.; Liu, J.; Pu, Y.; Qiu, L.; Zhang, L.; Liu, H.; Tan, W., Advances in the development of aptamer drug conjugates for targeted drug delivery. *Wiley Interdiscip. Rev. Nanomed. Nanobiotechnol.,* **2017,** *9* (3).

Chapter 5 Aptamer Chemistry

5.1 Introduction

Aptamers, artificial oligonucleotides with comparable binding affinities to most antibodies, are an attractive prospect when considering targeted drug delivery.[1] As most non-targeted drugs cause serious side effects to healthy tissue, the design of directed therapies using robust targeting vectors has become more appealing to the scientific community. Whilst monoclonal antibodies are at the forefront of the target therapy research push, aptamers might also be emerging as a suitable macromolecular drug, as discussed in several reviews and investigated in more detail in section 5.1.1.[2-4] Aptamers were first generated in 1990 by an *in vitro* selection technique (Systematic Evolution of Ligands by Exponential Enrichment, SELEX)[5] and displayed certain advantages over antibodies, the current standard for targeted delivery. These include a reduced size, less costly production, and easy chemical modification but also low immunogenicity and high chemical stability. Aptamers are also better able to penetrate tissue rapidly and are non-toxic, making them useful for drug delivery, as discussed in Chapter 1.[6-9]

The potential for aptamers to be used as vectors in targeted drug delivery has been studied extensively in recent years, with groups targeting growth factors,[10, 11] and viral proteins7,[12] amongst others, with several excellent reviews summarising these investigations as detailed in Chapter 1.2,[13, 14]

5.1.1 Aptamers as drugs

When investigating the role of aptamers as therapeutics, nucleic acids were found capable of preventing viral gene expression by overexpressing a response decoy in host cells.[15] More recently, Macugen was approved by the US Food and Drug Administration (FDA) for treatment against vascular endothelial growth factor (VEGF) of neovascular age-related

macular degeneration – the first therapeutic aptamer.[7] Aptamer AS1411 (currently in phase II clinical trials) can also recognise nucleolin, a BCL-2 mRNA binding protein associated with acute myelogenous leukaemia.[16]

Certain aptamers have been developed as anti-coagulants, which led to the investigation of them as potential therapeutics for the overexpression of thrombin.[17]

5.1.2 Aptamers as conjugated drug delivery systems

Targeted therapy is a way of selectively delivering toxic drugs to disease sites; this can effectively be achieved by conjugating the drug to the aptamer using a covalent linker or by intercalation.[18] Conjugation of aptamer sgc8 to therapeutics such as doxorubicin (Dox) was examined to determine release of the chemotherapeutic in acidic environments (pH 4.5-5.5).[19] Huang *et al*. found that the conjugate was capable of lowering toxicity towards non-target cells comparative to the unconjugated parent Dox. Unfortunately, there was a low copy number of drugs attached to each aptamer, a feat that was improved by Gmeiner and co-workers[7] and Wang *et al*.[20]

Noncovalent aptamer conjugation presents another attractive prospect for targeted drug delivery. Aptamer-tethered DNA nanotrains were designed with a modified sgc8 aptamer acting as the driving point for delivery whilst dsDNA nano-constructs carried multiple loads of Dox (Figure 66).[20, 21]

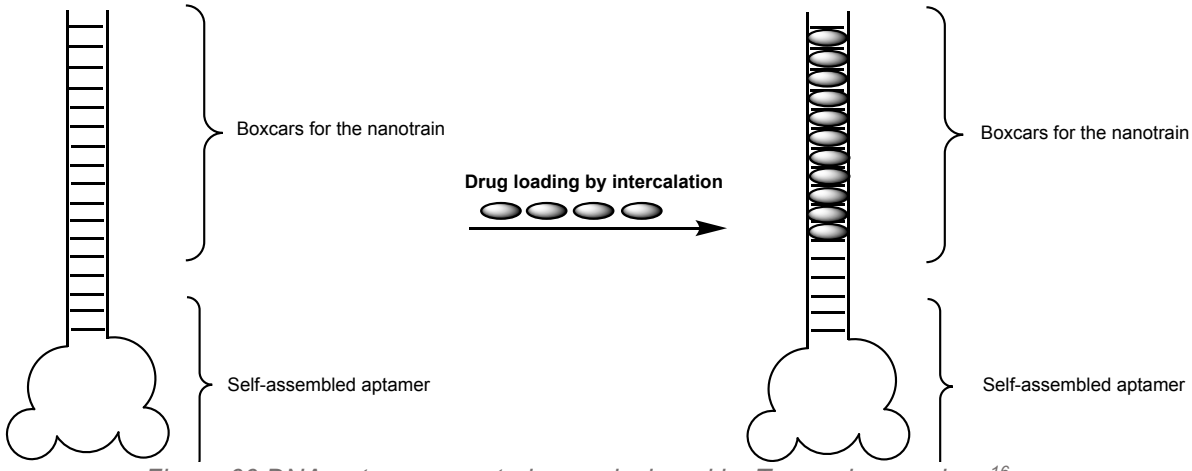


Figure 66 DNA-aptamer nanotrains as designed by Tan and co-workers[16]

The aptamer nanotrains were able to target the overexpressed human protein tyrosine kinase 7 (PTK7), a feat verified by flow-cytometric analysis. The nanotrains were also considered as carriers for multiple purposes, including a combination of chemical modification and physical intercalation. In this instance, 13 nm gold nanoparticles and chemotherapeutic drugs were loaded by attachment to the thiol groups and by GC base intercalation respectively.[22] Use of the gold allowed for transmission electron microscopy and also opened the opportunity for other cargo loading of therapeutics that might conjugate to gold.

Aptamers have also been shown to work in gate keeping for therapeutics contained within silica nanoparticles.[23] By conjugating an ATP-binding aptamer to mesoporous silica nanoparticles containing fluorescein, the pores of the complex could be closed until recognition of an ATP molecule (Figure 67).[23]

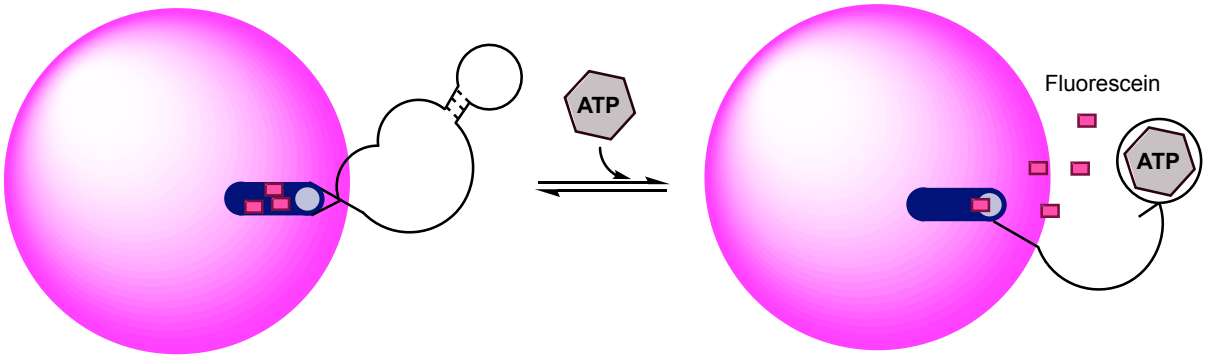


Figure 67 Diagram showing ATP-gated nanoparticles and recognition-dependent release of fluorescein (adapted from Ozalp et al. 2011)

This was one of the first examples of using aptamer recognition sites to control the release of a molecule, in this case fluorescein for easy sensing, and shows the untapped potential of aptamers for targeted delivery.

5.1.3 Thrombin binding aptamer

The coagulant serine protease thrombin is an essential part of the coagulation cascade designed to undergo haemostasis in the event of damage. The cascade itself was first described in 1964,[22] and thrombin is known to play a role in the last step, causing the cleavage of fibrinogen to fibrin monomers which can subsequently form a fibrin clot and stop bleeding.[24] Thrombin has also been identified as a possible cause of inflammation in certain diseases such as sepsis and multiple sclerosis.[25] In these cases, the coagulant factors enhance inflammation within both the bloodstream and also the tissue.

From this dual nature of thrombin, both release and capture of the coagulant could be desired in different disease models. In the case of multiple sclerosis for example, thrombin is overexpressed, requiring capture whilst thrombin should be delivered in sufferers of haemophilia. Of the inherited bleeding disorders for which thrombin is considered a suitable treatment, haemophilia is the best known and is characterised by an inability to generate sufficient thrombin for the clotting of blood vessel damage.[26]

There are two types of thrombin binding aptamer (TBA) designed to bind human α-thrombin (Figure 68). A 15-mer strand (here called TBA-15) described by Toole and co-workers forms a stable intramolecular antiparallel G-quadruplex,[27] and binds the fibrinogen-recognition exosite of thrombin. The other aptamer is a longer 29-mer (TBA-29) which binds the heparin-binding exosite and also contains an anti-parallel G-quadruplex.[27]

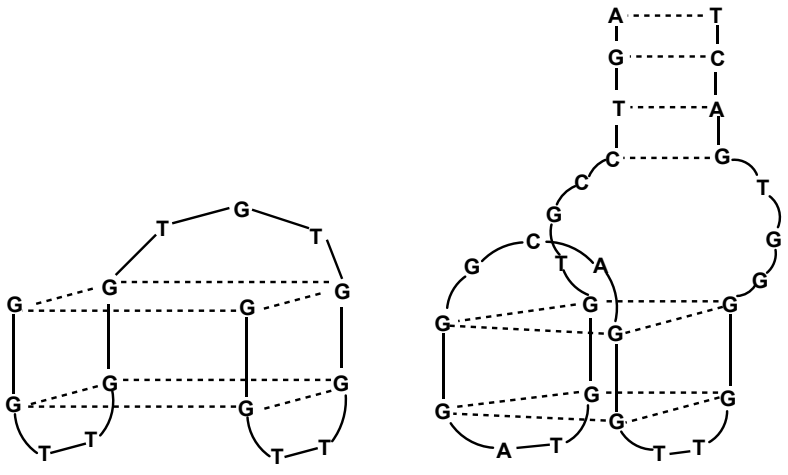


Figure 68 Two thrombin binding aptamers - both of which form G-quadruplexes in an antiparallel structure

The T-loops of TBA-15 are known to be the areas of the G-quadruplex involved in the binding of the DNA strand to the protein, as supported by work carried out modifying sections of the aptamer by Tucker and co-workers.[27] As such, any modifications to the TBA-15 strand should not disrupt either the G-quadruplex or the T-loops formed unless changing the thrombin binding affinity is desired.

5.2 Aims

A bis-ended aptamer capable of reversible drug capture and release on contact with a target was proposed, using the well-known TBA-15 sequence with a 3' extension to allow for release upon contact with a separate target. The long term aims of the project included the creation of a modified thrombin binding aptamer that could both deliver a coagulant upon binding to a target and selectively bind the protein in the case of overexpression.

First, the project aimed to design and synthesise a modified thrombin binding aptamer, then to test the binding capabilities of this modified strand in comparison to the well-known 15-mer of the classic TBA. Next, the project looked to analyse the capture and release ability of the aptamer for thrombin in the presence and absence of a segment of complementary DNA (Figure 69). Finally, the reversibility of the aptamer was to be investigated to determine the suitability of this design for future work.

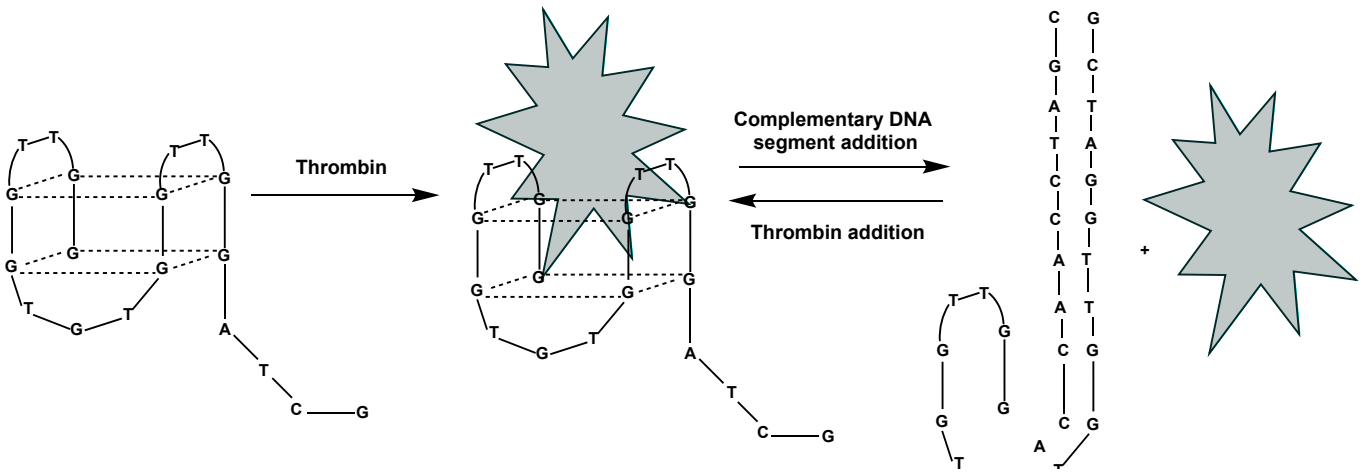


Figure 69 Graphical abstract for the proposed reversible thrombin catch and release design

5.3 Design and Synthesis of modified thrombin binding aptamer

The Tucker group had previously established that thrombin binding to TBA-15 was affected by disruption to the T loops of the G quadruplex,[27] so the first aim of this investigation was to determine how many bases of a complementary strand was necessary to cause a conformational change in the original G-quadruplex.

By modifying only the 3' end of the aptamer strand, a tail could be created (Figure 69) that should not inhibit the formation of a G quadruplex when existing as a single strand. A modified strand (TBA_L) with an additional four bases (5'-ATCG-3') was designed, along with the full complementary strand, and two segments of differing length complementary strands ($SHORT_C$ and $LONG_C$). Having purchased the DNA strands (Table 8) commercially from Merck, they were purified by semi-prep HPLC and characterised by mass spectrometry (Appendix 5.1).

TBA-15 readily forms an intramolecular G-quadruplex in buffers containing magnesium and potassium salt, but this conformation would be disrupted in the presence of a competing complementary DNA strand. As such, when attempting to design a release system for thrombin, disruption of the T loops of the G-quadruplex structure was important[28] and the complementary segments of DNA ($SHORT_C$ and $LONG_C$) were designed to bind one of these regions (Figure 70).

Table 8 DNA strands designed for thrombin catch and release investigations

STRAND	MASS (Da)	SEQUENCE (5'-3')
Thrombin binding aptamer (TBA)	4726	GGTTGGTGTGGTTGG
TBA complementary (TBA_C)	4420	CCAACCACACCAACC
TBA + linker (TBA_L)	5962	GGTTGGTGTGGTTGGATCG

TBA_L complementary (TBA_{LC})	5656	CGATCCAACCACACCAACC
Complementary segment 1 ($SHORT_C$)	2668	CGATCCAAC
Complementary segment 2 ($LONG_C$)	3270	CGATCCAACCA

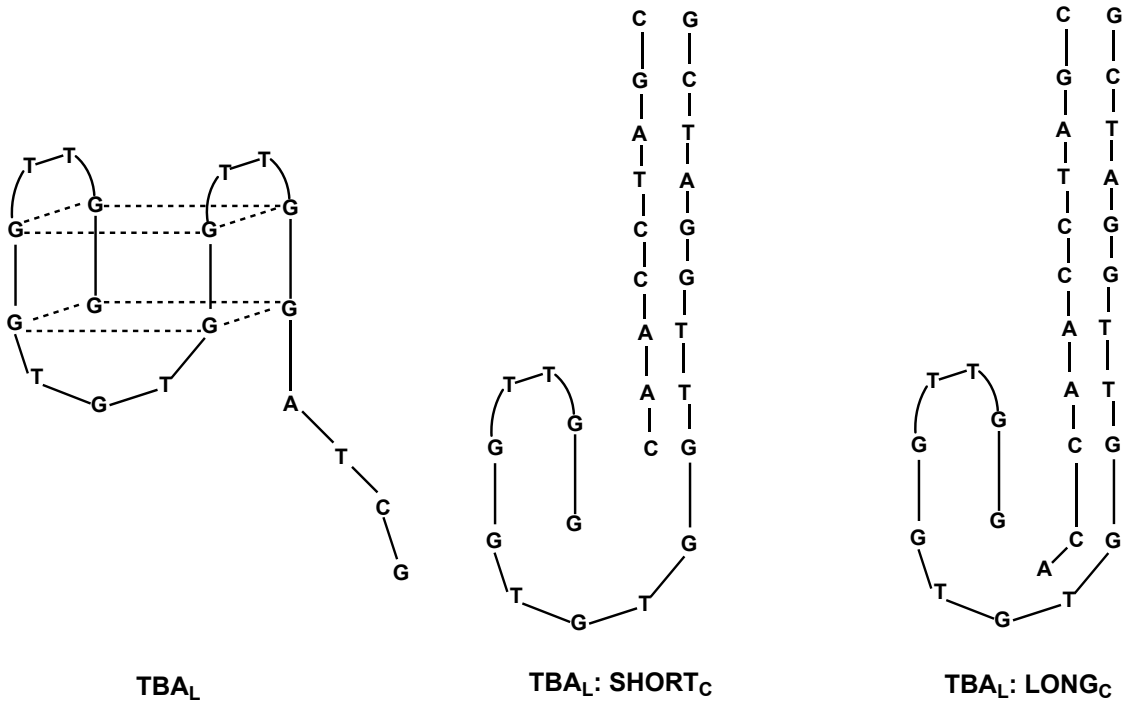


Figure 70 Anticipated G-quadruplex disruption on addition of complementary segments $SHORT_C$ and $LONG_C$

Strand $SHORT_C$ was prepared to have 5 complementary bases to the TBA-15 strand and 9 complementary bases to the modified TBA_L strand. Similarly, strand $LONG_C$ shows 7 complementary bases to the TBA-15 strands and 11 complementary bases to TBA_L strand. In contrast, the full complementary strands TBA_C and TBA_{LC} have 15 and 19 paired bases each respectively (Figure 70).

Formation of the G-quadruplex is dependent on the buffer used for the compound, with the secondary structure showing more stability in buffers containing potassium salts.[29, 30] As such, all experiments were carried out in both TBA buffer and duplex buffer (Table 9).

Table 9 Buffer components used in all thrombin aptamer investigations

BUFFER	COMPONENTS
TBA buffer	*20 mM Tris-HCl, 1 mM $MgCl_2$, 120 mM NaCl, 10 mM KCl, 2 mM $CaCl_2$ pH 7.38*
Duplex buffer	*10 mM sodium phosphate, 100 mM NaCl, pH 7.4*

5.3.1 Thermal characterisation of TBA-derived strands

The binding characteristics of duplex DNA can be investigated in several ways; thermal melting temperatures are a way of determining the relative stability of multiple duplex strands. By measuring the thermal melting temperature of the single strands alone, and of each combination of duplex in various buffer systems, the relative binding stabilities could be analysed, giving an indication of the effect of each buffer on the binding behaviour (Table 10). In this investigation, the T_Ms were determined by intercalating the strands with SYBR Green dye and measuring the fluorescence output at increasing temperature points. By determining the temperature required to disrupt the G quadruplex structure of both TBA-15 and TBA_L alone in these buffers (Figure 71 and Figure 72), comparisons could then be made when adding in various complementary strands.

Table 10 Thermal melts (T_Ms) of TBA and TBA_L strands alone and with their complementary strands in both duplex and TBA buffers

	AVERAGE T_M (˚C)
TBA (DUPLEX BUFFER)	N/A
TBA (TBA BUFFER)	44
TBA_L (DUPLEX BUFFER)	44
TBA_L (TBA BUFFER)	51
TBA: TBA_C (DUPLEX BUFFER)	70.5
TBA: TBA_C (TBA BUFFER)	73.3
TBA_L: TBA_{LC} (DUPLEX BUFFER)	73.5
TBA_L: TBA_{LC} (TBA BUFFER)	72

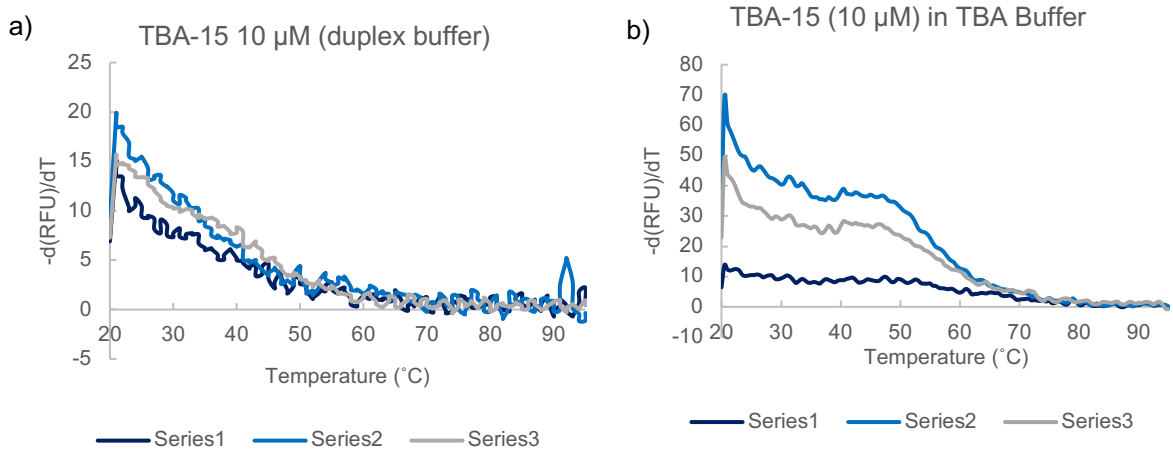


Figure 71 Graphical representation of the thermal character of TBA-15 in a) TBA b) duplex buffer

Interpreting the disruption of the G-quadruplex by the thermal melt character of the TBA-15 strand in each buffer was difficult due to a lack of significant peak in the T_M curves. However, the graph representing the T_M in duplex buffer did not show a peak, whereas there was a clear peak shown in potassium containing TBA buffer (44 °C). Similarly, the elongated strand TBA_L showed the same trend in each buffer (Figure 72) with T_Ms of 44 ˚C and 51 ˚C. Literature values for TBA-15 using differential scanning calorimetry show TBA to have a T_M of 50 ˚C in K^+ containing buffers.[31]

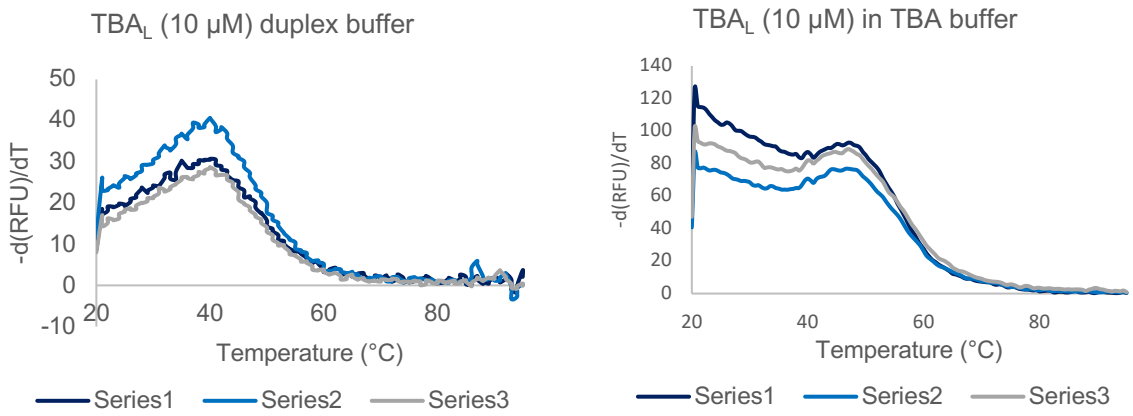


Figure 72 Graphical representation of the thermal character of TBA_L in a) duplex b) TBA buffer

Having determined the temperature required to disrupt the G-quadruplex structure in each TBA based strand, the T_M curves of the TBA, TBA_L and their full complementary strands were analysed (Figure 73). As expected, the T_Ms were greatly increased by the addition of a complementary strand, showing the temperature required to break the duplex DNA was 70.5 ˚C in duplex buffer and 73.3 ˚C in TBA buffer. TBA_L and TBA_{LC} strands showed similar behaviour with T_Ms of 73.5 and 72 ˚C. The longer TBA_L: TBA_{LC} duplex was anticipated to show a slightly higher T_Ms, due to the additional 4 bases having to be broken but was not expected to be significant.

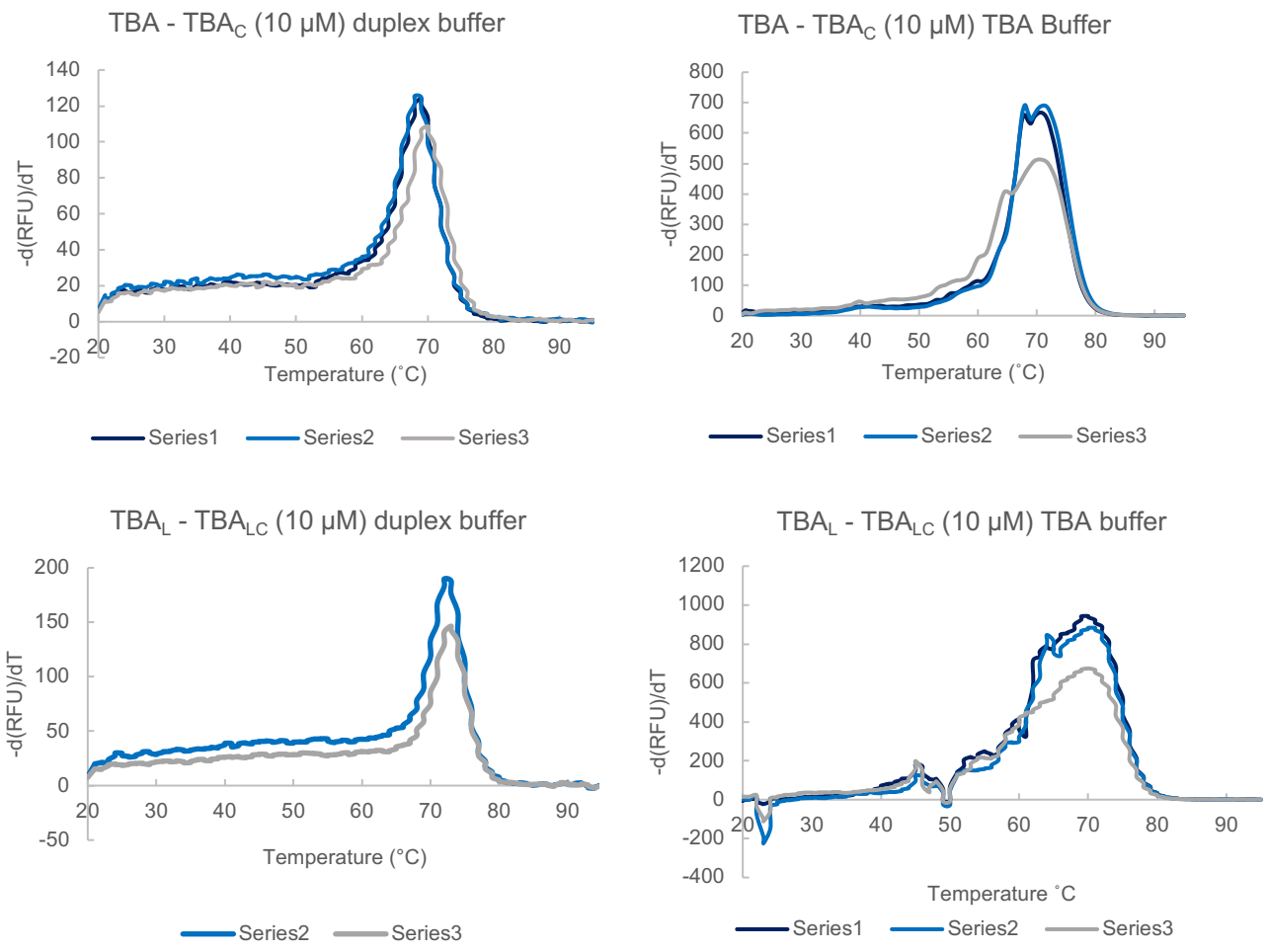


Figure 73 Graphical representation of the thermal character of TBA-TBA$_C$ and TBA$_L$-TBA$_{LC}$ strands in TBA and duplex buffers

Once the G-quadruplex and duplex characteristics of the DNA strands were established from the T_M data (Table 11), investigations into the binding behaviour of the shorter complementary segments $Short_C$ and $Long_C$ could begin (Figure 74) and (Figure 75).

Table 11 Thermal melts (T_Ms) of TBA and TBA_L strands complexed with either $SHORT_C$ or $LONG_C$ strands in both duplex and TBA buffers

	AVERAGE T_M (˚C)
TBA: $SHORT_C$ (DUPLEX BUFFER)	31.7
TBA: $SHORT_C$ (TBA BUFFER)	25
TBA_L: $SHORT_C$ (DUPLEX BUFFER)	47
TBA_L: $SHORT_C$ (TBA BUFFER)	53.3
TBA: $LONG_C$ (DUPLEX BUFFER)	47.7
TBA: $LONG_C$ (TBA BUFFER)	49.3
TBA_L: $LONG_C$ (DUPLEX BUFFER)	58.7
TBA_L: $LONG_C$ (TBA BUFFER)	62.3

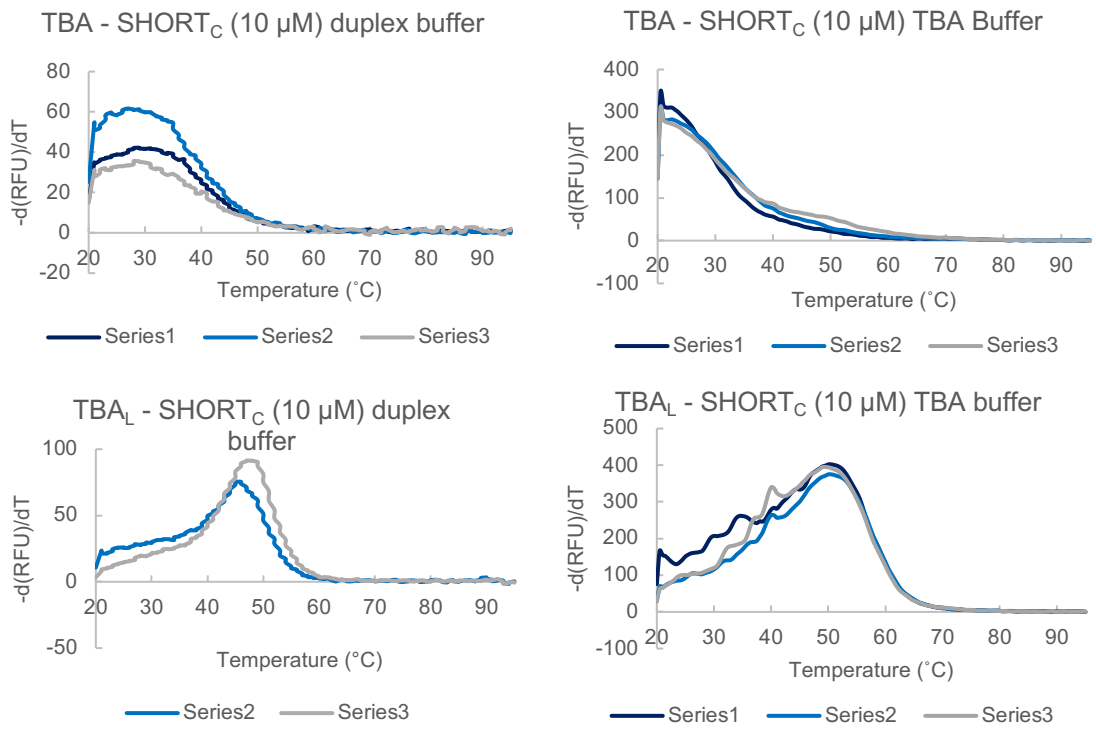


Figure 74 Graphical representation of the thermal of TBA and TBA$_L$ bound to SHORT$_C$ in TBA and duplex buffers

As expected, binding the TBA-15 strand to the short complementary strand SHORT$_C$ showed a very small T_M value in both duplex and TBA buffer (31.7 and 25 ˚C respectively), indicating weak duplex stability. However, in the longer TBA$_L$ strand, the T_M was seen to be 47 ˚C in duplex buffer and 53.3 °C in TBA buffer, which would indicate the additional 4 base pairs have a significant effect on stability of the duplex DNA.

In the same manner, LONG$_C$ was incubated with TBA-15 and TBA$_L$, and the TMs measured (Figure 75)

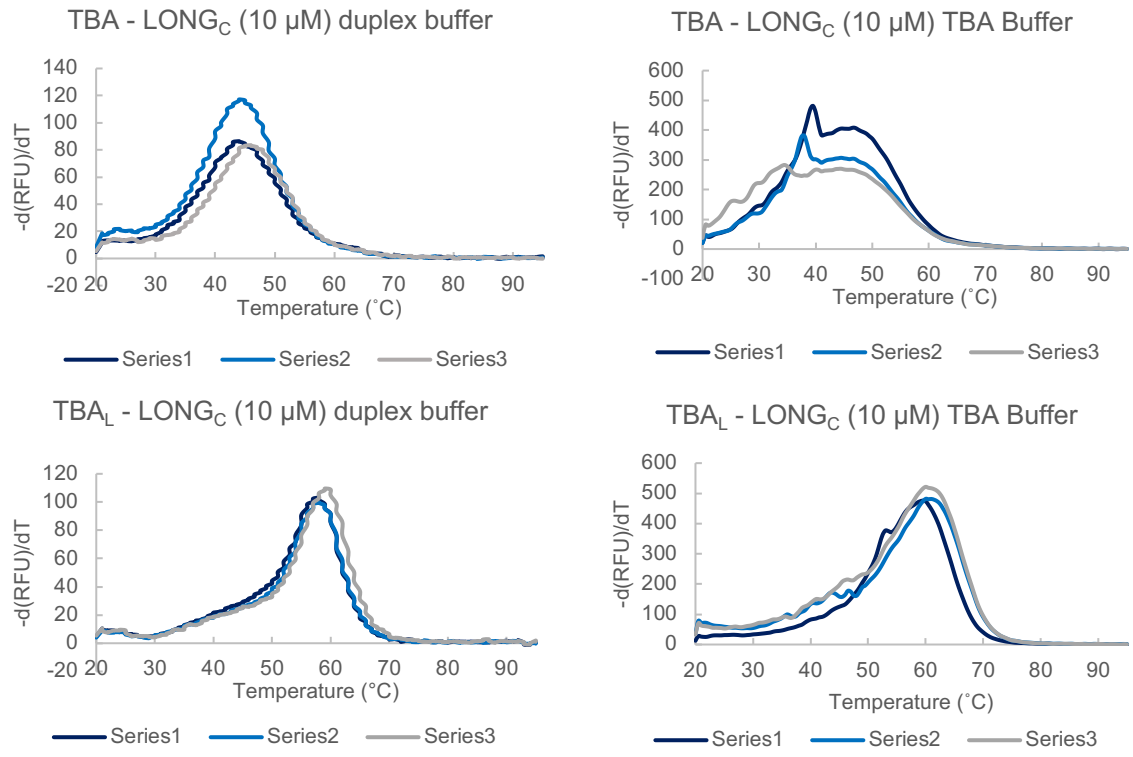


Figure 75 Graphical representation of the thermal of TBA and TBA$_L$ bound to LONG$_C$ in TBA and duplex buffers

The additional base pairing of the longer complementary segment LONG$_C$ is represented in the higher T_Ms observed when looking at these duplexes. The TBA strand in duplex buffer showed a T_M of 47.7 °C, 16 °C higher than seen when binding to strand SHORT$_C$. For the modified aptamer TBA$_L$, the increase is not as significant with a T_M of about 58.7 °C, a rise of 11.7 °C. What could be determined from such work though, was that the buffer composition had little effect on the overall stability of the duplex DNA but, did affect the thermal energy required to disrupt the G quadruplex sequence of single strands TBA and TBA$_L$.

5.3.2 CD determination of DNA secondary structure

An introduction to the spectroscopic technique of circular dichroism was discussed in section 3.4.6.5. Analysis of the CD of samples can enable the differentiation of DNA secondary structures, giving a qualitative way of identifying double strand DNA and secondary structures such as G-quadruplexes. The general structure of double stranded B-DNA gives a trace that is fairly different to that of a single stranded G-quadruplex DNA (Figure 76).[29, 32]

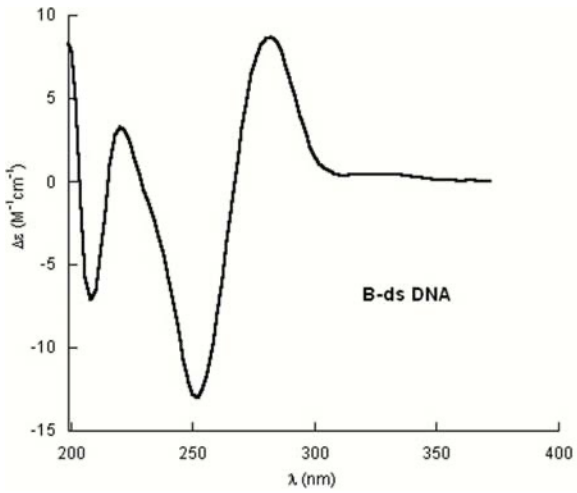


Figure 76 CD structure of B-DNA. Image taken from Dodero et al. 2011

The shape of the G-quadruplex is dependent on the way the strand is arranged into *syn-syn*, *anti-anti, syn-anti* or *anti-syn* and the specific structure can be roughly assigned by looking at the CD spectra.[33, 34] These can then be associated with particular G4 topologies (parallel, anti-parallel and hybrid) to aid determination of the style of G-quadruplex. In the case of TBA in the presence of metal ions such as potassium or calcium (K^+ or Ca^+), the aptamer forms an anti-parallel G-quadruplex as seen in the CD appearance (Figure 77).[35]

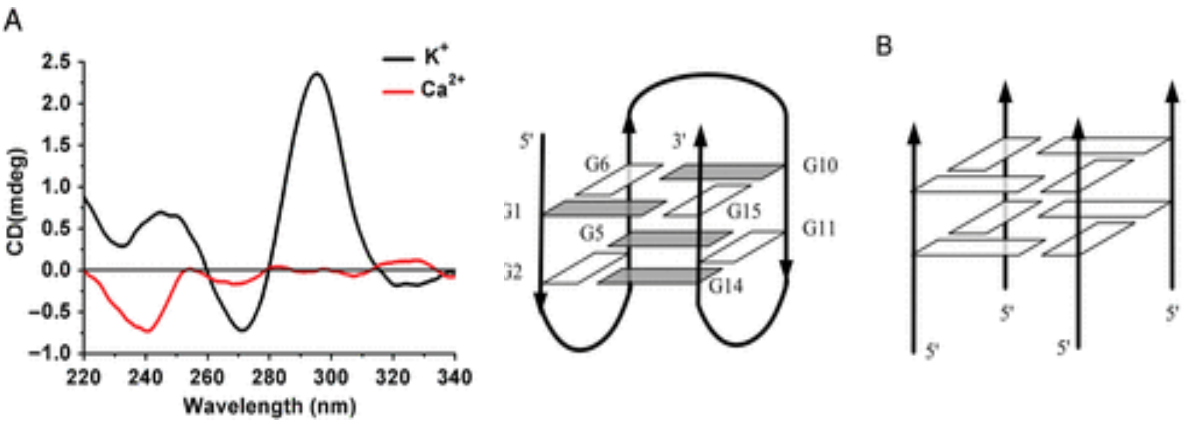


Figure 77 A) G-quadruplex CD structure in different salt conditions B) anti-parallel and parallel G-quadruplexes where the grey represents 'syn' and white represents 'anti' glycosidic conformations. Both images taken from Zhao et al. 2014.[29]

From these differences in structure, any changes in the secondary structure of the DNA can be noted. The 'catch and release' aptamer was designed specifically to exploit this adaptable morphology, where the G-quadruplex could be formed to bind the thrombin protein, but the presence of the complementary segments of DNA would disrupt one of the T loops and thereby collapse the quadruplex shape.

Detection of the change in morphology was investigated in both the duplex buffer and TBA buffer, to ensure that the presence of potassium and magnesium salts were included in any observations made. All measurements were taken at room temperature, in a range from 18 – 22 ˚C.

Before analysing CD spectra of the protein bound to each variant of thrombin binding aptamer the structure of the aptamers as both single stranded entities and as duplexes were investigated. By considering the spectra in each buffer, some conclusions about the role of salts in the secondary structure formation could be made (Figure 78, Figure 79).

The behaviour of the TBA-15 strand in the each buffer was analysed (Figure 78). The difference in the buffer effect on the TBA strand alone was seen to be prominent here, indicating that the 3' modification to TBA_L affects the G-quadruplex structure in duplex buffer.

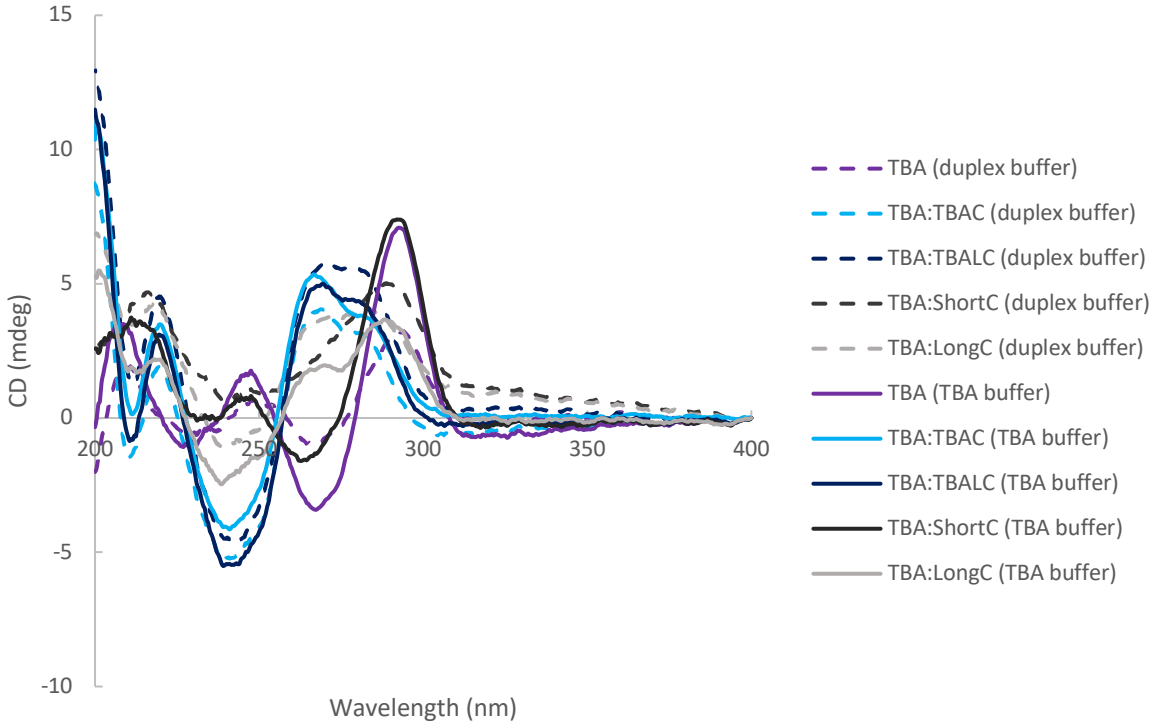


Figure 78 CD Spectra of TBA strands with each complementary strand option in both TBA and duplex buffer (15 μM)

The purple strands of the TBA-15 alone show a G-quadruplex type shape, matching that of Figure 77, and as expected the TBA: $SHORT_C$ duplex in TBA buffer also showed strong G-quadruplex characteristics. In comparison, the navy lines representing TBA: TBA_{LC} and the cyan lines representing TBA: TBA_C both showed more characteristics of the B-DNA CD spectra. The grey lines representing TBA: $LONG_C$ show different behaviours in each buffer, where the solid line (TBA buffer) showed a CD with more G-quadruplex behaviour, and the dotted line (duplex buffer) showed more B-DNA characteristics. This mirrored the results shown in the T_Ms, where the TBA: $LONG_C$ showed more duplex B-DNA characteristics and required more energy to disrupt.

Next, the TBA_L strands were analysed with the same complementary strands (Figure 79).

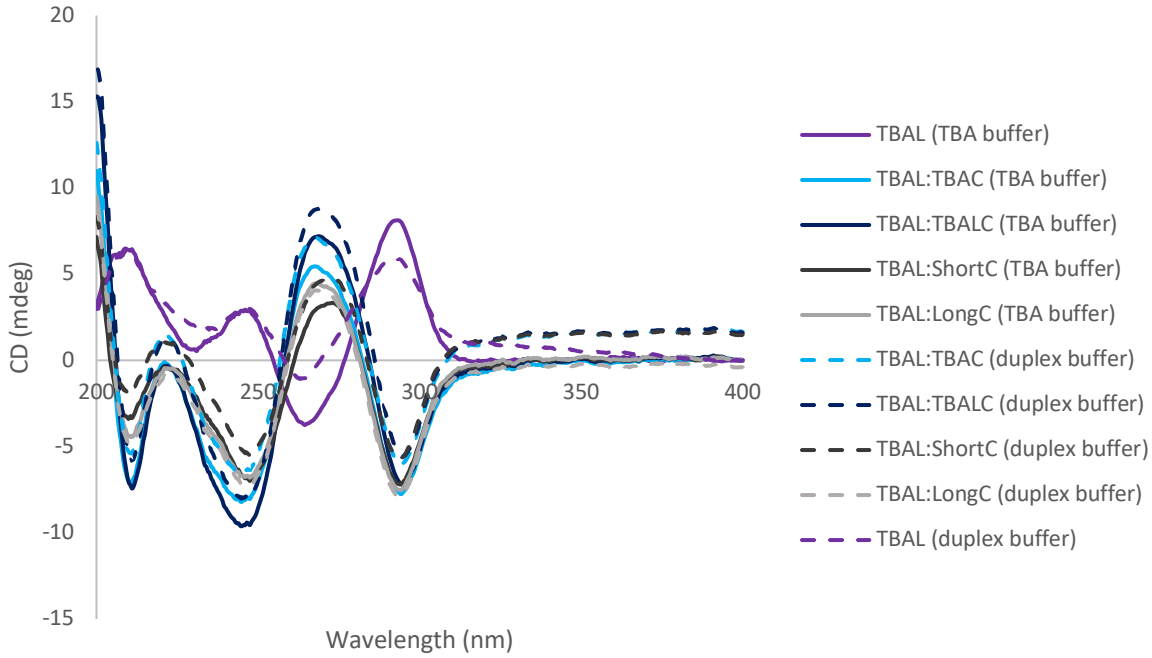


Figure 79 CD spectra of TBA_L strands with each complementary strand option in both duplex and TBA buffer (15 μM)

A slight shift in the overall structure was seen when comparing the CD spectra of TBA_L alone in each buffer. In both the duplex and TBA buffer though, both spectra resembled that of the G-quadruplex with a distinctive positive peak at 295 nm and negative peak at 265 nm.

As the complementary strands TBA_C and TBA_{LC} were added to the G-quadruplex, the CD spectra showed a shift to duplex B-DNA, as seen by the change of shape in spectra shown in Figure 79. Similarly, the segments of complementary DNA $SHORT_C$ and $LONG_C$ also showed that they bound TBA_L enough to induce a shift towards duplex DNA behaviour. The addition of the buffer had less of an effect on the double stranded DNA, but a slight shift overall can be seen between the duplex and TBA buffer samples. The T_Ms supported this, showing a higher overall amount of energy required to disrupt the duplex than TBA-15, no matter the complementary segment used.

Measuring the change in the conformation of the protein thrombin alone in different buffers also gave some insight into how the protein might fold differently in the presence or absence of certain metal salts (Figure 80).

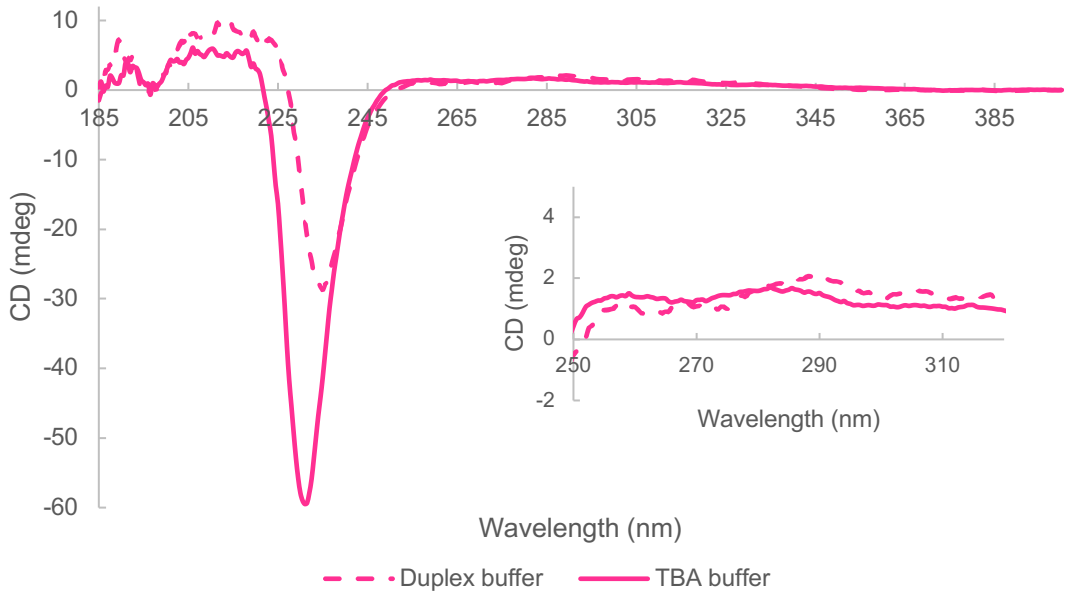


Figure 80 CD spectra of thrombin (5 μM) in TBA and duplex buffers

The CD spectra of thrombin is typically performed in K^+ and Ca^+ containing buffers to allow for stabilisation of the G-quadruplex. The peak at 290 nm did not show significant differences in each buffer, but the trough at 230-237 nm gave both a shift and a change in intensity. In duplex buffer, the trough was smaller and shifted to lower frequency wavelengths (237 nm) whilst the trough in TBA buffer had almost double the intensity and peaks at a slightly higher frequency (231 nm). This adaption in behaviour was thought to be due to the salts present in each buffer, and as such might give an indication into the state of the protein.

Having investigated the secondary structure of the aptamer in various environments, the effect of adding thrombin was analysed (Figure 81).

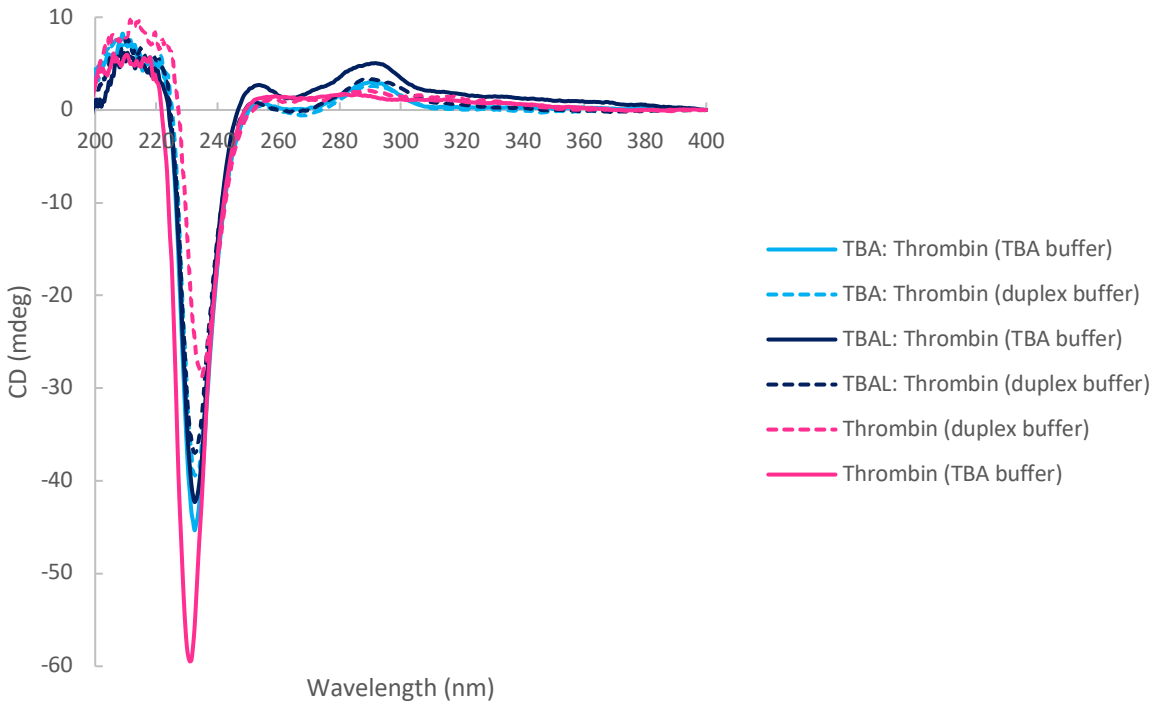


Figure 81 CD Spectra of TBA and TBA_L bound to thrombin in a 1:1 ratio (5 μM) in both TBA and duplex buffer

Thrombin alone in TBA buffer produced a trough signal at 231 nm of greater intensity than that shown by the combinations of TBA: thrombin or TBA_L: thrombin. Addition of complementary strands and segments (Figure 81) showed the changes induced by buffer environments. In TBA buffer, addition of the aptamers reduced the intensity of the trough whilst in duplex buffer the intensity was increased. A small peak at 290 nm and trough at 267 nm were also seen on addition of the G-quadruplex structure, indicating the aptamer maintained the same shape when binding the thrombin.

Next, the CD spectra of the TBA and TBA_L aptamers with complementary DNA strands and in the presence of thrombin were taken (Figure 82, Figure 83).

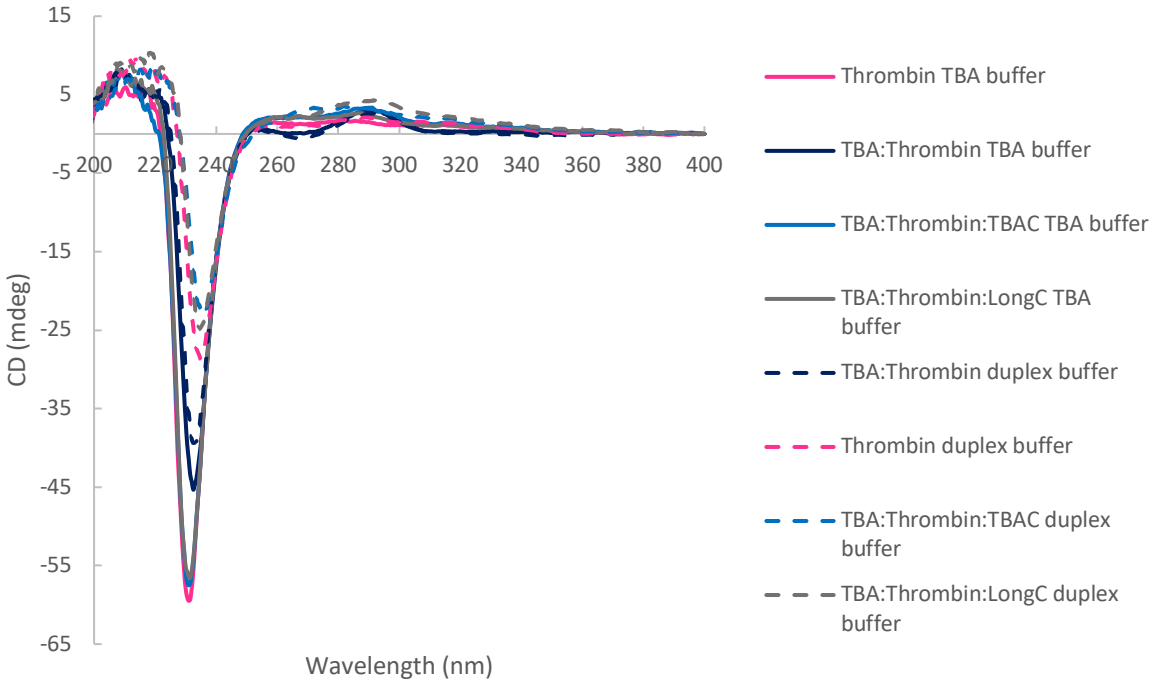


Figure 82 CD Spectra of TBA strands in the presence of thrombin and complementary strand segments TBA_C and $LONG_C$ in both TBA and duplex buffers

The trough at approximately 235 nm showed a difference upon addition of complementary segments of DNA. When looking at the aptamer alone, the trough increased in magnitude in duplex buffer but reduced in TBA buffer. Addition of the complementary DNA strands should cause the G-quadruplex to be disrupted if the aptamer bound the TBA_C or $LONG_C$ preferentially. From Figure 82, the trough showed that adding either DNA strand caused little change from the thrombin spectrum, a remarkable difference to that of the bound TBA: thrombin combination. These spectra would indicate that the TBA strand preferentially binds both TBA_C and $LONG_C$ to thrombin in a 1:1:1 ratio, regardless of buffer.

The same experiment was carried out on the modified aptamer TBA_L and complementary segment $LONG_C$ in the presence of thrombin (Figure 83).

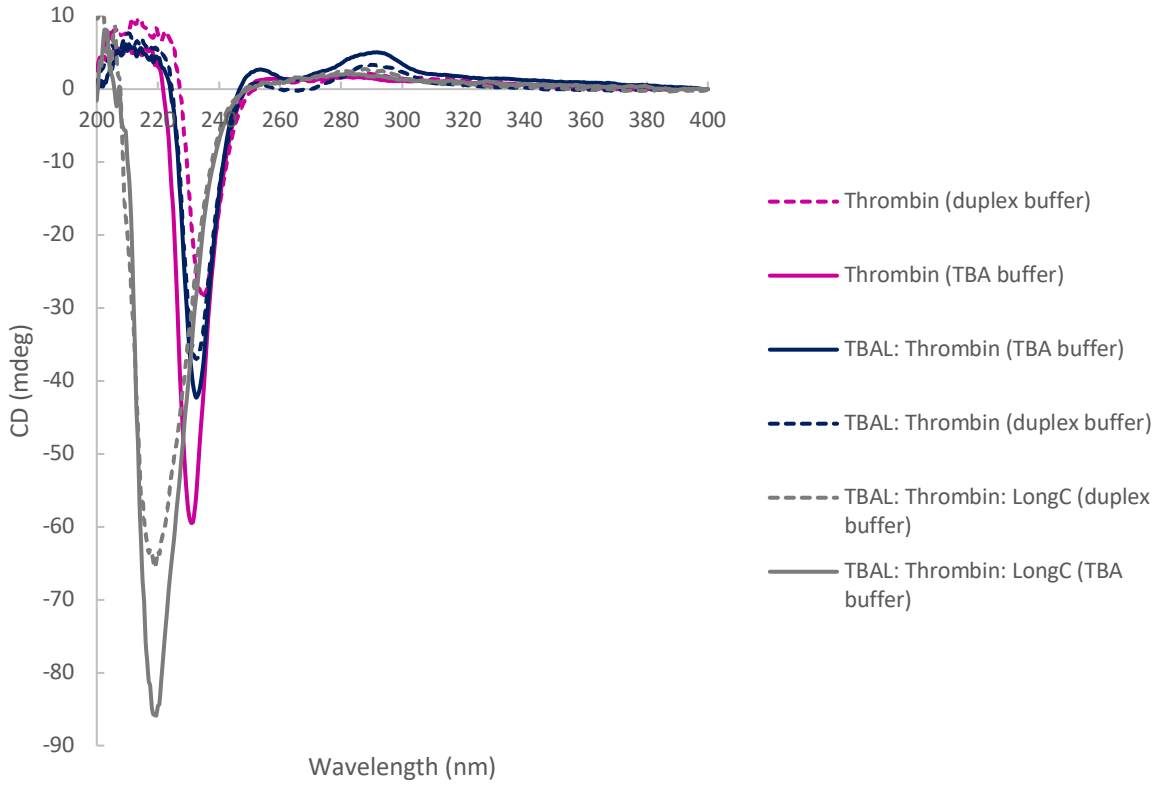


Figure 83 CD Spectra of TBA_L strands in the presence of thrombin and complementary strand segment $LONG_C$ in both TBA and duplex buffers

A large shift of the main trough (230 – 220 nm) was seen on addition of the $LONG_C$ complementary segment to the TBA_L: thrombin, indicating a change in behaviour, though this was not mirrored in the CD of free thrombin (shown in pink). The small peak and trough characteristic of G-quadruplex behaviour were not seen in the grey lines representing the TBA_L: thrombin: $LONG_C$ complex either, implying a lack of the secondary structure in the DNA. The buffer did not appear to make a difference in this experiment either, so all following experiments were carried out in TBA buffer alone.

5.3.3 PAGE analysis of thrombin binding aptamers

Polyacrylamide gel electrophoresis (PAGE) allows for analysis of DNA strands as bands differing based on their size, shape, and molecular weight. The use of PAGE could determine binding events between the aptamer, the complementary segments of DNA, and

between DNA and proteins. This, in conjunction with CD analysis, could allow some determination of the binding preference of the aptamer in the presence of multiple binding options. Measuring the intensity of the DNA bands stained with Diamond® DNA stain could also lead to quantification of the binding events by converting the bands to an area *via* use of the software ImageJ.

First, the gel of each aptamer (TBA and TBA_L) was required to determine the electrophoretic shift of the DNA with each complementary strand and segment (Figure 84). The gel was run as a 14% polyacrylamide doped with KCl to promote G-quadruplex formation. By setting each aptamer next to the bound aptamer and complementary strand, any difference between the single strand and duplex could be observed (Table 12).

Table 12 Lane components for PAGE experiments on TBA and TBA_L strands investigating the binding of complementary strands TBA_C and TBA_{LC}

LANE	**1**	**2**	**3**	**4**	**5**	**6**	**7**	**8**	**9**	**10**
TBA (10 μM, μL)			2.5		2.5			2.5		
TBA_L (10 μM, μL)				2.5		2.5			2.5	
TBA_C (10 μM, μL)					2.5					
TBA_{LC} (10 μM, μL)						2.5				
Thrombin (10 μM, μL)								6.25	6.25	
Glycerol (μL)			2	2	2	2	2	2	2	

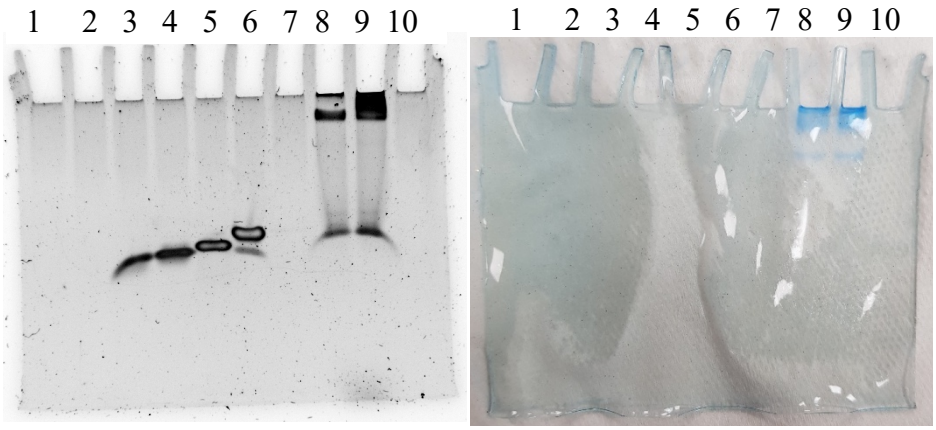


Figure 84 Native gels of TBA and TBA_L bound to TBA_C, TBA_{LC} and thrombin in TBA buffer (1μM) visualised with Diamond® DNA stain under UV light (left) and Instant Blue® Coomassie under visible light (right).

From lanes 3 and 4 of Figure 84 the single strands of TBA and TBA_L are clearly very similar in their shape and size. The duplexes with their complementary strands however showed a slight difference, with the longer duplex not moving as quickly through the gel (lane 6). Upon binding thrombin, a significant change was observed, with bands appearing at the very top of the gel indicating little to no movement through the gel. Given the large size of the protein (approximately 72 kDa), this lack of mobility was expected, and subsequent staining of the gel with Instant Blue® Coomassie showed protein present in the same area. The additional bands part-way down the gel in those lanes were attributed to unbound DNA.

Having determined the aptamers would bind both the complementary DNA and thrombin, more gels could be run to look at the binding of the shorter complementary segments $SHORT_C$ and $LONG_C$. The TBA strand was bound to both complementary segments and to increasing amounts of thrombin (0.5 – 2.5 μM) in an initial attempt to determine the concentration at which thrombin was preferentially bound (Table 13, Figure 85).

Table 13 Lane components for TBA bound to either $SHORT_C$ or $LONG_C$ with increasing amounts of thrombin in TBA buffer (10 μM)

LANE	**1**	**2**	**3**	**4**	**5**	**6**	**7**	**8**	**9**	**10**
TBA (10 μM, μL)		2.5	2.5	2.5	2.5	2.5	2.5	2.5	2.5	2.5
$SHORT_C$ (10 μM, μL)									2.5	2.5
LONGC (10 μM, μL)		2.5		2.5	2.5	2.5	2.5	2.5		
Thrombin (10 μM, μL)				1.25	2.5	3.75	5	6.25		5
Glycerol (μL)			2	2	2	2	2	2	2	2

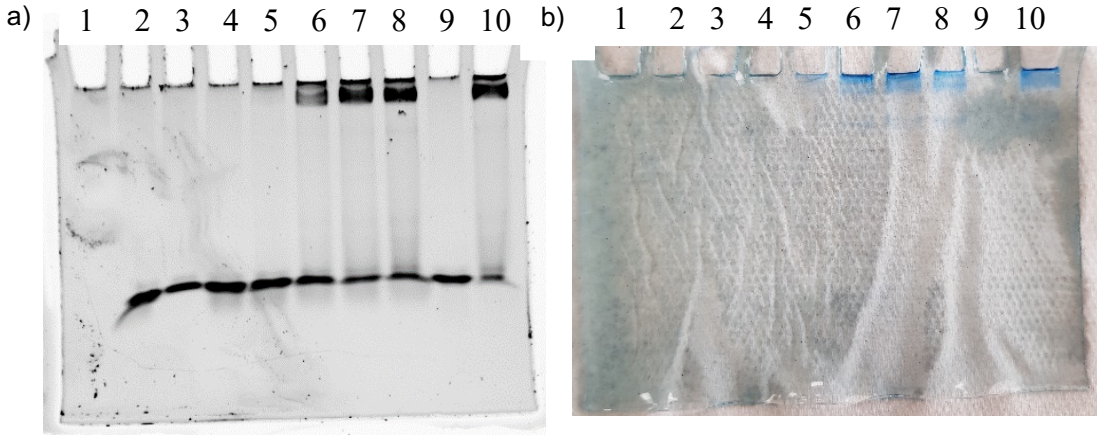


Figure 85 Native gel images of A) TBA with both $SHORT_C$ and $LONG_C$ complementary segments with increasing amounts of thrombin in TBA buffer (10 μM) B) shows the stained protein

The duplex DNA with both complementary segments in lanes 2 and 9 showed very little difference to the single stranded TBA in lane 3. At low concentrations of thrombin (lanes 4 - 5), very little change was observed, until an excess of thrombin was added in lane 6, where the presence of a second band at the top of the gel could be seen. From here, the intensity of that second band increased from lanes 6 – 8 as more thrombin was added, indicating a competing binding event occurring. Should the change in intensity be only due to increased amounts of thrombin, it was expected that the protein-stained images would show a similar

increase in intensity. Similarly, the thrombin bound preferentially when in excess to a mixture of TBA and $SHORT_C$ (lanes 7,8 and 10).

The modified aptamer TBA_L was also analysed in the presence of segments of complementary DNA and increasing concentrations of thrombin (Table 14, Figure 86).

Table 14 Lane components for TBA_L bound to either $SHORT_C$ or TBA_{LC} with increasing amounts of thrombin in TBA buffer (10 μM)

LANE	**1**	**2**	**3**	**4**	**5**	**6**	**7**	**8**	**9**	**10**
TBA_L (10 μM, μL)		2.5	2.5	2.5	2.5	2.5	2.5	2.5	2.5	2.5
$SHORT_C$ (10 μM, μL)			2.5	2.5	2.5	2.5	2.5	2.5		
TBA_{LC} (10 μM, μL)									2.5	2.5
Thrombin (10 μM, μL)				1.25	2.5	3.75	5	6.25		5
Glycerol (μL)			2	2	2	2	2	2	2	2

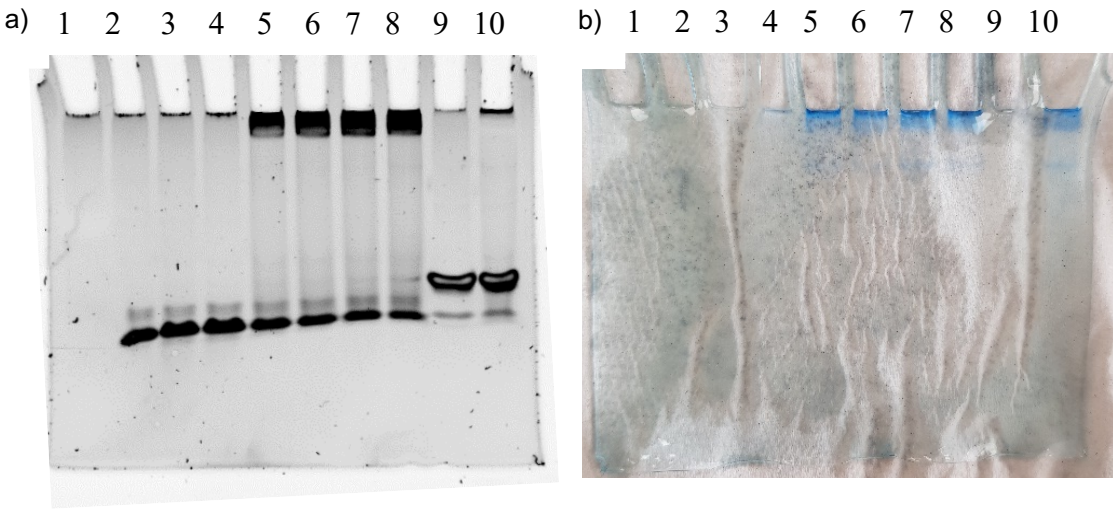


Figure 86 Native gel images of a) TBA_L with both $SHORT_C$ and TBA_{LC} complementary segments with increasing amounts of thrombin in TBA buffer (10 μM) b) shows the stained protein

The longer aptamer (TBA_L) also showed a difference in binding event upon the increase in thrombin concentration. In lane 5, at a 1:1:1 ratio, the appearance of a second DNA band showed binding of the aptamer to protein at the top of the gel, as corroborated by the protein-stained image in Figure 86b. From this, it was apparent that the longer aptamer had a preference for binding thrombin at lower concentrations, indicating the modification improved the stability of the G-quadruplex. When duplexed with the full complementary strand however, TBA_L did not form a G-quadruplex for protein binding at all.

ImageJ was used to quantify the DNA gel bands of Figure 85 and Figure 86, showing the intensity of the TBA or TBA_L DNA band as the concentration of thrombin was increased (Figure 87).

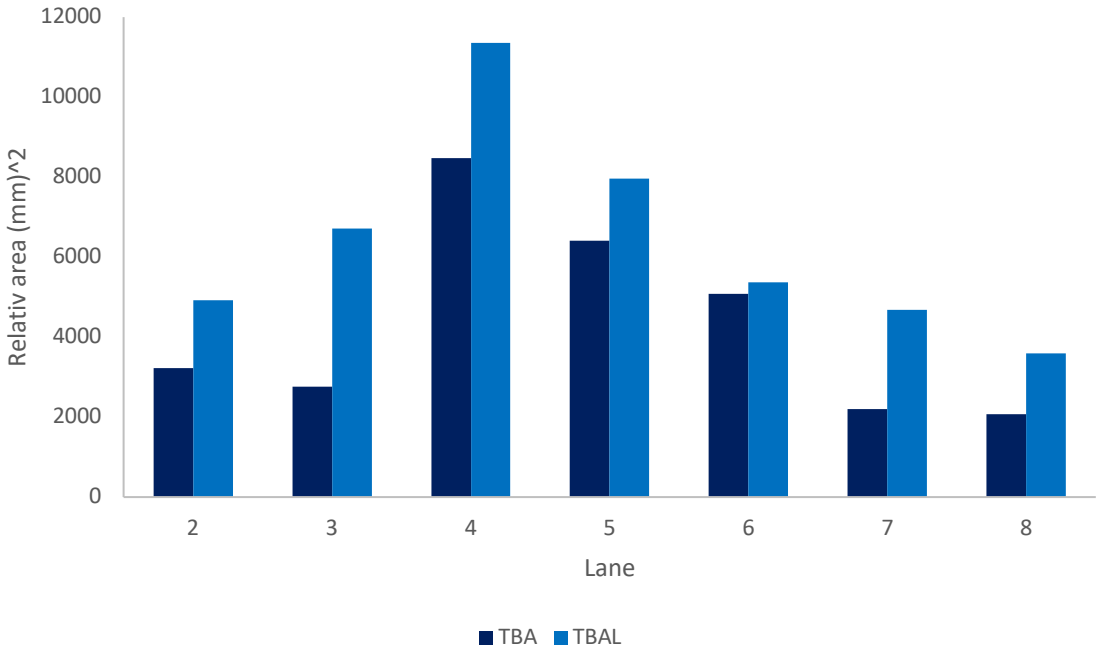


Figure 87 ImageJ analysis determining the intensity of the DNA bands of Figure 85 and 86 as the area of the band

The TBA-15 bands from Figure 85 shown in navy show that the intensity of the DNA band increases slightly as TBA_C was added to the TBA (lane 3 to lane 2). A larger increase in intensity was seen as thrombin was added (lane 4) though the protein should have no effect on this DNA band. Lanes 5 – 8 show a subsequent decrease in DNA intensity as the concentration of thrombin was increased, as anticipated if the thrombin was binding TBA preferentially to $LONG_C$. The light blue bands represented TBA_L intensity in Figure 86 and showed a similar behaviour, with an increase in intensity from lane 2 to lane 3 as the TBA_{LC} strand was added, creating a duplex. Again, an increase was seen on addition of the thrombin, and a subsequent decrease throughout lanes 5 – 8 as the relative concentration of thrombin increased.

The reduction in intensity past that of lane 3 (TBA) and lane 2 (TBA_L) shown in lanes 7 and 8 indicated that all the thrombin binding aptamer (TBA and TBA_L) were bound, and the complementary segment $SHORT_C$ was a smaller strand of DNA, so would be expected to have a lower intensity.

5.4 Studies into the reversible binding ability of thrombin binding aptamers

A combination of CD spectra and PAGE analysis was used to investigate the potential of these aptamers for reversible binding and release of thrombin in the presence of each complementary strand option. First, an experiment was designed looking at CD spectra of TBA: $LONG_C$ first, then adding one equivalent of thrombin followed by a subsequent equivalent of $Long_C$ in order to monitor the reversible nature of thrombin binding and release (Figure 88).

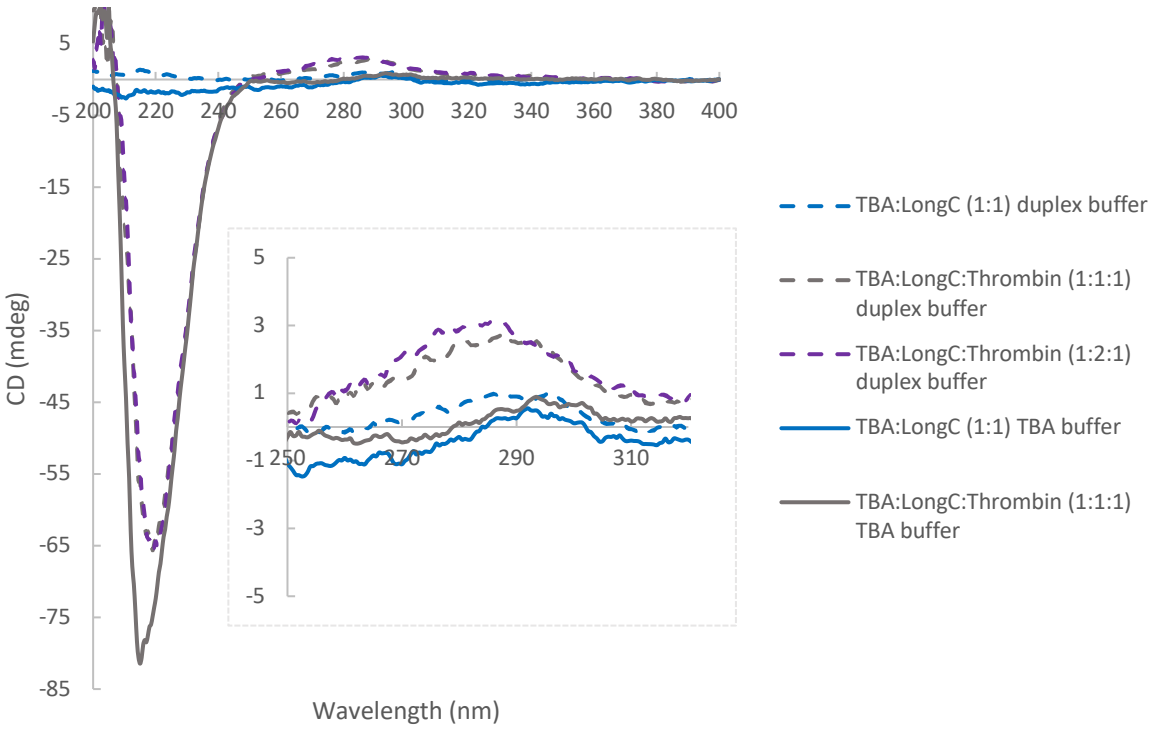


Figure 88 CD Spectra showing the reversibility study attempted on TBA with complementary segment $LONG_C$ in both TBA and duplex buffers (3 μM)

From the CD spectra above, the reversibility of binding complementary segment $Long_C$ in the absence and presence of thrombin was investigated. A weaker concentration was required to maintain a reasonable high tension (HT) value throughout the experiment, especially as the

thrombin protein was more prone to an overly high HT value at higher frequency wavelengths. By adding thrombin to the TBA: $LONG_C$ strands, a significant trough appeared, and showed no change on addition of a further equivalent of $LONG_C$ complementary DNA. Likewise, the peak at approximately 290 nm showed very little change on addition of an excess of $Long_C$. In TBA buffer, the peak showed no change even upon initial addition of thrombin, indicating no significant change in the secondary structure of the aptamer. Further evidence was required to make a decision regarding the reversible nature of the aptamer binding.

The same experiment was then attempted using the modified aptamer TBA_L, in order to determine if the behaviour would be changed by an additional 4 bases at the 3' end (Figure 89).

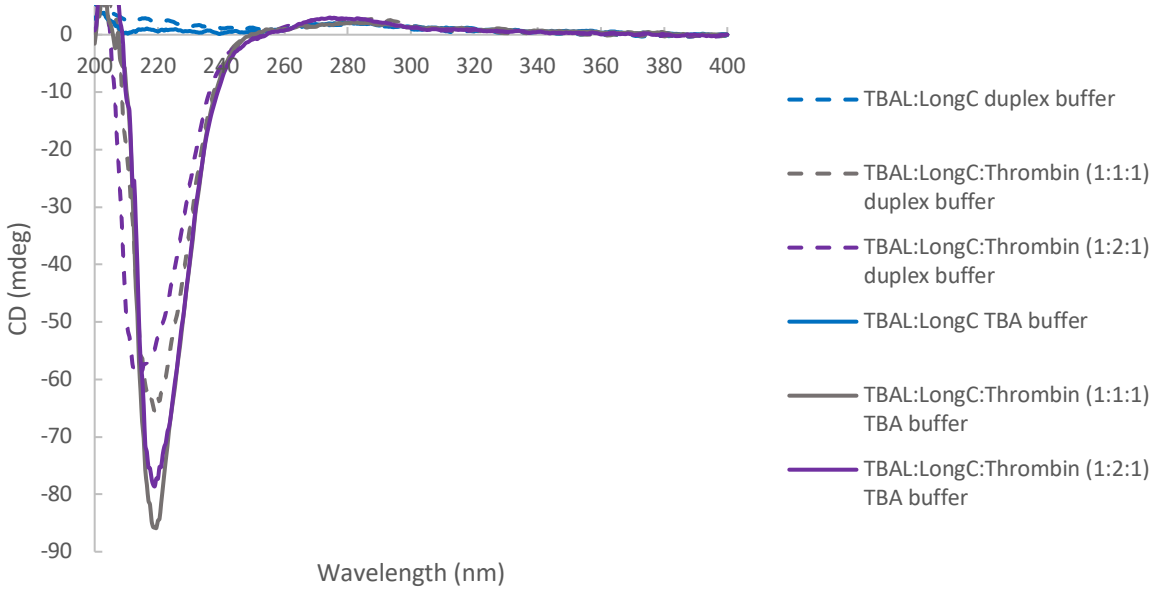


Figure 89 CD Spectra showing the reversibility study attempted on TBA_L with complementary segment $Long_C$ in both TBA and duplex buffers (3 μM)

The longer aptamer TBA_L showed different results to that of the original 15-mer, indicating a difference in reversibility. On addition of the thrombin to the aptamer TBA_L and $LONG_C$, the expected appearance of a large trough at approximately 220 nm was observed. Upon further addition of complementary segment $LONG_C$, there was a distinct change in the intensity of the trough, apparent in both buffer conditions. In each case, the intensity of the trough was reduced slightly, perhaps indicating a reduction in the amount of thrombin bound by the aptamer.

To further investigate the reversibility of binding, PAGE was used on aliquots of each step of the sequential reaction. Using the same gel conditions as previously described in 5.3.3, 2 repeats of both the TBA and TBA_L aptamer reversibility studies were run and analysed (Table 15).

Table 15 Lane components for PAGE experiments on TBA and TBA_L strands investigating reversible binding of thrombin at 4 ˚C

LANE	**1**	**2**	**3**	**4**	**5**	**6**	**7**	**8**	**9**	**10**
TBA/TBA_L (10 μM, μL)		2.5	2.5	2.5	2.5	2.5	2.5	2.5	2.5	2.5
$SHORT_C$ (10 μM, μL)			2.5	2.5	5	7.5				
$LONG_C$ (10 μM, μL)							2.5	2.5	5	7.5
Thrombin (10 μM, μL)				2.5	2.5	2.5		2.5	2.5	2.5
Glycerol (μL)		2	2	2	2	2	2	2	2	2

To ensure the reversible nature of the binding was investigated, a larger reaction mixture was prepared, and aliquots taken for each lane of the gel as the reaction progressed. For this investigation, the experiments were carried out in TBA buffer only. The first experiment

looked only at the original 15-mer aptamer TBA against each complementary segment (Figure 90).

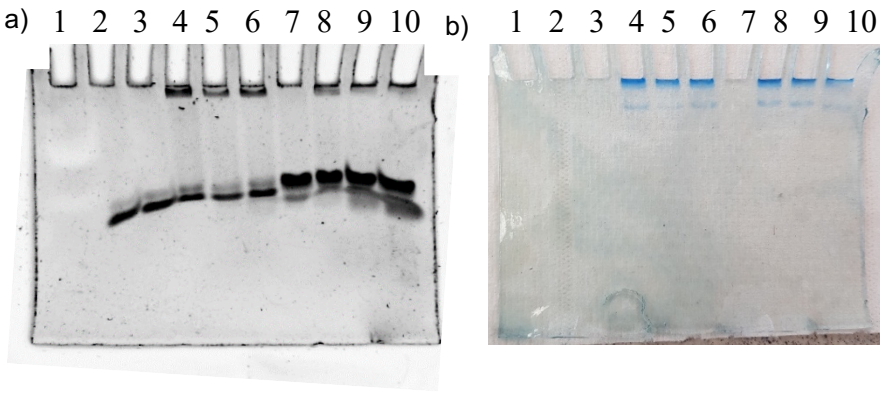


Figure 90 PAGE gel of TBA bound reversibly to various complementary segments of DNA $SHORT_C$ and $LONG_C$, and thrombin (10 μM). a) shows DNA containing bands whilst b) shows Coomassie stained protein containing bands

Lanes 2 and 3 of Figure 90 show the aptamer TBA alone and with the complementary segment $SHORT_C$, indicating very little difference in the electromobility of the bound and unbound DNA. However, there was a marked difference on addition of thrombin, as could be seen by the appearance of a second band at the top of lane 4. Measuring this against the protein-stained gel image Figure 90b shows that the DNA has bound to protein in this instance. Similarly, little change was seen in lanes 5 and 6.

More of a difference in the bound and unbound DNA was observed when coupling TBA to complementary segment $LONG_C$. Lane 7 showed a slightly higher band than that seen in lane 2, and very little binding to thrombin was observed in lanes 8, 9 and 10. Indeed, in lanes 9 and 10 the excess complementary segment DNA $LONG_C$ could be observed as a shadow band below. This gel indicates that in the case of aptamer TBA, the $SHORT_C$ strand did not disrupt thrombin binding in a 1:1:1 ratio but could compete for protein binding when in large excess. The longer complementary strand $LONG_C$ was more tightly bound though, and very little thrombin binding was observed.

The same experiment was carried out on the modified aptamer TBA_L (Figure 91) and the results analysed.

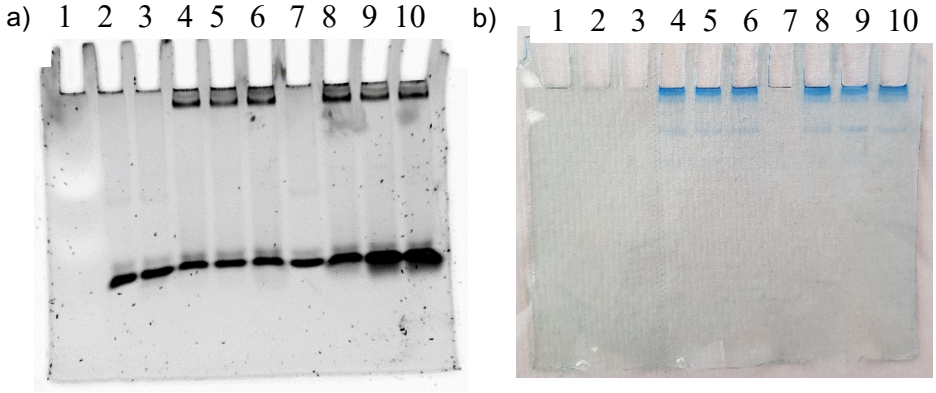


Figure 91 PAGE gel of TBA_L bound reversibly to various complementary segments of DNA $SHORT_C$ and $LONG_C$, and thrombin (10 μM). a) shows DNA containing bands whilst b) shows Coomassie stained protein containing bands

The observations made from Figure 91 were disappointing, demonstrating little evidence of significant reversibility in binding. While lane 4 showed the addition of a second band of DNA, matching with the protein stained in Figure 91b, but the intensity of the top band did not show any change as more equivalents of $SHORT_C$ DNA were added. This would indicate an irreversible binding event where the complementary DNA did not compete for the binding site.

In lanes 8 – 10, the binding of complementary DNA $LONG_C$ and thrombin was observed. Lane 8 showed that TBA_L bound thrombin when in a 1:1:1 ratio with $Long_C$ but did not release the protein entirely following addition of the DNA in excess. Analysis of the DNA band intensities were performed using ImageJ (Figure 92), showed little change in the band intensities on hybridisation of TBA to $SHORT_C$ (navy blue, lanes 3 – 6), indicating little binding of the complementary segment to the aptamer, as also seen in other techniques. However, the intensity of the duplex DNA band increased upon addition of rising amounts of complementary segment $LONG_C$, showing reversibility in the binding.

For the modified aptamer TBA_L, adding increasing concentrations of $SHORT_C$ showed a very slight increase in the duplex DNA band, indicating a slight level of reversibility. For lanes 8 – 10, a larger increase in the area was observed, indicating a better level of binding to the complementary segment $LONG_C$, though not as evident as seen in the TBA sample.

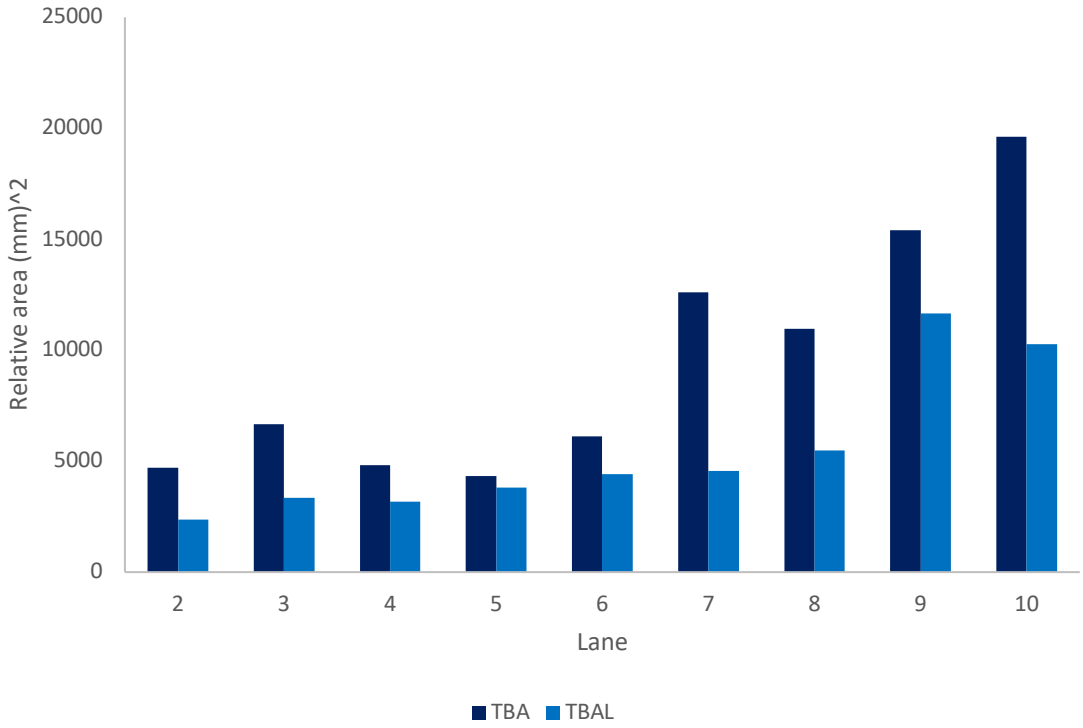


Figure 92 ImageJ analysis determining the intensity of the DNA bands of Figure 91 and 92 as the area of the band

The CD and PAGE results both show potential for a TBA-derived aptamer to have both binding and releasing capabilities. Investigating using PAGE showed potential for TBA-15 to bind thrombin in TBA buffer and to subsequently release the protein in large excess of the complementary DNA segment $SHORT_C$.

5.5 Conclusions and future work

The investigation into the design of an aptamer capable of both binding and releasing thrombin in varying conditions showed promise; slight modifications to the 15-mer aptamer TBA did not disrupt G-quadruplex formation nor disturb protein binding. Adding segments of complementary DNA to combinations of TBA, TBA_L and thrombin showed the potential for strategic release of the protein. This preliminary work demonstrates the potential for aptamers to be modified in ways suitable for targeted protein release or capture, meaning future design could lead to drugs suitable for treatment of either thrombin overproduction or shortage.

Whilst this work has not proceeded as far as discussed in the original aims, the preliminary results indicate potential for future work to incorporate the complementary segments of DNA ($SHORT_C$ and/or $LONG_C$) into a hairpin modification to the 3' end of the aptamer. By adding a hairpin of non-binding DNA, salt conditions could be modified to encourage or discourage secondary structure formation.

Ultimately, limited time in the lab towards the end of the PhD due to Covid-19 meant that this aim has been largely unmet, although synthesis of prototype strands have been formed for future work to commence. Another technique which would have been useful in investigating this project is Isothermal Calorimetry (ITC), an analytical technique capable of quantifying binding events.

5.6 References

1. Gijs, M.; Aerts, A.; Impens, N.; Baatout, S.; Luxen, A., Aptamers as radiopharmaceuticals for nuclear imaging and therapy. *Nucl. Med. Biol.,* **2016,** *43* (4), 253-71.
2. Kaur, H.; Bruno, J. G.; Kumar, A.; Sharma, T. K., Aptamers in the Therapeutics and Diagnostics Pipelines. *Theranostics* **2018,** *8* (15), 4016-32.
3. Ozalp, V. C.; Kavruk, M.; Dilek, O.; Bayrac, A. T., Aptamers: molecular tools for medical diagnosis. *Curr. Top Med. Chem.,* **2015,** *15* (12), 1125-37.
4. Santosh, B.; Yadava, P. K., Nucleic acid aptamers: research tools in disease diagnostics and therapeutics. *Biomed. Res. Int.,* **2014,** *2014*, 540451.
5. Alibolandi, M.; Ramezani, M.; Abnous, K.; Hadizadeh, F., AS1411 Aptamer-Decorated Biodegradable Polyethylene Glycol-Poly(lactic-co-glycolic acid) Nanopolymersomes for the Targeted Delivery of Gemcitabine to Non-Small Cell Lung Cancer In Vitro. *J. Pharm. Sci.,* **2016,** *105* (5), 1741-50.
6. Kang, L.; Yang, B.; Zhang, X.; Cui, L.; Meng, H.; Mei, L.; Wu, C.; Ren, S.; Tan, W., Enzymatic cleavage and mass amplification strategy for small molecule detection using aptamer-based fluorescence polarization biosensor. *Anal. Chim. Acta.,* **2015,** *879*, 91-6.
7. Chen, K.; Liu, B.; Yu, B.; Zhong, W.; Lu, Y.; Zhang, J.; Liao, J.; Liu, J.; Pu, Y.; Qiu, L.; Zhang, L.; Liu, H.; Tan, W., Advances in the development of aptamer drug conjugates for targeted drug delivery. *Wiley Interdiscip. Rev. Nanomed. Nanobiotechnol.,* **2017,** *9* (3).
8. Kalnins, A.; Thomas, M. N.; Andrassy, M.; Muller, S.; Wagner, A.; Pratschke, S.; Rentsch, M.; Klussmann, S.; Kauke, T.; Angele, M. K.; Bazhin, A. V.; Fischereder, M.; Werner, J.; Guba, M.; Andrassy, J., Spiegelmer Inhibition of MCP-1/CCR2--Potential as an Adjunct Immunosuppressive Therapy in Transplantation. *Scand. J. Immunol.,* **2015,** *82* (2), 102-9.
9. Ramaswamy, V.; Monsalve, A.; Sautina, L.; Segal, M. S.; Dobson, J.; Allen, J. B., DNA Aptamer Assembly as a Vascular Endothelial Growth Factor Receptor Agonist. *Nucleic Acid. Ther.,* **2015,** *25* (5), 227-34.
10. Koch, T. H.; Smith, D.; Tabacman, E.; Zichi, D. A., Kinetic analysis of site-specific photoaptamer-protein cross-linking. *J. Mol. Biol.,* **2004,** *336* (5), 1159-73.
11. Jeon, S. H.; Kayhan, B.; Ben-Yedidia, T.; Arnon, R., A DNA aptamer prevents influenza infection by blocking the receptor binding region of the viral hemagglutinin. *J. Biol. Chem.,* **2004,** *279* (46), 48410-9.
12. Sullenger, B. A.; Gallardo, H. F.; Ungers, G. E.; Gilboa, E., Overexpression of TAR sequences renders cells resistant to human immunodeficiency virus replication. *Cell* **1990,** *63* (3), 601-8.
13. Kim, T. H.; Lee, S. W., Aptamers for Anti-Viral Therapeutics and Diagnostics. *Int. J. Mol. Sci.,* **2021,** *22* (8).
14. Li, L.; Xu, S.; Yan, H.; Li, X.; Yazd, H. S.; Li, X.; Huang, T.; Cui, C.; Jiang, J.; Tan, W., Nucleic Acid Aptamers for Molecular Diagnostics and Therapeutics: Advances and Perspectives. *Angew. Chem. Int. Ed. Engl.,* **2021,** *60* (5), 2221-31.
15. Dobrovolsky, A. B.; Titaeva, E. V.; Khaspekova, S. G.; Spiridonova, V. A.; Kopylov, A. M.; Mazurov, A. V., Inhibition of thrombin activity with DNA-aptamers. *Bull. Exp. Biol. Med.,* **2009,** *148* (1), 33-6.
16. Huang, Y. F.; Shangguan, D.; Liu, H.; Phillips, J. A.; Zhang, X.; Chen, Y.; Tan, W., Molecular assembly of an aptamer-drug conjugate for targeted drug delivery to tumor cells. *ChemBioChem* **2009,** *10* (5), 862-8.
17. Gopinath, S. C., Anti-coagulant aptamers. *Thromb. Res.,* **2008,** *122* (6), 838-47.

18. Boyacioglu, O.; Stuart, C. H.; Kulik, G.; Gmeiner, W. H., Dimeric DNA Aptamer Complexes for High-capacity-targeted Drug Delivery Using pH-sensitive Covalent Linkages. *Mol. Ther. Nucleic Acids,* **2013,** *2*, e107.
19. Wang, R.; Zhu, G.; Mei, L.; Xie, Y.; Ma, H.; Ye, M.; Qing, F. L.; Tan, W., Automated modular synthesis of aptamer-drug conjugates for targeted drug delivery. *J. Am. Chem. Soc.,* **2014,** *136* (7), 2731-4.
20. Zhu, G.; Zheng, J.; Song, E.; Donovan, M.; Zhang, K.; Liu, C.; Tan, W., Self-assembled, aptamer-tethered DNA nanotrains for targeted transport of molecular drugs in cancer theranostics. *Proc. Natl. Acad. Sci. U S A,* **2013,** *110* (20), 7998-8003.
21. Macfarlane, R. G., An Enzyme Cascade in the Blood Clotting Mechanism, and Its Function as a Biochemical Amplifier. *Nature* **1964,** *202*, 498-9.
22. Gobel, K.; Eichler, S.; Wiendl, H.; Chavakis, T.; Kleinschnitz, C.; Meuth, S. G., The Coagulation Factors Fibrinogen, Thrombin, and Factor XII in Inflammatory Disorders-A Systematic Review. *Front. Immunol.,* **2018,** *9*, 1731.
23. Ozalp, V. C.; Schafer, T., Aptamer-based switchable nanovalves for stimuli-responsive drug delivery. *Chemistry* **2011,** *17* (36), 9893-6.
24. Negrier, C.; Shima, M.; Hoffman, M., The central role of thrombin in bleeding disorders. *Blood Rev.,* **2019,** *38*, 100582.
25. Bock, L. C.; Griffin, L. C.; Latham, J. A.; Vermaas, E. H.; Toole, J. J., Selection of single-stranded DNA molecules that bind and inhibit human thrombin. *Nature* **1992,** *355* (6360), 564-6.
26. Deng, B.; Lin, Y.; Wang, C.; Li, F.; Wang, Z.; Zhang, H.; Li, X. F.; Le, X. C., Aptamer binding assays for proteins: the thrombin example--a review. *Anal. Chim. Acta.,* **2014,** *837*, 1-15.
27. Ali, A.; Bullen, G. A.; Cross, B.; Dafforn, T. R.; Little, H. A.; Manchester, J.; Peacock, A. F. A.; Tucker, J. H. R., Light-controlled thrombin catalysis and clot formation using a photoswitchable G-quadruplex DNA aptamer. *Chem. Commun. (Camb)* **2019,** *55* (39), 5627-30.
28. Tasset, D. M.; Kubik, M. F.; Steiner, W., Oligonucleotide inhibitors of human thrombin that bind distinct epitopes. *J. Mol. Biol.,* **1997,** *272* (5), 688-98.
29. Zhao, X.; Liu, B.; Yan, J.; Yuan, Y.; An, L.; Guan, Y., Structure variations of TBA G-quadruplex induced by 2'-*O*-methyl nucleotide in K^+ and Ca^{2+} environments. *Acta. Biochim. Biophys. Sin. (Shanghai)* **2014,** *46* (10), 837-50.
30. Dodero, V. I.; Quirolo, Z. B.; Sequeira, M. A., Biomolecular studies by circular dichroism. *Front. Biosci. (Landmark Ed)* **2011,** *16*, 61-73.
31. Virgilio, A.; Petraccone, L.; Vellecco, V.; Bucci, M.; Varra, M.; Irace, C.; Santamaria, R.; Pepe, A.; Mayol, L.; Esposito, V.; Galeone, A., Site-specific replacement of the thymine methyl group by fluorine in thrombin binding aptamer significantly improves structural stability and anticoagulant activity. *Nucleic Acids Res.,* **2015,** *43* (22), 10602-11.
32. Del Villar-Guerra, R.; Trent, J. O.; Chaires, J. B., G-Quadruplex Secondary Structure Obtained from Circular Dichroism Spectroscopy. *Angew. Chem. Int. Ed. Engl.,* **2018,** *57* (24), 7171-5.
33. Zhao, D.; Dong, X.; Jiang, N.; Zhang, D.; Liu, C., Selective recognition of parallel and anti-parallel thrombin-binding aptamer G-quadruplexes by different fluorescent dyes. *Nucleic Acids Res.,* **2014,** *42* (18), 11612-21.

Chapter 6 Covid-19: Diagnosis of variants

6.1 Introduction

A highly transmissible novel coronavirus has disrupted the world from late 2019 to the current day, causing a pandemic of respiratory disease.[1] Severe acute respiratory syndrome coronavirus 2 (SARS-CoV-2) caused a global outbreak of viral pneumonia, surpassing similar coronaviruses of zoonotic origin such as SARS-CoV and MERS-CoV.[2] To date (August 2021) 4.36 million deaths have been attributed to the Covid-19 pandemic, as modelled by the Center for Systems Science and Engineering,[3] leading to worldwide devastation and disruption.

6.1.1. Origin and spread

Wuhan in the Hubei province in China began to report patients presenting viral pneumonia with an unknown cause in December 2019, with most cases of the first 30 hospitalised patients linked to the Huanan seafood wholesale market.[4] By the end of December 2019, the World Health Organisation (WHO) had been informed of a pneumonia outbreak of unknown cause.

Isolation of the virus from bronchoalveolar lavage fluid samples and metagenomic RNA sampling led to the identification of the disease as a new betacoronavirus.[2, 5] Spread of the disease occurred quickly, with familial clusters of cases reported and infection occurring in health-care facilities, indicating a strong case for human-to-human transmission.[6] The lunar New Year also accelerated viral spread, as many families travelled to other provinces of China for the celebrations. The Covid-19 outbreak reached an epidemic peak in China in February 2020, with an average infection rate of >3,000 new cases per day.[7] Since this point, the infection rate has risen quickly with the infection rate in the UK reaching a high of >80,000 per day and a current rate of ~34,000 per day (October 2021).[8]

By this stage, the global spread of Covid-19 was quickening, becoming characterised as a pandemic on 11th March 2020.[2] This spread continued, with new variants of the virus occurring throughout 2020 and 2021 leading to further disruption globally.

6.1.2 Genomics of SARS-CoV 2

The betacoronavirus SARS-CoV-2 has a shared genome organisation with other betacoronaviruses and shows 79% genome sequence identity with SARS-CoV.[7] In a betacoronavirus the six functional open reading frames (ORFs); replicase (R), spike (S), envelope (E), membrane (M) and nucleocapsid (N), are arranged in a 5' – 3' direction.[2] Most of the proteins encoded by SARS-CoV-2 are of similar length to the corresponding protein in SARS-CoV, though there is significant diversity in the spike (S) gene.[9]

As the spike protein shows the most unique behaviour, focus has concentrated on this when investigating the origins of this disease. The S protein is made up of 1273 amino acids, longer than that of SARS-CoV and bat SARS-CoV and distinct from the S proteins of most members in the subgenus Sarbecovirus.[10] An interesting feature of SARS-CoV-2 is the insertion of four amino acid residues at the junction of subunits S1 and S2 of the S protein, which generates a polybasic cleavage site effectively enabling cleavage by furin.[2, 11] Structural studies of this region indicated the furin-cleavage site could reduce stability of the S protein of SARS-CoV-2, enabling the conformational changes needed for binding of the receptor-binding domain to the receptor.[12] Whilst not yet confirmed, this additional cleavage-site might be associated with the higher transmissibility of the SARS-CoV-2 compared to SARS-CoV.

Human angiotensin-converting enzyme 2 (ACE2) acts as the receptor for SARS-CoV-2, though the virus also recognises the ACE2 from other mammals including pig, pangolin and dog.[2, 13] This receptor-binding domain was identified as a 211 amino acid region at the S1 C-

terminal domain of SARS-CoV-2 with a key role in virus entry and the primary target of antibodies.[2]

6.1.3 Clinical pathogenesis of SARS-CoV-2

The SARS-CoV-2 infection in humans manifests as a range from mild symptoms to severe respiratory failure (Figure 93). Having bound to epithelial cells in the respiratory tract of a human, the virus replicates and migrates to alveolar epithelial cells in the lungs. The replication within the lungs can be enough to trigger a strong immune response such as cytokine storm syndrome, the main cause of death in patients with Covid-19.[14]

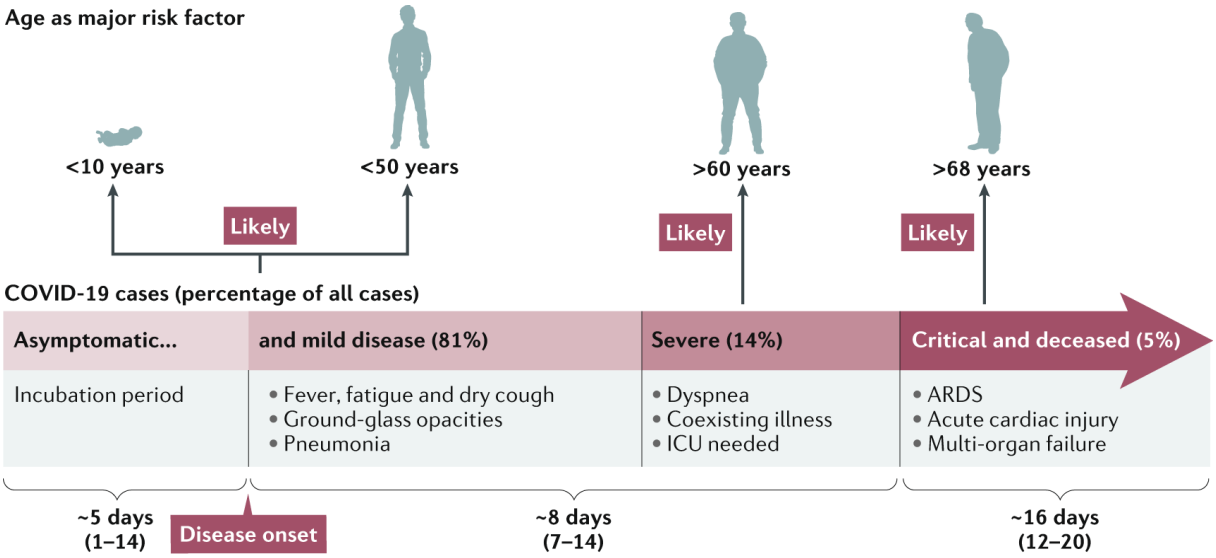


Figure 93 Clinical features of Covid-19 showing age as a major risk factor for disease. Image taken from Hu et al. 2021

Histopathological analyses of Covid-19 changes in the lungs showed bilateral diffused alveolar damage, hyaline membrane formation and fibrin deposits in severe cases.[15] Age was found to be a factor in the severity of disease phenotype, with older men more likely to develop severe respiratory illness whereas young adults and children presented with mild disease or no symptoms.[15]

6.1.4 Genetic variants of SARS-CoV-2

The virus SARS-CoV-2 has consistently mutated throughout the pandemic, meaning healthcare communities have had to adjust to cope with new transmission rates. Whilst coronaviruses mutate at a slower rate than most RNA viruses, due to the encoding of an enzyme capable of correcting some replication errors,[15] each mutation relies upon natural selection for survival, meaning those viruses with a competitive advantage for replication, transmission or immunity evasion will increase in frequency. Certain mutations have led to new variants of SARS-CoV-2 spreading throughout the globe (Table 16).[16]

Table 16 Covid-19 variants with common base mutations

WHO LABEL	SCIENTIFIC NAME	K417N (G→U)	K417N (A→C)	L452R (U→G)	E484K (G→A)	E484Q (G→C)	N501Y (A→U)
ALPHA	B.1.1.7						Yes
BETA	B.1.351	Yes			Yes		Yes
GAMMA	P.1		Yes		Yes		Yes
DELTA	B.1617.2			Yes		Yes	

The SARS-CoV-2 variant with lineage B.1.1.7 is a phylogenetic cluster originating in England (the Alpha variant), with an accumulated 17 lineage-defining mutations and, by December 2020 had appeared to outcompete other variants by spreading faster.[17] Many of the mutations in this lineage are in the spike glycoprotein, including N501Y (asparagine (N) to tyrosine (Y) mutation at the 501st codon), in the receptor-binding domain. 501Y variants are thought to have a higher affinity for human ACE2 and is also seen in a different variant originating from South Africa, the Beta variant.[17] Indeed, the amount of N501Y mutant

associated cases rose from 0.1 – 49.7% within 2 months in Autumn 2020 in the UK.[17] By using HADDOCK (a versatile flexible docking approach for the modelling of biomolecular complexes),[18] the protein-protein docking of ACE2 with various mutations of the viral RBD could be analysed. The wild-type docking score was reported as –122.6 kcal mol^{-1} and the N501Y mutant was predicted a very similar –122.4 kcal mol^{-1}.[17]

The E484K mutation (glutamic acid to lysine) in the viral RBD has also been identified as a common modification in successful Covid-19 variants, including the Beta variant. This substitution enables the fast spread and increased infectivity rates by building salt bridges and hydrogen bonding interactions.[19] Such a mutation might also reduce the efficacy of certain vaccines.[17, 20, 21] The E484K complex possessed a higher docking score to that of the wild-type, –128.8 kcal mol^{-1} respective to the wild-type –122.6 kcal mol^{-1} (Figure 94). [22]

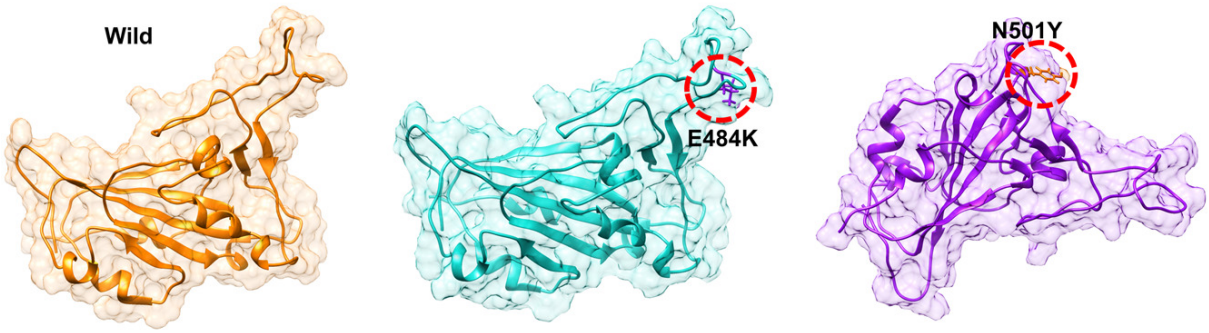


Figure 94 Structural representation of the spike protein, identifying the wild type, E484K and N501Y mutations in the receptor-binding domain. Image taken from Khan et al. 2021

6.1.5 Diagnosis of SARS-CoV-2 and variant detection

Controlling the spread of Covid-19 is imperative for worldwide healthcare and government agencies to prevent severe disease. Molecular detection of SARS-CoV-2 RNA is the gold

standard for diagnosis, with kits for the detection of ORF1b, N, E and S genes commercially available, as discussed in more detail below.

In most cases, amplification of viral nucleic acid from throat and nasopharyngeal swabs is necessary for molecular detection of the SARS-CoV-2. However, detection and confirmation of individual variants of Covid-19 requires full genetic sequencing, a far slower process. Globally, the capacity for genetic sequencing is low, as the cost is high. Lower economically developed countries with high infection rates have struggled to sequence the full genome with only 2.9 million of the >200 million cases having been sequenced (the majority of genetic sequencing occurring in the US and Europe).[23]

Controlling the spread of Covid-19 is imperative for worldwide healthcare and government agencies to prevent severe disease. Molecular detection of the SARS-CoV-2 nucleic acid is the current gold standard for diagnosis, with the detection of various genes commercially available as kits.[22-24] The use of polymerase chain reaction (PCR) to amplify the RNA and convert the material to DNA is used as the most sensitive widely used diagnostic aid.[25, 26] As new diagnostic methods are developed,[27] the cheap and easily used LF tests[28] have gained popularity due to their speed, although these tend to be less sensitive than amplification based nucleic acid tests. Alternative fast and sensitive new methods using alternative amplification techniques (e.g., EXPAR) show great promise.[29]

Unambiguous differentiation between the different SARS-CoV-2 variants typically requires full genetic sequencing but is a vital aspect of controlling the pandemic due to monitoring of viral evolution and tracking changes to the pandemic. Variant detection using assays has been investigated recently, for example PCR has been found capable of detecting subsets of variants by investigating S-gene dropout[30] and some tests have also been developed using CRISPR to deliver point of care diagnoses of Covid-19 variants.[31]

6.2 Aims

Detecting the variants of Covid-19 could provide governments with a way of controlling the spread of the virus worldwide more easily. Similarly, healthcare officials could use an easy determination of SARS-CoV-2 variants to help make decisions when deciding upon the most efficacious treatments for disease.

As such, the aim of this project was to design an anthracene-modified probe strand of DNA that was capable of selectively identifying certain single point changes present within Covid-19 variants. As the N501Y and E484K mutations have been identified as common areas of variation in the RNA virus, these were the key areas of focus for the design of probe DNA strands (Figure 95).

First, the project aimed to identify the single base mutation occurring at each point, N501Y and E484K, then to design anthracene-modified DNA strands capable of detecting the change from wild-type to mutant strands.

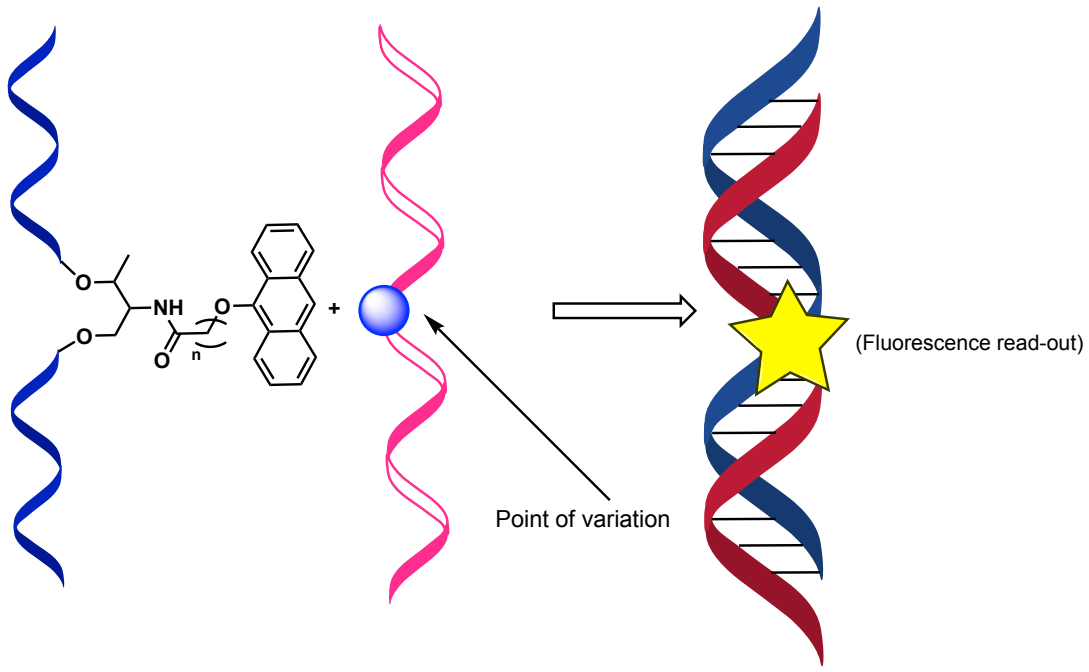


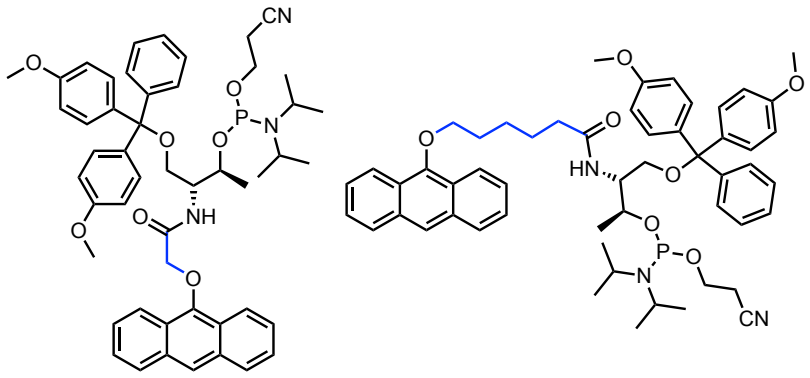
Figure 95 Diagram representation of anthracene-modified DNA probe duplexing with either wild type or mutated target DNA

From the synthesis of these modified DNA strands, the project then looked to test the ability of the oligomers to detect mutations in target strands and longer sequences. On success at this stage, detection would be done on PCR amplified products.

6.3 Design and synthesis of anthracene-modified DNA strands

Anthracene DNA chemistry has been studied intensively by the Tucker group over the past 20 years.[32] Previous work has included investigating the detection of single point variants in target strands through changes in fluorescence emission intensity of anthracene-modified DNA probes upon duplex formation.[32] In this work, Duprey *et al*. investigated the fluorescence emission changes of base adjacent and base opposite sensing in short segments of DNA.

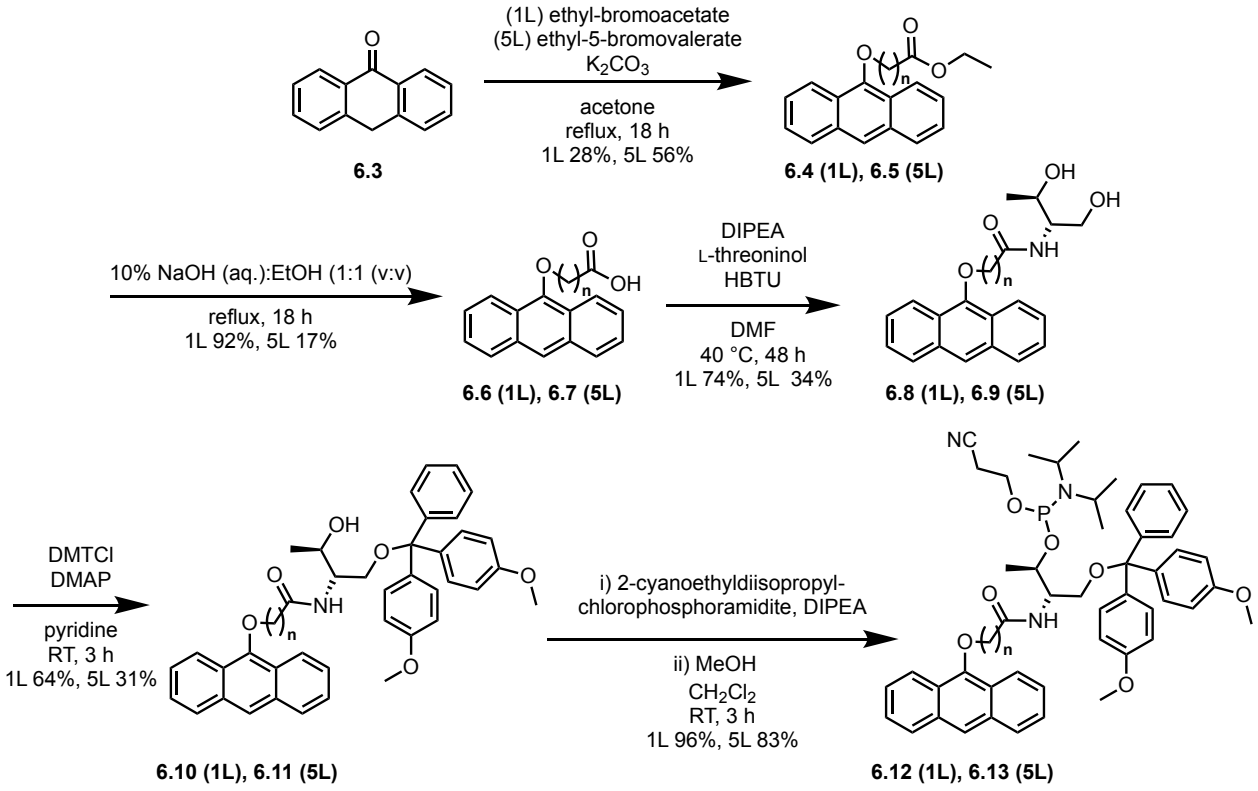
When investigating the modified DNA strands containing anthracene tags with linkers containing either L or D isomers of threoninol, large changes in fluorescence emission upon recognition of target strands with single point mutations were observed. The types of base variation were best recognised by anthracene modifications of varying flexibility and location within a probe strand.[33] Following the results described in this investigation, the L isomer of the anthracene phosphoramidites were decided upon, with two different chain lengths enabling a comparative study (Figure 96).



6.1 **6.2**

*Figure 96 1L (**6.1**) and 5L (**6.2**) anthracene tags designed for investigation into E484 and N501 base variant detection*

As described in Chapter 3, the phosphoramidites were prepared from commercially available anthrone (Scheme 55).



*Scheme 55 Synthesis of 1L and 5L anthracene phosphoramidites **6.12** and **6.13** from commercially available anthrone where n = 1 or 5*

Stepwise nucleophilic substitution, saponification and amide coupling with L-threoninol gave the desired isomer of the anthracene tags. In each synthesis there was a range in yield when synthesising tags of different carbon chain length – indicating different reactivities throughout the process. Subsequent DMT protection of the primary alcohol and phosphitylation of the remaining secondary alcohol gave the desired phosphoramidites **6.12** and **6.13**.

Having synthesised the anthracene phosphoramidites **6.12** and **6.13**, the tags were incorporated into specific DNA strands using the same procedure set out in 3.4.1 (Scheme 37). The sequence of the probe strands was specific to the DNA of SARS-CoV-2 and was adapted to work best with different anthracene tags. To incorporate previous findings from Duprey *et al*.[34] the anthracene 1L tag **6.12** was chosen for a 'base adjacent' probe system capable of detecting 'G' to 'A' E484K mutations whilst the more flexible 5L tag **6.13** was designed for a 'base opposite' probe system, capable of detecting 'A' nucleotide to 'T' N501Y mutations (Table 17).

Table 17 Strand design and sequence for modified DNA strands and their targets

STRAND	SEQUENCE (5'-3')
E484-T-WT-N501-T-WT	5'-TGT AAT GGT GTT GAA GGT TTT AAT TGT TAC TTT CCT TTA CAA TCA TAT GGT TTC CAA CCC ACT AAT GGT GTT GGT-3'
E484K-T-MUT-N501Y-T-MUT	5'-TGT AAT GGT GTT AAA GGT TTT AAT TGT TAC TTT CCT TTA CAA TCA TAT GGT TTC CAA CCC ACT TAT GGT GTT GGT-3'
E484-T-WT-N501Y-T-MUT	5'-TGT AAT GGT GTT GAA GGT TTT AAT TGT TAC TTT CCT TTA CAA TCA TAT GGT TTC

	CAA CCC ACT TAT GGT GTT GGT-3’
E484K-T-MUT-N501-T-WT	5’-TGT AAT GGT GTT AAA GGT TTT AAT TGT TAC TTT CCT TTA CAA TCA TAT GGT TTC CAA CCC ACT AAT GGT GTT GGT-3’
E484-T-WT	5'-AT GGT GTT GAA GGT TT-3'
E484K-T-MUT	5'-AT GGT GTT AAA GGT TT-3'
N501-T-WT	5'-A CCC ACT AAT GGT GT-3'
N501Y-T- MUT	5'-A CCC ACT TAT GGT GT-3'
E484K PROBE (BASE ADJ.)	5'-AA ACC TTC **X**AC ACC AT-3' (X = 1L, from **6.12**)
N501Y PROBE	5'-AC ACC AT**X** AGT GGG T-3' (X = 5L, from **6.13**)

The unmodified target strands were purchased from Merck and were characterised by analytical HPLC and MS, with further purification by semi-prep HPLC if the initial purity of the strand was <95% (Appendix 6.1). Having synthesised the probe strands, they were purified by HPLC and characterised by MS as described in Chapter 3 (see Appendix 6.2 for data).

6.4 Investigations into duplexes of probe and target strands

6.4.1 Fluorescence of N501 probe strand

The ε at 260 nm of anthracene was calculated to be 51444 M^{-1} cm^{-1}, determined by taking a known concentration of the anthracene monomer in 95:5 H_2O: MeCN and measuring the absorption at 260 nm.[33] This value was added to the epsilon calculated for the unmodified DNA strand, using the OligoAnalyzer tool from Integrated DNA Technologies (IDT).[35] Concentrations of the anthracene-modified probe strands were calculated using the Beer-Lambert law (Equation 1) and the absorbance at 260 nm, as determined by use of a NanoDrop spectrophotometer. As mentioned above, the anthracene-modified strand designed to detect base changes in the N501 position of the Covid-19 sequence made use of the 5L anthracene phosphoramidite **6.13** in a base-opposite sensing strand. Designed to sense an adenine to thymine mutation, the fluorescence emission of both the probe alone and in duplex with each target strand was recorded.

Equation 1 Beer Lambert law. A - absorbance, ε - molar absorptivity, ℓ - lenght of light path, C - concentration

$$A = \varepsilon \ell C$$

Following optimisation from previous work,[36] a ratio of 1:3 probe to target strand was used for the initial investigations using a probe concentration of 0.5 μM (Figure 97) in duplex buffer at pH 7.4 (buffer conditions given in Table 9).

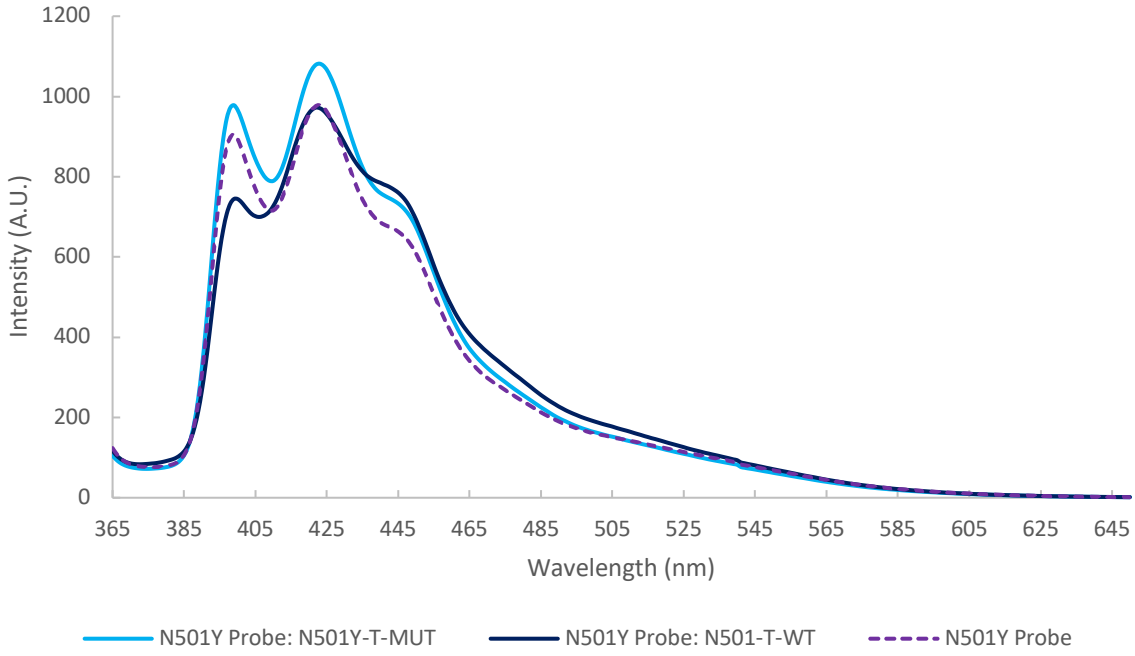


Figure 97 Fluorescence emission spectra (λexc = 350 nm) of N501Y probe: N501 WT and Mut strands (0.5:1.5 μM in duplex buffer)

The emission spectrum of the **N501Y probe** strand alone, when excited at 350 nm, was seen to be very similar to both that of the duplexes **N501Y probe: N501-T-WT** and **N501Y probe: N501Y-T-MUT** with a slight difference in intensity in the first vibrionic band. 'Base opposite' sensing can be affected by competition between the anthracene and the opposite base, typically the purines are thought to shift out of the duplex upon interaction with the anthracene, meaning higher emission of the fluorophore in the hydrophobic groove of the duplex.[37] The fluorescence emission was anticipated to be higher for the **N501Y probe: N501-T-WT** (a purine opposite) than that of the **N501Y probe: N501Y-T-MUT** (a pyrimidine opposite).[37] The fluorescence emission when forming a duplex of the **N501Y probe** with longer target strands were also measured (Figure 98).

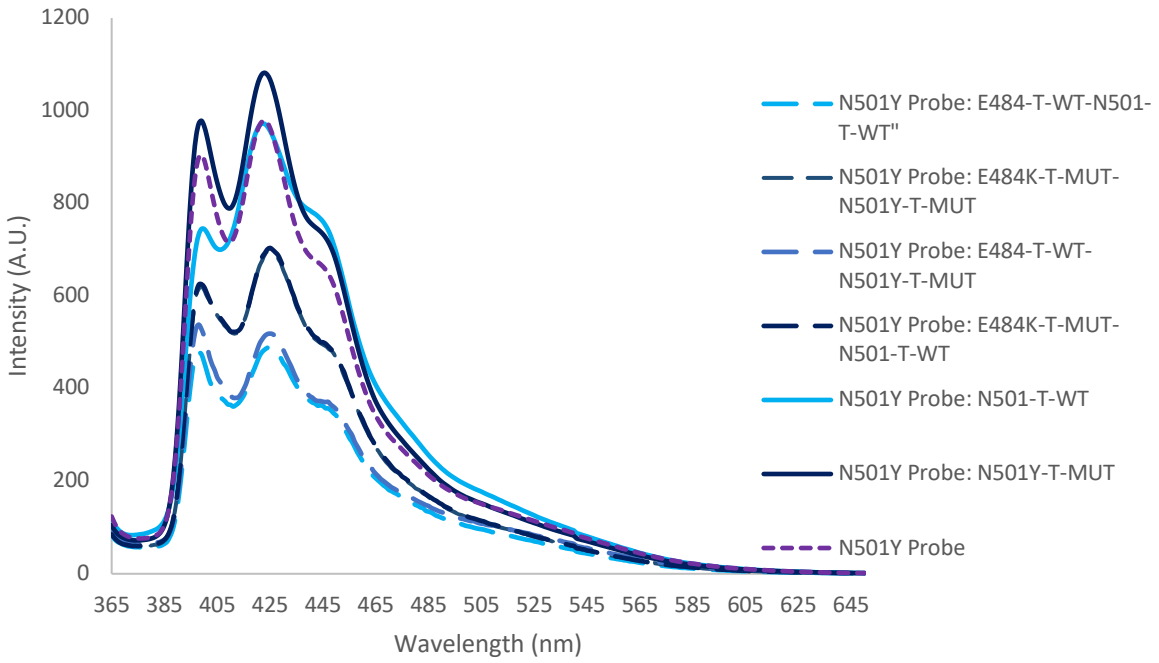


Figure 98 Analysis of fluorescence emission (λexc = 350 nm) of N501Y probe strand against various target strands (0.5:1.5 μM) duplex buffer

The emission of the anthracene probe complexed to the full target strands was expected to mirror the pattern seen in the **N501-T-WT** and **N501Y-T-MUT** strand duplexes, with little difference between each of the duplex emissions. However, from **Error! Reference source not found.**, there did not appear to be any significant pattern to the emission spectra. In fact, the duplex emission of **N501Y probe: E484-T-WT-N501-T-WT** appeared the same as that of **N501Y probe: E484-T-WT-N501Y-T-MUT** despite the strands having different variants at the target site.

Further investigation into the possible secondary structures of the **N501Y probe** and target strands showed the possibility of hairpins forming, which was a plausible explanation for the lack of consistency in the binding characteristics. Using Integrated DNA Technologies' OligoAnalyzer tool, two possible hairpin structures in the target strands were identified, with ΔG values for the folding interaction of –1.55 and –1.29 kcal mol^{-1}, and similar structures in

the probe strands showing ΔG values for the folding interaction of –1.88 and –1.81 kcal mol^{-1} (Appendix 6.3).[35] To determine if the presence of secondary structures could be negated by the use of large excesses of target strand, titration experiments were carried out in an attempt to determine the plateau point of fluorescence emission (Figure 99). In these experiments, an increasing amount of target N501 strand was added to a set concentration of the N501Y probe, to give ratios of 1:0 – 1:5.

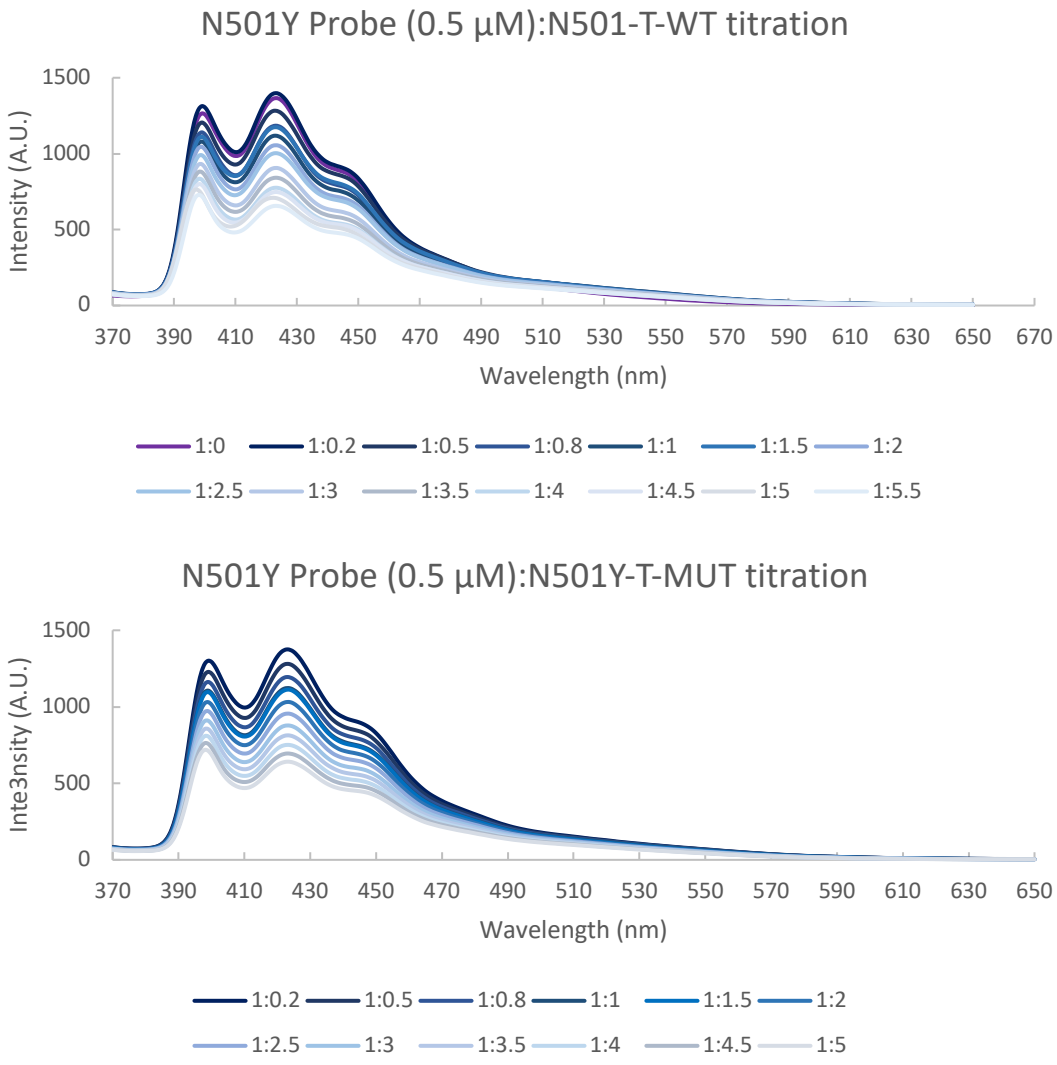


*Figure 99 Fluorescence emission titrations (λ_{exc} = 350 nm) of **N501Y probe**: target strands a) **N501-T-WT** b) **N501Y-T-MUT** in duplex buffer*

Titrations of the **N501Y probe** strand against each target strand showed very similar patterns, with no obvious sign of a plateau occurring as the duplex was formed, most likely due to competition from intramolecular interactions. This inability to form the duplex character even in the presence of 5 equivalents of target strand indicated that the N501Y mutation sequence chosen was not a suitable candidate for easy diagnosis of Covid-19 variants. The fluorescence emission profiles were also quite small and similar for each variant, again implying that diagnosis would not be accurate (Figure 100).

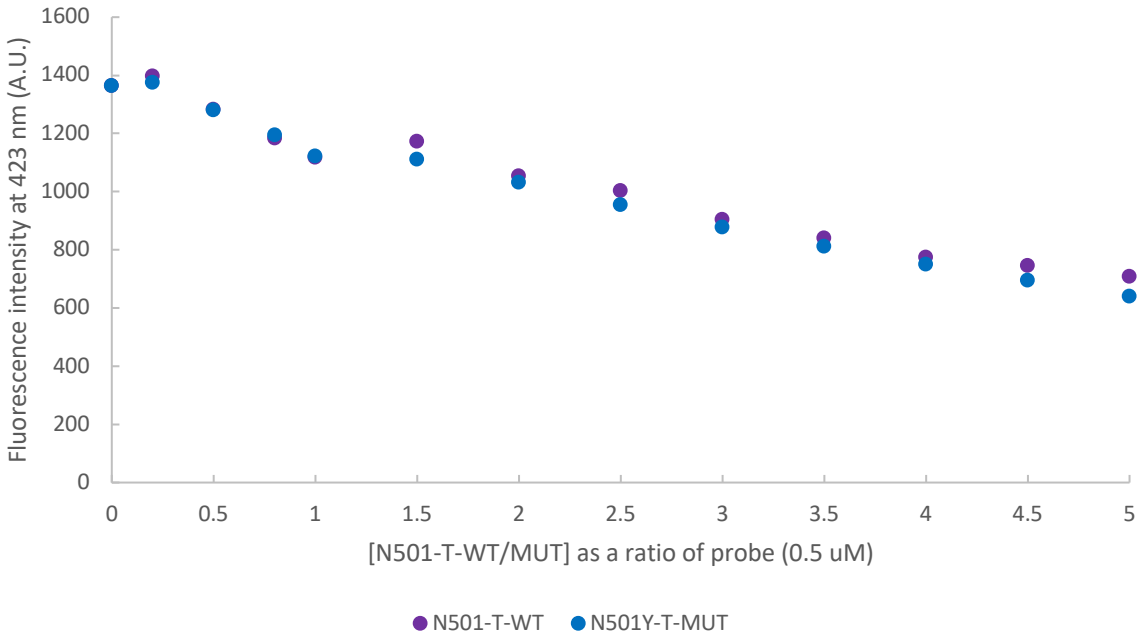


Figure 100 Emission intensity at 423 nm (λexc = 350 nm) from fluorescence titration studies of N501Y probe against target strands in duplex buffer

As such, work into designing a probe for the N501Y mutation was stopped at this point with efforts turned towards diagnosing the variation at the E484 site of the viral genome, as outlined below.

6.4.2 Fluorescence of E484 probe strand

Detecting the base variation at the 484th codon of the spike protein in the SARS-CoV-2 genome was designed to take place using the anthracene phosphoramidite **6.12** (n=1), having based the design on previous research by J-L. Duprey[34, 37] who determined the less flexible anthracene in the L conformation was superior for 'base-adjacent' G/A sensing.

Utilising the same parameters as in the N501 sensing investigations, the fluorescence emission spectra of the **E484K probe**, and duplexes of said probe with each target were recorded (Figure 101).

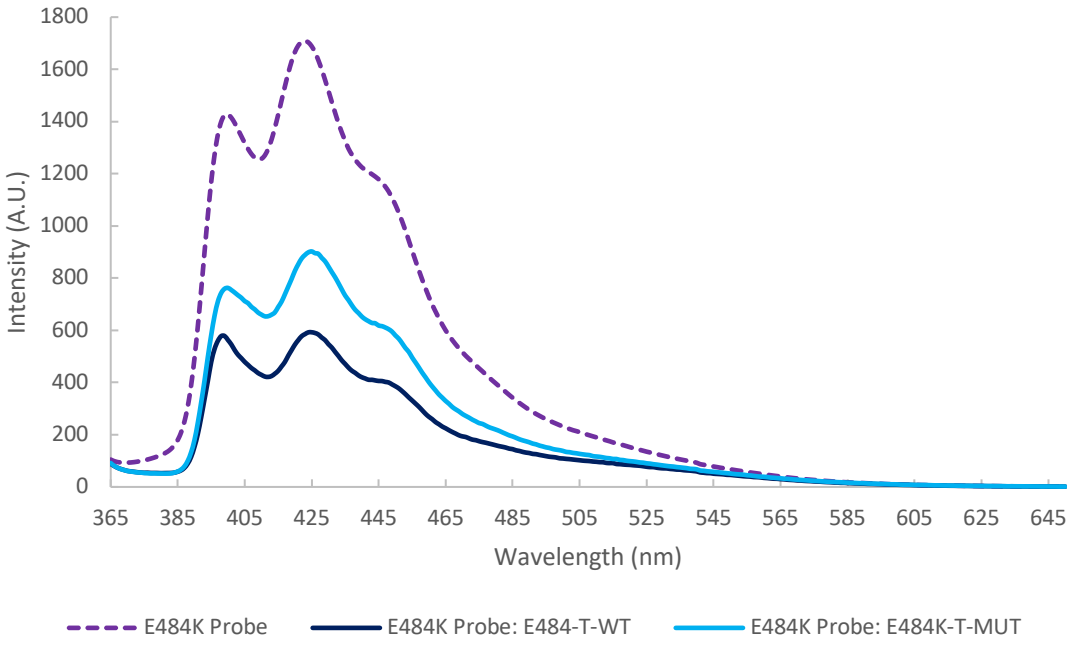


Figure 101 Fluorescence emission spectra of E484K probe and duplexes with each target strand (λexc = 350 nm, 0.5 μM:1.5 μM) in duplex buffer

From these emission spectra, the highly emissive single **E484K probe** strand showed a slightly different from anticipated pattern, with the **E484K-T-MUT** duplex showing less emission overall than the probe strand alone, but still more than the **E484-T-WT** duplex. The WT/MUT difference in fluorescence was expected as the **E484K probe: E484-T-WT** duplex was expected to be less emissive than the **E484K probe: E484K-T-MUT** duplex, as demonstrated by Duprey *et al*.[38]

The fluorescence emission of **E484K probe** duplexes with longer target strands were also measured and anticipated to show the same patterns. The duplexes of **E484K probe: E484-T-WT-N501-T-WT** and **E484-T-WT-N501Y-T-MUT** showed the G variant whilst **E484K probe: E484K-T-MUT-N501Y-T-MUT** and **E484K-T-MUT-N501-T-WT** showed the A base variant (Figure 102).

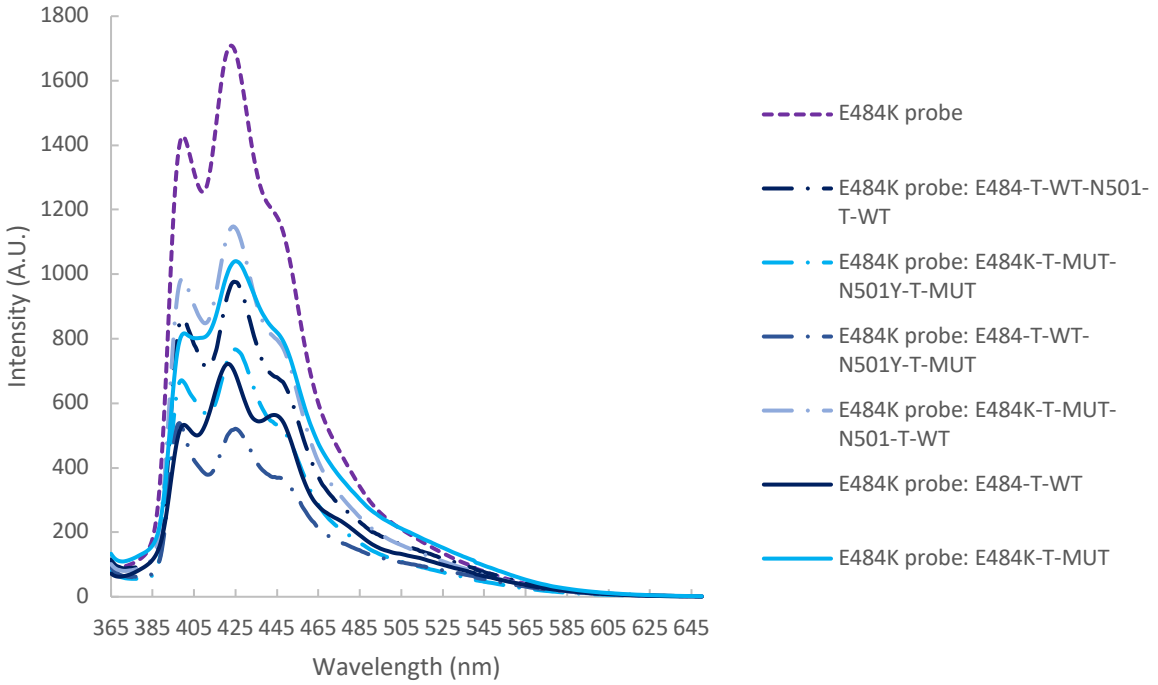


Figure 102 Fluorescence emission spectra of E484K probe strand: each target strand (λexc = 350 nm, 0.5 μM) in duplex buffer

The emission spectra above that the single probe is the most emissive. The duplexes of **E484K probe**: mutant targets strands (**E484K-T-MUT**, **E484K-T-MUT-N501Y-T-MUT**, **E484K-T-MUT-N501-T-WT**) showed a similar intensity of fluorescence emission, all more emissive than duplexes with the wild-type G variant in the base-adjacent position of the target strands. This pattern followed the expectations for the investigation and indicated that this mutation point might be a suitable candidate for diagnosis of Covid-19 variants – with less competition from intramolecular folding processes.

To determine the ratio of probe: target at which the expected duplex could form, titration fluorescence experiments were carried out in the same manner as had been performed for the N501Y mutation (Figure 103).

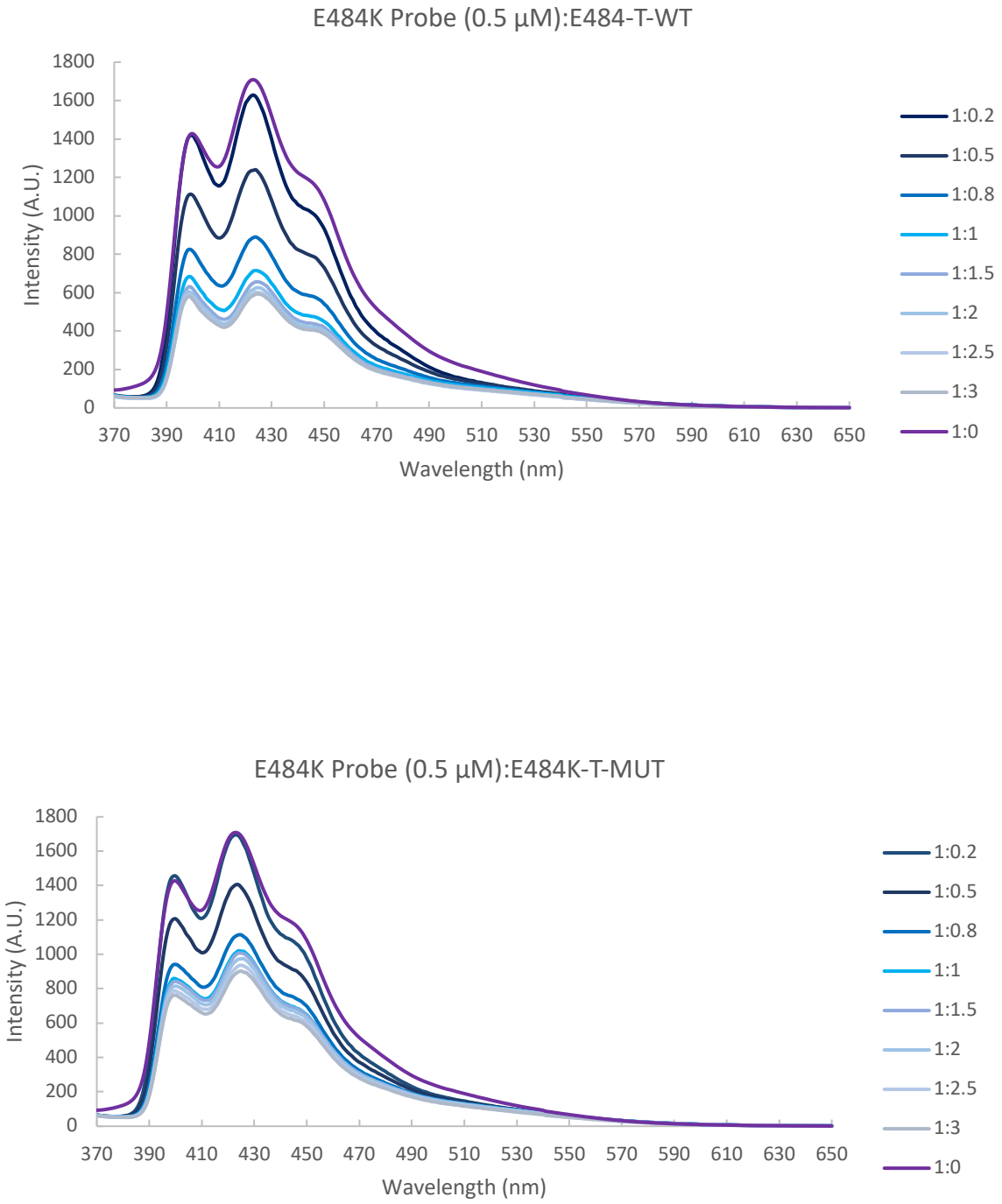


Figure 103 Fluorescence emission titrations (λ_{exc} = 350 nm) of E484K probe (0.5 µM): E484K target strands in duplex buffer

The titration experiments showed a clear plateau of emission decrease as the ratio of probe: target reached 1:1 and moved to an excess of target strand. In both the wild-type and the mutant target strands, the plateau was reached at approximately the same ratio, with both indicating the expected 1:1 complex (i.e., duplex) formation. The intensity of the emission at the point of plateau was also significantly different in the two duplexes formed. The **E484K probe: E484-T-WT** duplex had an emission intensity plateau at approximately 600 A.U. whereas the **E484K probe: E484K-T-MUT** plateau had an intensity of approximately 900. To ensure this difference was clear, the emission intensities at the emission maxima (λ_{max} = 423 nm) were plotted to investigate the significance of the shift in intensity (Figure 104).

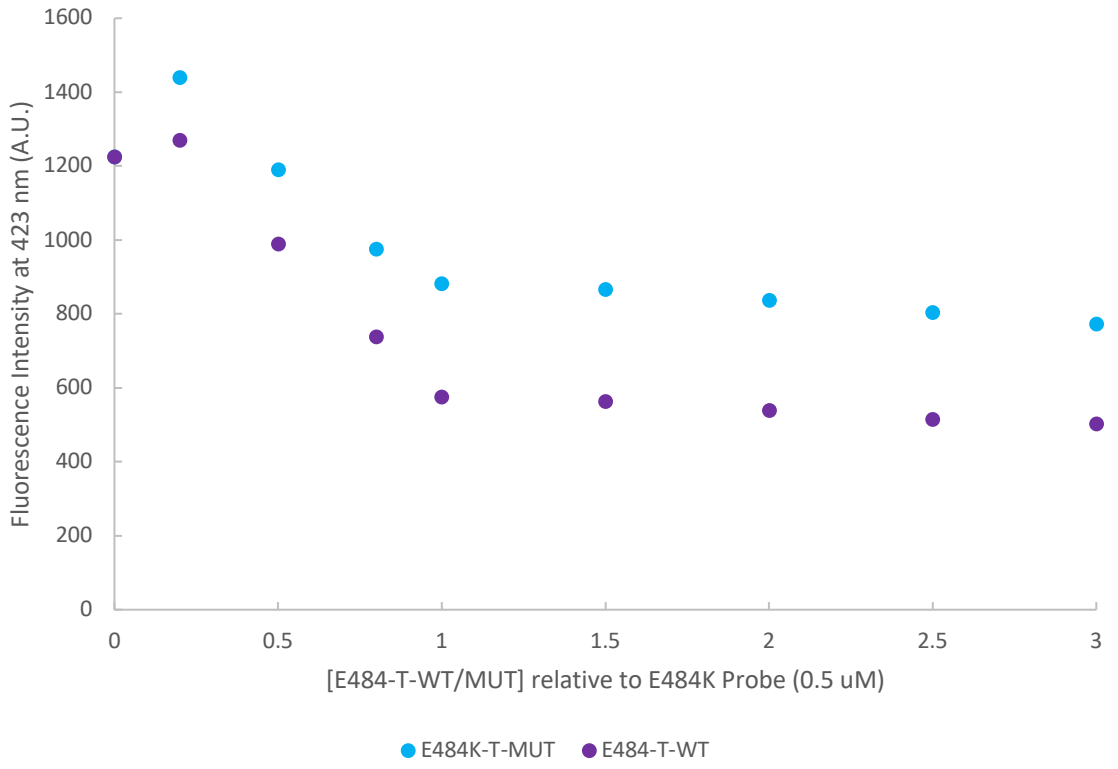


Figure 104 Plot of the emission intensity at the lamda max of fluorescence titrations of E484K probe: target strands (λexc = 350 nm, 0.5 μM) in duplex buffer

Plotting the data in this format clearly showed the point of plateau of emission decrease upon binding at 1:1, indicating that ratios of 1:2- 1:3 would be suitable for diagnostic testing. The difference in fluorescence emission was also significant, showing potential for clear diagnostic sensing. One concern over the use of only fluorescence as a diagnostic sensor is the concentration dependent nature of the emission results. Thoughts then turned to orthogonal fluorescence techniques such as anisotropy to provide further evidence for accurate base sensing.

6.4.3 Fluorescence anisotropy for base variant sensing

Fluorescence anisotropy utilises excitation with polarised light to determine the level of polarised emission from fluorescent samples. The extent of polarisation of the emission is the anisotropy (*r*), and samples with non-zero anisotropies are thought to display polarised emission.[34] The transition moments for absorption and emission that lie along specific directions of the fluorophore give the anisotropy, a homogenous solution would have a random orientation but on polarisation the transition moment with an orientation along the electric vector of the light is preferentially excited.[34]

Anisotropy measurements investigate the average angular displacement of the fluorophore between the absorption and emission of a photon. This displacement is determined by the rate and level of rotational diffusing during the lifetime of the excited state.[39] For biological molecules, such as the DNA duplexes created within this project, the anisotropy is altered dependent on the rotational diffusion and internal flexibility of the complex. As such, the slight disruption to a double helix formed by a mismatch in the duplex would result in a different anisotropy to that of the wild-type DNA.

The fluorescence anisotropy is a dimensionless quantity, meaning the results could be concentration independent and more of a ratio-metric measurement.[40] As such, a titration

experiment was carried out on the **E484K probe** strand and both the **E484-T-WT** and **E484K-T-MUT** strands (Figure 105).

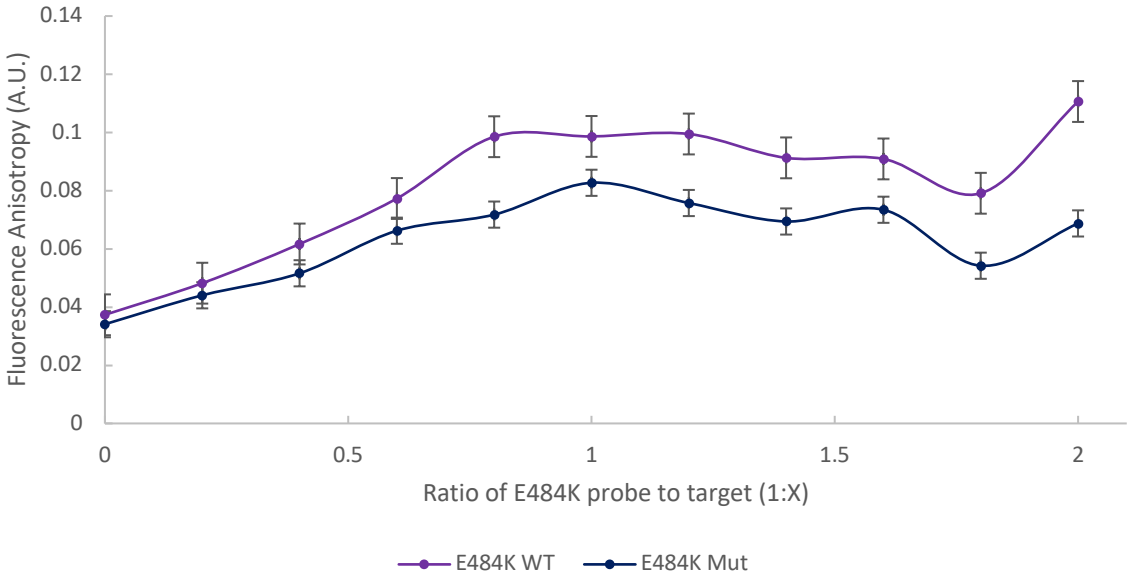


Figure 105 Fluorescence Anisotropy of E484K probe against target strands E484 WT and E484K Mut (λ_{exc} = 350 nm, emission at 425 nm, 0.5 μM: X in duplex buffer)

The fluorescence anisotropy showed a difference between the duplexes formed of each of the target strands, and a plateau starting to form at approximately a 1:1 ratio of probe: target strand. The difference in anisotropy between the **E484-T-WT** and **E484K-T-MUT** target strands showed a higher anisotropy value upon the formation of a duplex with the target **E484-T-WT**. This was thought to be due to the internal flexibility of the biomolecule. As anisotropy values are reduced upon increased flexibility, the more disrupted double helix of the E484K probe: E484K Mut was anticipated to show a lower value. Contrary to what was seen with the fluorescence system, the anisotropy increased slightly with an excess of target, which merits further investigation.

The fluorescence anisotropy experiments carried out provide further evidence of binding events occurring.

6.4.4 Melting temperatures of E484 system duplexes

The relative binding strengths of the E484K probe for each target were analysed by undertaking variable temperature fluorescence experiments to determine the melting temperatures of each duplex (T_Ms) (Table 18).

A higher T_M would indicate a stronger binding interaction between the probe and target strand (Figure 106). Each study was performed in triplicate, with the average values presented in Table 18.

Table 18 T_Ms of E484K probe strand with each target strand option (1 μM, duplex buffer). Expected confidence limit of 1 ˚C

	Average T_M (˚C)
E484K PROBE: E484-T-WT	62.5
E484K PROBE: E484K-T-MUT	57
E484K PROBE: WITH E484-T-WT-N501-T-WT	65.5
E484K PROBE: WITH E484-T-WT-N501Y-T-MUT	68.7
E484K PROBE: WITH E484K-T-MUT-N501Y-T-MUT	67 (minor peak 45)
E484K PROBE: WITH E484K-T-MUT-N501-T-WT	68 (minor peak 48)

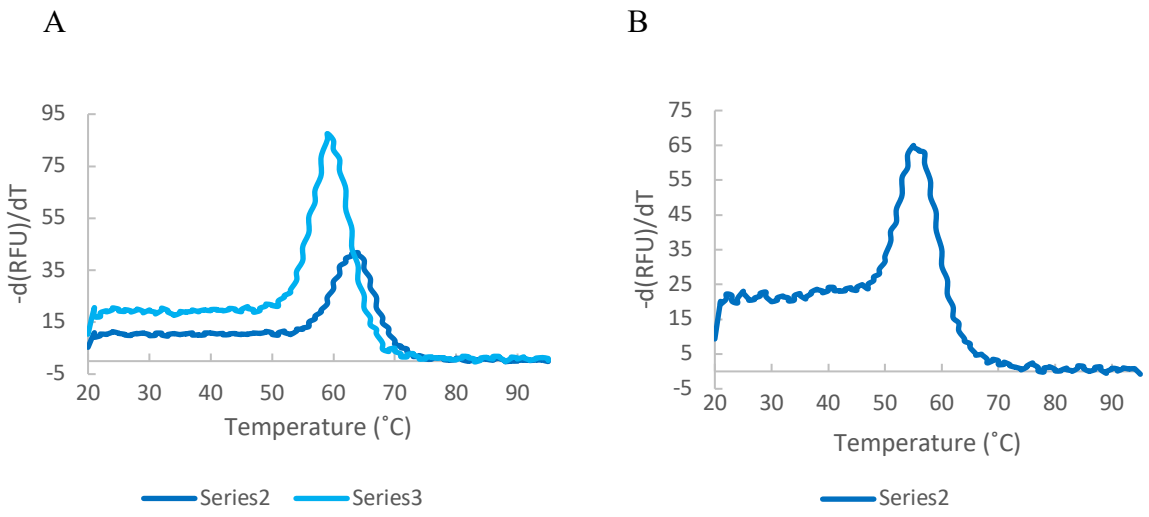


Figure 106 Graphical representation of the thermal profile of E484K probe: target strand (a)E484-T-WT, (b) E484K-T-MUT (10 μM, duplex buffer)

When analysing the difference in T_M of the **E484K probe**: E484K targets, the difference in melting temperature was seen to be minimal. The T_M of **E484K probe: E484-T-WT** was recorded at 62.5 ˚C whilst the **E484K probe: E484K-T-Mut** was destabilised at 57 ˚C.

The **E484K probe** was also duplexed with the longer 75-mer target strands (Appendix 6.4) to determine any change in the temperature required to disrupt the double helix. There was very little difference seen in the T_M of each duplex with longer strands, though the appearance of a secondary binding event was attributed to intramolecular binding interactions.

6.5 Conclusions and future work

The exploration into detecting Covid-19 variants has proved to be successful in its initial investigation, showing the capability of anthracene-modified DNA probes to detect single base point mutations in segments of spike protein sequence. Whilst the flexible nature of the N501Y probe and target strands meant that too many secondary structure possibilities could occur for effective diagnosis, the work investigating the E484K probe showed potential for variant detection. This will be continued further by testing the fluorescence anisotropy against the longer 75-mer target strands, and further to looking at larger segments of the viral sequence. As the work has focused on the DNA sequence, it relies upon amplification of the original RNA to c-DNA by use of PCR, so other directions of future work could look at the minimum concentration required for sensing, and the possibilities of detecting RNA sequences.

Future work in detecting Covid-19 variants will continue, first looking into single base mutations present within the Delta variant, a new and fast spreading variation of SARS-CoV-2 that is quickly becoming the primary cause of disease. Another anthracene phosphoramidite (D isomer, n=4) has been prepared and will be incorporated into a DNA probe looking to target the L452R mutation seen in the Delta variant. The leucine at position 452 in the receptor-binding motif mutating to an arginine is predicted to result in a stronger binding of the virus to the receptor, out competing neutralising antibodies.[41] As such, the design of a diagnostic sensing agent capable of detecting this mutation is thought to be useful in future management of the disease.

It is thought that quick and simple diagnoses of Covid-19 variants might allow healthcare agencies to make more informed choices in the treatments given, and to direct government officials in tracking the spread and evolution of variants worldwide.

6.6 References

1. Dong, E.; Du, H.; Gardner, L., An interactive web-based dashboard to track COVID-19 in real time. *Lancet Infect. Dis.,* **2020,** *20* (5), 533-4.
2. Hu, B.; Guo, H.; Zhou, P.; Shi, Z. L., Characteristics of SARS-CoV-2 and COVID-19. *Nat. Rev. Microbiol.,* **2021,** *19* (3), 141-54.
3. Wu, F.; Zhao, S.; Yu, B.; Chen, Y. M.; Wang, W.; Song, Z. G.; Hu, Y.; Tao, Z. W.; Tian, J. H.; Pei, Y. Y.; Yuan, M. L.; Zhang, Y. L.; Dai, F. H.; Liu, Y.; Wang, Q. M.; Zheng, J. J.; Xu, L.; Holmes, E. C.; Zhang, Y. Z., Author Correction: A new coronavirus associated with human respiratory disease in China. *Nature* **2020,** *580* (7803), E7.
4. Zhou, P.; Yang, X. L.; Wang, X. G.; Hu, B.; Zhang, L.; Zhang, W.; Si, H. R.; Zhu, Y.; Li, B.; Huang, C. L.; Chen, H. D.; Chen, J.; Luo, Y.; Guo, H.; Jiang, R. D.; Liu, M. Q.; Chen, Y.; Shen, X. R.; Wang, X.; Zheng, X. S.; Zhao, K.; Chen, Q. J.; Deng, F.; Liu, L. L.; Yan, B.; Zhan, F. X.; Wang, Y. Y.; Xiao, G. F.; Shi, Z. L., Addendum: A pneumonia outbreak associated with a new coronavirus of probable bat origin. *Nature* **2020,** *588* (7836), E6.
5. Chan, J. F.; Yuan, S.; Kok, K. H.; To, K. K.; Chu, H.; Yang, J.; Xing, F.; Liu, J.; Yip, C. C.; Poon, R. W.; Tsoi, H. W.; Lo, S. K.; Chan, K. H.; Poon, V. K.; Chan, W. M.; Ip, J. D.; Cai, J. P.; Cheng, V. C.; Chen, H.; Hui, C. K.; Yuen, K. Y., A familial cluster of pneumonia associated with the 2019 novel coronavirus indicating person-to-person transmission: a study of a family cluster. *Lancet* **2020,** *395* (10223), 514-23.
6. Organisation, W. H. Coronavirus disease 2019 (COVID-19). Situation report - 51. https://www.who.int/docs/default-source/coronaviruse/situation-reports/20200311-sitrep-51-covid-19.pdf?sfvrsn=1ba62e57_10 (accessed 16.08.2021).
7. Lu, R.; Zhao, X.; Li, J.; Niu, P.; Yang, B.; Wu, H.; Wang, W.; Song, H.; Huang, B.; Zhu, N.; Bi, Y.; Ma, X.; Zhan, F.; Wang, L.; Hu, T.; Zhou, H.; Hu, Z.; Zhou, W.; Zhao, L.; Chen, J.; Meng, Y.; Wang, J.; Lin, Y.; Yuan, J.; Xie, Z.; Ma, J.; Liu, W. J.; Wang, D.; Xu, W.; Holmes, E. C.; Gao, G. F.; Wu, G.; Chen, W.; Shi, W.; Tan, W., Genomic characterisation and epidemiology of 2019 novel coronavirus: implications for virus origins and receptor binding. *Lancet* **2020,** *395* (10224), 565-74.
8. UK Summary. https://coronavirus.data.gov.uk (accessed 02.10.2021).
9. Coutard, B.; Valle, C.; de Lamballerie, X.; Canard, B.; Seidah, N. G.; Decroly, E., The spike glycoprotein of the new coronavirus 2019-nCoV contains a furin-like cleavage site absent in CoV of the same clade. *Antiviral Res.,* **2020,** *176*, 104742.
10. Anderson, K. G., Rambaut, A., Lipkin, W. I., Holmes, E. C., Garry, R. F., The proximal origin of SARS-CoV-2. *Nat. Med.,* **2020,** *26*, 450-2.
11. Wrobel, A. G.; Benton, D. J.; Xu, P.; Roustan, C.; Martin, S. R.; Rosenthal, P. B.; Skehel, J. J.; Gamblin, S. J., Author Correction: SARS-CoV-2 and bat RaTG13 spike glycoprotein structures inform on virus evolution and furin-cleavage effects. *Nat. Struct. Mol. Biol.,* **2020,** *27* (10), 1001.
12. Shi, J.; Wen, Z.; Zhong, G.; Yang, H.; Wang, C.; Huang, B.; Liu, R.; He, X.; Shuai, L.; Sun, Z.; Zhao, Y.; Liu, P.; Liang, L.; Cui, P.; Wang, J.; Zhang, X.; Guan, Y.; Tan, W.; Wu, G.; Chen, H.; Bu, Z., Susceptibility of ferrets, cats, dogs, and other domesticated animals to SARS-coronavirus 2. *Science* **2020,** *368* (6494), 1016-20.
13. Huang, C.; Wang, Y.; Li, X.; Ren, L.; Zhao, J.; Hu, Y.; Zhang, L.; Fan, G.; Xu, J.; Gu, X.; Cheng, Z.; Yu, T.; Xia, J.; Wei, Y.; Wu, W.; Xie, X.; Yin, W.; Li, H.; Liu, M.; Xiao, Y.; Gao, H.; Guo, L.; Xie, J.; Wang, G.; Jiang, R.; Gao, Z.; Jin, Q.; Wang, J.; Cao, B., Clinical features of patients infected with 2019 novel coronavirus in Wuhan, China. *Lancet* **2020,** *395* (10223), 497-506.
14. Wu, Z.; McGoogan, J. M., Characteristics of and Important Lessons From the Coronavirus Disease 2019 (COVID-19) Outbreak in China: Summary of a Report of 72314

Cases From the Chinese Center for Disease Control and Prevention. *JAMA* **2020,** *323* (13), 1239-42.
15. Lauring, A. S.; Hodcroft, E. B., Genetic Variants of SARS-CoV-2-What Do They Mean? *JAMA* **2021,** *325* (6), 529-31.
16. Tracking SARS-CoV-2 variants. https://www.who.int/en/activities/tracking-SARS-CoV-2-variants/ (accessed 02.10.2021).
17. Khan, A.; Zia, T.; Suleman, M.; Khan, T.; Ali, S. S.; Abbasi, A. A.; Mohammad, A.; Wei, D. Q., Higher infectivity of the SARS-CoV-2 new variants is associated with K417N/T, E484K, and N501Y mutants: An insight from structural data. *J. Cell. Physiol.,* **2021**, 10.1002/jcp.30367.
18. van Zundert, G. C.; Bonvin, A. M., Modeling protein-protein complexes using the HADDOCK webserver "modeling protein complexes with HADDOCK". *Methods Mol. Biol.,* **2014,** *1137*, 163-79.
19. Liu, Y.; Liu, J.; Xia, H.; Zhang, X.; Fontes-Garfias, C. R.; Swanson, K. A.; Cai, H.; Sarkar, R.; Chen, W.; Cutler, M.; Cooper, D.; Weaver, S. C.; Muik, A.; Sahin, U.; Jansen, K. U.; Xie, X.; Dormitzer, P. R.; Shi, P. Y., Neutralizing Activity of BNT162b2-Elicited Serum. *N. Engl. J. Med.,* **2021,** *384* (15), 1466-8.
20. Wang, P.; Nair, M. S.; Liu, L.; Iketani, S.; Luo, Y.; Guo, Y.; Wang, M.; Yu, J.; Zhang, B.; Kwong, P. D.; Graham, B. S.; Mascola, J. R.; Chang, J. Y.; Yin, M. T.; Sobieszczyk, M.; Kyratsous, C. A.; Shapiro, L.; Sheng, Z.; Huang, Y.; Ho, D. D., Antibody resistance of SARS-CoV-2 variants B.1.351 and B.1.1.7. *Nature* **2021,** *593* (7857), 130-5.
21. collaborations, W. 2,952,265 sequence entries with complete collection date information shared via GISAID. https://www.gisaid.org/index.php?id=208 (accessed 27th August 2021).
22. Ishige, T.; Murata, S.; Taniguchi, T.; Miyabe, A.; Kitamura, K.; Kawasaki, K.; Nishimura, M.; Igari, H.; Matsushita, K., Highly sensitive detection of SARS-CoV-2 RNA by multiplex rRT-PCR for molecular diagnosis of COVID-19 by clinical laboratories. *Clin. Chim. Acta.,* **2020,** *507*, 139-42.
23. Corman, V. M.; Landt, O.; Kaiser, M.; Molenkamp, R.; Meijer, A.; Chu, D. K.; Bleicker, T.; Brunink, S.; Schneider, J.; Schmidt, M. L.; Mulders, D. G.; Haagmans, B. L.; van der Veer, B.; van den Brink, S.; Wijsman, L.; Goderski, G.; Romette, J. L.; Ellis, J.; Zambon, M.; Peiris, M.; Goossens, H.; Reusken, C.; Koopmans, M. P.; Drosten, C., Detection of 2019 novel coronavirus (2019-nCoV) by real-time RT-PCR. *Euro Surveill.,* **2020,** *25* (3).
24. Konrad, R.; Eberle, U.; Dangel, A.; Treis, B.; Berger, A.; Bengs, K.; Fingerle, V.; Liebl, B.; Ackermann, N.; Sing, A., Rapid establishment of laboratory diagnostics for the novel coronavirus SARS-CoV-2 in Bavaria, Germany, February 2020. *Euro Surveill.,* **2020,** *25* (9).
25. Dao Thi, V. L.; Herbst, K.; Boerner, K.; Meurer, M.; Kremer, L. P.; Kirrmaier, D.; Freistaedter, A.; Papagiannidis, D.; Galmozzi, C.; Stanifer, M. L.; Boulant, S.; Klein, S.; Chlanda, P.; Khalid, D.; Barreto Miranda, I.; Schnitzler, P.; Krausslich, H. G.; Knop, M.; Anders, S., A colorimetric RT-LAMP assay and LAMP-sequencing for detecting SARS-CoV-2 RNA in clinical samples. *Sci. Transl. Med.,* **2020,** *12* (556).
26. Nicol, T.; Lefeuvre, C.; Serri, O.; Pivert, A.; Joubaud, F.; Dubee, V.; Kouatchet, A.; Ducancelle, A.; Lunel-Fabiani, F.; Le Guillou-Guillemette, H., Assessment of SARS-CoV-2 serological tests for the diagnosis of COVID-19 through the evaluation of three immunoassays: Two automated immunoassays (Euroimmun and Abbott) and one rapid lateral flow immunoassay (NG Biotech). *J. Clin. Virol.,* **2020,** *129*, 104511.
27. Carter, J. G.; Orueta Iturbe, L.; Duprey, J. H. A.; Carter, I. R.; Southern, C. D.; Rana, M.; Whalley, C. M.; Bosworth, A.; Beggs, A. D.; Hicks, M. R.; Tucker, J. H. R.; Dafforn, T. R., Ultrarapid detection of SARS-CoV-2 RNA using a reverse transcription-free exponential amplification reaction, RTF-EXPAR. *Proc. Natl. Acad. Sci. U S A* **2021,** *118* (35).

28. ECDC, W. R. O. f. E. *methods for the detection and identification of SARS-CoV-2 variants*; European Centre for Disease Prevention and Control: Technical Report, 2021.
29. de Puig, H.; Lee, R. A.; Najjar, D.; Tan, X.; Soekensen, L. R.; Angenent-Mari, N. M.; Donghia, N. M.; Weckman, N. E.; Ory, A.; Ng, C. F.; Nguyen, P. Q.; Mao, A. S.; Ferrante, T. C.; Lansberry, G.; Sallum, H.; Niemi, J.; Collins, J. J., Minimally instrumented SHERLOCK (miSHERLOCK) for CRISPR-based point-of-care diagnosis of SARS-CoV-2 and emerging variants. *Sci. Adv.,* **2021,** *7* (32).
30. Moran, N.; Bassani, D. M.; Desvergne, J. P.; Keiper, S.; Lowden, P. A. S.; Vyle, J. S.; Tucker, J. H. R., Detection of a single DNA base-pair mismatch using an anthracene-tagged fluorescent probe. *Chem. Commun.,* **2006**, (48), 5003-5.
31. Duprey, J. L. H. A.; Bassani, D. M.; Hyde, E. I.; Ludwig, C.; Rodger, A.; Vyle, J. S.; Wilkie, J.; Zhao, Z. Y.; Tucker, J. H. R., Anthracene-modified oligonucleotides as fluorescent DNA mismatch sensors: discrimination between various base-pair mismatches. *Supramol. Chem.,* **2011,** *23* (3-4), 273-7.
32. Duprey, J. H. A.; Bassani, D. M.; Hyde, E. I.; Jonusauskas, G.; Ludwig, C.; Rodger, A.; Spencer, N.; Vyle, J. S.; Wilkie, J.; Zhao, Z. Y.; Tucker, J. H. R., Rationalisation of a mechanism for sensing single point variants in target DNA using anthracene-tagged base discriminating probes. *Org. Biomol. Chem.,* **2018,** *16* (35), 6576-85.
33. Duprey, J.-L. H. A. Studies On Anthracene Tagged Oligonucleotides. PhD, University of Birmingham, 2010.
34. Fluorescence Anisotropy. In *Principles of Fluorescence Spectroscopy*, Lakowicz, J. R., Ed. Springer US: Boston, MA, 2006, 10.1007/978-0-387-46312-4_10pp 353-82.
35. OligoAnalyzer. https://eu.idtdna.com/calc/analyzer (accessed 25.09.2021).
36. Leck, G. Fluorescent Nucleic Acid Probes for DNA Sensing and Imaging. University of Birmingham, 2021.
37. Duprey, J. L. H. A.; Zhao, Z. Y.; Bassani, D. M.; Manchester, J.; Vyle, J. S.; Tucker, J. H. R., Detection of DNA base variation and cytosine methylation at a single nucleotide site using a highly sensitive fluorescent probe. *Chem. Commun.,* **2011,** *47* (23), 6629-31.
38. Duprey, J. L. H. A.; Bassani, D. M.; Hyde, E. I.; Jonusauskas, G.; Ludwig, C.; Rodger, A.; Spencer, N.; Vyle, J. S.; Wilkie, J.; Zhao, Z. Y.; Tucker, J. H. R., Rationalisation of a mechanism for sensing single point variants in target DNA using anthracene-tagged base discriminating probes. *Org. Biomol. Chem.,* **2018,** *16* (35), 6576-85.
39. Tchesnokova, V.; Kulasekara, H.; Larson, L.; Bowers, V.; Rechkina, E.; Kisiela, D.; Sledneva, Y.; Choudhury, D.; Maslova, I.; Deng, K.; Kutumbaka, K.; Geng, H.; Fowler, C.; Greene, D.; Ralston, J.; Samadpour, M.; Sokurenko, E., Acquisition of the L452R mutation in the ACE2-binding interface of Spike protein triggers recent massive expansion of SARS-CoV-2 variants. *J. Clin. Microbiol.,* **2021**, 10.1128/JCM.00921-21, JCM0092121.
40. Horiba What is Fluorescence Anisotropy or Fluorescence Polarization? https://www.horiba.com/gbr/technology/measurement-and-control-techniques/spectroscopy/fluorescence-spectroscopy/what-is-fluorescence-anisotropy-or-fluorescence-polarization/ (accessed 13.09.2021).
41. Poppas, A.; Rounds, S., Congestive heart failure. *Am. J. Respir. Crit. Care Med.,* **2002,** *165* (1), 4-8.

Chapter 7 Techniques, Experimental and Methods

7.1 Techniques

7.1.2.3 Melting temperature (T_m) procedure

Thermal melting can be used to probe oligonucleotide duplex formation dependent on the hyperchromic effect which relates to the relative UV absorbance of the stacking of bases within the single or duplex strand. Duplexed strands absorb less UV light due to the stacking of the aromatic nucleobases within the double helix. Duplexed, hairpin and G-quadruplex DNA (10 or 15 μM, 19 μL) and SsoAdvanced™ universal SYBR® (1 μL) (supplied by BioRad) were added to PCR Eppendorf tubes and annealed at 95 ˚C for 5 min. A Bio-RadiQ™5 Multicolour Real-Time PCR Detection System was used to run and collect thermal stability data in triplicate, from which the Tm of the duplex could be determined. This was calculated from the peak height of the negative first derivative of the melting curves. The measurements were taken as the duplexes were heated from 20 – 95 ºC and cooled back to 20 ºC at a rate of 1 ºC min^{-1} and values were obtained from the maxima of the negative first derivative of the melting curve.

7.1.2.4 Circular dichroism procedure

Circular dichroism is seen when optically active molecules absorb circularly polarised light differently dependent on the direction of the polarisation. The difference can be projected as a measure of ellipticity on a CD spectropolarimeter. Positive CD signals absorb left-handed circularly polarised light best whilst negative signals show the reverse.[1]

A spectropolarimeter measures the absorption difference between R and L polarised light:

$$\Delta A = A_L - A_R \ (M^{-1}\ cm^{-1})$$

And reports the data in terms of the ellipticity (θ) in degrees.[2] The relationship between this and the change in absorption is as follows:

$$\theta = 32.98\,\Delta A$$

As such, a CD spectrum is measured as a function of the wavelength. When looking at the CD spectra of DNA, certain shapes represent duplex DNA in different structural forms, such as the widely prevalent right-handed double helix B DNA and the left-handed Z DNA.[2]

The typical B form of a DNA duplex strand shows the base pairs as perpendicular to the phosphate axes, meaning the overall chirality is weak.[2] The nature of the base pair content and the overall salt content of the buffer both play large roles in the CD spectrum of a duplex DNA sample. For example, as the AT content of a duplex strand increases, the negative trough increases in strength, whilst the increasing Na^+ concentration causes the long wavelength region of the CD spectrum to decrease slowly.[3]

In contrast, hairpin structures of single-strand DNA have differing CD spectra, often with weaker signal intensities. Most hairpins are formed of small single strand loops within a duplex structure, and as such, a change from duplex to hairpin structure can be observed (Figure 107).[4]

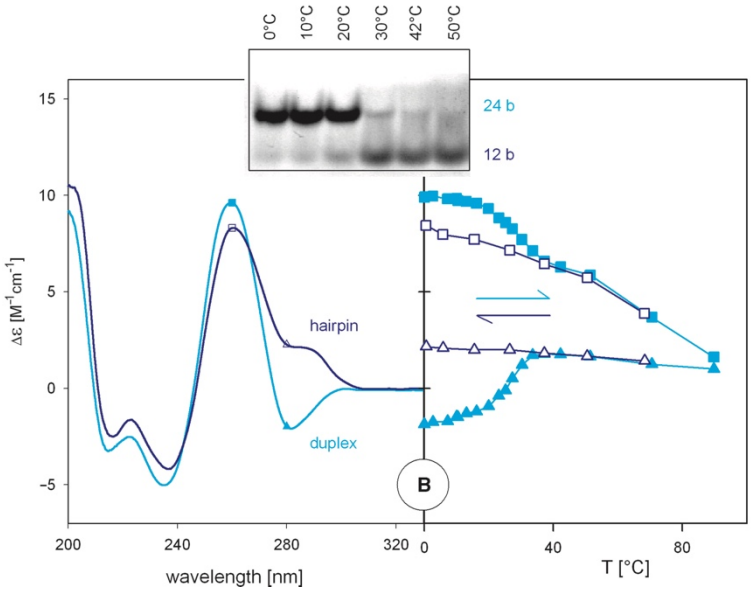


Figure 107 Irreversible temperature dependent duplex to hairpin transition of d(C6G6) DNA complex in 1 mM Na phosphate, 0.3 mM EDTA, pH 7. PAGE (20% polyacrylamide) of the samples at various temperatures. Image taken from J. Kypr et al., 2009 to show the CD structure of B-DNA and hairpin DNA.

Studies were carried out on single strand and duplexed DNA (3, 5, 10 or 15 μM, 200 μL) in either TBA buffer or duplex buffer using a Jasco 1500 CD Spectrophotometer and a quartz cuvette of 10 mm pathlength. Parameters as described below:

Table 19 General parameters for circular dichroism spectroscopy

RANGE	200 – 400 nm
DATA PITCH	0.5 nm
SCAN SPEED	100 nm min^{-1}
BANDWIDTH	1.00 nm
ACCUMULATIONS	3
SCALE	200 mdeg/1.0 dOD

Baselines were corrected manually from the solvent blank, offsetting results at 400 nm. All buffers used in CD spectra were as described below:

Table 20 Buffer components for aptamer spectroscopy experiments

BUFFER	COMPONENTS
TBA BUFFER	*20 mM Tris-HCl, 1 mM $MgCl_2$, 120 mM NaCl, 10 mM KCl, 2 mM $CaCl_2$ pH 7.38*
DUPLEX BUFFER	*10 mM sodium phosphate, 100 mM NaCl, pH 7.4*

7.1.2.5 Polyacrylamide Gel Electrophoresis procedure

Native polyacrylamide gel electrophoresis (PAGE) was performed on DNA samples to identify duplex formation, purity and changes in electromobility. Biomolecular interactions of DNA and proteins could be shown to differ according to the electrophoretic mobility of the molecule or complex. Complexation adds mass to the biomolecule, reducing mobility which results in a higher band in the gel, meaning that single stranded DNA moves further than double stranded, and DNA bound to proteins move least of all.

Polyacrylamide gels (12, 14 or 20% w/w, 40 mL) were prepared in sets of 4 using bis-acrylamide solution. For 14% gel: bis-acrylamide soln. (40% w/w, 17 mL), TBE buffer (5×, 8 mL) and Milli-Q water (17.8 – 18.0 mL), In cases where potassium doping to improve G-quadruplex formation was required, 200 µL of KCl (2 M) was used. The gel was then activated by the addition of APS (10% in H_2O, 300 µL) and TEMED (30 µL).

DNA samples (1 µM, 23 µL) were prepared in either TBA or duplex buffer (Table 20) with the addition of glycerol (30%, 2 µL). The samples were then loaded onto the gel (10 µL) with all gels prepared in duplicate. Lane 1 of each gel plate was loaded with a visual representation of the electromobility shift (this gel loading dye included bromo-phenol blue and xylene-cyanoFF).

The gels were run in TBE buffer (1× dilution from 5 × stock: 54 g Tris base, 27.5 g boric acid, 3.7 g EDTA in H_2O (1 L)) when running DNA samples in duplex buffer and KCl (10 mM) spiked TBE buffer (1×) when running DNA samples in TBA buffer on Bio-Rad PowerPac at 100 V for 70 – 200 minutes, with a 15 minute pre-run. The gels were then removed and washed in de-ionised H_2O before being rocked in a solution of Diamond™ stain nucleic acid dye (5 µL per 2 gels) in TBE buffer (1×, 50 mL) for 15 minutes. An AlphaImager HP Gel Imaging System (from Alpha Innotech) was used to visualise the gels under UV (310 nm).

If proteins were included in the gel, protein imaging was accomplished by staining with Instant Blue® Coomassie after visualisation of the DNA for 30 min. The stain shows protein as blue in visible light.

7.1.2.6 Ultraviolet visible spectroscopy

Ultraviolet visible (UVvis) spectroscopy is an absorption-based technique that determines the amount of light is absorbed by a molecule at any given wavelength between 200 – 800 nm. Upon absorbing the photon of light, the an electron can be excited to a higher energy state in a manner described by the following equation: Equation 2

Equation 2 The energy of a molecule after absorbing a specific wavelength of light (∆E is the change in energy, h is Planck's constant, v is the frequency of light, c is the speed of light and λ is the wavelength of light absorbed)

$$\Delta E = hv = \frac{hc}{\lambda}$$

A CARY 5000 UV spectrophotometer was used to determine the UVvis absorbance of each molecule. Quartz cuvettes (Starna Scientific Ltd, UK) were used with a path length of 1.0 cm and parameters shown in the table below (Table 21).

Table 21 UVvis parameters

RANGE	200 – 800 nm (source changeover set to 200 nm)
RESPONSE	medium
DATA PITCH	0.5 nm
SCAN SPEED	200 nm min^{-1}
BAND WIDTH	1.0 nm

7.1.2.7 Fluorescence characterisation

Fluorescence spectra are recorded as fluorescent compounds absorb a photon of light, causing an electron to promote to a higher energy level. At this stage, the species becomes electronically excited (Equation 3).

Equation 3 Excitation of fluorescent molecule M by photon

$$M + h\nu \rightarrow M^*$$

The excited molecule loses excess energy to return to a stable ground state and can do so by emitting the photon via fluorescence, luminescence, or phosphorescence. Fluorescence, the short-lived spin allowed downward transition can be a very useful property for sensing as detection can be achieved at low concentrations using relatively simple equipment. Comparatively, phosphorescence emission occurs when the molecules in an excited single state (S_1) go via a spin conversion (intersystem crossing) to a triplet state (T_1).

Recording the fluorescence spectra relies on absorption of the light at a particular wavelength, so the UV spectrum is usually taken first, then the absorbance maxima used as the excitation wavelength of the molecule. The wavelength of the emission is lower energy

than that of the absorption, due to energy lost through internal conversion of the energy bands down to the lowest vibrational energy of S_1 required for fluorescence to occur and the difference is the Stokes shift. All fluorescence spectra were taken using a Jasco FP-8500 fluorometer.

Organic samples for fluorescence were prepared as a range of concentrations in a range of organic solvents using a three-window sub-micro quartz cuvette (Starna Scientific Ltd, UK) and a 3 mm pathlength. General settings are described in Table 22 with the excitation and emission wavelength ranges described individually throughout Chapter 4.

Table 22 General parameters for fluorescence spectroscopy

RANGE (DNA SAMPLES ONLY)	365 – 650 nm
DATA INTERVAL	1 nm
ACCUMULATIONS	3
SENSITIVITY	high
EXCITATION BAND WIDTH	5 nm
EMISSION BAND WIDTH	5 nm
SCAN SPEED	200 nm min^{-1}
EXCITATION WAVELENGTH (DNA SAMPLES ONLY)	350 nm

DNA probe samples were made up in H_2O (MilliQ, 0.5 μM) in a 1:3 ratio with target strands and incubated at room temperature in the dark for 5 min before the spectra were recorded.

7.1.2.8 Fluorescence anisotropy

Fluorescence anisotropy is the measurement of the change in orientation of a molecule in space, respective of the time between the absorption and emission events. Absorption and emission are indicative of the spatial alignment of the molecule's dipole relative to the electric vector of the electromagnetic wave of excitation and emitted light.[5] The amount of emitted light retaining the polarisation is based upon the speed of rotation of the molecule in solution (Figure 108).

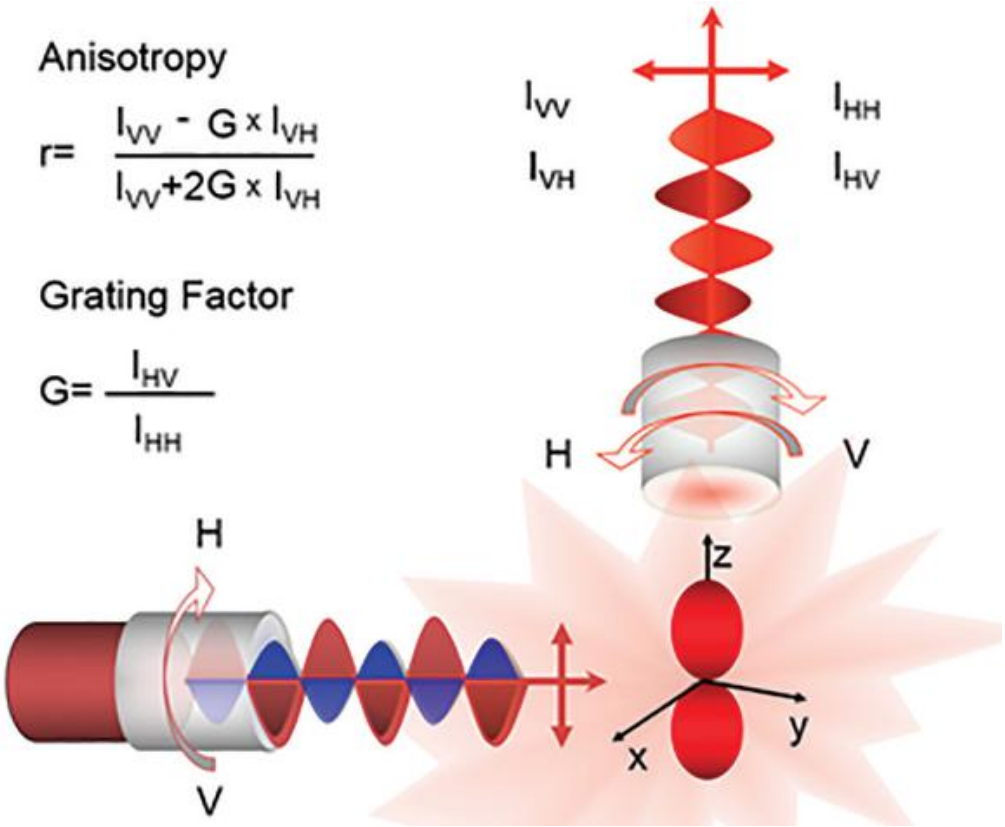


Figure 108 Depiction of fluorescence anisotropy experiment with excitation and emission polarisers rotating to 0 and 90 ˚ orientations. H = horizontal, V = vertical Image taken from Horiba.com2

The grating factor (G factor) is used as a correction for the instrument's differential transmission of the orthogonal vector orientations.[5] All fluorescence anisotropy data was recorded using a Jasco FP-8500 fluorometer using additional polarisers and the general parameters are listed below.

Table 23 General parameters for fluorescence anisotropy

EXCITATION BAND WIDTH	20 nm
G FACTOR	0.9674
EXCITATION WAVELENGTH	350 nm
EMISSION WAVELENGTH	425 nm
ACCUMULATIONS	5

7.1.2.9 Mass Spectrometry Fourier-transform ion cyclotron resonance (FT-ICR)

The instrument consists of an ion trap (a Penning trap) which contains both a magnetic field to prevent movement perpendicular to the magnet, and an electric field to stop ions moving along the length of the magnetic field. This results in the ions circling the magnetic field in tiny orbits with frequencies similar to cyclotron frequencies.[32] The MS instrument can then separate these orbits by weight using radio frequency pulses emitted through electrodes in the excitation plates. These pulses are relative to the cyclotron frequencies which acts as a function of mass and separates the ions in this manner. The changes in potential of the ions upon this excitation are recorded as an ICR signal and analysed by Fourier transformation to give a molecular weight reading.[20] FT-ICR is considered the gold standard for high mass accuracy and is a popular technique for direct sample infusion. It was hoped that the different technique would minimise the chance of hydrolysis occurring during the running of the mass

spectrometry, but the data showed the same hydrolysed product molecular weights (Appendix 3.5).

7.2 General Experimental

7.2.1 Materials

Solvents and reagents were purchased from Sigma Aldrich, Fischer, Fluorochem, VWR or Acros Organics and used without further purification unless otherwise stated. All solvents were anhydrous unless otherwise stated. Anhydrous THF, PhMe and CH_2Cl_2 were collected from a Pure Solv-MD solvent purification system and purged under argon for 15 min prior to use. The following cooling baths were used; 0 ˚C (ice/water). For overnight reactions at 0 ˚C, a Julabo FT902 immersion cooler was used in an acetone bath. All reactions in non-aqueous solvents were carried out under argon in oven-dried glassware. Column chromatography was carried out using open columns packed with Merck grade 60 silica gel unless otherwise stated. Analytical TLC was carried out on Merck aluminium-backed silica gel 60 plates. Short wave UV (254 nm), long wave UV (365 nm), ninhydrin, vanillin or $KMnO_4$ were used to visualise the compounds. In the case of determining compounds with DMT protecting groups, TLC plates were cast over hydrochloric acid vapour. Bovine thrombin from Helena Biosciences was used in PAGE experiments described in Chapter 5. Activation of the thrombin was achieved by dissolution of the dry protein in 175 µL buffer (either TBA or duplex), incubation at RT for 15 min, then on ice for 30 min to give a 10 µM solution which could be stable at 4 ˚C for 7 days.

7.2.2 General procedures

Nuclear magnetic resonance (NMR) (^1H, ^{13}C and ^{31}P) were determined by either a Bruker AV400 spectrometer or a Bruker Avance NEO 400 spectrometer (^1H – 400 MHz. ^{13}C – 101 MHz). Spectra were recorded in $CDCl_3$ referenced to residual $CHCl_3$ (^1H, 7.26 ppm; ^{13}C, 77.48, 77.16, 76.84 ppm), CD_3CN referenced to residual CH_3CN (^1H, 1.94 ppm; ^{13}C 1.32,

118.26 ppm) or DMSO-d6 referenced to residual DMSO (^{1}H, 2.50 ppm; ^{13}C, 39.4 ppm). Chemical shifts (d) are reported in ppm and coupling constants (*J*) are reported in Hz. The following abbreviations are used to describe multiplicity; s-singlet, d-doublet, dd-double doublet, t-triplet, q-quartet, m-multiplet, app-apparent. In all cases where anthracene aromatic protons are seen as 2 peaks, the splitting pattern can be described as AA'BB' in ODCB type splitting. All coupling constants are reported as observed and not averaged. Data was acquired using Bruker Topspin v3.2 and analysed using either MestReNova v12.0.2-20910 or MestReNova v12.0.3-21384.

Mass spectra were recorded on either a Waters micromass LCT Time of flight mass spectrometer, a Waters Xevo G2-XS Mass Spectrometer or a Waters Xevo G2-XS mass spectrometer for oligo samples and are reported as *m/z*(%).

IR spectra were recorded neat on a Perkin Elmer Spectrum 100 FT-IR spectrometer. The following abbreviations are used to report stretch shape; s–strong, sh-sharp, br-broad.

Melting points were carried out in triplicate, reporting the average values as a range, using a Stuart SMP10 melting point apparatus with open glass capillary tubes.

Milli-Q water used in DNA sample preparation, purification and DNA containing experiments was purified with a Millipore Elix-Gradient A10 system (resistivity > 18 MΩ.cm, TOC ≤ 5 ppb, Millipore, France).

Unless otherwise stated, all reactions were carried out under argon using anhydrous solvent. When the reaction was required to be in the dark, the flask containing the reaction mixture was wrapped in aluminium foil for the duration. For such reactions, all workups and purifications were also carried out in foil wrapped containers and flasks. Room temperature (RT) was a range from 19 ˚C – 24 ˚C. Unless otherwise stated, TLC eluent systems are the same as the column conditions.

7.1.2 DNA synthesis and characterisation general procedure

7.1.2.1 Synthesis of unmodified and modified DNA strands

Standard phosphoramidites (Bz-dA, iBu-dG, Ac-dC, and dT) were purchased from Link Technologies, and 5'-hexynyl phosphoramidite (Glen Research) were used for synthesis. The phosphoramidites were dissolved in anhydrous MeCN to 0.1 M prior to synthesis. Strands were synthesised at a 1 μmol scale on SynBaseTM CPG 1000/110 solid supports from Link Technologies. The resins have average pore sizes of 1000 Å, nominal particle sizes of 110 μm, and nucleoside loadings of 25-40 μmol g^{-1}. Phosphoramidites were activated with 5- ethylthio-1*H*-tetrazole (0.5 M) in MeCN prior to coupling. Coupling times of 25 seconds and 10 minutes were used for the nucleosides and hexynyl group respectively. Acetic anhydride and methylimidazole were added to cap unreacted material, and then iodine (0.1 M) in THF: pyridine: H_2O (78:20:2) was added to oxidise the phosphotriester formed. Upon sequence completion, oligonucleotides were treated with aqueous ammonia (30%) for 1 hour to cleave the strands from the resin. Protecting groups on the strands were removed by heating in aqueous ammonia (30%) at 60 °C for 6 hours. The solvent was then removed on a Thermo Scientific speed vac in preparation for purification.

Ultramild syntheses differed on several counts. The phosphoramidites (Pac-dA, iPr-Pac-dG, Ac-dC, dT) from Link Technologies were used to all ultramild syntheses. Phosphoramidites were activated with 5-ethylthio-1*H*-tetrazole (0.25M) in acetonitrile prior to coupling. Coupling times of 25 seconds was used for the nucleoside phosphoramidites, and 10 minutes for non-standard anthracene-derived phosphoramidites. Phenoxyacetic anhydride and methylimidazole were added to cap unreacted material, and iodine (0.02 M) in THF: pyridine: H_2O (7:2:1) was added to oxidise the phosphotriester formed. Upon sequence completion, the resins were placed in freshly prepared 1 mL solutions of potassium carbonate (0.05 M) in EtOH and left overnight to cleave strands from the resin and remove protecting groups. The solutions were neutralised with AcOH (6 μL) and the solvent was removed on a Thermo

Scientific speed vac. The dried powders were redissolved in 1 mL Milli-Q H_2O and desalted with a NAP-10 column from GE Healthcare to remove residual resin and potassium carbonate. The solutions were then concentrated to 1 mL and stored in the freezer for purification.

7.1.2.2 Annealing of duplexes and preparation of samples

For all experiments involving cycloadduct containing DNA, the samples were dissolved in degassed 100 mM $NaIO_4$ (aq.) in MeOH unless otherwise stated. See section 3.4.3 for the sample preparation of each experiment. General experimental for DNA-based cycloaddition seen on page *XLVIII.*

For melting temperature studies, the duplexes or secondary order single strand DNA samples were annealed by heating at 80 ºC for 5 minutes in a pre-heated heating mantle before being left to cool to room temperature (~1 hour). For all other studies, the duplexes were left at room temperature for a minimum of 30 minutes before taking any measurements.

7.1.2.3 HPLC Purification

Semi preparative HPLC purification was performed on an Agilent Technologies 1260 Infinity system using a Phenomenex Clarity 5µm Oligo-RP LC 250 x 10 mm column. 1 ml of sample was injected with a run time of 45 minutes for each sample, at a flow rate of 3 ml/min. The column was heated to 60 °C prior to sample injection for unmodified DNA sequences. Modified DNA sequences were run at RT. The UV/vis absorbance of each run was monitored at 260 nm and 360 nm for modified strands. The solvent gradients used are listed in the table below (Table 24):

Table 24 HPLC methods table with gradients and temperature

Temperature (˚C)	Total run length (min)	Gradient (buffer D:	Cleaning procedure

			MeCN)	
DMT on	60	45	85:15 – 40:60 (0 – 30 min)	100% MeCN 30 -40 min, 85:15 Buffer D: MeCN 40-45 min
Short oligo	60	45	95:5 – 82:18 (0 – 25 min)	100% MeCN 25 -40 min, 95:5 Buffer D: MeCN 40-45 min
Anth-modified oligo	60	50	75:25 – 85:15 (0 – 30 min)	100% MeCN 30 -40 min, 75:25 Buffer D: MeCN 40-50 min
Diels-Alder oligo	25	45	85:15 – 75:25 (0 – 30 min)	100% MeCN 30 -40 min, 85:15 Buffer D: MeCN 40-45 min

Collected fractions were evaporated to dryness, diluted to 1 mL in Milli-Q H_2O, and desalted using a NAP-10 column (GE Healthcare), whilst eluting to 1.5 mL. Purity of oligonucleotides was determined by analytical HPLC using a Phenomenex Clarity 5 µm Oligo RP LC 250 x 4.6 mm column on an Agilent Technologies 1260 Infinity system. The column was heated to 60 °C prior to sample injection for unmodified strands and at RT for modified DNA strands. 10 µL of sample was injected with a run time of 45 minutes for each sample, at a flow rate of 1 mL min^{-1}. Solvent gradients used were identical to those used in semi-preparative HPLC

(Table 24). The UV/vis absorbance of each run was monitored at 260nm and 360 nm for modified strands.

7.1.2.5 Characterisation and concentration determination

Samples showing >95% purity by analytical HPLC were deemed sufficiently pure for use in experiments. Samples showing <95% purity were repurified by semi preparative HPLC. The characterisation of pure oligonucleotide samples was performed by negative mode electrospray mass spectrometry. Sample concentrations were determined by optical density at 260 nm using a BioSpec- nano micro-volume UVvis spectrophotometer (nanodrop) from Shimadzu and the Beer Lambert law, with extinction coefficients obtained from Integrated DNA Technologies' OligoAnalyzer.[6]

7.2.3 List of novel compounds

2.43 – 3,3'-(anthracene-9,19-diyl)bis(propan-1-ol)

2.57 – 9-((2-(bis(4-methoxyphenyl)(phenyl)methoxy)ethoxy)methyl)-10-(chloromethyl)anthracene

2.61 – 9,10-bis(((4-vinylbenzyl)oxy)methyl)anthracene

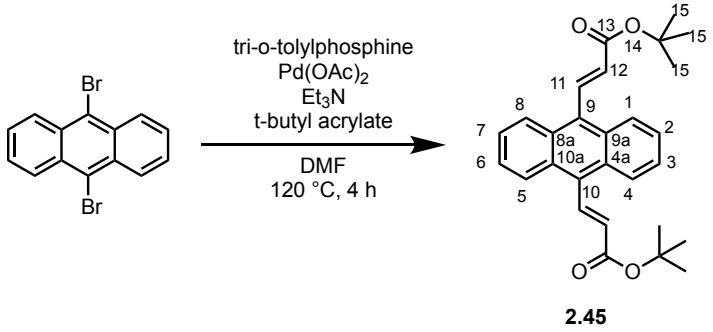
2.88 – 1-((9s,10s)-9-methoxy-9,10-dihydro-9,10-(epoxyimino)anthracen-11-yl)ethan-1-one

4.30 – 2-(anthracen-9-ylmethoxy)isoindoline-1,3-dione

4.27 – *O*-(anthracen-9-ylmethyl)hydroxylamine (novel procedure)

7.2.4 Experimental

***Compound 2.45**: di tert-butyl 3,3'-(9,10-anthracenediyl)bis 2-propenoate*

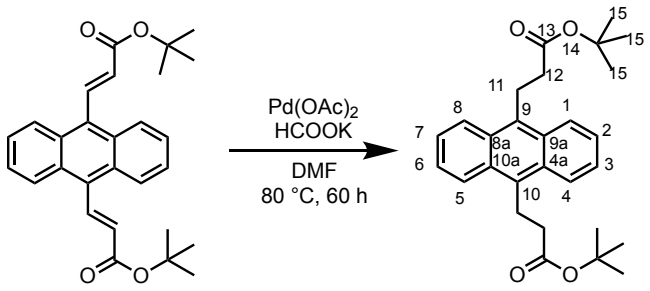


2.45

Commercially available 9,10-dibromoanthracene (3360 mg, 10.0 mmol), palladium(II) acetate (247 mg, 1.10 mmol) and tri-*o*-tolyl phosphine (669 mg, 2.20 mmol) were added to a solution of *t*-butyl acrylate (29 mL, 200 mmol) and triethylamine (28 mL, 200 mmol) in DMF (50 mL) and heated at 120 ˚C for four hours under argon. Upon completion, the reaction mixture was allowed to cool to room temperature and H_2O (10 mL) and EtOAc (10 mL) were added. The organic layer was then extracted and washed with H_2O (3 × 10 mL) and brine (1 × 10 mL). The organic layer was dried over $MgSO_4$, filtered, and the solution removed under reduced pressure to give a crude yellow solid. Purification was achieved via flash column chromatography (EtOAc:hexane = 1:20) to give the title compound as a yellow crystalline solid (2843 mg, 66%); MP: decomposition observed 209 – 215 ºC (recrystallised from CH_2Cl_2:hexane); IR (ν_{max}/cm^{-1}): 2978 (sh, C=CH), 2937 (ArCH), 1709 (s, sh, C=O), 1637 (sh, C=C), 1148 (s, sh, C-O); ^{1}H NMR (300MHz, $CDCl_3$) δ 8.51 (d, *J* = 16.1 Hz, 2H, *H11*), 8.26 (m, 4H, m(AA'BB' in ODCB type splitting), *H1, H4, H5, H8* or *H2, H3, H6, H7*), 7.54 (m, 4H, m(AA'BB' in ODCB type splitting), *H1, H4, H5, H8* or *H2, H3, H6, H7*), 6.33 (d, *J* = 16.1 Hz, 2H, *H12*), 1.63 (s, 9H, *H15*). ^{13}C NMR (101MHz, $CDCl_3$) δ 165.6 (CO, *C13*), 140.8 (CH, *C11 or 12*), 129.7 (CH, *C11 or 12*), 126.0 (ArCH, *C1, C4, C5, C8 or C2, C3, C6, C7*), 125.9 (ArCH, *C1, C4, C5, C8 or C2, C3, C6, C7*), 28.3 (CH_3, *C15*); *m/z* (TOF MS ES+) calculated

mass [M + Na]: 453.53, observed mass: 453.21. Data in agreement with those reported in the literature.[7]

***Compound 2.44**: di tert-butyl 9,10-anthracene dipropanoate*

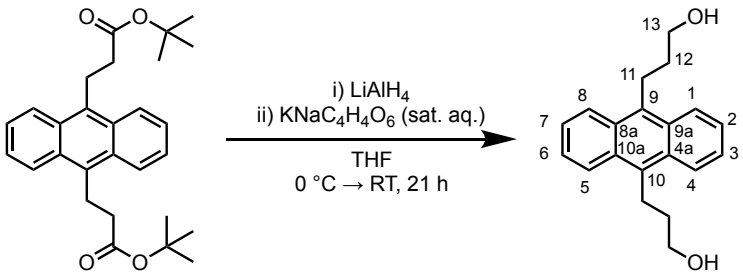


2.45 **2.44**

Fresh potassium formate (245 mg, 2.91 mmol, recrystallised from MeOH/Et_2O) and palladium(II) acetate (26.1 mg, 0.12 mmol) were added to a solution of the propenoate **2.45** (250 mg, 0.581 mmol) in DMF (10 mL) and heated at 80 °C for 16 h. Upon completion, the reaction mixture was allowed to cool to room temperature and H_2O (20 mL) and EtOAc (20 mL) were added. Once passed through filter paper to remove excess palladium, the organic layer was extracted with EtOAc (3 × 10 mL) then CH_2Cl_2 (3 × 10 mL) washed with H_2O (2 × 10 mL) and brine (1 × 10 mL), dried over Na_2SO_4 and filtered. The solvent was removed under reduced pressure and the yellow residue subsequently purified via flash column chromatography (hexane: CH_2Cl_2 = 8:2) to give first the title product (102.2 mg, 41%), IR (ν_{max}/cm^{-1}): 2913 (Ar CH), 1697 (s, sh C=O) ^{1}H NMR ($CDCl_3$, 300MHz) δ 8.33 (m(AA'BB' in ODCB type splitting), 4H, *H1, H4, H5, H8*), 7.54 (m(AA'BB' in ODCB type splitting), 4H, *H2, H3, H6, H7*), 3.92 (m, 4H, *H11 or H12*), 2.69 (m, 4H, *H11 or H12*), 1.49 (s, 18H, *H15*), ^{13}C NMR ($CDCl_3$, 101MHz) δ 172.5 (CO, *C13*), 132.1 (*C11/C12*), 129.4 (*C11/C12*), 125.4 (ArCH, *C1, C4, C5, C8 or C2, C3, C6, C7*), 124.9 (ArCH, *C1, C4, C5, C8 or C2, C3, C6, C7*), 80.6, 68.0, 36.7, 31.6, 28.2 (3 × C15). *m/z* (TOF MS ES+) calculated mass [M + K]: 473.68, observed mass: 473.15.

Data in agreement with those reported in the literature.[7]

***Compound 2.43**: 3,3'-(anthracene-9,19-diyl)bis(propan-1-ol)*

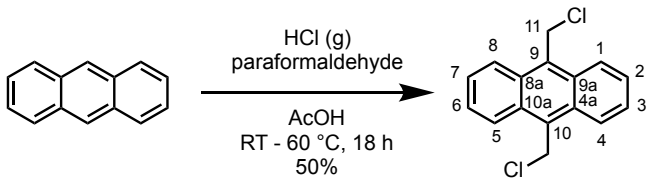


2.44 **2.43**

$LiAlH_4$ (1 M in THF, 5.60 mL, 5.60 mmol) was added dropwise to a solution of the di-*tert*-butyl ester **2.44** (608 mg, 1.40 mmol) in anhydrous THF (30 mL) at 0˚C under argon over a period of 10 min. The reaction mixture was then stirred at room temperature under argon for 21 h. The reaction mixture was cooled to 0˚C and opened to the atmosphere before quenching via addition of sat. aq. Rochelle salt dropwise (3 mL). The yellow solid was re-dissolved in Et_2O (10 mL) before extraction with EtOAc (2 × 10 mL) and washing with brine (1 × 10 mL). The organic layer was then dried over $MgSO_4$, filtered, and the solvent removed under reduced pressure. The product was purified via flash column chromatography (CH_2Cl_2:MeOH = 98:2) to give the title compound as a yellow solid (325.5mg, 79%); IR (ν_{max}/cm^{-1}): 3287 (br, OH), 2920 (s, Ar C-H) and 2879 (s, Ar C-H); ^1H NMR (400 MHz, DMSO-d_6) δ 8.38 (m(AA'BB' in ODCB type splitting), 4H, *H1, H4, H5, H8*), 7.54 (m(AA'BB' in ODCB type splitting), 4H, *H2, H3, H6, H7*), 4.71 (t, *J* = 5.0 Hz, 2H, *H14*), 3.63 (m, 8H, *H11/13*), 1.87 (m, 4H, *H12*). ^{13}C NMR (101 MHz, DMSO) δ 133.8 (Ar C-H, *C9, C10*), 129.4 (ArC-H, *C4a, C8a, C9a, C10a*), 125.6 (ArC-H, *C1, C4, C5, C8 or C2, C3, C6, C7*), 125.5 (ArC-H, *C1, C4, C5, C8 or C2, C3, C6, C7*), 61.1 (CH_2, *C13*), 34.9 (CH_2, *C12*), 24.5 (CH_2, *C11*). *m/z* (ES+): 317.15 ([294.39 + Na]+, 100%).

Compound known via Patent: US-2007123600-A1 – no experimental procedure or characterisation given.

***Compound 2.48**: 9,10-Bis-chloromethyl-anthracene*

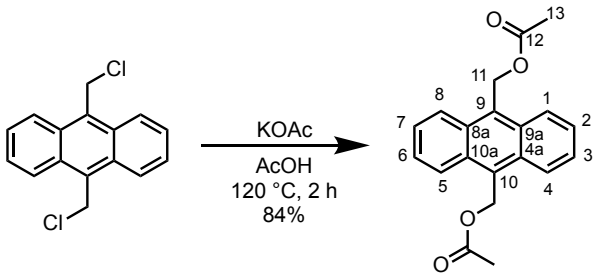


2.47 **2.48**

A slurry of paraformaldehyde (3000 mg, 34.16 mmol) and 20 mL glacial acetic acid were combined in a 2-neck flask. Gaseous HCl (generated *in situ* from concentrated H_2SO_4 and NaCl) was bubbled through the stirred suspension until the solution became clear. Anthracene (7000 mg, 39.28 mmol) and a further 20 mL glacial acetic acid was added to the 2-neck flask and the reaction stirred at 60 ˚C under argon for 24 h before being poured onto ice. The solid was filtered and dried under reduced pressure to give the crude product as a yellow solid. The residue was then recrystallized from hot chlorobenzene, giving the title compound as yellow crystals (4224 mg, 45%); MP: decomposition to black solid at 193-195 ºC (recrystalised from $CDCl_3$, IR (ν_{max}/cm^{-1}): 3070 (ArCH), 2923 (ArCH), 2852 (ArCH), 1665 (ArCC), 752 (C-Cl). ^{1}H NMR (DMSO, 300MHz, d; ppm) 8.53 (m(AA'BB' in ODCB type splitting), 4H, *H1, H4, H5, H8*), 7.73 (m(AA'BB' in ODCB type splitting), 4H, *H2, H3, H6, H7*), 5.89 (s, 4H, *H11*). ^{13}C NMR (DMSO, 101MHz, d; ppm). Solubility insufficient for carbon data, few peaks seen 131.2, 129.7, 127.3, 125.3. *m/z* (TOF MS ASAP+) calculated mass: 274.0316 (100%), 276.0289 (67%), observed mass: 274.0320 (100%), 276.0295 (70%) (3 isotope peaks used for i-FIT, i-FIT: 34.4).

Data in agreement with those reported in the literature.[8]

***Compound 2.49**: Anthracene-9,10-diylbis(methylene) diacetate*

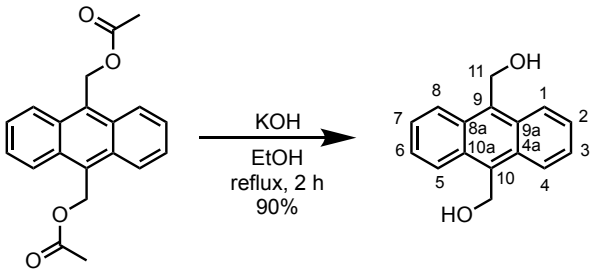


2.48 **2.49**

A suspension of 9,10-bischloromethyl anthracene **2.48** (1.000 g, 3.66 mmol) was prepared in glacial acetic acid (20 mL) and potassium acetate (2.876 g, 29.3 mmol) was added. The reaction mixture was stirred at reflux (120 ˚C) for 1 h. The reaction mixture was then poured onto ice and the title compound separated by filtration under suction to give a yellow solid (993.6 mg, 84%); MP: decomposition at 223-227 ºC (recrystallised from $CHCl_3$), IR (ν_{max}/cm^{-1}): 3085 (ArCH), 1728 (C=O), 1247 (C-O ester), ^{1}H NMR ($CDCl_3$, 300MHz, d; ppm) 8.45-8.39 (m(AA'BB' in ODCB type splitting), 4H, *H1, H4, H5, H8 or H2, H3, H6, H7*), 7.67-7.60 (m(AA'BB' in ODCB type splitting), 4H, *H1, H4, H5, H8 or H2, H3, H6, H7*), 6.20 (s, 4H, *H11*), 2.09 (app d, *J* = 12.7 Hz, 6H, *H13*). ^{13} C NMR ($CDCl_3$, 101MHz, d; ppm) 171.2 (2 × *C12*), 130.8 (*C4a, C10a or C8a, C9a*), 128.7 (*C4a, C10a or C8a, C9a*), 126.4 (*C1, C4, C5, C8 or C2, C3, C6, C7*), 124.7 (*C1, C4, C5, C8 or C2, C3, C6, C7*), 58.8 (2 × *C11)*, 21.0 (2 × *C13*), *m/z* (TOF MS ASAP+) calculated mass: 322.1205, observed mass: 322.1210.

Data in agreement with those reported in the literature.[9]

***Compound 2.50**: anthracene-9,10-diyldimethanol*

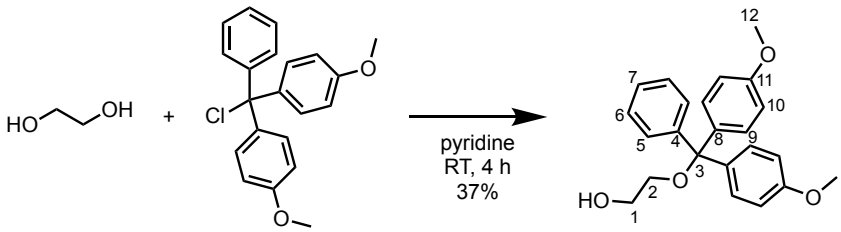


2.49 **2.50**

Bis-acetate **2.49** (29.4 mg, 0.0912 mmol) was prepared in solution with KOH (71.3 mg, 1.27 mmol) in EtOH (15 mL) and stirred at reflux for 2 h until consumption of the starting material by TLC (9:1 hexane: EtOAc). Upon completion, the reaction mixture was allowed to cool to room temperature and subsequently cooled in ice to aid precipitation. The resultant crystals were filtered under reduced pressure to yield the title compound as a yellow solid (19.6 mg, 90%). ν_{max}/cm^{-1}: 3400 (OH), 2909 (Ar-CH), ^{1}H NMR (400 MHz, DMSO-d_6) δ 8.50 (m(AA'BB' in ODCB type splitting), 4H, *H1, H4, H5, H8 or H2, H3, H6, H7*), 7.57 (m(AA'BB' in ODCB type splitting), 4H, *H1, H4, H5, H8 or H2, H3, H6, H7*), 5.45 (s, 4H, *H11*), 5.36 (s, 2H, OH), ^{13}C NMR (101 MHz, DMSO) δ 133.8 (*C4a, C10a or C8a, C9a*), 130.1 (*C4a, C10a or C8a, C9a*), 125.8 (*C1, C4, C5, C8 or C2, C3, C6, C7*), 125.7 (*C1, C4, C5, C8 or C2, C3, C6, C7*), 55.9 (2 × *C11*), *m/z* (TOF MS ES+): [M + NH_4] calculated mass: 256.1338, observed mass: 256.1336.

Data in agreement with those reported in the literature.[9]

Compound 2.56: *2-(bis(4-methoxyphenyl)(phenyl)methoxy)ethan-1-ol*

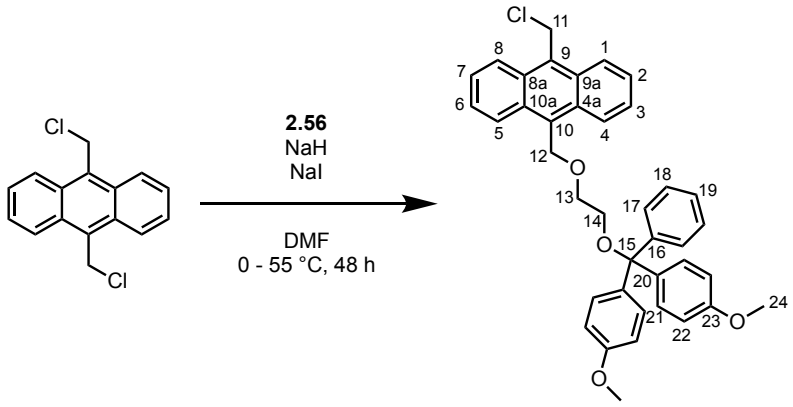


2.54 **2.55** **2.56**

A solution of anhydrous ethylene glycol **2.54** (0.06 mL, 1.062 mmol) in pyridine (5 mL) was prepared and DMTCl **2.55** (200 mg, 0.590 mmol) added to the reaction mixture at RT. The reaction mixture was stirred at RT for 4 h until consumption of the starting material DMTCl by TLC (70:29:1 hexane: EtOAc: Et_3N). At this point the reaction mixture was diluted with CH_2Cl_2 (5 mL) and washed twice with $NaHCO_3$ (sat. aq. soln. 2 × 15 mL), dried over $MgSO_4$ and filtered before removal of the solvent under reduced pressure. The crude residue was purified by flash chromatography (70:29:1 hexane:EtOAc:Et_3N) to yield the bis-protected form as a colourless oil (85.7 mg, 22%) and the mono-protected title compound as a colourless oil (80.4 mg, 37%), IR ν_{max}/cm^{-1}: 3394 (br, OH), 2931 (ArCH), 1242 (s, C-O, ether), ^{1}H NMR (400 MHz, CD_3CN) δ 7.51 – 7.43 (m, 2H, *H5*), .37 – 7.31 (m, 4H, *H9 or H10*), 7.31 – 7.27 (m, 2H, *H6*), 7.26 – 7.17 (m, 1H, *H7*), 6.90 – 6.82 (m, 4H, *H9 or H10*), 3.76 (s, 6H, *H12*), 3.62 (t, *J* = 4.9 Hz, 2H, *H1*), 3.06 (dd, *J* = 5.4, 4.6 Hz, 2H, *H2*) 2.90 (s, 1H, *OH*), ^{13}C NMR (101 MHz, CD_3CN) δ 159.1 (*2 × C11)*, 146.0 (*C3*), 136.9 (*C4*), 130.6 (*2 × C9 or C10)*, 128.7 (*C5*), 128.3 (*C6*), 127.3 (*C7)*, 117.9 (*2 × C8*), 113.0 (*2 × C9 or C10)*, 86.2, 65.8 (*C2*), 61.8 (*C1*), 55.4 (*2 × C12*), *m/z* (TOF MS AP+ve) calculated mass (M+H) 364.44, observed mass: 303.1388 (DMT fragment).

Data in agreement with those reported in the literature.[10]

***Compound 2.57**:9-((2-(bis(4-methoxyphenyl)(phenyl)methoxy)ethoxy)methyl)-10-(chloromethyl)anthracene*



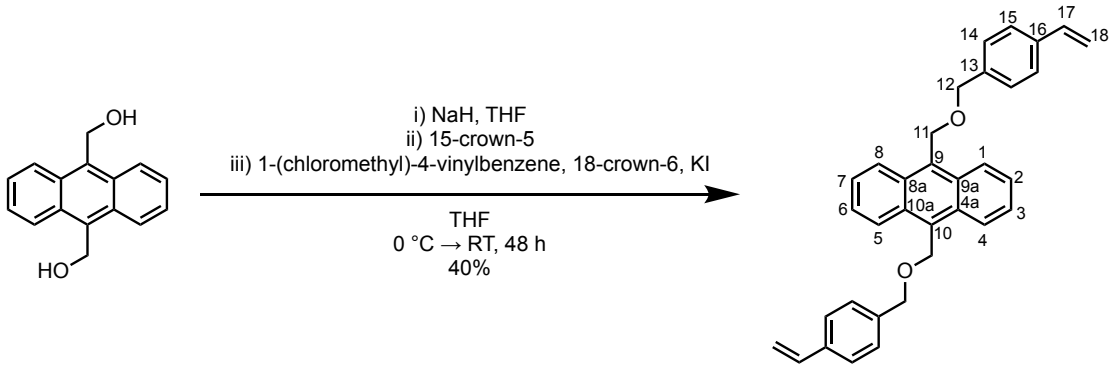
2.48 **2.57**

A solution of DMT protected ethylene glycol **2.56** (502.3 mg, 1.38 mmol) and NaI (82.7 mg, 0.552 mmol) in DMF (4 mL) was stirred at 0 ºC for 10 min before addition of **2.48** (379.4 mg, 1.38 mmol). During this, a solution of NaH (167.0 mg, 1.38 mmol, 60% dispersion in mineral oil) was prepared in DMF (3 mL) and subsequently added to the reaction mixture at 0 ºC over 5 min. The reaction mixture was allowed to come up to room temperature and stirred for 24 h at this temperature, then heated at 55 ºC for a further 24 h until consumption of the starting material by TLC (2:2:1 PhMe: $CHCl_3$: EtOAc). The reaction mixture was allowed to cool to RT then diluted with H_2O (25 mL) and extracted into EtOAc (3 × 10 mL). The aqueous layer was washed further with CH_2Cl_2 (5 × 5 mL), the organic layers combined and dried over Na_2SO_4 and filtered, then the solvent removed under reduced pressure. The residue was purified via flash column chromatography (2:2:1 PhMe: $CHCl_3$: EtOAc) to yield the title compound as an orange-yellow oil (69.1 mg, 18%), IR (in DMSO-d6) (ν_{max}/cm^{-1}): 3453 (br, OH), 1024 (s, C-O, primary alcohol), ^{1}H NMR (300 MHz, $CDCl_3$) δ 8.44 – 8.35 (m (AA'BB' in ODCB type splitting), 4H, *H1, H4, H5, H8*), 7.71 – 7.62 (m (AA'BB' in ODCB type splitting), 4H, *H2, H3, H6, H7*), 7.46 – 7.41 (m, 2H, *H18*), 7.36 – 7.28 (m, 6H, *H17, H21*), 7.23 – 7.17 (m, 1H, *H19*), 6.86 – 6.79 (m, 4H, *H22*), 5.62 (4H, *H11, H12*), 3.79 (s, 6H, *H24*), 3.76 – 3.70 (m, 2H, *H13 or*

H14), 3.25 (m, 2H, *H13 or H14*).^{13}C NMR (101 MHz, DMSO) (Fragmented compound observed only) δ 158.5 (*2 × C23*), 145.7 (qC, *2 × C20*), 136.5 (*2 × C21)*, 130.2 (*2 × C17*), 129.4(*2 × C18*), 128.2 (qC, *C16*), 127.0 (*C19*), 113.6 (*4 × C22*), 85.5 (qC, *C15*), 65.6 (*C13 or C14*), 60.8 (*C13 or C14*), 55.5 (*2 × C24*), *m/z* (TOF MS ES +) calculated mass: 602.22 observed mass: 303.14 (DMT fragment).

Data shows this compound fragments easily, the ethylene glycol moiety becoming removed from the anthracene.

***Compound 2.61**: 9,10-bis(((4-vinylbenzyl)oxy)methyl)anthracene*

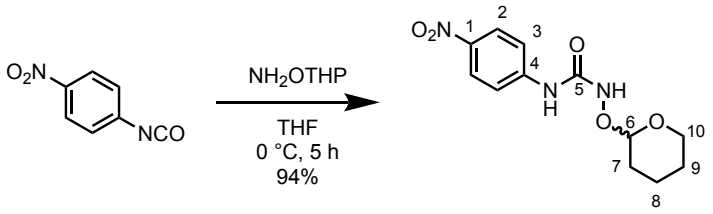


2.50 **2.61**

Diol **2.50** (250 mg, 1.05 mmol) was added to a flask containing sodium hydride (167 mg, 3.47 mmol) in THF (20 mL) at 0 ºC before addition of 15-crown-5 (764 mg, 3.47 mmol). The reaction mixture was stirred at 0 ºC for 30 min, whilst a solution of 1-(chloromethyl)-4-vinylbenzene (401 mg, 2.63 mmol), 18-crown-6 (695 mg, 2.63 mmol) and potassium iodide (437 mg, 2.63 mmol) in THF (15 mL) was prepared. The styrene mixture was added to the reaction mixture dropwise at 0 ºC over 10 min and the resultant reaction mixture was stirred at room temperature for 20 h until the starting material was consumed by TLC. The reaction mixture was subsequently extracted with EtOAc (3 × 20 mL), dried over $MgSO_4$, filtered and the solvent removed under reduced pressure to give an orange oil. The residue was purified by flash column chromatography (1:8 EtOAc: hexane, dry loaded) to yield the product as a fluffy yellow solid (189 mg, 40%). IR (ν_{max}/cm^{-1}): 2922 (ar C-H), 2857 (ar C-H), 1087 (aliphatic C-O), ^{1}H NMR (400 MHz, $CDCl_3$) δ 8.36 (m (AA'BB' in ODCB type splitting), *H1, H4, H5, H8 or H2, H3, H6, H7*), 7.60 – 7.48 (m, (AA'BB' in ODCB type splitting), 4H, *H1, H4, H5, H8 or H2, H3, H6, H7*), 7.46 – 7.39 (m, 4H, *H14*), 7.36 (m, 4H, *H15*), 6.74 (dd, *J* = 18.0, 11.0 Hz, 2H, *H17*), 5.77 (dd, *J* = 17.7, 1.1 Hz, 2H, *H18 or H19*), 5.50 (s, 4H, *H11 or H12*) 5.26 (dd, *J* = 10.9, 1.1 Hz, 2H, *H18 or H19*), 4.69 (s, 4H, *H11 or H12*), ^{13}C NMR (101 MHz, $CDCl_3$) δ 138.0 (qC), 137.1 (qC), 136.6 (CH=C, *C17*), 130.8 (qC), 130.3 (qC), 128.3 (Ar C, 4 × *C15*), 126.3 (Ar C, 4 × *C13 or C14*), 125.7 (Ar C, *C1, C4, C5, C8 or C2, C3, C6, C*), 125.0

(Ar C, *C1, C4, C5, C8 or C2, C3, C6, C*), 113.9 (C=CH_2, *C18,19*), 72.1 (CH_2, *C11 or C12*), 64.1 (CH_2, *C11 or C12*). *m/z* (TOF MS ASAP+ve) calculated mass: 470.2246, observed mass: 470.2250.

Compound 2.71: *1-(4-nitrophenyl)-3-((tetrahydro-2H-pyran-2-yl)oxy)urea*

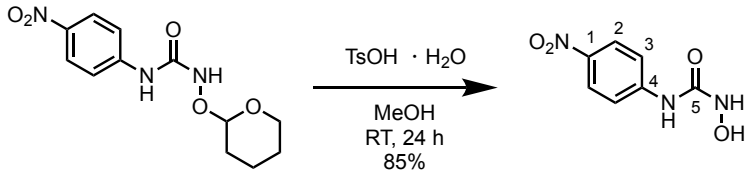


2.70 **2.71**

A solution of NH_2OTHP (357 mg, 3.05 mmol) in THF (3 mL) was added dropwise over 5 min to a solution of 4-nitrophenyl isocyanate **2.70** (500 mg, 3.05 mmol) in THF (10 mL) at 0 ˚C. The reaction mixture was stirred at 0 ˚C for 5 h. Upon allowing to warm to room temperature, the solvent was removed under reduced pressure and the residue purified via flash column chromatography (EtOAc: hexane 2:3) to give the title compound as a yellow solid (763.4 mg, 94%); MP: 146-149 ºC (recrystalised from $CDCl_3$), IR (ν_{max}/cm^{-1}): 3353 (NH), 3179, 3092, 2949 (CH_2), 2934 (CH_2), 2921 (CH_2), 1691 (CO), 1501 (NO). ^1H NMR (400 MHz, $CDCl_3$) δ 8.62 (s, 1H, CN*H*), 8.25 – 8.13 (m, 2H, *H2)*, 7.65 – 7.60 (m, 2H, *H3)*, 4.91 – 4.81 (m, 1H, *H6)*, 4.15 – 4.02 (m, 1H, *H10a)*, 3.87 – 3.41 (m, 1H, *H10b)*, 1.94 – 1.85 (m, 2H, *H8)*, 1.70 – 1.33 (m, 4H, *H7, H9)*. ^{13}C NMR (101 MHz, $CDCl_3$) δ 157.5 *(C5)*, 143.9 *(C1 or C4)*, 143.1 *(C1 or C4)*, 125.1 *(C2)*, 118.5 *(C3)*, 106.0 *(C6)*, 65.8 *(C10)*, 29.0 *(C7 or C9)*, 24.7 *(C7 or C9)*, 20.9 *(C8)*. *m/z* (TOF MS ASAP+ve) calculated mas: 282.1083, observed mass: 282.1082.

Data in agreement with that reported in literature[7]

Compound 2.65: *1-hydroxy-3-(4-nitrophenyl)urea*



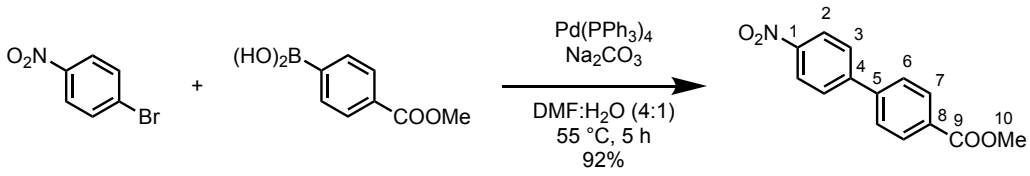
2.71 **2.65**

Known compound – procedure followed as described in literature.[7]

Acid TsOH.H_2O (36.1 mg, 0.190 mmol) was added to a solution of protected hydroxyurea **2.71** (500 mg, 1.89 mmol) in MeOH (20 mL) and stirred for 24 h at RT. The solvent was removed under reduced pressure and the residue purified via flash column chromatography (EtOAc: hexane 2:1) to give a yellow crystalline solid (314 mg, 85%); MP: 150-152 ºC (recrystalised from EtOAc and *hexane*), IR (ν_{max}/cm^{-1}): 3364 (NH), 3324 (NH), 3151, 2871 (OH), 1689 (C=O), 1548 (NO), 1326 (OH); ^{1}H NMR (400 MHz, DMSO-d_6) δ 9.52 (s, 1H, O*H*), 9.29 (s, 1H, ArN*H*) or N*H*OH), 9.16 (s, 1H, ArN*H*) or N*H*OH), 8.29 – 8.03 (m, 2H, *H2)*, 8.03 – 7.80 (m, 2H, *H3)*; ^{13}C NMR (101 MHz, DMSO) δ 158.2 *(C5)*, 146.8 *(C1)*, 141.7 *(C4),* 125.2 *(C2),* 118.8 *(C3)*; *m/z* (TOF MS ES−) 196.03 (100%).

Data in agreement with that reported in the literature.[7]

Compound 2.74: *methyl 4'-nitro-[1,1'-biphenyl]-4-carboxylate*



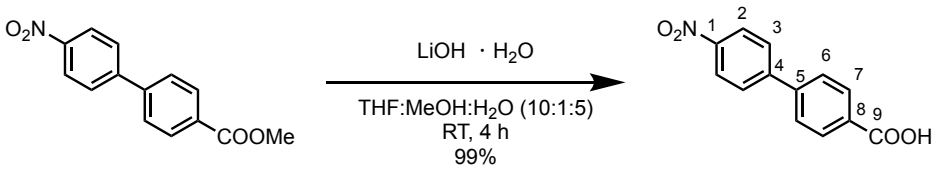
2.72 **2.73** **2.74**

Known compound – procedure followed as described in literature.[7]

A solution of 1-bromo-4-nitrobenzene (374 mg, 1.85 mmol), $Pd(PPh_3)_4$ (111 mg, 0.096 mmol) and Na_2CO_3 (393 mg, 3.70 mmol) in DMF (10 mL) and H_2O (3 mL) was prepared and 4-methoxycaronylboronic acid (500 mg, 2.78 mmol) was added and the reaction mixture was heated at 55 ºC for 16 h. On evidence of starting material consumption by TLC, the reaction mixture was allowed to cool to RT and diluted with H_2O (15 mL) before being extracted into EtOAc (3 × 10 mL) and filtered over celite. The organic layer was then washed with brine (1 × 10 mL) and dried over $MgSO_4$ and the solvent removed under reduced pressure to reveal a creamy brown residue. The residue was then purified by flash column chromatography (3:1 PhMe:$CHCl_3$) to give the title compound as a white solid (342.3 mg, 72%), MP: 185-190 ºC (recrystalised from $CHCl_3$), IR (ν_{max}/cm^{-1}): 1717 (C=O), ^{1}H NMR (300 MHz, $CDCl_3$) δ 8.55 – 8.26 (m, 2H, *H2)*, 8.22 – 8.11 (m, 2H, *H3*), 7.81 – 7.74 (m, 2H, *H6)*, 7.72 – 7.66 (m, 2H, *H7*), 3.96 (s, 3H, *H10)*. ^{13}C NMR (101 MHz, $CDCl_3$) δ 166.9 (CO, *C9*), 145.4 (C), 141.9 (C), 131.0 (C), 130.1 (CH, *C7*), 128.3 (CH), 127.5 (CH), 124.2 (CH, *C2*). *m/z* (TOF ASAP +ve) 258.08 (100%).

Data in agreement with the literature.[7]

Compound 2.75: *4'-nitro-[1,1'-biphenyl]-4-carboxylic acid*



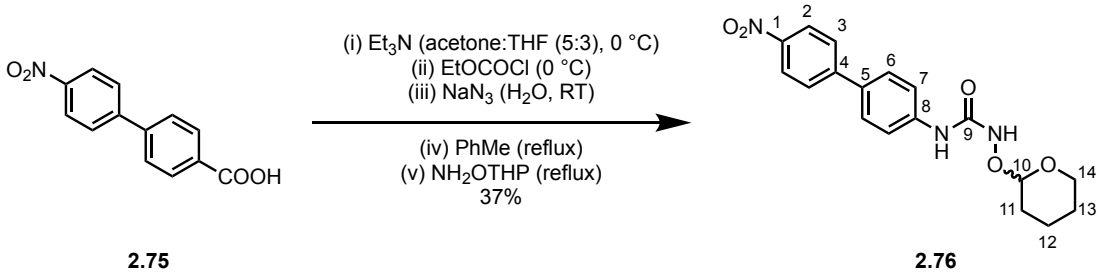
2.74 **2.75**

Known compound – procedure followed as described in literature.[7]

A solution of ester **2.67** (57 mg, 0.22 mmol) in THF (15 mL) and MeOH (15 mL) was prepared and stirred at RT. A solution of $LiOH{\cdot}H_2O$ (46 mg, 1.1 mmol) in H_2O (5 mL) was prepared and added to the reaction mixture at RT, then the mixture left stirring for 3 h until consumption of the starting material by TLC (3:1 PhMe: $CHCl_3$). H_2O (20 mL) was added to the reaction mixture and the mixture washed with Et_2O (2 × 10 mL). The aqueous layer was acidified with HCl (2 M, 2 mL) dropwise and the white precipitate formed was collected by filtrating under suction to yield the title compound as a white solid (53 mg, >99%). MP: decomposition to yellow at 187-190 ºC (recrystallised from THF: hexane), IR (ν_{max}/cm^{-1}): 2942 (Ar C-H), 2603 (s, br, CO*OH*), 1805 (C=O), ^{1}H NMR (400 MHz, DMSO-d_6) δ 13.13 (s, 1H, *OH*), 8.39 – 8.30 (m, 2H, *H2 or H7*), 8.13 – 7.99 (m, 4H, *H3,H6*), 7.96 – 7.89 (m, 2H, *H2 or H7*), ^{13}C NMR (101 MHz, DMSO) δ 167.4 (CO, *C9*), 147.7 (qC), 145.9 (qC), 142.3 (qC), 131.5 (qC), 130.6 (qC), 130.5 (*2 × C3 or C6*), 128.8 (*2 × C3 or C6*), 128.0 (*2 × C2 or C7*), 124.7 (*2 × C2 or C7*), *m/z* (TOF MS ASAP+) calculated mass: 244.0623 observed mass: 244.0632.

Data in agreement with the literature.[7]

Compound 2.76: *1-(4'-nitro-[1,1'-biphenyl]-4-yl)-3-((tetrahydro-2H-pyran-2-yl)oxy) urea*



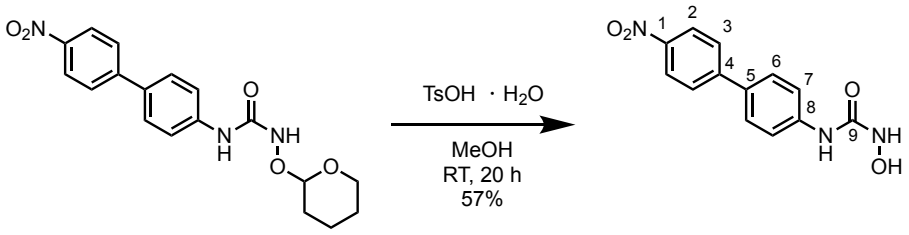
2.75 **2.76**

Acid **2.75** (298 mg, 1.23 mmol) was dissolved in acetone (6 mL, dried over $MgSO_4$) and THF (3 mL), cooled to 0 °C and Et_3N (0.22 mL, 1.60 mmol) was added, turning the yellow suspension to a red solution. After 10 min stirring at 0 °C, EtOCOCl (200 mg,1.85 mmol) was added to the reaction mixture. After loss of the starting material was observed by TLC (70:30:1 *hexane*: EtOAc: Et_3N) and IR, a solution of NaN_3 (288 mg, 4.43 mmol) in H_2O (2 mL) was added dropwise over 2 min and the reaction mixture was allowed to warm to room temperature and stirred for a further 2 h. On appearance of the azide by TLC and IR, the reaction mixture was diluted with H_2O (10 mL), extracted into PhMe (3 × 5 mL), washed with Na_2CO_3 (10 mL) and brine (10 mL) then concentrated under reduced pressure to approx. 5 mL. The reaction mixture was subsequently heated at reflux until full conversion to the isocyanate was seen by TLC and IR, then NH_2OTHP (721 mg, 6.15 mmol) was added to the reaction mixture and heated at reflux for a further 16 h. Upon completion, the reaction mixture was concentrated under reduced pressure and purified by flash column chromatography (70:30:1 *hexane*: EtOAc: Et_3N) to give the title compound as a yellow-orange solid (162.7 mg, 37%), MP: 134 -136 ºC (recrystallised from $CDCl_3$), IR (ν_{max}/cm^{-1}): 3017 (Ar C-H), 2944 (Ar C-H), 1215 (C-N), ^1H NMR (300 MHz, $CDCl_3$) δ 8.33 – 8.17 (m, 2H, *H2 or H7*), 7.73 – 7.62 (m, 2H, *H3 or H6*), 7.52 – 7.39 (m, 2H, *H2 or H7*), 6.83 – 6.68 (m, 2H, *H3 or H6*), 5.47 (s, 2H, *NH*), 4.71 (t, *J* = 3.8 Hz, 1H, *H10*), 3.98 – 3.81 (m, 3H), 3.65 – 3.50

(m, 1H), 1.74 (m, 1H), 1.27 (m, 2H). ^{13}C NMR (101 MHz, $CDCl_3$) δ 157.71, 146.99, 138.67, 133.81, 128.47, 128.02, 127.30, 126.48, 124.18, 119.83, 115.38, 105.52, 65.43, 29.00, 24.79, 20.78, *m/z* (TOF MS ES+) calculated mass [M+Na]: 380.36, observed mass: 380.12.

Data differs to that of the literature (only ^{1}H NMR given) and different procedure was required.[7]

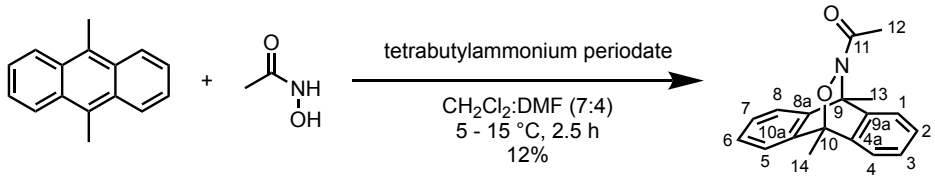
***Compound 2.69**: 1-hydroxy-3-(4'-nitro-[1,1'-biphenyl]-4-yl) urea*



2.76 **2.69**

The protected hydroxyurea **2.76** (11.3 mg, 0.032 mmol) was dissolved in MeOH (3 mL) and TsOH · H_2O (2 mg, 0.006 mmol) was added to the reaction mixture and stirred at RT for 20 h until consumption of the starting material by TLC (1:2:1 PhMe: $CHCl_3$: EtOAc). A colour change from an orange solution to colourless was observed on addition of the TsOH · H_2O. The solvent was removed under reduced pressure and the residue purified via flash column chromatography (1:2:1 PhMe: $CHCl_3$: EtOAc) to give the title compound as an orange crystalline solid (4.9 mg, 57%). MP: 184 -186 ºC (recrystallised from MeOH), IR (ν_{max}/cm^{-1}): 3413 (*NH*), 2918 (Ar CH), 2460, 1588 (CO, *C9*), 1493 (NO), ^{1}H NMR (300 MHz, CD_3OD) δ 8.25 – 8.21 (m, 2H, *H2 or H7*), 7.79 – 7.75 (m, 2H, *H3 or H6*), 7.52 – 7.49 (m, 2H, *H2 or H7*), 6.81 – 6.79 (m, 2H, *H3 or H6*), 4.58 (s, 1H, *OH*). ^{13}C NMR (101 MHz, $CDCl_3$) δ 147.6 (CO, *C9*), 128.5 (2 × *C2 or C7*), 128.1 (qC, *C1, C8 or C4, C5*), 127.3 (qC, *C1, C8 or C4, C5*), 126.5 (2 × *C3 or C6*), 124.2 (2 × *C2 or C7*), 115.4 (2 × *C3 or C6*), *m/z* (TOF MS ES+) calculated mass: 273.07, observed mass: 215.09 (expect fragmentation of C=ONHOH, leaving the amine + H^+ (calculated mass of amine: 214.7).

Compound 2.78: *1-((9S,10Ss)-9,10-dimethyl-9,10-dihydro-9,10-(epoxyimino) anthracen-11-yl) ethan-1-one*

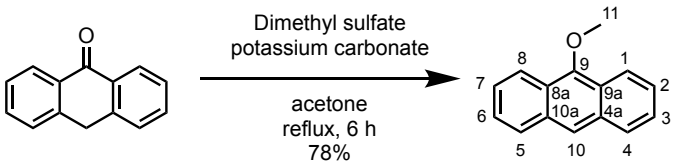


2.14 **2.77** **2.78**

Commercially available 9,10-dimethyl anthracene **2.14** (150 mg, 0.727 mmol) was dissolved in CH_2Cl_2 (7 mL) and cooled to 5 ˚C before addition of tetrabutylammonium periodate (473mg, 1.09 mmol). The reaction mixture was stirred at 5 ˚C for 10 min, then a solution of acetohydroxamic acid **2.77** (82.0 mg, 1.09 mmol) in DMF (4 mL) was added dropwise to the reaction mixture over 3 min and the reaction temperature allowed to range from 5 – 15 ˚C whilst stirring for 2.5 h until consumption of the starting material by TLC (95:5 hexane: EtOAc). The reaction mixture was diluted with CH_2Cl_2 (10 mL, cooled in an ice bath) and washed with sat. aq. $NaHCO_3$ (2 × 10 mL, cooled in an ice bath), brine (2 × 10 mL, cooled in an ice bath) and dried over Na_2SO_4 before filtration and the removal of solvent under reduced pressure. The residue was purified by flash column chromatography (95:5 *hexane*: EtOAc gradient to 90:10 hexane: MeOH) to give the title compound as a pale yellow crystalline solid (24.5 mg, 12%), IR (ν_{max}/cm^{-1}): 2983 (Ar C-H), 1675 (C=O, amide), 1281 (C-N), ^{1}H NMR (400 MHz, $CDCl_3$) δ 7.50 – 7.43 (m, 2H, *H1, H8 or H4, H5*), 7.39 – 7.33 (m, 2H, *H1, H8 or H4, H5*), 7.30 – 7.20 (m, 4H, *H2, H3, H6, H7*), 2.70 (s, 3H, *H13 or H14*), 2.22 (s, 3H, *H13 or H14*), 1.83 (s, 3H, *H12*), ^{13}C NMR (101 MHz, $CDCl_3$) δ 176.7 (CO, *C11*), 141.3 (qC, *C9 or C10*), 141.1 (qC, *C9 or C10*), 127.5 (*C2, C7 or C3, C6*), 127.2 (*C2, C7 or C3, C6*), 121.4 (*C1, C8 or C4, C5*), 120.6 (*C1, C8 or C4, C5*), 79.6 (*C8a, C9a or C4a, C10a*), 63.8 (*C8a, C9a or C4a, C10a*), 24.9 (*C12*), 16.81 (*C13 or C14*), 15.1 (*C13 or C14*), *m/z* (TOF MS ASAP+) calculated mass]: 280.1338, observed mass: 280.1343.

Data in agreement with the literature though different procedure used.[11]

Compound 2.87: *9-methoxyanthracene*

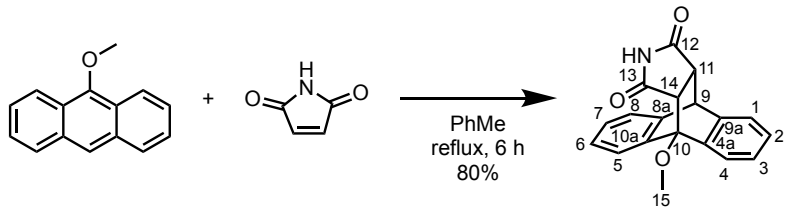


2.87

Commercially available anthrone (300 mg, 1.55 mmol) was dissolved in acetone (15 mL) and purged under argon before potassium carbonate (939 mg, 6.80 mmol) was added. Dimethyl sulfate (0.32 mL, 3.32 mmol) was added and the reaction mixture was heated at reflux for 6 h until consumption of the starting material by TLC (95:5 hexane: EtOAc). Upon completion, the reaction mixture was allowed to cool to room temperature and poured over CH_2Cl_2 (20 mL) and hexane (20 mL). The organic layer was subsequently washed with water (20 mL) and brine (20 mL), dried over Na_2SO4, filtered and the solvent removed under reduced pressure. Purification by flash chromatography (95:5 hexane: EtOAc) gave the title compound as a white crystalline solid (244.2 mg, 78%); 92-94 °C (from CH_2Cl_2 and hexane), IR (ν_{max}/cm^{-1}): 3047 C-H aromatic, 2961 C-H, 1728 CO carbonyl, 1458 CH, 1041 CO vinyl ether; ^{1}H NMR (400 MHz, $CDCl_3$) δ 8.38 – 8.35 (m, 2H, *H4, H5*), 8.26 (s, 1H, *H10*), 8.08 – 7.98 (m, 2H, *H1,H8*), 7.61 – 7.44 (m, 4H, *H2,H3,H6,H7*), 4.19 (s, 3H, *H11*), ^{13}C NMR (101 MHz, $CDCl_3$) δ 152.0 (*C9*), 132.2 (*C8a,C9a or C4a,C10a*), 128.3 (*C1,C8*), 125.3 (*C2,C7 or C3,C6*), 125.0 (*C2,C7 or C3,C6*), 124.2 (*C8a,C9a or C4a,C10a*), 122.1 (*C4,C5 or C10)*, 122.0 (*C4,C5 or C10*), 63.0 (*C11*), *m/z* (TOF MS ASAP+) calculated mass: 209.0966, observed mass: 209.0972 (M+H).

Data in agreement with the literature.[12]

***Compound 2.89**: (9R,10R,11R,15R)-9-methoxy-9,10-dihydro-9,10-[3,4] epipyrroloanthracene-12,14-dione*

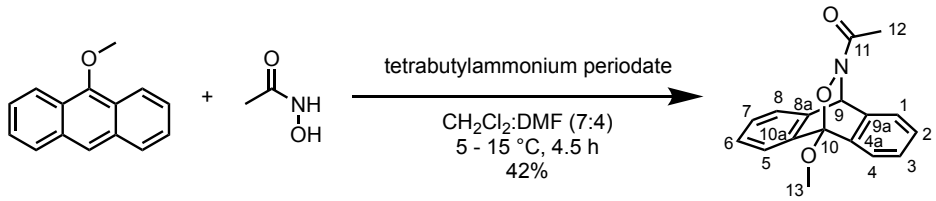


2.87 **2.88** **2.89**

Reaction procedure based on similar literature:[13]

A solution of 9,10 dimethyl anthracene (57 mg, 0.273 mmol) was prepared in PhMe (7 mL) and maleimide (26.5 mg, 0.273 mmol) was added at room temperature. The reaction mixture was then heated at reflux for 6 h until consumption of starting material by TLC (95:5 hexane: EtOAc). The reaction mixture was then allowed to cool to room temperature and the resulting precipitate was collected by filtration under reduced pressure to yield the title compound as a white crystalline solid (67 mg, 80%), IR (ν_{max}/cm^{-1}): 3184 (NH), 3072 (Ar C-H), 2841 (Ar C-H), 1701 (CO, *C18/19*), 1343 (CN, *C18/19*), 1083 (C-O, *C15*),^{1}H NMR (400 MHz, DMSO-d6) δ 10.83 (s, 1H, *NH*), 7.53 – 7.46 (m, 1H, *One of H1, H8, H4, H5*), 7.42 (td, *J* = 7.6, 1.5 Hz, 2H, *H1, H8 or H4, H5*), 7.29 – 7.08 (m, 5H, *H2, H3, H6, H7* and either *H1, H8, H4, H5*), 4.67 (d, *J* = 3.3 Hz, 1H, *H9*), 3.97 (s, 3H, *H15*), 3.75 (d, *J* = 8.8 Hz, 1H, *H11 or H14*), 3.37 (d, *J* = 3.4 Hz, 1H, *H11 or H14*), ^{13}C NMR (101 MHz, DMSO-d6) δ 178.1 (CO, *C12 or C13*), 176.2 (CO, *C12 or C13*), 142.4 (qC, *C4a, C8a, C9a or C10a*), 141.7 (qC, *C4a, C8a, C9a or C10a*), 141.3 (qC, *C4a, C8a, C9a or C10a*), 138.1 (qC, *C4a, C8a, C9a or C10a*), 126.9 (*C2, C3, C6 or C7*), 126.8 (*C2, C3, C6 or C7*), 126.8 (*C2, C3, C6 or C7*), 126.4 (*C2, C3, C6 or C7*), 124.8 (*One of C1, C8, C4, C5*), 121.7 (*C1, C8 or C4, C5*), 81.7 (qC, *C10*), 54.1 (*C15*), 48.9 (*C11 or C14*), 46.1 (*C11 or C14*), 43.8 (*C9*), *m/z* (TOF MS ASAP+) calculated mass: 306.1130, observed mass: 306.1133 (M+H). Data in agreement with similar compounds in literature[13]

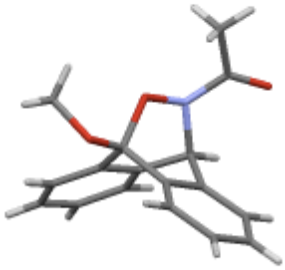
Compound 2.88: *1-((9s,10s)-9-methoxy-9,10-dihydro-9,10-(epoxyimino)anthracen-11-yl)ethan-1-one*



2.87 **2.77** **2.90**

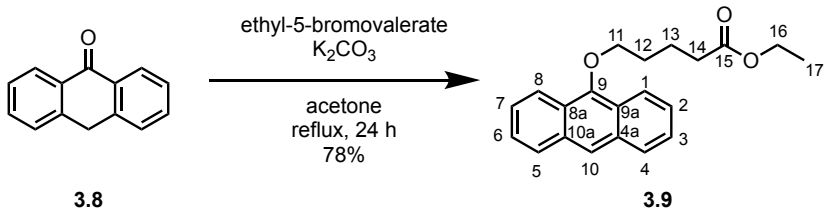
Methoxy-anthracene **2.85** (120 mg, 0.576 mmol) was dissolved in CH_2Cl_2 (7 mL) over heat-activated molecular sieves and cooled to 5 ˚C using an ice-water bath. The acetohydroxamic acid **2.77** (216 mg, 2.88 mmol) was dissolved in DMF (4 mL) and added dropwise to the reaction mixture over 5 min at 5 ˚C. The reaction mixture was stirred for 4.5 h at a temperature range of 5 – 15 ˚C until consumption of the starting material by TLC (95:5 hexane: EtOAc). The reaction mixture was washed with $NaHCO_3$ (sat. aq. soln., cold) and extracted into CH_2Cl_2 (3 × 10 mL) before drying over Na_2SO_4, filtering and removing the solvent under reduced pressure. The residue was purified by flash column chromatography (gradient 95:4:1 - 5:94:1 *hexane*: EtOAc: Et_3N) to give the title compound as an orange crystalline solid (68.5 mg, 42%) Product was determined to be unstable and subject to decomposition within 2 h; ^{1}H NMR (400 MHz, $CDCl_3$) δ 7.58 – 7.51 (m, 2H, *H1, H8*), 7.46 – 7.38 (m, 2H, *H4, H5*), 7.33 – 7.19 (m, 4H, *H2, H3, H6, H7*), 6.60 (s, 1H, *H9*), 4.07 (s, 3H, *H13*), 1.97 (s, 3H, *H12*), ^{13}C NMR (101 MHz, $CDCl_3$) δ 172.4 (CO, *C11*), 138.7 (qC, *C4a, C10a or C8a, C9a*), 138.3 (qC, *C4a, C10a or C8a, C9a*), 128.0 (*C2, C7 or C3, C6*), 127.4 (*C2, C7 or C3, C6*), 123.5 (*C4, C5*), 121.0 (*C1, C8*), 105.7 (qC, *C10*), 56.8 (*C9*), 54.2 (*C13*), 21.8 (*C12*), *m/z* (TOF MS ASAP+) calculated mass: 282.1130, observed mass: 282.1136. Regioisomer determined by X-ray crystallography: Crystal Data for $C_{17}H_{15}NO_3$ (*M* =281.30 g/mol): monoclinic, space group $P2_1/n$ (no. 14), *a* = 9.2271(3) Å, *b* = 12.3386(6) Å, *c* = 11.9834(5) Å, *β* = 93.774(4)°, *V* = 1361.35(10) Å^3, *Z* = 4, *T* = 100.01(10) K, μ(Cu Kα) = 0.771 mm^{-1}, *Dcalc* = 1.372 g/cm^3, 10024 reflections measured (10.302° ≤ 2Θ ≤ 146.05°), 2688

unique (R_{int} = 0.0291, R_{sigma} = 0.0228) which were used in all calculations. The final R_1 was 0.0383 (I > 2σ(I)) and wR_2 was 0.1050 (all data). Crystals grown by evaporation from flash chromatography eluent.



Decomposition species IR: (neat, cm $^{-1}$): ν = 3201 (OH), 2933 (Ar C-H), 1671 (CO), 1652 (CO).

***Compound 3.9**: ethyl 5-(anthracen-9-yloxy) pentanoate*



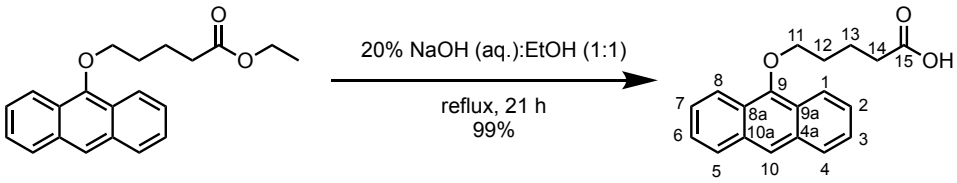
3.8 **3.9**

Known compound - procedure followed as described in literature.[14, 15]

A solution of degassed acetone (20 mL), anthrone (3.000 g, 15.45 mmol) and K_2CO_3 (2.135 g, 15.45 mmol) were added together and stirred at room temperature in the absence of light for 15 min. Keeping the flask in the dark, ethyl 5-bromovalerate (1.00 mL, 6.318 mmol) was added and the reaction mixture was heated at reflux for 24 h. The reaction mixture was then allowed to cool to room temperature, filtered to remove salts and the solvent removed under reduce pressure. The crude residue was re-dissolved in CH_2Cl_2 (25 mL), washed with H_2O (3 × 10 mL), dried over $MgSO_4$ and the solvent removed under reduced pressure to give an orange oil which solidified upon standing. Purification of the crude residue by flash column chromatography (9:1 hexane: EtOAc) gave in order of elution, the oxidation product anthraquinone (yellow solid) and the title compound as a white solid (1.5943g, 78 %) (R_f = 0.40 in 9:1 hexane: EtOAc); MP 71-74 °C (from CH_2Cl_2); IR (ν_{max}/cm^{-1}): 3047 (Ar C-H)*,* 2961 *C-H*, 1728 (C=O*, C15*) 1458 (CH*)*, 1041 (*C-O vinyl ether, C16*); ^{1}H NMR (400 MHz, $CDCl_3$) δ 8.35 – 8.23 (2H, m, *H1,H8*), 8.22 (1H, s, *H10*), 8.05 – 7.94 (2H, m, *H4, H5*), 7.58 – 7.39 (4H, m, *H2,H3,H6,H7*), 4.35 – 3.93 (4H, m, *H11,H16*), 2.50 (2H, t, *J* = 7.1 Hz, *H14*), 2.16 – 1.98 (4H, m, *H12,H13*), 1.29 (3H, t, *J* = 7.1 Hz, *H17*); ^{13}C NMR (101 MHz, $CDCl_3$) δ 173.5 (CO, *C15*), 151.3 (C, *C9*), 132.5 (C, *C4a, C10a*), 128.5 (CH, *C4, C5*), 125.5 (CH, *C2, C7*), 125.2 (CH*, C3, C6*), 124.7 (C, *C8a, C9a*), 122.4 (CH, *C1, C8*), 122.1 (CH, *C10*), 75.5 (CH_2, *C11*), 60.4 (CH_2, *C16*), 34.2 (CH_2, *C14*), 30.1 (CH_2, *C13*), 21.9 (CH_2, *C12*), 14.3 (CH_3, *C17*); *m/z*

(TOF MS ES+) calculated mass [M + Na]: 345.1467, observed mass: 345.1469. Data in agreement with the literature.[14]

Compound 3.10: *5-(anthracen-9-yloxy)pentanoic acid*



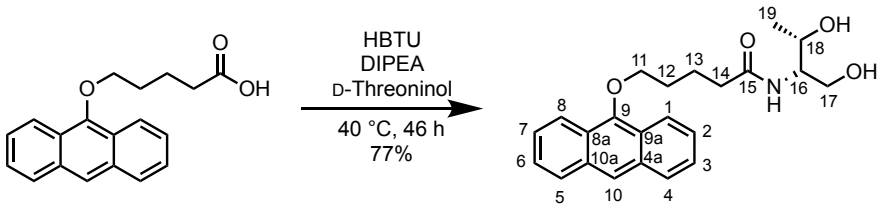
3.9 **3.10**

Known compound - procedure followed as described in literature.[14, 15]

A solution of (1:1 v:v) NaOH (20% w:v, aq.) in EtOH (not anhydrous) (40 mL total vol.) and ester **3.9** (2.200 g, 6.194 mmol) were added together and the reaction mixture heated at reflux in the absence of light for 21 h. Upon consumption of the starting material, the reaction mixture was allowed to cool to room temperature and subsequent dropwise addition of HCl (conc., 2 mL) over 5 min gave a cream precipitate which was collected by suction filtration. The solid was washed with H_2O (20 mL) and dried under vacuum to give the title compound as a cream solid (1.813 g, 99%). MP: 96 - 99 °C (from CH_2Cl_2), IR (ν_{max}/cm^{-1}): 3054 (*C-H aromatic*), 2871 *C-H*, 1708 (*CO carbonyl*), ^{1}H NMR (400 MHz, DMSO-d_6) δ 8.38 (1H, s, *H10*), 8.31 – 8.16 (2H, m, *H4,H5*), 8.14 – 8.01 (2H, m, *H1,H8*), 7.63 – 7.46 (4H, m, *H2,H3,H6,H7*), 4.15 (2H, t, *J* = 6.3 Hz, *H11*), 3.06 (1H, s, O*H*), 2.47 (2H, t, *J* = 7.2 Hz, *H14*), 2.08 – 1.82 (m, 4H, m, *H12,H13*); ^{13}C NMR (101 MHz, DMSO) δ 172.8 (CO, *C15*), 150.7 (C, *C*9), 131.9 (C, *C*4a*,C*10a), 128.5 (CH, *C*4*,C*5), 125.7 (CH, *C*2*,C*7), 125.5 (CH, *C*3*,C*6), 124.1 (C, *C*8a*,C*9a), 121.9 (CH, *C*1*,C*8, C*10*), 75.4 (CH_2, *C*11), 33.3 (CH_2, *C*14), 29.4 (CH_2, *C*12), 21.4 (CH_2, *C*13). *m/z* (TOF MS ES+) calculated mass [M + Na]: 317.1154, observed mass: 317.1155.

Data in agreement with the literature (melting point differs from literature value (104 ˚C)).[14, 15]

***Compound 3.11**: 5-(anthracen-9-yloxy)-N-((2S,3S)-1,3-dihydroxybutan-2-yl)pentanamide*



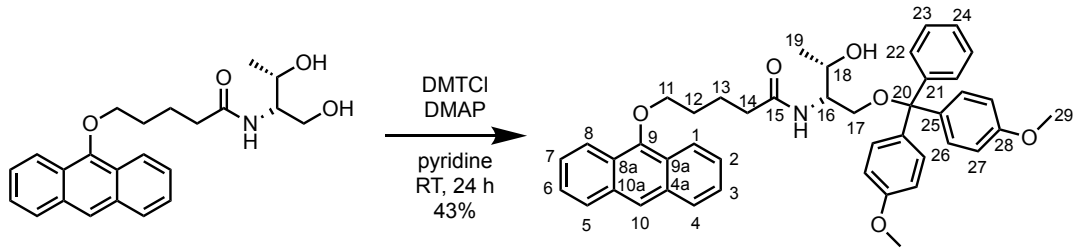
3.10 **3.11**

Known compound – procedure followed as described in literature.[14, 15]

To a solution of carboxylic acid **3.7** (323.8 mg, 1.100 mmol) in DMF (7 mL) was added HBTU (417.1 mg, 1.100 mmol) and the reaction mixture was stirred at RT for 15 min. Next, D-threoninol (115.7 mg, 1.100 mmol) and DIPEA (0.19 mL, 1.100 mmol) were added to the reaction mixture under argon and the resulting solution was stirred at 40 ˚C for 46 h. On disappearance of starting material by TLC, the reaction mixture was allowed to cool to RT, diluted with MeOH:CH_2Cl_2 (1:3, 20 mL) then washed with H_2O (3 × 10 mL) and dried over $MgSO_4$. The orange solution was filtered, and the solvent removed under reduced pressure to give an orange-red solid. The residue was purified by flash column chromatography (100:0 CH_2Cl_2 to 98:2 CH_2Cl_2: MeOH) to give the title compound as an orange oil which solidified upon standing to a fluffy yellow solid (321.1 mg, 77%). MP: 91 – 96 °C (from EtOAc: *hexane*), IR (ν_{max}/cm^{-1}): 3403 (*C-H*), 3229 (br, *OH*), 2967 (Ar C-H), 1641 (*CO carbonyl*), ^{1}H NMR (400 MHz, $CDCl_3$) δ 8.30 – 8.22 (m, 2H, *H4,H5)*, 8.20 (s, 1H, *H10)*, 8.03 – 7.95 (m, 2H, *H1,H8)*, 7.52 – 7.37 (m, 4H, *H2,H3,H6,H7)*, 6.43 (d, 2H, *NH)*, 4.24 – 4.14 (m, 3H, *H11,H18)*, 3.92 – 3.84 (m, 1H, *H16)*, 3.82 (dd, *J* = 4.1, 2.6 Hz, 2H, *H17)*, 2.46 (t, *J* = 8.0 Hz, 2H, *H14)*, 2.11 – 2.03 (m, 4H, *H12,H13)*, 1.20 (d, *J* = 6.4 Hz, 3H, *H19)*; ^{13}C NMR (101 MHz, $CDCl_3$) δ 173.9 *(C15)*, 151.1 *(C9)*, 132.4 *(C4a,C10a)*, 128.5 *(C4.C5)*, 125.5 *(C3,C6)*, 125.3 *(C2,C7)*, 124.7 *(C8a,C9a)*, 122.3 *(C1,C8)*, 122.2 *(C10)*, 75.6 *(C11)*, 68.7 *(C18)*, 65.0 *(C17)*, 54.8

(C16), 36.7 *(C14)*, 30.1 *(C12)*, 22.7 *(C13)*, 20.6 *(C19)*; *m/z* (TOF MS ES+) calculated mass [M + Na]: 382.2026, observed mass: 382.2023. Data in agreement with the literature.[14, 15]

***Compound 3.12**: 5-(anthracen-9-yloxy)-N-((2S,3S)-1-(bis(4-methoxyphenyl)(phenyl)methoxy)-3-hydroxybutan-2-yl)pentanamide*



3.11 **3.12**

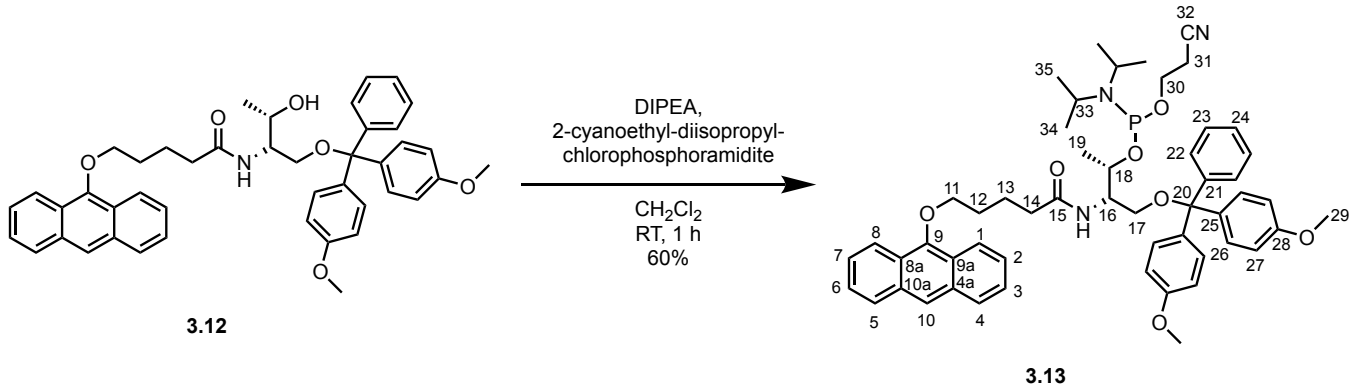
Known compound – procedure followed as described in literature.[14, 15]

To a foil-wrapped flask containing diol **3.10** (321.1 mg, 0.842 mmol) in pyridine (5 mL) was added DMTCl (285.3 mg, 0.842 mmol) and DMAP (15.4 mg, 0.842 mmol) sequentially and the reaction mixture was stirred at RT for 24 h. The reaction mixture was then poured over H_2O (30 mL), extracted with CH_2Cl_2 (3 × 20 mL) and dried over $MgSO_4$. The residue was then filtered, and the solvent removed under reduced pressure to give the crude product as an orange oil. Flash column chromatography (hexane: EtOAc: Et_3N 40:59:1) gave the title compound as a fluffy yellow solid (247 mg, 43%). MP: 68 – 71 °C (from EtOAc: hexane), IR (ν_{max}/cm^{-1}): 3328 (OH), 2945 (Ar C-H), 1640 (NH), 1507 (C=O, *C15*), (400 MHz, CD_3CN) δ 8.33 (s, 1H, *H10)*, 8.32 – 8.26 (m, 2H, *H4,H5)*, 8.13 – 8.02 (m, 2H, *H1,H8)*, 7.60 – 7.44 (m, 6H, *H26, H22*), 7.37 – 7.29 (m, 4H, *H27*), 7.27 – 7.18 (m, 1H, *H24*), 6.92 – 6.79 (m, 4H, *H2,H3,H6,H7)*, 6.46 (d, *J* = 8.9 Hz, 1H, *NH)*, 4.20 (t, *J* = 6.2 Hz, 2H, *H11)*, 4.01 – 3.94 (m, 2H, *H16,H18)*, 3.73 (s, 6H, *H29)*, 3.18 (dd, *J* = 9.1, 5.2 Hz, 1H, *H17a)*, 3.12 – 2.99 (m, 2H, *H17b, OH)*, 2.41 (t, *J* = 7.1 Hz, 2H, *H14)*, 2.13 – 2.06 (m, 2H, *H12,H13)*, 1.07 (d, *J* = 6.2 Hz, 3H, *H19)*; ^{13}C NMR (101 MHz, CD_3CN) δ 173.3 (CO, *C15*), 159.2 (*C21*), 136.6 (*2 × C25*), 132.9 (*C4a,C10a*), 130.5 (*4 × C26*), 128.9 (*C4,C5*), 128.6 (*2 × C22*), 128.4 (*2 × C23*), 127.3 (*C24*), 126.3 (*C2,C7*), 125.9 (*C3,C6*), 125.1 (*C8a,9a*), 122.8 (*C1,C8*), 122.5 (*C10*), 113.6 (*4 ×*

C27), 76.3 (*C11*), 66.9 (*C18*), 64.2 (*C17*), 55.4 (*2 × C29*), 54.8 (*C16*), 36.3 (*C14*), 30.4 (*C12 or C13*), 23.1 (*C12 or C13*), 20.2 (*C19*). *m/z* (TOF MS ASAP+) fragments observed: 303.14 (100%), 382.20 (30%) – anticipate loss of DMT protecting group (MW: 303).

- NB. Limited solubility so some peaks missing in ^{13}C compared to previous literature data[14]

Compound 3.13: *(2S,3S)-3-(5-(anthracen-9-yloxy) pentanamido)-4-(bis(4-methoxyphenyl)(phenyl)methoxy)butan-2-yl (2-cyanoethyl) diisopropyl phosphoramidite*

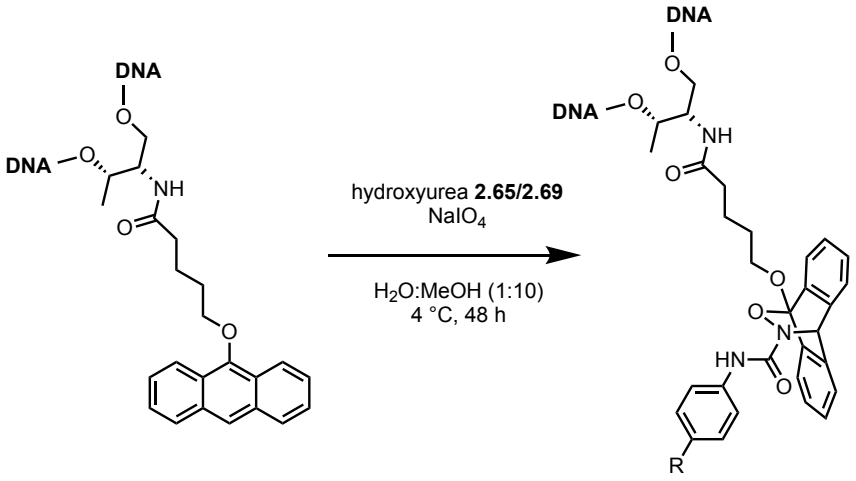


3.12 **3.13**

To a flask containing compound **3.12** (159 mg, 0.248 mmol) in Ch_2Cl_2 (15 mL) was added DIPEA (0.13 mL, 0.99 mmol) and 2-cyanoethyl-diisopropylchlorophosphoramidite (0.07 mL, 0.3 mmol) and the reaction mixture stirred at RT for 1 h in the absence of light. Solid supported benzyl alcohol (0.03 g, 0.05 mmol) was then added to the flask and the reaction mixture stirred for a further 30 min. The resulting solution was filtered, diluted with EtOAc (10 mL) and washed sequentially with $NaHCO_3$ (2 × 50 mL), water (50 mL) and brine (50 mL). The soln. was then dried over $MgSO_4$, filtered and the solvent removed under reduced pressure. Purification was achieved via column chromatography using activated basic alumina (EtOAc: hexane: Et_3N 59:40:1) to give the title compound as an orange oil (110 mg, 60%). ^{1}H NMR (300 MHz, CD_3CN) δ 8.29 (s, 1H, *H10*), 8.28 – 8.21 (m, 2H, *H4, H5*), 8.08 – 8.00 (m, 2H, *H1, H8*), 7.53 – 7.40 (m, 6H, *H2, H3, H6, H7 or H27, H23*), 7.35 – 7.25 (m, 6H, *H26, H22*), 7.23 – 7.13 (m, 1H, *H24*), 6.89 – 6.78 (m, 4H, *H2, H3, H6, H7 or H28*), 6.28 (d, *J* = 8.9 Hz, 1H, *NH*), 4.17 (t, *J* = 6.0 Hz, 2H, *H11*), 3.69 – 3.68 (m, 6 H, *H29*), 3.21 – 3.03 (m, 2H, *H17*), 2.70 – 2.68 (m, 2H, *H30 or H33*), 2.60 – 2.53 (m, 2H, *H30 or H33*), 2.51 – 2.43 (m, 4H, *H14, H11*), 2.39 (t, *J* = 6.8 Hz, 2H, *H31*), 2.12 – 1.99 (m, 4H, *H12, H13*), 1.26 (dd, *J* = 6.8, 5.4 Hz, 3H, *H19*), 1.12 – 1.04 (m, 12H, *H34, H35*), ^{31}P NMR (121 MHz, CD_3CN) δ

148.90, 147.05, 146.98, *m/z* (TOF MS ES+) [M + K]: calculated mass: 922.39, observed mass: 922.42.

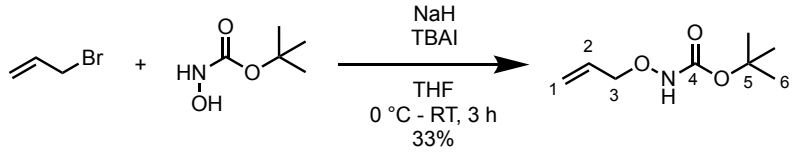
DNA cycloaddition general experimental



A solution of hydroxyurea **2.65** or **2.69** in MeOH (100 μM, 200 μL) and $NaIO_4$ in MeOH (100 μM, 200 μL) were degassed and vortexed in a refrigerator for 1 h before addition of anthracene-modified DNA **HP-A** in degassed H_2O: MeOH (20 μM, 25:175 μL) and subsequent vortexing for a further 23 h. The solvent from the reaction mixture was then removed via speed-vac and the reaction mixture resuspended in de-ionised H_2O (MiliQ, 1000 μL). The crude mixture was purified first by Nap10 size-exclusion column, and the resultant mixture collected in de-ionised H_2O (MiliQ, 1500 μL). This filtrate was purified by HPLC at RT using a Phenomenex Clarity 5 μm Oligo RP LC 250 × 4.6 mm column on analytical HPLC (Agilent Technologies 1260 Infinity system) following the Diels-Alder oligo method described in Table 24.

HPLC purification of anthracene containing products was monitored at 260 nm and 360 nm whereas cycloadduct containing products were monitored at 260 nm and 320 nm. Starting material HP-A eluted at 3.1 min and product eluted at 4.2 min. Fractions were then characterised by MS using either XEVO, Waters or FT-ICR instruments (Appendices 3.3, 3.4, 3.5).

Compound 4.28: *tert-butyl (allyloxy)carbamate*

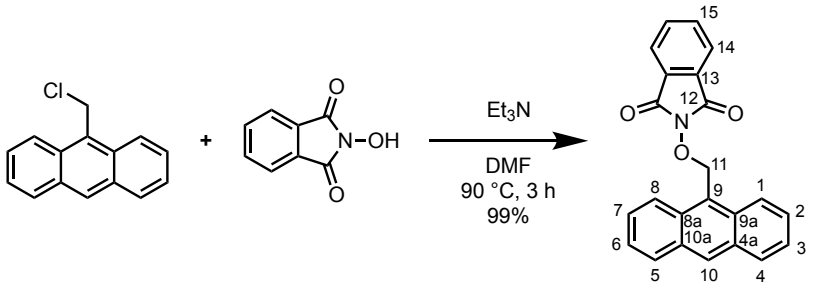


4.27 **4.26** **4.28**

Commercially available NaH (60% in mineral oil, 36.2 mg, 0.376 mmol) was triturated in *hexane* (3 × 10 mL), dissolved in THF (3 mL) and cooled to 0 ˚C. A solution of *N*-boc hydroxylamine (50 mg, 0.376 mmol) in THF (2 mL) was added to the reaction mixture and stirred at RT for 1.5 h. A solution of allyl bromide (0.02 mL, 0.251 mmol) and TBAI (111.2 mg, 0.301 mmol) in THF (2 mL) was prepared and added to the reaction mixture, then the entire reaction mixture was further stirred at RT for 45 min until consumption of the starting material observed by TLC (3:1 *hexane*: EtOAc, stained with vanillin and $KMnO_4$). The reaction mixture was diluted with H_2O (40 mL) and extracted into CH_2Cl_2 (3 × 15 mL), then dried over Na_2SO_4, filtered and the solvent removed under reduced pressure to give the title compound in crude as a colourless oil (14.3 mg, 33%). IR (ν_{max}/cm^{-1}): 3209 (NH), 2966 (Ar C-H), 1728 (C=O, *C4*), ^{1}H NMR (400 MHz, $CDCl_3$) δ 7.02 (s, 1H, *NH*), 6.05 – 5.74 (m, 1H, *H2*), 5.44 – 4.99 (m, 2H, *H1*), 4.33 (ddt, *J* = 6.4, 2.5, 1.2 Hz, 1H, *H3a*), 4.17 (d, *J* = 6.1 Hz, 1H, *H3b*), 1.29 – 1.02 (m, 9H, *H6*), ^{13}C NMR (101 MHz, $CDCl_3$) δ 158.2 (CO, *C4*), 132.7 (*C2*), 118.6 (*C1*), 76.3 (*C3*), 29.7 (*3 × C6*). *m/z* (mass hidden by presence of tetrabutyl ammonium ions).

- NB. Limited amount of compound therefore, not all ^{13}C peaks expected observed.

Compound 4.30: *2-(anthracen-9-ylmethoxy)isoindoline-1,3-dione*

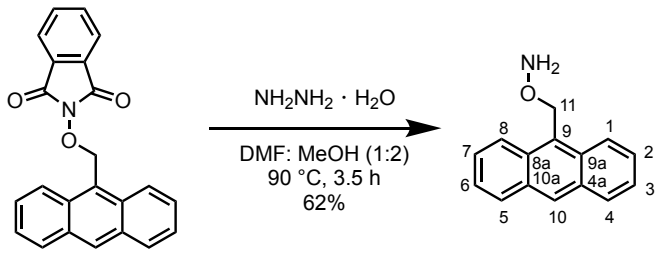


4.25 **4.29** **4.30**

Procedure adapted from literature: Teng *et al.,* 2015[16]

Commercially available 9-chloromethyl anthracene **4.25** (700 mg, 2.54 mmol) and *N*-hydroxyphthalimide **4.29** (415 mg, 2.54 mmol) were dissolved in DMF (7 mL) and stirred at RT for 5 min. Et_3N (0.85 mL, 6.10 mmol) was added to the reaction mixture and heated at 90 ºC for 3 h until consumption of the starting material by TLC (3:2 hexane: EtOAc). The reaction mixture was allowed to cool for 5 min then diluted with ice-cold H_2O (50 mL) and the mixture placed in an ice bath. The resulting precipitate was filtered under suction to give the title product as a yellow solid (897 mg, 99%), MP (decomposition 246 – 249 ˚C, recrystallised from CH_2Cl_2), IR (ν_{max}/cm^{-1}): 3057 (Ar C-H), 1726 (C=O, *C12*), ^{1}H NMR (400 MHz, $CDCl_3$) δ 8.73 (dd, *J* = 8.9, 1.0 Hz, 2H, *H4, H5*), 8.56 (s, 1H, *H10*), 8.04 (dd, *J* = 8.5, 0.7 Hz, 2H, *H1, H8*), 7.93 – 7.84 (m, 2H, *H14 or H15*), 7.82 – 7.73 (m, 2H, *H14 or H15*), 7.68 (ddd, *J* = 8.9, 6.5, 1.3 Hz, 2H, *H3, H6*), 7.52 (ddd, *J* = 8.5, 6.5, 1.0 Hz, 2H, *H2, H7*), 6.21 (s, 2H, *H11*), ^{13}C NMR (101 MHz, $CDCl_3$) δ 207.0 (2 × *C12*), 163.7, (qC, *2 × C13*) 134.6 (*2 × C14 or C15*), 132.0 (qC, *C9*), 131.3 (qC, *C8a, C9a*), 130.2 (*C10*), 129.1 (qC, *C4a, C10a*), 129.0 (*C4, C5*), 127.2 (*C3, C6*), 125.2 (*C2, C7*), 124.1 (*C1, C8*), 123.8 (*2 × C14 or C15*), 72.1 (*C11*), *m/z* (TOF MS ES+) calculated mass: 376.0968, observed mass: 376.0960.

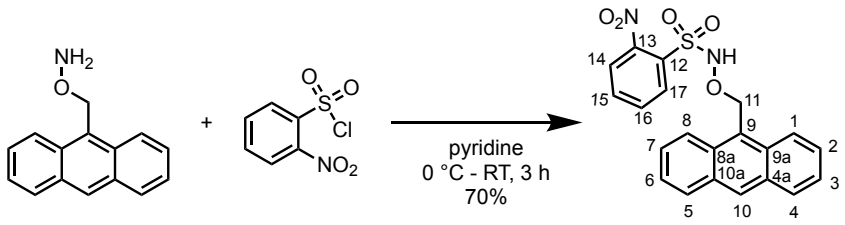
***Compound 4.27**: O-(anthracen-9-ylmethyl)hydroxylamine*



4.30 **4.27**

A suspension of anthracene derivative **4.30** (620 mg, 1.75 mmol) in DMF (3 mL) and MeOH (6 mL) was prepared, and $NH_2NH_2{\cdot}H_2O$ (0.25 mL, 5.25 mmol) was added. The reaction mixture was heated at 90 ˚C for 3.5 h until consumption of the starting material was observed by TLC (6:5 EtOAc: hexane). The reaction mixture was then allowed to cool to room temperature, diluted with H_2O (20 mL) and extracted with EtOAc (3 × 10 mL), washed with brine (10 mL), dried over Na_2SO_4 and filtered. The solvent was removed under reduced pressure and the residue purified by flash column chromatography (1:1 EtOAc: hexane) to give the title compound as a yellow solid (242 mg, 62%). MP: 87-88 ˚C (recrystallised from $CHCl_3$: hexane), IR (ν_{max}/cm^{-1}): 3310 (NH_2), 2907 (Ar CH), ^{1}H NMR (400 MHz, $CDCl_3$) δ 8.47 (d, *J* = 7.7 Hz, 2H, *H4, H5*), 8.44 (s, 1H, *H10*), 8.02 (dd, *J* = 8.3, 1.4 Hz, 2H, *H1, H8*), 7.57 (ddd, *J* = 8.9, 6.5, 1.4 Hz, 2H, *H3, H6*), 7.49 (ddd, *J* = 7.8, 6.5, 1.1 Hz, 2H, *H2, H7*), 5.73 (s, 2H, *H11*), 5.57 (s, 2H, *NH_2*), ^{13}C NMR (101 MHz, $CDCl_3$) δ 131.4 (qC, *C4a, C10a or C8a, C9a*), 131.3 (qC, *C4a, C10a or C8a, C9a*), 129.0 (*C1, C8 or C4, C5*), 128.7 (*C1, C8 or C4, C5*), 127.8 (qC, *C9*), 126.3 (*C3, C6*), 125.0 (*C2, C7*), 124.4 (*C10*), 69.9 (*C11*), *m/z* (TOF MS ASAP+) calculated mass: 223.10, observed data: 223.08 (30%) (high-res data not obtainable).

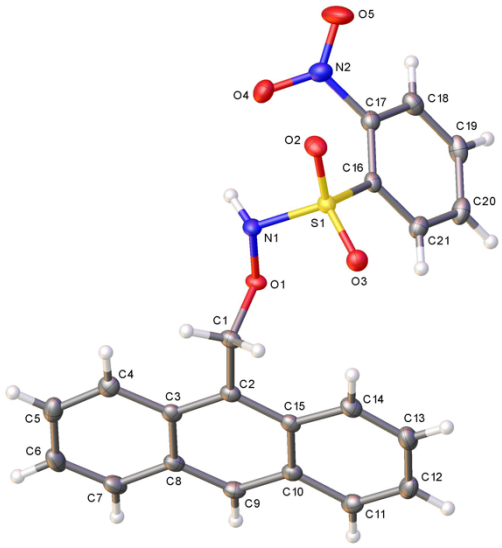
Compound 4.22: *N-(anthracen-9-ylmethoxy)-2-nitrobenzenesulfonamide*



4.27 **4.37** **4.22**

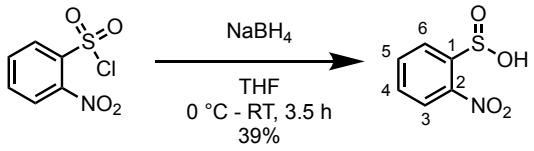
O-Hydroxylamine **4.27** (680 mg, 2.82 mmol) was dissolved in pyridine (10 mL) and cooled to 0 ˚C before addition of the sulfonyl chloride (938 mg, 4.23 mmol). The reaction mixture was stirred at RT for 3 h until consumption of the starting material was observed by TLC (1:1:0.1 EtOAc: hexane: Et_3N). The reaction mixture was then poured over H_2O (20 mL) and extracted into EtOAc (3 × 10 mL), washed with $NaHCO_3$ (10 mL) and brine (10 mL), dried over Na_2SO_4 and filtered before the solvent was removed under reduced pressure. The residue was purified by recrystallisation in CH_2Cl_2 with dropwise addition of hexane to give the title compound as a yellow crystalline solid (808 mg, 70%). MP: decomposition at 170 – 171 ˚C, IR (ν_{max}/cm^{-1}): 3271 (NH), 2921, 1532 (NO), 1346 (NO), 1171 (S=O), ^{1}H NMR (400 MHz, DMSO-d6) δ 11.32 (s, 1H, *NH*), 8.70 (s, 1H, *H10*), 8.38 (dd, *J* = 8.9, 1.0 Hz, 2H, *H4, H5*), 8.16 – 8.08 (m, 2H, *H1, H8*), 7.99 (ddd, *J* = 10.0, 7.9, 1.4 Hz, 2H, *H15, H16*), 7.81 (dtd, *J* = 24.8, 7.6, 1.4 Hz, 2H, *H14, H17*), 7.62 (ddd, *J* = 8.9, 6.5, 1.4 Hz, 2H, *H3, H6*), 7.55 (ddd, *J* = 7.7, 6.6, 1.0 Hz, 2H, *H2, H7*), 5.95 (s, 2H, *H11*), ^{13}C NMR (101 MHz, DMSO) δ 149.0 (*C12 or C13*), 135.5 (*C14 or C17*), 133.1 (*C14 or C17*), 131.4 (*C8a or C9a*), 131.3 (*C8a or C9a*), 130.4 (*C15 or C16*), 129.7 (*C4a, C10a*), 129.3 (*C1, C8*), 127.3 (*C3, C6*), 125.9 (*C9, C12 or C13*), 125.8 (*C9, C12 or C13*), 125.1 (*C15 or C16*), 124.6 (*C4, C5*), 71.2 (*C11*), m/z (TOF MS ASAP+) calculated mass: 431.0672, observed mass: 431.0668. Crystal Data for C21H16N2O5S (M =408.42 g/mol): monoclinic, space group P21/c (no. 14), a = 8.1066(2) Å, b = 12.6889(4) Å, c = 18.1114(6) Å, β = 94.652(3)°, V = 1856.87(10) Å3, Z =

4, T = 100.01(10) K, μ(CuKα) = 1.882 mm-1, Dcalc = 1.461 g/cm3, 7112 reflections measured (8.518° ≤ 2Θ ≤ 148.748°), 3677 unique (Rint = 0.0242, Rsigma = 0.0334) which were used in all calculations. The final R1 was 0.0328 (I > 2σ(I)) and wR2 was 0.0856 (all data).



Procedure adapted from similar literature (Kawaguchi *et al*., 2018)[17]

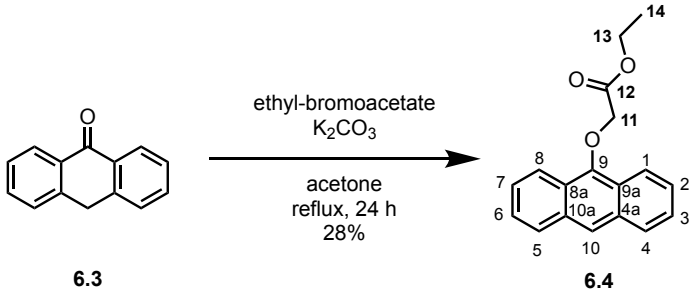
***Compound 4.17**: 2-nitrobenzenesulfinic acid*



Commercially available 2-nitrobenzene sulfonyl chloride **4.37** (200 mg, 0.902 mmol) was dissolved in THF (10 mL) and cooled to 0 ˚C before addition of $NaBH_4$ (170.5 mg, 4.51 mmol) in 3 equal portions. The reaction mixture was subsequently stirred at 0 ˚C for 3 h until consumption of starting material observed by TLC (1:1:0.1 EtOAc: hexane: Et_3N). The reaction mixture was quenched with H_2O (20 mL) in an ice bath and acidified with HCl (2M, 5 mL) to pH 2 at the same temperature. The reaction mixture was then extracted with CH_2Cl_2 (3 × 10 mL), dried over Na_2SO_4, and filtered before removal of the solvent under reduced pressure. The residue was purified by crystallisation from CH_2Cl_2 and dropwise addition of hexane to give the title compound as a pale yellow crystalline solid (66 mg, 39%). MP: 117 – 118 ˚C, IR (ν_{max}/cm^{-1}): 3200 (OH), 1523 (NO), 1348 (S=O), ^{1}H NMR (400 MHz, DMSO-d_6) δ 8.21 (dd, *J* = 8.1, 1.2 Hz, 1H, *H3 or H6*), 8.11 (dd, *J* = 7.8, 1.5 Hz, 1H, *H3 or H6*), 8.00 (td, *J* = 7.5, 1.2 Hz, 1H, *H4 or H5*), 7.82 (ddd, *J* = 8.0, 7.3, 1.5 Hz, 1H, *H4 or H5*), 6.57 (s, 1H, OH), ^{13}C NMR (101 MHz, DMSO) δ 146.3 (*C1 or C2*), 145.0 (*C1 or C2*), 135.4 (*C4 or C5*), 133.0 (*C4 or C5*), 125.8 (*C3 or C6*), 125.5 (*C3 or C6*), *m/z* (TOF MS ES-) [M-H] calculated mass: 185.9861, observed mass: 185.9865.

Data in agreement with the literature.[18]

***Compound 6.4**: ethyl 2-(anthracen-9-yloxy)acetate*

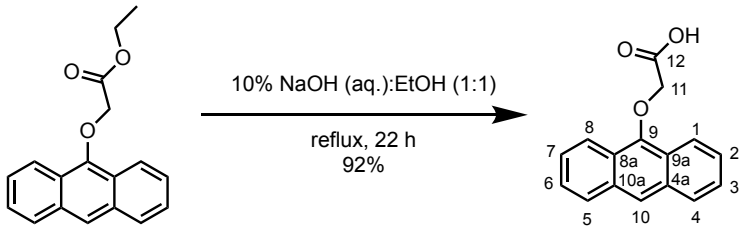


Known compound - procedure followed as described in literature.[14, 15]

A solution of degassed acetone (80 mL), anthrone (2.27 g, 11.69 mmol) and K_2CO_3 (1.616 g, 11.69 mmol) were added together and stirred at room temperature in the absence of light for 15 min. Keeping the flask in the dark, ethyl-bromoacetate (1.3 mL, 11.69 mmol) was added and the reaction mixture was heated at reflux for 24 h. The reaction mixture was then allowed to cool to room temperature, filtered to remove salts and the solvent removed under reduce pressure. The crude residue was re-dissolved in CH_2Cl_2 (25 mL), washed with H_2O (3 × 10 mL), dried over $MgSO_4$ and the solvent removed under reduced pressure to give an orange oil which solidified upon standing. Purification of the crude residue by flash column chromatography (9:1 hexane: EtOAc) gave the title compound as a yellow crystalline solid (904 mg, 28 %), IR (ν_{max}/cm^{-1}): 3050 (Ar CH), 2988 (Ar CH), 1755 (CO), ^{1}H NMR (400 MHz, $CDCl_3$) δ 8.44 – 8.34 (m, 2H, *H4, H5*), 8.27 (s, 1H, *H10*), 8.03 – 7.93 (m, 2H, *H1, H8*), 7.58 – 7.41 (m, 4H, *H2, H3, H6, H7*), 4.81 (s, 2H, H11), 4.38 (q, *J* = 7.2 Hz, 2H, *H13*), 1.37 (t, *J* = 7.2 Hz, 3H, *H14*), ^{13}C NMR (101 MHz, $CDCl_3$) δ 169.1 (CO, *C12*), 150.3 (qC, *C9*), 132.3 (qC, *C4a, C10a or C8a, C9a*), 128.4 (*C1, C8*), 125.7 (*C2, C3, C6, C7*), 124.3 (qC, *C4a, C10a or C8a, C9a*), 123.1 (*C10*), 122.2 (*C4, C5*), 72.1 (*C11*), 61.4 (*C13*), 14.3 (*C14*). *m/z* (TOF MS ES+) calculated mass: 281.1178, observed mass: 281.1172.

Data in agreement with the literature.[14]

***Compound 6.6**: 2-(anthracen-9-yloxy) acetic acid*



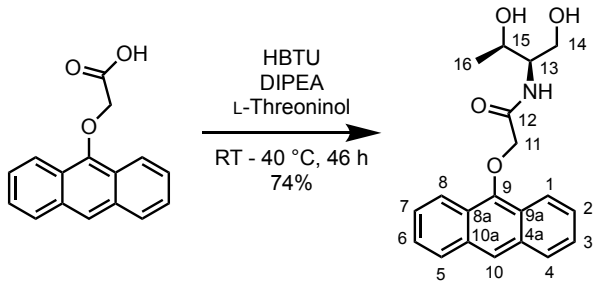
6.4 **6.6**

Known compound - procedure followed as described in literature.[14, 15]

A solution of 10% aq. NaOH in EtOH (not anhydrous) (80 mg, 40 mL total vol.) and ester **6.4** (827 mg, 2.949 mmol) were added together and the reaction mixture heated at reflux in the absence of light for 21 h. Upon consumption of the starting material, the reaction mixture was allowed to cool to room temperature and subsequent dropwise addition of HCl (conc., 2 mL) over 5 min gave a cream precipitate which was collected by suction filtration. The solid was washed with H_2O (20 mL) and dried under vacuum to give the title compound as a cream solid (687.7 mg, 92%). IR (ν_{max}/cm^{-1}): 3058 (Ar CH), 1729 (CO, *C12*), ^{1}H NMR (400 MHz, $CDCl_3$) δ 8.32 (s, 1H, *H10*), 8.30 – 8.23 (m, 2H, *H4, H5*), 8.10 – 7.94 (m, 2H, *H1, H8*), 7.52 (dddd, *J* = 17.2, 7.9, 6.6, 1.3 Hz, 4H, *H2, H3, H6, H7*), 4.88 (s, 2H, *H11*), ^{13}C NMR (101 MHz, $CDCl_3$) δ 168.1 (CO, *C12*), 132.3 (qC), 128.6 (*C1, C8*), 126.1 (*C2, C3 or C6, C7*), 125.7 (*C2, C3 or C6, C7*), 123.7 (*C10*), 121.5 (*C4, C5*), 71.2 (*C11*), *m/z* (TOF MS ES-): [M-H] calculated mass: 251.0708, observed mass: 251.0715.

Data in agreement with the literature.[14]

***Compound 6.8**: 2-(anthracen-9-yloxy)-N-((2R,3R)-1,3-dihydroxybutan-2-yl) acetamide*



6.6 **6.8**

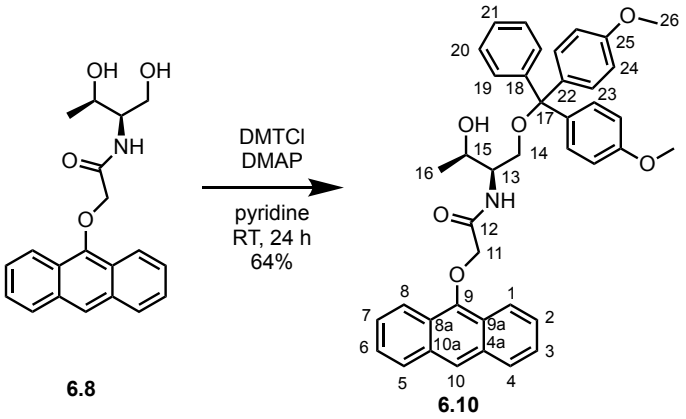
Known compound – procedure followed as described in literature.[14, 15]

A solution of carboxylic acid **6.6** (685.0 mg, 2.496 mmol) in DMF (10 mL) was prepared and HBTU (946.6 mg, 2.496 mmol) added before the reaction mixture was stirred at RT for 15 min. Next, L-threoninol (262.5 mg, 2.496 mmol) and DIPEA (0.44 mL, 2.496 mmol) were added to the reaction mixture under argon and the resulting solution was stirred at 40 ˚C for 46 h. On disappearance of starting material observed by TLC (95:5 CH_2Cl_2: MeOH), the reaction mixture was allowed to cool to RT, diluted with MeOH:CH_2Cl_2 (1:3, 20 mL) then washed with H_2O (3 × 10 mL) and dried over $MgSO_4$. The orange solution was filtered, and the solvent removed under reduced pressure to give an orange-red solid. The residue was purified by flash column chromatography (100:0 CH_2Cl_2 to 98:2 CH_2Cl_2: MeOH) to give the title compound as an orange oil which solidified upon standing to a fluffy yellow solid (630.0 mg, 74%), IR (ν_{max}/cm^{-1}): 3413 (NH), 3220 br (OH), 2969, 1651 (C=O, *C12*), 1328 (C-N), ^{1}H NMR (400 MHz, DMSO-d_6) δ 8.44 (s, 1H, *H10*), 8.36 – 8.26 (m, 2H, *H4, H5*), 8.16 – 8.06 (m, 2H, *H1, H8*), 7.82 (d, *J* = 8.9 Hz, 1H, *NH*), 7.61 – 7.48 (m, 4H, *C2, C3, C6, C7*), 4.83 (dd, *J* = 4.8, 3.2 Hz, 1H, *H11*), 4.78 (q, *J* = 5.4, 3.7 Hz, 1H, *H11*), 4.06 – 3.94 (m, 1H, *H15*), 3.84 (dtd, *J* = 9.2, 6.4, 2.8 Hz, 1H, *H13*), 3.54 (dtd, *J* = 21.7, 10.7, 6.0 Hz, 2H, *H14*), 1.13 (d, *J* = 6.4 Hz, 3H, *H16*), ^{13}C NMR (101 MHz, DMSO) δ 168.2 (CO, *C12*), 150.3 (qC, *C9*), 132.3 (qC, *C4a, C10a or C8a, C9a*), 128.9 (*C1, C8*), 126.3 (*C2, C3, C6, C7*), 124.4 (qC, *C4a, C10a or C8a,*

C9a), 123.2 (*C10*), 122.4 (*C4, C5*), 64.5 (*C15*), 61.1 (*C14*), 56.1 (*C13*), 20.9 (*C16*), *m/z* (TOF MS ES+): calculated mass: 340.1549, observed mass: 340.1554.

Data in agreement with the literature.[14]

***Compound 6.10**: 2-(anthracen-9-yloxy)-N-((2R,3R)-1-(bis(4-methoxyphenyl)(phenyl) methoxy)-3-hydroxybutan-2-yl) acetamide*



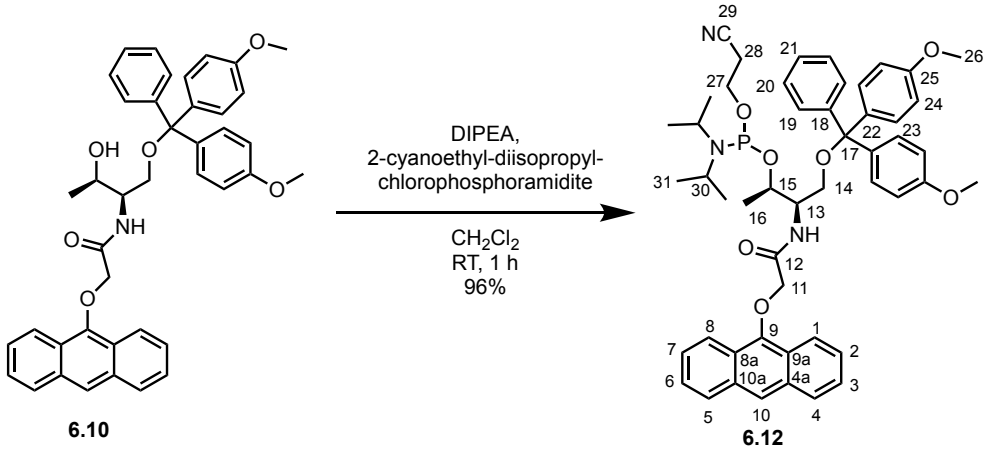
Known compound – procedure followed as described in literature.[14, 15]

Diol **6.8** (624.4 mg, 1.841 mmol) was dissolved in pyridine (7 mL) and DMTCl (623.8 mg, 1.841 mmol) and DMAP (33.7 mg, 0.276 mmol) were added sequentially and the reaction mixture was stirred at RT for 24 h until consumption of the starting material was observed by TLC (60:39:1 hexane: EtOAc: Et_3N). The reaction mixture was then poured over H_2O (30 mL), extracted with CH_2Cl_2 (3 × 20 mL) and dried over $MgSO_4$. The residue was then filtered, and the solvent removed under reduced pressure to give the crude product as an orange oil. Flash column chromatography (60:39:1 hexane: EtOAc: Et_3N) gave the title compound as a fluffy yellow solid (751.3 mg, 64%), IR (ν_{max}/cm^{-1}): 2932 (Ar CH), 1508 (C=O, *C12*), 1248 (C-O), ^{1}H NMR (400 MHz, CD_3CN) δ 8.39 (s, 1H, *H10*), 8.26 (m, 2H, *H4, H5*), 8.08 (m, 2H, *H1, H8*), 7.53 – 7.47 (m, 5H, *NH + H3, H6, H2, H7 or H24*), 7.46 – 7.36 (m, 6H, *H19, H23*), 7.33 – 7.27 (m, 2H, *H20*), 7.25 – 7.19 (m, 1H, *H21*), 6.88 – 6.82 (m, 4H, *H3, H6, H2, H7 or H24*), 4.70 (d, *J* = 1.8 Hz, 2H, *H11*), 4.22 – 4.09 (m, 1H, *H13*), 3.73 (d, *J* = 1.9 Hz, 6H, *H26*), 3.33 (dd, *J* = 9.2, 5.4 Hz, 1H, *H15*), 3.26 – 3.18 (m, 2H, *H14*), 1.21 – 1.18 (m, 3H, *H16*), ^{13}C NMR (101 MHz, CD_3CN) δ 168.8 (CO, *C12*), 159.2 (qC, *2 × C25*), 149.8 (qC, *C9*), 145.8 (qC, *C18*), 136.7 (*C22*), 136.6 (*C22*), 132.9 (*4 × C23*), 130.6 (*C4, C5*), 129.1 (*2 × C19*), 128.6 (*2 ×*

C20), 127.4 (*C21*), 126.6 (*C2, C7 or C3, C6*), 126.4 (*C2, C7 or C3, C6*), 124.7 (qC, *C4a, C10a C8a, C9a*), 123.7 (*C10*), 122.2 (*C1, C8*),113.6 (*4* × *C24*), 86.5 (qC, *C17*), 74.3 (*C11*), 66.8 (*C15*), 63.9 (*C14*), 55.4 (*2* × *C26*), 54.8 (*C13*), 20.4 (*C16*), *m/z* (TOF MS ES+): calculated mass: 664.2688, observed mass: 664.2689.

Data in agreement with the literature.[14]

Compound 6.12: *(2R,3R)-3-(2-(anthracen-9-yloxy)acetamido)-4-(bis(4-methoxyphenyl)(phenyl)methoxy)butan-2-yl (2-cyanoethyl) diisopropyl phosphoramidite*



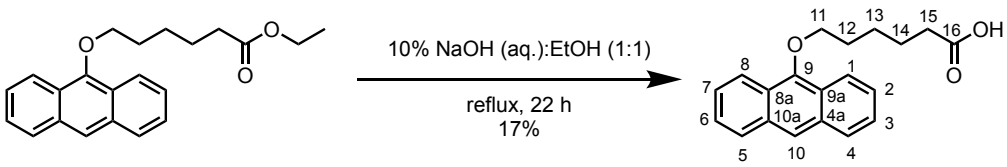
Known compound – procedure followed as described in literature.[14, 15]

To a flask containing compound **6.10** (304.6 mg, 0.475 mmol) in CH_2Cl_2 (10 mL) was added DIPEA (0.33 mL, 1.90 mmol) and 2-cyanoethyl-diisopropylchlorophosphoramidite (0.13 mL, 0.546 mmol) and the reaction mixture stirred at RT for 1 h in the absence of light. MeOH (1.5 mL) was then added to the flask and the reaction mixture stirred for a further 30 min. The solution was filtered, diluted with EtOAc (10 mL) and washed sequentially with $NaHCO_3$ (2 × 50 mL), water (50 mL) and brine (50 mL). The soln. was then dried over $MgSO_4$, filtered and the solvent removed under reduced pressure. Purification was achieved via column chromatography using activated basic alumina (EtOAc: hexane: Et_3N 59:40:1) to give the title compound as a yellow oil (384 mg, 96%), ^{1}H NMR (400 MHz, CD_3CN) δ 8.35 (s, 1H, *H10*), 8.22 (dq, *J* = 8.7, 1.0 Hz, 2H, *H4, H5*), 8.08 – 7.97 (m, 2H, *H1, H8*), 7.57 – 7.44 (m, 5H, *NH* + *H2, H3, H6, H7 or H24*), 7.43 – 7.36 (m, 6H, *H19, H23*), 7.30 (m, 2H, *H20*), 7.24 – 7.17 (m, 1H, *H21*), 6.89 – 6.80 (m, 4H, *H2, H3, H6, H7 or H24*), 4.79 – 4.64 (m, 2H, *H11*), 4.46 – 4.26

(m, 2H, *H13, H15*), 3.87 – 3.74 (m, 2H), 3.74 – 3.66 (d, 6H, *H26*), 3.47 – 3.30 (m, 5H, *H14, H27, H30*), 2.64 (td, *J* = 6.0, 0.8 Hz, 2H, *H28*), 1.18 – 1.15 (m, 12H, *H31*), 1.04 (d, *J* = 6.8 Hz, 3H, *H16*), ^{31}P NMR (162 MHz, CD_3CN) δ 148.41, 146.08, *m/z* (TOF MS ES+): calculated mass: 864.3777, observed mass: 864.3770.

Data in agreement with the literature.[14]

Compound 6.5: *ethyl 6-(anthracen-9-yloxy) hexanoate*



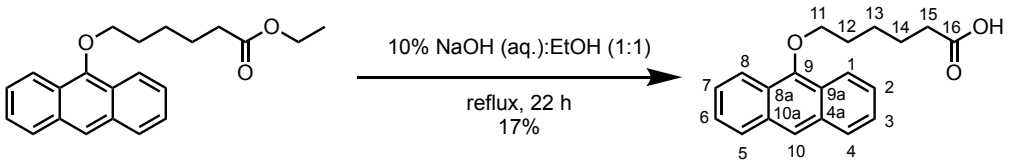
6.5 **6.7**

Known compound - procedure followed as described in literature.[14, 15]

A solution of degassed acetone (80 mL), anthrone (2.00 g, 10.30 mmol) and K2CO3 (1.423 g, 10.30 mmol) were added together and stirred at room temperature in the absence of light for 15 min. Keeping the flask in the dark, ethyl-6-bromohexanoate (1.83 mL, 10.30 mmol) was added and the reaction mixture was heated at reflux for 24 h. The reaction mixture was then allowed to cool to room temperature, filtered to remove salts and the solvent removed under reduce pressure. The crude residue was re-dissolved in CH_2Cl_2 (25 mL), washed with H2O (3 × 10 mL), dried over $MgSO_4$ and the solvent removed under reduced pressure to give an orange oil which solidified upon standing. Purification of the crude residue by flash column chromatography (9:1 hexane: EtOAc) gave the title compound as a pale yellow crystalline solid (1.945 g, 56 %), IR (ν_{max}/cm^{-1}): 2887 (Ar CH), 1676 (C=O, *C16*), ^{1}H NMR (400 MHz, Chloroform-*d*) δ 8.32 – 8.26 (m, 2H, *H4, H5 or H1, H8*), 8.14 (s, 1H, *H10*), 7.98 – 7.83 (m, 2H, *H4, H5 or H1, H8*), 7.45 (dddd, *J* = 17.6, 8.0, 6.5, 1.4 Hz, 4H, *H2, H3, H6, H7*), 4.25 – 4.00 (m, 4H, *H11, H17*), 2.39 (t, *J* = 7.3 Hz, 2H, *H15*), 2.14 – 1.98 (m, 2H, *H12, H13 or H14*), 1.86 – 1.74 (m, 2H, *H12, H13 or H14*), 1.74 – 1.63 (m, 2H, *H12, H13 or H14*), 1.26 (dt, *J* = 11.7, 7.1 Hz, 3H, *H18*), ^{13}C NMR (101 MHz, $CDCl_3$) δ 184.30 (CO, *C16*), 140.47 (qC), 133.53 (qC), 132.76, 132.06 (qC), 128.48 (*C4, C5 or C1, C8*), 127.63 (*C4, C5 or C1, C8*), 127.05, 32.39, *m/z* (TOF MS ASAP+): calculated mass: 336.1725, observed mass: 336.1731. (^{13}C NMR – some data missing due to low concentration)

Data in agreement with the literature.[14]

Compound 6.7: *6-(anthracen-9-yloxy) hexanoic acid*



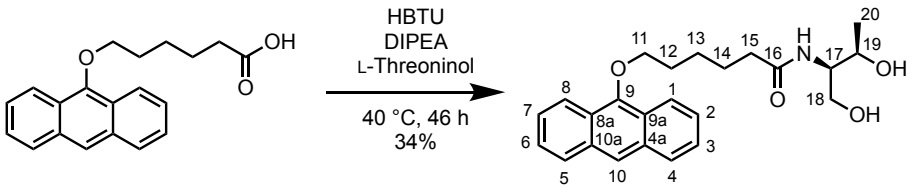
6.5 **6.7**

Known compound - procedure followed as described in literature.[14, 15]

A solution of (1:1 v:v) NaOH (10% w:v, aq.) in EtOH (not anhydrous) (40 mL total vol.) and ester **6.5** (1.684 g, 5.01 mmol) were added together and the reaction mixture heated at reflux in the absence of light for 21 h. Upon consumption of the starting material, the reaction mixture was allowed to cool to room temperature and subsequent dropwise addition of HCl (conc., 2 mL) over 5 min gave a cream precipitate which was collected by suction filtration. The solid was washed with H_2O (50 mL) and dried under vacuum to give the title compound as a cream solid (261.5 mg, 17%). IR (ν_{max}/cm^{-1}): 3068 (OH), 2928 (Ar CH), 1700 (C=O, *C16*), ^{1}H NMR (400 MHz, $CDCl_3$) δ 8.30 – 8.24 (m, 2H, *H4, H5*), 8.22 (s, 1H, *H10*), 8.04 – 7.96 (m, 2H, *H1, H8*), 7.52 – 7.41 (m, 4H, *H2, H3, H6, H7*), 4.20 (t, *J* = 6.5 Hz, 2H, *H11*), 2.48 (t, *J* = 7.2 Hz, 2H, *H15*), 2.14 – 2.01 (m, 2H, *H12*), 1.80 (dtdd, *J* = 22.2, 16.4, 9.4, 4.4 Hz, 4H, *H13, H14*), ^{13}C NMR (101 MHz, $CDCl_3$) δ 179.0 (CO, *C16*), 151.3 (qC, *C9*), 132.4 (qC, *C8a, C9a or C4a, C10a*), 128.5 (*C1, C8*), 125.5 (*C2, C7 or C3, C6*), 125.1 (*C2, C7 or C3, C6*), 124.7 (qC, *C8a, C9a or C4a, C10a*), 122.4 (*C4, C5*), 122.1 (*C10*), 75.8 (*C11*), 33.9 (*C15*), 30.4 (*C12*), 25.8 (*C13 or C14*), 24.7 (*C13 or C14*), *m/z* (TOF MS ES-): calculated mass: 307.1353, observed mass: 307.1349.

Data in agreement with the literature.[14]

Compound 6.9: *6-(anthracen-9-yloxy)-N-((2R,3R)-1,3-dihydroxybutan-2-yl) hexanamide*



6.7 **6.9**

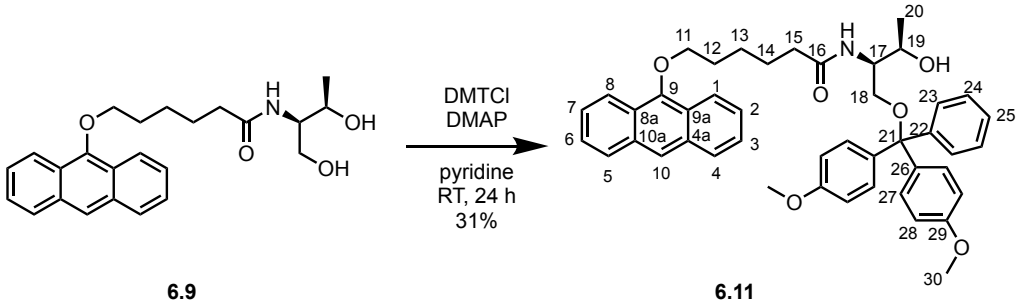
Known compound – procedure followed as described in literature.[14, 15]

To a solution of carboxylic acid **6.7** (261.5 mg, 0.848 mmol) in DMF (6 mL) was added HBTU (321.6 mg, 0.848 mmol) and the reaction mixture was stirred at RT for 15 min. Next, L-threoninol (89.2 mg, 0.848 mmol) and DIPEA (0.15 mL, 0.848 mmol) were added to the reaction mixture under argon and the resulting solution was stirred at 40 ˚C for 46 h. On disappearance of starting material observed by TLC (95:5 CH_2Cl_2: MeOH), the reaction mixture was allowed to cool to RT, diluted with MeOH: CH_2Cl_2 (1:3, 20 mL) then washed with H_2O (3 × 10 mL) and dried over $MgSO_4$. The orange solution was filtered, and the solvent removed under reduced pressure to give an orange-red solid. The residue was purified by flash column chromatography (100:0 CH_2Cl_2 to 98:2 CH_2Cl_2: MeOH) to give the title compound as an orange oil which solidified upon standing to a fluffy yellow solid (112.7 mg, 34%), IR (ν_{max}/cm^{-1}): 3353 (OH), 2940 (Ar CH), 1647 (C=O, *C16*), 1340 (C-N), ^{1}H NMR (300 MHz, DMSO-d_6) δ 8.38 (s, 1H, *H10*), 8.28 – 8.18 (m, 2H, *H4, H5*), 8.13 – 8.06 (m, 2H, *H1, H8*), 7.60 – 7.47 (m, 4H, *H2, H3, H6, H7*), 7.38 (d, *J* = 8.8 Hz, 1H, *NH*), 4.58 (t, *J* = 5.2 Hz, 2H, *H11*), 4.13 (t, *J* = 6.4 Hz, 2H, *H18*), 3.88 (ddd, *J* = 6.5, 5.2, 2.8 Hz, 1H, *H17 or H19*), 3.67 (qd, *J* = 9.0, 7.7, 2.8 Hz, 1H, *H17 or H19*), 2.25 (q, *J* = 4.7, 3.2 Hz, 2H, *H12*), 2.00 (t, *J* = 6.8 Hz, 2H, *H15*), 1.72 – 1.55 (m, 4H, *H13, H14*), 1.01 (d, *J* = 6.4 Hz, 3H, *H20*), ^{13}C NMR (101 MHz, CD_3CN) δ 174.0 (CO, *C16*), 150.2 (qC, *C9*), 133.0 (qC, *C4a, C10a*), 128.9 (qC, *C8a, C9a*), 126.3 (*C2,C7 or C3, C6*), 125.9 (*H17 or H19*), 125.1 (*C2,C7 or C3, C6*), 122.8 (*C1,*

C8), 122.5 (*C10*), 76.4 (*C11*), 66.9 (*C19*), 63.2 (*C18*), 46.3 (*C17*), 36.5 (*C15*), 30.7 (*C12*), 26.6 (*C13, C14*), 20.2 (*C20*), *m/z* (TOF MS ES+): [M + Na] calculated mass: 418.1986, observed mass: 418.1988.

Data in agreement with the literature.[14]

***Compound 6.11**: 6-(anthracen-9-yloxy)-N-((2R,3R)-1-(bis(4-methoxyphenyl)(phenyl) methoxy)-3-hydroxybutan-2-yl)hexanamide*



6.9 **6.11**

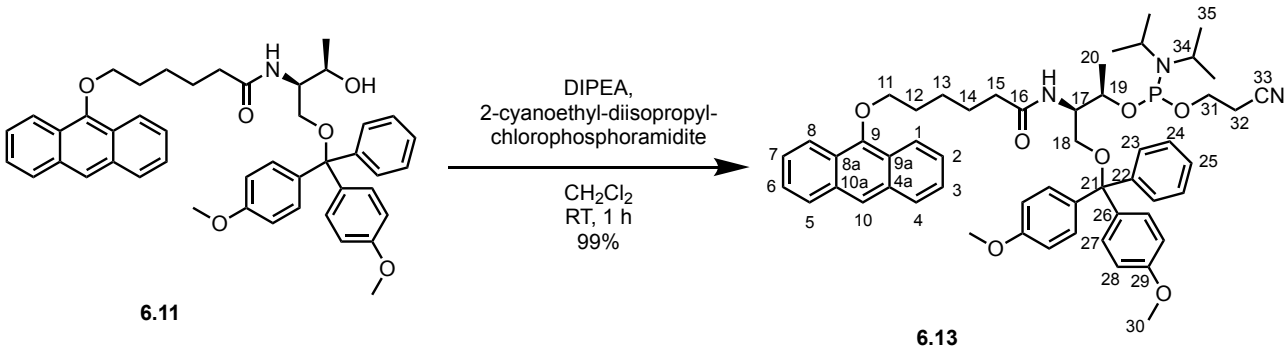
Known compound – procedure followed as described in literature.[14, 15]

To a foil-wrapped flask containing diol **6.9** (106.5 mg, 0.269 mmol) in pyridine (5 mL) was added DMTCl (91.1 mg, 0.269 mmol) and DMAP (5 mg, 0.04 mmol) sequentially and the reaction mixture was stirred at RT for 24 h until consumption of the starting material was observed by TLC (60:39:1 hexane: EtOAc: Et_3N). The reaction mixture was then poured over H_2O (20 mL), extracted with CH_2Cl_2 (3 × 10 mL) and dried over $MgSO_4$. The residue was then filtered, and the solvent removed under reduced pressure to give the crude product as an orange oil. Flash column chromatography (60:39:1 hexane: EtOAc: Et_3N) gave the title compound as a fluffy yellow solid (58.4 mg, 31%), IR (ν_{max}/cm^{-1}): 3301 (OH), 2938 (Ar CH), 1647 (C=O, *C16*), 1248 (C-O), ^{1}H NMR (400 MHz, CD_3CN) δ 8.29 (s, 1H, *H10*), 8.27 – 8.20 (m, 2H, *H4, H5*), 8.06 – 8.01 (m, 2H, *H1, H8*), 7.52 – 7.44 (m, 4H, *H28 or H2, H3, H6, H7*), 7.44 – 7.38 (m, 2H, *H24*), 7.32 – 7.23 (m, 6H, *H27, H23*), 7.20 – 7.09 (m, 1H, *H25*), 6.88 – 6.73 (m, 4H, *H28 or H2, H3, H6, H7*), 6.49 (d, *J* = 8.9 Hz, 1H, *NH*), 4.11 (t, *J* = 6.6 Hz, 2H, *H11*), 3.94 (dtq, *J* = 18.1, 5.8, 3.2 Hz, 2H, *H17, H19*), 3.69 (s, 6H, *H30*), 3.18 – 3.08 (m, 3H, *H18, OH*), 2.30 (t, *J* = 7.1 Hz, 2H, *H15*), 2.06 – 2.00 (m, 2H, *H12*), 1.79 – 1.62 (m, 4H, *H13, H14*), 1.27 (t, *J* = 7.3 Hz, 3H, *H20*), ^{13}C NMR (101 MHz, CD_3CN) δ 173.6 (CO, *C16*), 159.1 (qC, *2 × C29*), 151.8 (qC, *C9*), 145.8 (qC, *C22*), 136.7 (qC, *2 × C26*), 133.0 (qC, *C4a, C10a or C8a, C9a*), 130.5 (4 × *C27*), 128.9 (*C4, C5*), 128.6 (2 × *C23 or 2 × C24*), 128.3 (2 × *C23*

or 2 × C24), 127.3(*C25*), 126.2 (*C2, C7 or C3, C6*), 125.9 (*C2, C7 or C3, C6*), 125.3 (qC, *C4a, C10a or C8a, C9a*), 122.8 (*C1, C8*), 122.5 (*C10*), 113.5 (4 × *C28*), 86.3 (qC, *C21*), 76.4 (*C11*), 66.8 (*C19*), 64.2 (*C18*), 55.4 (*2 × C30*), 54.8 (*C17*), 36.5 (*C15*), 30.7 (*C12*), 26.2 (*C13, C14*), 20.2 (*C20*), *m/z* (TOF MS ES+): [M + Na] calculated data: 720.3301, observed data: 720.3301.

Data in agreement with the literature.[14]

Compound 6.13: *(2R,3R)-3-(6-(anthracen-9-yloxy)hexanamido)-4-(bis(4-methoxy phenyl)(phenyl)methoxy)butan-2-yl (2-cyanoethyl) diisopropyl phosphoramidite*



6.11 **6.13**

Known compound – procedure followed as described in literature.[14, 15]

To a flask containing compound **6.11** (58.4 mg, 0.084 mmol) in Ch_2Cl_2 (5 mL) was added DIPEA (0.06 mL, 0.335 mmol) and 2-cyanoethyl-diisopropylchlorophosphoramidite (0.03 mL, 0.096 mmol) and the reaction mixture stirred at RT for 1 h in the absence of light. MeOH (1.0 mL) was then added to the flask and the reaction mixture stirred for a further 30 min. The solution was filtered, diluted with EtOAc (10 mL) and washed sequentially with $NaHCO_3$ (2 × 30 mL), water (30 mL) and brine (30 mL). The soln. was then dried over $MgSO_4$, filtered and the solvent removed under reduced pressure. Purification was achieved via column chromatography using activated basic alumina (EtOAc: hexane: Et_3N 59:40:1) to give the title compound as a yellow oil (75.0 mg, 99%), ^{1}H NMR (400 MHz, CD_3CN) δ 8.29 (s, 1H, *H10*), 8.28 – 8.22 (m, 2H, *H4, H5*), 8.07 – 8.01 (m, 2H, *H1, H8*), 7.51 – 7.45 (m, 4H, *H2, H3, H6, H7 or H28*), 7.44 – 7.39 (m, 2H, *H24*), 7.33 – 7.23 (m, 6H, *H27, H23*), 7.20 – 7.14 (m, 1H, *H25*), 6.85 – 6.77 (m, 4H, *H2, H3, H6, H7 or H28*), 6.21 (d, *J* = 8.9 Hz, 1H, *NH*), 4.13 (t, *J* = 6.6 Hz, 2H, *H11*), .72 – 3.68 (m, 6H, *H30*), 3.11 (qd, *J* = 9.2, 5.9 Hz, 2H, *H18*), 2.71 – 2.66 (m, 4H, *H31, H34*), 2.46 (t, *J* = 6.0 Hz, 2H, *H32*), 2.30 (t, *J* = 7.1 Hz, 2H, *H15*), 2.04 (p, *J* =

6.8 Hz, 2H, *H12*), 1.83 – 1.63 (m, 4H, *H13, H14*), 1.33 (dd, *J* = 6.9, 2.3 Hz, 3H, *H20*), 3H, 1.13 – 1.06 (m, 12H, *H35*), ^{31}P NMR (162 MHz, CD_3CN) δ 148.92, 146.96, 140.33.

Data in agreement with the literature.[14]

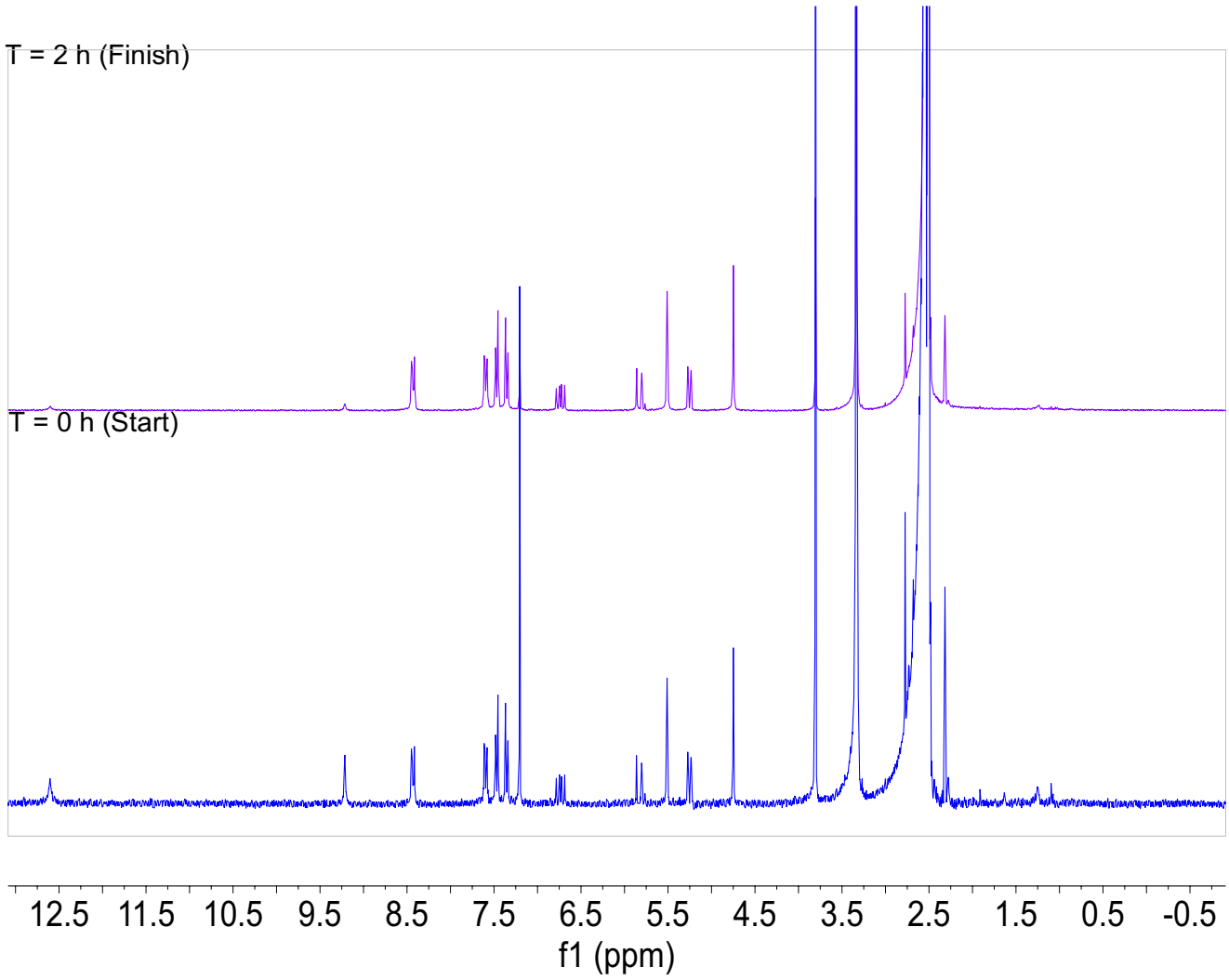
7.2 Experimental References

1. Urbach, A. R., Circular Dichroism Spectroscopy in the Undergraduate Curriculum. *J. Chem. Educ.,* **2010,** *87*, 891-3.
2. Kypr, J.; Kejnovska, I.; Renciuk, D.; Vorlickova, M., Circular dichroism and conformational polymorphism of DNA. *Nucleic Acids Res.,* **2009,** *37* (6), 1713-25.
3. Matsuo, K.; Nakagawa, H.; Adachi, Y.; Kameda, E.; Aizawa, K.; Tsumoto, H.; Suzuki, T.; Miyata, N., Photoinduced Upregulation of Calcitonin Gene-Related Peptide in A549 Cells through HNO Release from a Hydrophilic Photocontrollable HNO Donor. *Chem. Pharm. Bull.,* **2012,** *60* (8), 1055-62.
4. DuMond, J. F.; King, S. B., The chemistry of nitroxyl-releasing compounds. *Antioxid. Redox Signal,* **2011,** *14* (9), 1637-48.
5. Horiba What is Fluorescence Anisotropy or Fluorescence Polarization? https://www.horiba.com/gbr/technology/measurement-and-control-techniques/spectroscopy/fluorescence-spectroscopy/what-is-fluorescence-anisotropy-or-fluorescence-polarization/ (accessed 13.09.2021).
6. OligoAnalyzer. https://eu.idtdna.com/calc/analyzer (accessed 25.09.2021).
7. Adachi, Y.; Nakagawa, H.; Matsuo, K.; Suzuki, T.; Miyata, N., Photoactivatable HNO-releasing compounds using the retro-Diels-Alder reaction. *Chem. Commun.,* **2008**, (41), 5149-51.
8. Cloninger, M. J.; Whitlock, H. W., A Synthetic Receptor Which Uses Multiple Edge-Face Interactions To Bind Aromatic Guests. *J. Org. Chem.,* **1998,** *63* (18), 6153-9.
9. Qiu, L.; Zhu, C.; Chen, H.; Hu, M.; He, W.; Guo, Z., A turn-on fluorescent Fe(3+) sensor derived from an anthracene-bearing bisdiene macrocycle and its intracellular imaging application. *Chem. Commun. (Camb)* **2014,** *50* (35), 4631-4.
10. Ferreira, F.; Meyer, A.; Vasseur, J. J.; Morvan, F., Universal solid supports for the synthesis of oligonucleotides via a transesterification of *H*-phosphonate diester linkage. *J. Org. Chem.,* **2005,** *70* (23), 9198-206.
11. Gary E. Keck, R. R. W., John B. Yates, A versatile method for carbon-nitrogen bond formation via ene reactions of acylnitroso compounds. *Tetrahedron* **1981,** *37* (23), 4007-16.
12. Hirao, Y.; Saito, T.; Kurata, H.; Kubo, T., Isolation of a hydrogen-bonded complex based on the anthranol/anthroxyl pair: formation of a hydrogen-atom self-exchange system. *Angew. Chem. Int. Ed. Engl.,* **2015,** *54* (8), 2402-5.
13. Goksu, H.; Topal, M.; Keskin, A.; Gultekin, M. S.; Celik, M.; Gulcin, I.; Tanc, M.; Supuran, C. T., 9,10-Dibromo-N-aryl-9,10-dihydro-9,10-[3,4]epipyrroloanthracene-12,14-diones: Synthesis and Investigation of Their Effects on Carbonic Anhydrase Isozymes I, II, IX, and XII. *Arch. Pharm. (Weinheim)* **2016,** *349* (6), 466-74.
14. Duprey, J.-L. H. A. Studies On Anthracene Tagged Oligonucleotides. PhD, University of Birmingham, 2010.
15. Duprey, J. L. H. A.; Bassani, D. M.; Hyde, E. I.; Jonusauskas, G.; Ludwig, C.; Rodger, A.; Spencer, N.; Vyle, J. S.; Wilkie, J.; Zhao, Z. Y.; Tucker, J. H. R., Rationalisation of a mechanism for sensing single point variants in target DNA using anthracene-tagged base discriminating probes. *Org. Biomol. Chem.,* **2018,** *16* (35), 6576-85.
16. Teng, Y.; Suwanarusk, R.; Ngai, M. H.; Srinivasan, R.; Ong, A. S.; Ho, B.; Renia, L.; Chai, C. L., An amidation/cyclization approach to the synthesis of *N*-hydroxyquinolinones and their biological evaluation as potential anti-plasmodial, anti-bacterial, and iron(II)-chelating agents. *Bioorg. Med. Chem. Lett.,* **2015,** *25* (3), 607-10.
17. Kawaguchi, M.; Tani, T.; Hombu, R.; Ieda, N.; Nakagawa, H., Development and cellular application of visiblelight- controllable HNO releasers based on caged Piloty's acid. *Chem. Commun.,* **2018,** *54* (73), 10371-4.

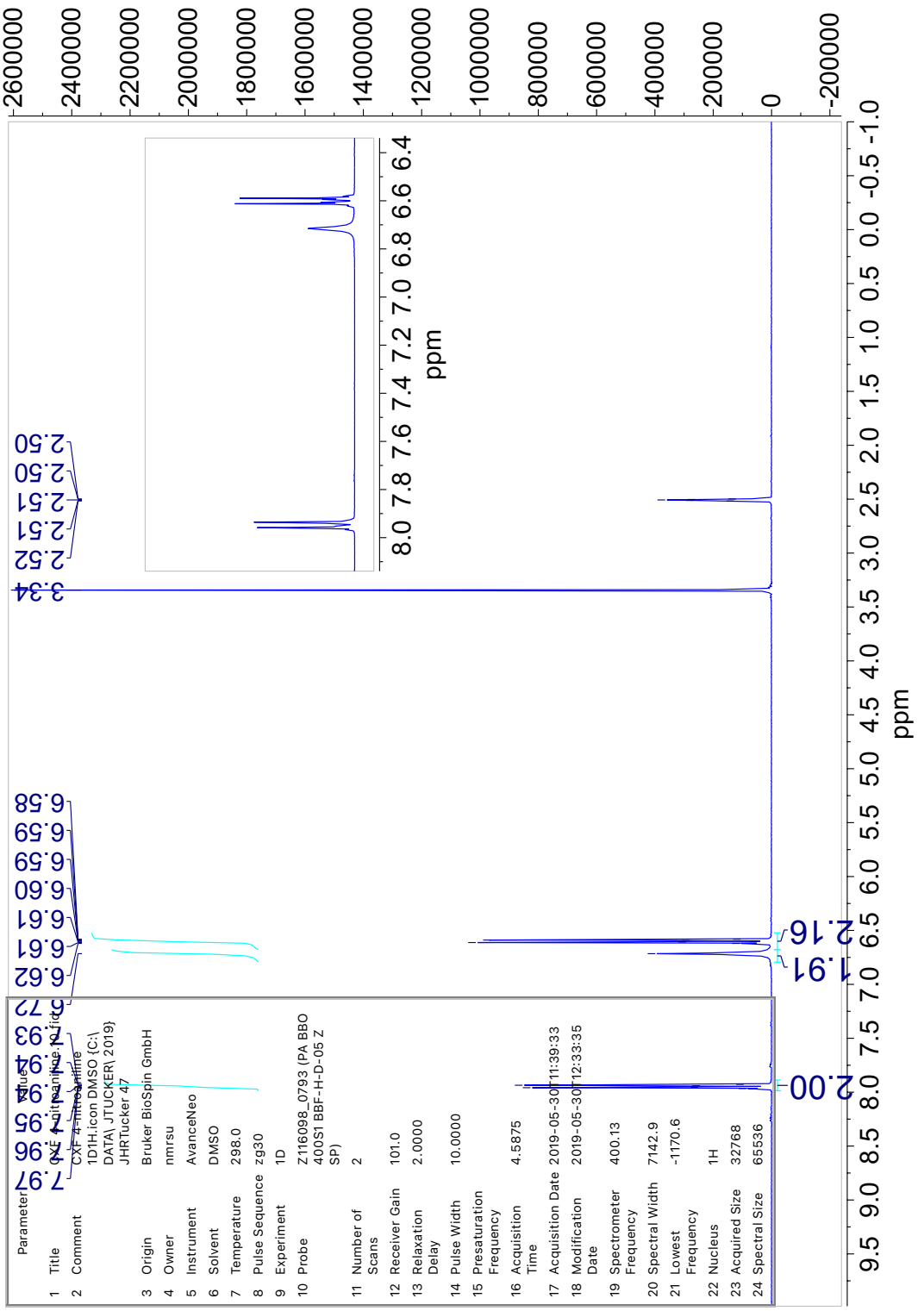
18. Aizawa, K.; Nakagawa, H.; Matsuo, K.; Kawai, K.; Ieda, N.; Suzuki, T.; Miyata, N., Piloty's acid derivative with improved nitroxyl-releasing characteristics. *Bioorg. Med. Chem. Lett.,* **2013,** *23* (8), 2340-3.

Chapter 8 Appendices

2.1 ^{1}H NMR stack of polymerisation attempt (2.61)



2.2 ^{1}H NMR of 4-nitroaniline

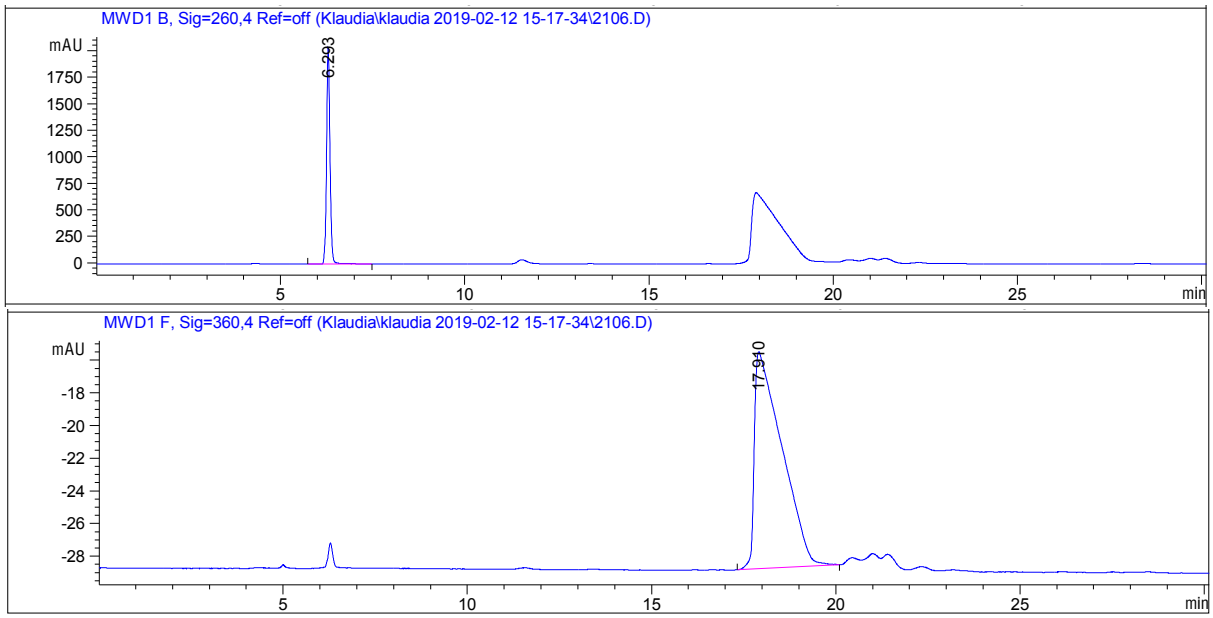


3.1 HPLC traces and MS of Chapter 3 DNA

Lin-A - 5'-TGGACTC(**X**)CTCAATG-3'

```
======================================================================
Acq. Operator   : SYSTEM                        Seq. Line :   1
Acq. Instrument : SemiPrep                       Location :   1
Injection Date  : 2/12/2019 3:18:36 PM               Inj :   1
                                                Inj Volume : Manually
Acq. Method     : C:\Chem32\1\Data\Klaudia\klaudia 2019-02-12 15-17-34\FcNA Anth 60oC.M
Last changed    : 2/12/2019 3:17:34 PM by SYSTEM
Analysis Method : C:\Chem32\1\Data\Klaudia\klaudia 2019-02-12 15-17-34\FcNA Anth 60oC.M (
                  Sequence Method)
Last changed    : 10/4/2021 8:48:29 AM by SYSTEM
                  (modified after loading)
Method Info     : Short Oligo

Additional Info : Peak(s) manually integrated
```

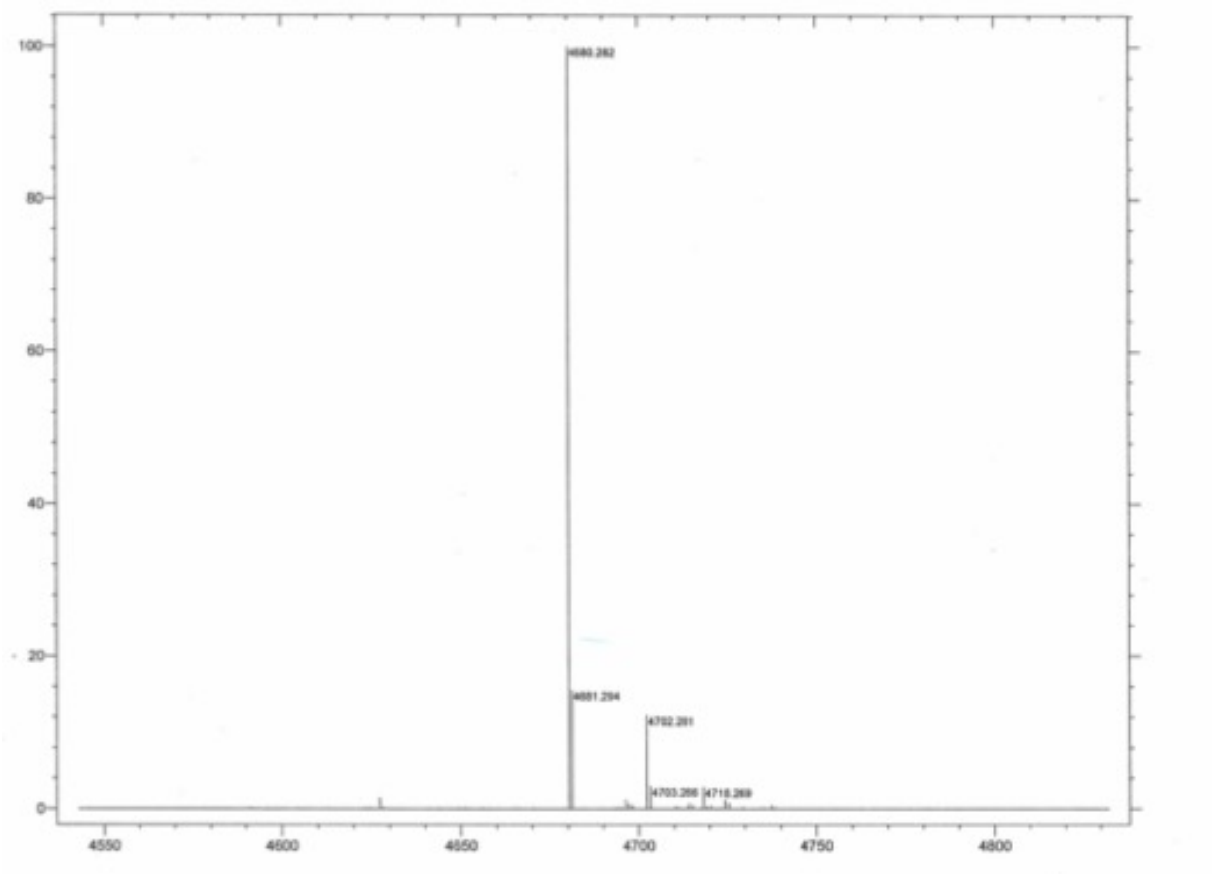



```
Signal 2: MWD1 B, Sig=260,4 Ref=off

Peak RetTime Type  Width     Area      Height     Area
  #   [min]        [min]   [mAU*s]     [mAU]       %
----|-------|----|-------|----------|----------|--------|
   1   6.293 BV R  0.0956 1.29834e4  2043.30457 100.0000

Totals :                  1.29834e4  2043.30457

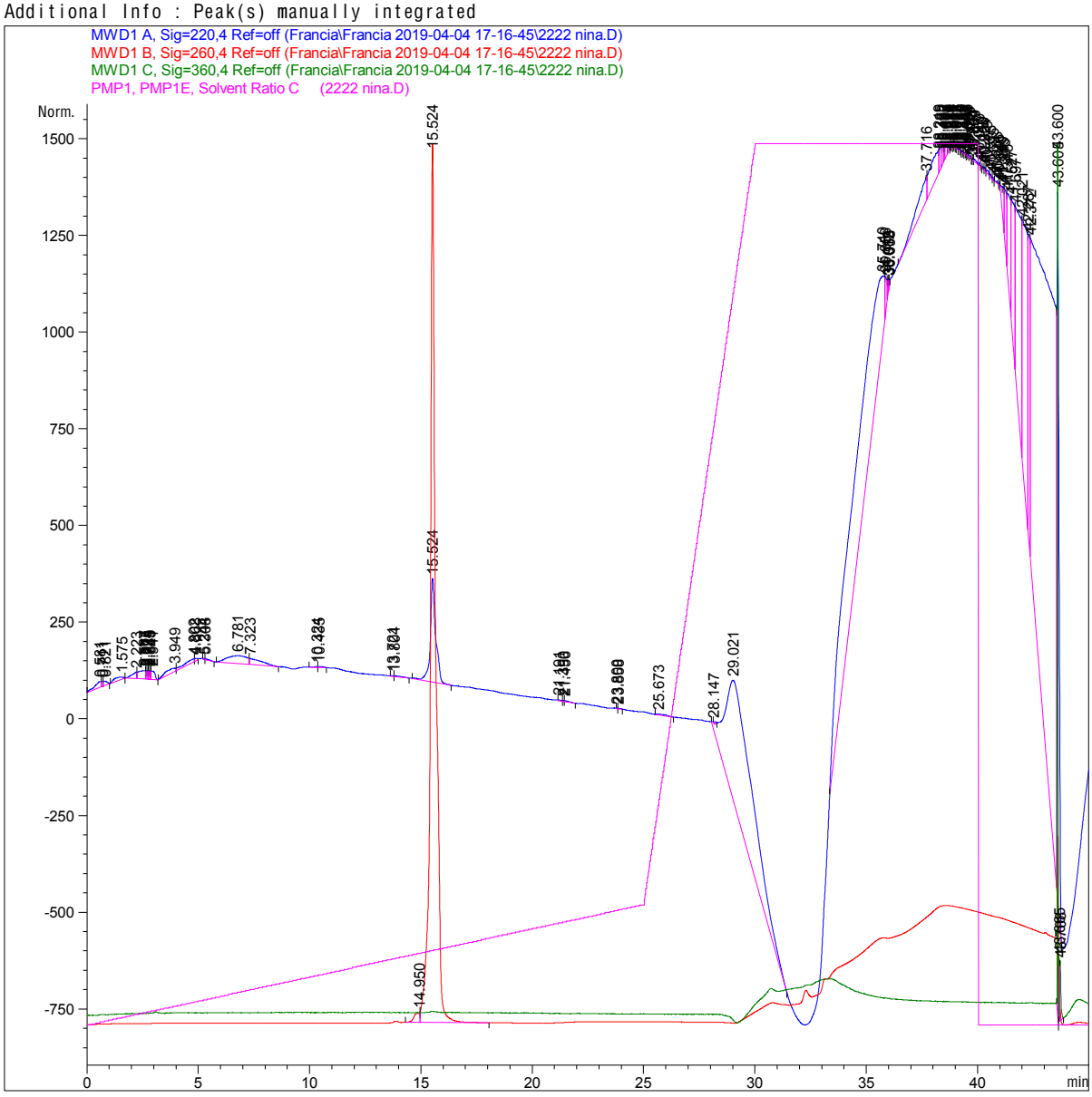
======================================================================
                          *** End of Report ***
```


100
80
60
40
20
0
4680.282
4681.294
4702.291
4703.266
4716.269
4550
4600
4650
4700
4750
4800

Lin-U - 5’-TGGACTC**C**CTCAATG-3’

```
======================================================================
Acq. Operator   : SYSTEM                          Seq. Line :   2
Acq. Instrument : LC-FC                            Location :   3
Injection Date  : 04-Apr-19 6:03:46 PM                 Inj :   1
                                                  Inj Volume : 15.000 µl
Different Inj Volume from Sample Entry!  Actual Inj Volume : 10.000 µl
Acq. Method     : C:\Chem32\3\Data\Francia\Francia 2019-04-04 17-16-45\Short Oligo 60°C.M
Last changed    : 06-Mar-19 1:42:46 PM by SYSTEM
Analysis Method : C:\Chem32\3\Data\Francia\Francia 2019-04-04 17-16-45\Short Oligo 60°C.M (
                  Sequence Method)
Last changed    : 05-Apr-19 8:41:29 AM by SYSTEM
Sample Info     : 2222 nina

Additional Info : Peak(s) manually integrated
```

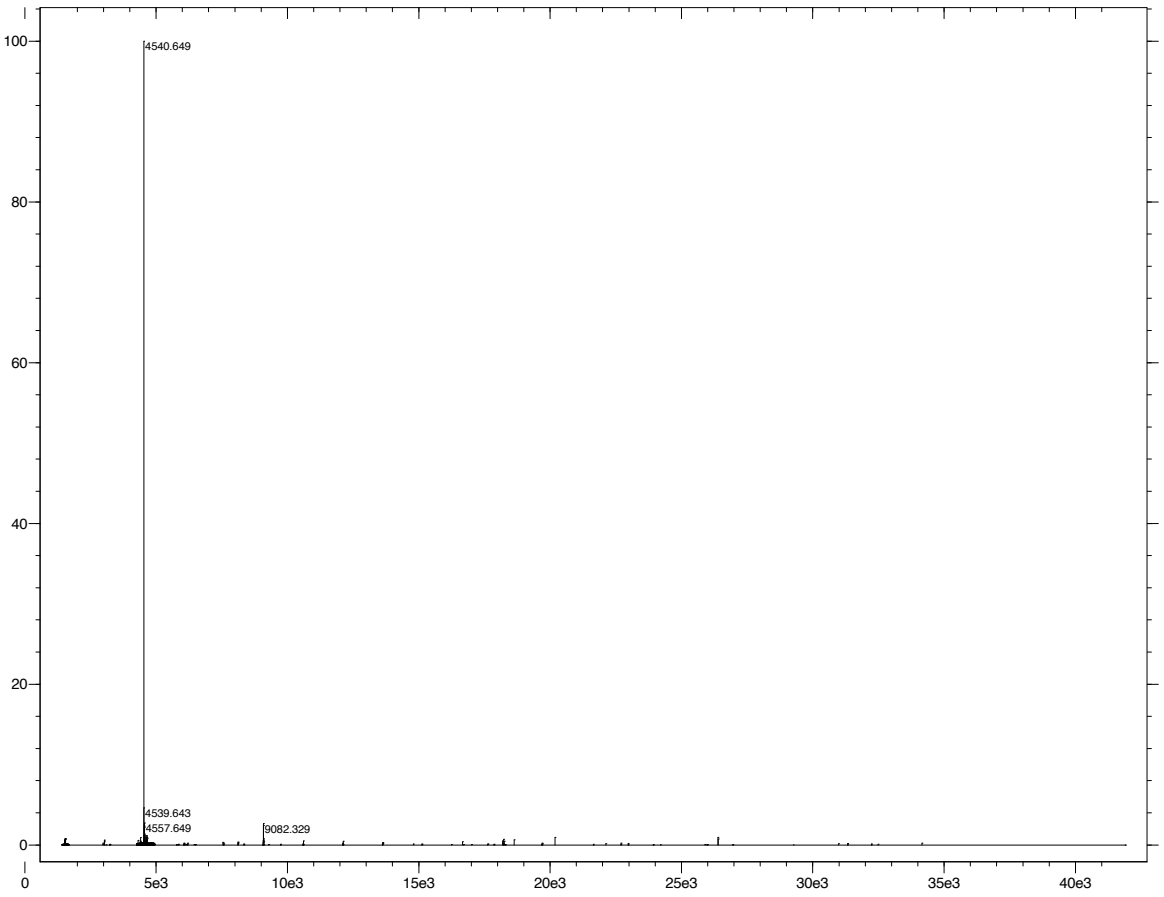


Signal 2: MWD1 B, Sig=260,4 Ref=off

Peak #	RetTime [min]	Type	Width [min]	Area [mAU*s]	Height [mAU]	Area %
1	14.950	MF	0.2731	73.52168	4.48698	1.0776
2	15.524	FM	0.2837	6749.26660	396.55170	98.9224
Totals :				6822.78828	401.03868	

*** End of Report ***

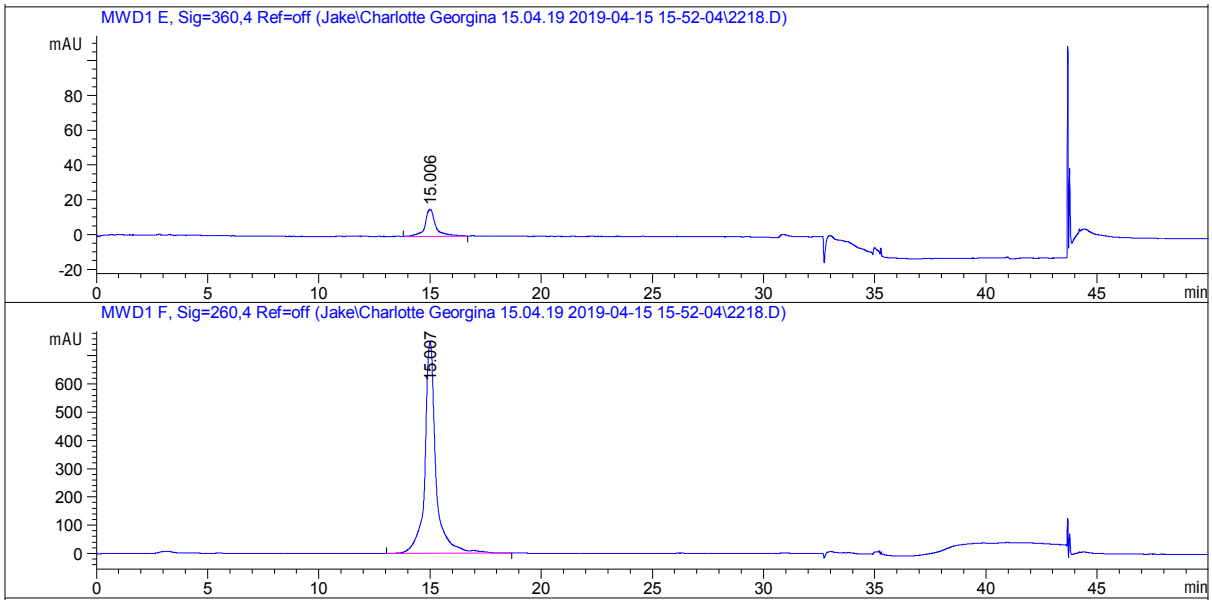
MS:



HP-A - 5’-CACGTT(**X**)TTCGTG-3’

```
=====================================================================
Acq. Operator   : SYSTEM                        Seq. Line :   2
Acq. Instrument : LC-FC                          Location :   41
Injection Date  : 15-Apr-19 4:47:18 PM                Inj :   1
                                               Inj Volume : 20.000 µl
Method          : C:\Chem32\3\Data\Jake\Charlotte Georgina 15.04.19 2019-04-15 15-52-04\FcNA
                  Anth 60oC.M (Sequence Method)
Last changed    : 15-Apr-19 3:48:45 PM by SYSTEM
Sample Info     : 2218

Additional Info : Peak(s) manually integrated
```




```
Signal 2: MWD1 E, Sig=360,4 Ref=off

Peak RetTime Type  Width     Area      Height     Area
  #   [min]        [min]   [mAU*s]     [mAU]       %
----|-------|----|-------|----------|----------|--------|
   1  15.006 BB    0.4927  515.63635   15.47502 100.0000

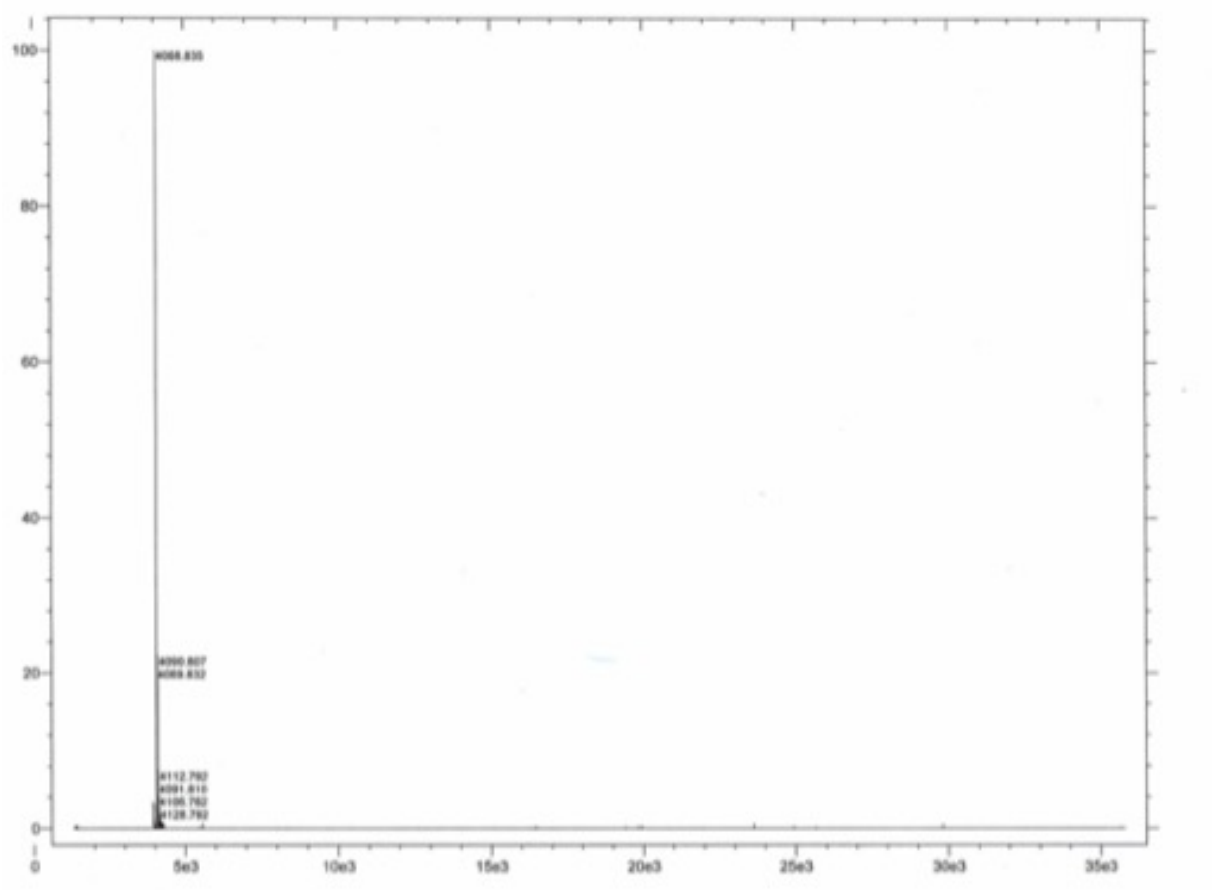
Totals :                   515.63635   15.47502


Signal 3: MWD1 F, Sig=260,4 Ref=off

Peak RetTime Type  Width     Area      Height     Area
  #   [min]        [min]   [mAU*s]     [mAU]       %
----|-------|----|-------|----------|----------|--------|
   1  15.007 VV R  0.5026 2.58798e4   749.20447 100.0000

Totals :                  2.58798e4   749.20447

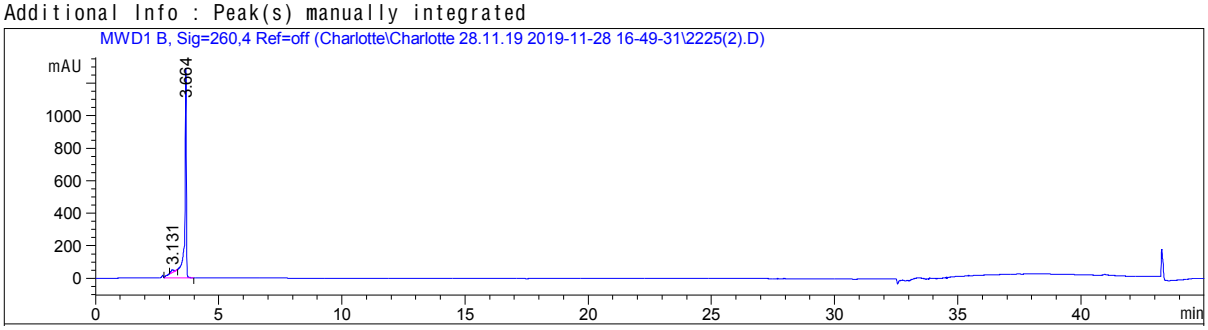

=====================================================================
                        *** End of Report ***
```


100
80
60
40
20
0
4068.835
4090.807
4069.832
4112.792
4091.810
4135.782
4128.792
0
5e3
10e3
15e3
20e3
25e3
30e3
35e3

HP-U - 5’-CACGTTTTTCGTG-3’

```
======================================================================
Acq. Operator   : SYSTEM                        Seq. Line :   2
Acq. Instrument : LC-FC                          Location :   2
Injection Date  : 28-Nov-19 5:36:31 PM                Inj :   1
                                               Inj Volume : 50.000 µl
Different Inj Volume from Sample Entry!  Actual Inj Volume : 10.000 µl
Method          : C:\Chem32\3\Data\Charlotte\Charlotte 28.11.19 2019-11-28 16-49-31\FcNA Anth
                  Charlotte D-A.M (Sequence Method)
Last changed    : 08-Aug-19 12:27:19 PM by SYSTEM
Sample Info     : 2225(2)

Additional Info : Peak(s) manually integrated
```

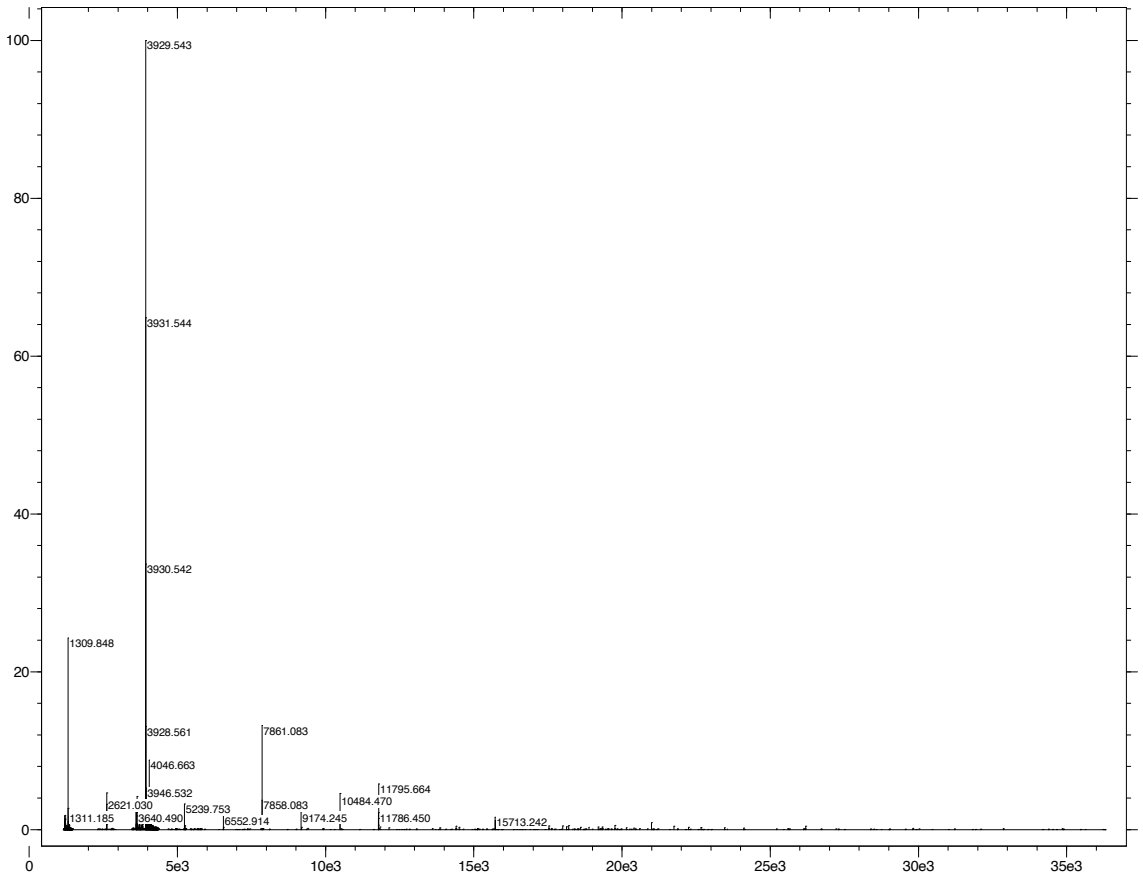



```
Signal 1: MWD1 B, Sig=260,4 Ref=off

Peak RetTime Type  Width     Area      Height     Area
  #   [min]        [min]   [mAU*s]     [mAU]       %
----|-------|----|-------|----------|----------|--------|
   1   3.131 BV E  0.1295  130.23422   15.91506   1.9333
   2   3.664 VB R  0.0736 6606.26660 1292.76123  98.0667

Totals :                  6736.50082 1308.67629

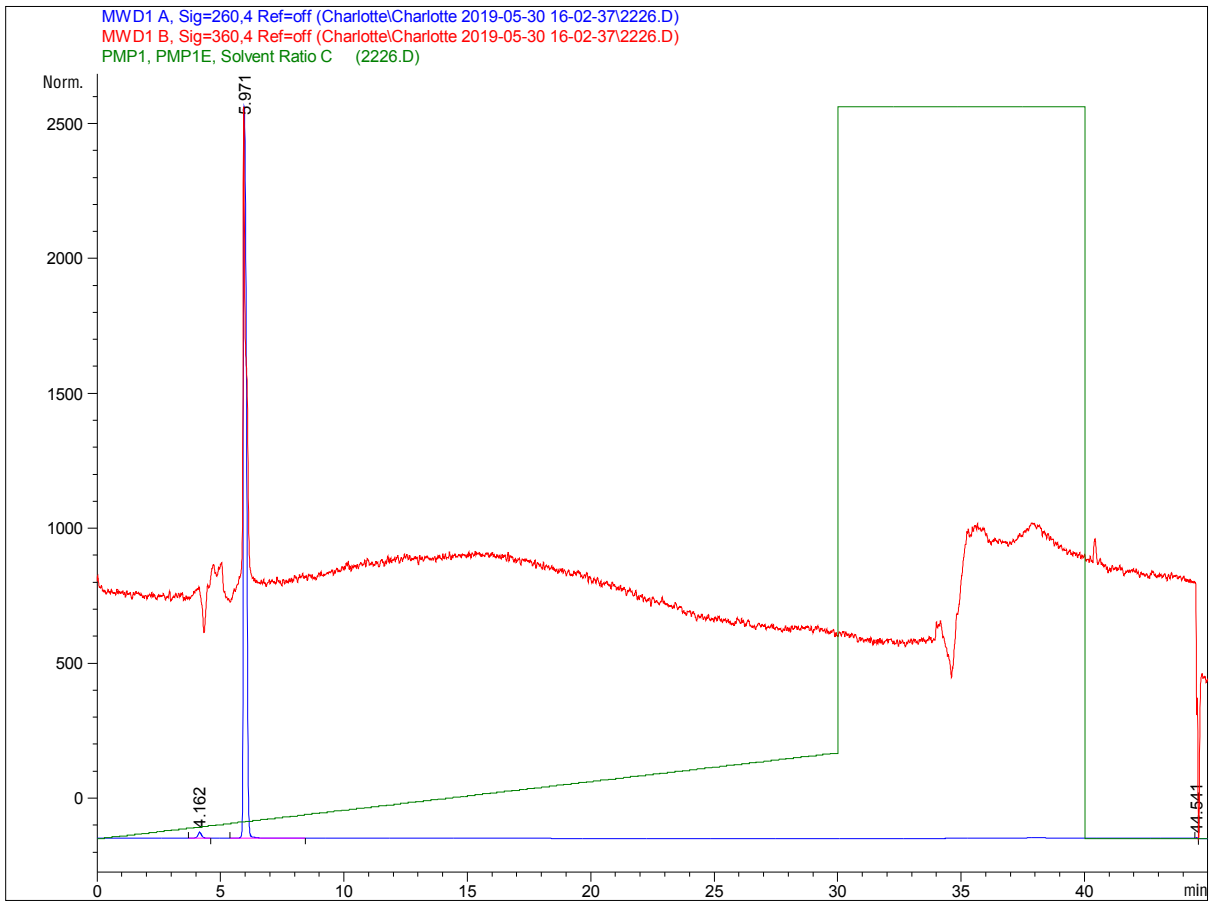
======================================================================
                          *** End of Report ***
```


100
80
60
40
20
0
3929.543
3931.544
3930.542
1309.848
3928.561
4046.663
3946.532
2621.030
5239.753
1311.185
3640.490
6552.914
7861.083
7858.083
9174.245
10484.470
11795.664
11786.450
15713.242
0
5e3
10e3
15e3
20e3
25e3
30e3
35e3

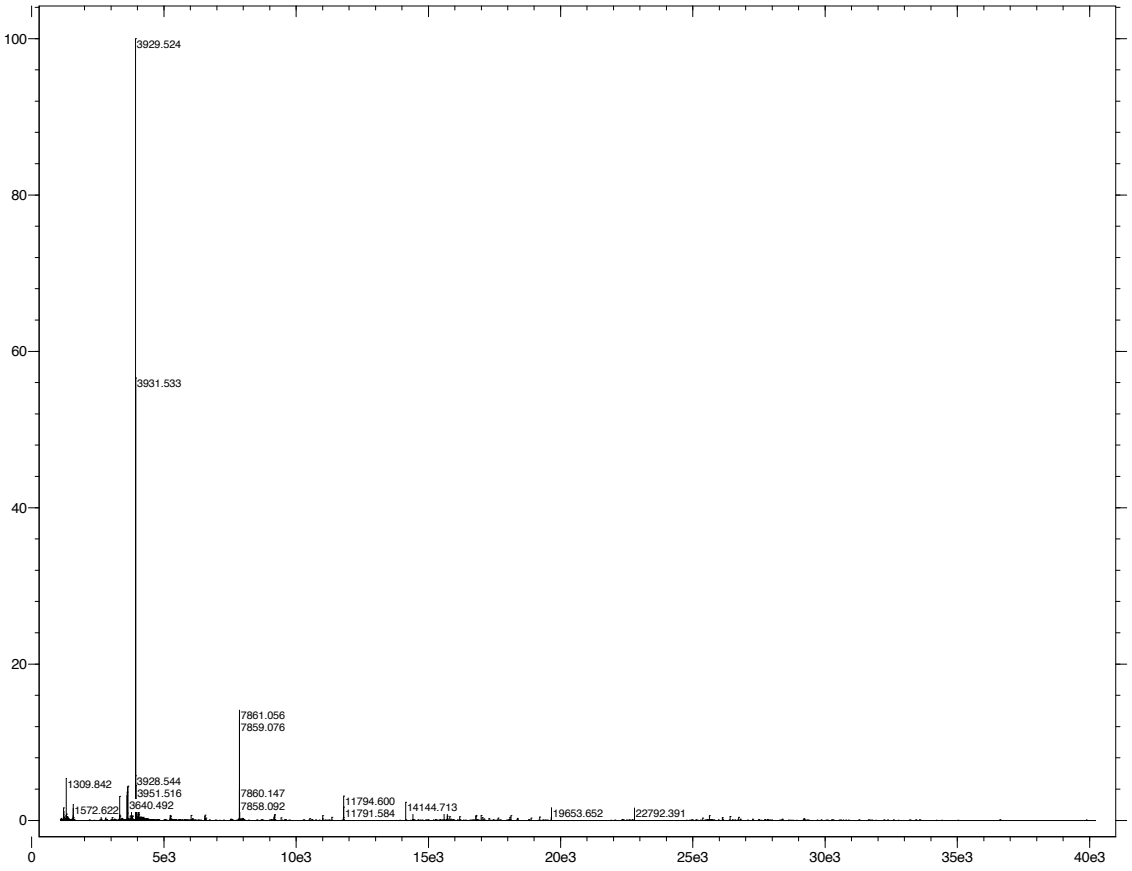
X

HP-C - 5’-GTGCAAAAAGCAC-3’

```
Acq. Operator    : SYSTEM                          Seq. Line :   1
Acq. Instrument  : SemiPrep                         Location :   1
Injection Date   : 5/30/2019 4:03:46 PM                 Inj :   1
                                                  Inj Volume : Manually
Method           : C:\Chem32\1\Data\Charlotte\Charlotte 2019-05-30 16-02-37\FcNA Anth 60oC
                   Hairpins.M (Sequence Method)788  98.9439
Last changed     : 5/30/2019 4:02:37 PM by SYSTEM1   0.0277
Method Info      : Short Oligo
 Totals :                 2.12740e4  2464.25828
Sample Info      : 2226
```



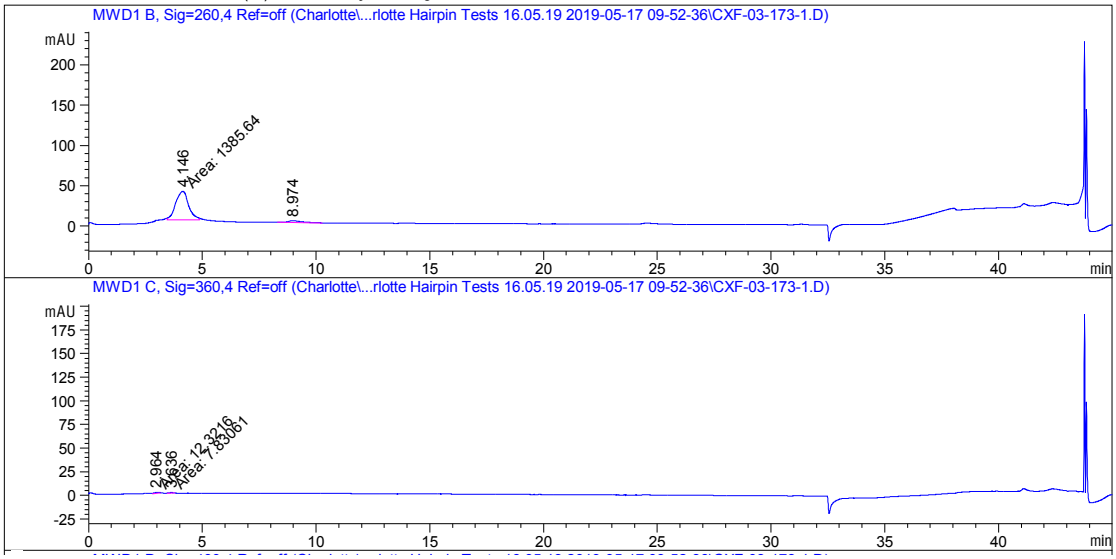
MS:


100
80
60
40
20
0
3929.524
3931.533
7861.056
7859.076
1309.842
3928.544
3951.516
1572.622
3640.492
7860.147
7858.092
11794.600
11791.584
14144.713
19653.652
22792.391
0
5e3
10e3
15e3
20e3
25e3
30e3
35e3
40e3

3.2 HPLC trace of HP-cycloaddition

```
=====================================================================
Acq. Operator   : SYSTEM                        Seq. Line :   3
Acq. Instrument : LC-FC                          Location :   62
Injection Date  : 17-May-19 11:27:51 AM               Inj :   1
                                                Inj Volume : 20.000 µl
Different Inj Volume from Sample Entry!  Actual Inj Volume : 100.000 µl
Acq. Method     : C:\Chem32\3\Data\Charlotte\Charlotte Hairpin Tests 16.05.19 2019-05-17 09-
                  52-36\FcNA Anth Charlotte D-A.M
Last changed    : 17-May-19 9:49:50 AM by SYSTEM
Analysis Method : C:\Chem32\3\Data\Charlotte\Charlotte Hairpin Tests 16.05.19 2019-05-17 09-
                  52-36\FcNA Anth Charlotte D-A.M (Sequence Method)
Last changed    : 17-May-19 2:21:11 PM by SYSTEM
Sample Info     : CXF-03-173-1

Additional Info : Peak(s) manually integrated
```




```
Signal 1: MWD1 B, Sig=260,4 Ref=off

Peak RetTime Type  Width     Area      Height     Area
  #   [min]        [min]   [mAU*s]     [mAU]       %
----|-------|----|-------|----------|----------|--------|
   1   4.146 MM    0.6572 1385.64417   35.14069  93.8591
   2   8.974 BB    0.4918   90.65867    2.33059   6.1409

Totals :                  1476.30283   37.47128


Signal 2: MWD1 C, Sig=360,4 Ref=off

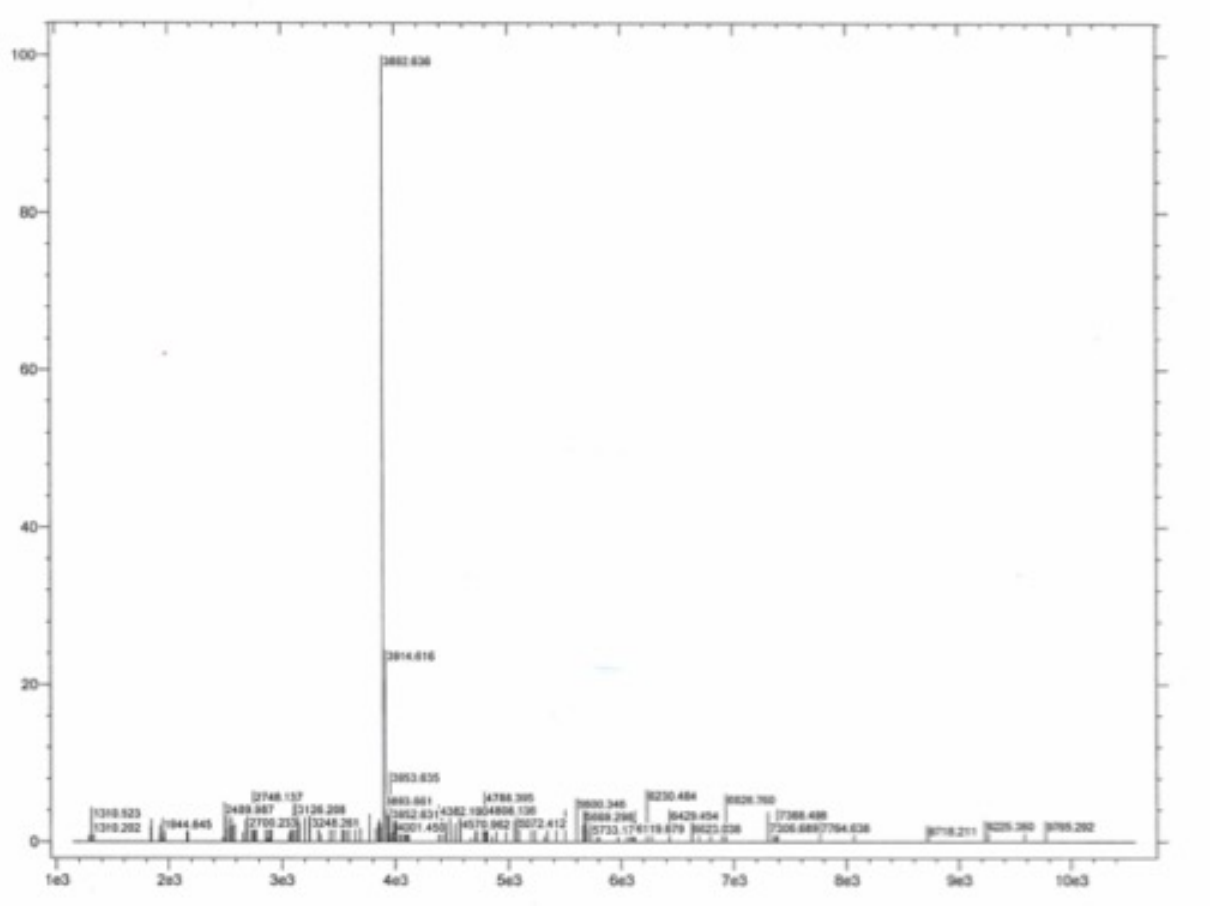
Peak RetTime Type  Width     Area      Height     Area
  #   [min]        [min]   [mAU*s]     [mAU]       %
----|-------|----|-------|----------|----------|--------|
   1   2.964 MM    0.1936   12.32160    1.06066  61.1427
   2   3.636 MM    0.2417    7.83061 5.39966e-1  38.8573

Totals :                    20.15220    1.60062

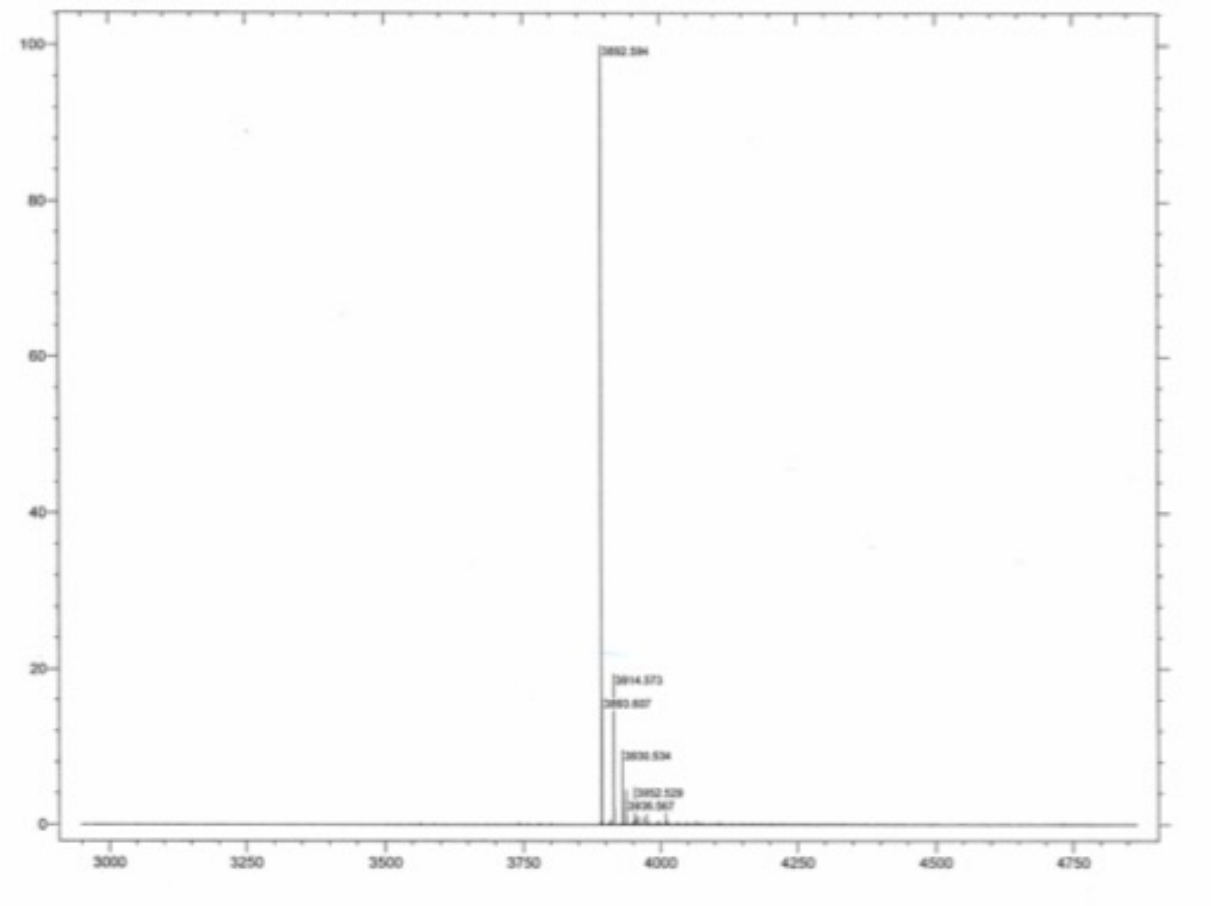
=====================================================================
                        *** End of Report ***
```

3.3 MS of HP-cycloaddition

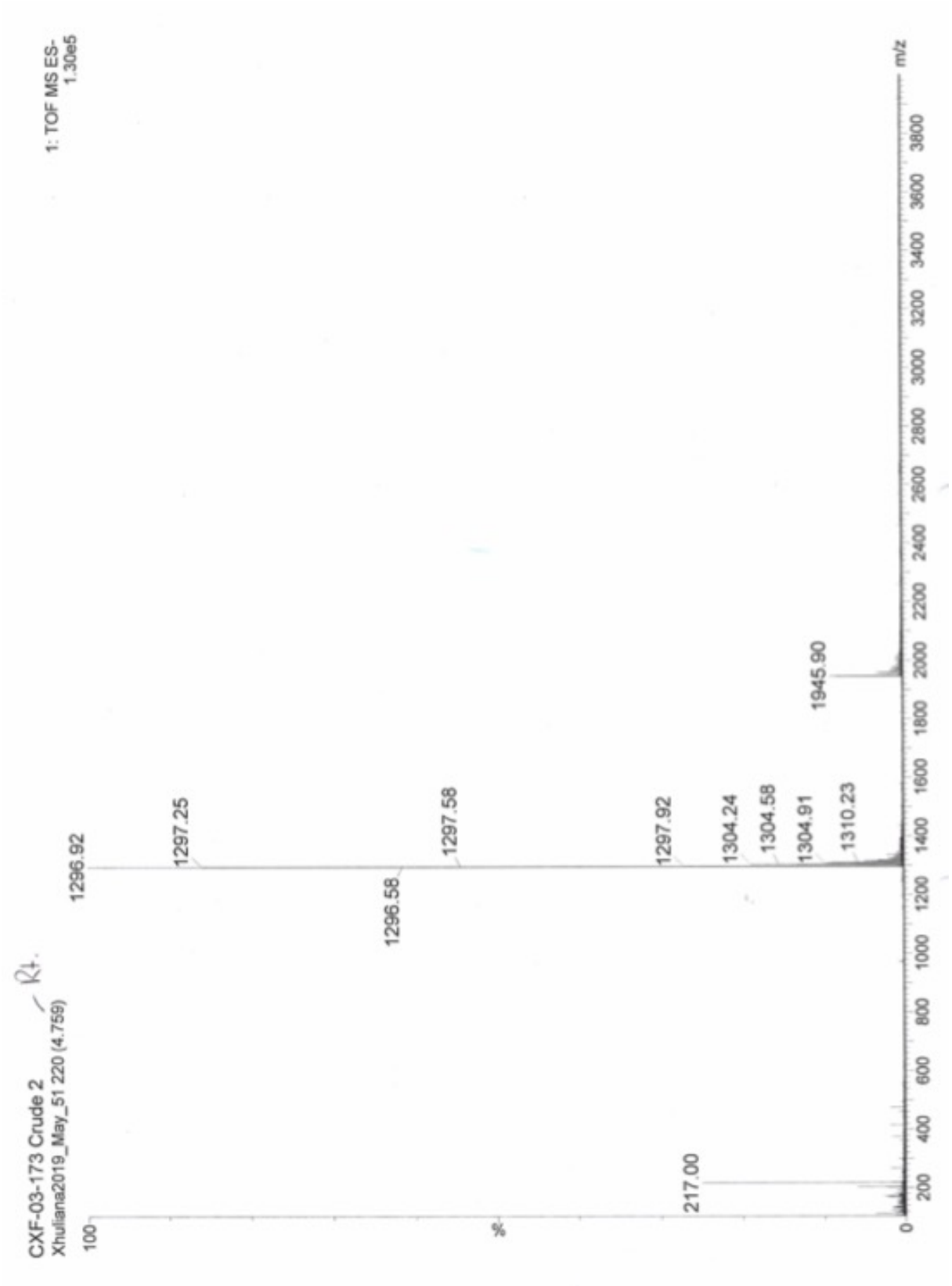
Fraction 3:



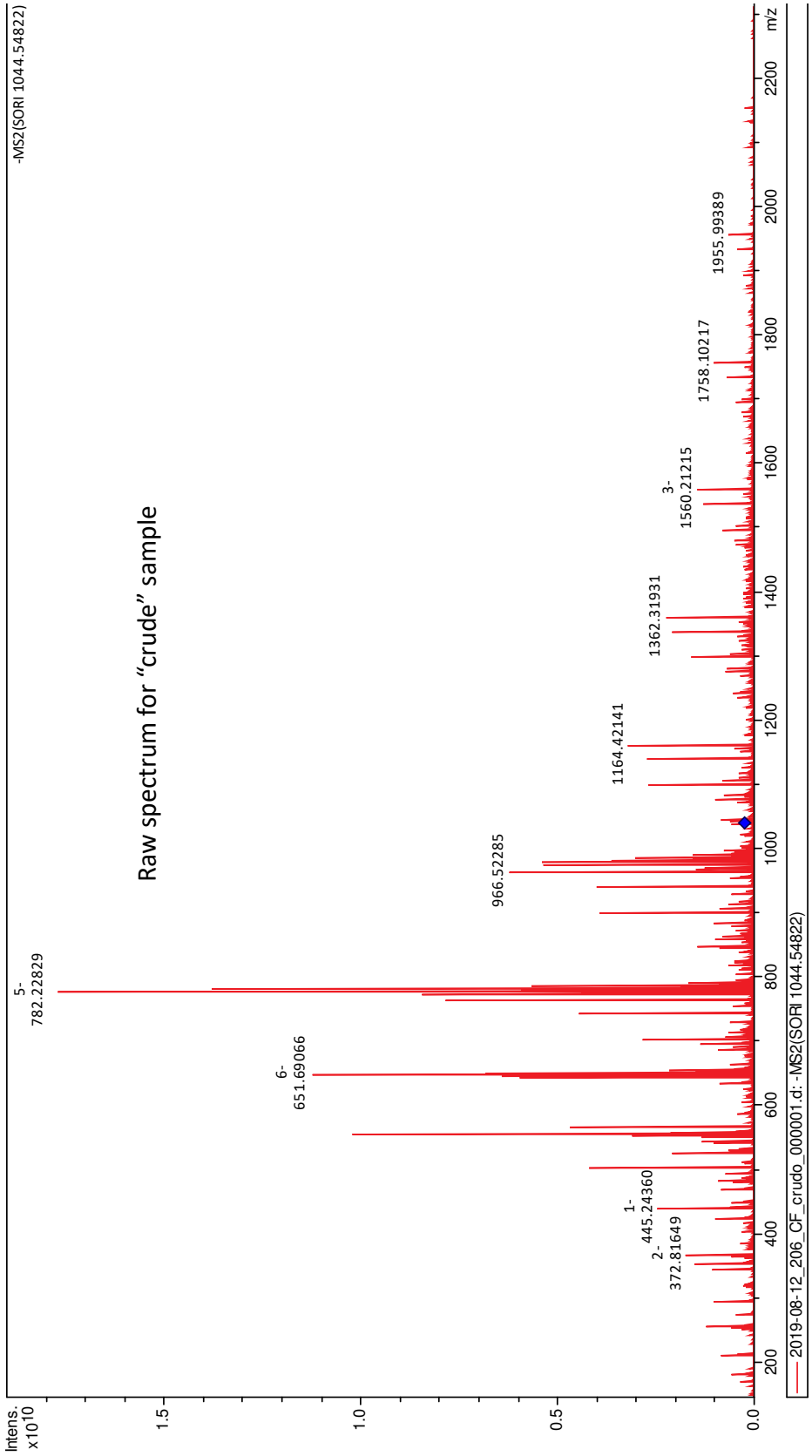
Crude:

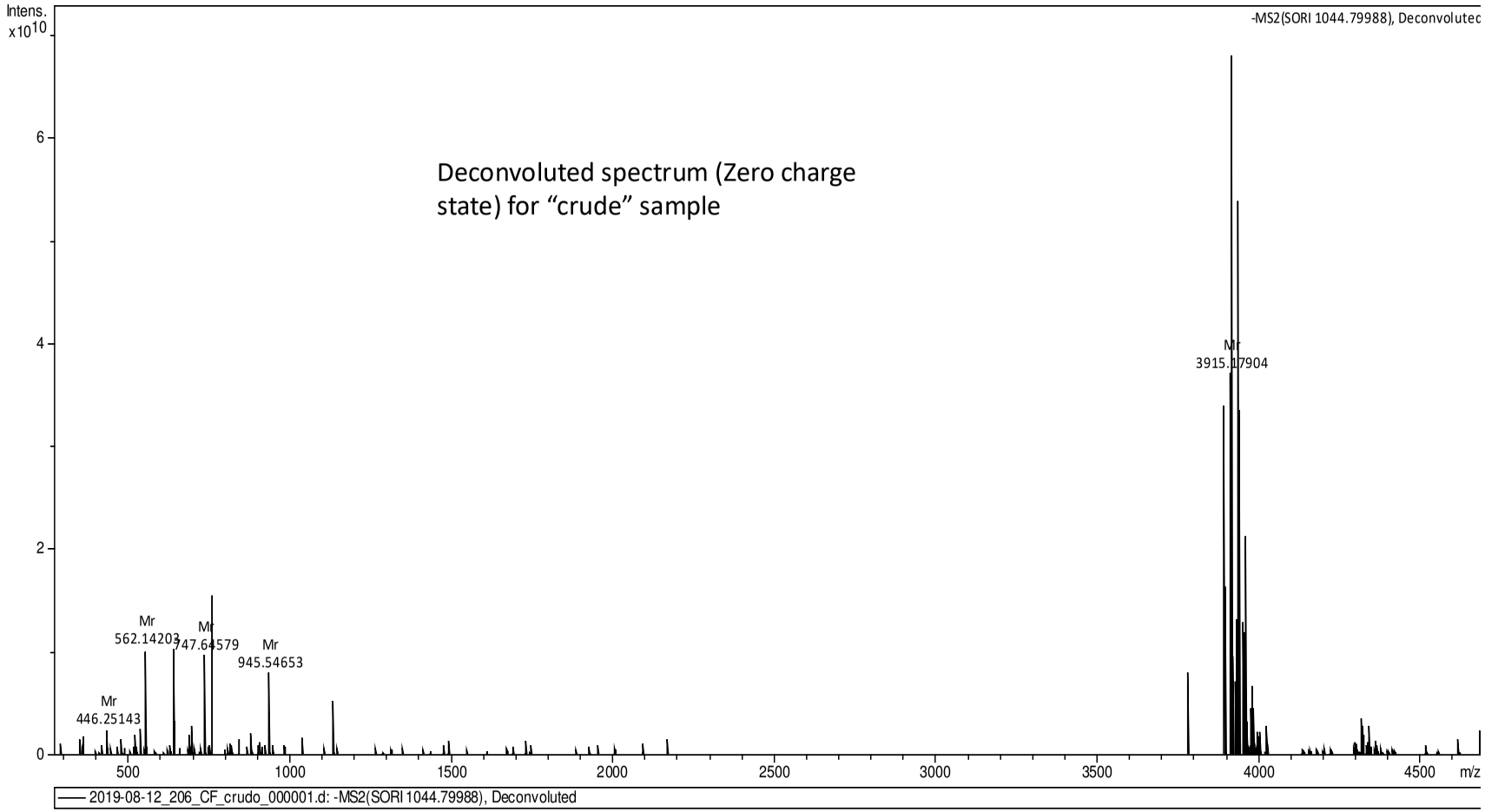


3.4 Extended range MS of HP-cycloaddition (raw data)

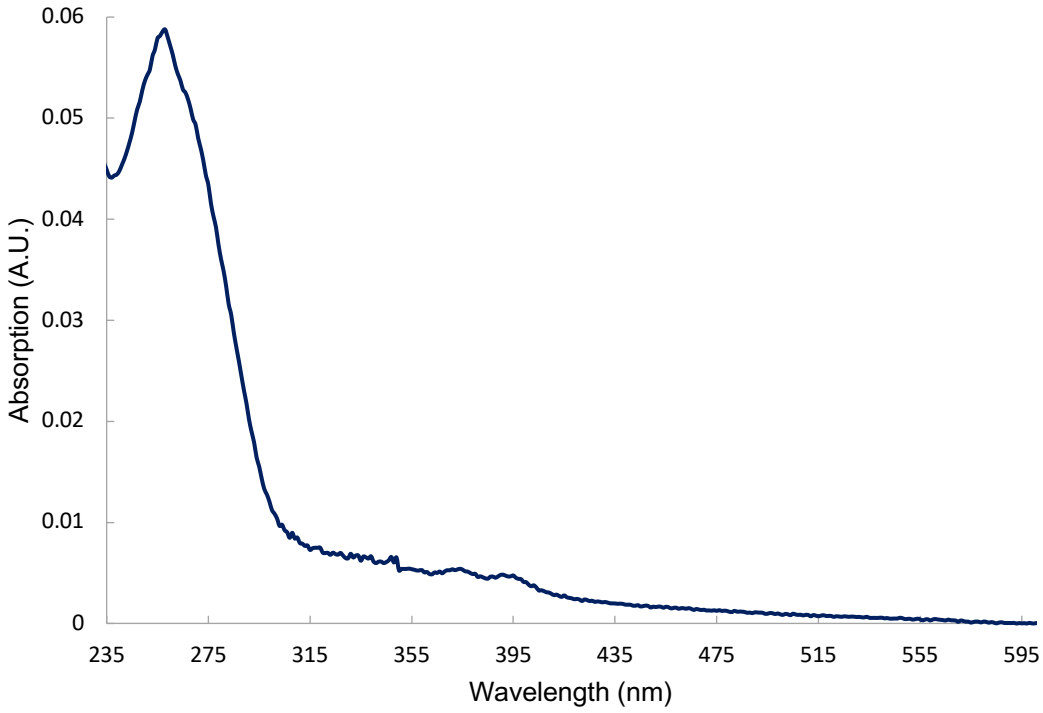


3.5 FT-ICR MS of HP-cycloaddition



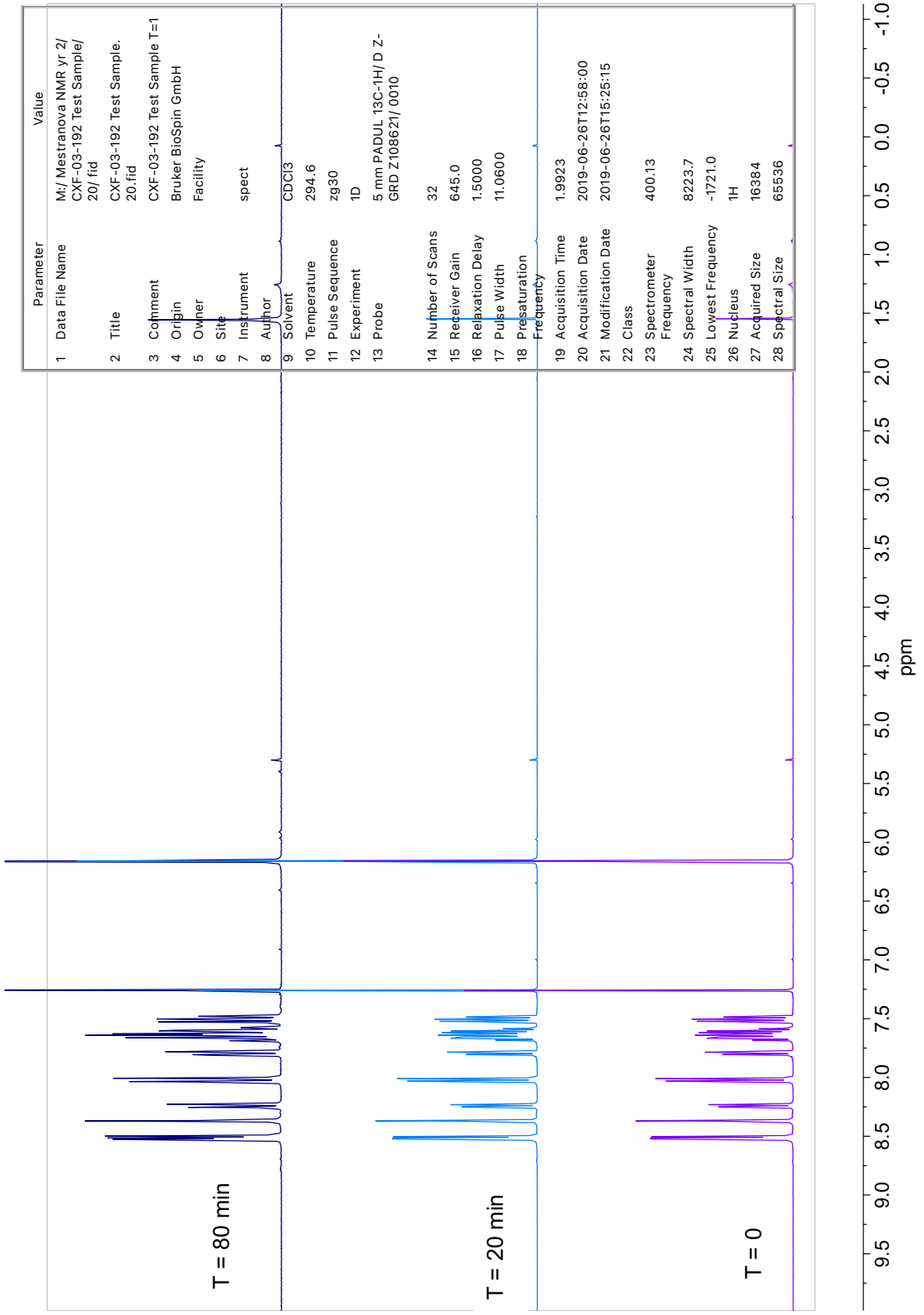

Intens.
x10^10
-MS2(SORI 1044.79988), Deconvolutec
Deconvoluted spectrum (Zero charge state) for “crude” sample
Mr
3915.17904
Mr
562.14203
Mr
747.64579
Mr
945.54653
Mr
446.25143
0
2
4
6
500
1000
1500
2000
2500
3000
3500
4000
4500
m/z
2019-08-12_206_CF_crudo_000001.d: -MS2(SORI 1044.79988), Deconvoluted

3.6 UV vis of HP-U



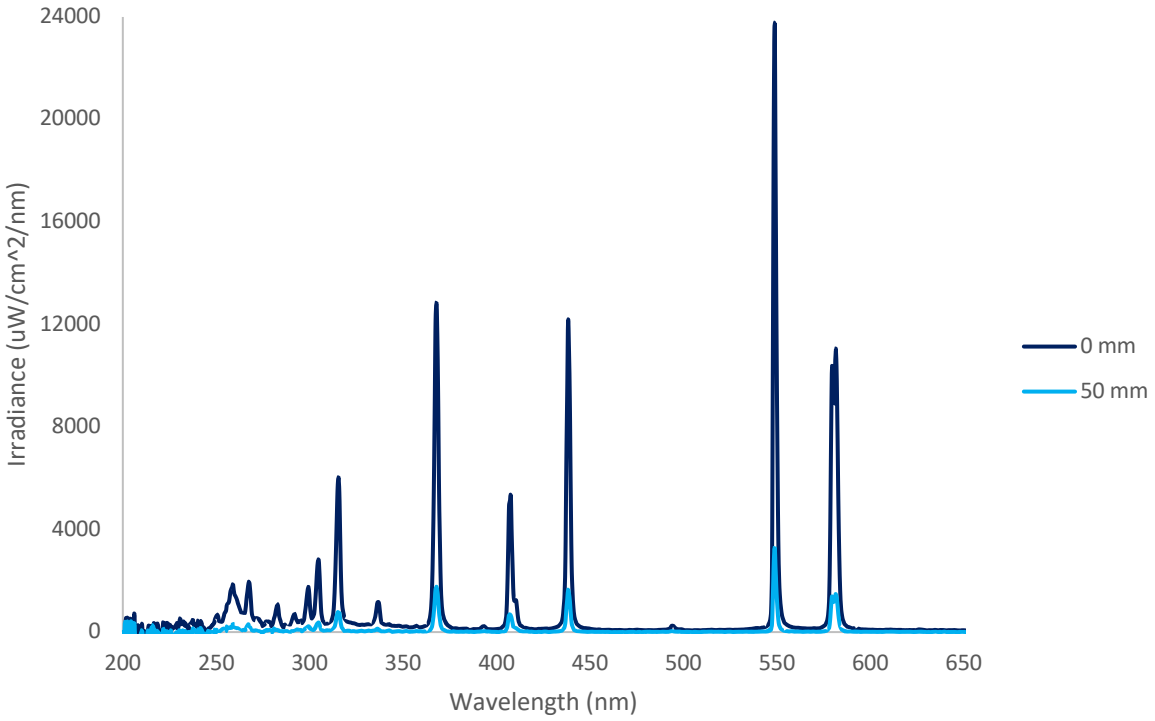
Appendix Figure 1 UV vis spectrum of HP-U (Mili Q H_2O)

4.1 ^{1}H NMR stack of Piloty's acid analogue 4.22 photo-irradiation using 125 W mercury lamp and 365 nm bandpass filter



	Parameter	Value
1	Data File Name	M:/ Mestranova NMR yr 2/ CXF-03-192 Test Sample/ 20/ fid
2	Title	CXF-03-192 Test Sample. 20.fid
3	Comment	CXF-03-192 Test Sample T=1
4	Origin	Bruker BioSpin GmbH
5	Owner	Facility
6	Site	
7	Instrument	spect
8	Author	
9	Solvent	CDCl3
10	Temperature	294.6
11	Pulse Sequence	zg30
12	Experiment	1D
13	Probe	5 mm PADUL 13C-1H/ D Z-GRD Z108621/ 0010
14	Number of Scans	32
15	Receiver Gain	645.0
16	Relaxation Delay	1.5000
17	Pulse Width	11.0600
18	Presaturation Frequency	
19	Acquisition Time	1.9923
20	Acquisition Date	2019-06-26T12:58:00
21	Modification Date	2019-06-26T15:25:15
22	Class	
23	Spectrometer Frequency	400.13
24	Spectral Width	8223.7
25	Lowest Frequency	-1721.0
26	Nucleus	1H
27	Acquired Size	16384
28	Spectral Size	65536

4.2 Irradiance of 125 W mercury lamp (0 mm and 50 mm distance of sensor from the lamp)

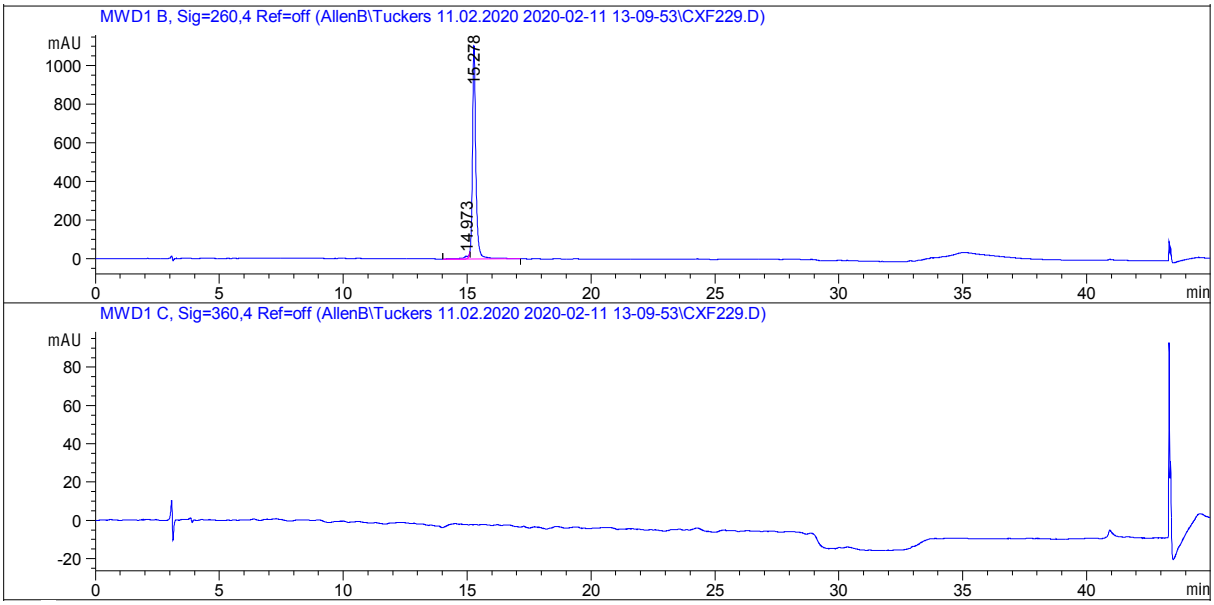


5.1 HPLC traces and MS of aptamer DNA strands

TBA:

```
======================================================================
Acq. Operator   : SYSTEM                        Seq. Line :   7
Acq. Instrument : LC-FC                          Location :   55
Injection Date  : 11-Feb-20 5:01:45 PM                Inj :   1
                                               Inj Volume : 15.000 µl
Different Inj Volume from Sample Entry!  Actual Inj Volume : 10.000 µl
Method          : C:\Chem32\3\Data\AllenB\Tuckers 11.02.2020 2020-02-11 13-09-53\Short Oligo
                  60°C.M (Sequence Method)
Last changed    : 06-Mar-19 1:42:46 PM by SYSTEM
Sample Info     : CXF229

Additional Info : Peak(s) manually integrated
```



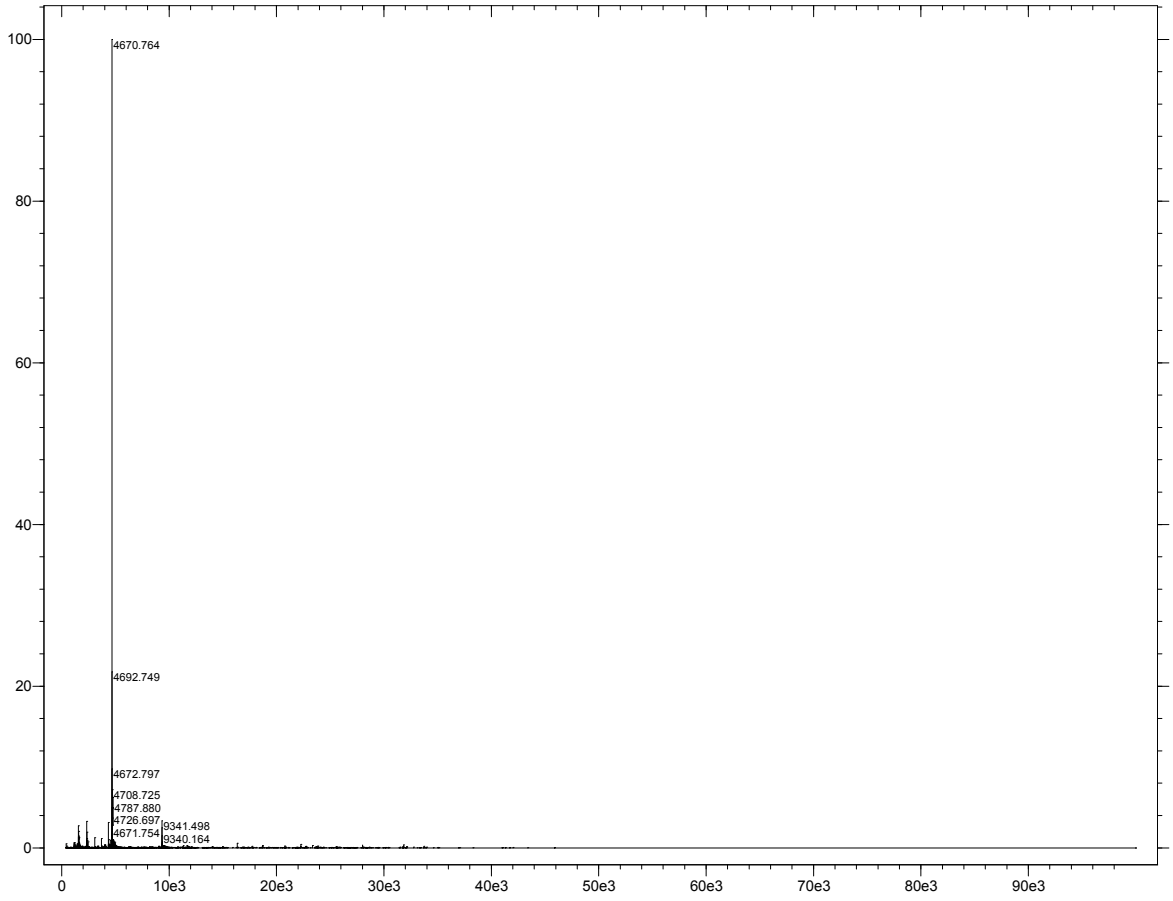

```
Signal 2: MWD1 B, Sig=260,4 Ref=off

Peak RetTime Type  Width     Area      Height     Area
  #   [min]        [min]   [mAU*s]     [mAU]       %
----|-------|----|-------|----------|----------|--------|
   1  14.973 BV E  0.2354  247.31860   13.65082   2.2596
   2  15.278 VV R  0.1407 1.06979e4  1107.35889  97.7404

Totals :                  1.09453e4  1121.00970


Signal 3: MWD1 C, Sig=360,4 Ref=off

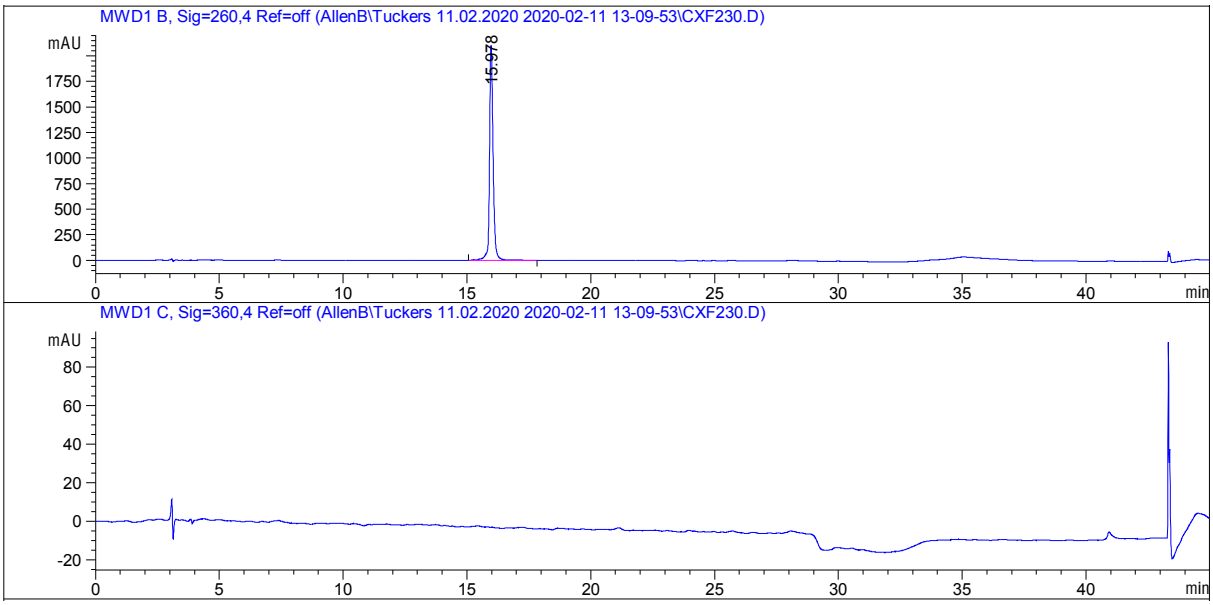
======================================================================
                        *** End of Report ***
```


100
80
60
40
20
0
4670.764
4692.749
4672.797
4708.725
4787.880
4726.697
4671.754
9341.498
9340.164
0
10e3
20e3
30e3
40e3
50e3
60e3
70e3
80e3
90e3

TBA$_L$:

```
=====================================================================
Acq. Operator   : SYSTEM                        Seq. Line :   8
Acq. Instrument : LC-FC                          Location :   56
Injection Date  : 11-Feb-20 5:47:45 PM               Inj :   1
                                                Inj Volume : 15.000 µl
Different Inj Volume from Sample Entry!  Actual Inj Volume : 10.000 µl
Method          : C:\Chem32\3\Data\AllenB\Tuckers 11.02.2020 2020-02-11 13-09-53\Short Oligo
                  60°C.M (Sequence Method)
Last changed    : 06-Mar-19 1:42:46 PM by SYSTEM
Sample Info     : CXF230

Additional Info : Peak(s) manually integrated
```



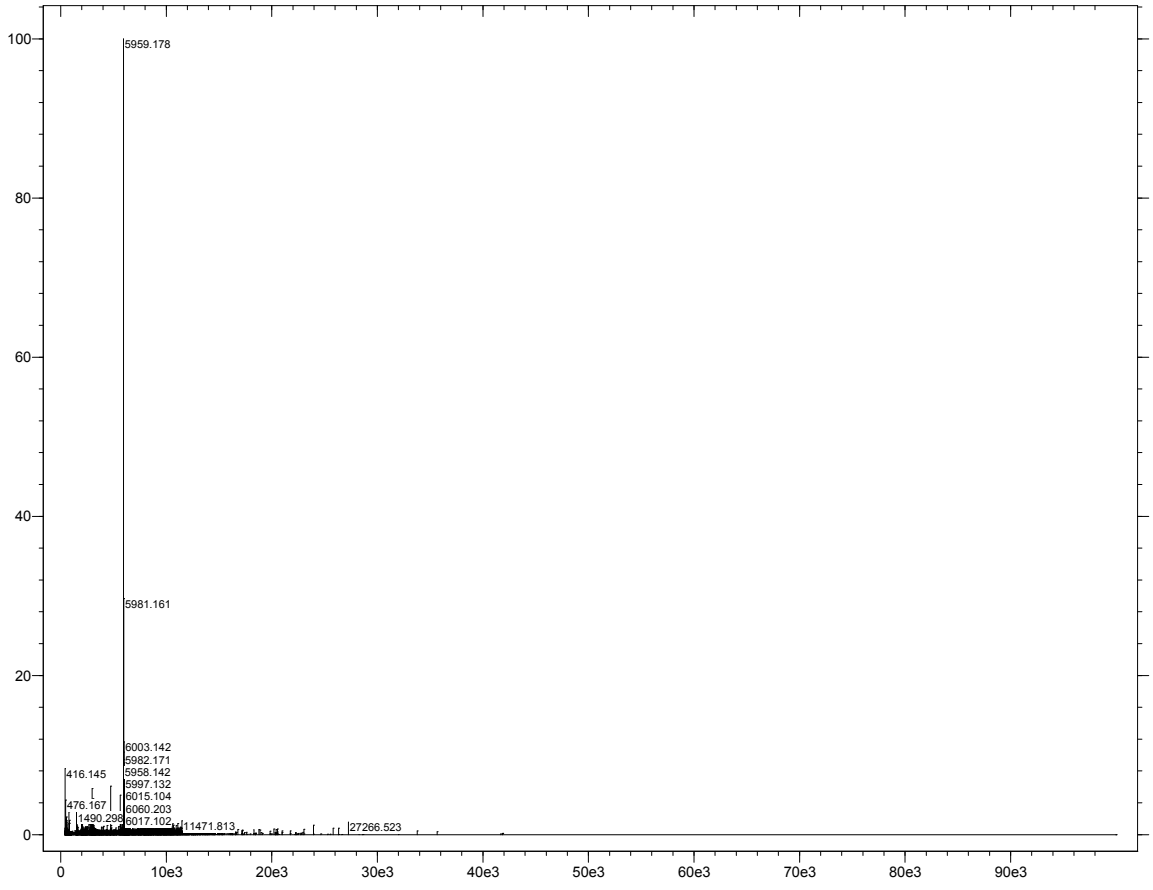

```
Signal 2: MWD1 B, Sig=260,4 Ref=off

Peak RetTime Type  Width     Area      Height     Area
  #   [min]        [min]   [mAU*s]     [mAU]       %
----|-------|----|-------|----------|----------|--------|
   1  15.978 VV R  0.1504 2.10605e4  2102.38989 100.0000

Totals :                  2.10605e4  2102.38989


Signal 3: MWD1 C, Sig=360,4 Ref=off

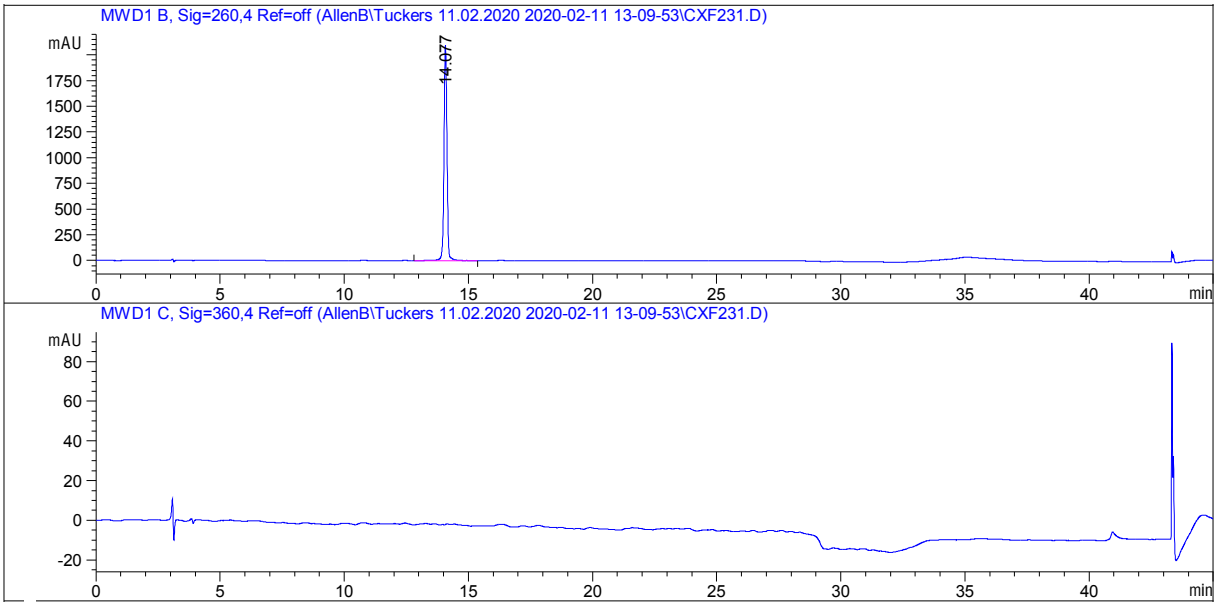
=====================================================================
                          *** End of Report ***
```


100
80
60
40
20
0
5959.178
5981.161
6003.142
5982.171
5958.142
5997.132
6015.104
6060.203
6017.102
416.145
476.167
1490.298
11471.813
27266.523
0
10e3
20e3
30e3
40e3
50e3
60e3
70e3
80e3
90e3

TBA$_C$:

```
=====================================================================
Acq. Operator   : SYSTEM                          Seq. Line :   9
Acq. Instrument : LC-FC                            Location :   57
Injection Date  : 11-Feb-20 6:33:45 PM                 Inj :   1
                                                  Inj Volume : 15.000 µl
Different Inj Volume from Sample Entry!  Actual Inj Volume : 10.000 µl
Method          : C:\Chem32\3\Data\AllenB\Tuckers 11.02.2020 2020-02-11 13-09-53\Short Oligo
                  60°C.M (Sequence Method)
Last changed    : 06-Mar-19 1:42:46 PM by SYSTEM
Sample Info     : CXF231

Additional Info : Peak(s) manually integrated
```



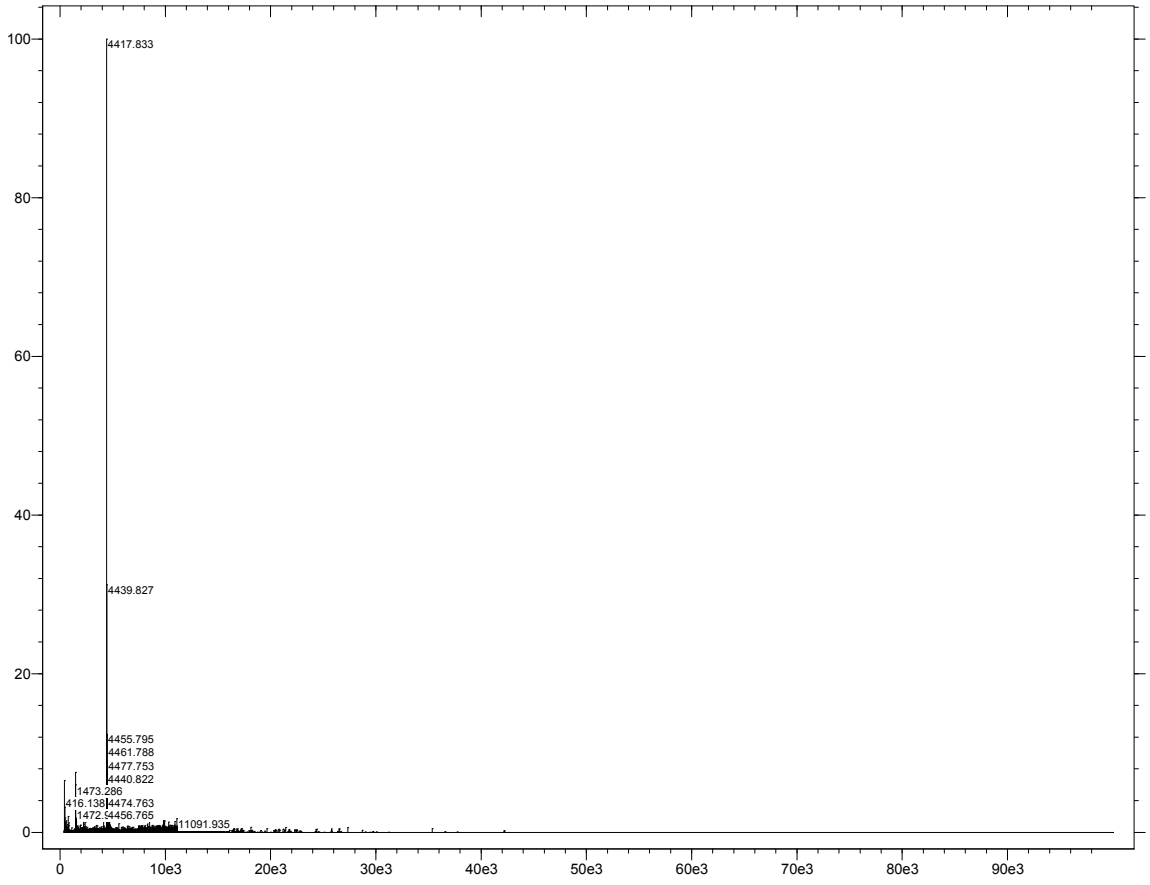

```
Signal 2: MWD1 B, Sig=260,4 Ref=off

Peak RetTime Type  Width     Area      Height     Area
  #   [min]        [min]   [mAU*s]     [mAU]       %
----|-------|----|-------|----------|----------|--------|
   1  14.077 BV R  0.1269 1.74355e4  2099.16089 100.0000

Totals :                  1.74355e4  2099.16089


Signal 3: MWD1 C, Sig=360,4 Ref=off

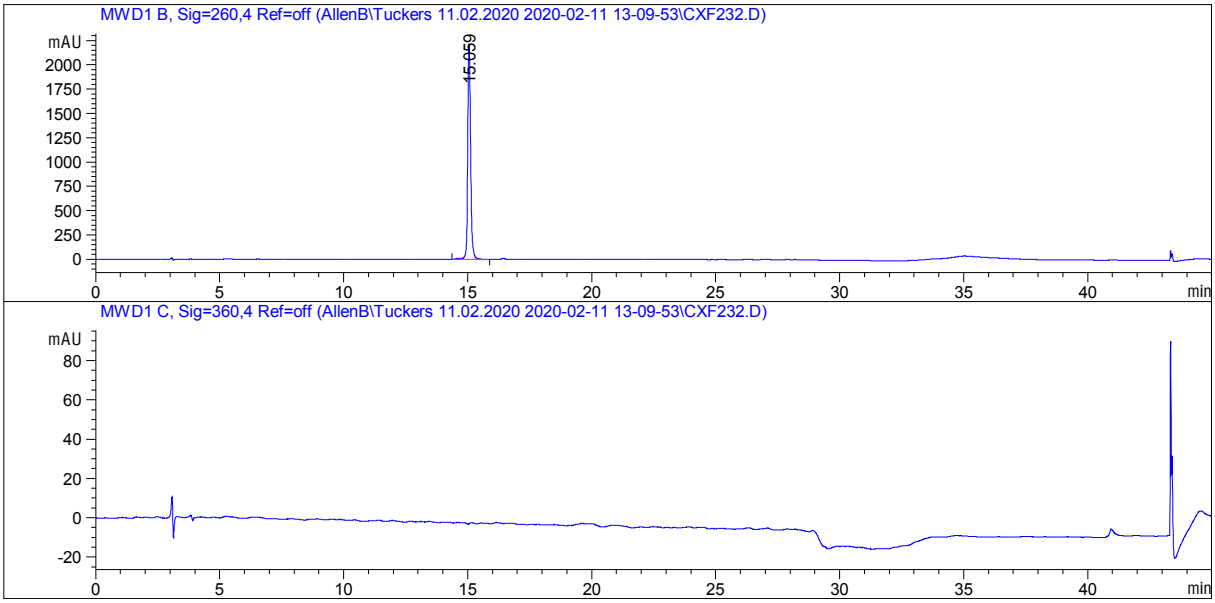
=====================================================================
                        *** End of Report ***
```


100
80
60
40
20
0
4417.833
4439.827
4455.795
4461.788
4477.753
4440.822
1473.286
416.138
4474.763
1472.5
4456.765
11091.935
0
10e3
20e3
30e3
40e3
50e3
60e3
70e3
80e3
90e3

TBA_{LC}:

```
=====================================================================
Acq. Operator   : SYSTEM                          Seq. Line :  10
Acq. Instrument : LC-FC                            Location :  58
Injection Date  : 11-Feb-20 7:19:44 PM                 Inj :  1
                                                  Inj Volume : 15.000 µl
Different Inj Volume from Sample Entry!  Actual Inj Volume : 10.000 µl
Method          : C:\Chem32\3\Data\AllenB\Tuckers 11.02.2020 2020-02-11 13-09-53\Short Oligo
                  60°C.M (Sequence Method)
Last changed    : 06-Mar-19 1:42:46 PM by SYSTEM
Sample Info     : CXF232

Additional Info : Peak(s) manually integrated
```



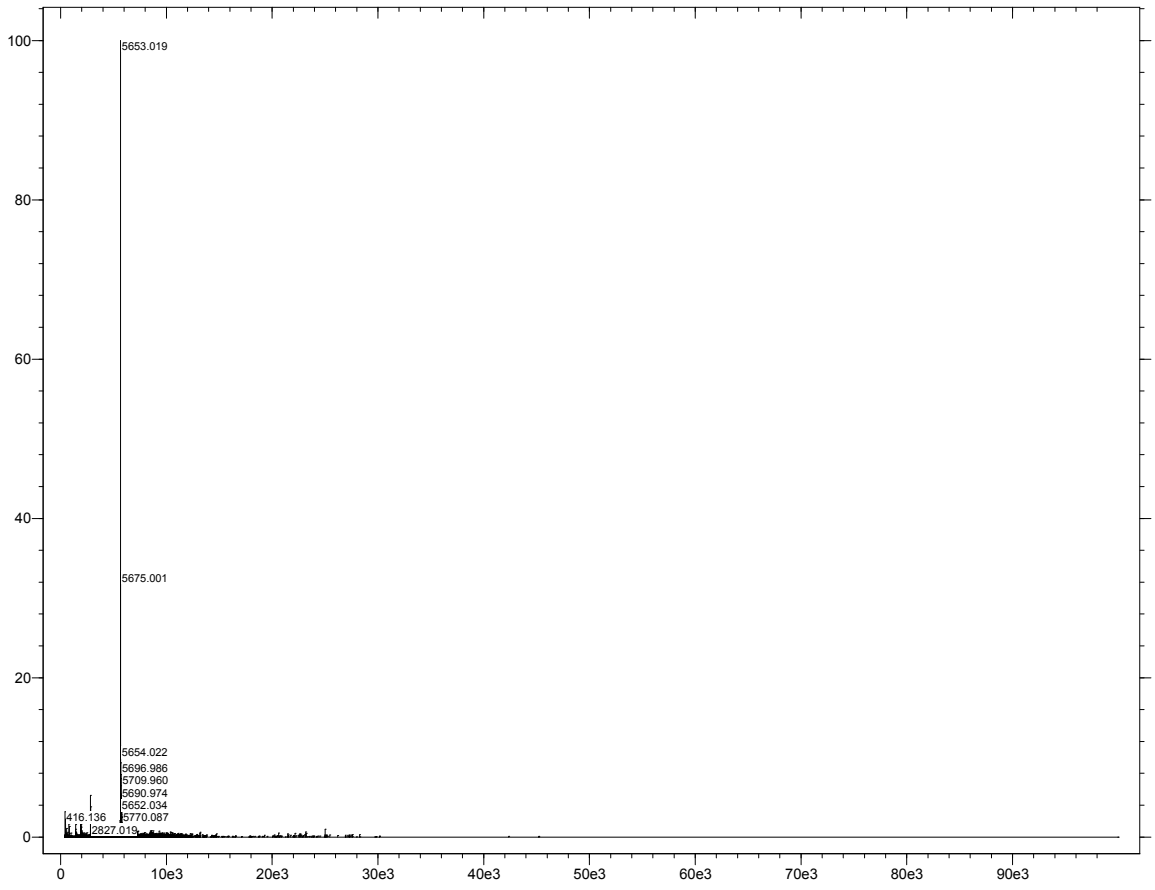

```
Signal 2: MWD1 B, Sig=260,4 Ref=off

Peak RetTime Type  Width     Area      Height     Area
  #   [min]        [min]   [mAU*s]     [mAU]       %
----|-------|----|-------|----------|----------|--------|
   1  15.059 VB R  0.1237 1.78960e4  2215.84497 100.0000

Totals :                  1.78960e4  2215.84497


Signal 3: MWD1 C, Sig=360,4 Ref=off

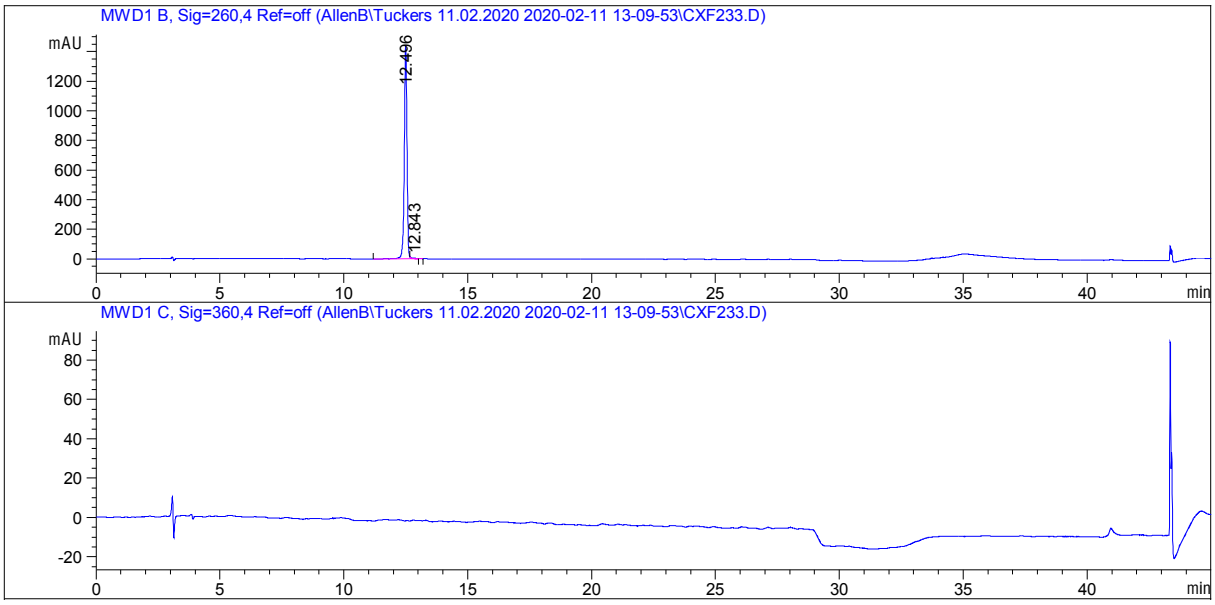
=====================================================================
                          *** End of Report ***
```


100
80
60
40
20
0
5653.019
5675.001
5654.022
5696.986
5709.960
5690.974
5652.034
5770.087
416.136
2827.019
0
10e3
20e3
30e3
40e3
50e3
60e3
70e3
80e3
90e3

SHORT$_C$:

```
======================================================================
Acq. Operator   : SYSTEM                          Seq. Line :  11
Acq. Instrument : LC-FC                            Location :   59
Injection Date  : 11-Feb-20 8:05:44 PM                  Inj :   1
                                                 Inj Volume : 15.000 µl
Different Inj Volume from Sample Entry!  Actual Inj Volume : 10.000 µl
Method          : C:\Chem32\3\Data\AllenB\Tuckers 11.02.2020 2020-02-11 13-09-53\Short Oligo
                  60°C.M (Sequence Method)
Last changed    : 06-Mar-19 1:42:46 PM by SYSTEM
Sample Info     : CXF233

Additional Info : Peak(s) manually integrated
```




```
Signal 2: MWD1 B, Sig=260,4 Ref=off

Peak RetTime Type  Width     Area      Height     Area
  #   [min]        [min]   [mAU*s]     [mAU]       %
----|-------|----|-------|----------|----------|--------|
   1  12.496 VV R  0.1123 1.06962e4  1445.73669  99.4978
   2  12.843 VV E  0.1642   53.99231    4.69454   0.5022

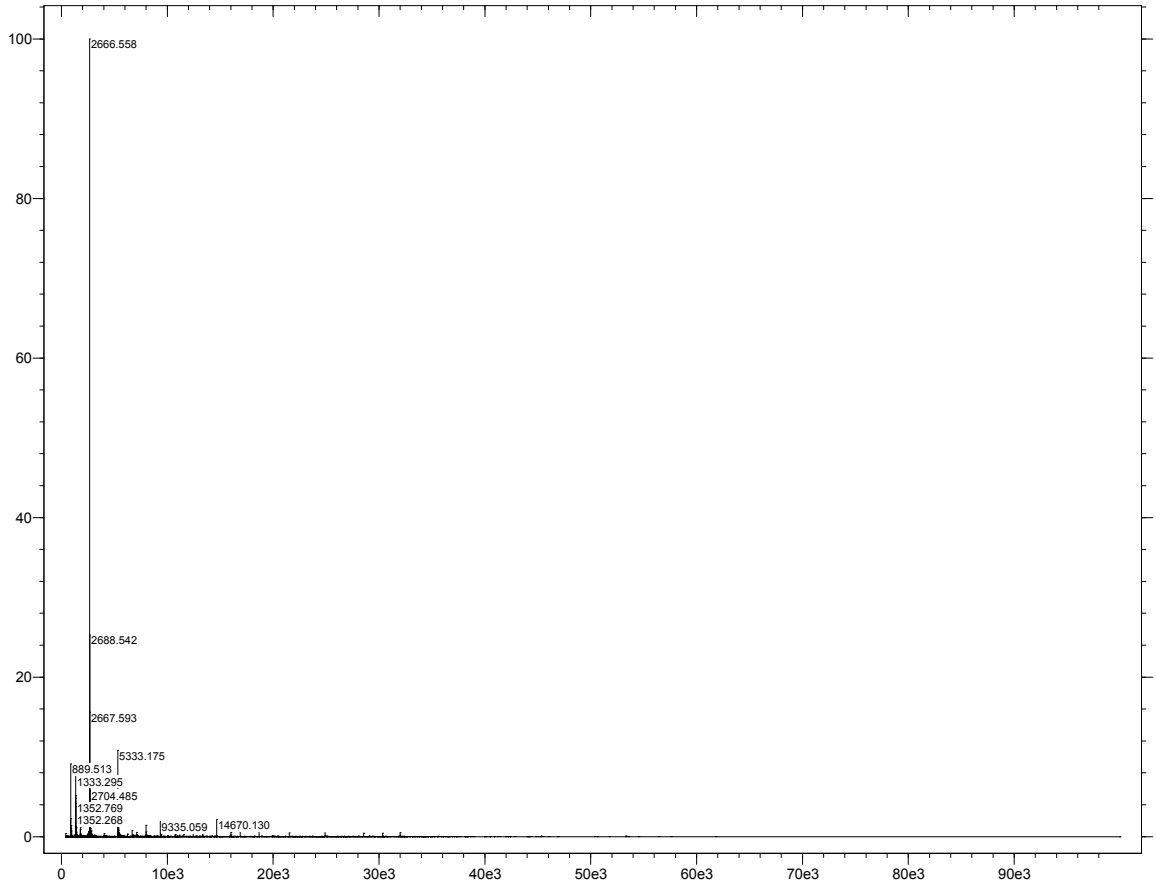
Totals :                  1.07502e4  1450.43123



Signal 3: MWD1 C, Sig=360,4 Ref=off

======================================================================
                          *** End of Report ***
```

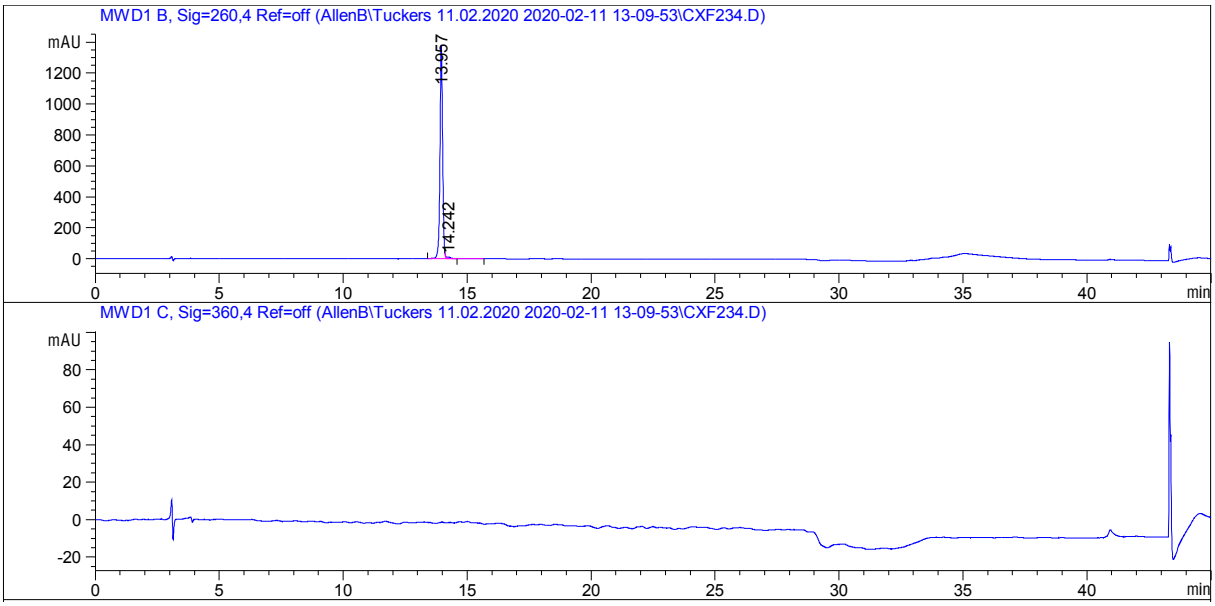
XXX


100
80
60
40
20
0
2666.558
2688.542
2667.593
5333.175
889.513
1333.295
2704.485
1352.769
1352.268
9335.059
14670.130
0
10e3
20e3
30e3
40e3
50e3
60e3
70e3
80e3
90e3

LONG$_C$:

```
======================================================================
Acq. Operator   : SYSTEM                          Seq. Line :  12
Acq. Instrument : LC-FC                            Location :  60
Injection Date  : 11-Feb-20 8:51:44 PM                 Inj :  1
                                                  Inj Volume : 15.000 µl
Different Inj Volume from Sample Entry!  Actual Inj Volume : 10.000 µl
Method          : C:\Chem32\3\Data\AllenB\Tuckers 11.02.2020 2020-02-11 13-09-53\Short Oligo
                  60°C.M (Sequence Method)
Last changed    : 06-Mar-19 1:42:46 PM by SYSTEM
Sample Info     : CXF234

Additional Info : Peak(s) manually integrated
```



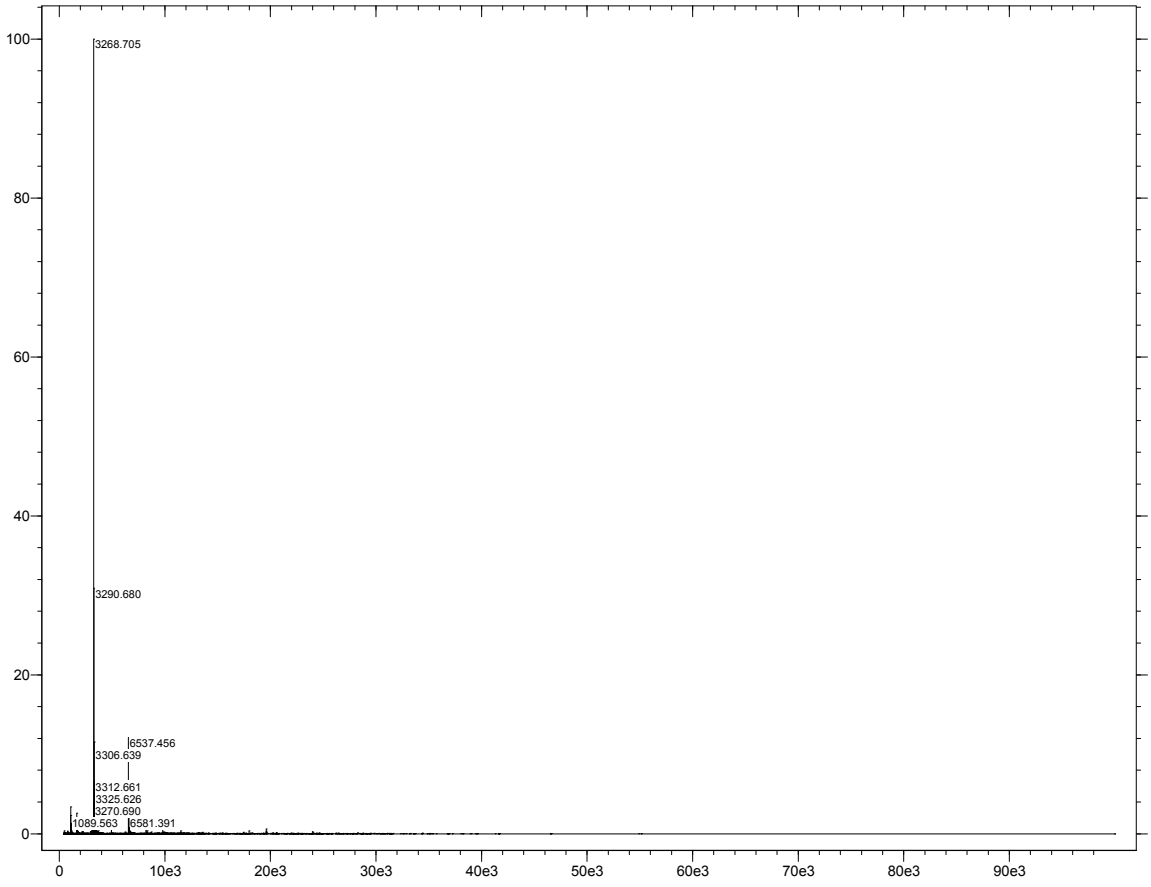

```
Signal 2: MWD1 B, Sig=260,4 Ref=off

Peak RetTime Type  Width     Area      Height     Area
  #   [min]        [min]   [mAU*s]     [mAU]       %
----|-------|----|-------|----------|----------|--------|
   1  13.957 BV R  0.1169 1.05836e4  1384.37305  98.9093
   2  14.242 VV E  0.1664  116.71143    9.83632   1.0907

Totals :                 1.07003e4  1394.20937


Signal 3: MWD1 C, Sig=360,4 Ref=off

======================================================================
                          *** End of Report ***
```

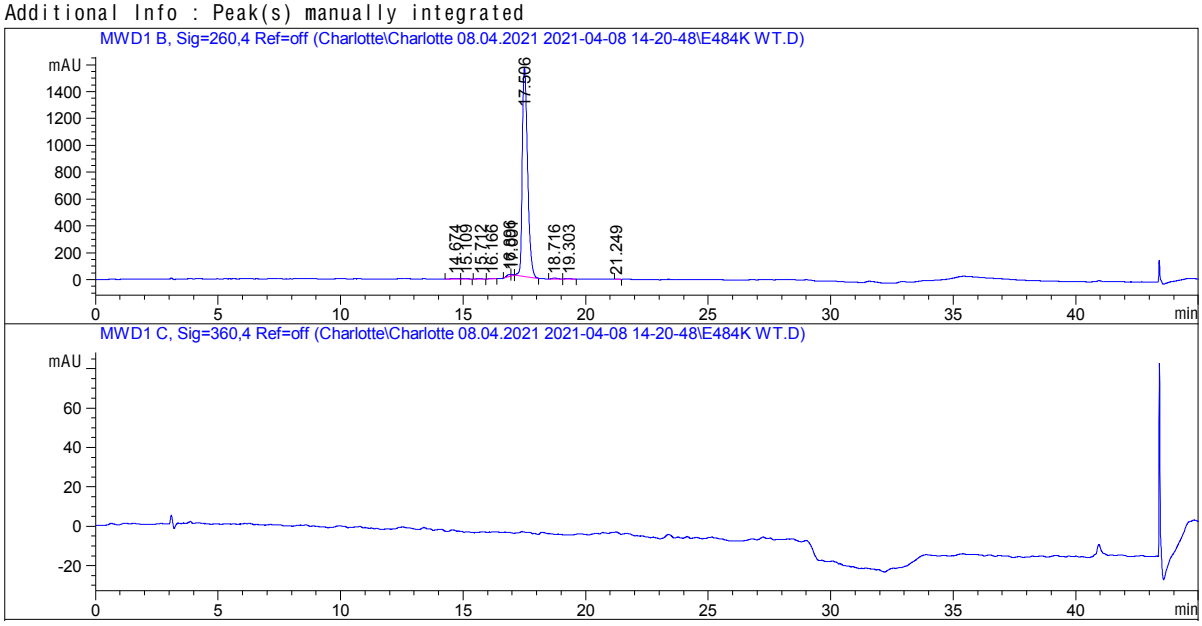

100
80
60
40
20
0
3268.705
3290.680
6537.456
3306.639
3312.661
3325.626
3270.690
1089.563
6581.391
0
10e3
20e3
30e3
40e3
50e3
60e3
70e3
80e3
90e3

6.1 HPLC traces and MS of Covid-19 target strands

E484 WT

```
=====================================================================
Acq. Operator    : SYSTEM                          Seq. Line :   8
Acq. Instrument : LC-FC                             Location :   8
Injection Date  : 08-Apr-21 7:58:46 PM                  Inj :   1
                                                  Inj Volume : 15.000 µl
Different Inj Volume from Sample Entry!  Actual Inj Volume : 10.000 µl
Method          : C:\Chem32\3\Data\Charlotte\Charlotte 08.04.2021 2021-04-08 14-20-48\Short
                  Oligo 60°C.M (Sequence Method)
Last changed    : 08-Apr-21 2:18:49 PM by SYSTEM
Sample Info     : E484K WT

Additional Info : Peak(s) manually integrated
```

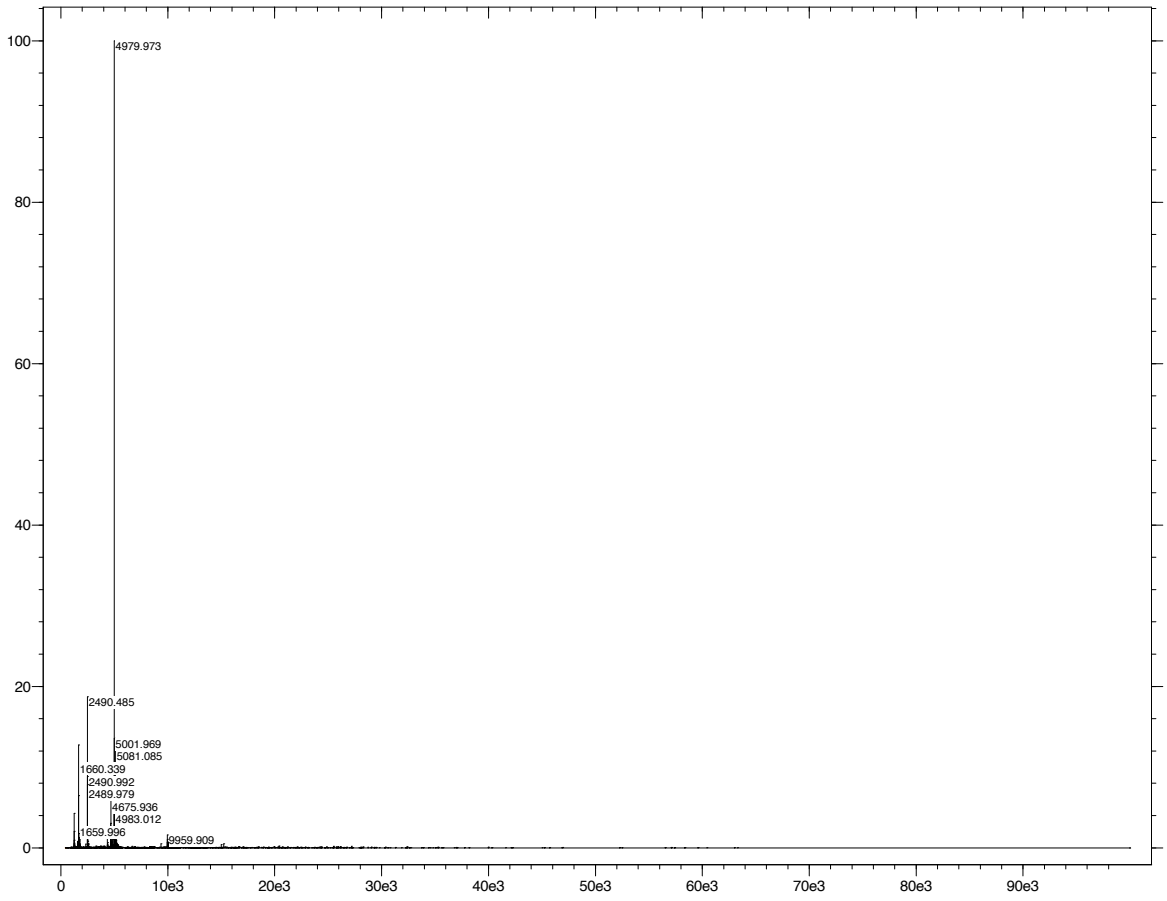


Signal 1: MWD1 B, Sig=260,4 Ref=off

Peak #	RetTime [min]	Type	Width [min]	Area [mAU*s]	Height [mAU]	Area %
1	14.674	BV	0.3221	62.53039	3.03830	0.2597
2	15.109	VB	0.2234	45.07866	2.83662	0.1872
3	15.712	BB	0.2345	36.39946	2.11830	0.1512
4	16.166	BB	0.2027	41.96766	3.24914	0.1743
5	16.896	BV	0.1799	177.51942	15.46553	0.7373
6	17.001	VB	0.0935	55.65745	9.33972	0.2312
7	17.506	BB	0.2316	2.34197e4	1556.15381	97.2749
8	18.716	BV	0.2290	122.65557	7.82038	0.5095
9	19.303	VB	0.2406	94.92122	6.06307	0.3943
10	21.249	VB	0.1426	19.37143	1.87474	0.0805
Totals :				2.40758e4	1607.95959	

Signal 2: MWD1 C, Sig=360,4 Ref=off

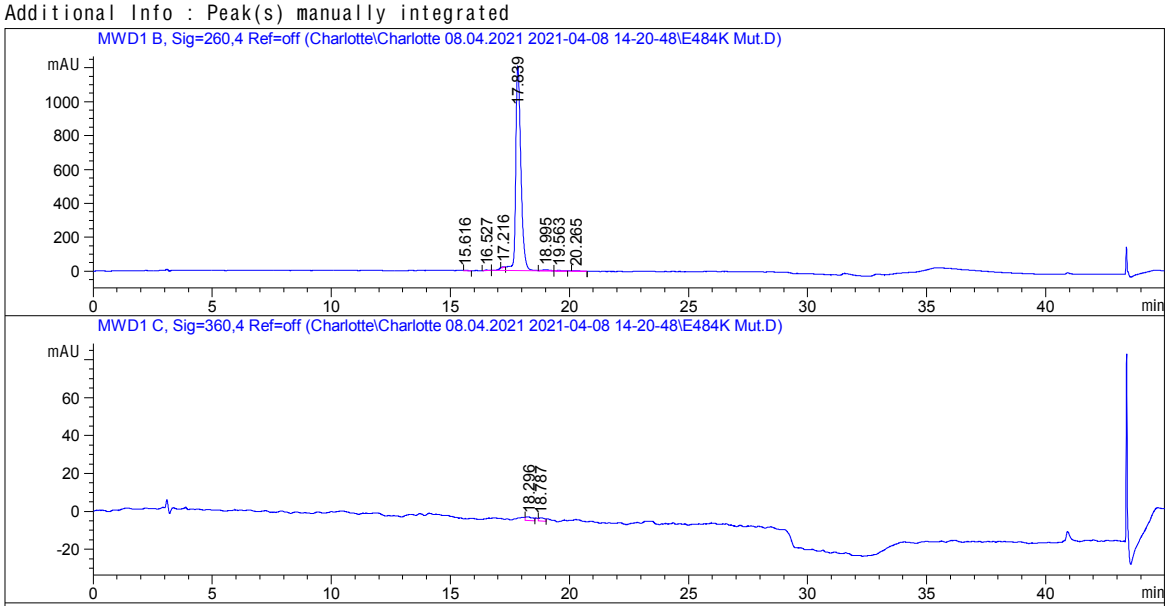
```
=====================================================================
                        *** End of Report ***
```


100
80
60
40
20
0
4979.973
2490.485
5001.969
5081.085
1660.339
2490.992
2489.979
4675.936
4983.012
1659.996
9959.909
0
10e3
20e3
30e3
40e3
50e3
60e3
70e3
80e3
90e3

E484K Mut

```
======================================================================
Acq. Operator   : SYSTEM                        Seq. Line :   9
Acq. Instrument : LC-FC                          Location :   9
Injection Date  : 08-Apr-21 8:44:48 PM               Inj :   1
                                               Inj Volume : 15.000 µl
Different Inj Volume from Sample Entry!  Actual Inj Volume : 10.000 µl
Method          : C:\Chem32\3\Data\Charlotte\Charlotte 08.04.2021 2021-04-08 14-20-48\Short
                  Oligo 60°C.M (Sequence Method)
Last changed    : 08-Apr-21 2:18:49 PM by SYSTEM
Sample Info     : E484K Mut

Additional Info : Peak(s) manually integrated
```



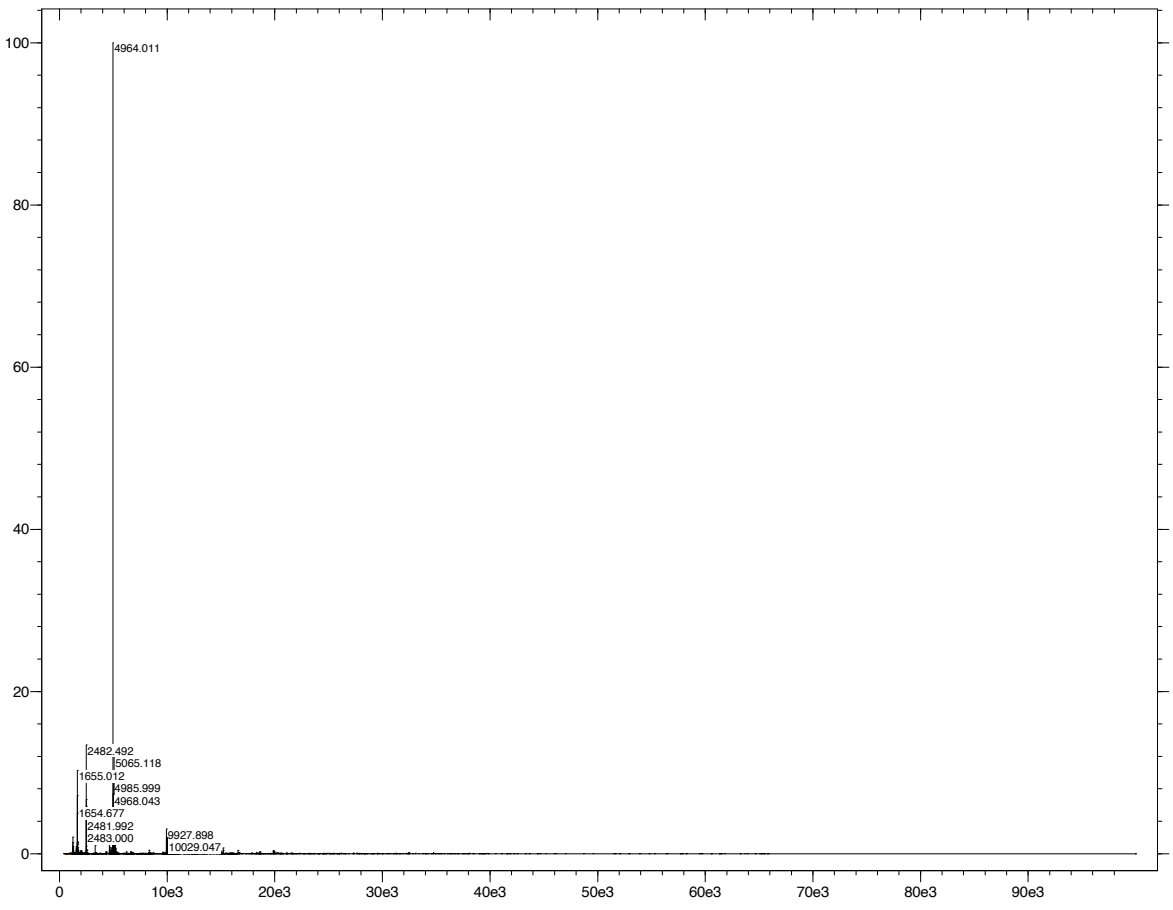
Signal 1: MWD1 B, Sig=260,4 Ref=off

Peak #	RetTime [min]	Type	Width [min]	Area [mAU*s]	Height [mAU]	Area %
1	15.616	VB	0.1395	18.44060	1.93019	0.0978
2	16.527	BB	0.1912	41.86012	3.41056	0.2220
3	17.216	BV E	0.1385	33.97612	4.47713	0.1802
4	17.839	VV R	0.2332	1.84949e4	1203.78296	98.0719
5	18.995	VV E	0.3009	133.78568	6.42695	0.7094
6	19.563	VV E	0.2551	79.40957	4.07885	0.4211
7	20.265	VB E	0.2797	56.14453	2.68739	0.2977
Totals :				1.88585e4	1226.79402	

Signal 2: MWD1 C, Sig=360,4 Ref=off

Peak #	RetTime [min]	Type	Width [min]	Area [mAU*s]	Height [mAU]	Area %
1	18.296	VV	0.2762	41.37206	1.88412	57.0756
2	18.787	VV	0.2285	31.11435	1.75750	42.9244
Totals :				72.48641	3.64162	

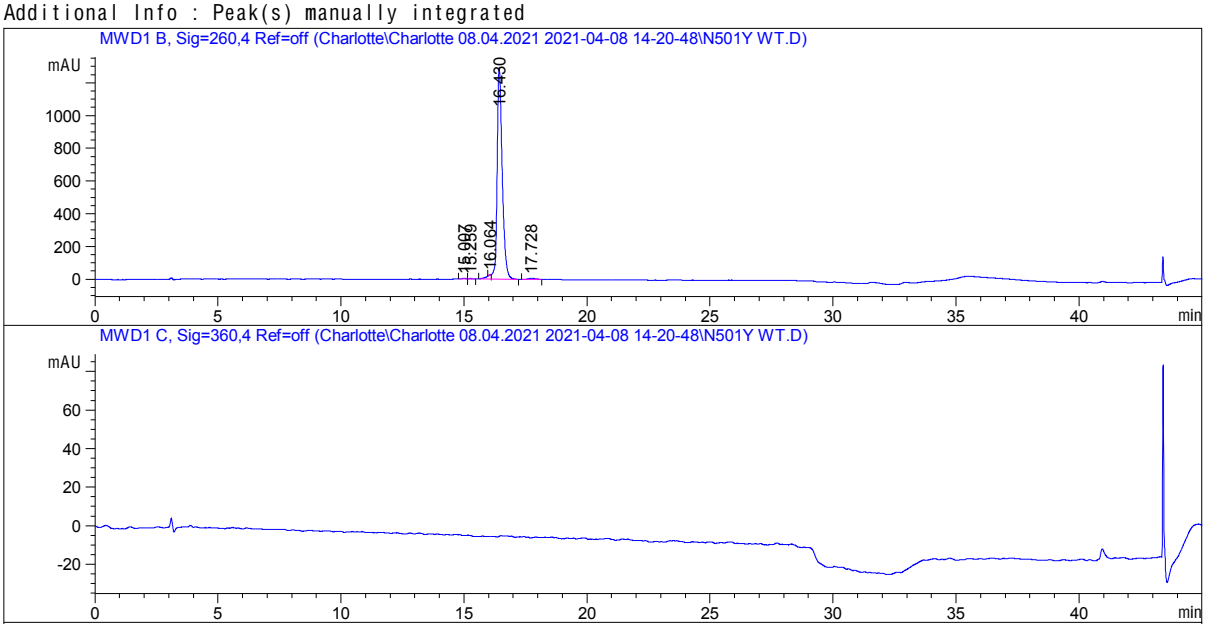
```
======================================================================
                        *** End of Report ***
```


100
80
60
40
20
0
4964.011
2482.492
5065.118
1655.012
4985.999
4968.043
1654.677
2481.992
2483.000
9927.898
10029.047
0
10e3
20e3
30e3
40e3
50e3
60e3
70e3
80e3
90e3

N501 WT

```
=====================================================================
Acq. Operator   : SYSTEM                        Seq. Line :   6
Acq. Instrument : LC-FC                          Location :   6
Injection Date  : 08-Apr-21 6:26:46 PM               Inj :   1
                                                Inj Volume : 15.000 µl
Different Inj Volume from Sample Entry!  Actual Inj Volume : 10.000 µl
Method          : C:\Chem32\3\Data\Charlotte\Charlotte 08.04.2021 2021-04-08 14-20-48\Short
                  Oligo 60°C.M (Sequence Method)
Last changed    : 08-Apr-21 2:18:49 PM by SYSTEM
Sample Info     : N501Y WT

Additional Info : Peak(s) manually integrated
```

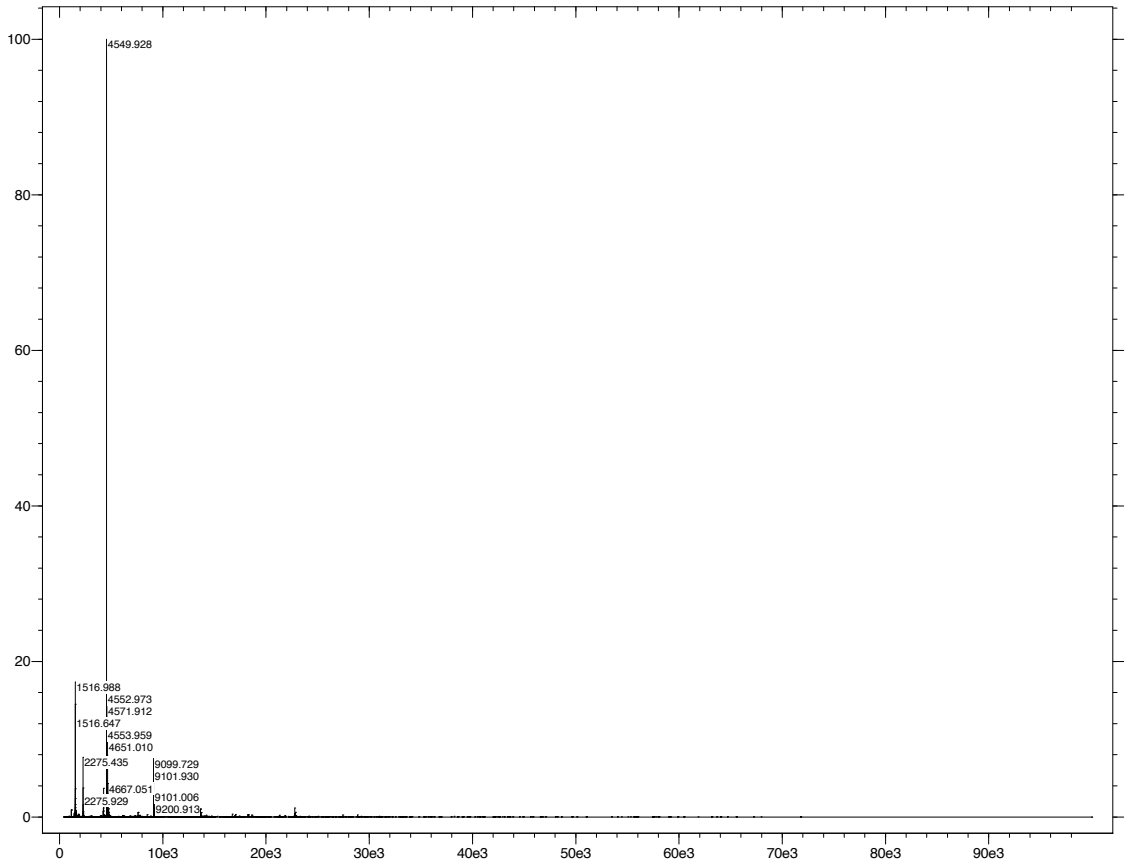


Signal 1: MWD1 B, Sig=260,4 Ref=off

Peak #	RetTime [min]	Type	Width [min]	Area [mAU*s]	Height [mAU]	Area %
1	15.007	BV	0.1995	39.14278	3.05375	0.2043
2	15.259	VB	0.1483	22.65705	2.16205	0.1182
3	16.064	BV E	0.1066	19.99253	3.04694	0.1043
4	16.430	VB R	0.2213	1.89569e4	1290.97400	98.9338
5	17.728	VB R	0.2796	122.50011	6.50943	0.6393
Totals :				1.91612e4	1305.74618	

Signal 2: MWD1 C, Sig=360,4 Ref=off

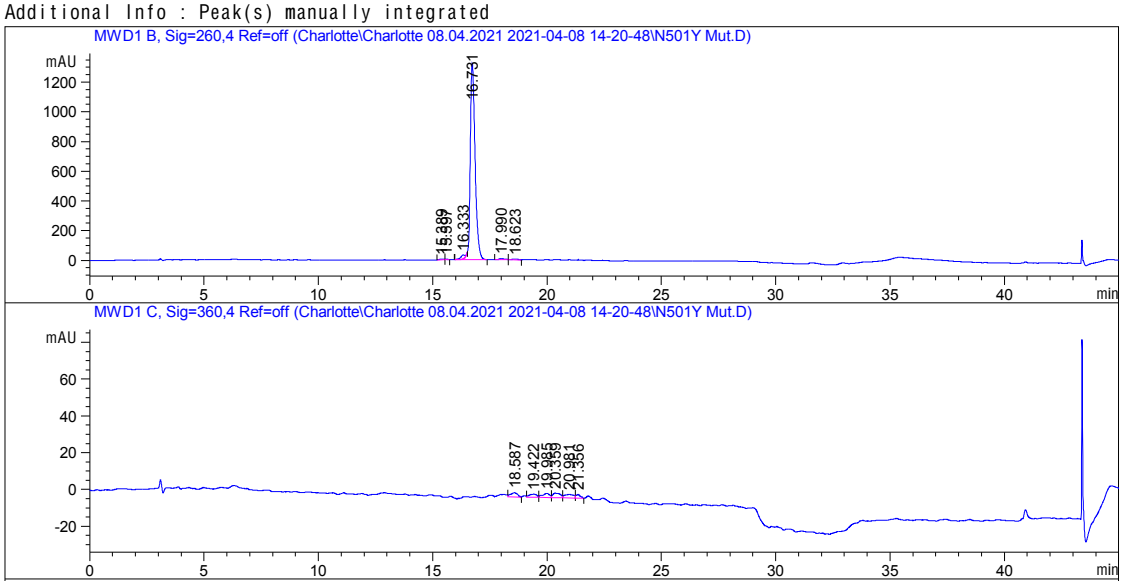
```
=====================================================================
                        *** End of Report ***
```


100
80
60
40
20
0
4549.928
1516.988
4552.973
4571.912
1516.647
4553.959
4651.010
2275.435
9099.729
9101.930
4667.051
2275.929
9101.006
9200.913
0
10e3
20e3
30e3
40e3
50e3
60e3
70e3
80e3
90e3

N501Y Mut

```
======================================================================
Acq. Operator   : SYSTEM                        Seq. Line :   7
Acq. Instrument : LC-FC                          Location :   7
Injection Date  : 08-Apr-21 7:12:45 PM               Inj :   1
                                                Inj Volume : 15.000 µl
Different Inj Volume from Sample Entry!  Actual Inj Volume : 10.000 µl
Method          : C:\Chem32\3\Data\Charlotte\Charlotte 08.04.2021 2021-04-08 14-20-48\Short
                  Oligo 60°C.M (Sequence Method)
Last changed    : 08-Apr-21 2:18:49 PM by SYSTEM
Sample Info     : N501Y Mut

Additional Info : Peak(s) manually integrated
```



Signal 1: MWD1 B, Sig=260,4 Ref=off

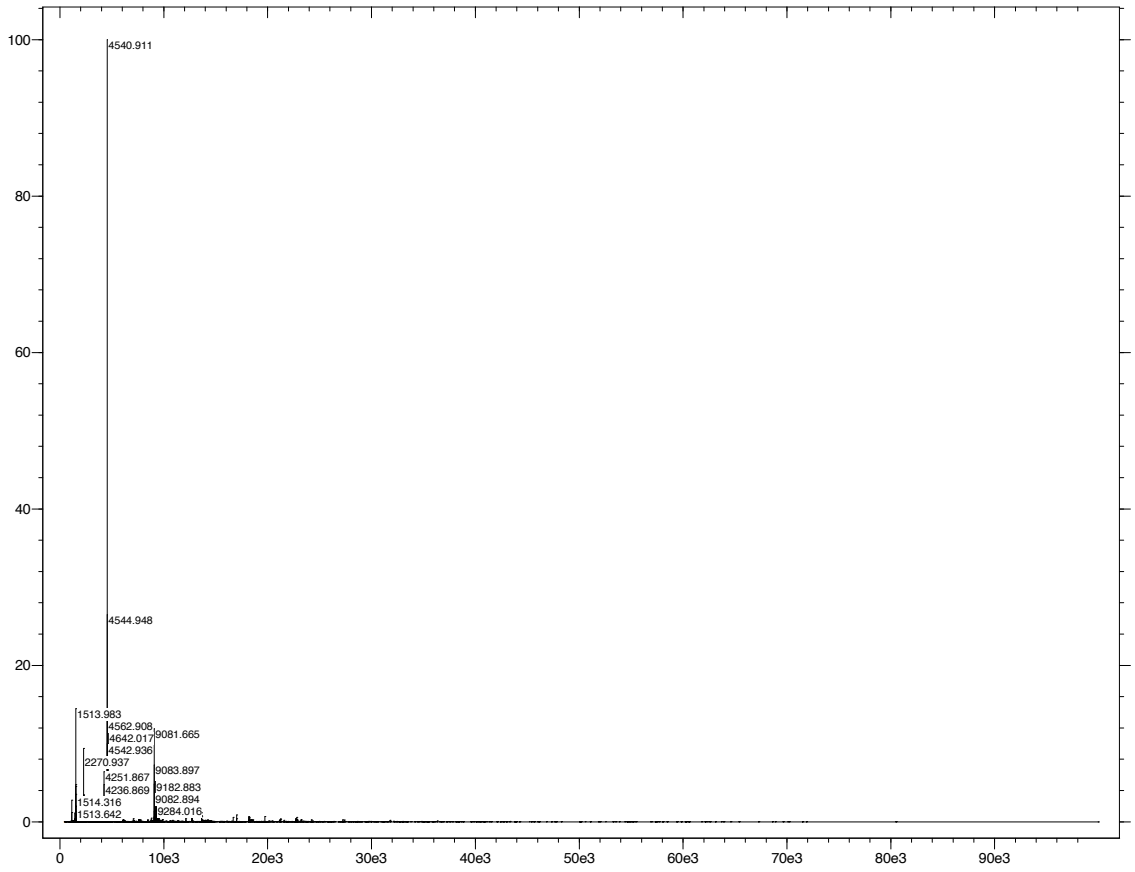
Peak #	RetTime [min]	Type	Width [min]	Area [mAU*s]	Height [mAU]	Area %
1	15.389	BV	0.1920	56.41018	4.44627	0.2826
2	15.597	VB	0.1228	22.91575	2.82078	0.1148
3	16.333	BV E	0.1946	352.56100	25.93547	1.7660
4	16.731	VB R	0.2222	1.92858e4	1321.72437	96.6018
5	17.990	BV	0.2555	142.21223	8.07446	0.7123
6	18.623	VB	0.3076	104.32716	4.68798	0.5226
Totals :				1.99643e4	1367.68932	

Signal 2: MWD1 C, Sig=360,4 Ref=off

Peak #	RetTime [min]	Type	Width [min]	Area [mAU*s]	Height [mAU]	Area %
1	18.587	VB	0.2814	48.18769	2.30963	17.9231
2	19.422	VV	0.2766	38.15313	1.72135	14.1908
3	19.985	VV	0.3182	48.96054	2.19494	18.2106
4	20.359	VV	0.3062	56.13926	2.44231	20.8807
5	20.981	VV	0.3581	52.84515	1.91387	19.6554
6	21.356	VB	0.1898	24.57202	1.88857	9.1394
Totals :				268.85778	12.47067	

```
======================================================================
                        *** End of Report ***
```

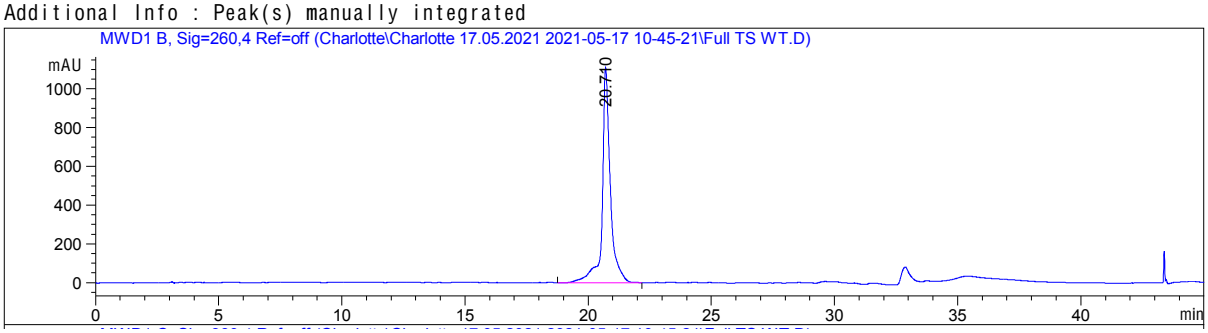
XL


100
80
60
40
20
0
4540.911
4544.948
1513.983
4562.908
4642.017
4542.936
9081.665
2270.937
4251.867
9083.897
4236.869
9182.883
1514.316
9082.894
1513.642
9284.016
0
10e3
20e3
30e3
40e3
50e3
60e3
70e3
80e3
90e3

Full TS WT

```
======================================================================
Acq. Operator   : SYSTEM                        Seq. Line :   2
Acq. Instrument : LC-FC                          Location :   2
Injection Date  : 17-May-21 11:33:23 AM               Inj :   1
                                               Inj Volume : 15.000 µl
Different Inj Volume from Sample Entry!  Actual Inj Volume : 10.000 µl
Method          : C:\Chem32\3\Data\Charlotte\Charlotte 17.05.2021 2021-05-17 10-45-21\Short
                  Oligo 60°C.M (Sequence Method)
Last changed    : 12-May-21 12:49:09 PM by SYSTEM
Sample Info     : Full TS WT

Additional Info : Peak(s) manually integrated
```




```
Signal 1: MWD1 B, Sig=260,4 Ref=off

Peak RetTime Type  Width     Area      Height     Area
  #   [min]        [min]   [mAU*s]     [mAU]       %
----|-------|----|-------|----------|----------|--------|
   1  20.710 BV R  0.3235 2.56689e4  1111.31006 100.0000

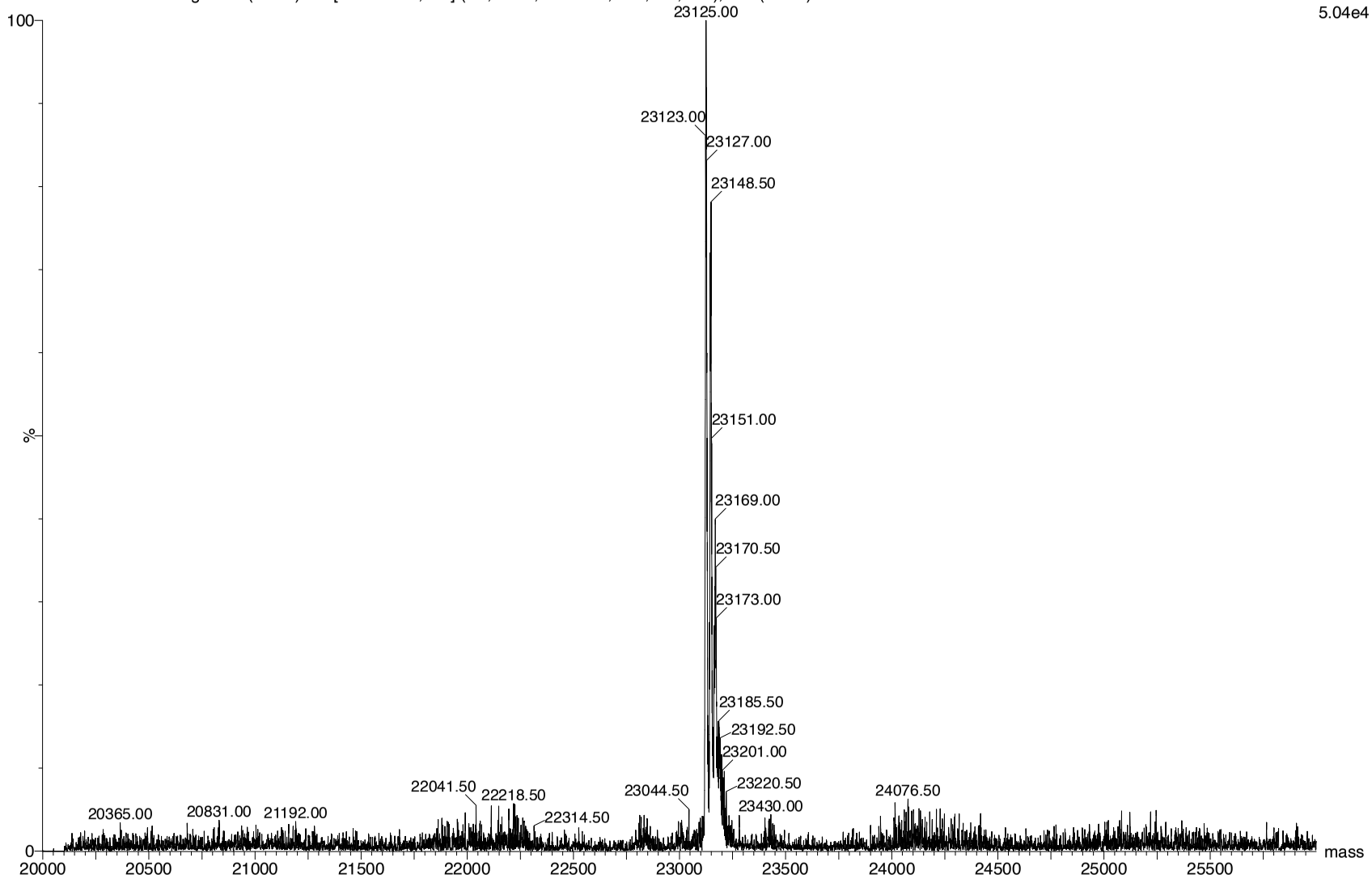
Totals :                  2.56689e4  1111.31006

======================================================================
                        *** End of Report ***
```

Full TS WT Oligo MW=23125
Charlotte Farrow
JT-CXF-3PRXX-nESI-Neg-1 55 (0.947) M1 [Ev-736136,It24] (Gs,0.050,120:2400,0.50,L33,R33); Cm (54:59)

University of Birmingham, School of Chemistry
Waters Synapt G2-S

21-May-2021
1: TOF MS ES-
5.04e4

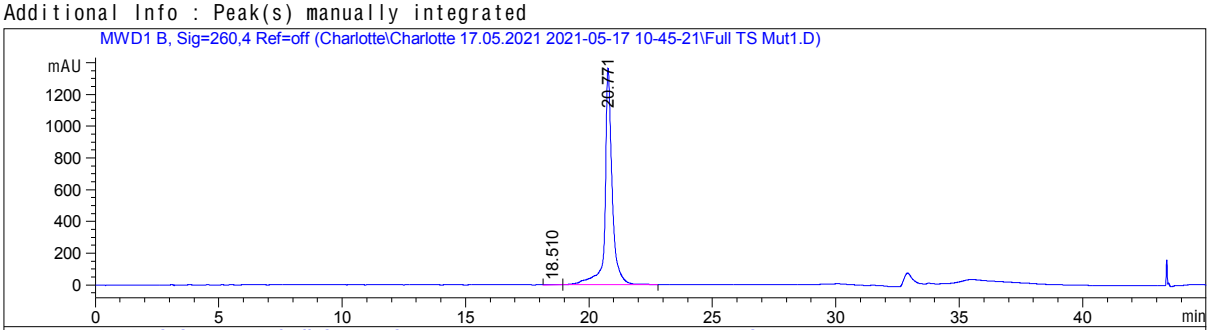


XLIII

Full TS Mut1

```
======================================================================
Acq. Operator   : SYSTEM                        Seq. Line :   3
Acq. Instrument : LC-FC                          Location :   3
Injection Date  : 17-May-21 12:19:55 PM               Inj :   1
                                                Inj Volume : 15.000 µl
Different Inj Volume from Sample Entry!  Actual Inj Volume : 10.000 µl
Method          : C:\Chem32\3\Data\Charlotte\Charlotte 17.05.2021 2021-05-17 10-45-21\Short
                  Oligo 60°C.M (Sequence Method)
Last changed    : 12-May-21 12:49:09 PM by SYSTEM
Sample Info     : Full TS Mut1

Additional Info : Peak(s) manually integrated
```




```
Signal 1: MWD1 B, Sig=260,4 Ref=off

Peak RetTime Type  Width     Area      Height     Area
  #   [min]        [min]   [mAU*s]     [mAU]       %
----|-------|----|-------|----------|----------|--------|
   1  18.510 VB    0.4345   67.49635    1.88143   0.2454
   2  20.771 BV R  0.2828 2.74359e4  1362.98669  99.7546

Totals :                  2.75034e4  1364.86812
======================================================================
                          *** End of Report ***
```

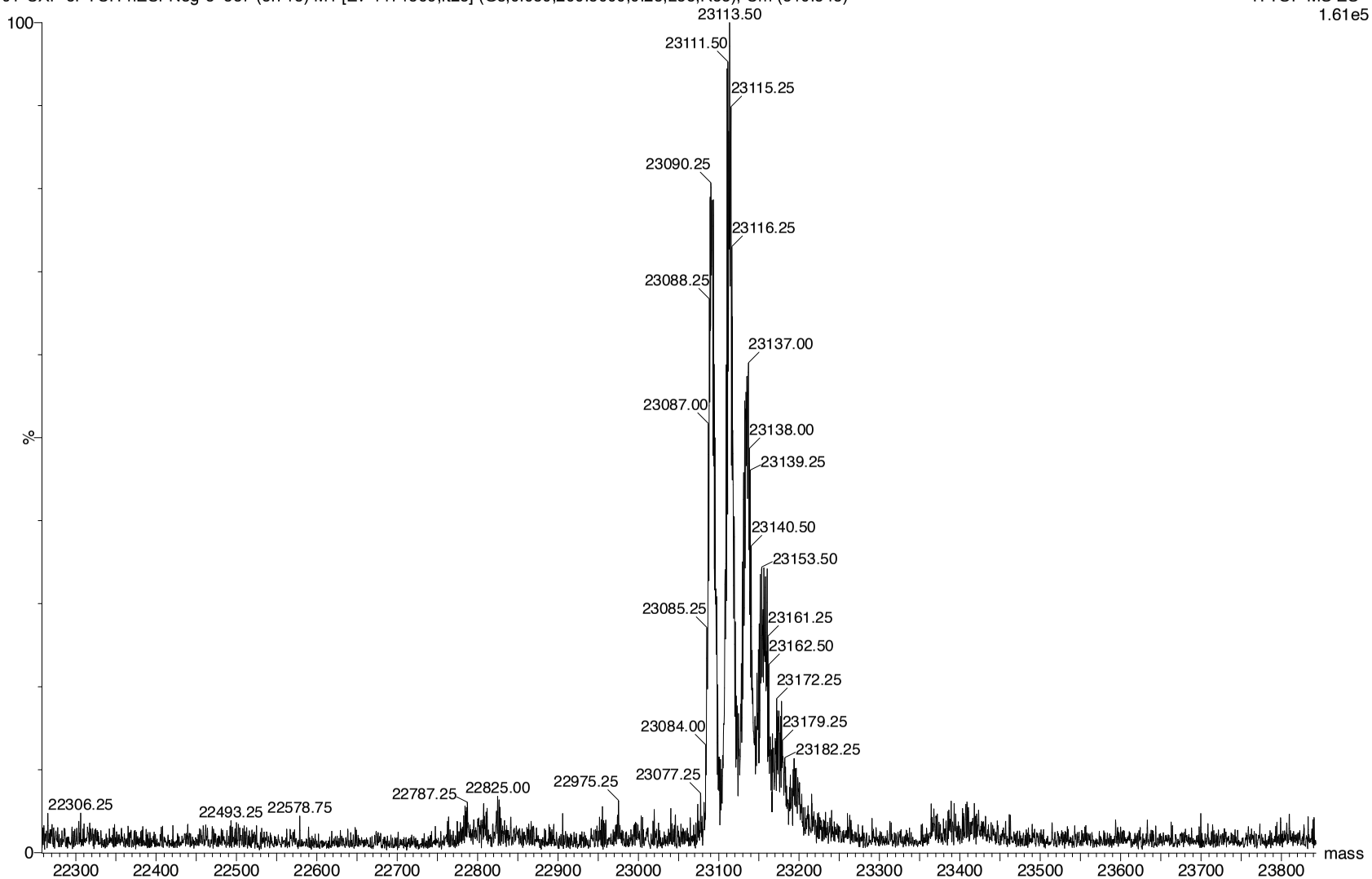
Full TS Mut1 Oligo MW=23092
Charlotte Farrow

University of Birmingham, School of Chemistry
Waters Synapt G2-S

21-May-2021

JT-CXF-3PTCH-nESI-Neg-5 337 (5.715) M1 [Ev-1471369,It25] (Gs,0.050,200:5000,0.25,L33,R33); Cm (310:343)

1: TOF MS ES-
1.61e5

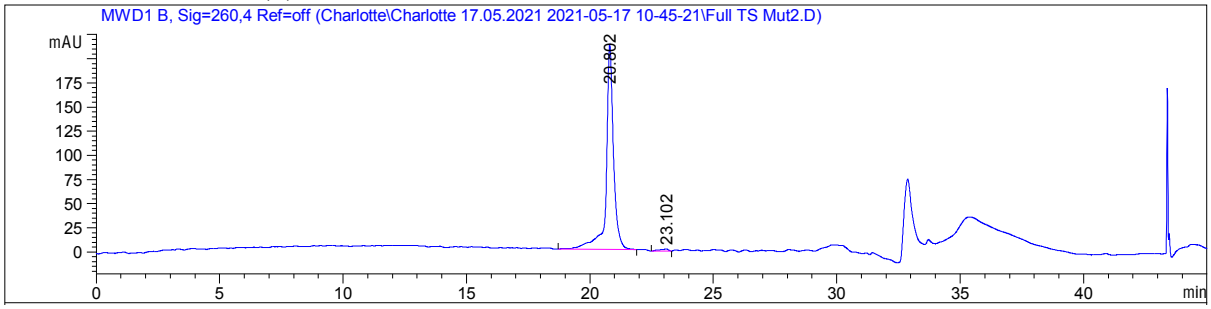


XLV

Full TS Mut2

```
==========================================================================
Acq. Operator   : SYSTEM                        Seq. Line :   4
Acq. Instrument : LC-FC                          Location :   4
Injection Date  : 17-May-21 1:06:30 PM                Inj :   1
                                                Inj Volume : 15.000 µl
Different Inj Volume from Sample Entry!  Actual Inj Volume : 10.000 µl
Method          : C:\Chem32\3\Data\Charlotte\Charlotte 17.05.2021 2021-05-17 10-45-21\Short
                  Oligo 60°C.M (Sequence Method)
Last changed    : 12-May-21 12:49:09 PM by SYSTEM
Sample Info     : Full TS Mut2

Additional Info : Peak(s) manually integrated
```




```
Signal 1: MWD1 B, Sig=260,4 Ref=off

Peak RetTime Type  Width     Area      Height     Area
  #   [min]        [min]   [mAU*s]     [mAU]       %
----|-------|----|-------|----------|----------|--------|
   1  20.802 VB R  0.2926 4376.24658  212.24667  98.8451
   2  23.102 BB    0.3328   51.13216    1.97001   1.1549

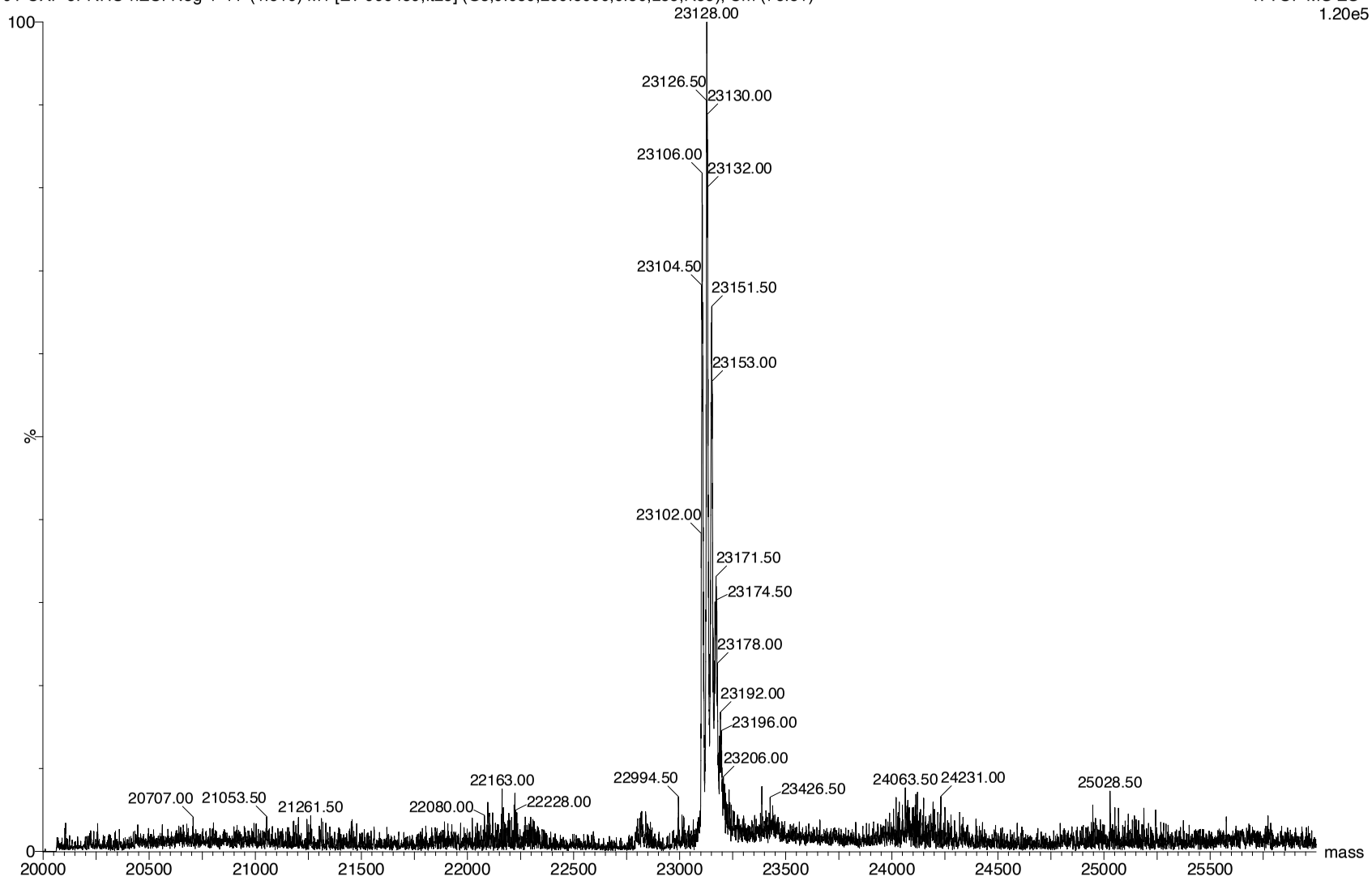
Totals :                  4427.37874  214.21669

==========================================================================
                         *** End of Report ***
```

Full TS Mut2 Oligo MW=23107
Charlotte Farrow
JT-CXF-3PRHU-nESI-Neg-1 77 (1.319) M1 [Ev-996489,lt25] (Gs,0.050,200:5000,0.50,L33,R33); Cm (73:81)

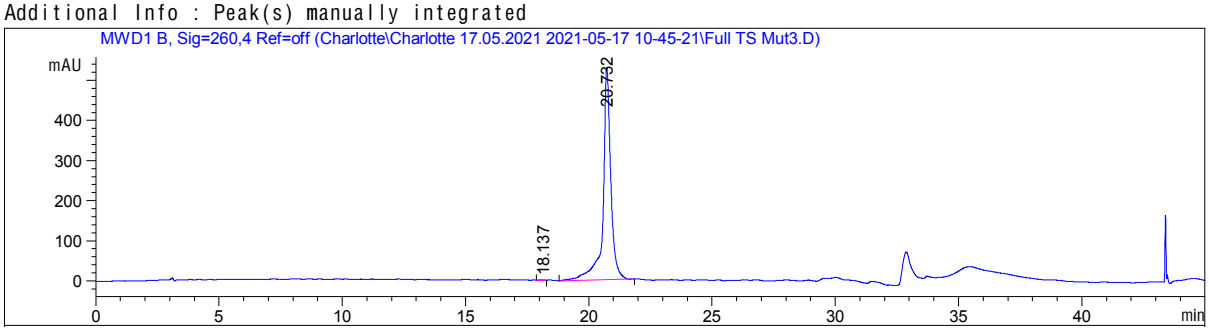
University of Birmingham, School of Chemistry
Waters Synapt G2-S

21-May-2021
1: TOF MS ES-
1.20e5



```
==================================================================
Acq. Operator   : SYSTEM                        Seq. Line :   5
Acq. Instrument : LC-FC                          Location :   5
Injection Date  : 17-May-21 1:53:03 PM               Inj :   1
                                                Inj Volume : 15.000 µl
Different Inj Volume from Sample Entry!  Actual Inj Volume : 10.000 µl
Method          : C:\Chem32\3\Data\Charlotte\Charlotte 17.05.2021 2021-05-17 10-45-21\Short
                  Oligo 60°C.M (Sequence Method)
Last changed    : 12-May-21 12:49:09 PM by SYSTEM
Sample Info     : Full TS Mut3

Additional Info : Peak(s) manually integrated
```




```
Signal 1: MWD1 B, Sig=260,4 Ref=off

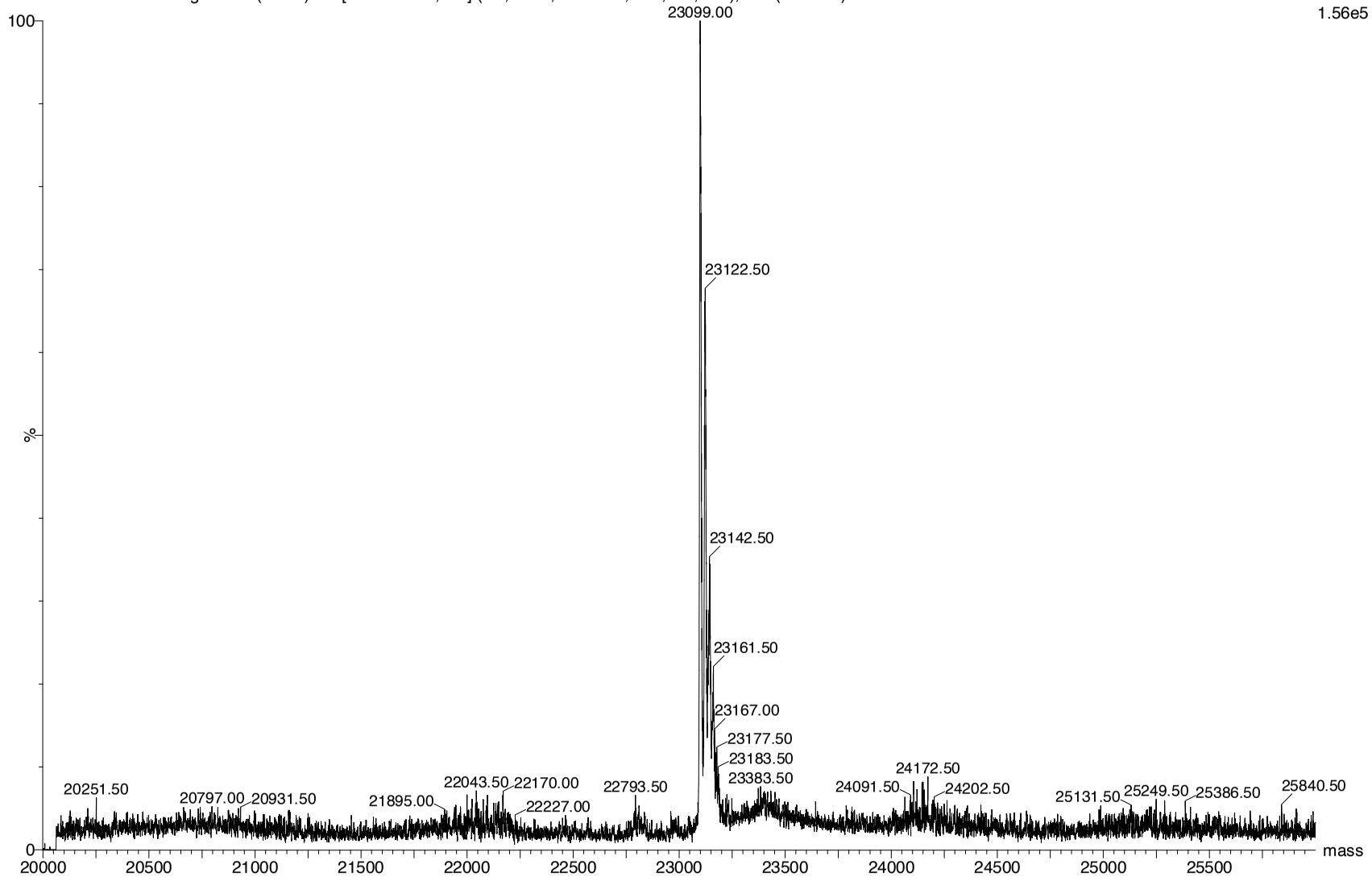
Peak RetTime Type  Width     Area      Height     Area
  #   [min]        [min]   [mAU*s]     [mAU]       %
----|-------|----|-------|----------|----------|--------|
   1  18.137 VV    0.2148   26.37163    1.78100   0.2257
   2  20.732 BV R  0.3093 1.16606e4   528.68530  99.7743

Totals :                  1.16869e4   530.46631

==================================================================
                        *** End of Report ***
```

Full TS Mut3

Full TS Mut3 Oligo MW=23100
Charlotte Farrow
University of Birmingham, School of Chemistry
Waters Synapt G2-S
21-May-2021
JT-CXF-3PRKK-nESI-Neg-1 477 (8.081) M1 [Ev-1149857,It23] (Gs,0.050,200:5000,0.50,L33,R33); Cm (458:496)
1: TOF MS ES-
1.56e5

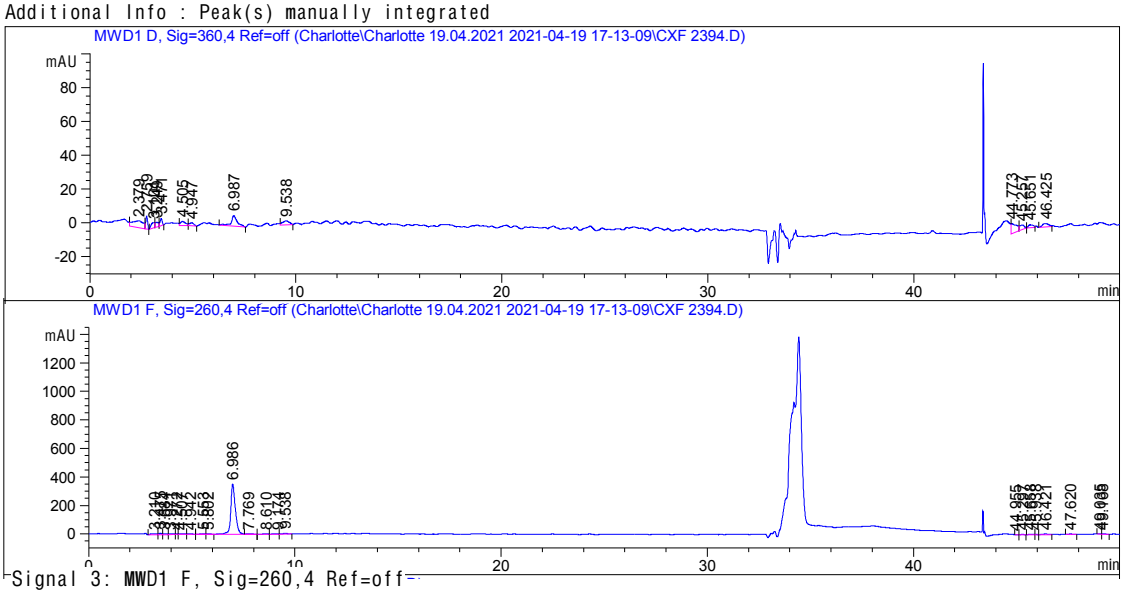


6.2 HPLC traces and MS of modified Covid-19 probe strands

E484K Probe

```
======================================================================
Acq. Operator   : SYSTEM                        Seq. Line :   2
Acq. Instrument : LC-FC                          Location :   2
Injection Date  : 19-Apr-21 6:05:10 PM                Inj :   1
                                                Inj Volume : 20.000 µl
Different Inj Volume from Sample Entry!  Actual Inj Volume : 10.000 µl
Method          : C:\Chem32\3\Data\Charlotte\Charlotte 19.04.2021 2021-04-19 17-13-09\FcNA
                  Anth 60oC.M (Sequence Method)
Last changed    : 19-Apr-21 5:07:29 PM by SYSTEM
Sample Info     : CXF 2394

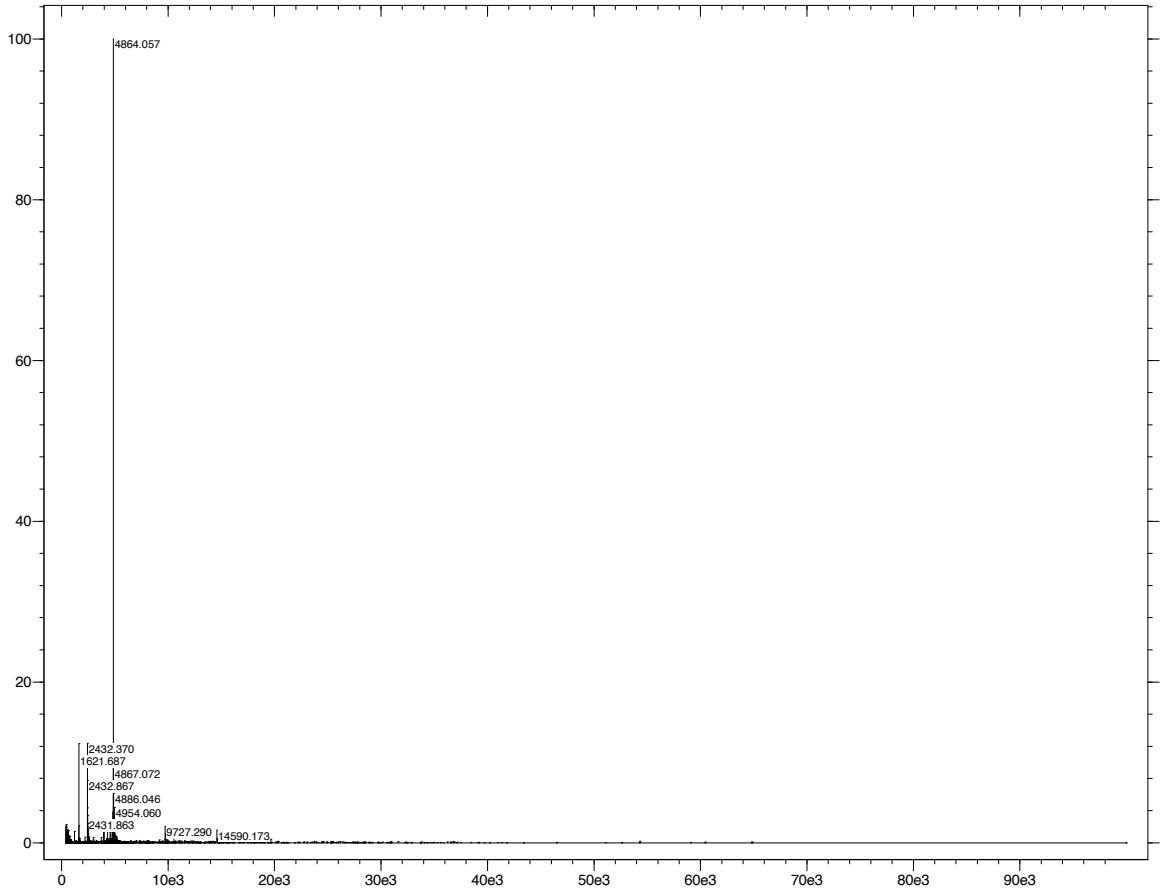
Additional Info : Peak(s) manually integrated
```




```
Signal 3: MWD1 F, Sig=260,4 Ref=off
```

Peak #	RetTime [min]	Type	Width [min]	Area [mAU*s]	Height [mAU]	Area %
1	3.210	BV	0.2781	154.94408	6.74133	2.3000
2	3.475	VV	0.1310	104.05035	10.93828	1.5446
3	3.684	VV	0.1870	66.90205	4.78816	0.9931
4	3.971	VV	0.2548	91.44994	4.66234	1.3575
5	4.272	VV	0.1075	27.24685	3.63099	0.4045
6	4.507	VV	0.2696	100.98149	5.41515	1.4990
7	4.942	VB	0.2416	54.76556	3.33419	0.8130
8	5.553	BV E	0.2389	56.36457	3.33941	0.8367
9	5.802	VV E	0.2146	49.43892	3.15859	0.7339
10	6.986	VV R	0.2260	5514.88232	353.48520	81.8650
11	7.769	VB E	0.3116	57.00878	2.68603	0.8463
12	8.610	VB R	0.2283	39.84402	2.63695	0.5915
13	9.174	BV	0.2422	32.46988	1.78492	0.4820
14	9.538	VB	0.2928	95.66273	4.37953	1.4201
15	44.955	VB	0.1166	15.72165	2.07065	0.2334
16	45.297	BB	0.2017	24.73418	2.06624	0.3672
17	45.658	BV	0.2406	55.89475	3.31755	0.8297
18	45.938	VB	0.1157	13.93381	1.85291	0.2068
19	46.421	BV	0.3114	93.49208	3.99025	1.3878
20	47.620	VB	0.2223	48.40673	2.96739	0.7186
21	49.035	BV	0.1337	17.88859	2.09251	0.2655
22	49.168	VB	0.1583	20.47620	1.77941	0.3040
Totals :				6736.55955	431.11796	

L

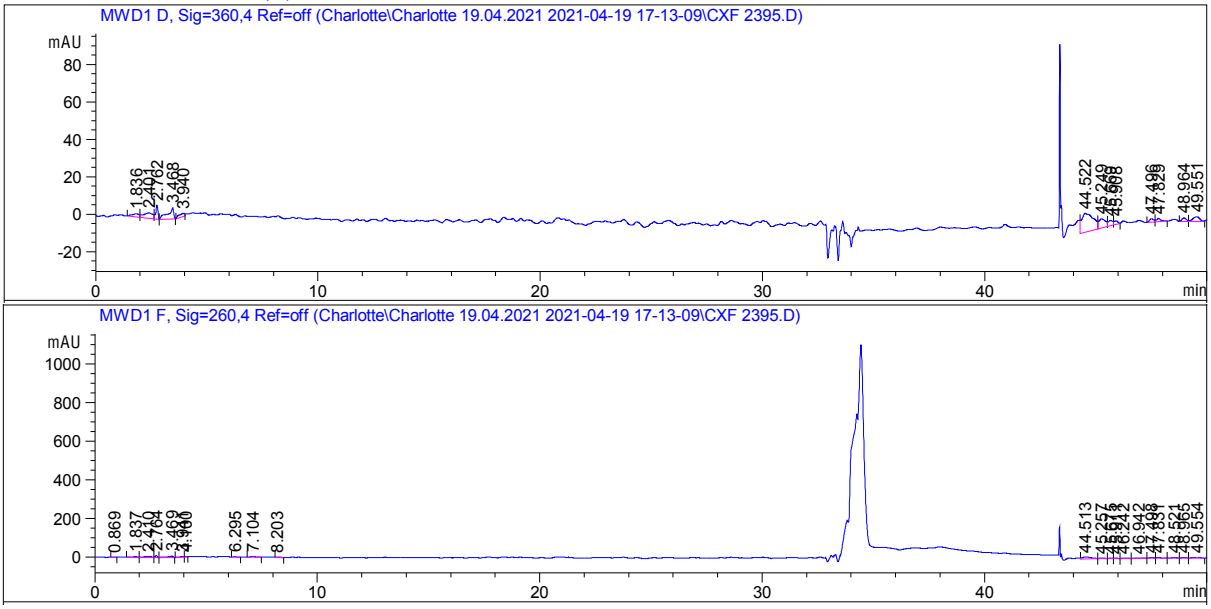

100
80
60
40
20
0
4864.057
2432.370
1621.687
4867.072
2432.867
4886.046
4954.060
2431.863
9727.290
14590.173
0
10e3
20e3
30e3
40e3
50e3
60e3
70e3
80e3
90e3

LI

N501Y Probe

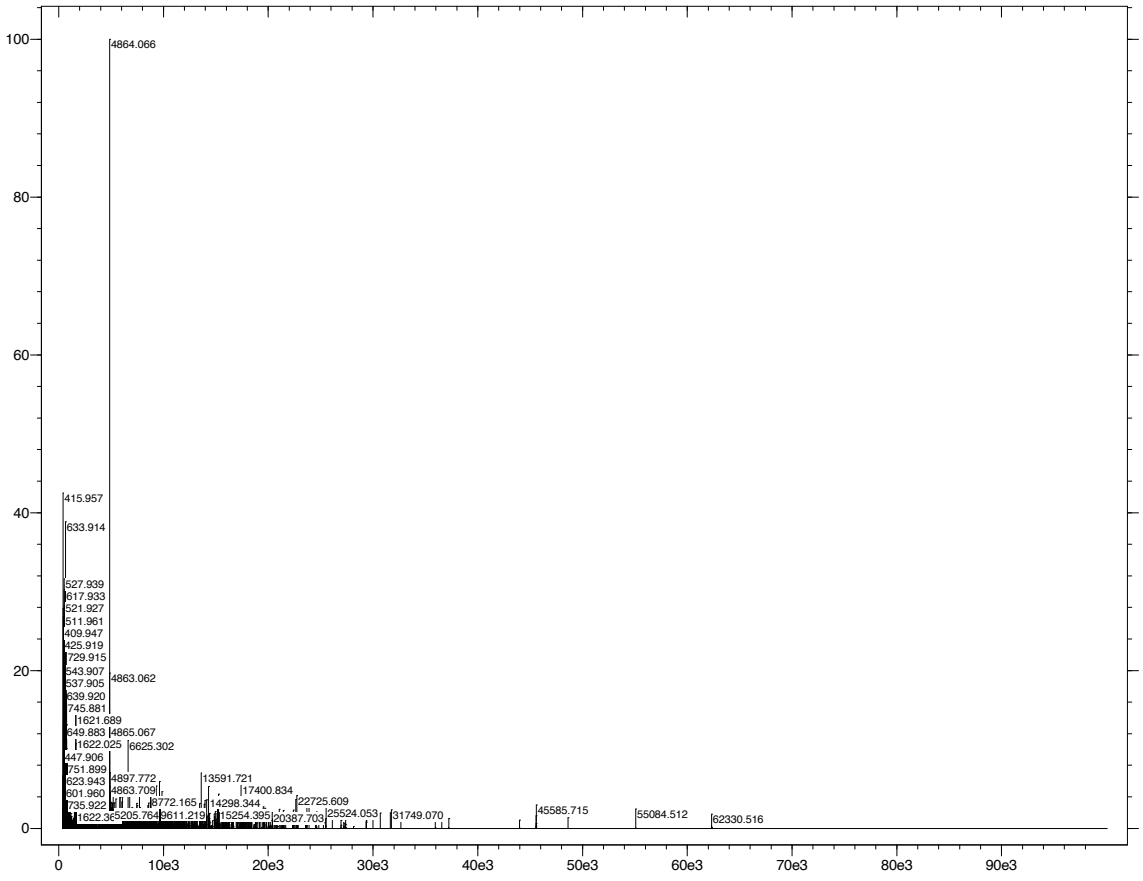
```
======================================================================
Acq. Operator   : SYSTEM                        Seq. Line :   3
Acq. Instrument : LC-FC                          Location :   3
Injection Date  : 19-Apr-21 6:56:08 PM                Inj :   1
                                                Inj Volume : 20.000 µl
Different Inj Volume from Sample Entry!  Actual Inj Volume : 10.000 µl
Method          : C:\Chem32\3\Data\Charlotte\Charlotte 19.04.2021 2021-04-19 17-13-09\FcNA
                  Anth 60oC.M (Sequence Method)
Last changed    : 19-Apr-21 5:07:29 PM by SYSTEM
Sample Info     : CXF 2395

Additional Info : Peak(s) manually integrated
```



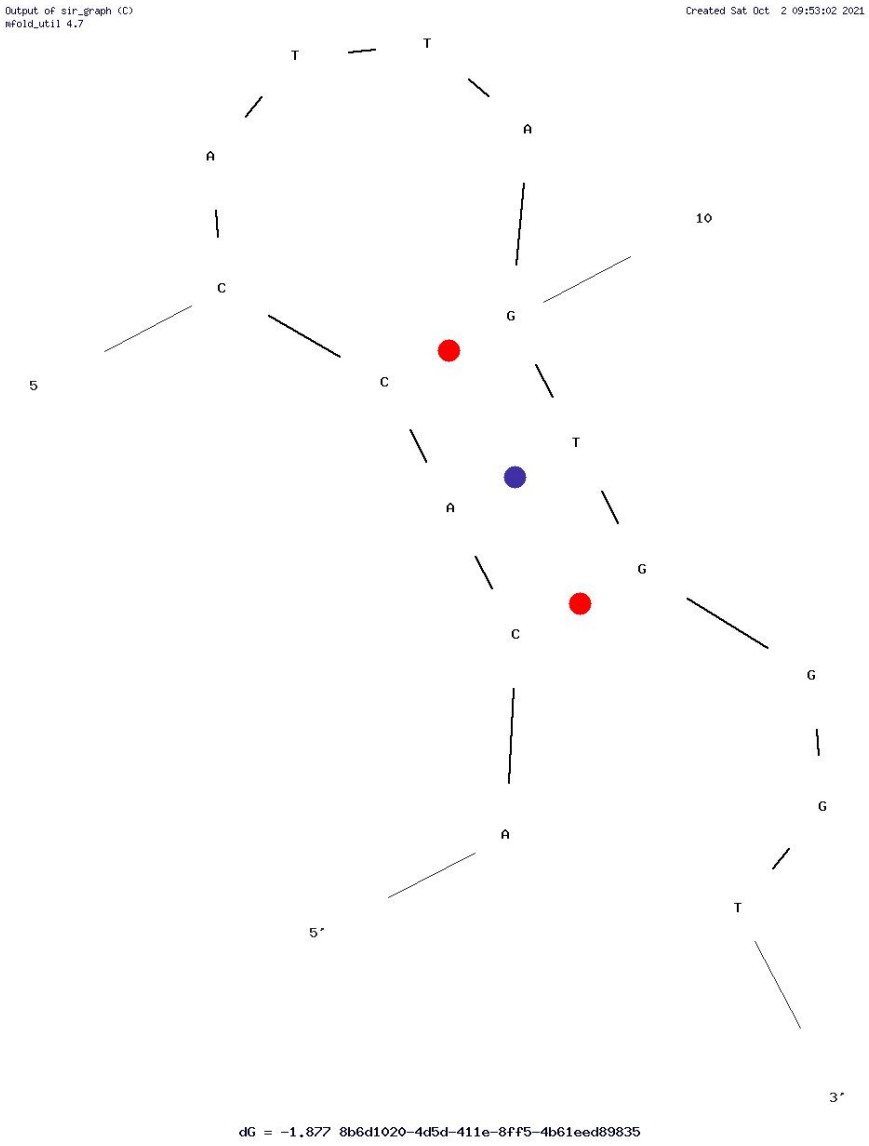
Signal 1: MWD1 D, Sig=360,4 Ref=off

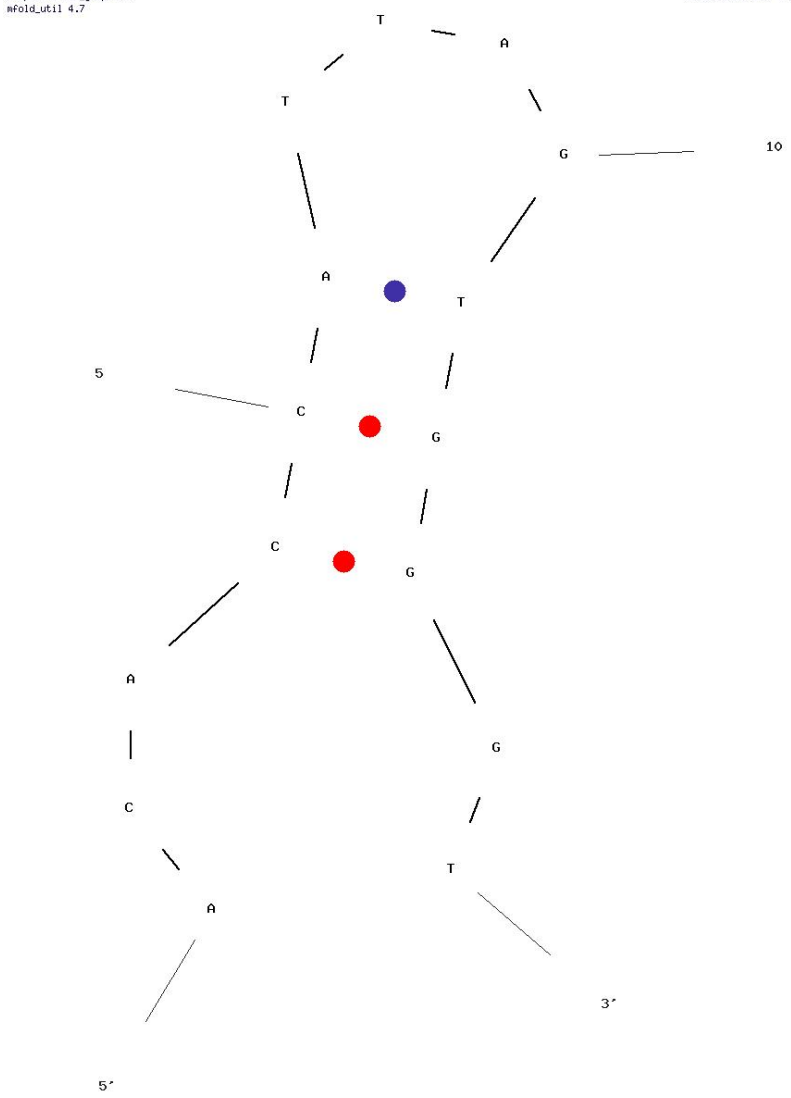
Peak #	RetTime [min]	Type	Width [min]	Area [mAU*s]	Height [mAU]	Area %
1	1.836	BV	0.2919	35.57837	1.71567	3.7227
2	2.401	VV	0.3820	84.06584	2.80240	8.7962
3	2.762	VB	0.1023	49.49886	7.37936	5.1793
4	3.468	BB	0.2433	108.36170	5.76589	11.3384
5	3.940	BV	0.2600	32.75198	1.70558	3.4270
6	44.522	VV	0.4581	357.57492	9.97849	37.4146
7	45.249	VV	0.2742	102.46238	4.89421	10.7211
8	45.669	VV	0.1945	38.36949	2.78928	4.0148
9	45.908	VB	0.1678	21.99133	1.88934	2.3011
10	47.496	BV	0.1856	22.98258	1.79248	2.4048
11	47.829	VB	0.1981	24.62827	1.75115	2.5770
12	48.964	BV	0.2378	26.30856	1.87383	2.7528
13	49.551	VB	0.2917	51.13414	2.38948	5.3504
Totals :				955.70844	46.72716	


100
80
60
40
20
0
4864.066
415.957
633.914
527.939
617.933
521.927
511.961
409.947
425.919
729.915
543.907
537.905
939.920
745.881
1621.689
649.883
4865.067
1622.025
6625.302
447.906
751.899
623.943
4897.772
601.960
4863.709
735.922
8772.165
14298.344
1622.365205.764
9611.219
15254.395
20387.703
13591.721
17400.834
22725.609
25524.053
31749.070
45585.712
55084.512
62330.516
0
10e3
20e3
30e3
40e3
50e3
60e3
70e3
80e3
90e3

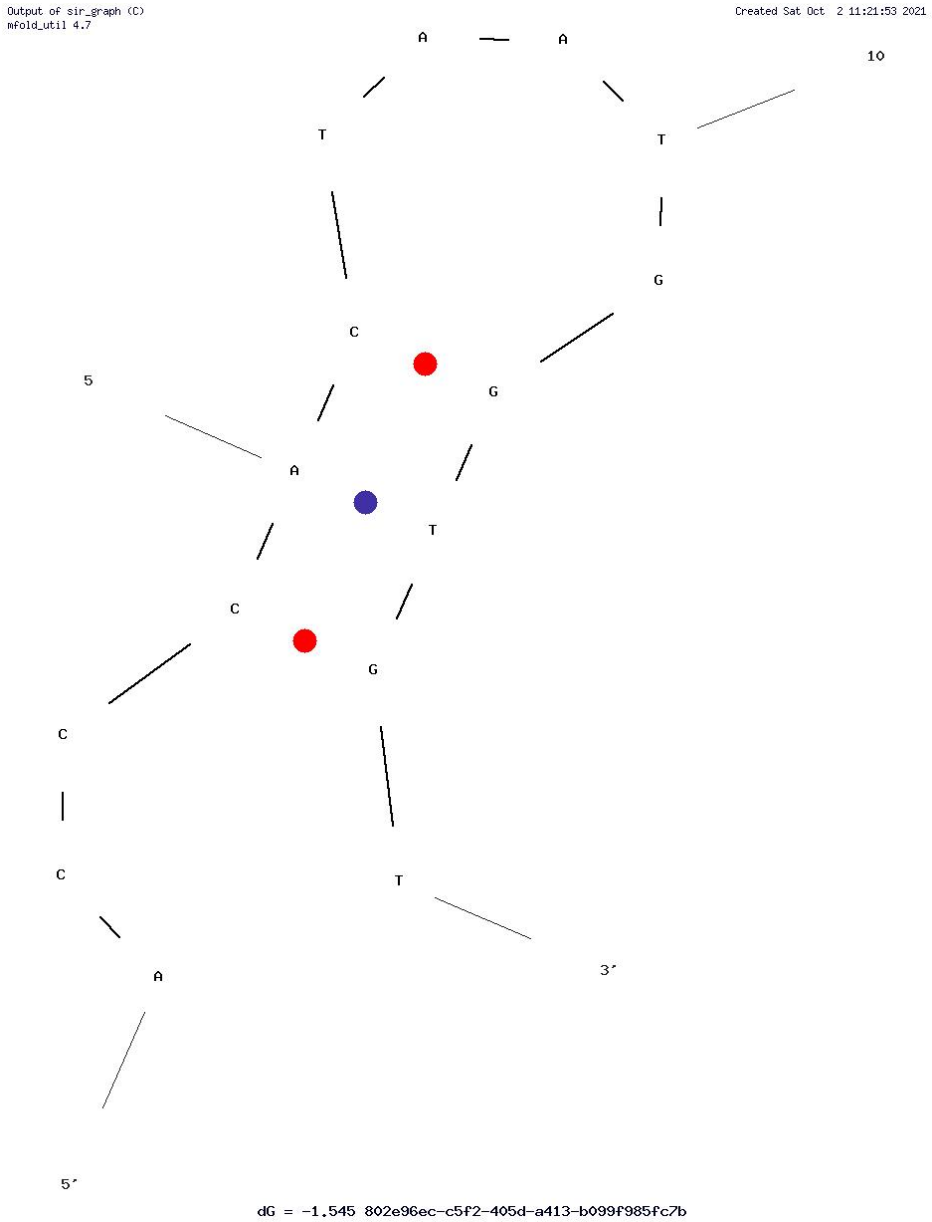
6.3 IDT hairpin secondary structure possibilities[1]

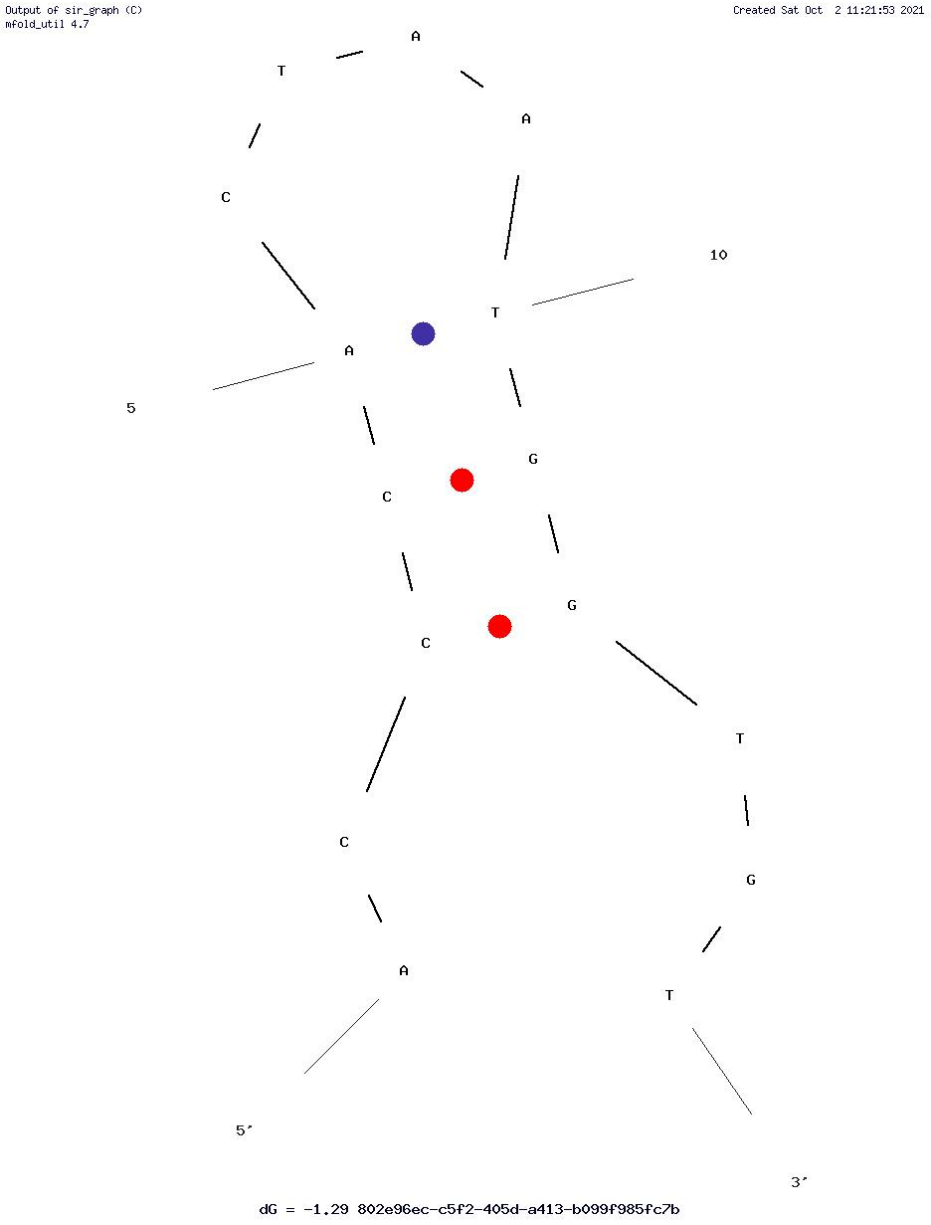
N501Y probe strand possible structures:



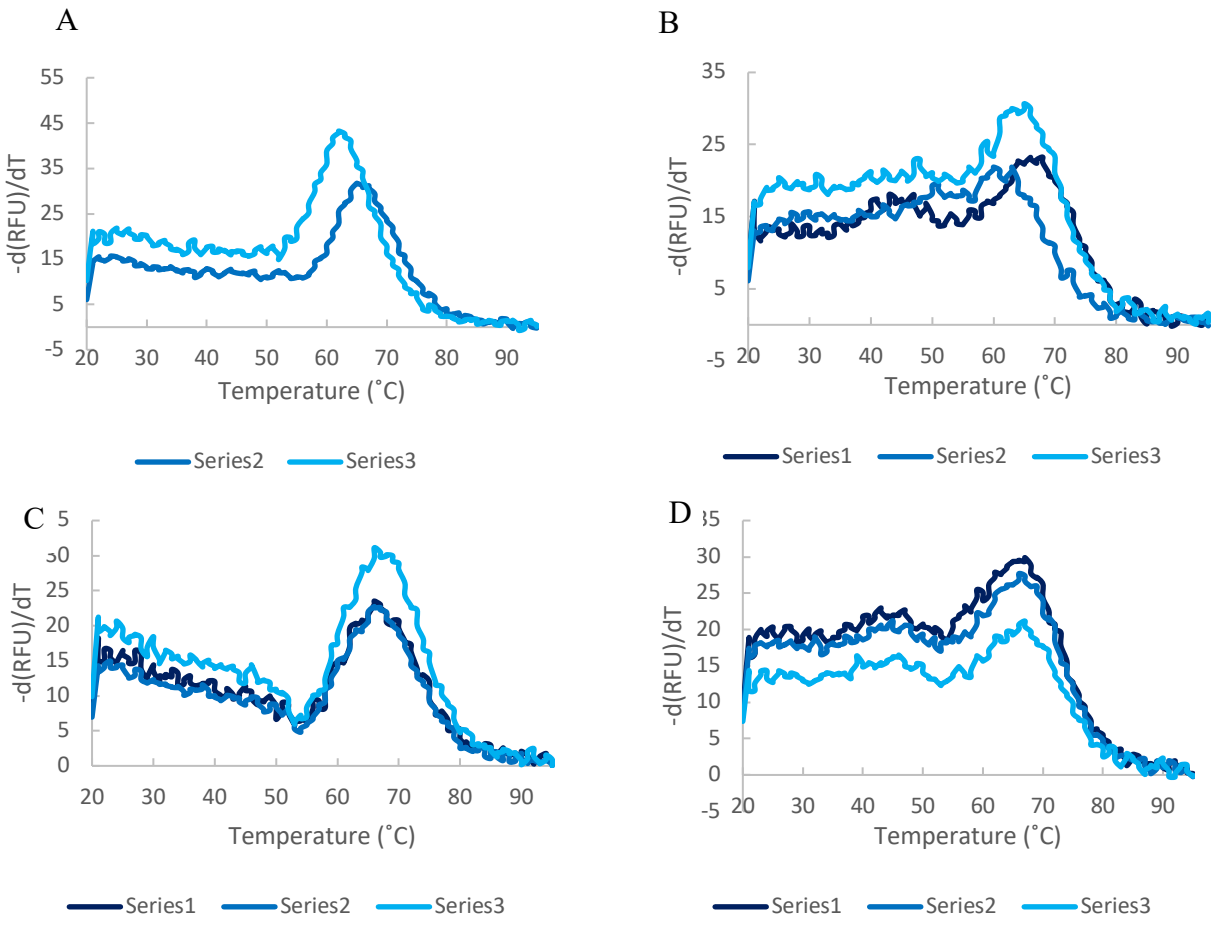

Output of sir_graph (C)
mfold_util 4.7
Created Sat Oct 2 09:53:02 2021
T
A
T
G
10
A
T
5
C
G
C
G
A
G
C
T
A
3'
5'
dG = -1.807 8b6d1020-4d5d-411e-8ff5-4b61eed89835

N501-T-WT possible structures:



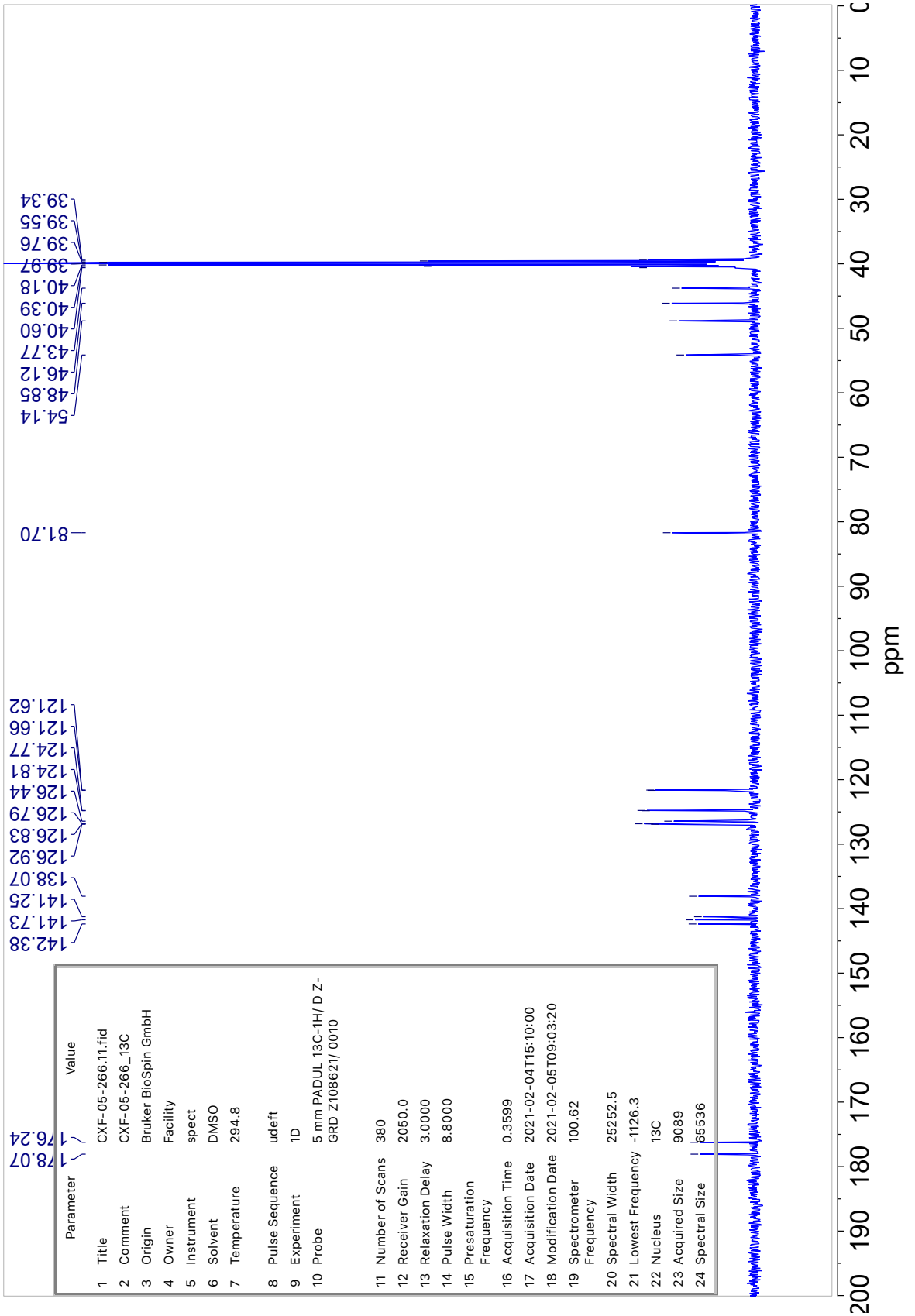

Output of sir_graph (C)
mFold_util 4.7
Created Sat Oct 2 11:21:53 2021
A
T
A
C
10
T
A
5
G
C
G
C
T
C
G
A
T
5′
3′
dG = -1.29 802e96ec-c5f2-405d-a413-b099f985fc7b

6.4 Graphical representation of melting temperatures of E484K probe duplexes with longer target strands

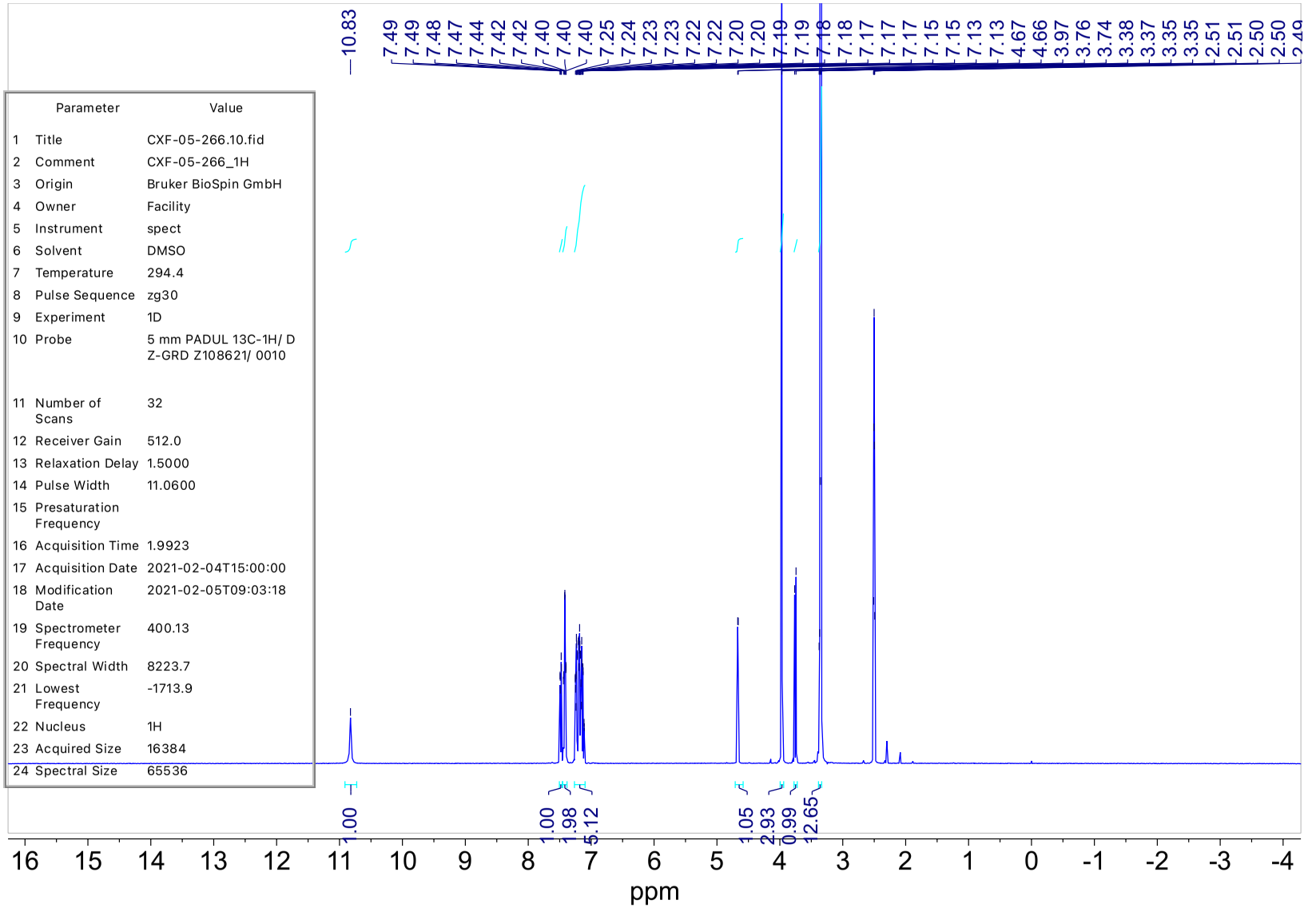


Appendix Figure 2 Thermal profile graphs depicting the temperature required to disrupt the double helix of ***E484K probe*** *against each long target strand. A):* ***E484-T-WT-N501-T-WT****, B)* ***E484K-T-MUT-N501Y-T-MUT*** *C):* ***E484-T-WT-N501Y-T-MUT*** *D)* ***E484K-T-MUT-N501-T-WT*** *(10 µM, duplex buffer)*

7.1 ^{1}H and ^{13}C NMR of 2.89



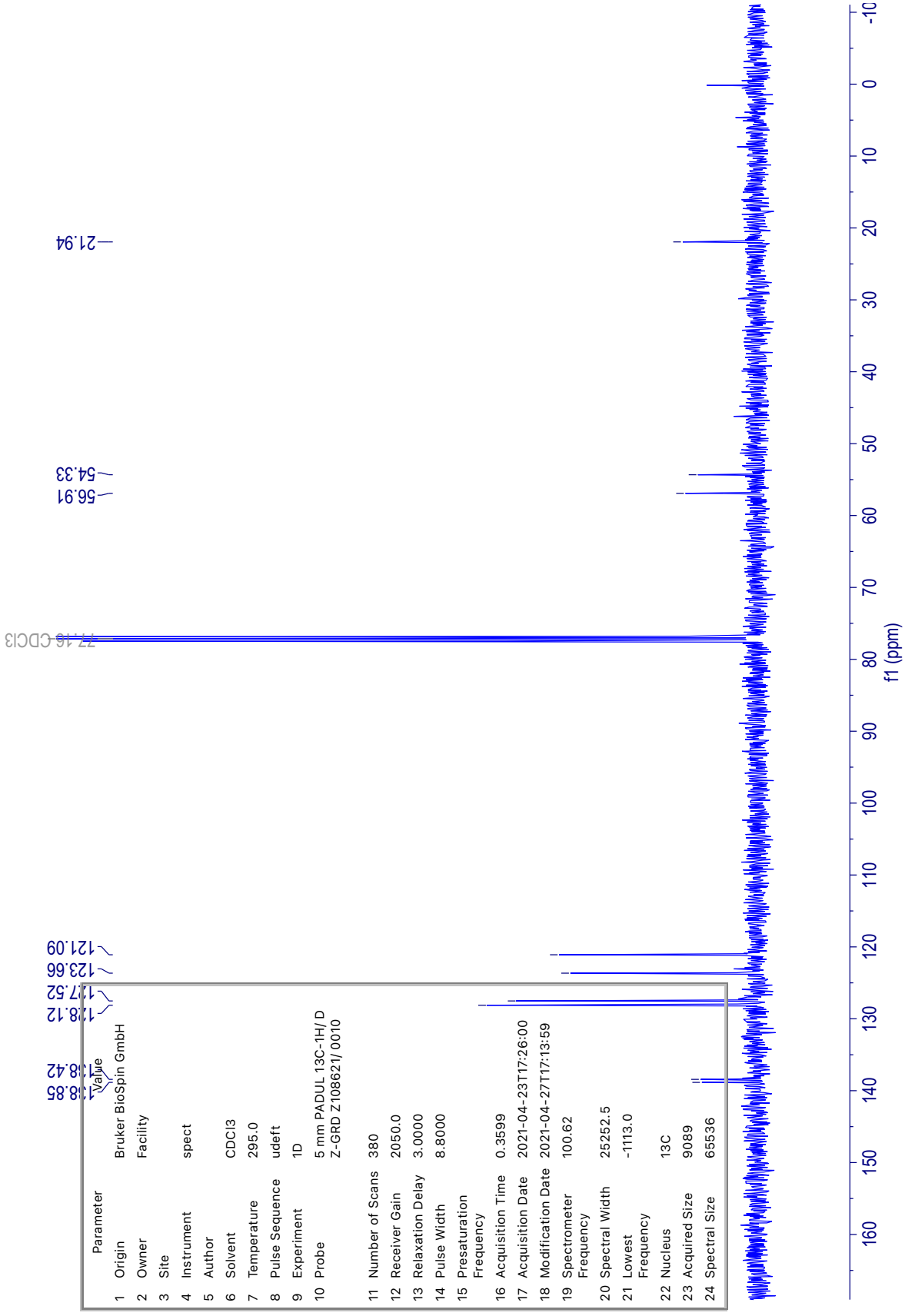
	Parameter	Value
1	Title	CXF-05-266.11.fid
2	Comment	CXF-05-266_13C
3	Origin	Bruker BioSpin GmbH
4	Owner	Facility
5	Instrument	spect
6	Solvent	DMSO
7	Temperature	294.8
8	Pulse Sequence	udeft
9	Experiment	1D
10	Probe	5 mm PADUL 13C-1H/ D Z-GRD Z108621/ 0010
11	Number of Scans	380
12	Receiver Gain	2050.0
13	Relaxation Delay	3.0000
14	Pulse Width	8.8000
15	Presaturation Frequency	
16	Acquisition Time	0.3599
17	Acquisition Date	2021-02-04T15:10:00
18	Modification Date	2021-02-05T09:03:20
19	Spectrometer Frequency	100.62
20	Spectral Width	25252.5
21	Lowest Frequency	-1126.3
22	Nucleus	13C
23	Acquired Size	9089
24	Spectral Size	65536

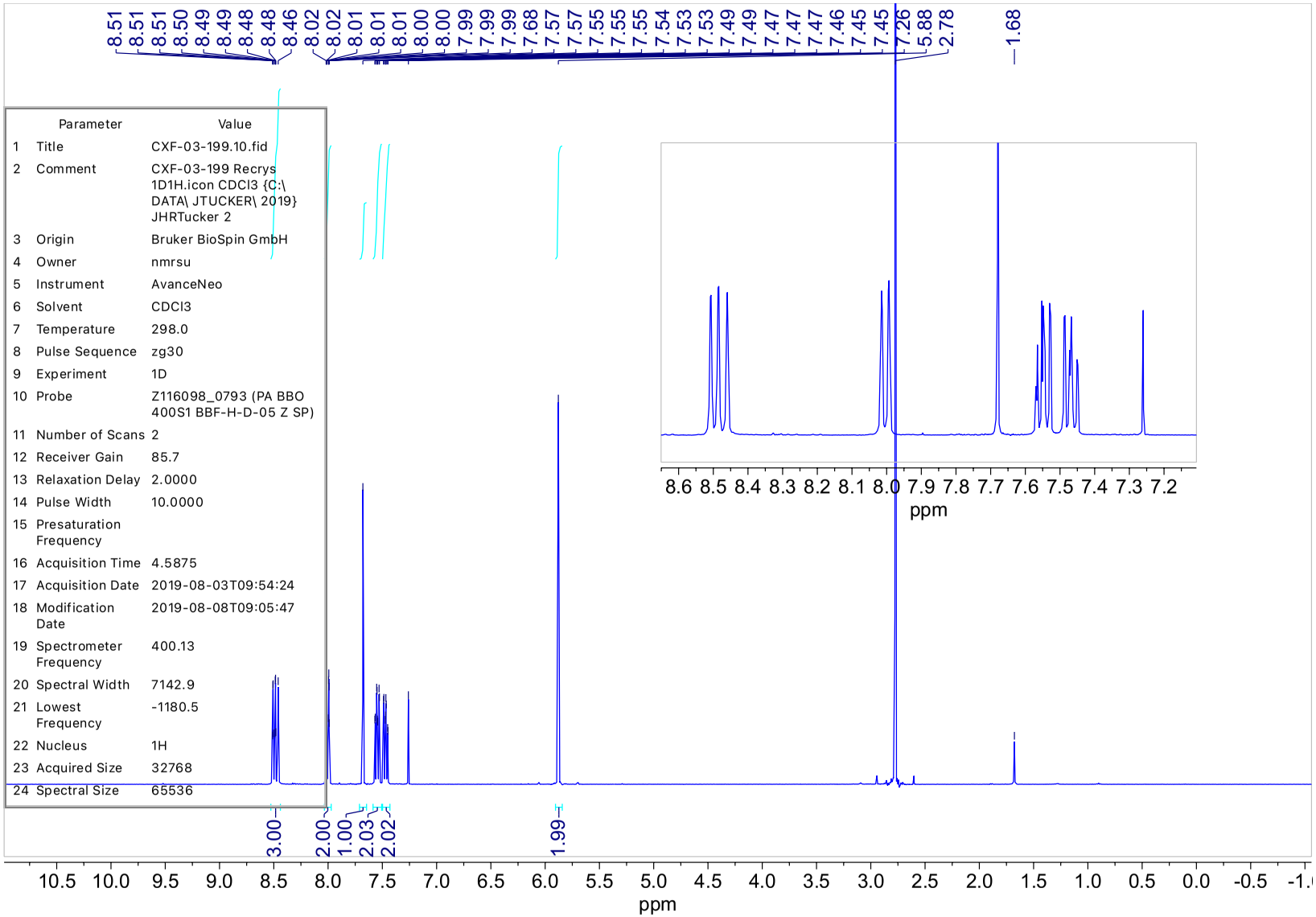


	Parameter	Value
1	Title	CXF-05-266.10.fid
2	Comment	CXF-05-266_1H
3	Origin	Bruker BioSpin GmbH
4	Owner	Facility
5	Instrument	spect
6	Solvent	DMSO
7	Temperature	294.4
8	Pulse Sequence	zg30
9	Experiment	1D
10	Probe	5 mm PADUL 13C-1H/ D Z-GRD Z108621/ 0010
11	Number of Scans	32
12	Receiver Gain	512.0
13	Relaxation Delay	1.5000
14	Pulse Width	11.0600
15	Presaturation Frequency	
16	Acquisition Time	1.9923
17	Acquisition Date	2021-02-04T15:00:00
18	Modification Date	2021-02-05T09:03:18
19	Spectrometer Frequency	400.13
20	Spectral Width	8223.7
21	Lowest Frequency	-1713.9
22	Nucleus	1H
23	Acquired Size	16384
24	Spectral Size	65536

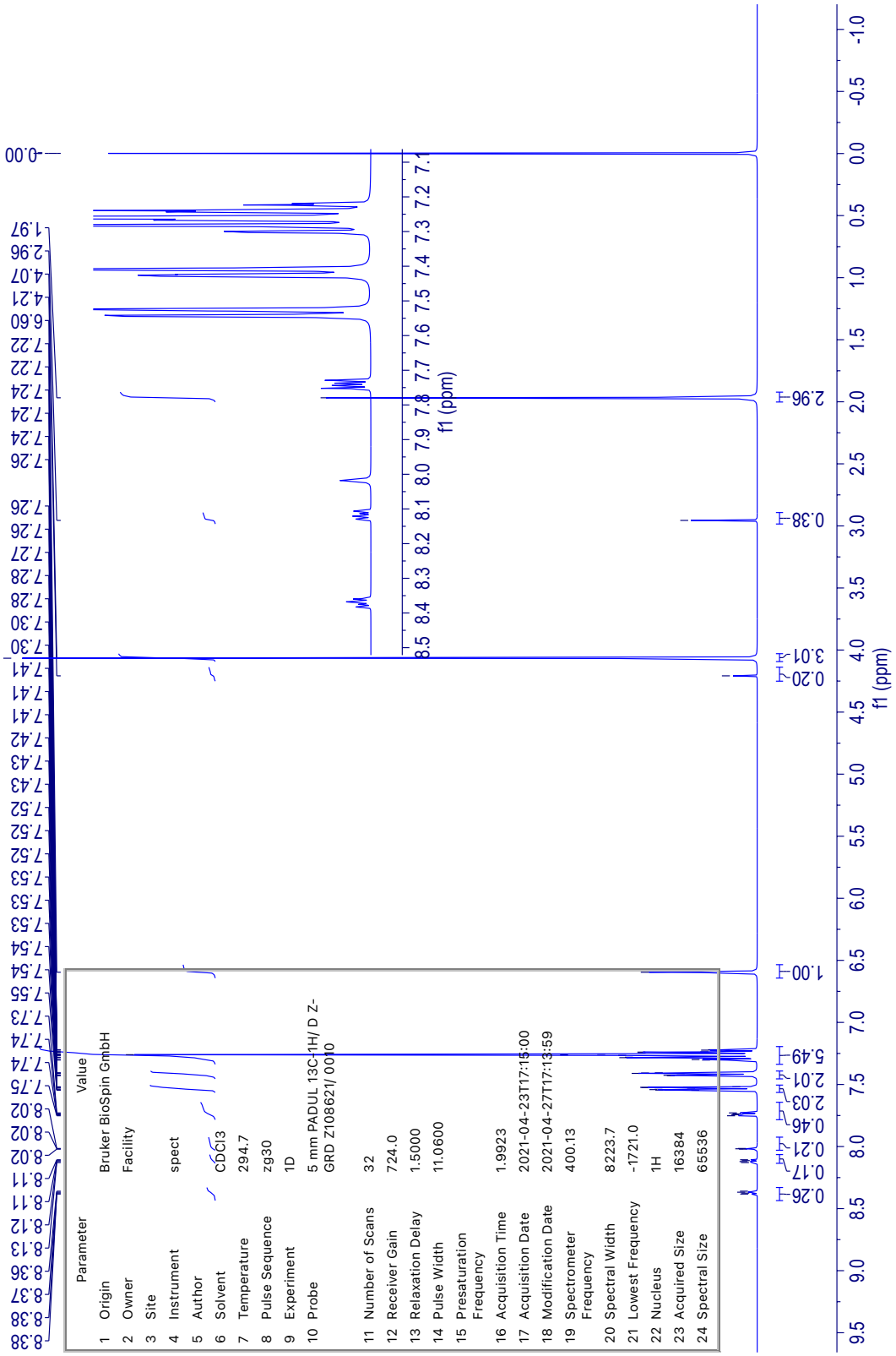
LX

7.2 ^{1}H and ^{13}C NMR of 2.88

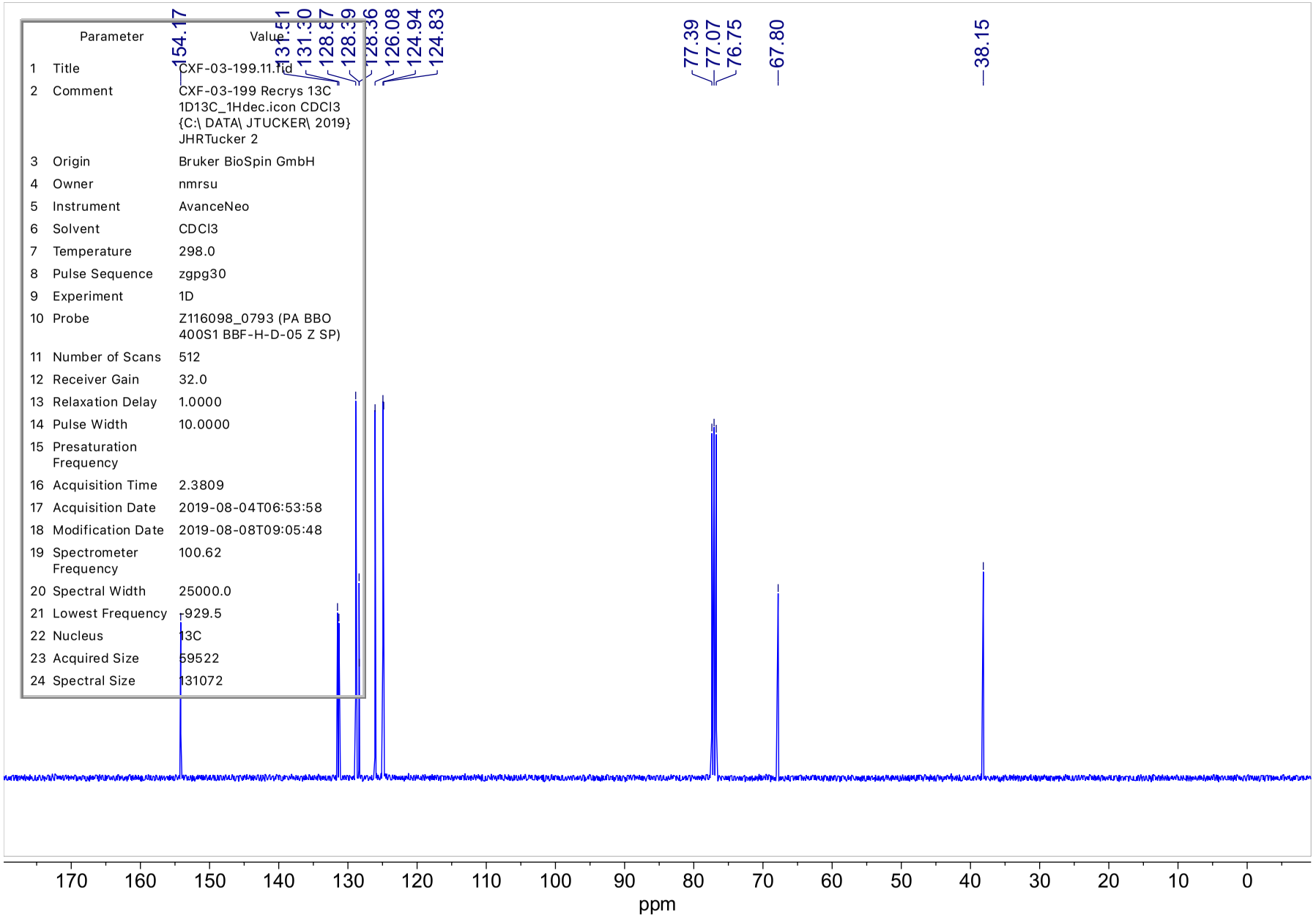



8.51 8.51 8.51 8.50 8.49 8.49 8.48 8.48 8.46 8.02 8.02 8.01 8.01 8.01 8.00 8.00 7.99 7.99 7.99 7.68 7.57 7.57 7.55 7.55 7.55 7.54 7.53 7.53 7.49 7.49 7.47 7.47 7.47 7.46 7.45 7.45 7.26 5.88 2.78 1.68
Parameter Value
1 Title CXF-03-199.10.fid
2 Comment CXF-03-199 Recrys 1D1H.icon CDCl3 {C:\ DATA\ JTUCKER\ 2019} JHRTucker 2
3 Origin Bruker BioSpin GmbH
4 Owner nmrsu
5 Instrument AvanceNeo
6 Solvent CDCl3
7 Temperature 298.0
8 Pulse Sequence zg30
9 Experiment 1D
10 Probe Z116098_0793 (PA BBO 400S1 BBF-H-D-05 Z SP)
11 Number of Scans 2
12 Receiver Gain 85.7
13 Relaxation Delay 2.0000
14 Pulse Width 10.0000
15 Presaturation Frequency
16 Acquisition Time 4.5875
17 Acquisition Date 2019-08-03T09:54:24
18 Modification Date 2019-08-08T09:05:47
19 Spectrometer Frequency 400.13
20 Spectral Width 7142.9
21 Lowest Frequency -1180.5
22 Nucleus 1H
23 Acquired Size 32768
24 Spectral Size 65536
8.6 8.5 8.4 8.3 8.2 8.1 8.0 7.9 7.8 7.7 7.6 7.5 7.4 7.3 7.2
ppm
3.00 2.00 1.00 2.03 2.02 1.99
10.5 10.0 9.5 9.0 8.5 8.0 7.5 7.0 6.5 6.0 5.5 5.0 4.5 4.0 3.5 3.0 2.5 2.0 1.5 1.0 0.5 0.0 -0.5
ppm

7.3 ^{1}H and ^{13}C NMR of 4.22



LXIV



	Parameter	Value
1	Title	CXF-03-199.11.fid
2	Comment	CXF-03-199 Recrys 13C 1D13C_1Hdec.icon CDCl3 {C:\ DATA\ JTUCKER\ 2019} JHRTucker 2
3	Origin	Bruker BioSpin GmbH
4	Owner	nmrsu
5	Instrument	AvanceNeo
6	Solvent	CDCl3
7	Temperature	298.0
8	Pulse Sequence	zgpg30
9	Experiment	1D
10	Probe	Z116098_0793 (PA BBO 400S1 BBF-H-D-05 Z SP)
11	Number of Scans	512
12	Receiver Gain	32.0
13	Relaxation Delay	1.0000
14	Pulse Width	10.0000
15	Presaturation Frequency	
16	Acquisition Time	2.3809
17	Acquisition Date	2019-08-04T06:53:58
18	Modification Date	2019-08-08T09:05:48
19	Spectrometer Frequency	100.62
20	Spectral Width	25000.0
21	Lowest Frequency	-929.5
22	Nucleus	13C
23	Acquired Size	59522
24	Spectral Size	131072

1. OligoAnalyzer. https://eu.idtdna.com/calc/analyzer (accessed 25.09.2021).